NOVEMBER 1, 1990

Analytical CHEMISTRY

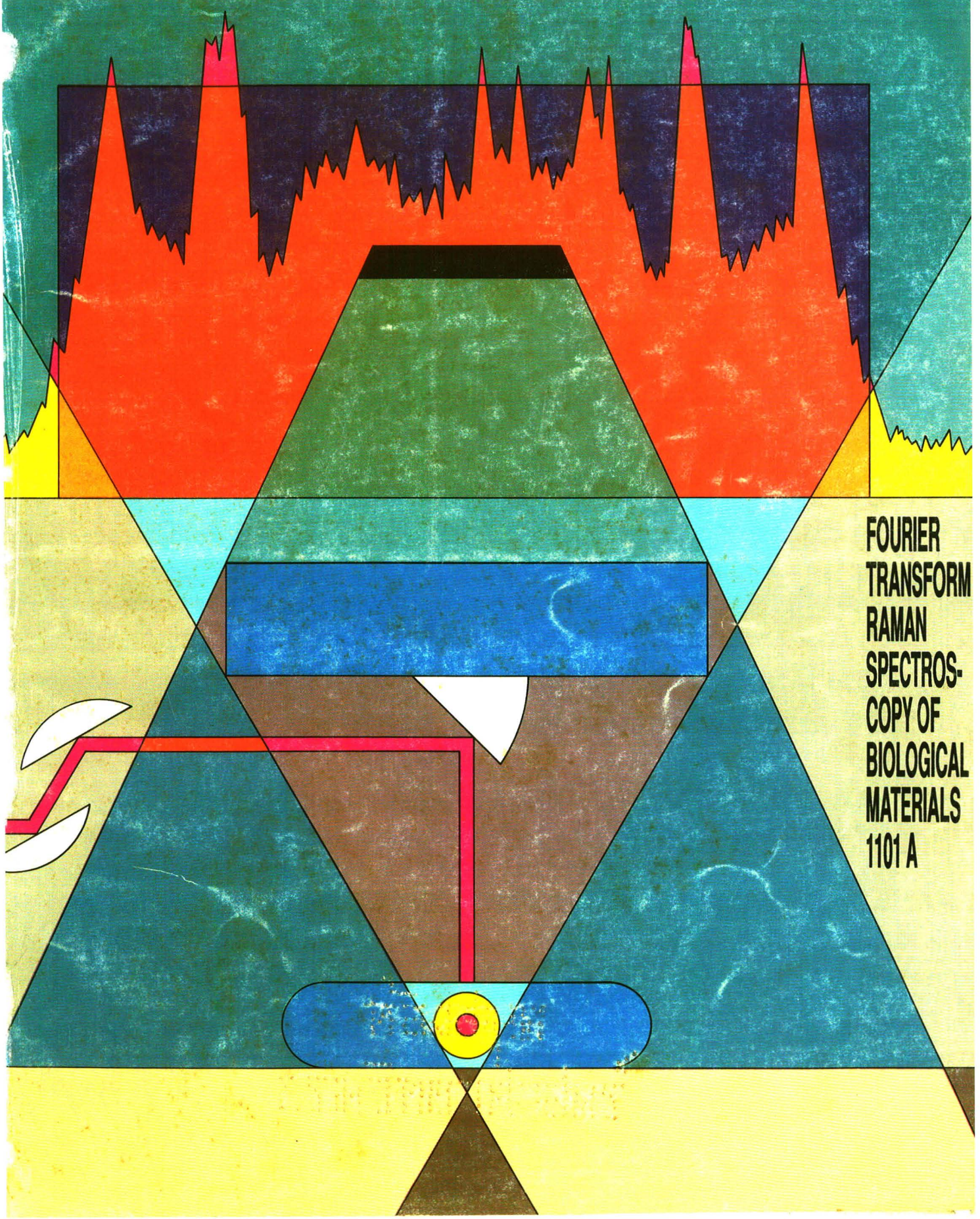

FOURIER TRANSFORM RAMAN SPECTROSCOPY OF BIOLOGICAL MATERIALS 1101 A

You're right. It's new.

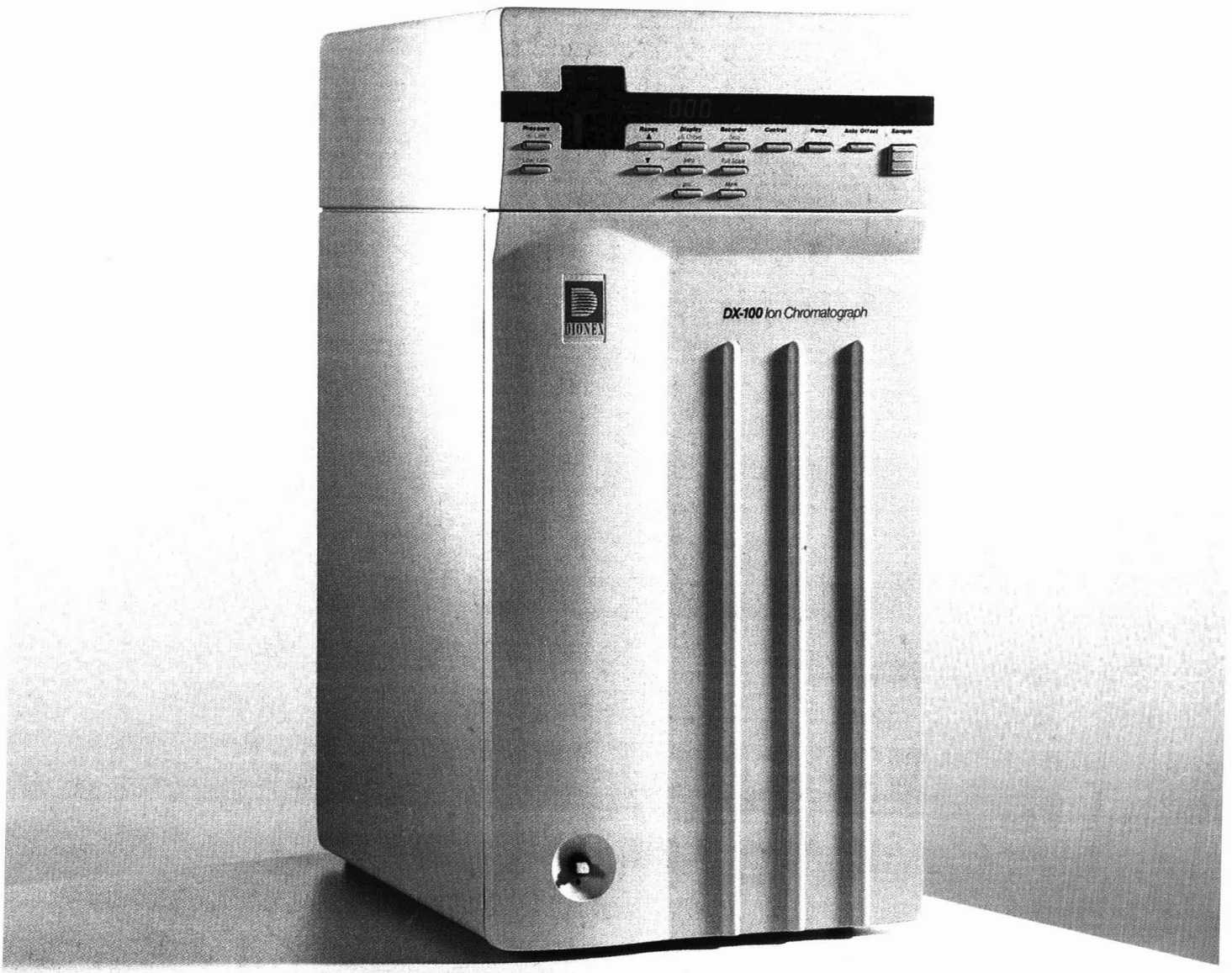

The DX-100 for Ion Analysis.

A new, easy-to-use Ion Chromatograph designed for quick set-up and push button operation— a complete system with a small footprint. You're right, ***it's simple.***

A system which provides excellent resolution and sensitivity by combining a new conductivity detector, high performance Dionex columns, and industry standard MicroMembrane™ Chemical Suppressors. High pressure metal-free pump and components ensure long-term, reliable operation. You're right, ***it performs.***

A system priced far less than you would expect for an Ion Chromatograph of this caliber—backed by the proven chemistry and service support of Dionex, the leader in IC. Right again, ***it's value.***

For more information, contact your local Dionex representative or (in U.S.A.) call **1-800-227-1817, ext. 424** today.

DIONEX
A BETTER SOLUTION

Dionex Corporation, P.O. Box 3603, Sunnyvale, CA 94088-3603, **Canada** Dionex Canada Ltd., (416)855-2551, **England** Dionex (UK) Ltd., (0276)691722, **West Germany** Dionex GmbH, (06126)6036, **France** Dionex S.A., (1)46216666, **Italy** Dionex S.r.l., (06)3792979, **Netherlands** Dionex B.V., (076)714800

Micromembrane is a trademark of Dionex Corporation © 1990 Dionex Corporation

CIRCLE 28 ON READER SERVICE CARD

GILSON 232-401

Transform your HPLC system into a complete auto-analyser.

Increase laboratory throughput, reduce cost per analysis, improve the consistency of your test results... add Gilson's 232-401 Automatic Sample Processor to your chromatograph.

Gilson has designed the first high capacity sample processor with system control.

It handles more samples, faster. It simplifies your chromatogram. It offers precision and repeatibility. Fully programmable, it can be associated with other analytical instruments, computers, and various sample preparation satellites.

The 232-401 is all you need to automate routine handling of large series of LC analytes, from sampling and pretreatment procedures, up to the end report.

The 232-401 is described in our brochure, which explains how to implement such modern techniques as sample clean-up and sample concentration, column backflushing, fraction collection in sealed vials, and reinjection for tests of purity or bioactivity.

GILSON

To receive your copy, please contact your nearest representative, or write to :
Gilson, BP 45 - 95400 Villiers-le-Bel, France - Tel. : (1) 34 29 50 00 - Tlx : 606 682
Fax : (1) 39 94 51 83

CIRCLE 51 ON READER SERVICE CARD

Because each step is critical for peak performance in chromatography.

J.T.Baker High Purity Solvents

For HPLC and GC analyses that place you on the leading edge of separations technology, J.T.Baker high purity solvents assure you accurate, reproducible results.

J.T.Baker manufactures high purity solvents by methods that push purification technology to the limits.

When there's no time to retrace your steps, select the high performance solvents that are manufactured and characterized for your specific application: 'BAKER ANALYZED'® HPLC grade for HPLC mobile phases; 'BAKER RESI-ANALYZED'® and 'BAKER CAPILLARY-ANALYZED'* grades for demanding trace analyte extractions.

Specify J.T.Baker high purity solvents for your next requirement.

World leading rock climber Stefan Glowacz of West Germany, during his free ascent of the 5.12C rated (Extreme Difficulty) world class "Chain Reaction" at Smith Rocks, Oregon.

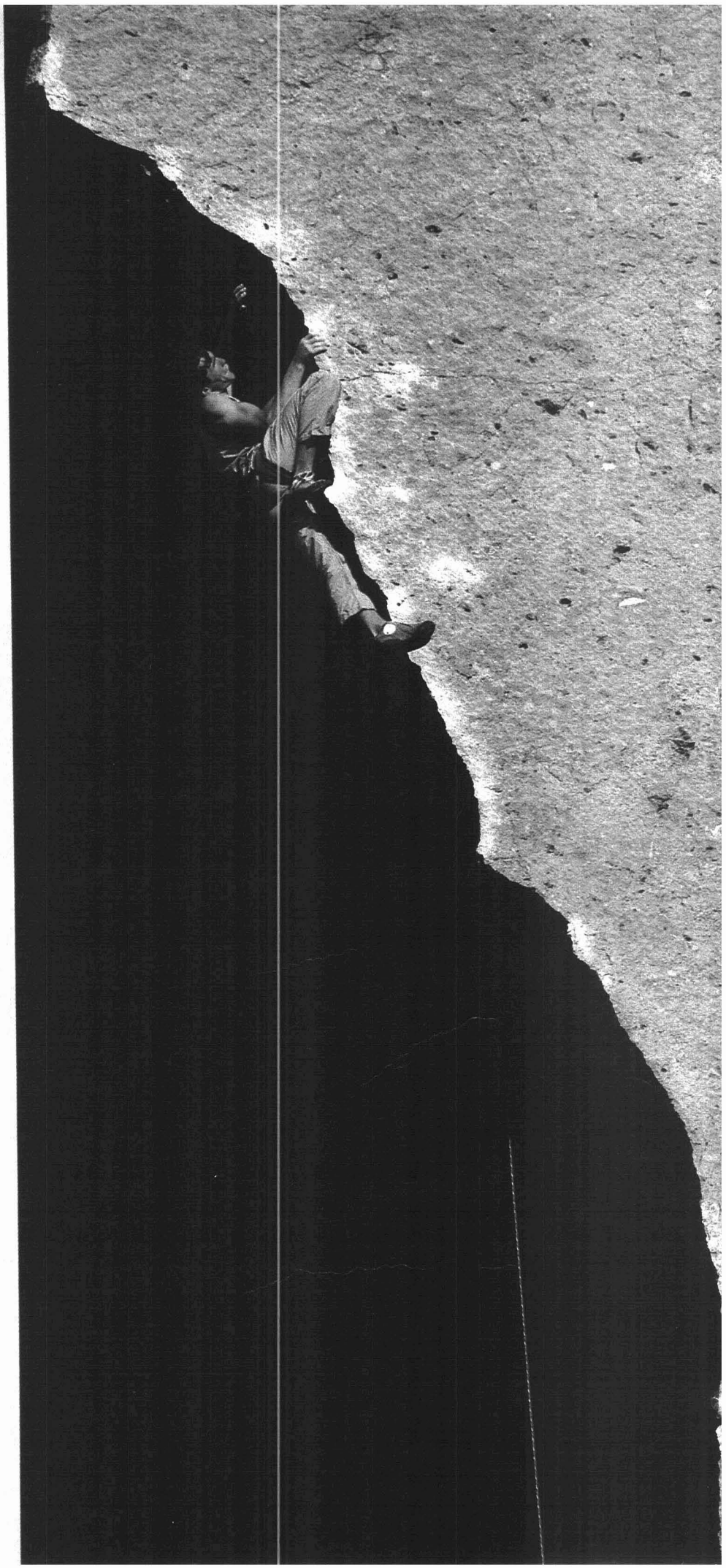

J.T.Baker®

J.T.Baker Inc. ■ 222 Red School Lane
Phillipsburg, NJ 08865
1-800-JTBAKER; in NJ 201-859-2151
Telex: 299514 BAKR UR ■ FAX: 201-859-9318

CIRCLE 18 ON READER SERVICE CARD.

'BAKER ANALYZED'®, 'BAKER RESI-ANALYZED'® and 'BAKER CAPILLARY-ANALYZED'* are trademarks of J.T.Baker Inc.

NOVEMBER 1, 1990
VOLUME 62
NUMBER 21

The Audit Bureau

ANCHAM
62(21) 1081A–1132A/2257–2416 (1990)
ISSN 0003-2700

Registered in U.S. Patent and Trademark Office; Copyright 1990 by the American Chemical Society

ANALYTICAL CHEMISTRY (ISSN 0003-2700) is published semimonthly by the American Chemical Society at 1155 16th St., N.W., Washington, DC 20036. Editorial offices are located at the same ACS address (202-872-4570; FAX 202-872-4574; TDD 202-872-8733). Second-class postage paid at Washington, DC, and additional mailing offices. Postmaster: Send address changes to ANALYTICAL CHEMISTRY Member & Subscriber Services, P.O. Box 3337, Columbus, OH 43210.

Claims for missing numbers will not be allowed if loss was due to failure of notice of change of address to be received in the time specified; if claim is dated (a) North America: more than 90 days beyond issue date, (b) all other foreign: more than one year beyond issue date, or if the reason given is "missing from files."

Copyright Permission: An individual may make a single reprographic copy of an article in this publication for personal use. Reprographic copying beyond that permitted by Section 107 or 108 of the U.S. Copyright Law is allowed, provided that the appropriate per-copy fee is paid through the Copyright Clearance Center, Inc., 27 Congress St., Salem, MA 01970. For reprint permission, write Copyright Administrator, Publications Division, ACS, 1155 16th St., N.W., Washington, DC 20036.

Registered names and trademarks, etc., used in this publication, even without specific indication thereof, are not to be considered unprotected by law.

Advertising Management: Centcom, Ltd., 500 Post Rd. East, Westport, CT 06880 (203-226-7131)

1990 subscription rates include air delivery outside the U.S., Canada, and Mexico

	1 yr	2 yr
Members		
Domestic	$ 29	$ 49
Canada and Mexico	64	119
Europe	96	183
All Other Countries	118	227
Nonmembers		
Domestic	59	100
Canada and Mexico	94	170
Europe	186	336
All Other Countries	208	380

Three-year and other rates contact: Member & Subscriber Services, ACS, P.O. Box 3337, Columbus, OH 43210 (614-447-3776 or 800-333-9511).

Subscription orders by phone may be charged to VISA, MasterCard, or American Express. Call toll free 800-333-9511 in the continental United States; in the Washington, DC, metropolitan area and outside the continental United States, call 202-872-8065. Mail orders for new and renewal subscriptions should be sent with payment to American Chemical Society, Department L-0011, Columbus, OH 43268-0011.

Subscription service inquiries and changes of address (Include both old and new addresses with ZIP code and *recent mailing label*) should be directed to the ACS Columbus address noted above. Please allow six weeks for changes to become effective.

ACS membership information: Lorraine Bowlin (202-872-4567)

Single issues, current year, $8.00 except review issue, $14.00, and LabGuide, $49.00; **back issues and volumes and microform editions** available by single volume or back issue collection. For information or to order, call the number listed for subscription orders by phone; or write the Microform & Back Issues Office at the Washington address.

Nonmembers rates in Japan: Rates above do not apply to nonmember subscribers in Japan, who must enter subscription orders with Maruzen Company Ltd., 3–10 Nihonbashi 2-chome, Chuo-ku, Tokyo 103, Japan. Tel: (03) 272-7211.

Analytical® CHEMISTRY

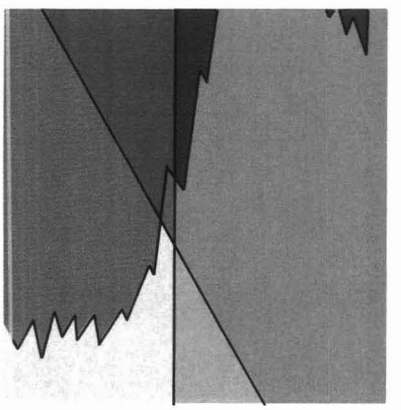

REPORT **1101 A**

On the cover. **FT-Raman spectroscopy of biological materials.** The flexibility and inherent advantages of near-IR FT-Raman spectroscopy make it the vibrational spectroscopic method of choice for most biomolecular preparations. Ira W. Levin and E. Neil Lewis of the National Institutes of Health describe the principles and instrumentation involved in the application of FT-Raman spectroscopy to membrane biophysical studies

ANALYTICAL APPROACH **1123 A**

Archaeological textiles and dyes. Archaeological chemists have recently begun to examine organic materials in an effort to answer questions about historic and prehistoric cultures. J. E. Katon and coworkers of Miami University and Kathryn A. Jakes of The Ohio State University discuss how molecular microspectroscopy can be used to provide clues about prehistoric Peruvian dyeing technology

BRIEFS **1088 A**

EDITORIAL **1097 A**

Euroanalysis VII. On August 26–31, more than 1000 scientists from around the world attended Euroanalysis VII in Vienna, Austria. Organized by the Working Party on Analytical Chemistry of the Federation of European Chemical Societies, this event involved the presentation of more than 750 papers in all areas of analytical chemistry

NEWS **1099 A**

Endowment for **Kolthoff Awards.** ▶ College grants. ▶ Methane surprise. ▶ Nuclear waste agreement

FOCUS **1113 A**

Perspectives on the future of analytical mass spectrometry. This year's Summer Symposium on Analytical Chemistry featured talks on the newest developments and future directions of analytical mass spectrometry. Cecilia Basic, Jody Freeman, and Richard Yost of the University of Florida report on the highlights of the meeting, hosted by Oak Ridge National Laboratory

NEW PRODUCTS & MANUFACTURERS' LITERATURE **1120 A**

AUTHOR INDEX **2257**

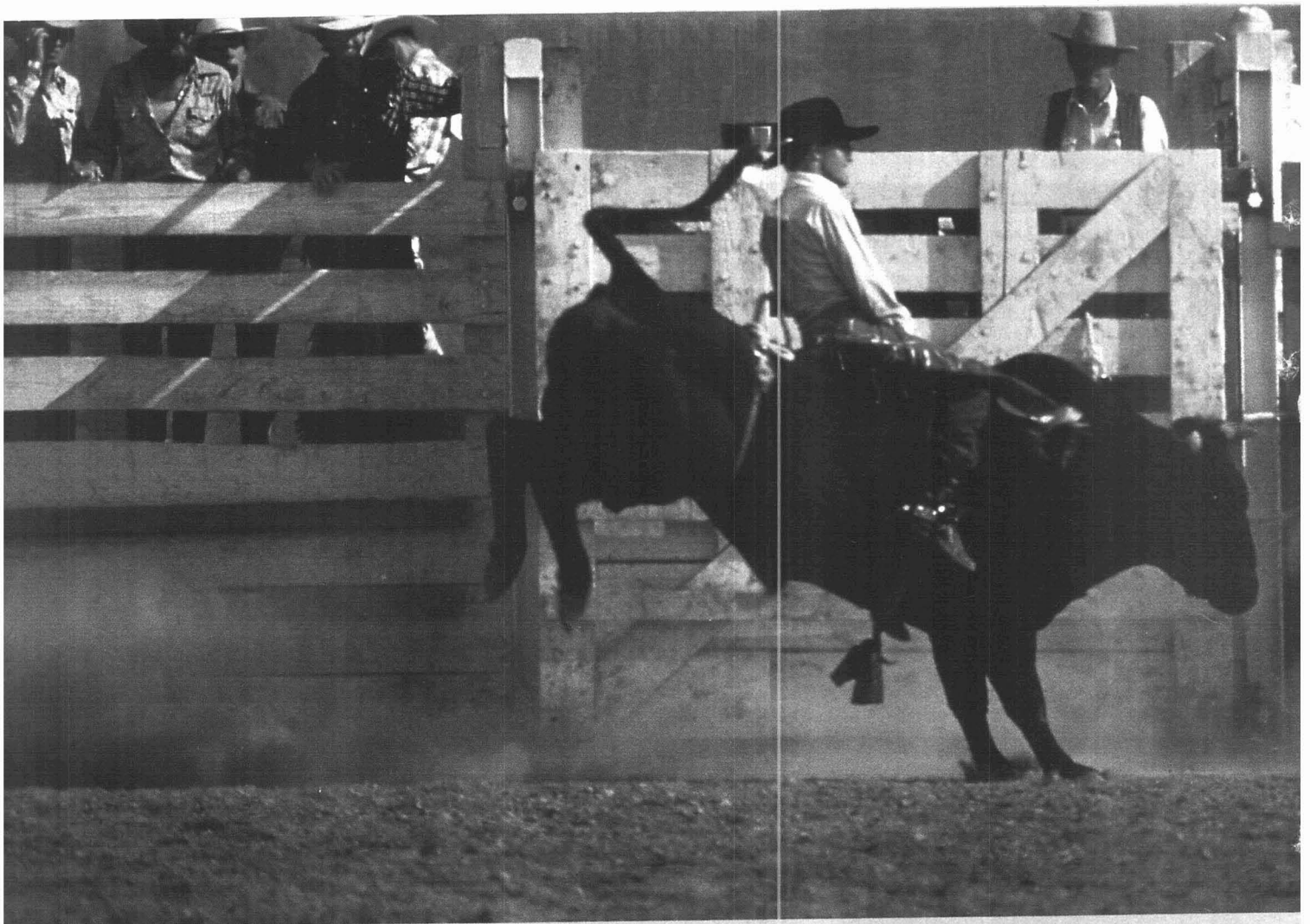

sartorius

0 100 %

1%

95.000 g

R 2

T

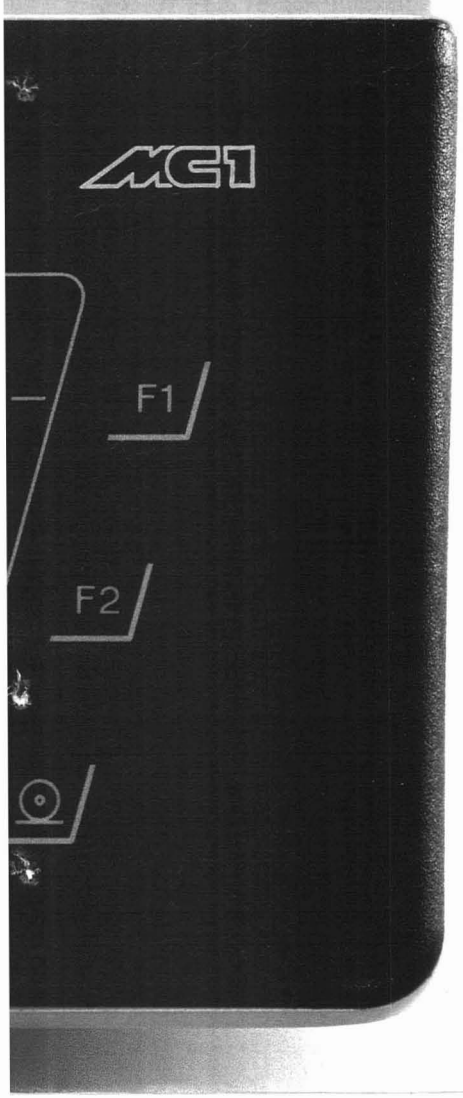

With 1 mg readability, this is how your balance perceives the shock of loading a sample

Perception is a matter of perspective. For an ordinary balance with 1 mg readability, a sample placed on the pan is as challenging as any rodeo bull. Just watch the way the digits flicker. Or, rather, try waiting for the digits to stop flickering.

Even once the reading has stabilized, a casual draft is a typhoon. Fingers drumming a tabletop are the pounding of hooves. And digits are sent fluttering wildly again. Scientists call these common laboratory occurrences "ambient conditions." But for ordinary precision balances, these common events present an uncommon challenge. And those fingers drumming the table usually belong to disgruntled researchers, waiting for their balance to stabilize.

Sartorius balances with MC 1 technology are the only balances available with a built-in microcomputer—a functioning intelligence *beyond* microprocessors—programmed to filter out noise, vibrations, and other disturbances and give you the precise weight of your sample. Instantly. And its performance does not suffer as the sample weight increases. Regardless of sample size, the display stabilizes in *less than half the time* of what might be described as "competition."

With MC 1 technology, your balance will keep its balance, and your results will be true to your world.

For more information on this breakthrough in balance technology, call, write, or circle the number below. Sartorius Instruments, 1430 Waukegan Rd., McGaw Park, IL 60085. Phone: 800•544•3409 FAX: 708•689•2038.

sartorius

Sure. Smart. Sartorius.

CIRCLE 127 ON READER SERVICE CARD

BRIEFS

Perspective: Analytical Biotechnology

Applications of Dioxetane Chemiluminescent Probes to Molecular Biology 2258

DNA probes and synthetic oligonucleotides are key tools in modern molecular biology research and are becoming increasingly important in commercial applications. Details of one of the most promising methods, based on enzymatically triggered chemiluminescence, are presented.

Stephan Beck* and Hubert Köster, MilliGen/Biosearch, 186 Middlesex Turnpike, Burlington, MA 01803

Articles

Dissociation of Tetrahexylammonium Picrate Ion Pairs Adsorbed at the Chloroform–Water Interface 2270

The ion pair tetrahexylammonium picrate and its cation tetrahexylammonium ion are adsorbed, but its anion picrate is not. The ion pair dissociation constant at the interface is $(1.2 \pm 0.1) \times 10^{-5}$ mol/L.

Lawrence Amankwa and Frederick F. Cantwell*, Department of Chemistry, University of Alberta, Edmonton, Alberta, Canada T6G 2G2

Determination of Carbon-Centered Radicals in Aqueous Solution by Liquid Chromatography with Fluorescence Detection 2275

Radicals are trapped by an amino nitroxide, and the alkoxyamines formed are derivatized with fluorescamine. The precision is ~5% at 1–10 nM, and the detection limit is in the sub-nM range.

David J. Kieber and Neil V. Blough*, Chemistry Department, Woods Hole Oceanographic Institution, Woods Hole, MA 02543

Selective Sorption of Alkali-Metal Cations by Carboxylic Acid Resins Containing Acyclic or Cyclic Polyether Units 2283

Good sorption selectivity for Na^+ over other alkali cations is obtained by using a 16-crown-5 carboxylic acid resin.

Takashi Hayashita, Mi-Ja Goo, Jong Chan Lee, Jong Seung Kim, Jan Krzykawski, and Richard A. Bartsch*, Department of Chemistry and Biochemistry, Texas Tech University, Lubbock, TX 79409-1061

Influence of Alkyl Chain Length on the Stability of *n*-Alkyl-Modified Reversed Phases. 1. Chromatographic and Physical Analysis 2288

Ligand alkyl chain length affects the stability of reversed phases. Short ligand-modified phases change substantially under aggressive eluent conditions. Longer ligand-modified phases are preferable for a longer column lifetime.

Martin J. J. Hetem*, Jan W. de Haan, Henk A. Claessens, Leo J. M. van de Ven, and Carel A. Cramers, Laboratory of Instrumental Analysis, Eindhoven University of Technology, P.O. Box 513, 5600 MB Eindhoven, The Netherlands and **Joachim N. Kinkel,** E. Merck, Frankfurterstrasse 250, D-6100 Darmstadt 1, West Germany

Influence of Alkyl Chain Length on the Stability of *n*-Alkyl-Modified Reversed Phases. 2. Model Dissolution Study 2296

Longer *n*-alkyl ligands gradually show better substrate-shielding properties. Above a certain critical ligand length, shielding by longer ligands inhibits the dissociation rate by affecting the hydrolysis and dissolution processes.

Martin J. J. Hetem*, Jan W. de Haan, Henk A. Claessens, Leo J. M. van de Ven, and Carel A. Cramers, Laboratory of Instrumental Analysis, Eindhoven University of Technology, P.O. Box 513, 5600 MB Eindhoven, The Netherlands, **Peter W. J. G. Wijnen,** Laboratory of Inorganic Chemistry, Eindhoven University of Technology, P.O. Box 513, 5600 MB Eindhoven, The Netherlands, and **Joachim N. Kinkel,** E. Merck, Frankfurterstrasse 250, D-6100 Darmstadt 1, West Germany

Prediction of Retention Times in Serially Linked Open-Tubular Gas Chromatographic Columns and Optimization of Column Lengths 2300

Serial column theory provides a way to predict sample component retention times with linked open-tubular columns. Window analysis permits the calculation of relative and total column lengths needed for baseline separation of all sample components.

Jeffrey R. Jones and J. Howard Purnell*, Department of Chemistry, University College of Swansea, Singleton Park, Swansea SA2 8PP, Wales, U.K.

Hydrodynamic Relaxation and Sample Concentration in Field-Flow Fractionation Using Permeable Wall Elements 2306

The use of frit elements, embedded in FFF channel walls, to achieve hydrodynamic relaxation and thus stopless flow injection, is proposed and evaluated.

J. Calvin Giddings, Field-Flow Fractionation Research Center, Department of Chemistry, University of Utah, Salt Lake City, UT 84112

*Corresponding author

■ Supplementary material available

Did you check everything?

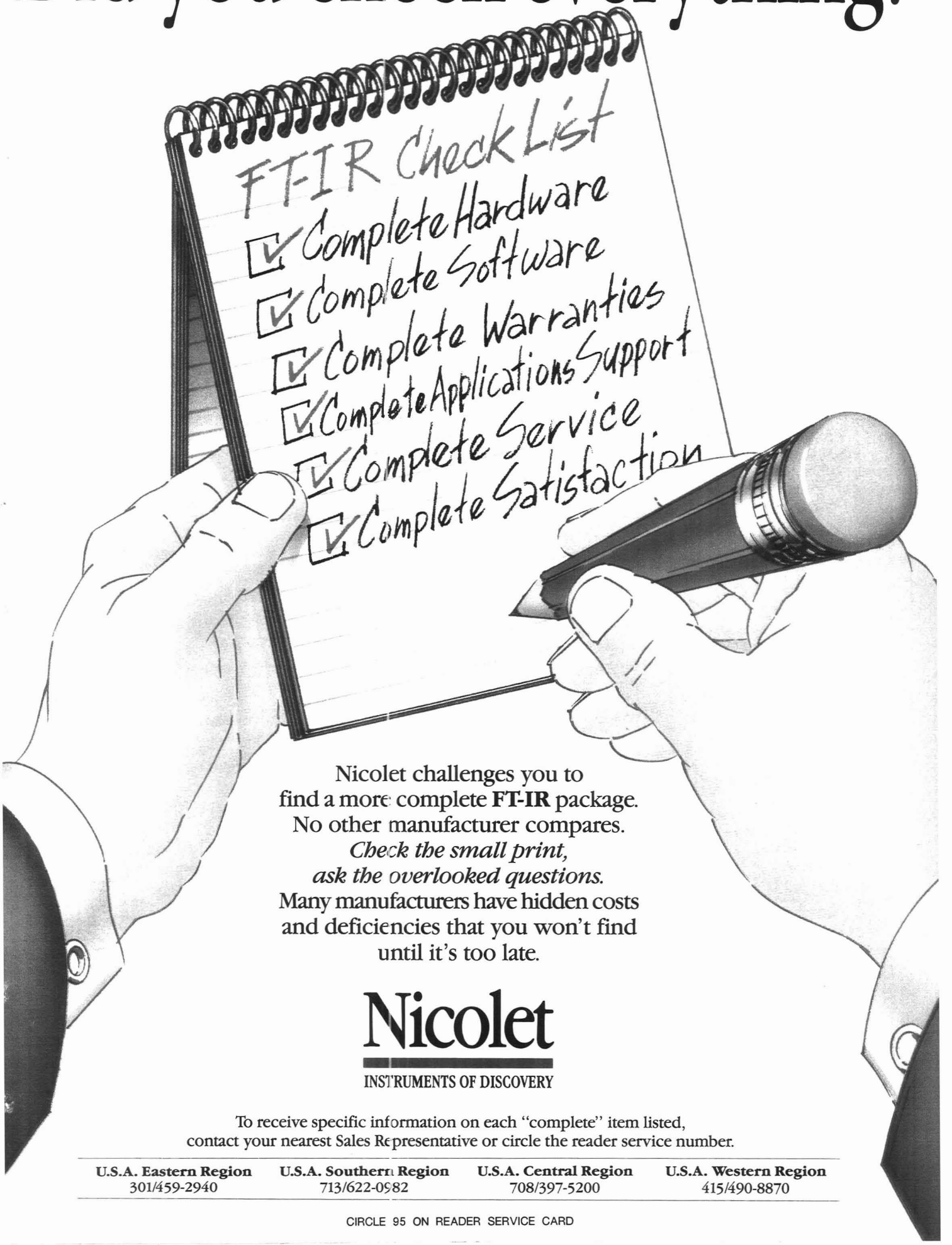

Nicolet challenges you to find a more complete **FT-IR** package. No other manufacturer compares.

Check the small print, ask the overlooked questions.

Many manufacturers have hidden costs and deficiencies that you won't find until it's too late.

Nicolet

INSTRUMENTS OF DISCOVERY

To receive specific information on each "complete" item listed, contact your nearest Sales Representative or circle the reader service number.

U.S.A. Eastern Region	U.S.A. Southern Region	U.S.A. Central Region	U.S.A. Western Region
301/459-2940	713/622-0982	708/397-5200	415/490-8870

CIRCLE 95 ON READER SERVICE CARD

Simultaneous Determination of Bruneaur–Emmett–Teller and Inverse Gas Chromatography Surface Areas of Solids 2313

Two methods, which involve inverse GC with Ar as the probe and tracer pulse GC with $^{15}N_2$ as the tracer, are developed for the measurement of surface areas of solids. The measurements are carried out by using a mixed carrier gas of helium and nitrogen at 77 K.

Hengchang Song and Jon F. Parcher*, Department of Chemistry, University of Mississippi, University, MS 38677

Prediction of Gas and Liquid Chromatographic Retention Indices of Polyhalogenated Biphenyls 2318

GC and LC retention indices of 53 polyhalogenated biphenyl compounds are predicted using descriptors derived directly from the molecular structures.

M. N. Hasan and P. C. Jurs*, Department of Chemistry, 152 Davey Laboratory, The Pennsylvania State University, University Park, PA 16802

Development and Use of Charged Partial Surface Area Structural Descriptors in Computer-Assisted Quantitative Structure–Property Relationship Studies 2323■

A series of structural descriptors is presented that allows for the application of QSPR techniques to diverse data sets and to properties that are strongly influenced by polar intermolecular interactions.

David T. Stanton and Peter C. Jurs*, Chemistry Department, Davey Laboratory, Penn State University, University Park, PA 16802

Whole-Column Computer Simulation in Nonlinear Liquid Chromatography. The Traveling Characteristics of the Concentration Waves of a Binary Mixture 2330

Computer calculations of the solution of mass balance equations of chromatography for a binary mixture provide the individual band profiles along the column at each moment as well as the elution profiles at each point.

Zidu Ma and Georges Guiochon*, Department of Chemistry, University of Tennessee, Knoxville, TN 37996-1600, and Division of Analytical Chemistry, Oak Ridge National Laboratory, Oak Ridge, TN 37831-6120

Surface Studies of the Silver Sulfide Ion Selective Electrode Membrane 2339

The surface of the silver sulfide ion-selective electrode is examined by X-ray photoelectron spectroscopy and scanning electron microscopy. Chemical pathways are proposed for the interference of Hg^{2+}, Fe^{3+}, and halide ions.

Roland De Marco, Robert W. Cattrall*, John Liesegang, and Graeme L. Nyberg, School of Physical Sciences, La Trobe University, Melbourne, Victoria 3083, Australia and **Ian C. Hamilton,** BHP Central Research Laboratories, Newcastle, New South Wales 2287, Australia

Stearate-Modified Carbon Paste Electrodes for Detecting Dopamine in Vivo: Decrease in Selectivity Caused by Lipids and Other Surface-Active Agents 2347

The ability of stearate-modified carbon paste electrodes to distinguish between the oxidations of dopamine and ascorbic acid is significantly decreased following contact with brain tissue, lipids, or other surfactants.

Paul D. Lyne and Robert D. O'Neill*, Chemistry Department, University College, Belfield, Dublin 4, Ireland

Polynomial Filters for Data Sets with Outlying or Missing Observations: Application to Charge-Coupled-Device-Detected Raman Spectra Contaminated by Cosmic Rays 2351

Missing-point filters use a polynomial fit to the data surrounding, but not including, outlying or missing points. The procedure efficiently bridges gaps in data sets with minimal distortion.

G. R. Phillips and J. M. Harris*, Department of Chemistry, University of Utah, Salt Lake City, UT 84112

Chemiresistor Gas Sensors Based on Photoconductivity Changes in Phthalocyanine Thin Films: Enhancement of Response toward Ammonia by Photoelectrochemical Deposition with Metal Modifiers 2357

Photoelectrochemical modification of phthalocyanine-coated interdigitated array microcircuits with various transition metals improves the performance of chemiresistors. Detection limits of 1.0 ppt are obtained for NH_3 in air for the Hg-modified assemblies.

Rossella Brina, Greg E. Collins, Paul A. Lee, and Neal R. Armstrong*, Department of Chemistry, The University of Arizona, Tucson, AZ 85721

Environmental Factors Affecting Micellar Stabilized Room-Temperature Phosphorescence Lifetimes 2365

A kinetic decay model of triplet molecules is proposed to describe the effects of triplet quenchers and external heavy atoms on phosphorescence lifetimes in micellar solutions.

Haidong Kim and Stanley R. Crouch*, Department of Chemistry, Michigan State University, East Lansing, MI 48824 and **Matthew J. Zabik* and Salah A. Selim,** Pesticide Research Center, Michigan State University, East Lansing, MI 48824

Figures of Merit for Furnace Atomization Plasma Emission Spectrometry 2370

Figures of merit are presented for Ag, Fe, Ni, Cd, Pb, Be, Bi, Cu, and P in an effort to broadly characterize the analytical potential of the furnace atomization plasma emission spectrometric technique.

R. E. Sturgeon*, S. N. Willie, V. Luong, and S. S. Berman, Division of Chemistry, National Research Council of Canada, Ottawa, Ontario, Canada K1A 0R9

Buy Yourself Some Time.

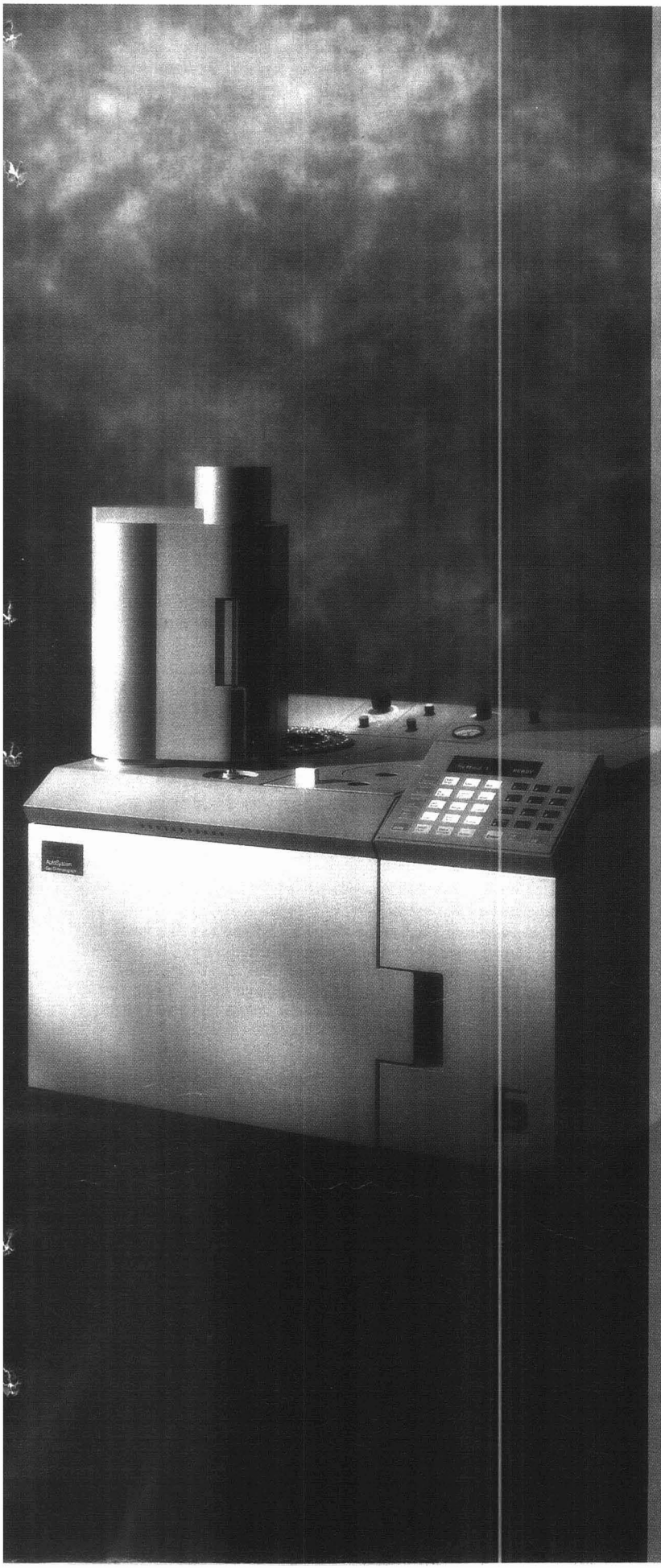

The premise behind Perkin-Elmer's new GC is quite simple: design a gas chromatograph that will let you get more done.

Meet the AutoSystem GC.

It's the first gas chromatograph with a totally integrated liquid autosampler, giving you unmatched flexibility in GC sampling.

We built in new standards of reliability and versatility to ensure maximum productivity in high throughput labs.

Together, the AutoSystem GC and PE Nelson's data handling capability bring a new level of communication and control to gas chromatography.

And with PE XPRESS, all the in-stock consumables you need are shipped within 24 hours.

For more information, or a demonstration of the AutoSystem GC, contact your local Perkin-Elmer office. For product literature call 1-800-762-4000.

Anytime.

PERKIN ELMER

The Perkin-Elmer Corporation
Norwalk, CT 06859-0012

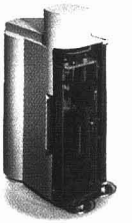

A built-in liquid autosampler for new levels of flexibility and control.

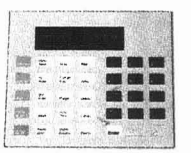

One simplified keyboard, with color-coded function keys, controls autosampler and GC.

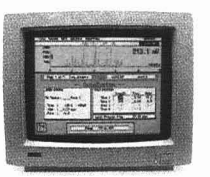

PE Nelson's OMEGA AutoSystem Controller combines GC control with multi-tasking data handling.

PE Nelson's Model 1020 Personal Integrator with screen-driven graphics and a 20-MB hard disk.

Perkin-Elmer combines experience, expertise, and worldwide resources to provide unmatched products, service, and support for analytical laboratories.

Information Only #111
Sales Call #112

NEW From the makers of SigmaPlot™

PeakFit™

Quantitative Peak Analysis... on your own PC.

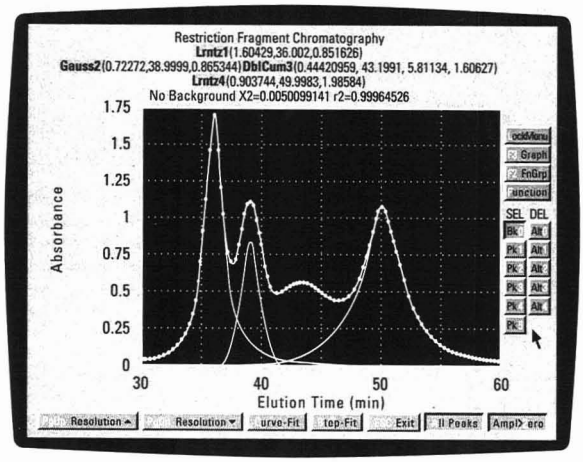

Introducing PeakFit™ dedicated peak analysis software! Designed for anyone who needs to separate peaks or multiple functional forms for analysis and calculation, PeakFit gives you the unique ability to observe and control algorithm performance on screen, iteration by iteration, for fast and accurate determination of the best fit for your data. PeakFit's state-of-the-art tools include:

- ***Unique graphical visual interaction with data*** — you control the non-linear curve-fitting operation by manipulating the curve placement and parameter values right on the screen.
- ***Quantitative analysis*** — areas, centers, amplitudes and widths of individual peaks automatically calculated.
- ***Full numerical review*** — parameter/fit statistics include standard error, confidence limits, F-statistics, residuals, t-values, etc.
- ***Extensive built-in equation library*** — 26 different specialized functions, including Gaussian, Lorentzian, Voigt, Pearson VII, Symmetric Double Cumulative, even user-defined functions.
- ***Numerous input/output options*** — dot matrix, LaserJet™, PostScript™ printers. SigmaPlot 4.0™, Lotus, ASCII and other formats.
- ***Easy to use*** — Industry standard mouse-driven interface.
- ***Applications*** — Chromatography, Spectroscopy, Electrophoresis, Electronics, Pharmacology, Statistical Analysis and Engineering.

Priced within reach of most research budgets, PeakFit is backed by a full money-back guarantee... and one of the strongest support staffs in the industry. To find out more about PeakFit or other scientific and engineering software from Jandel, just call us: **1-800-874-1888** (inside U.S.), or **1-415-924-8640** (outside U.S.).

Jandel SCIENTIFIC
65 Koch Road • Corte Madera, CA 94925
Phone: 415-924-8640 FAX: 415-924-2850
In Europe: Schimmelbuschstr. 25 • 4006 Erkrath 2 • FRG
02104/36098 • 02104/36099

Call for free brochure: **800-874-1888**

CIRCLE 70 ON READER SERVICE CARD

BRIEFS

Oxygen Optrode for Use in a Fiber-Optic Glucose Biosensor 2377

The optical fiber oxygen sensor is based on the dynamic quenching of the luminescence of tris(1,10-phenanthroline)-ruthenium(II) cation by molecular oxygen. Oxygen is monitored continuously in the 0–750 Torr range, and the detection limit is 0.7 Torr.

Maria C. Moreno-Bondi and Otto S. Wolfbeis*, Analytical Division, Institute of Organic Chemistry, Karl-Franzens University, 8010 Graz, Austria and **Marc J. P. Leiner and Bernhard P. H. Schaffar,** AVL-List GmbH, Biomedical Division, Kleist-Strasse 48, 8020 Graz, Austria

Nonenzymatic Method for the Determination of Hydrogen Peroxide in Atmospheric Samples 2381

A nonenzymatic method is developed and compared with the enzymatic (*p*-hydroxyphenyl)acetic acid method. The method is based on the Fe(II)-catalyzed oxidation of benzoic acid by H_2O_2 to form isomeric hydroxybenzoic acids.

Jai H. Lee* and Ignatius N. Tang, Environmental Chemistry Division, Brookhaven National Laboratory, Upton, NY 11973 and **Judith B. Weinstein-Lloyd,** Chemistry/Physics Program, State University of New York/Old Westbury, Old Westbury, NY 11568

Spatially Resolved Laser Transfer of Organic Surface Films for Infrared Analysis 2385

A laser transfer sampling technique is described and applied to obtain IR spectra of organic surface films. Spatially resolved transfer across a vacuum gap is demonstrated at 1064 and 248 nm.

M. S. de Vries, H. E. Hunziker*, and H. R. Wendt, Almaden Research Center, IBM Research Division, San Jose, CA 95120 and **D. D. Saperstein,** IBM General Products Division, San Jose, CA 95193

Endothermic Ion–Molecule Reactions. 4. Site-Directed Fragmentation in N-Acetylated Oligosaccharides at Low Beam Energies 2388

Site-directed fragmentation of N-acetylated sugars is observed at very low beam energies when reactive (endothermic) collisions are used.

Ron Orlando* and Catherine Fenselau, Structural Biochemistry Center, Department of Chemistry and Biochemistry, University of Maryland Baltimore County, Baltimore, MD 21228 and **Robert J. Cotter*,** Middle Atlantic Mass Spectrometry Facility, Department of Pharmacology and Molecular Sciences, Johns Hopkins University School of Medicine, Baltimore, MD 21205

Recognition of Trypsin Autolysis Products by High-Performance Liquid Chromatography and Mass Spectrometry 2391

The major peptides produced by complete autolysis of trypsin are characterized by HPLC and MS so that they are recognized as artifacts in tryptic digests of proteins.

Martha M. Vestling*, Constance M. Murphy, and Catherine Fenselau, Department of Chemistry and Biochemistry, University of Maryland Baltimore County, Baltimore, MD 21228

Full Power FTIR Spectroscopy

Integrated sampling solutions with Mattson Instruments' Galaxy™ series of FTIR spectrometers.

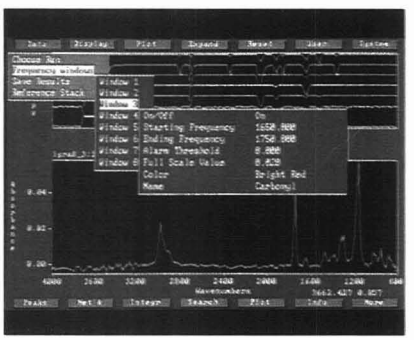

Mattson Instruments' Galaxy series of FTIR spectrometers provides the highest value ever available in infrared analysis.

- ☐ Reliable, high performance operation for analysis of your toughest samples.
- ☐ Research grade interferometer control.
- ☐ Enhanced speed of analysis.
- ☐ Small instrument footprint.
- ☐ Compatible with all standard sampling accessories.

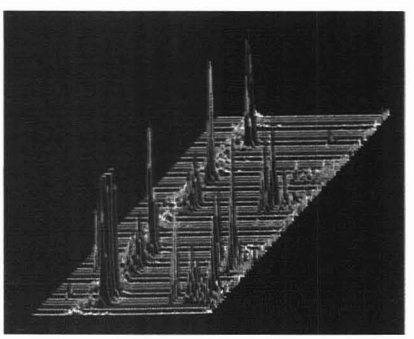

Grob test mixture with the Series 100 GC-FTIR interface; Entropy reconstruction and 3-D spectral display.

Full-featured data analysis software with real-time spectral acquisition.

- ☐ Real-time display of infrared spectrum and reconstructed chromatogram or thermal data.
- ☐ Up to eight functional group specific reconstructions for instant compound recognition.
- ☐ Full access to all spectral acquisition parameters allows operator selection of time based resolution.
- ☐ The substantial FIRST™ Software package that includes PLS Quant, Deconvolution, Curve Fitting, Macro capability and quality graphics.

For Less Than You Would Expect

Compare our specifications, capabilities and price. Call us for a quote!

GC-FTIR
TGA-FTIR
FT-RAMAN
FTIR-Microscopy
Galaxy™ Series FTIR

Mattson Instruments, Inc.
1001 Fourier Drive
Madison, WI 53717
Tel. (608) 831-5515
Fax: (608) 831-2093

CIRCLE 88 ON READER SERVICE CARD

Chromatography Products Catalogue

Chromatography products

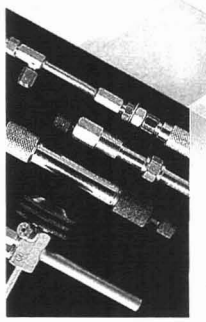

- Syringes
- Accesories
- HPLC Columns, Cartridges & Accessories
- Capillary Columns
- Instruments

For your free Catalogue contact your local office or dealer:
SGE Australia (Head Office) Tel: (03) 874 6333 Fax: (03) 874 5672
SGE UK Tel: (0908) 56 8844 Fax: (0908) 56 6790
SGE USA Tel: (512) 837 7190 Fax: (512) 836 9159
SGE Germany Tel: (6150) 2078 Fax: (6150) 14768
SGE France Tel: (1) 438 22943 Fax: (1) 438 24268

perfection in chromatography

CIRCLE 130 ON READER SERVICE CARD

Attention ACS Members

Support the American Chemical Society's CAMPAIGN FOR CHEMISTRY

- to promote scientific literacy.
- to ensure a future generation of scientists and researchers.
- to meet the long-term technical demands of our society.

When it's your turn to give...

remember your investment in the Campaign for Chemistry is an investment in everyone's future.

For details:
Phone 202/872-4094

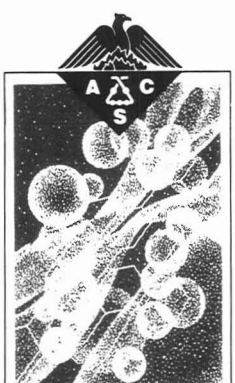

BRIEFS

Fast Atom Bombardment Mass Spectrometric Quantitative Analysis of Methionine-Enkephalin in Human Pituitary Tissues 2395

Picomole levels of endogenous methionine-enkephalin per mg protein are measured by FABMS in individual human pituitary tissue extracts using a deuterated internal standard following multidimensional chromatographic purification.

Jozef J. Kusmierz, R. Sumrada, and Dominic M. Desiderio*, Charles B. Stout Neuroscience Mass Spectrometry Laboratory and Departments of Immunology–Virology, Neurology, and Biochemistry, University of Tennessee—Memphis, 800 Madison Avenue, Memphis, TN 38163

Laser Ionization Gas Chromatography/Mass Spectrometry of Tetraethyltin 2400

Detection limits of 2.5 pg of tetraethyltin/mL or 1.5 fg of tetraethyltin absolute are obtained. This corresponds to values of 1.3 pg tin/mL or 750 pg of tin absolute.

Steven M. Colby, Michael Stewart, and James P. Reilly*, Department of Chemistry, Indiana University, Bloomington, IN 47405

Correspondence

Enzyme Immunoassay of Insulin by Semiconductor Laser Fluorometry 2404

Totaro Imasaka, Hiroyuki Nakagawa, Takashi Okazaki, and Nobuhiko Ishibashi*, Faculty of Engineering, Kyushu University, Hakozaki, Fukuoka 812, Japan

Technical Notes

Reversed Injector Loading Technique for Simultaneous Determinations by Flow Injection Analysis 2405

José Luis Pérez Pavón*, Carmelo García Pinto, Bernardo Moreno Cordero, and Jesús Hernández Méndez, Department of Analytical Chemistry, Bromatology and Food Sciences, University of Salamanca, Salamanca, Spain

Bottle-Calibration Static Head Space Method for the Determination of Methane Dissolved in Seawater 2408

Kenneth M. Johnson*, Jeffrey E. Hughes, Percy L. Donaghay, and John McN. Sieburth, Graduate School of Oceanography, University of Rhode Island, Narragansett, RI 02882

Separation of Yttrium-90 and Strontium-90 on Papers Impregnated with Ionizable Crown Ethers 2412

C. M. Wai* and H. S. Du, Department of Chemistry, University of Idaho, Moscow, ID 83843

On-Valve Electrochemical Detector for High-Speed Flow Injection Analysis 2414

Joseph Wang* and Ruiliang Li, Department of Chemistry, New Mexico State University, Las Cruces, NM 88003

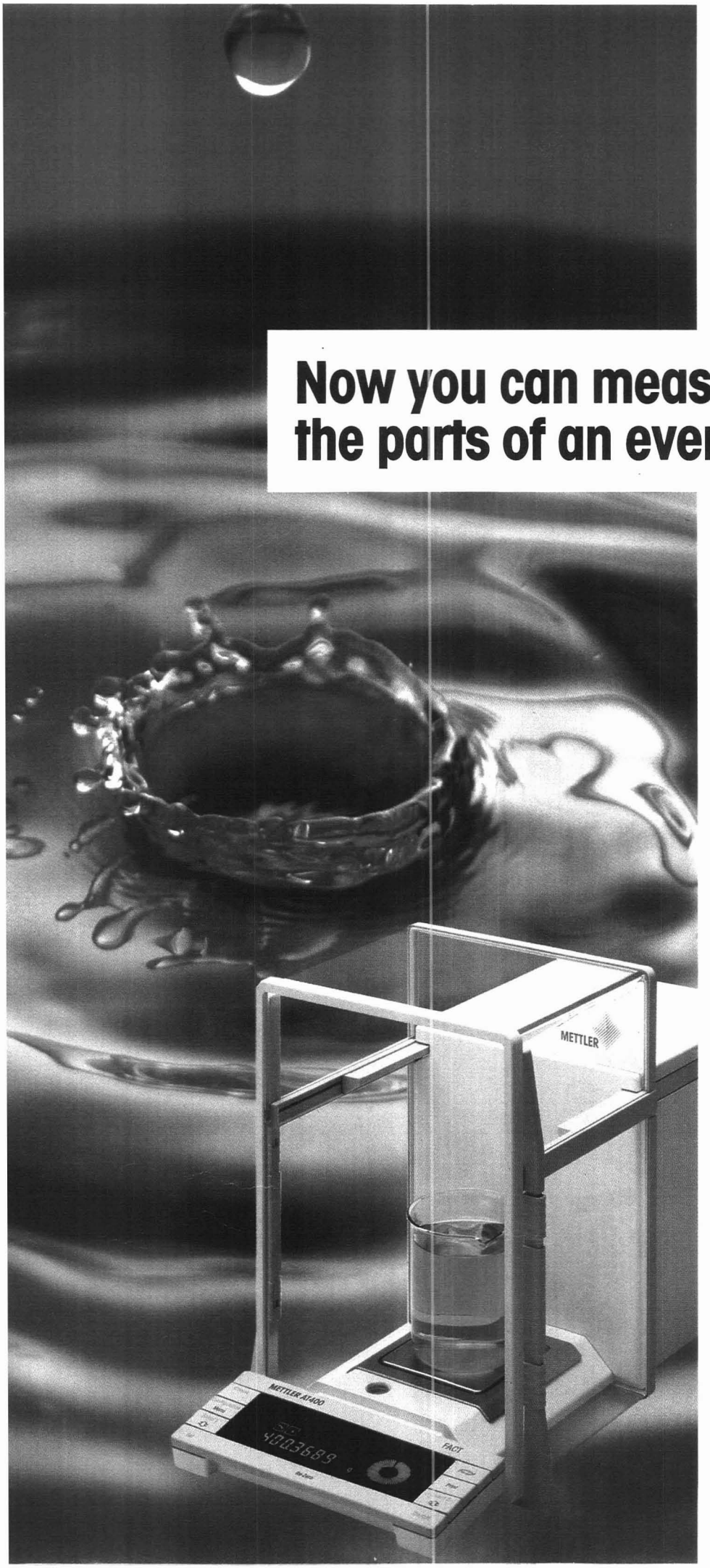

Now you can measure the sum of the parts of an even larger whole.

Presenting the 405 g METTLER AT400.

No matter how you add it up, the AT400 represents a giant leap forward in weighing capacity. At 405 g, it doubles the limit for a 4 place balance, while its METTLER AT technology remains unequalled.

Which is why seeing the advantages of the AT400 requires only the most basic calculations:

Start with the ability to weigh larger samples more accurately and with greater ease. Add the ergonomic AT family design, with automatic draft shield. Factor in the revolutionary METTLER DeltaTrac®, and METTLER's Fully Automatic Calibration Technology (FACT) – for the absolute precision you expect from a METTLER balance. Plus, consider the fact that it's also available as the METTLER AT460 DeltaRange®, with a movable fine range of 62 g.

Then multiply it all by METTLER Service Plus®, your assurance that we stand behind every balance we sell.

For the answers to your most weighty problems, call us. We'll help you find the perfect solution.

CIRCLE 86 ON READER SERVICE CARD

Mettler Instrument Corporation
Box 71
Hightstown, NJ 08520
1-800-METTLER
(NJ 609-448-3000)

METTLER

We understand.
Precisely.

6955.73

Leak-tight Valves & Fittings for Analytical Instrument Applications

The leak-tight technology of the SWAGELOK Companies is built into all the products you see here.

They work with each other to give you design flexibility. You can select sizes, shapes, materials and ratings to handle ***your*** service conditions.

They're all manufactured to the same standards of precision and quality control. You can count on consistent tolerances, compatible end connections, and reliable seals.

They're available locally from Authorized Sales and Service representatives. You can save money through efficient purchasing, controlled inventories, and on-time delivery.

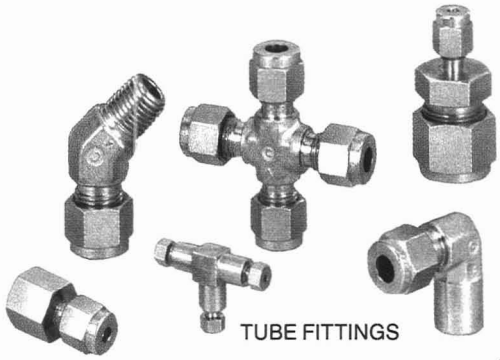

TUBE FITTINGS

BALL & PLUG VALVES

FILTERS

METERING VALVES

CHECK & RELIEF VALVES

QUICK-CONNECTS

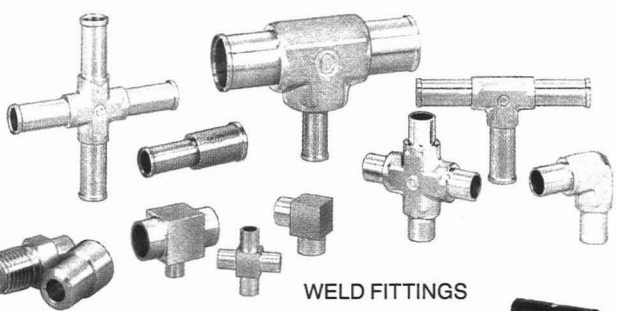

WELD FITTINGS

O-RING & METAL GASKET FACE SEAL FITTINGS

NEEDLE VALVES

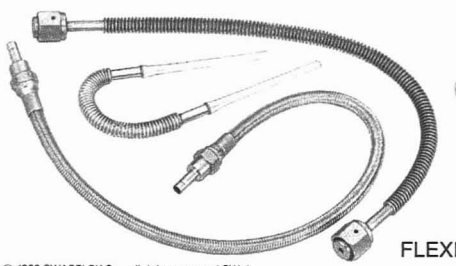

FLEXIBLE HOSE

© 1988 SWAGELOK Co., all rights reserved SW-4

SWAGELOK Co.
Solon, Ohio 44139
SWAGELOK Canada Ltd., Ontario

These Products are subjects of patent or patents pending

the SWAGELOK companies

CIRCLE 125 ON READER SERVICE CARD

Euroanalysis

One of the highlights in the worldwide field of analytical chemistry, Euroanalysis VII, took place in Vienna August 26–31, 1990. Euroanalysis is a broad-scope analytical chemistry conference organized by the Working Party on Analytical Chemistry (WPAC) of the Federation of European Chemical Societies (FECS), representing 32 member societies from 26 European countries. Six observers from China, Egypt, Israel, Japan, Romania, and IUPAC also take part in ongoing WPAC activities.

This conference is a European effort rivaling the highly successful 41-year-old Pittsburgh Conference on Analytical Chemistry and Applied Spectroscopy held in the United States. The first Euroanalysis was held in Heidelberg in 1972, followed by Budapest in 1975, Dublin in 1978, Helsinki in 1981, Cracow in 1984, Paris in 1987, and Vienna this August. The next conference will be held in Edinburgh in 1993.

The Vienna conference was organized by the Austrian Society for Analytical Chemistry on behalf of the WPAC of the FECS; the Secretary General of the conference was Manfred Grasserbauer of the Technical University of Vienna. The scientific program consisted of 70 invited lectures and 680 contributed oral and poster presentations on applications of analytical chemistry (environmental systems and food, pharmaceutical and biomedical science, biotechnology, materials science, and arts and archaeology) and methodological developments in analytical chemistry (including atomic spectroscopy, molecular spectroscopy, separation techniques, electrochemical methods, sensors, radiochemical and nuclear techniques, thermal analysis, local and surface analysis, structural analysis of solids, and immunoassay).

Special sessions were held on sample preparation for inorganic and organic trace analysis, computer-based analytical chemistry, quality assurance in analytical chemistry, and education and training in analytical chemistry. Approximately 1100 active participants from 48 countries attended, including 20 non-European countries. More than 30% were industrial participants. Spain contributed the largest number of papers (96). Germany was second with 71 papers and Austria third with 66 papers. The United States contributed 20 papers. All invited lectures will be published in a special volume of *Mikrochimica Acta*.

Of particular significance was a WPAC report on the teaching of analytical chemistry in Europe, based on evaluation of questionnaires from 314 European universities. There is obviously a wide diversity of curricula, and the WPAC issued a number of recommendations to provide a basic equivalence of undergraduate programs in Europe, particularly in view of the economic unification planned by 1992.

Euroanalysis VII was one of the best broad-based international conferences on analytical chemistry I have ever attended. The meeting was well organized, the program was comprehensive, and the opportunity to meet colleagues from around the world was most pleasurable.

G. H. Morrison

ONLY THE BEST FOR THE BEST.

Can your HPLC system pump champagne? Can your HPLC system reliably pump ANY solvent without costly, time consuming degassing procedures?

Only one HPLC pump can — the Varian LC Star 9010. Our 9010 can pump ANY HPLC solvent, without prior preparation, with reliable results, everytime.

Let's face it. If you can't count on your pump, it doesn't matter how well the other parts of your HPLC system work. High performance isn't enough when one tiny bubble can shut down your whole operation.

The unique, patented design of the Star 9010 delivers high performance and dependability with any mobile phase. It eliminates pump cavitation, so your HPLC system can operate for hours on end, even overnight, unattended.

The net result is that, over the long run, you can have more analyses completed in less time, and with greater confidence.

Let us show you how dependable and productive a pump can be. For more information on the Star 9010 Pump and the entire Varian LC Star System, call **800-231-8134**. In Canada, call **416-457-4130**.

CIRCLE 140 ON READER SERVICE CARD

LC WITH A FUTURE varian

Endowment Funds Sought for Kolthoff Awards

The Division of Analytical Chemistry is asking for donations to establish an endowment for the Kolthoff Enrichment Awards for Undergraduate Studies. Established in 1989 by the Division, the awards recognize outstanding junior-year-level students who plan to pursue careers in analytical chemistry. Over the past two years the Division has provided funds ranging from $500 to $1000 for 11 student awards. The endowment would provide a more stable source of funds.

Contributions by check should be made out to the Division of Analytical Chemistry and sent to Division treasurer David Curran, Department of Chemistry, University of Massachusetts, Amherst, MA 01003. Include a note to indicate that the funds are for the Kolthoff endowment.

The Division has issued a special appeal for donations from I. M. Kolthoff's professional progeny. In addition, a genealogy delineating Kolthoff's scientific offspring through several generations is being compiled by Herbert Laitinen, who asks that anyone with information contact him at the Department of Chemistry, University of Florida, Gainesville, FL 32611 (904-392-0541, FAX 904-392-8758). Information about nominations for the award can be found in the August 1 NEWS.

Small College Grants

Small colleges with enrollments of 2500 students or less are invited to apply for the 1991 Pittsburgh Conference Memorial National College Grants Awards. The grants can be used for the purchase of scientific equipment, teaching aids, and/or library materials, but not exclusively for research materials. Schools receiving grants in previous years are not eligible for another award for three years.

The grants are supported by the Pittsburgh Conference on Analytical Chemistry and Applied Spectroscopy, the Spectroscopy Society of Pittsburgh, and the Society for Analytical Chemists of Pittsburgh. At least 10 schools will receive awards, which can be for as much as $3000. For more information, contact Paul Bauer, Pittsburgh Conference—PCMNCG, 300 Penn Center Blvd., Suite 332, Pittsburgh, PA 15235. Applications must be submitted by March 1, 1991.

Methane Surprise

Unusually high levels of methane have been detected in cities within eastern Europe by researchers from the University of California at Irvine. Methane, a key contributor to the greenhouse effect, increased in the atmosphere during the 1980s at the rate of 1% per year. Unlike other greenhouse gases, methane's lifetime in the atmosphere is short—about 10 years. The University of California scientists estimate that a 10% reduction in methane emissions could stabilize the global concentration of the gas. The methane measurements were directed by atmospheric chemist F. Sherwood Rowland, a pioneer in recognizing the danger of chlorofluorocarbons to the ozone layer.

Sherwood's team collected air samples at ground level for the study and analyzed them by GC. High methane levels were found in Berlin, Budapest, Krakow, and Prague. Lower levels of methane, comparable to U.S. values, were measured in Vienna and Zagreb. The researchers attribute the high methane levels to poor controls on the transport and handling of natural gas.

Nuclear Waste Agreement

The U.S. and the U.S.S.R. have signed an agreement that pledges cooperation in the area of environmental restoration and nuclear waste management. The agreement, signed in Austria, identifies several areas of cooperation that are being clarified in joint meetings. Cooperative areas may include analyses and investigations related to waste partitioning to facilitate permanent disposal as well as analyses and investigations related to geologic disposal of radioactive waste.

For Your Information

The Design Institute for Physical Property Data (DIPPR) **Data Compilation of Pure Compound Properties,** 1990, has been expanded to include 39 properties on 1117 chemicals. For more information, contact the Standard Reference Data Program, A320 Physics Bldg., NIST, Gaithersburg, MD 20899 (301-975-2208).

Spectra-Physics is offering a **free grants assistance program** to aid researchers and teachers at not-for-profit institutions in securing monies for chromatography, capillary electrophoresis, or data management systems. For more information, call 301-345-8256.

Paul Lauterbur of the University of Illinois at Urbana–Champaign will receive the **first Bower Award for Achievement in Science** (see February 15 NEWS). Lauterbur, a leader in the development of magnetic resonance imaging, will receive $290 000 and a gold medal.

The American Association for Clinical Chemistry (AACC) Press has published **five new books:** *DORA '90–'91: Directory of Rare Analyses, Clinical Chemistry Quiz, The Laboratory Pocket Guide to Abused Drugs, Hazardous Waste: Facts and Fallacies,* and *Impact of AIDS on the Clinical Chemistry Laboratory.* For more information, contact Mona Alcazar, AACC, Dept. PR, 2029 K St., N.W., Washington, DC 20006.

NIST is offering four new **glass density standard reference materials** for calibrating densitometers and other instruments. Each standard has a density value certified to the sixth place. For more information, contact Standard Reference Materials Program, Room 204, Bldg. 202, NIST, Gaithersburg, MD 20899 (301-975-6776, FAX 301-948-3730).

Before you go through another column, it pays to go through Whatman.

If you're not using the right sample prep with your HPLC system, you could be wasting valuable time and money. That's why it pays to go through the Whatman Sample Prep System.

Whatman sample prep filters help yield purer filtrates, to ensure reproducible results–which means *less* repeat testing for you and *more* life for your column.

The Whatman Sample Prep System includes:

Puradisc™ 25 (AS/TF/PP)–Syringe-tip filters are available with various membranes to help avoid generation of extractables: polysulfone, for aqueous applications (Puradisc 25 AS); PTFE, for solvent-based applications (Puradisc 25 TF); and polypropylene, for solvent/aqueous applications (Puradisc 25 PP).

SPEC–The only solid-phase extraction device that contains an integral 0.2 micron polypropylene membrane to eliminate the need for secondary filtration.

Solvent and Aqueous IFD™–The only filter device that filters and degasses mobile phases in-line to save time and extend the life of the HPLC column.

So before you go through another HPLC column, go through Whatman.

Contact Whatman Inc. for more information on receiving a FREE column.

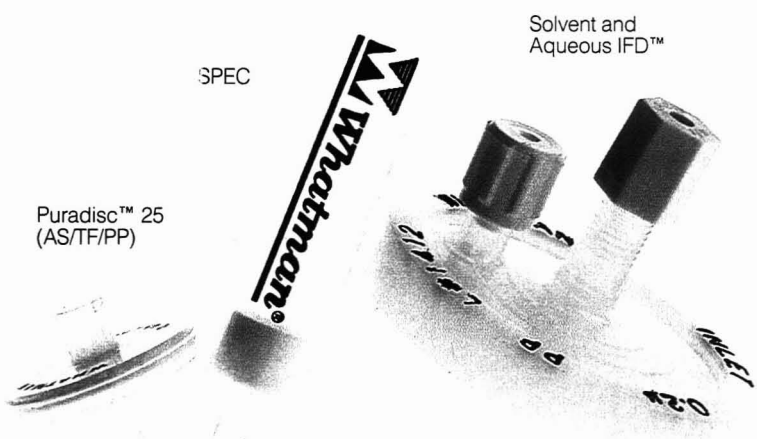

Whatman®

Whatman Laboratory Division

Whatman Inc., 9 Bridewell Place, Clifton, New Jersey 07014
Telephone: 201-773-5800 Telex: 133426 FAX: 201-472-6949

Whatman (word and device) and Whatman (word only) are trademarks of Whatman Paper Ltd. 746-11-174
Puradisc, Solvent IFD, and Aqueous IFD are trademarks of Arbor Technologies, Inc.

CIRCLE 146 ON READER SERVICE CARD

FOURIER TRANSFORM RAMAN SPECTROSCOPY OF BIOLOGICAL MATERIALS

Ira W. Levin and E. Neil Lewis
Laboratory of Chemical Physics
National Institute of Diabetes and Digestive and Kidney Diseases
National Institutes of Health
Bethesda, MD 20892

REPORT

Since its discovery more than 60 years ago, the spontaneous Raman effect has enjoyed spectacular success in applications spanning the physical, chemical, biological, and engineering fields. Following the initial excitement generated primarily by physicists in the 1930s, Raman spectroscopy was used almost exclusively by chemists for about 20 years for vibrational studies of polyatomic molecules. In the early to middle 1960s, visible light lasers as convenient sources of radiation stimulated an enormous amount of interest in Raman spectroscopy. As conventional and resonance-enhanced Raman studies proliferated throughout the 1960s and 1970s, new nonlinear Raman phenomena, distinguished by a plethora of colorful acronyms from CARS to RIKES, were developed and applied to systems of chemical interest.

In 1986, when many Raman spectroscopists were sensing the serenity of a rapidly maturing field, several investigators (*1–3*) successfully demonstrated the coupling of Raman-scattered radiation to a Michelson interferometer, replacing the traditional monochromator with a multiplexing instrument. These studies stimulated scientific and economic interest from both the vibrational spectroscopic community and the manufacturers of FT-IR spectrometers.

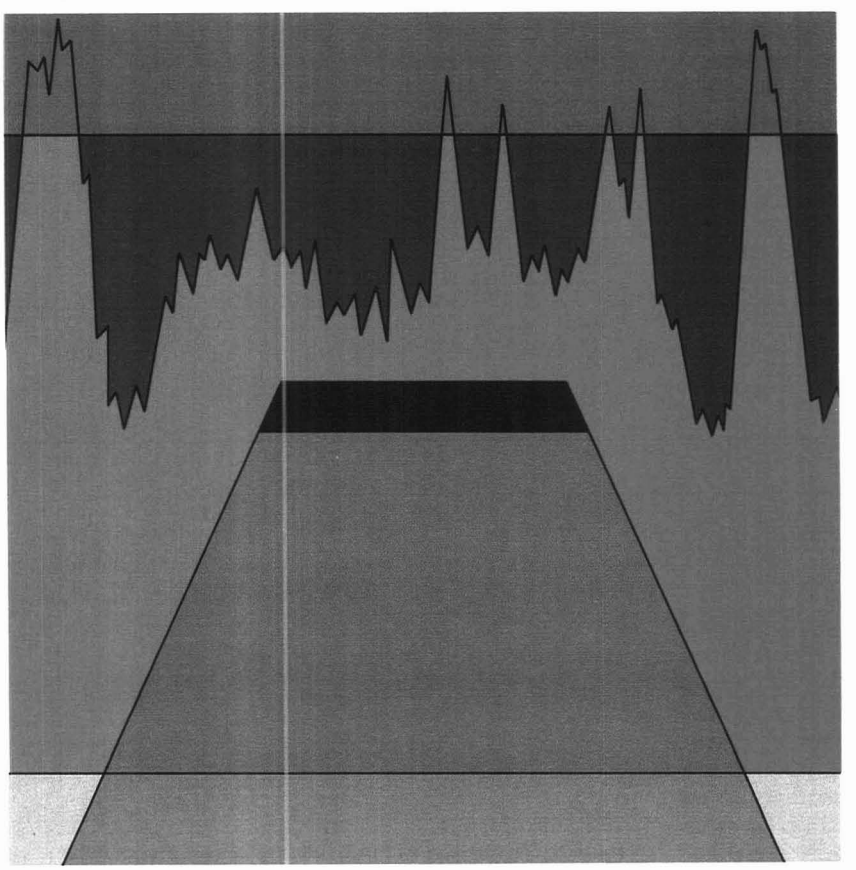

In the past few years, near-IR FT-Raman spectroscopy has evolved as a viable technique for obtaining vibrational Raman spectra of many chemical systems that are either intractable to visible laser excitation or can benefit from the capabilities of interferometric instrumentation (*4–9*). Although applications to biophysical and biochemical materials have not developed as rapidly as those pertaining to traditional chemical characterizations, FT-Raman spectroscopy holds great promise for providing vibrational data on vast numbers of biomolecular systems that are not immediately amenable to general Raman and IR techniques.

FT-Raman spectroscopy

The advantages of FT-Raman spectroscopy over conventional dispersive Raman techniques, which employ visible laser excitation and photomultiplier detection, include long-wavelength excitation to frustrate or eliminate sample fluorescence and improved instrumental performance of FT spectrometers over standard monochromators. The first advantage should not be understated; for

This article not subject to U.S. copyright
Published 1990 American Chemical Society

typical industrial or biological samples, the presence of a dominant fluorescence signal induced by either visible or UV laser radiation often precludes measurement of the weakly scattered Raman light.

Because the intensity of the Raman signal is inversely proportional to the fourth power of the excitation wavelength, the near-IR 1064-nm radiation from the Nd:YAG lasers generally used in FT-Raman instrumentation is less efficient by factors of 18–40 in generating Raman data than, for example, argon-ion sources delivering 514.5-nm emission. In the FT-Raman experiment, this decrease in sensitivity is somewhat compensated for by the interferometer's intrinsic throughput and multiplex characteristics, referred to as Jacquinôt's and Fellgett's advantages, respectively. To achieve an effective multiplex advantage, however, we assume that the experiment is detector noise limited, as is the case for the currently available cooled photoconductive germanium (Ge) and indium gallium arsenide (InGaAs) devices. (Although future improvements are expected in detector performance, existing photoconductors now function near their theoretical detection limits).

Finally, the capability for precise spectral frequency measurements, which is also implicit in interferometric instrumentation (Connes' advantage), can influence the decision to use FT-Raman equipment rather than scanning, dispersive instruments. For example, in using dispersive instrumentation, one must be sure to maintain the fidelity of the resulting spectral data, particularly after lengthy signal averaging efforts to increase the signal-to-noise characteristics of weakly scattering samples. Furthermore, frequency precision is critical in data manipulations involving spectral subtractions.

For neat liquids, dilute solutions, or polycrystalline samples, the ability to rapidly record high-quality reproducible Raman spectra with a near-IR Nd:YAG laser and FT instrumentation is as straightforward as the conventional procedures involving visible laser excitation and dispersive monochromators. Another advantage over dispersive instruments accrues in the use of an interferometer to record moderately high-resolution (0.25 cm^{-1}) Raman spectra. Once a sample is aligned with the entrance aperture of the interferometer in the FT experiment, changes in spectral resolution can be made using only computer keystrokes. (For dispersive instruments, matching the alignment of a sample capillary to an entrance slit corresponding to even 1-cm^{-1} spectral resolution is neither routine nor trivial.)

Despite the general advantages and utility of near-IR FT-Raman spectroscopy, the technique has developed more slowly in biology than in chemistry. This more deliberate advancement within the biological disciplines stems from several fundamental problems, including the intrinsic fragility and weakly scattering nature of most native preparations; the ubiquitous and unrelenting fluorescent properties, often representative of biological samples, which can unaccountably affect baseline contours and relative spectral intensities; the difficulties in both monitoring and controlling temperatures of aqueous dispersions; and the rather different aggregation characteristics encountered in intact cellular and model biomolecular systems that make preparation of each new biological sample a separate alignment and focusing effort.

The benefits of near-IR laser radiation accrue rapidly when dealing with biological samples—particularly when persistent fluorescing contaminants are introduced during lengthy sample handling and purification procedures. Because biomolecular samples tend to be fragile, dilute, and weakly scattering aggregates, the intensity of the Raman scattering can be increased dramatically by pelleting the biological suspension directly in the capillary sample tube by ultracentrifugation, a nontrivial exercise. (During centrifugation, the hydrated pellet, which is ultimately illuminated by the laser in the FT-Raman experiment, will experience a force of about 150 000–170 000 g. This necessary sample packing effect can be compared with normal methods for visible laser approaches, in which the pelleting of lipid suspensions requires only a hematocrit centrifuge operating at a force of about 10 000 g.) In many cases, the ultracentrifugation step is required not only to record a spectrum effectively, but is necessary even to observe a signal.

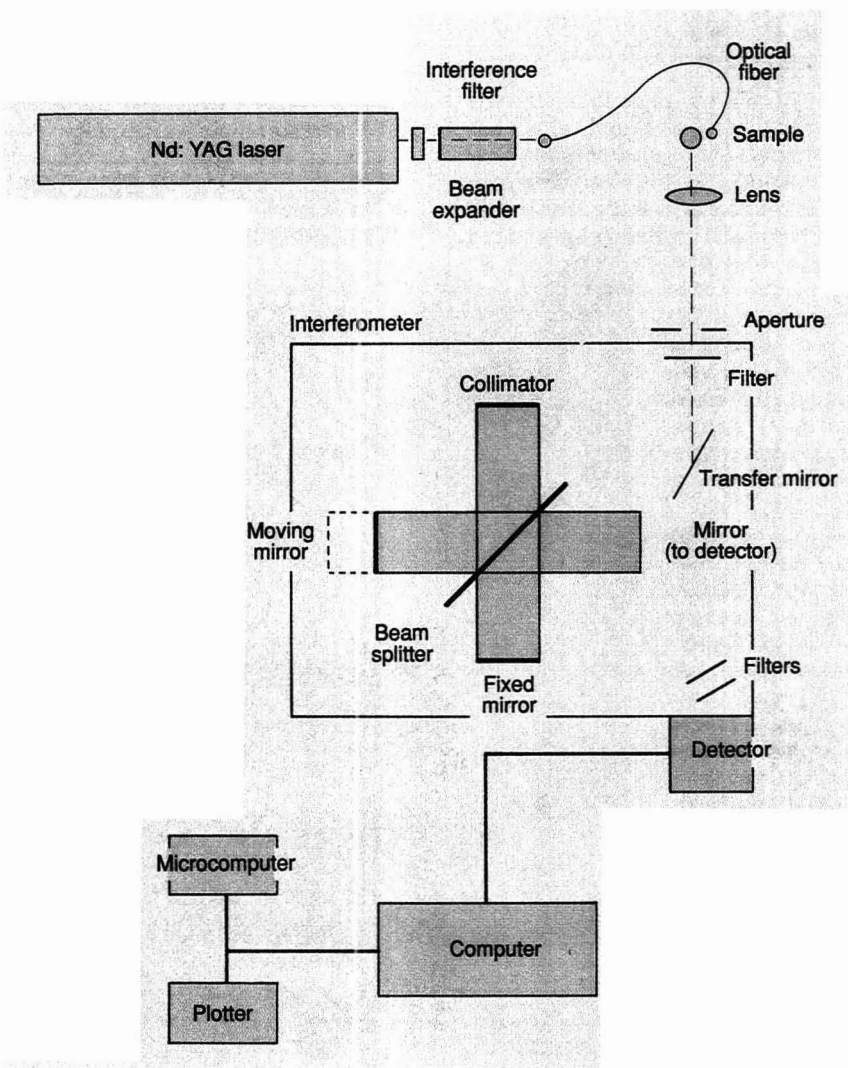

Figure 1. Schematic of the FT-Raman experiment using a 90° scattering geometry.

Disadvantages arise when using near-IR laser radiation with samples dispersed in aqueous media. The overtone region of water absorbs radiation from both the Rayleigh signal at the exciting wavelength (9394.5 cm^{-1} for the Nd:YAG laser) and the longer Raman scattered wavelengths corresponding to the C–H stretching modes (6500 cm^{-1} in absolute wavenumbers) of the sample. In addition to the loss of Raman scattered intensity for the C–H stretching vibrations, reproducible temperature measurements become a critical concern. In these cases, one resorts to the use of either reference cells or internal temperature calibrations that are based on the spectral sensitivity of the water spectrum. Temperature control can also be maintained by manipulating the incident laser spot size or by using fiber-optic bundles to carry the exciting and scattered radiation in conjunction with sample cooling techniques.

Experimental overview

Either a 90° or a 180° backscattering geometry can be used to collect the Raman emission, which is subsequently coupled to a Michelson interferometer. We have used primarily the classic right-angle sampling geometry (Figure 1), initially adopting this approach to accommodate a variety of sampling accessories and optical arrangements (*6–9*). For samples capable of absorbing 1064-nm Nd:YAG illumination, such as dilute aqueous biological dispersions, a backscattering geometry (Figure 2) may be more appropriate.

Although a single fiber-optic bundle is shown bringing near-IR radiation to the sample in Figure 1, a second fiber-optic collection bundle passing between the sample and the IR source compartment can also be used. In this case, the Raman scattered radiation emanating from the end of the collection fiber replaces the interferometer's IR source, maximizing the coupling of the scattered radiation to the instrumental optics. Removal of both fibers quickly provides the 90° scattering geometry. Whenever even minor changes occur in the arrangement of the optical components or sampling accessories, with respect to the 90° instrumentation, a new phase spectrum must be obtained to ensure accurate spectral representation. Data processing of the enormous numbers of spectra generated is facilitated by using removable disk cartridge systems and a laboratory computer network.

The most critical aspects of the FT-Raman technique using Nd:YAG laser excitation lie in efficiently rejecting the extremely intense Rayleigh and reflected signals prior to detection and in choosing suitable, sensitive near-IR detectors. In the 90° system, up to three dielectric notch or narrow bandpass filters act to discriminate against the Rayleigh scattering, and a solid-state cooled InGaAs detector provides the necessary detection capability for this region of the spectrum (*6*). Although efficient Rayleigh line rejection can be obtained by placing the filters perpendicular to the optical axis, an accompanying loss of Raman intensity—particularly for small wavenumber shifts—becomes evident.

By carefully rotating one or two of the filters, one can tune the Raman instrument to record spectra closer to the exciting line. For example, we can obtain spectra down to 100 cm^{-1} (*9*). To extend the high-frequency limits of the spectrum, the temperature of the detector can be increased. Increasing the detector temperature from −196 °C to −38 °C extends the frequency range from ~2990 cm^{-1} to ~3300 cm^{-1} (*9*). Under these conditions, we experience only a marginal degradation in the signal-to-noise ratio.

A suitable mixing of cold and ambient-temperature nitrogen gas provides a wide range of detector temperatures stable to ±1 °C and precludes the necessity of constructing separate thermoelectric coolers for the detector element. Rapid improvements will be forthcoming in both filter and detector technology for extending the high and low frequency limits of the Raman spectrum collected by FT techniques.

Membrane biophysical studies

Conventional bilayer assemblies. To understand the conformational and dynamic properties contributing to the complex physiological and pharmacological processes occurring at biological interfaces, a detailed architectural view of cellular membranes at the molecular level is required. For almost two decades, the most productive hypothesis for generating and extending membrane models has been the fluid mosaic construct, in which amphipathic lipids form a bilayer matrix for the expression of a variety of peripheral and integral membrane components (*10*). Although most molecular bilayer information pertains to the cellular plasma membrane, the membranes of intracellular organelles exhibit varying properties, functions, and molecular compositions, further demonstrating the richness and complexities intrinsic to biomembranes. In discussing applications designed to elucidate the properties of biomembranes, we will outline several related studies from which both advantages and snares of the FT-Raman approach can be seen.

Among the many physical techniques used to investigate the structural, dynamic, thermodynamic, and functional properties of biomembranes, vibrational spectroscopy provides an extraordinarily sensitive, noninvasive

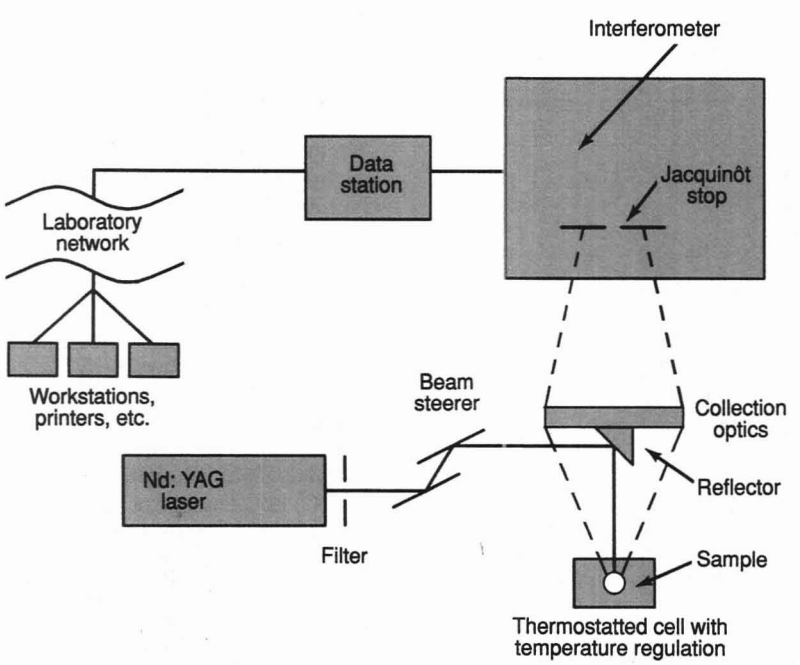

Figure 2. Schematic illustrating a 180° backscattering sample configuration.

means for probing the many intra- and intermolecular interactions defining the membrane matrix (*11*).

Unlike artificial membranes, biological membrane assemblies that have been subjected to several isolation and purification steps yet remain sufficiently free from fluorescence effects to allow Raman spectra to be recorded with visible laser excitation are rare. Figure 3 shows the FT-Raman spectrum of a bovine synaptic plasma membrane preparation obtained with 1.6 W of near-IR Nd:YAG laser power at a 4-cm^{-1} spectral resolution. For this sample preparation, which contains integral bilayer proteins and a peripheral protein clathrin coat surrounding the lipid vesicle, it is necessary to pellet the dilute aqueous membrane dispersion received from the cell biologist in the same sample capillary that is ultimately used in the FT-Raman experiment.

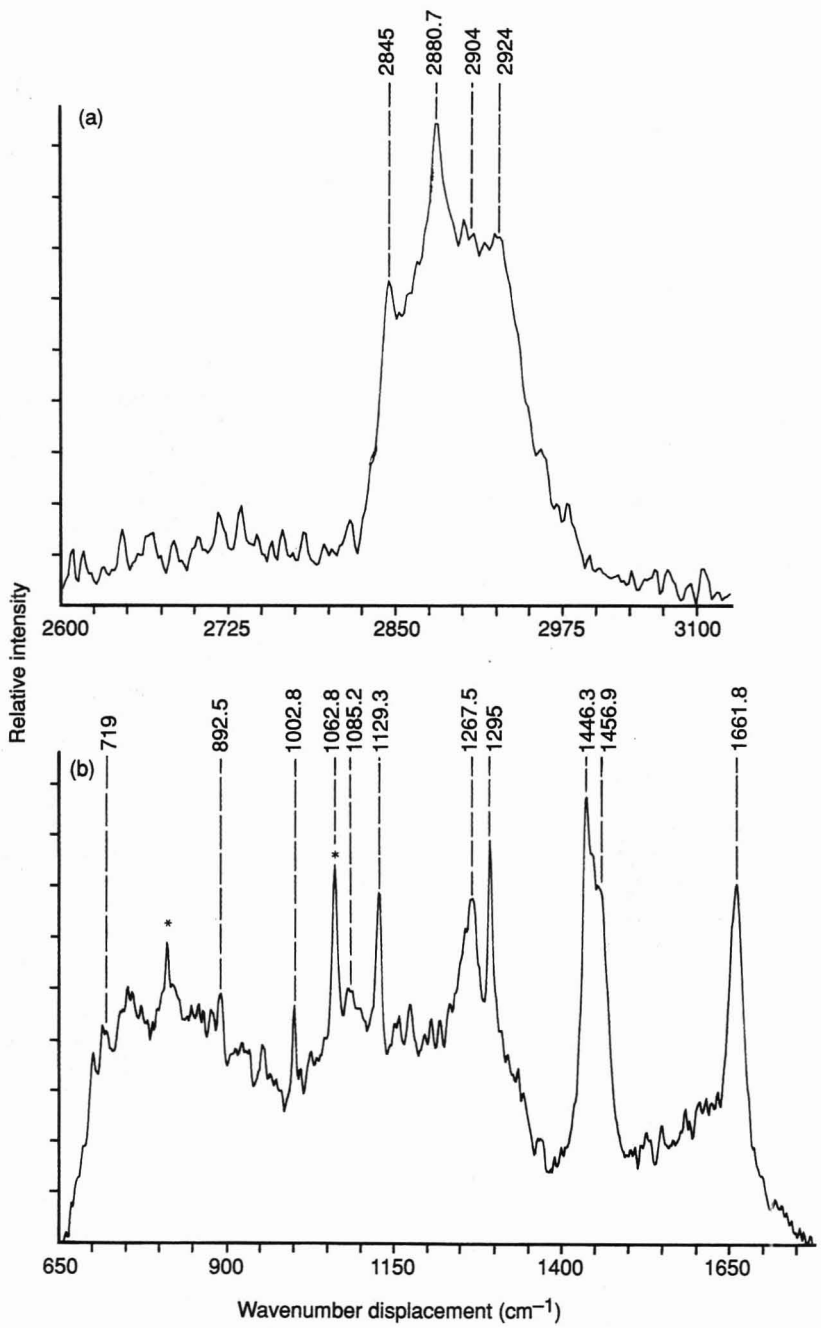

Figure 3. FT-Raman spectra of an aqueous dispersion of bovine synaptic membranes in (a) the 2900-cm^{-1} C–H stretching mode region and (b) the 1700–650-cm^{-1} spectral region showing attainable frequency precision of the spectra.
(Peaks marked by an asterisk contain small contributions from nonfiltered laser lines.)

The membrane is hydrated in an aqueous medium, making heating effects from the 1064-nm laser line substantial. To prevent diffusion of the biomembrane out of the exciting beam and to prevent protein denaturation, the sample is cooled to approximately −40 °C by gently streaming cold nitrogen gas across the capillary. After a two-and-a-half-hour acquisition time, the unsmoothed spectrum (shown in Figure 3) is again representative of an ordered form of a natural membrane.

Intact biomembranes often remain liquid crystalline to temperatures below even −20 °C and thus are not routinely examined as a lipid gel phase, as are model systems. The low-temperature phase is specifically characterized by the intensity patterns in the 2845- and 2880-cm^{-1} acyl chain methylene C–H stretching mode regions and in the 1085- and 1129-cm^{-1} acyl chain C–C stretching mode regions.

The frequency values on the spectra illustrate Connes' advantage in the determination of vibrational Raman frequencies with interferometric instrumentation. Because the accuracy of these frequencies depends on measured displacements from the exciting line, the absolute wavenumber of the Nd:YAG fundamental is measured at the same resolution of the experiment, but without the rejection filters. A precise and accurate measurement of an undistorted lineshape of the exciting fundamental thus can be obtained. If spectra of these dilute, fragile membranes could be recorded dispersively with a scanning monochromator and visible laser excitation, signal averaging times would be so great—even with the intensity advantage of the incident visible radiation—that reliable frequency measurements would probably not be obtainable because of the mechanical limitations of the monochromator. Precise frequency data are important because subtle membrane reorganizations are reflected in frequency shift information; shifts of tenths of a wavenumber are significant, for example, in characterizing gel to liquid crystalline phase transitions.

Figure 4 shows the spectra of a model lipid bilayer system consisting of 1-palmitoyl-2-oleoylphosphatidylcholine (POPC) and lanosterol in both the gel (a and b) and liquid crystalline (c and d) phases. Lanosterol, a precursor of various sterols in animals, is used as a membrane perturbant. POPC, with one saturated and one unsaturated chain, mimics a general mammalian membrane. The two phases exhibit markedly different intensity and fre-

The New VG TRIO-1 S Ultra Sensitive GC/MS/DS.

The *NEW* VG TRIO-1 S takes GC/MS into a new realm of sensitivity. It can produce full scan, library searchable EI spectra from just 10 picograms of sample. With the options of differential pumping and negative/positive chemical ionization, detection limits are even lower. No mass selective detector or ion trap compares.

TRIO-1 S is the only GC/MS able to perform both high and low concentration analyses, even with high background levels, co-elution or isotope dilution.

The LAB-BASE™ data system, now available with a 25 MHz computer platform, enables fully automatic sample handling and data processing. When time is critical, HyperSearch (option) produces instantaneous library search results, with chemical structures.

New TRIO-1 S, the clear choice when you demand analytical certainty.

VG INSTRUMENTS

FISONS Instruments

UNITED KINGDOM. VG Masslab, Crewe Road, Manchester, M23 9BE. Tel: 061-946 1060.
USA. VG Instruments Inc. 32 Commerce Center, Cherry Hill Drive, Danvers, MA 01923. Tel: (508) 777 8034.
CANADA. VG Instruments Canada Inc. 115 Place Frontenac, Pointe-Claire, Quebec, H9R 4Z7. Tel: (514) 695-6257.
WEST GERMANY. VG Instruments GmbH. Hasengartenstraße 14,Postfach 5869, 6200 Wiesbaden. Tel: (06121) 71090.
FRANCE. VG Instruments. 5 Avenue Gallieni, 94250 Gentilly. Tel: (1) 47406160.
ITALY. VG Instruments. Viale Dell'Assunta 101, 20063 Cernusco Sul Naviglio, Milano. Tel: (2) 924 8808.
THE NETHERLANDS. VG Instruments BV. PO Box 171, 1380 AD. Weesp. Tel: (2940) 80484.
BELGIUM. VG Instruments NV. Excelsiorlaan 1 Box 2, 1930 Zaventem. Tel: 322 725 2410.
SCANDINAVIA. VG Instruments AB. Box 45199, S-104 30 Stockholm. Tel: 08-311035.
CHINA. VG Instruments. Apartment 1008 Beijing Yanshan Hotel, Beijing 100086. Tel: 1 256 4309. Telex: 211203.
KOREA. VG Instruments Korea. Dong-il Building, 58-6 Nonhyun-dong, Kangnam-Ku, Seoul. Tel: (01) 548 2983. Telex: 28523.
JAPAN. Jasco International Co. Ltd. 2-4-21 Sennin-cho, Hachioji City, Tokyo 193. Tel: 010813 42666 1321. Telex: 2862515.

CIRCLE 142 ON READER SERVICE CARD

quency patterns. Because lanosterol is a bulkier molecule than cholesterol, we have compared temperature-dependent spectra of liposomes reconstituted separately with lanosterol and cholesterol to deduce the modulating effects of sterols on the dynamic and packing properties of the membranes.

Interdigitated chain bilayers: lipid/antibiotic interactions. The fluid mosaic model serves as the working hypothesis for modeling membrane behavior, although the initial simplistic view of integral proteins floating in a sea of lipids has been refined. We now recognize, for example, that protein–protein contacts within the membrane are common and that the protein influences its surrounding matrix lipids through the formation of annular rings of boundary lipids.

Recently, the suggestion and demonstration of explicit domain structures within the bilayer have begun to provide a basis for further understanding the role of various lipid–lipid and lipid–protein interactions in modifying membrane function. Among the different types of domains available to the bilayer matrix, partially and completely interdigitated bilayer lipid chains are of current biophysical interest (*12*). In interdigitated chain bilayers, the lipid hydrocarbon chain moieties penetrate across the bilayer center; for completely interdigitated systems, the terminal methyl groups from the hydrophobic region of an opposing monolayer pack near the membrane's more polar interfacial region. In this packing motif, saturated chain diacylphospholipids, for example, exhibit four hydrocarbon chains per head group instead of the usual two chains per head group in the conventional bilayer. As a consequence of chain interdigitation, model membrane systems show a decrease in the thickness of the bilayer and a concomitant ordering of the lipid chains.

Consider the interaction of a series of macrolide polyenes, amphotericin B, amphotericin A, and nystatin A_1 (Figure 5), with a model bilayer composed entirely of the saturated chain diacyl lipid 1,2-dipalmitoylphosphatidylcholine (DPPC). These polyene antibiotics represent a class of natural products with potent antifungal properties. Although it is clear that the mechanism involving antibiotic–cellular interaction occurs at the level of the membrane interface, the nature of the interaction by which cell death is induced by these antibiotics is not fully understood. One common hypothesis suggests that the formation of transmembrane polyene–sterol channels may be involved in allowing cellular components to leak out by increasing the

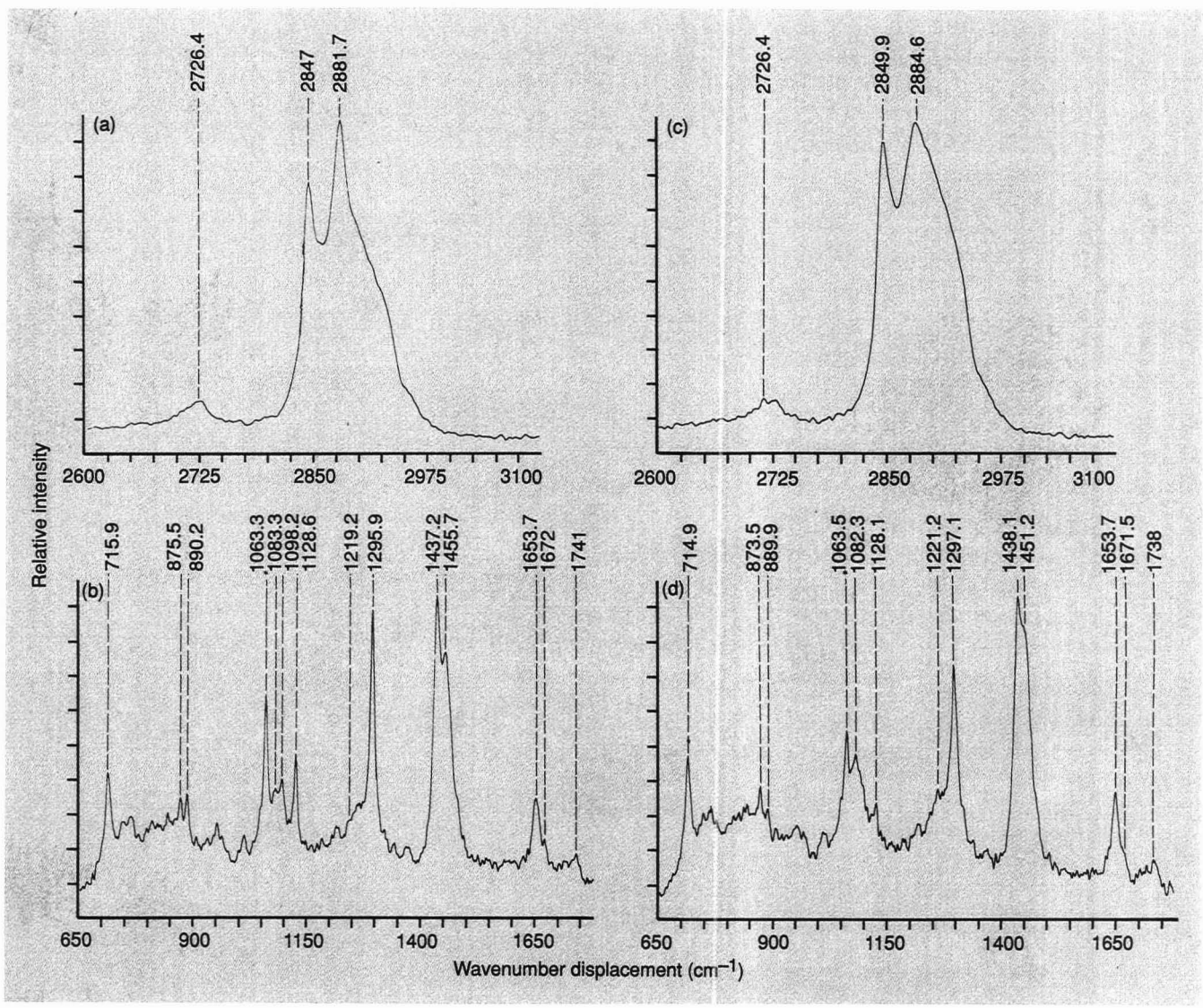

Figure 4. FT-Raman spectra of an aqueous dispersion of 1-palmitoyl-2-oleoylphosphatidylcholine (POPC) bilayer assemblies containing 18 mol % lanosterol in the gel (a and b) and liquid crystalline (c and d) phases.

membrane's permeability characteristics. Our approach is to examine the morphological response of DPPC bilayers, reconstituted both with and without cholesterol, to the binding activity of amphotericin B and amphotericin A.

Figure 6 shows both the conventional dispersive Raman spectrum and the FT-Raman spectrum of the DPPC/amphotericin B complex in the C–H stretching mode region. Because the hydrophobic conjugated polyene portions of the antibiotic ring lead to highly colored yellow–orange compounds, the selective resonance or preresonance enhancement and fluorescent effects induced by visible and UV laser radiation preclude a complete characterization of the various possible membrane complexes. Thus the upper curve in Figure 6, obtained with argon-ion radiation, is virtually featureless in the important 2900-cm^{-1} spectral region of the DPPC bilayer. In contrast, the near-IR FT-Raman spectrum reflects the bilayer complex in its low-temperature gel phase.

The spectral region in Figure 6 is dominated by the two lipid chain methylene features at ~2850 and 2880 cm^{-1}, which correspond to the CH_2 symmetric (in-phase) and antisymmetric (out-of-phase) stretching modes, respectively. In monitoring bilayer responses and membrane perturbations, the peak height intensity ratios I_{2850}/I_{2880} and I_{2935}/I_{2880}, determined as a function of temperature, provide useful indices for gauging lipid packing effects and determining relative bilayer order/disorder parameters. In particular, the I_{2850}/I_{2880} index reflects primarily interchain interactions whereas the I_{2935}/I_{2880} intensity ratio measures effects originating from changes in intrachain *trans/gauche* isomerization superimposed on the chain–chain interactions (*11*).

Comparisons of the chain–chain interactions between pure multilamellar DPPC assemblies and bilayer complexes of amphotericin A and B, in the presence and absence of cholesterol, are summarized in Figure 7 in terms of the relevant I_{2850}/I_{2880} intensity parameters. The head and tail of each arrow, representing a specific liposomal assembly or complex, correspond to temperatures of approximately 41.5 °C and 25 °C, respectively. The values of the I_{2850}/I_{2880} indices at these two temperatures provide a measure of the intermolecular lipid chain order for the aqueous dispersion of each liposome. (Because of slight differences in the physical antibiotic–lipid packing characteristics, the low gel-phase temperatures may deviate several degrees from the 25 °C DPPC reference bilayer. The possible small discrepancies in temperature are not problematic, however, because we are concerned primarily with the trends displayed in the figure.) Thus for the pure DPPC multilamellar system, the I_{2850}/I_{2880} peak height intensity ratio of about 0.77 for the 25 °C gel phase is characteristic of a bilayer whose chains are hexagonally packed. A value of about 0.98 reflects a normal liquid crystalline DPPC phase. (The phase transition temperature T_m between the gel and liquid crystalline states of aqueous, uncomplexed DPPC dispersions is 41 °C.)

Both amphotericin A and B significantly order the bilayer chains (lower values of I_{2850}/I_{2880}); in particular, the 25 °C spectra reflect intensity ratios of 0.67 and 0.65, respectively, for the two complexes. Because other membrane surface-active species (such as polymyxin B, another cyclic antibiotic) are known from X-ray diffraction studies to induce bilayer chain interdigitation, and because the observed I_{2850}/I_{2880} ratios in the 25 °C regime correspond to Raman data for known interdigitated systems, we interpret the lipid-ordering properties of these two polyene macrolide antibiotics as originating from the induced interdigitated chain membrane morphology. In contrast to the

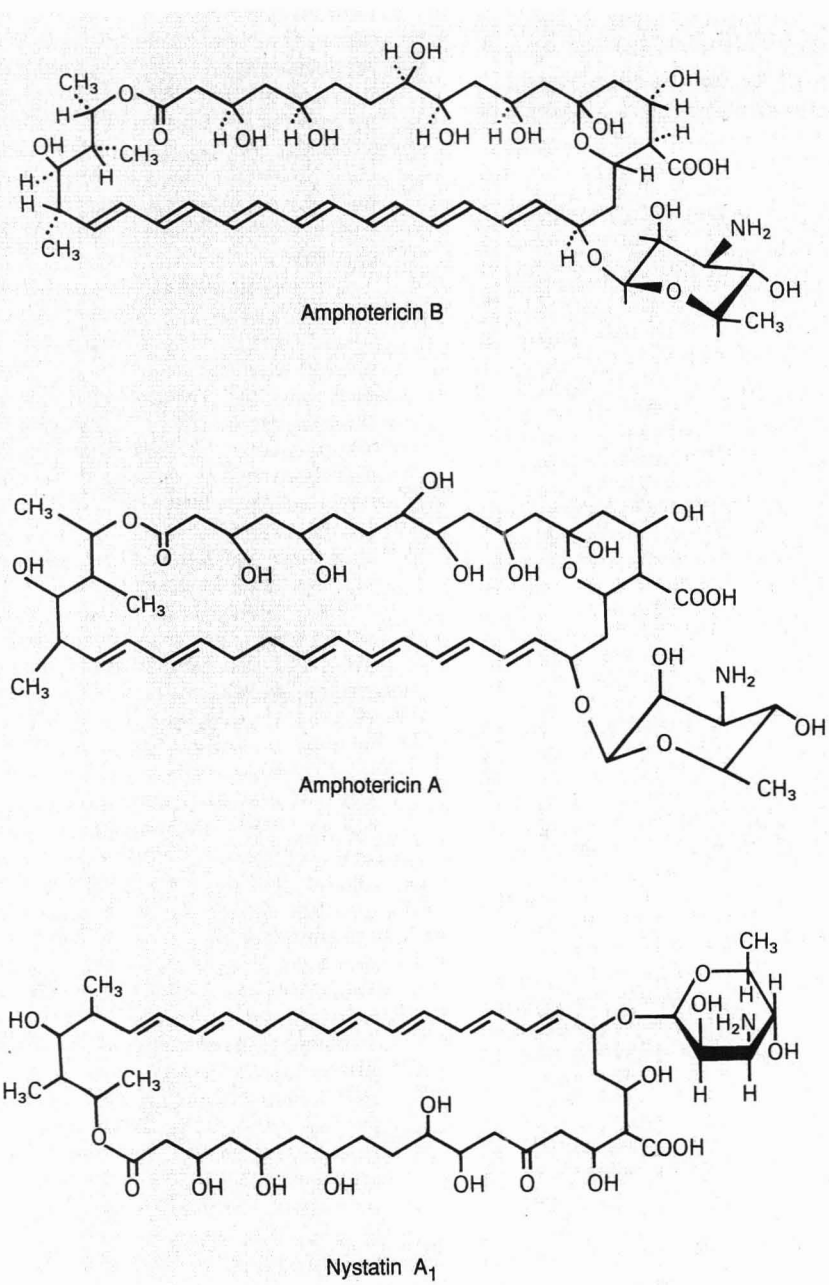

Figure 5. Structures of amphotericin B, amphotericin A, and nystatin A_1.

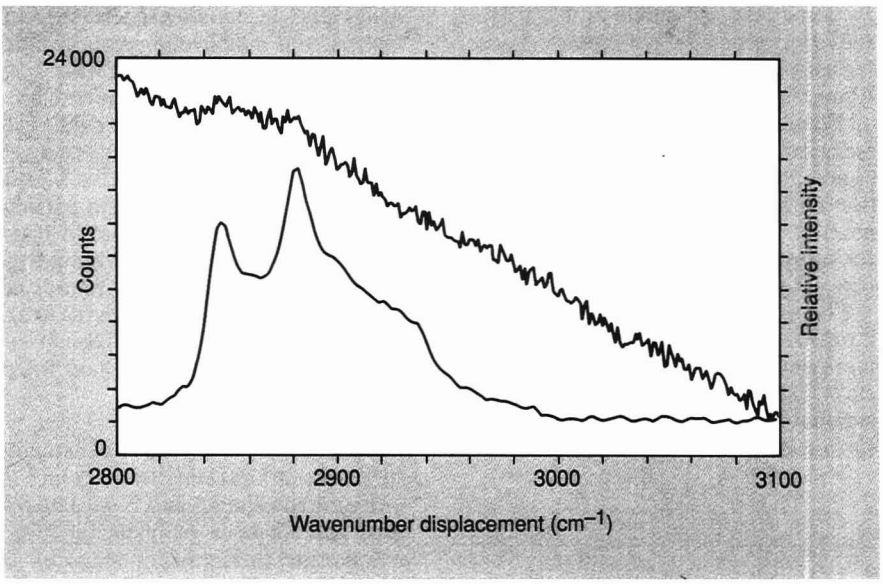

Figure 6. Dispersive Raman spectrum (top) and FT-Raman spectrum (bottom) of polycrystalline 1,2-dipalmitoylphosphatidylcholine (DPPC) bilayers containing amphotericin B.

(DPPC: Amphotericin B mole ratio equals 24:1.)

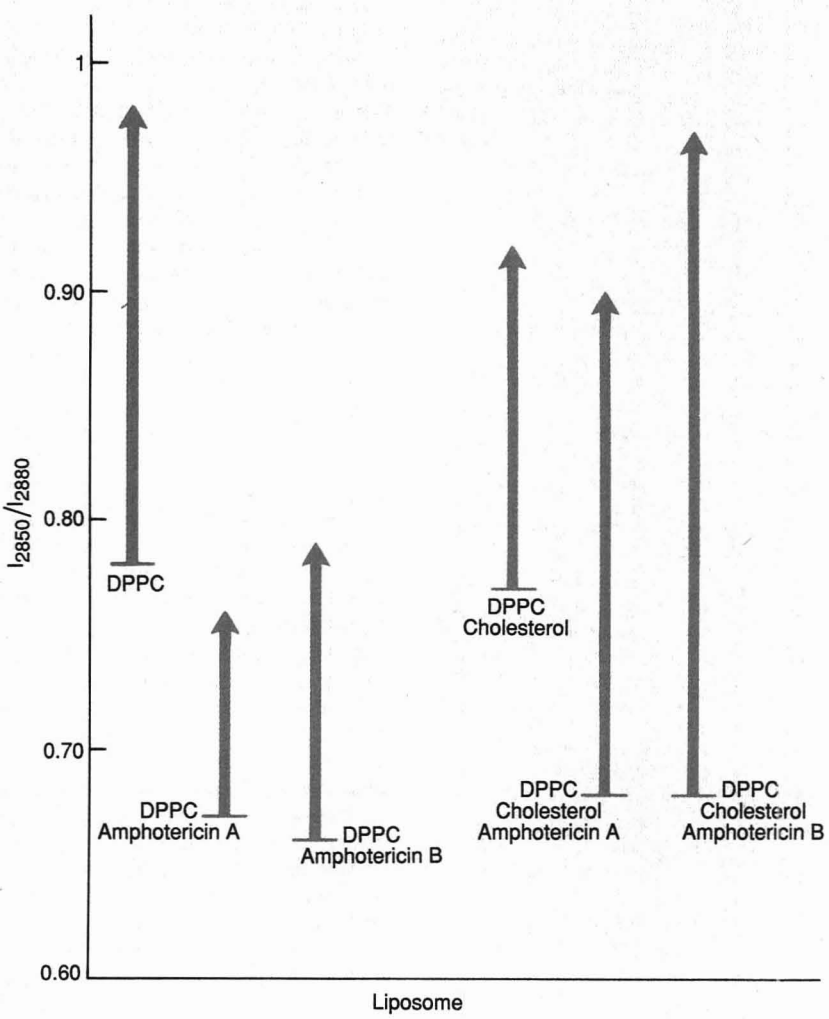

Figure 7. Ordering effects of polyene antibiotics on DPPC multilayers.

The I_{2850}/I_{2880} intensity ratio represents the interchain order parameter for the various liposomes at ~25 °C (tail of arrow) and 41.5 °C (head of arrow).

spectroscopic and diffraction data derived from model systems, evidence for even partially interdigitated bilayers in native or intact membrane assemblies is limited (*13*). Despite this paucity of information, interdigitated chain arrangements may represent a potentially important biological membrane architecture (*13, 14*).

As mentioned earlier, membrane cholesterol, an intrabilayer component, is known to modulate the order/disorder parameters of the lipid matrix. A comparison of the I_{2850}/I_{2880} order parameters for the various liposomes shown in Figure 7 demonstrates that cholesterol orders the liquid crystalline properties of DPPC multilayers. Although high concentrations of cholesterol generally disorder the gel phase, the lower concentrations of sterol in this experiment (18 mol %) exhibit less of an effect. When either amphotericin A or B with 18 mol % cholesterol is added, the I_{2850}/I_{2880} order/disorder parameters for the membrane chains indicate a gel-phase bilayer ordering that is comparable to systems without cholesterol.

If a sterol–antibiotic complex were formed within the bilayer, the gel-phase disorder would be substantially greater than that reported in Figure 7 because of the disrupting properties of the complex on the lipid chain packing arrangements. Thus, the data suggest that the sterol is expelled from the interior of the bilayer in the low-temperature phase; we again speculate about the possibility of interdigitated bilayer chains in these assemblies.

Also, referring to Figure 7, we observe that at higher temperatures (41.5 °C) the DPPC–cholesterol–amphotericin A complex is slightly more ordered than the reference DPPC–cholesterol systems. Surprisingly, the DPPC–cholesterol–amphotericin B complex is as disordered as liquid crystalline DPPC multilayers. It appears that amphotericin A and B, whose conjugated polyene moieties differ slightly, form rather dissimilar cholesterol complexes with the zwitterionic lipid substrate. That is, in the liquid crystalline phase, cholesterol binds externally more strongly to amphotericin B and is removed from the bilayer. In the amphotericin A complex, cholesterol may still remain within the bilayer, ordering the matrix slightly. Antibiotics in the presence of sterol, however, do not have quite the strong bilayer ordering properties observed in the binary lipid–antibiotic systems. (To minimize the differences in preparing the complexes, binary and ternary systems were hydrated from lyophilized mixtures of the appropriate components.)

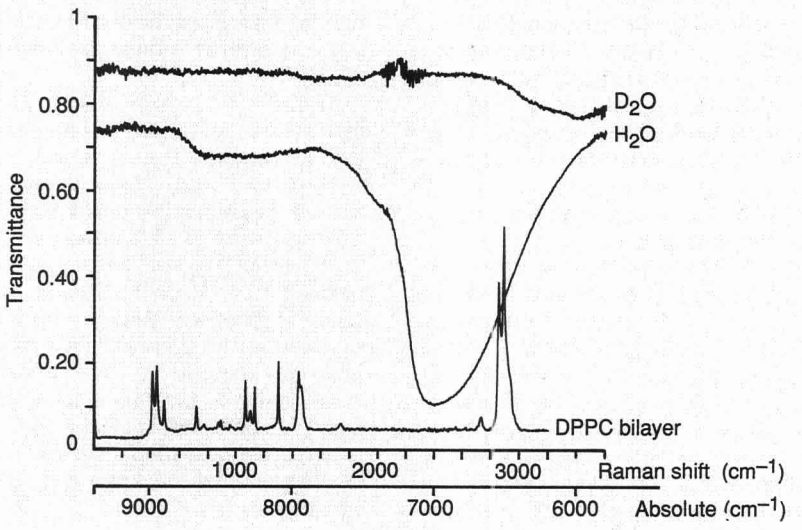

Figure 8. Near-IR absorption spectra of H_2O and D_2O superimposed on the gel-phase, near-IR FT-Raman spectrum of a DPPC bilayer.

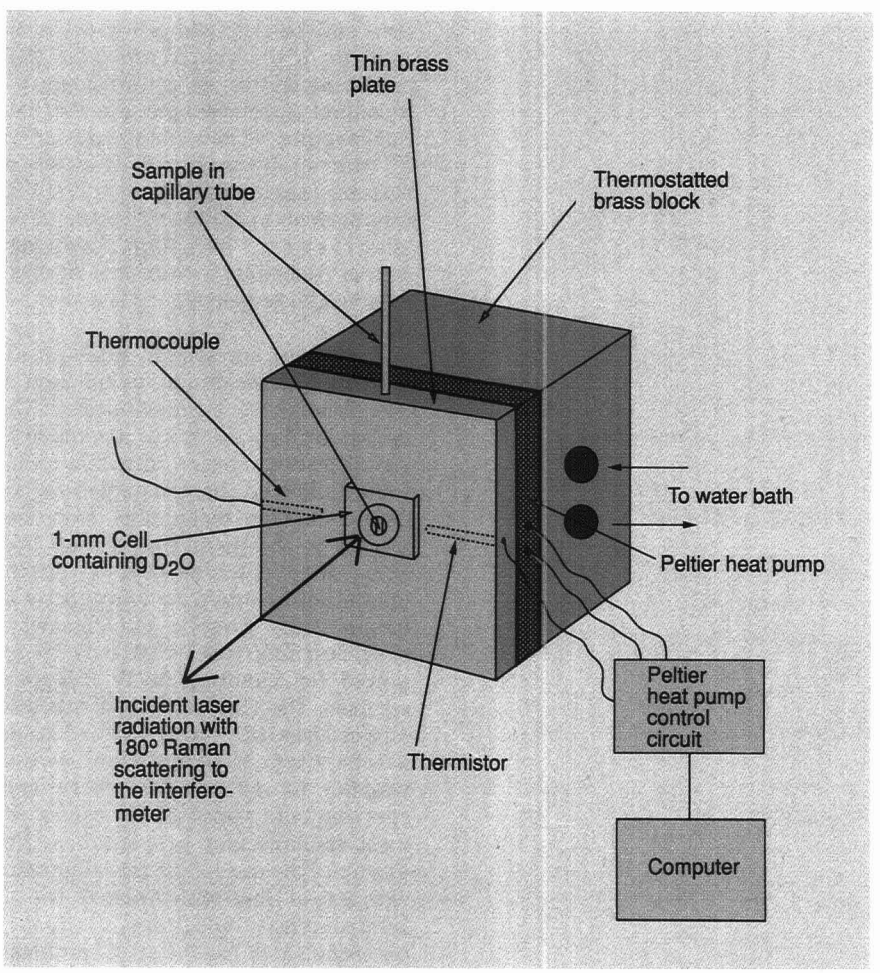

Figure 9. Schematic of thermostatted sample assembly for 180° backscattering geometry.

Temperature measurement in aqueous dispersions. In experiments involving lipid–antibiotic interactions, the temperatures of the systems were measured with externally placed thermocouples in which the sampling geometry was calibrated against a known system (such as pure DPPC liposomes) whose temperature behavior has been well characterized. To exploit fully the FT-Raman methodology in elucidating membrane properties, as in the determination of temperature profiles, it is necessary to measure sample temperatures precisely.

The problem of assessing temperatures of aqueous dispersions is illustrated in Figure 8. The absorption spectra of H_2O and D_2O are superimposed on the FT-Raman spectrum of DPPC. Although it is not shown, the exciting Nd:YAG line at 1064 nm falls in the wings of H_2O overtone bands, and the resulting absorption of radiation by the aqueous medium leads to significant sample heating.

Increasing the Raman scattered signal by increasing the incident Nd:YAG power levels can dramatically increase the temperature of the dispersion. (Because the overtone manifold is different for D_2O, the heating effect is diminished for D_2O dispersions.) In an H_2O medium, moderate heating effects often lead to a channeling in the sample and subsequently to sample diffusion in the capillary. Also, the Raman scattered C–H stretching mode photons, which are in a particularly important spectral region for interpreting bilayer reorganizations, are absorbed by another H_2O overtone, leading to a decrease in the intensity of the observed C–H stretching mode vibrations. Thus one should hydrate model bilayer systems with D_2O when possible; most native systems, however, are best spectroscopically surveyed as H_2O dispersions. For these cases the loss in C–H stretching mode signal can often be tolerated; it is virtually impossible, however, to measure the sample temperature within a desired ±0.3 °C error with either externally or internally placed thermocouples.

To obviate the temperature measurement difficulties discussed above, an "internal" standard is used. A small reference cell, containing an internal standard (usually D_2O) is placed in a thermostatted cell assembly such that the incident Nd:YAG beam passes first through the reference cell and then through the contiguous sample capillary with its biological dispersion in an H_2O medium. Thus the D_2O is in intimate thermal contact with the sample capillary.

Figure 9 presents a schematic of the thermostatted cell fabricated for the 180° backscattering geometry. Because the D_2O stretching modes reflect a sensitive temperature dependence, and because these D_2O features occur in the 2500 cm^{-1} spectral window, library

curves can easily be generated for determining accurate sample temperatures. (If the sample is dispersed in D_2O, no reference cell is required.) A separate D_2O reference cell is ideal for investigating lipid–protein complexes, because D_2O in the sample capillary would exchange with peripheral membrane protein segments. Using a thermostatted sample chamber and a Peltier device for precise temperature control, we are able to generate library spectra with a dispersive instrument employing visible laser excitation. From data reduction techniques, temperature measurements well within ±0.3 °C can be attained from the FT-Raman D_2O spectra excited with near-IR radiation.

Figure 10 shows the differences in measuring the gel to liquid crystalline phase transition region for DPPC using an externally attached thermocouple and the D_2O reference calibration method. (In this example the model bilayer assembly was hydrated directly with D_2O.) Although fewer temperature points were recorded than are usually required for a complete profile, a temperature-dependent curve in terms of the I_{2850}/I_{2880} order/disorder parameters may still be fit to a two-state model (*15*) to extract reliable phase transition temperatures T_m.

The central curves on the figure represent least-squares fits of the spectral data. The outer curves represent the calculated curves plus and minus three standard deviations, respectively. Although the gel phase and liquid crystalline phase order/disorder parameters are correct for the externally placed thermocouple, the highly cooperative, narrow phase transition region characteristic of pure DPPC liposomes is, instead, quite broad, yielding a low T_m. For the D_2O internal temperature calibration method, however, the correct DPPC temperature profile is obtained, exhibiting a sharp, first-order gel to liquid crystalline phase transition at 41.3 °C.

The ability to merge under computer control the operations of changing the sample temperature, by means of the solid-state Peltier heat pump, with sample equilibration and spectral acquisition enables us to obtain routinely both ascending and descending temperature profiles, which are subsequently processed through our laboratory computer network. This methodology has been successfully applied to a wide variety of model and intact membrane dispersions in studies designed to illuminate the predominant molecular interactions occurring at biological interfaces.

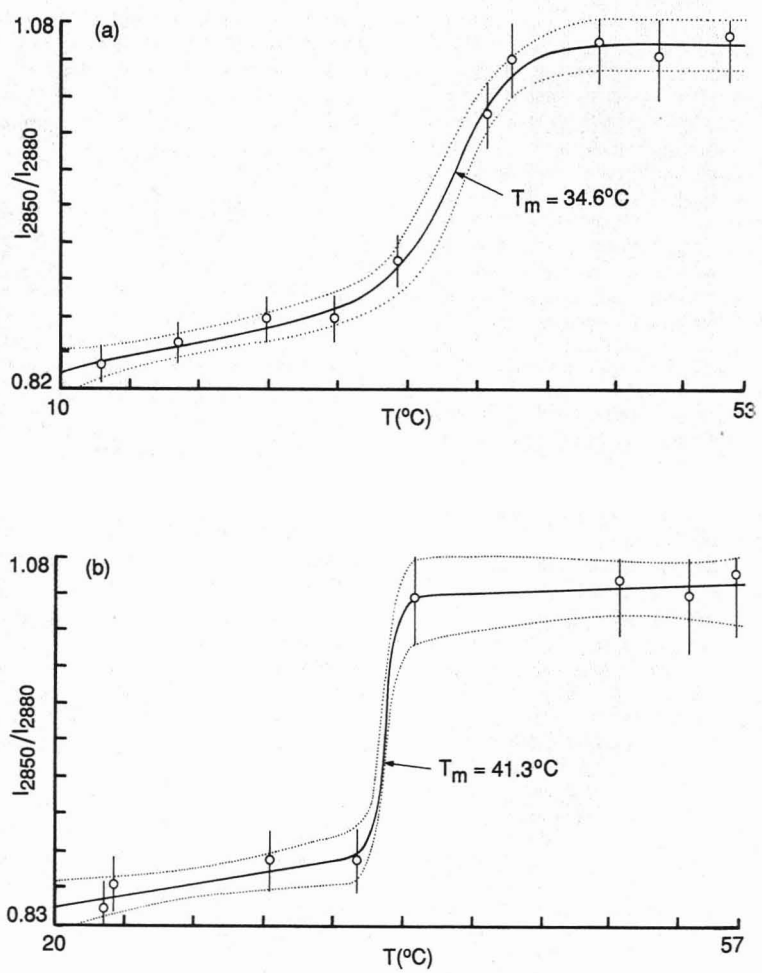

Figure 10. Temperature profile showing the change in intermolecular order of pure DPPC multilamellar assemblies using (a) an external thermocouple to determine spectral temperatures and (b) D_2O as an internal temperature calibrant.

Conclusion

We have attempted to convey both the flavor of using long-wavelength excitation coupled to interferometric instrumentation and the idea that biophysicists and biochemists can provide insight on biomolecular problems that prove unyielding to conventional vibrational spectroscopic approaches. For example, we have obtained near-IR FT-Raman spectra for a wide variety of systems ranging from human and calf lung surfactants to specific proteins related to cataract formation, the expression of Alzheimer's syndrome, and the insecticidal properties of particular bacilli.

In the past our general guide for examining biological samples has been to use dispersive instrumentation if the molecular dispersion was amenable to visible laser excitation with either photomultiplier or charge-coupled device detectors. Our techniques have improved to the point that we are now going directly to the near-IR instrumentation to obtain Raman spectra of biomolecules. Despite the somewhat steep learning curve that may be required for handling many biological samples, the flexibility and inherent advantages of near-IR FT-Raman spectroscopy offer sufficient overall benefits to make it the vibrational spectroscopic approach of choice for most biomolecular preparations. For example, the ease of sample alignment with sets of fiber-optic bundles; the interferometer's multiplex, frequency precision, and resolution advantages; and the ability to control and determine precisely the temperatures of dilute, fragile molecular aggregates all justify an optimistic outlook toward applying FT-Raman spectroscopy to even the more recalcitrant biological systems.

We would like to thank the Perkin-Elmer Corporation for the generous loan of an FT-Raman spectrometer. We would also like to acknowledge the participation of R. G. Adams and V. F. Kalasinsky in these studies.

References

(1) Hirschfeld, T.; Chase, D. B. *Appl. Spectrosc.* **1986,** *40,* 133–37.
(2) Chase, D. B. *J. Am. Chem. Soc.* **1986,** *108,* 7485–88.
(3) Jennings, D. E.; Weber, A.; Brault, J. W. *Appl. Opt.* **1986,** *25,* 284–90.
(4) Zimba, C. G.; Hallmark, V. M.; Swalen, J. D.; Rabolt, J. D. *Appl. Spectrosc.* **1987,** *41,* 721–26.
(5) Jennings, D. E.; Weber, A.; Brault, J. W. *J. Mol. Spectrosc.* **1987,** *126,* 19–28.
(6) Lewis, E. N.; Kalasinsky, V. F.; Levin, I. W. *Appl. Spectrosc.* **1988,** *42,* 1188–93.
(7) Lewis, E. N.; Kalasinsky, V. F.; Levin, I. W. *Anal. Chem.* **1988,** *60,* 2658–61.
(8) Lewis, E. N.; Kalasinsky, V. F.; Levin, I. W. *Anal. Chem.* **1988,** *60,* 2306–09.
(9) Lewis, E. N.; Kalasinsky, V. F.; Levin, I. W. *Appl. Spectrosc.* **1989,** *43,* 156–59.
(10) Nicolson, G. L.; Singer, S. J. *Science* **1972,** *175,* 720–31.
(11) Levin, I. W. In *Advances in Infrared and Raman Spectroscopy*; Clark, R.J.M.; Hester, R.E., Eds.; Wiley-Heyden: New York, 1984; Vol. 11, pp. 1–48.
(12) McIntosh, T. J.; Daniel, R. F.; Simon, S. A. *Biochim. Biophys. Acta* **1983,** *731,* 109–14.
(13) Lewis, E. N.; Levin, I. W.; Steer, C. J. *Biochim. Biophys. Acta* **1989,** *986,* 161–66.
(14) Levin, I. W.; Thompson, T. E.; Barenholz, Y.; Huang, C. *Biochemistry* **1985,** *24,* 6282–86.
(15) Kirchoff, W. H.; Levin, I. W.; *J. Res. Nat. Bur. Stand.* **1987,** *92,* 113–28.

Ira W. Levin, deputy chief of the Laboratory of Chemical Physics and chief of the section on Molecular Biophysics at the National Institute of Diabetes and Digestive and Kidney Diseases at NIH, received a B.S. degree from the University of Virginia and a Ph.D. from Brown University. Since joining NIH in 1963, his interests have ranged from absolute intensity studies and normal coordinate analyses to elucidating the lipid–lipid and lipid–protein interactions governing reorganizations in biological membranes. Current interests include application of IR and Raman spectroscopies to characterize novel lipid morphologies.

E. Neil Lewis received a B.S. degree and a Ph.D. from the Polytechnic of Wales in the United Kingdom. His research interests include the use of Raman and IR spectroscopies for studying biomembranes and related macromolecular systems of biophysical relevance.

Malvern - the complete answer to particle characterization

Malvern offer the most comprehensive and advanced range of particle sizing and zeta potential equipment available anywhere.

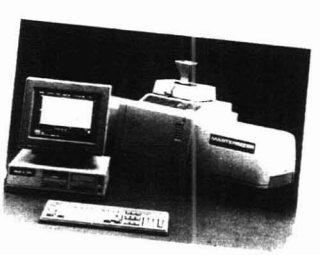

Direct dry powder analysis with MasterSizer - already the world's most popular laser particle sizer, its new Dry Powder Feeder makes it even quicker and more versatile. Overall size range is 0.1-600 microns and MasterSizer is the only one to offer genuine Mie analysis.

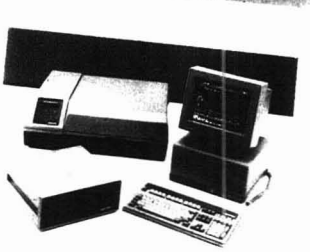

Zeta potential and submicron particle sizing - the Malvern ZetaSizer 3 offers the ultimate in PCS particle sizing using unique multi-angle analysis for reliable, detailed size distributions from 3 nanometres to 3 microns. Its electrophoresis capabilities extend from strong electrolyte media to non-polar liquids such as hydrocarbons with full zeta potential distributions measured in seconds. For characterizing colloidal dispersions, it has no equal.

The Malvern API AeroSizer uses aerodynamic techniques combined with advanced laser technology to give extremely high resolution particle size analysis of powders from 0.5 to 200 microns.

MALVERN

Malvern Instruments Inc.
10 Southville Rd, Southborough, MA 01772, USA
Tel: (508) 480 0200 Fax: (508) 460 9692

Malvern Instruments Limited
Spring Lane South, Malvern, Worcs. WR14 1AQ, UK.
Telephone: (0684) 892456 Telex: 339679 Fax: (0684) 892789

CIRCLE 92 ON READER SERVICE CARD

DIALOG INTRODUCES ANOTHER TABLE OF BASIC ELEMENTS FOR YOUR LAB.

There's no symbol for *information* in the Periodic Table. Yet nothing could be more crucial to your research than complete, accurate technical and business information.

That's why many chemists consider DIALOG™ an essential element in the modern lab.

As the world's largest online knowledgebank, DIALOG gives you access to a whole world of critical information. Right in your own lab.

For starters, you can tap into the crucial scientific data. DIALOG has detailed information on everything from compound identification to chemical safety data, property data, substance and substructure.

Then you can expand your focus by accessing important, related data that will enable you to look at your work in a broader context.

For example, you can investigate patents, competitive projects, new product markets, and worldwide industry trends. In fact, you can investigate any topic, anytime.

And you won't have to sacrifice depth for the sake of breadth. DIALOG is updated continuously, so the data is always comprehensive and current. And many citations can be conveniently retrieved in full text.

Call today for more information and a free Periodic Table Reference Card. Once you've examined them, you'll see how DIALOG can become a basic element of all your research.

Call us toll free at 800-3-DIALOG, (800-334-2564). Or request information by Fax at 415-858-7069.

DIALOG INFORMATION SERVICES, INC.
A Knight-Ridder Company

The world's largest online knowledgebank.

© 1989 Dialog Information Services, Inc., 3460 Hillview Avenue, Palo Alto, California 94304. All rights reserved. DIALOG is a service mark of Dialog Information Services, Inc. Registered U.S. Patent and Trademark Office.

CIRCLE 30 ON READER SERVICE CARD

Perspectives on the FUTURE OF ANALYTICAL MASS SPECTROMETRY

Cecilia Basic, Jody A. Freeman, and Richard A. Yost
University of Florida
Department of Chemistry
Gainesville, FL 32611

So read a billboard leading to the new city of Oak Ridge, TN, in late 1942. In direct contrast to the spirit of the "secret city" of the early 1940s Manhattan Project, attendees of the 43rd Annual Summer Symposium on Analytical Chemistry gathered July 24–27, 1990, to openly discuss the current and future directions of the rapidly growing field of analytical mass spectrometry (MS). The last summer symposium to feature analytical MS was held in 1981; it was time, therefore, to compare progress notes gathered over the past nine years and to focus once again on what has proven to be an active and exciting area of analytical chemistry.

The symposium was hosted by W. D. "Dub" Shults, director of the Division of Analytical Chemistry at Oak Ridge National Laboratory (ORNL)—the only division of its kind in the national labs—and chaired by Dave Donohue, also from ORNL. Active participation from the audience throughout the symposium was encouraged by program chair Graham Cooks of Purdue University, thus setting an atmosphere for the free exchange of ideas.

The oral sessions commenced with a marathon Wednesday, reminiscent of the 24-hour-per-day pace of the early physicists of Oak Ridge; three sessions ran from 8:30 A.M. to 10:30 P.M., testing the stamina of experts and neophytes alike. Wednesday's sessions, coupled with those on Friday, amounted to 27 invited talks along with six submitted posters and a special graduate student session on Thursday. (Details of the symposium program can be found in the April 1, 1990, issue of ANALYTICAL CHEMISTRY.)

In keeping with the theme of the fu-

0003-2700/90/A362-1113/$02.50/0
© 1990 American Chemical Society

ture of analytical MS, young mass spectrometrists—the future of our discipline—played an important role in the conference. Young academics met during part of the dinner hour on Wednesday to share their early experiences as academicians and to offer both advice and encouragement to those considering a future career in academics. To prove that analytical MS in an academic environment can be both challenging and rewarding, an afternoon session was appended to Friday's agenda featuring talks from four young academic mass spectrometrists.

A new feature of the summer symposium, introduced this year by Cooks, was the National Graduate Student Award Competition—a first-hand "look at the future of mass spectrometry." The competition, focusing on the research efforts of students during their graduate careers, included six oral and six poster presentations by finalists (Table I) chosen from entries nationwide. The finalists' presentations were of high quality, making selection of the top oral and top poster for cash prizes a difficult task for the jury.

The winners in each category are pictured above. The winner of the oral competition was James Gord, working with Ben Freiser at Purdue University, whose talk was entitled "Probing Gas-Phase Ion–Molecule Reaction Dynamics through the Measurement of Product Ion Kinetics by Using FT-ICR Mass Spectrometry." Jeffrey Klingler, working with Willard Harrison at the University of Florida, won the poster competition with a presentation entitled "Time-Resolved Glow Discharge Mass Spectrometry (GDMS)."

The 45 presentations made during the symposium provided a comprehensive perspective on the state of the art in analytical MS and on future directions in the field. Many of the exciting developments discussed were in the areas of new instrumentation, analysis of high molecular weight species, and the incorporation of chemistry (i.e., gas- and solution-phase reactions) into mass spectrometric techniques.

Instrumentation development

Analytical MS is known for its diversity of instrumentation, as seen not only in the variety of mass spectrometers in use but also in the creative engineering of interfaces between MS and other analytical methods (e.g., GC/MS, LC/MS, GC/IR/MS). The presentations made at the summer symposium not only reflected this diversity but proved that instrumental development will continue to be a flourishing area of research.

The National Graduate Student Award winners along with conference organizers: (from left) Graham Cooks, program chair; Dub Shults, host; Jeffrey Klingler, poster winner; James Gord, oral winner; and Dave Donohue, general chairman.

Table I. National Graduate Student Award Competition Finalists

Finalist	University/Adviser	Topic
Orals		
James Boyle	Yale L. D. Pfefferle	Combustion diagnostics by vacuum-UV photoionization TOF-MS
James Gord	Purdue Ben Freiser	Probing gas-phase ion–molecule reaction dynamics with an FT-ICR mass spectrometer
David Hrubowchak	Penn State Nick Winograd	Surface characterization by ion-induced desorption and multiphoton resonance ionization
Michael Ikonomou	Alberta Paul Kebarle	Electrospray and ion spray ionization MS
Kuangnan Qian	Delaware Jean Futrell	CID of polyatomic ions by angle-resolved crossed-beam MS/MS
Mingda Wang	Ohio State Alan Marshall	Improvements in FT-ICR trapping techniques
Posters		
Jody Freeman	Florida Rick Yost	Modeling in vivo mutagenicity by MS/MS
Kent Henry	Cornell Fred McLafferty	Electrospray ionization on an FT-ICR mass spectrometer
Jeffrey Klingler	Florida Willard Harrison	Time-resolved glow discharge MS
Arthur Moseley	North Carolina Jim Jorgenson	Nanoscale LC/MS interfaces
Lynn Teesch	Emory Jeannette Adams	Fragmentation mechanisms of peptide–metal ion complexes
Gert von Helden	California at Santa Barbara Mike Bowers	LDMS of metal ion clusters

Of particular note is the increasing use of ion-trapping techniques—both Fourier transform ion cyclotron resonance (FT-ICR) and quadrupole ion trap mass spectrometry (QITMS)—in analytical MS. At the 1981 symposium only one paper concerning ion traps was presented; in 1990 almost one-third of the presentations used ion traps in some form. Ion traps are unique in the control they allow over the mass and energy of ions stored for extended periods of time; thus, ion–neutral interactions can be enhanced and the resulting gas-phase processes studied. Sequential stages of MS analysis (i.e., MS/MS/MS . . . MS^n) can also be performed, extending the analytical capabilities of ion-trapping techniques.

Fundamental studies of the effect of the various trapping parameters—such as pressure, time, and excitation—on the resultant mass spectra of simple to complex molecules could be considered a subtopic of this year's symposium. James Gord from Purdue University studied the dynamics of the reaction between the cations of several transition metals and benzene. Measurement of the product ion translational energies provided details of the potential energy surfaces of the reactions (*1*). Such detail will aid in understanding the fragmentation of larger, more complex molecular systems in FT-ICR mass spectrometers. Jennifer Brodbelt-Lustig from the University of Texas used a QIT mass spectrometer to study the degree of adduct formation and subsequent dissociation and reactivity of a series of small molecular systems (e.g., oxyaromatics). These studies lend insight into the changes in the ion populations as a function of reaction time, sample pressure, and excitation voltages (*2*).

Ben Freiser of Purdue University described the combination of lasers and MS as the "perfect marriage." Indeed, lasers of all varieties (dye, CO_2, Nd:YAG) are becoming more popular as ionization, desorption, and photodissociation sources with trapping and other mass spectrometric techniques. Freiser used lasers and FT-ICR to study potential energy surfaces, kinetic energy releases, and collisional and radiative relaxation rates for transition metal complexes. The first stable, doubly charged mixed metal dimer, $LaFe^{2+}$, was observed by photodesorption of La^{2+} and subsequent reaction with $FeCO_5$ to produce $LaFe(CO)_2^{2+}$ followed by argon collision-induced dissociation (CID) to give the doubly charged metal dimer (*3*).

Murray Johnston from the University of Delaware used a coherent source of vacuum-ultraviolet (vacuum-UV) radiation (Nd:YAG laser tripled twice to 118 nm [10.5 eV]) with a time-of-flight (TOF) mass spectrometer to study neutral decomposition chemistry by first photodecomposing a neutral gas-phase species and then photoionizing the decomposition products. The main drawback of laser systems is their relatively high cost; thus, Dave Russell's studies obtained with a $3000 N_2 laser on a new hybrid EB TOF mass spectrometer were received with great interest. The introduction of these low-cost N_2 lasers may bring about even greater use of lasers in MS studies (*4*).

Paralleling the growth of lasers is a resurgence in the use of TOF mass spectrometers, as seen in the work of Russell and Johnston. The intrinsic pulsed operation and low cost of TOF mass spectrometers make them attractive counterparts in laser studies. Further studies using a laser TOF mass spectrometer were presented by Bob Cotter from The Johns Hopkins University, who performed both IR and UV matrix-assisted laser desorption (LD)-TOF-MS with a pulsed extraction lens to study the mass spectra of biomolecules up to 116 000 Da (β-galactosidase of *E. coli*) (*5*). John Boyle of Yale University coupled a ceramic microjet reactor designed by John Fenn to a TOF mass spectrometer with vacuum-UV photoionization to study stable and labile combustion intermediates.

Analysis of high-mass molecules

At the 1981 summer symposium, compounds ranging from 1000 to 10 000 Da were considered to be "high mass." Today, biomolecular species 10 times that weight are being analyzed. As the mass range accessible to MS continues to increase, there will be a greater demand for successful interfacing of separation and ionization techniques that are amenable to answering questions of biochemical concern.

Dick Smith from Pacific Northwest Laboratory illustrated the current capabilities of capillary zone electrophoresis/electrospray ionization (CZE/ES) MS in biomolecular analysis by presenting the structurally specific spectra of a 23-fmol sample of cytochrome *c* (*6*). He found that for well-behaved systems, the charged states are sufficiently resolved to permit molecular weight determination with precision of $< 0.001\%$ in the 100-kDa range. Currently, however, CZE/ES is limited by the large background currents arising

SMALL WONDERS.

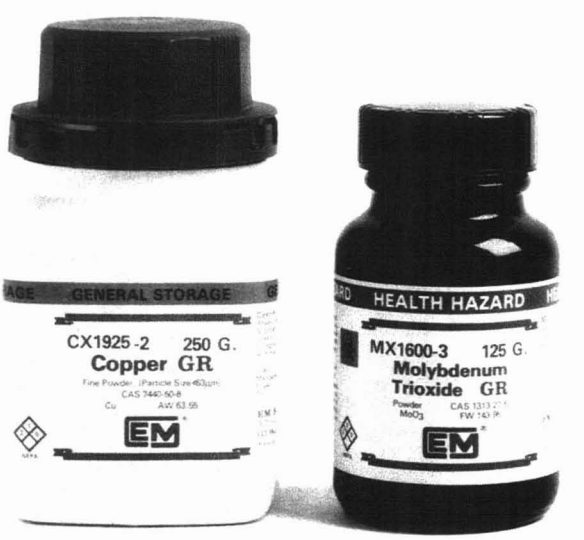

Good things come in small packages. And it's true. Our downsized reagents ensure purity and reduce disposal costs. All are unconditionally guaranteed. For a free catalog, call **1-800-222-0342.**

A Division of EM Industries, Inc.
480 Democrat Road, P.O. Box 70
Gibbstown, NJ 08027
Associate of E. Merck, Darmstadt, W. Germany

EM®
EM SCIENCE
We have service down to a science.

CIRCLE 32 ON READER SERVICE CARD

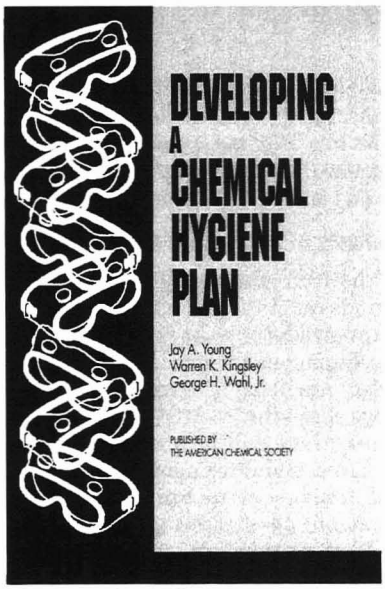

Developing a Chemical Hygiene Plan

This essential "how-to" book tells you what you need to know to comply with the federal regulation known as the "OSHA Laboratory Standard" which requires chemical hygiene plans. Developed by the ACS Committee on Chemical Safety, the guide presents hygiene plans that can be modified according to the particulars of individual laboratories. Among the topics covered in this valuable book you'll find

- **application of the OSHA Laboratory Standard**
- **history of the OSHA Laboratory Standard**
- **standard operating procedures**
- **control measures and equipment**
- **records and recordkeeping**

In addition, several appendices are provided, including employee information and training techniques, exposure assessment procedures, the elements of an emergency procedure plan, the OSHA Laboratory Standard, a list of contacts for states that have OSHA-approved state plans, and a list of acronyms.

This reference is critical to all lab supervisors who must have in place by January 31, 1991, a chemical hygiene plan that outlines specific work practices and procedures ensuring employee protection from health hazards associated with hazardous chemicals.

by Jay A. Young, Warren K. Kingsley, and George H. Wahl
Developed by the Committee on Chemical Safety of the American Chemical Society

72 pages (1990) Paperbound
ISBN 0-8412-1876-5 LC 90-46721
$18.95

O • R • D • E • R F • R • O • M

American Chemical Society
Distribution Office, Dept. 87
1155 Sixteenth St., N.W.
Washington, DC 20036
or CALL TOLL FREE

800-227-5558
(in Washington, D.C. 872-4363) and use your credit card!

from the CZE-supporting electrolyte. Smith suggested that the development of isotachophoresis/ES MS might overcome the problems caused by the electrolyte. He projected that improved MS interfacing techniques may begin to fulfill the increasing demand for information regarding the microheterogeneity of biomolecular species.

Evan Williams from Stanford University presented a unique combination of CZE and pulsed laser ionization, which used the continuous ice formation witnessed at the end of the CZE tip. He found that biomolecular species could be ablated from the ice into the gas phase and laser ionized. Following the laser pulse, the ice reforms, and the next sample can be ablated, thus coupling the intrinsic continuous-flow operation of CZE with the pulsed nature of a laser system.

Ken Busch of the Georgia Institute of Technology has accessed species of even greater mass (up to ≈100 000 Da) than those analyzed thus far by CZE by developing a new interface between planar gel electrophoresis and continuous-flow fast atom bombardment (FAB) MS.

The interfacing of supercritical fluid chromatography (SFC) and MS is seen as another new area of research. Susan Olesik of The Ohio State University investigated the energetics of the cluster ions formed in the jet expansion region of a combined SFC/field-enhanced ionization MS interface. Based on her studies, Olesik predicts that it will be possible to control the internal energy of the cluster ions—and thus the subsequent degree of fragmentation—by scanning through the phase transition region of the supercritical fluid carrier. Molecular weight and spectral reproducibility problems arise because of difficulties in reproducing restricter cone tips. Olesik was able to overcome these limitations with improved machining technology.

The analysis of large biomolecules will be facilitated by the successful interfacing of ESI with FT-ICR (ES-FTMS), presented by Kent Henry from Cornell University (*7*). The extremely high resolution afforded at low m/z (< 3000) permits accurate isotopic ^{13}C peak assignments. This may provide a means of assigning masses to multiply charged fragment ions following MS/MS biomolecules in an FT-ICR mass spectrometer.

Unraveling the mechanism of the ionization of large molecules in these new interface regions, as well as in ES, secondary ion mass spectrometry (SIMS), FAB, and LD, continues to be an active area of research. Kelsey Cook of the University of Tennessee studied the effect of changes in the sample matrix of electrohydrodynamically ionized mono- and di-quaternary ammonium salts to model the solution processes that may be occurring in FAB and SIMS. These processes are difficult to monitor directly with these techniques because of interferences from the primary atom beam (*8*).

Jerry Hunt of Argonne National Laboratory probed the axial and radial energy distributions of a variety of ions formed by LD and photoionization in a TOF mass spectrometer by imaging the ions with a position-sensitive detector. The velocity distributions of the ions were on the order of 1 eV.

Williams also reported the use of a vapor-deposited Pt resistance thermometer to measure the temperature of a quartz surface during nonmatrix-assisted LD. The temperatures were found to be in good agreement with theoretical calculations on the same surface (*9*).

An important conclusion of Michael Ikonomou's investigation into the mechanism of ES and ion spray ionization at the University of Alberta is that droplet charging occurs at the sprayer tip and not as the droplet travels toward the counterelectrode (*10*). These and other studies presented at the symposium indicate that rapid progress is being made in understanding the mechanisms of biomolecular ionization.

Chemical reactions in analytical MS

The study and use of chemical reactions—in both the gas and solution phases—is becoming increasingly widespread in analytical MS. Understanding gas-phase ion–molecule processes in an effort to manipulate the chemistry either before or after the mass spectrometric step is extending the analytical capabilities of MS.

Jon Amster at the University of Georgia selectively varied the exothermicity of the chemical ionization reaction of a laser-desorbed dipeptide (Ala-Val) by changing the reagent gas (from NH_3 to C_2H_4 to N_2O) to produce increasingly "hotter" ions and in so doing manipulated the fragmentation pattern of the peptide.

Scott McLuckey's search for "an analytically useful reaction" at ORNL led to the study of the proton transfer reaction between multiply protonated myoglobin (formed from electrospray with a QIT mass spectrometer) and the bases dimethylamine and 1,6-hexanediamine. The decrease in the charge state of the protein was found to vary as a function of both the proton affinity of the reagent base and the trapping time of the reaction (*11*). This use of

Introducing

BAIRD ENVIRONALYSIS+

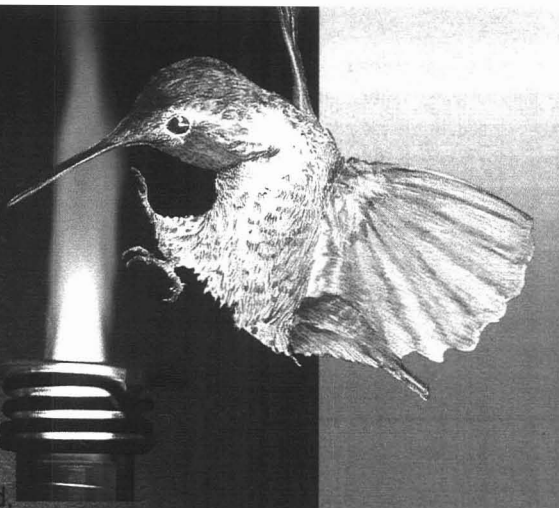

Speed and Precision for the Analytical Laboratory

For the chemist concerned with environmental analysis of water and waste, Baird has designed Environalysis+, the most carefully coordinated, modular ICP laboratory system available – the instruments and software you need to make the fastest, most delicate determinations possible (and make government requirements routine).

1 Meet or exceed EPA and CLP detection sensitivities.

The new 60-channel BAIRD ICP 2000 is assured to determine the 25 EPA-approved elements in ppb quantities better than those listed in *Method 200.7* for water and wastes analysis. In tandem with the BAIRD UDX Ultrasonic Nebulizer, it also meets the CLP sensitivity requirements for As, Se, Pb, and Tl – comprehensively and *simultaneously* accommodating every CLP analyte except Hg. Could this mean the end of expensive, one-sample-at-a-time graphite furnace AA? Yes.

2 Automate multielement determinations and save on per-sample cost.

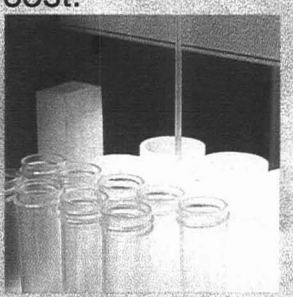

The BAIRD ICP 2000 works with a variety of random-access autosamplers having a wide range of sample/size capacities. Q.C. check and recheck can be at any preselected intervals, and, in the event of a Q.C. failure, the choice of action, including repeat analysis, is inherent in the program's software. Standardization and restandardization are routine. This tightly controlled automation is in complete compliance with all government requirements, including the CLP protocol for quality assurance and control.

3 Produce reports as quickly and easily as your analyses.

BAIRD Plasmacomp® software is fully compatible with a variety of packages that routinely generate reports required by the CLP on CLP-specified forms, as well as the computer-deliverables described by *Statement of Work 788*. And Plasmacomp's many diverse options are easily customized to meet all the needs of any ICP analytical laboratory.

Write or call today for complete information on Environalysis+.
Baird Analytical Instruments Division,
125 Middlesex Turnpike, Bedford, MA 01730.
Telephone (617) 276-6163.

IMO
Imo Industries Inc.

BAIRD ICP

CIRCLE 14 ON READER SERVICE CARD

NEW MICROWAVE DIGESTION BOMBS

PAT. PENDING

Now in two sizes, 23 ml and 45 ml.

The speed and convenience of microwave heating can now be applied to the digestion of inorganic, organic, or biological materials in a Teflon Lined Bomb. The new Parr Microwave Digestion Bombs have been designed to combine the advantages of closed high-pressure and high temperature digestion with the requirements of microwave heating. Many samples can be dissolved or digested with less than one minute heating times. As with all Parr Digestion Vessels, careful design and testing effort have gone into the safety and sealing aspects of this unique vessel and operating environment.

Call or write for Bulletin 4781 with complete technical details.

PARR INSTRUMENT COMPANY
211 Fifty-third Street
Moline, IL 61265
Phone: (309) 762-7716
Telex: 270226

CIRCLE 114 ON READER SERVICE CARD

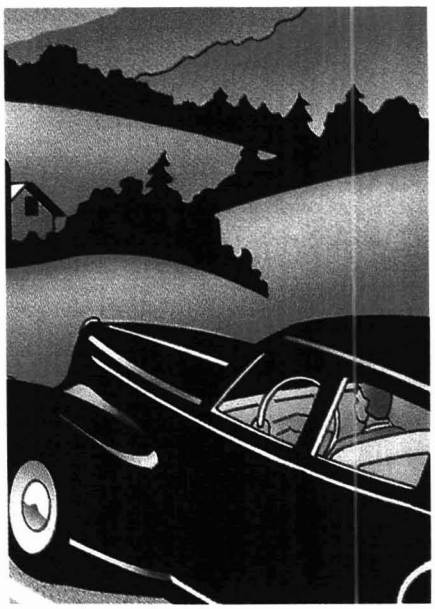

Rapid progress is being made in understanding the mechanisms of biomolecular ionization.

a basic reagent to partially deprotonate multiply protonated species can aid in peptide structure determination when multiple stages of MS are performed.

Jim Delmore of the Idaho Falls National Engineering laboratory used the gas-phase autoneutralization reaction of SF_6^- to produce a fast beam of neutrals, allowing neutral-beam SIMS analysis of cocaine on a dollar bill and malathion on an untreated leaf.

Eric Grimsrud from Montana State University described the variety of gas-phase and surface-induced reactions that can yield unexpected negative ions under electron-capture negative chemical ionization (ECNCI) conditions; he concluded that not only is CO_2 a more efficient buffer gas than CH_4 or N_2, but it also minimizes side reactions arising from radical and reduction mechanisms. These studies are of value in analyses that use ECNCI.

The successful use of chemical reactions in analytical MS has been extended from the familiar gas phase to the largely unexplored solution phase. John Bartmess of the University of Tennessee has developed a series of solution-phase reactions whose gas-phase neutral products readily form anions via dissociative detachment (*12*). For example, the in situ combination of isoamyl nitrile with a few drops of methanol produces methyl nitrate—a species that readily forms NO_2^- and $^-OCH_2NO$ ions in the gas phase. Although there is no single carbanion-forming compound, relatively simple synthesis can lead to species containing heteroatoms that form anions spanning the acidity scale.

Jeannette Adams of Emory University and her student Lynn Teesch have studied interactions between peptides and alkali and alkaline earth metal ions. By using CID of the cationized peptides produced by FAB, they concluded that the metal ions preferentially bind to the amide carbonyl sites of the peptides and not the other side chain locations, as previously suggested (*13*).

Finally, our group at the University of Florida has used electrochemistry and enzymes on line with thermospray MS/MS to elucidate the pathways of solution-phase biochemical redox reactions (*14*). We have also studied the gas-phase reactivity of known carcinogens with various nucleophiles using MS/MS. These studies clearly demonstrate the power of "chemistry" inside (or on line with) a mass spectrometer (*15*).

Summary

Unlike the secrecy of the early scientists of Oak Ridge, the free exchange of ideas between scientists at the 43rd Annual Summer Symposium on Analytical Chemistry led to the open discussion of new areas of instrumental development, new interfacing techniques, and increasingly challenging analytical problems. Chief among these challenges is the search for improved methods of analysis of high molecular weight species as questions of biochemical concern enter the realm of analytical MS. Furthermore, increasing attention is being focused on the use of chemical reactions in both the gas and solution phases to enhance the analytical capabilities of MS. By highlighting the interests of young mass spectrometrists, the symposium organizers succeeded not only in presenting the future areas of research in analytical MS but in introducing the people who will be pursuing these directives. We encourage everyone to attend the 44th Summer Symposium on Analytical Chemistry, featuring the characterization of polymers, to be held July 28–August 1, 1991, at Miami University in Oxford, OH.

References

(1) Gord, J.; Freiser, B. S. *J. Chem. Phys.* **1989,** *91,* 7530–36.
(2) Brodbelt, J.; Cooks, R. G. *Anal. Chim. Acta* **1988,** *206,* 239.
(3) Huang, Y.; Freiser, B. S. *J. Am. Chem. Soc.* **1988,** *110,* 4434–35.
(4) Strobel, F; White, M. A.; Preston, L. M.; Solonki, J.; Russell, D. H., *J. Am. Soc. Mass Spectrom,* in press.
(5) Spengler, B.; Cotter, R. J. *Anal. Chem.* **1990,** *62,* 793.
(6) Smith, R. D.; Loo, J. A.; Edmonds, C. G.; Barinaga, C. J.; Udseth, H. R. *Anal. Chem.* **1990,** *62,* 882–99.
(7) Henry, K. D.; Williams, E. R.; Wang, B. H.; McLafferty, F. W.; Shabanowitz, J.; Hunt, D. F. *Proc. Natl. Acad. Sci.* **1989,** *86,* 9075–78.
(8) Reynolds, J. D.; Cook, K. D. *J. Am. Soc. Mass Spectrom.* **1990,** *1,* 233–37.
(9) Philippoz, J.; Zenobi, R.; Zare R. N. *Chem. Phys. Lett.* **1989,** *158,* 12–17.
(10) Ikonomou, M. G.; Blades, A. T.; Kebarle, P. *Anal. Chem.* **1990,** *62,* 957–67.
(11) McLuckey, S. A.; van Berkel, G. J.; Glish, G. L. *J. Am. Chem. Soc.* **1990,** *112,* 5668–70.
(12) Thomas, D. A.; Bloor, J. E.; Bartmess, J. E. *J. Am. Soc. Mass Spectrom.* **1990,** *1,* 295–300.
(13) Teesch, L. M.; Adams, J. *J. Am. Chem. Soc.* **1990,** *112,* 5098–5104.
(14) Volk, K. J.; Yost, R. A.; Brajter-Toth, A. *Anal. Chem.* **1989,** *61,* 1709–17.
(15) Freeman, J. A.; Johnson, J. V.; Hail, M. E.; Yost, R. A.; Kuehl, D. W. *J. Am. Soc. Mass Spectrom.* **1990,** *1,* 110–15.

Jody A. Freeman (left) received her B.S. degree in chemistry from Notre Dame College of Ohio in 1986 and is working on her Ph.D. in analytical chemistry at the University of Florida. Her graduate research involves developing innovative methods for identification of DNA adducts and estimating the mutagenic/carcinogenic potential of chemicals by ion–molecule reactions in a tandem quadrupole mass spectrometer.

Cecilia Basic (right) completed her B.Sc. degree in chemistry at the University of Winnipeg, Canada, in 1985. She was introduced to MS at the University of Toronto, where she completed her M.Sc. degree in 1988. She is currently working on her Ph.D. in analytical chemistry at the University of Florida. Her studies involve probing the energetics of ions in a quadrupole ion trap mass spectrometer.

Richard A. Yost, professor of chemistry at the University of Florida, received his B.S. degree in chemistry from the University of Arizona in 1974 and his Ph.D. in analytical chemistry from Michigan State University in 1979. His interests include the education of future generations of analytical mass spectrometrists, and the instrumentation, fundamentals, and applications of tandem MS.

From pesticides/residues to food and feed processing

Journal of Agricultural and Food Chemistry

Now published monthly!

Editor:
Irvin E. Liener
University of Minnesota

Associate Editors:
G. Wayne Ivie
USDA
Marshall Phillips
USDA

Let the **Journal of Agricultural and Food Chemistry** keep you up to date on the production and safety of foods, feeds, fibers, and other agricultural products, as well as the chemical, biochemical, and nutritional aspects of foods and feeds.

As a monthly publication, the journal promises to deliver an additional 700 pages per year. Read wide-ranging reports and original research used by your colleagues virtually every working day!

1990 Rates	ACS Member** 1 Year	ACS Member** 2 Years	Nonmember 1 Year
U.S.	$ 25	$ 45	$204
Canada & Mexico	$ 41	$ 77	$220
Europe*	$ 52	$ 99	$231
All Other Countries*	$ 61	$ 117	$240

*Includes Air Service
**Member rates are for personal use only
For nonmember rates in Japan , contact Maruzen Co., Ltd.

For more information or to subscribe, contact:
American Chemical Society
Sales and Distribution Dept.
1155 Sixteenth Street, NW
Washington, DC 20036

In a hurry? Call Toll Free 1-800/227-5558 (U.S. only).
In D.C. and outside the U.S.: (202) 872-4363.

NEW PRODUCTS

UV Crosslinker binds nucleic acid samples to hybridization membranes in 15–30 s. Four modes of operation are provided. Fisher Scientific **401**

Oil. OCMA-220 oil content analyzer, designed for the determination of oil in water and soil samples, uses a halogenated solvent to separate oil from water for subsequent IR analysis. The solvent is insoluble in water and does not absorb IR energy in the 2–4.5-μm band. Horiba Instruments **405**

Clinical analysis. ES 300 immunoassay analyzer is a multichannel system capable of processing up to 100 tests per hour. Tests include T4, TSH-S, FT4, T uptake, T3, TBG, ferritin, IgE, LH, FSH, prolactin, HCG, insulin, cortisol, and digoxin. Boehringer Mannheim **406**

Oxygen. Model 3060 ultratrace oxygen analyzer features ranges of 0–50/0–100 ppb and 0–1.0/0–10 ppm O_2, 1 ppb O_2 sensitivity, and ± 2% full-scale accuracy. The instrument automatically selects the appropriate range for a given measurement. Teledyne Analytical Instruments **407**

Solvent delivery. Model 325 metal-free digital HPLC pump, which can be controlled remotely via an RS-232 connection, includes a self-flush pump head, built-in pulse dampener, and 40 front-panel diagnostics. The flow rate is programmable from 0.05 to 10.0 mL/min. Alltech Associates **408**

Process analysis. Model 206 IR analyzer is designed for the determination of a single component in either a liquid or gas stream. Features include separate housings for the source and detector, an isolated sample cell, remote readout, and computer-control capability. Anacon **409**

Electron microscopy. CM20 FEG is a 200-kV TEM/STEM system equipped with a thermal field emission gun. Capabilities include high-resolution imaging in macromolecular structure research, STEM imaging, electron holography, and EELS near-edge studies. Philips **410**

LC/MS. Benchmark bench-top LC/MS system is designed for QC, routine methods development, organic synthesis, and new pharmaceutical compound analysis. Features include a mass range of 2000 Da; ion profile, scanning, and SIM modes of operation; and scanning speed of 4000 Da/s. Extrel **411**

Spectrophotometer. HP 8452A option 003 diode array spectrophotometer incorporates a tungsten lamp and an optical system with no optically active moving parts. Wavelength range is 470–1100 nm. Scanning speed is 0.1 s for a full spectrum. Hewlett-Packard **412**

Ion measurement. CM-X, designed for the microanalysis of pH, Ca^{2+}, Na^{+}, and other ions in living cells, features a xenon excitation source, a dual-wavelength illumination configuration that interfaces directly to an epifluorescence microscope via a fiber-optic cable, and photon-counting detection of fluorescence. Spex **413**

Software

Graphs. Grafit generates graphs and charts for interpretation and presentation of technical data. Features include curve smoothing and regression, text formatting, full axial control, and multiple chart composition. Graphicus **416**

Electrophoresis. Database includes more than 250 articles on the technology, development, and applications of capillary electrophoresis. The search system allows users to sort by molecule type, separation technique, and detection method, as well as by author, title, and journal. Waters Chromatography Division of Millipore **417**

Manufacturers' Literature

Newsletter. *Retention Times*, Vol. 13, No. 1, includes information on a GC/MS system for analysis of drug and environmental samples and on cholesterol determination by LC/FID. Tracor Instruments **419**

Environmental analysis. Brochure describes the use of HPLC for environmental monitoring and analyses. PAHs, phenols, phthalates, carbamates, herbicides, and pesticides are discussed. LDC Analytical **422**

Spectrophotometry. Application note discusses the optimization of UV–vis spectrophotometry for the quantitative analysis of microvolume samples of nucleic acids and proteins. Beckman Instruments **423**

For more information on listed items, circle the appropriate numbers on one of our Readers' Service Cards

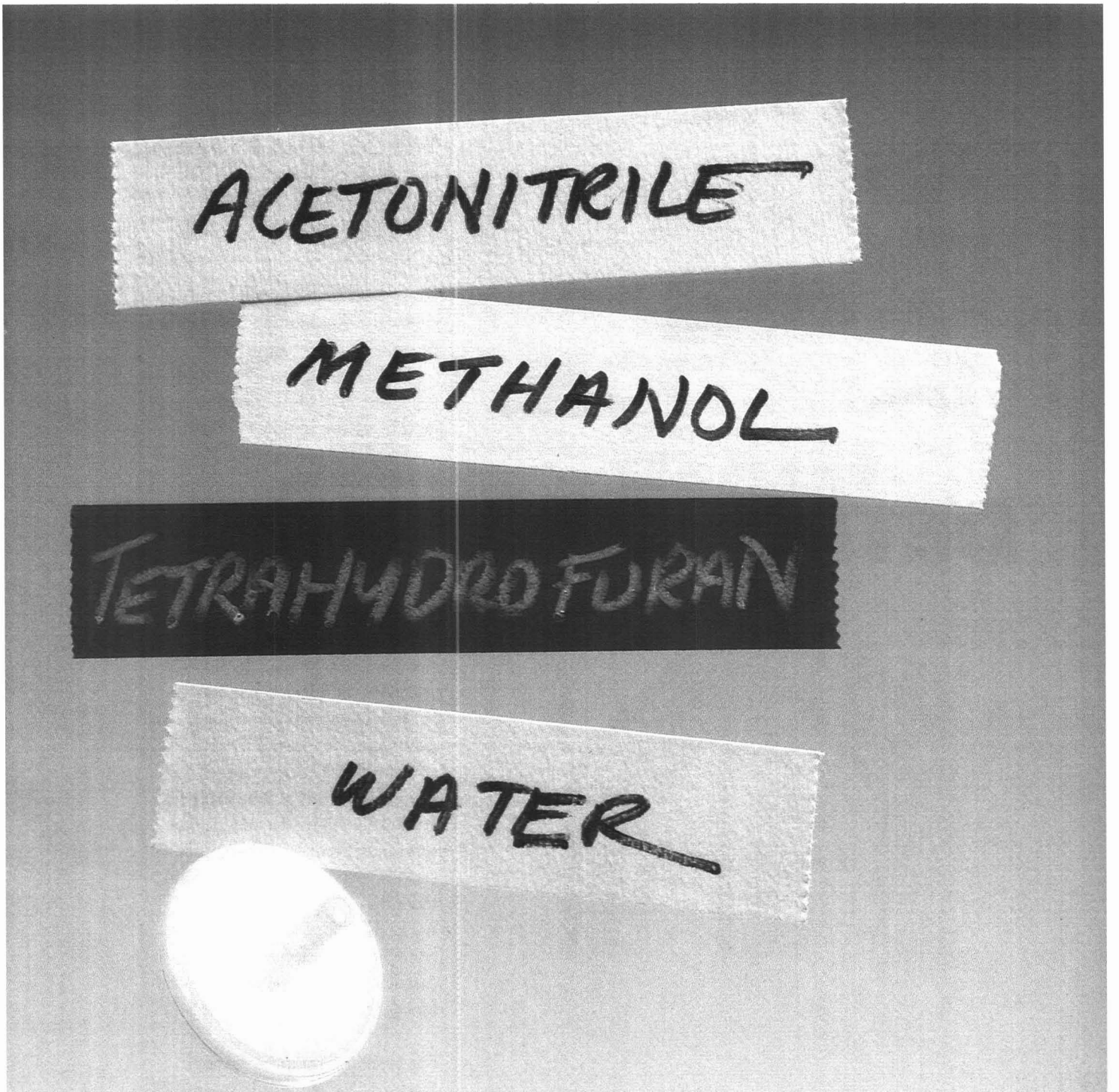

One filter fits all.

The new Millex®-LCR Filter Unit is compatible with all common aqueous or organic-based HPLC solvents—from water to methanol to tetrahydrofuran.

Its special membrane produces no organic or inorganic contaminants. So risk of introducing unwanted variables and artifacts into your work is eliminated.

Particulates are reduced below detectable limits, which keeps frits from plugging and extends column life.

Test the HPLC-certified Millex-LCR Filter Unit yourself. Send in the coupon, or call 800-225-1380 (in Mass., call 617-275-9200) for a free sample and technical brief.

MILLIPORE

CIRCLE 90 ON READER SERVICE CARD

Try the Millex-LCR Unit. Free.

Send to: Joe Peters
Millipore Corporation
80 Ashby Road
Bedford, MA 01730

Name _____

Title _____

Co./Inst. _____

Department _____

Address _____

City _____

State _____ Zip _____

Phone ( ) _____ Best time to call _____

PA 900008 © 1990 Millipore Corporation

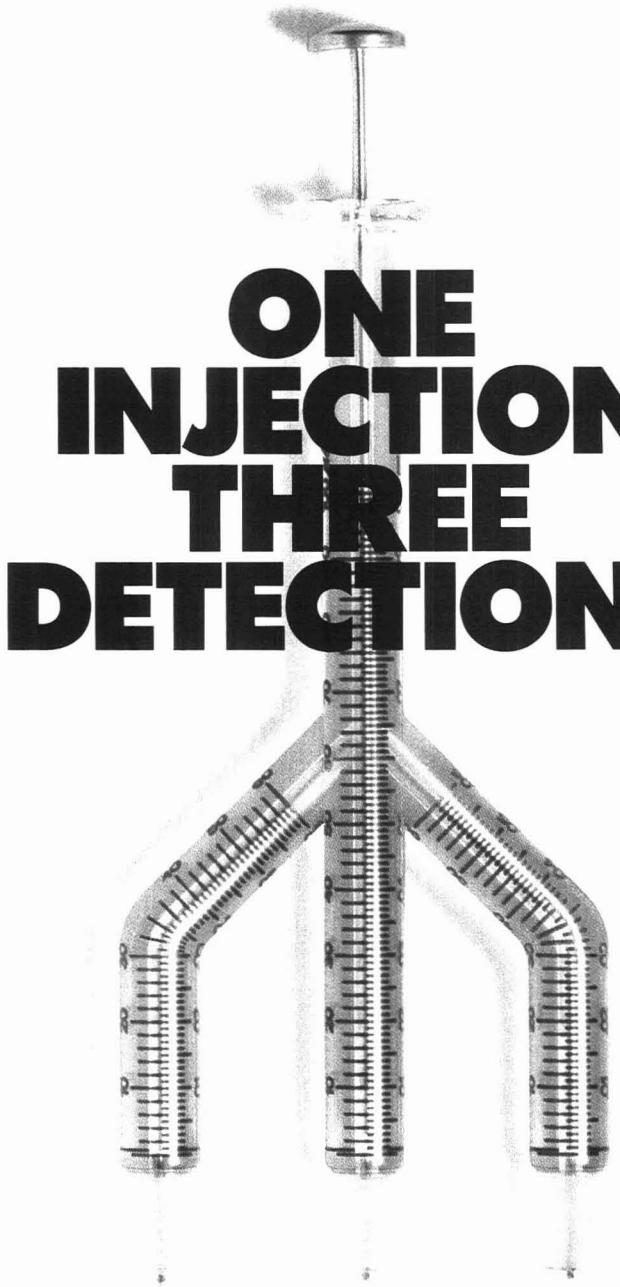

ONE INJECTION. THREE DETECTIONS.

THE 3D HPLC SYSTEM FROM BACHARACH COMBINES THREE DETECTORS IN ONE

Now, you can monitor UV, fluorescence and conductivity separately or simultaneously—with one injection—using a single, compact unit. The 3D HPLC is ideal for laboratory use in quality control, screening and teaching applications.

UV DETECTION

In the UV mode, it is a fixed wavelength detector at 254 nm, where up to 65% of all analytical HPLC applications are performed.

FLUORESCENCE DETECTION

In the fluorescence mode it monitors total emission above 280 nm. The selectivity of fluorescence can confirm the presence of components which may be masked by other UV-absorbing compounds.

CONDUCTIVITY DETECTION

As a conductivity detector, it monitors ionic species—inorganic anions, cations, organic acids and certain vitamins.

The 3D HPLC System comes complete with pump, injector, cartridge column, recorder and trifunctional detector—for under $7000.

For more information, contact:
Bacharach Coleman Instruments,
625 Alpha Drive, Pittsburgh, PA 15238; (412) 963-2107.

BACHARACH
Coleman® Instruments

CIRCLE 16 ON READER SERVICE CARD

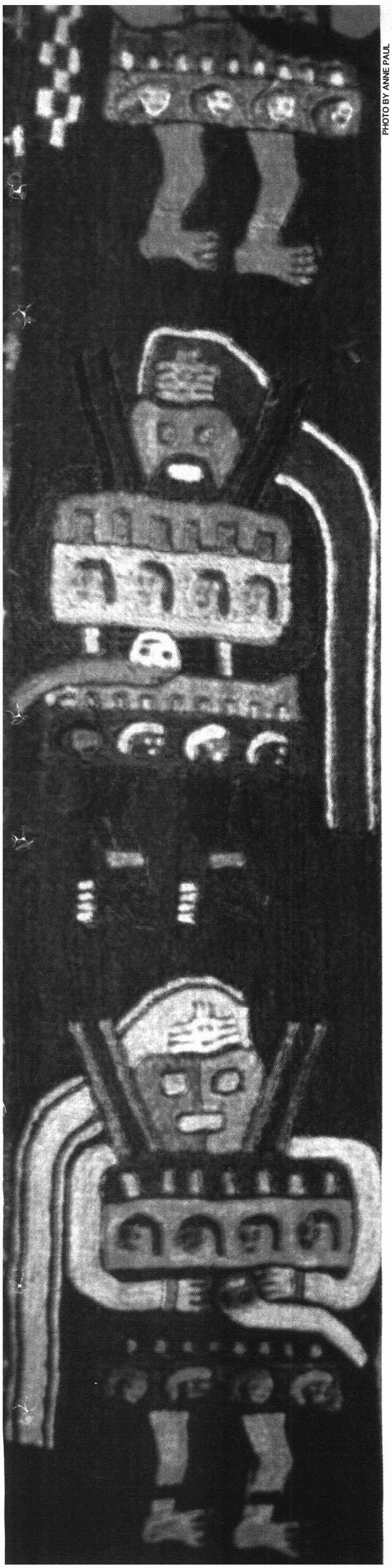

PHOTO BY ANNE PAUL

ANALYTICAL APPROACH

Unlocking THE SECRETS OF THE PAST

The Analysis of Archaeological Textiles and Dyes

Pamela A. Martoglio, Steven P. Bouffard, André J. Sommer, and J. E. Katon
Molecular Microspectroscopy Laboratory
Department of Chemistry
Miami University
Oxford, OH 45056

Kathryn A. Jakes
College of Human Ecology
Department of Textiles and Clothing
The Ohio State University
Columbus, OH 43210-1295

In recent years, archaeological chemists have begun to examine organic materials. Previously ignored because only small quantities survive in the archaeological context, these fragmentary and fragile organic remains have been analyzed by using new instrumental methods. For example, by examining seeds from soil flotation samples and residues inside pots, new information concerning prehistoric dietary patterns has been revealed. Differences in amber composition reflect differences in the original plants from which the resin came. Examination of textile fragments can help to elucidate prehistoric and historic technology. In this article, we will describe how microspectroscopy is being used to study textile fragments and their coloration.

Molecular microspectroscopy is a powerful method for identifying organic compounds because it provides both molecular and structural information. In addition, the technique is particularly well suited for studying archaeological textiles because of its nondestructive nature and ability to analyze extremely small sample sizes.

Previously, dyed archaeological textiles were analyzed by destructive techniques requiring relatively large amounts of sample. Through methods involving solvent stripping, a small portion of the sample was boiled in a variety of sequential solvents. The colors observed can lead to dye classification. For example, red and violet madder dyeings on aluminum potassium sulfate (alum) or on iron sulfate mordanted wool turn orange and produce a yellow solution when boiled in 10% sulfuric acid. The presence of the hydroxyanthraquinone dye can be verified by analyzing the yellow solution (after washing with ethyl acetate) using thin-layer chromatography with a 9:1 solvent mixture of toluene and glacial acetic acid (*1*).

The same dye class can also be identified by wetting several milligrams of textile with concentrated sulfuric acid, diluting the acid solution with water, and extracting the dyes with ethyl acetate. Visible spectrophotometry comparisons with a known dye extract confirmed the identification (*2*).

IR spectral analysis of archaeological textiles found in the Bar Kochba cave in the Judean Desert was also used to identify different dyes. Alizarin (a hydroxyanthraquinone dye) was identified by extracting the sample with hydrochloric acid followed by extraction with carbon tetrachloride. The extract was dried and purified by sublimation before precipitation with 0.1 N sulfuric acid. The IR spectra (using KBr pellets) were compared with known dye

0003-2700/90/A362-1123/$02.50/0
© 1990 American Chemical Society

spectra for identification (*3*).

Not only did these techniques require the destruction of large amounts of sample, but variations within the sample—such as differently colored fibers blended into a yarn—are not distinguishable. In addition, the process of stripping the dye from the fiber destroys the dye–fiber complex, leading to the loss of potentially useful information concerning the dyeing process. Thus alternative nondestructive methods were developed.

Molecular microspectroscopy

IR spectroscopy is often used to identify textile fibers, coatings, and finishes. For example, blend composition of fabrics and contaminants on textiles have been identified (*4*, *5*). The crystallinity of different cellulosic materials has been measured by comparing the IR intensity ratio of absorbances at 1372 cm^{-1}/2900 cm^{-1} (*6*). Compositional changes resulting from oxidative degradation of linen aldehyde groups to carboxyl groups have also been monitored by IR spectroscopy (*7*).

By using molecular microspectroscopy, many of the disadvantages inherent in the destructive techniques can be eliminated. Lang et al. (*8*) have shown that single fibers can be identified by both IR and Raman microspectroscopies. These methods are useful for identifying archaeological fibers when the characteristic surface features used for fiber identification by optical microscopy have been degraded by use and burial conditions.

Previous work also indicates that it might be possible to identify dyes or other compounds that exist along with the fibers. We hoped that by using microspectroscopy, we could identify dyes and characterize dyeing procedures used by historic and prehistoric civilizations.

Development of the analytical technique

Prior to microspectroscopic analysis, fibers and yarns removed from textile fragments are studied by light microscopy and by scanning electron microscopy (SEM) to observe any surface characteristics that could indicate fiber type (e.g., cotton or hair) as well as variances in fiber colors or types within the yarns. Energy-dispersive X-ray spectroscopy (EDS) is used to identify any possible mordanting of the fibers. Once the fiber type and the mordant are known, IR microspectroscopy is used to analyze the dyes on the fibers. Visible microspectroscopy serves mainly to verify the IR results, with the exception of the purpurin dye. This dye does not have any strong bands in the IR region that are distinct from the absorbance bands of the fiber and thus can only be identified with the visible technique.

IR spectra are obtained on an Analect AQS-20M IR microspectrophotometer system with an MCT narrow-band detector. Single fibers are prepared for analysis by flattening with a metal probe and transferring to a 1-mm-thick KCl plate (*9*). Typical sample areas range from 30 to 50 μm in diameter. Spectra are collected at 4 cm^{-1} resolution and apodized using a Happ–Genzel apodization function. Each spectrum reflects the ratios of 128 background scans to 128 sample scans. Band positions are determined from first-derivative spectra of the samples. Spectral subtractions are performed by normalizing the absorbances of a band common to the dyed and undyed fibers. (Initial subtractions involved the use of several common bands for normalization. However, because no differences were observed between the resultant spectra, the C–H stretch of the wool band located near 2960 cm^{-1} was employed for the remaining subtractions.) The subtracted spectra of the dye on the fiber are then compared with spectra of known dyes to identify the sample.

To test the dye detection limits on a typical fiber, a series of wool yarns is dyed with amounts of Acid Red 52 dye, which nominally range from 0.01 to 4.4 wt % on the fiber. Acid Red 52 (a rhodamine-type dye) has several strong IR absorption bands that do not overlap with those of wool. In the highly loaded fibers, the dye can be identified without spectral manipulations. In the samples with lower dye concentration, the dye can be identified only after spectral subtraction of the undyed fiber spectrum from that of the dyed fiber.

Figure 1 compares an Acid Red 52 spectrum obtained by subtraction with one obtained from the pure dye. Out of 17 band matches between the two spectra, the more distinct similarities are seen at 1593, 1078, and 1037 cm^{-1}. The peak present around 1700 cm^{-1} in the subtraction is disregarded because it results from an unsubtracted portion of one of the amide bands. This false peak is present whenever one wool fiber is subtracted from another. Peak assignments are aided by examining first-derivative spectra.

The Acid Red 52 dyed fibers can also be analyzed by visible microspectroscopy. This analysis is done with an Instruments SA Ramanor U-1000 Raman microspectrometer that was modified to obtain absorption spectra in the visible region. Basically, the tungsten–halogen light source of the microscope is imaged onto the sample using a rectangular aperture. This aperture is placed at a coincident image plane of the sample and the source, and sample areas as small as 20 × 20 μm are defined. Specific details of the modification are described elsewhere (*10*).

Samples are prepared in a manner similar to that of the IR studies. The ratios of single-beam spectra of the sample to a background spectrum mea-

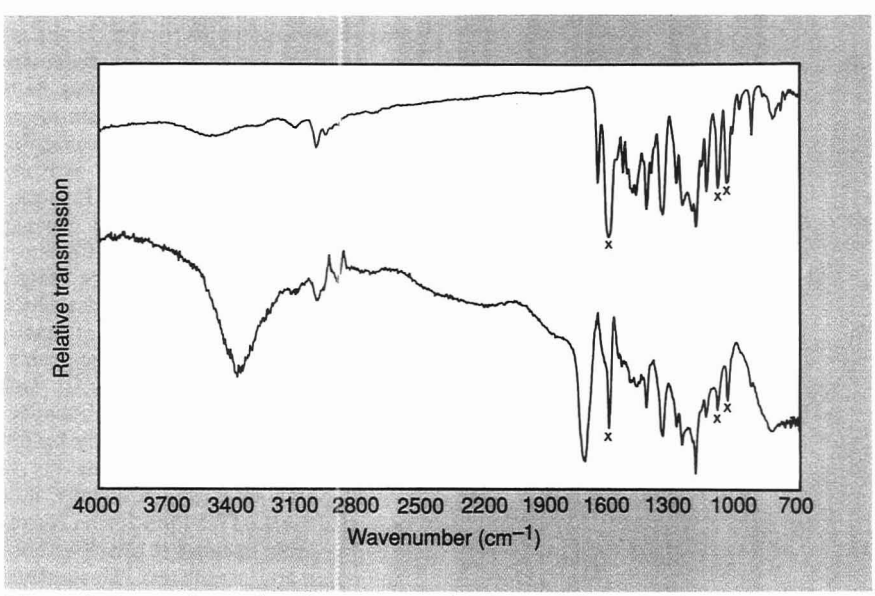

Figure 1. Comparison of an IR spectrum of Acid Red 52 dye (upper trace) with a spectrum obtained by spectral subtraction of undyed wool from Acid Red 52 dyed wool (4.4 wt % on fiber) (lower trace).

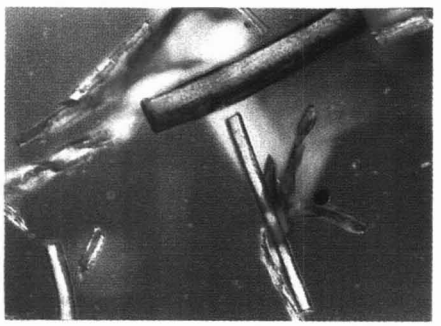

Figure 2. Fiber fragments from a Paracas archaeological textile sample.
Both plant and hair fibers are seen, some of which are dyed blue, red, or amber.

sured adjacent to the sample area are obtained to yield absorbance spectra. The spectra are collected over the range of 400–800 nm with an effective resolution of 1 nm. Spectra obtained on the dyed fibers are then compared with reference spectra obtained on the pure dyes. The dye is easily detected in all of the samples because the molar absorptivities of bands observed in the visible region are always much greater than those for bands in the IR. Another advantage in visible region work is that white, undyed wool has no distinct absorption bands in the visible region. Thus the spectrum observed could be directly related to the dye on the fiber.

Peruvian archaeological fabrics and dyes

South America has a rich history of prehistoric civilizations, and Peruvian textiles embody one expression of that history. A significant source of archaeological textiles can be found in the funerary bundles of the Paracas culture (400 B.C.–400 A.D.) located on the southern coast of Peru on the Paracas peninsula.

The very dry climate of this region helped to preserve the elaborate textiles buried with the elite leaders of the period. The spectacular embroidered garments were wrapped in multiple layers on the body, interleaved with yards of plain woven textiles. Some of these funerary bundles reached 7 ft in diameter.

The textiles reflect a complex and advanced society through their symbolism, wide range of colors, and intricate fabric manufacture (*11–13*). (Fibers from one of the samples are shown in Figure 2.) Art historians have described the many images embroidered on these textiles and have inferred their meaning in terms of prehistoric ritual. Little is known about the methods used to dye these ancient textiles, although some inferences have been made from the ethnographic literature and from chemical analyses. A recent article describes 56 different plants that are potential local sources of dyes for textile use in Peru (*14*). However, other dyes must be considered if trade with other cultures across Central and South America existed.

Saltzman (*2*) and Fester (*15*) have identified the source of some of the red, brown, black, green, and yellow colors found in pre-Columbian South American textiles. They attribute the red colors in Paracas textiles to the purpurin from plants in the genus *Relbunium*. Many species of *Relbunium* are native to the area, and no differentiation of species has been accomplished to date. Red colors in textiles from the later Nazca and Chimu periods have been attributed to cochineal, a dye found in the cacti insect *Dactylopius coccus* that is native to areas of Mexico. Thus the textiles found in southern and northern Peru in periods later than the Paracas give evidence of some system of trade through South and Central America.

Some botanists disagree on whether plants classified as *Relbunium* actually belong to the genus *Gallium*. The latter genus, present in North America, is very similar to madder plants of the genus *Rubia* found throughout Europe and Asia. Although both yield similar red colors on textiles, *Relbunium* and

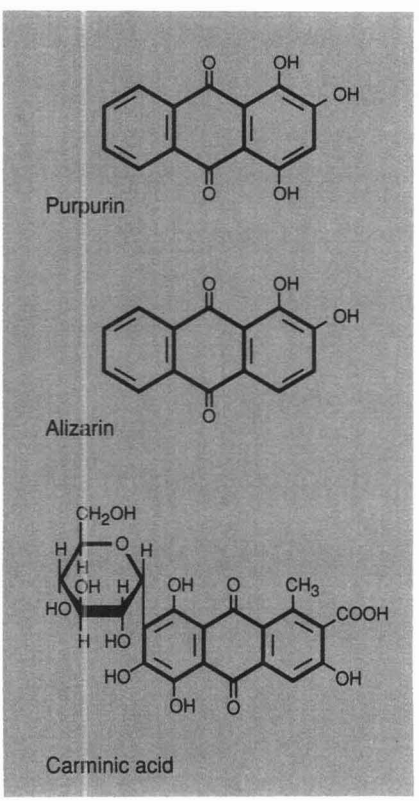

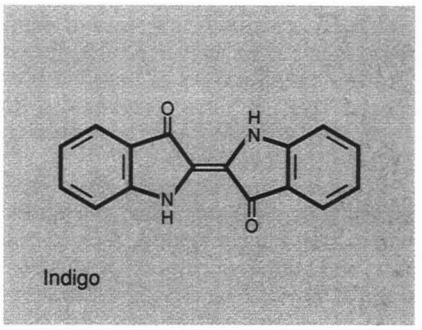

Rubia can be differentiated from each other by the relative concentrations of alizarin and purpurin present in the dyeing material. *Rubia* contains a high concentration of alizarin, whereas *Relbunium* contains a high concentration of purpurin as the main coloring agent. Carminic acid, the coloring agent in cochineal, is also chemically distinct.

The structures of the three compounds are shown in the box. Although all three yield red colors and are anthraquinone dyes, differences in their chemical compositions can be used for identification.

Fester (*15*) and Saltzman (*2*) attribute blue colors in Paracas textiles to indigo. This dye could have been derived from either *Indigofera suffructicosa* or *Cybistax antisyphilitica*, both of which grow in the same vicinity in Peru (*14*). Figure 3 compares an IR spectrum obtained by subtraction of an undyed wool spectrum from that of a blue Paracas fiber with one obtained from a pure sample of indigo. Eight absorptions associated with the dye are observed in the resultant subtraction spectrum. Some distinctive similarities are seen at 1460, 1481, 1170, and 1194 cm^{-1}.

Minerals readily available from the environment were used in combination with natural dyes to provide a link between the fiber and the dye, forming a mordant "lake." Color brightness and fastness are improved by the use of mordants in the dyeing process. Fester (*15*) cites the use of aluminum- and iron-containing minerals, but the exact procedure for the mordanting and dyeing of prehistoric yarns in Paracas is unknown.

Investigation of natural Peruvian dyes

To establish techniques for dye identification, wool fibers were dyed with cochineal or purpurin standards. These two dyes previously had been identified in pre-Columbian fabrics by other techniques and thus provided verification of our results. Purpurin and indigo have been identified in Paracas textiles. The presence of carminic acid

would be possible if a system of trade had been established at that time. In addition, the number of possible blue or red dyes is small compared with those used for yellows or browns, simplifying the investigation.

Standard undyed, unfinished wool yarns (test fabrics) were mordanted with alum, cupric sulfate, ferrous sulfate, and stannous chloride, and subsequently dyed. The first dye standard used was prepared from raw cochineal insects instead of from extracted and purified carminic acid, so the exact concentration of dye on the fibers is unknown. Only two mordants, alum and stannous chloride (in addition to the unmordanted sample), were examined for the purpurin-dyed standards. The exact concentration of the purpurin on the fibers is also unknown because dye precipitation occurred when mordanted fibers were added to the dye bath.

IR and visible spectra of the dyed standards were obtained and spectral subtractions were performed as for the Acid Red 52 dyed samples. Neither cochineal nor purpurin could be detected in the IR spectra unless spectral subtractions were performed. After spectral subtraction, the dye could easily be identified in all of the dyed samples (see Figure 4). Cochineal was identified by the band at 1548 cm^{-1} and the doublet around 1050 cm^{-1}. The mordant had no apparent effect on the IR spectra, although mordant effects were seen in the visible spectra. The addition of a mordant increased the absorbance of the dye bands in the visible region. These increased absorbance values support the theory that mordanting strengthens the dye–fiber complex, leading to higher concentrations of dye on the fibers. Interestingly, even though different colors were obtained with different mordants, the visible spectra of the mordanted, dyed fibers did not exhibit peak shifts compared to those of the unmordanted dyed fibers. The reason for this observation is still under investigation.

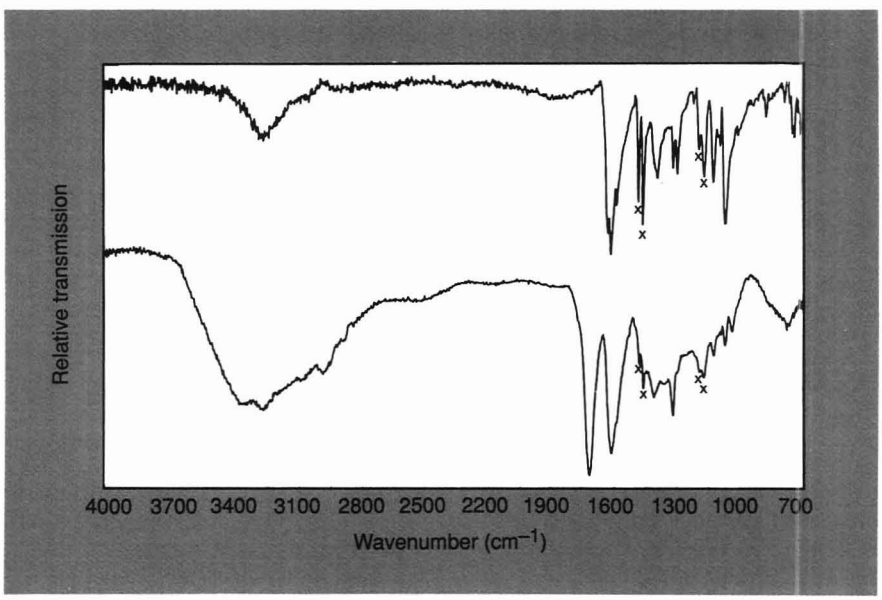

Figure 3. Comparison of IR spectra.
The upper trace is of indigo dye. The lower trace is obtained after spectral subtraction of an undyed wool spectrum from that of a blue Paracas archaeological fiber.

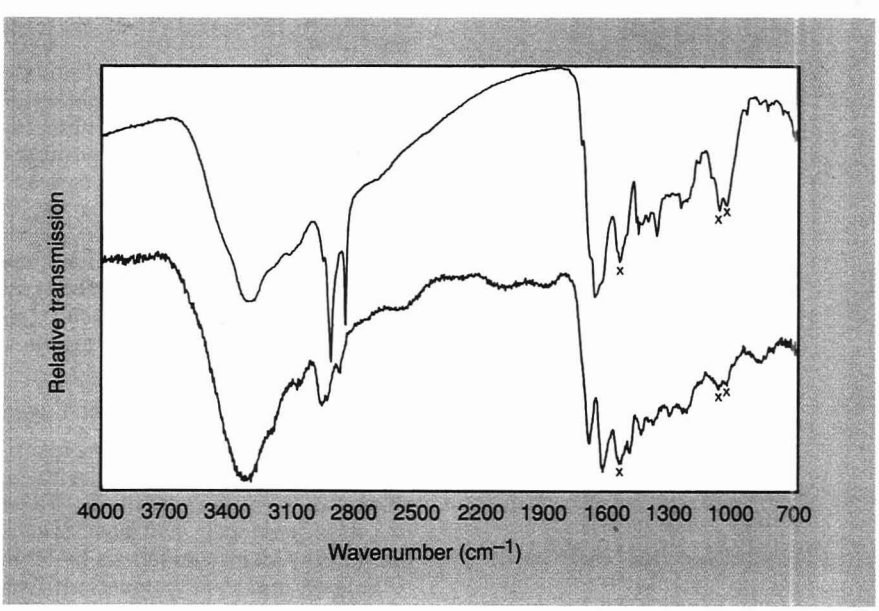

Figure 4. Comparison of IR spectra.
The upper trace is of cochineal dye. The lower trace is obtained after spectral subtraction of an undyed wool spectrum from that of a cochineal-dyed wool fiber.

An alum-mordanted alpaca wool yarn dyed with *Relbunium* plants collected in Peru was obtained from the Laboratory for Historic Colorants, University of California. The IR and visible spectra of a single fiber were obtained and compared with those of the purpurin-dyed wool. Both the IR spectra of the *Relbunium*-dyed, alum-mordanted fibers and the spectral subtractions of the undyed, mordanted wool from the *Relbunium*-dyed wool matched those of the purpurin-dyed, alum-mordanted wool spectra and spectral subtractions, respectively. The visible spectra of the *Relbunium*-dyed, alum-mordanted wool fibers were identical to the visible spectra of the purpurin-dyed, alum-mordanted wool fibers, with two peaks at 512 and 550 nm. These results, which are expected because purpurin is the main coloring component in *Relbunium*, support the accuracy of the microspectroscopic technique.

Application to archaeological samples

Six specimens of yarn or fibers were chosen from a larger collection of samples obtained from Paracas funerary textiles housed in the Museo Nacional de Antropología y Arqueología in Lima, Peru. The samples in the collection were not cut directly from the textiles (because of museum regulations) but were obtained by collecting loose fibers and yarns in or on the textiles. It was assumed that these samples originated from the textiles with which they were stored. The specimens investigated came from a turban, various skirts or skirt fringes, and a mantle (a type of

cloak or wrap).

Five of the specimens selected are single yarns or accumulations of loose fibers taken from colored sections of the embroidered textiles. These contain two or more differently colored fibers. The sixth specimen, taken from the base fabric of a skirt rather than from a surface embroidery yarn, is assumed to be undyed because of its yellow/brown coloration (which is typical of an aged fiber) and its function in the embroidered textile.

Fibers from the specimens were examined microscopically using bright-field, phase contrast, polarized light, and differential interference contrast techniques. The characteristic scalar structure of hair fibers and twisting shape of cotton fibers were observed. IR microspectroscopic analyses of the samples confirmed the identification of the fibers' sources as protein and cellulose. The combination of different types of hair fibers and cotton indicates the possibility of purposeful fiber blending by prehistoric people of Paracas. The combination of differently colored fibers within single yarns indicates the possibility of fiber dyeing prior to yarn production.

Further discussion of the Paracas textiles and analytical techniques—including light microscopy, SEM, EDS, and microspectroscopy—as well as the technology for textile production used by these prehistoric people may be found in other publications (*16*, *17*).

IR and visible microspectroscopies subsequently were used to identify the dyes present in fibers representative of each color within the samples. The mantle sample, for example, contained amber, red, blue, and colorless fibers (Figure 2). The colorless fibers are cellulosic and, because of their microscopic appearance, it can be concluded that they are immature cotton fibers. Some of the colored fibers are protein; because of their microscopic appearance, it can be concluded that they are hair fibers. Indigo was identified in the blue fibers by both IR and visible microspectroscopies. Purpurin was identified as the coloring component in the red fibers of the yarns in this mantle. Figure 5 compares the visible spectra of *Relbunium*-dyed wool with a red Paracas fiber.

For comparison, a portion of this Paracas period yarn was examined and purpurin was identified by solution spectroscopy at the Laboratory for Historical Colorants. Of the remaining fiber samples, indigo was identified in all blue or dark green fibers and purpurin in all red fibers. Carminic acid and the other coloring agents in cochineal were not found in any of the samples, which is consistent with previous analyses that did not identify cochineal in textiles produced earlier than the Nazca and Chimu periods (*2*). Discovery of cochineal in Paracas textiles would indicate trade routes between Mexico and Peru.

EDS analysis of cross sections of the fibers revealed a concentration of heavy elements on the surface of the fibers from soil encrustation. The presence of aluminum throughout the fibers indicated that they probably were mordanted with alum in the dyeing process, as Fester (*15*) states.

Future work

Our research has shown the potential of microspectroscopy for analyzing dyes in archaeological textile fibers. Establishment of a standard dye spectrum library that includes natural dyes native to Peru would help to provide clues about prehistoric Peruvian dyeing technology. Similar work can be performed on other textiles from different periods of history and regions of the world. We believe that microspectroscopy will continue to serve as a powerful tool for unlocking the secrets of the past.

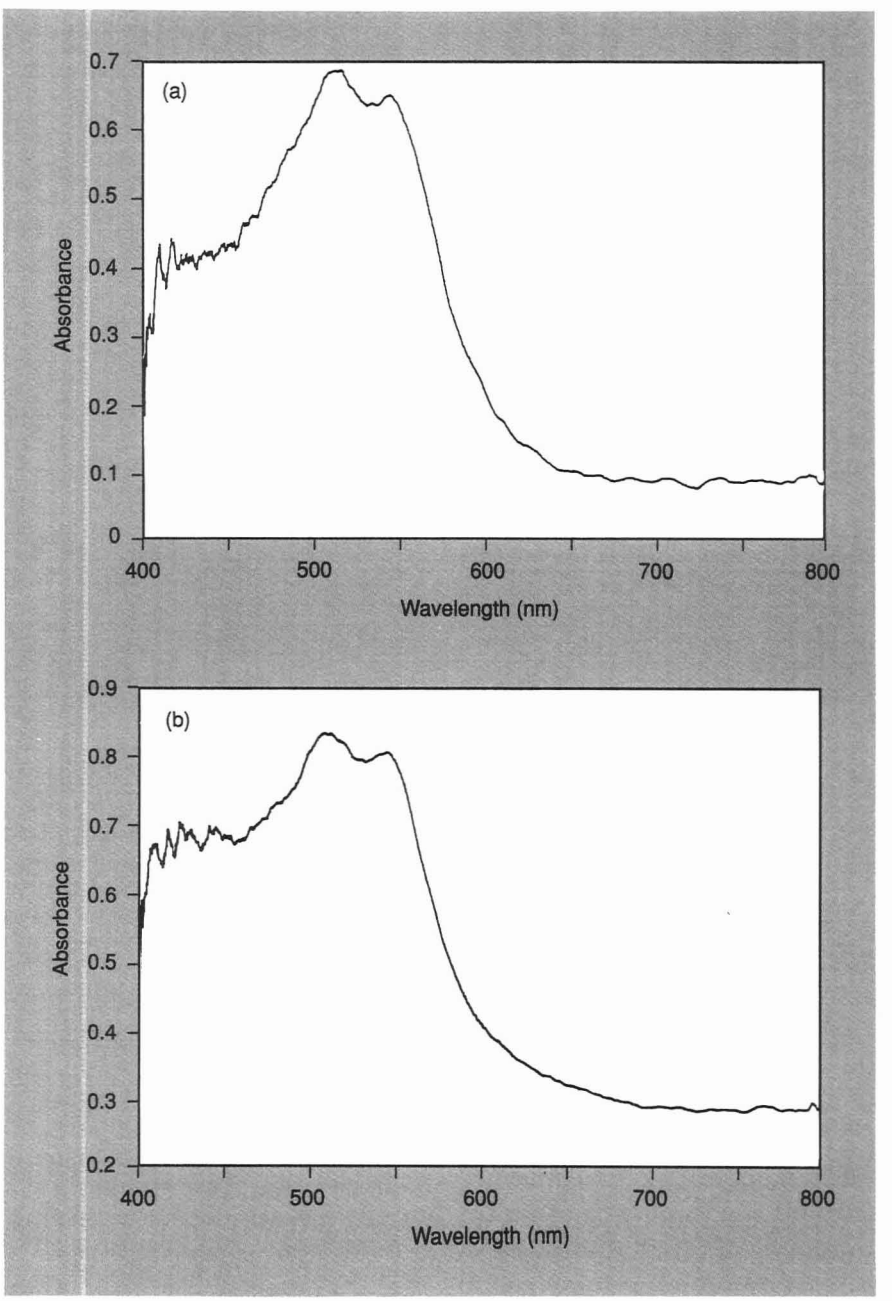

Figure 5. Comparison of visible spectra.

(a) *Relbunium*-dyed wool and (b) red wool fiber from a Paracas mantle sample.

LABORATORY
SERVICE CENTER

PARTICLE SIZE STANDARDS

NBS traceable calibration standards and controls. Large assortment of diameters from 0.02 to 2000 μm. Microspheres of polystyrene, glass and fluorescent materials. Free catalog available. Toll Free 800-334-3883. In Calif. 415-962-1100. FAX 415-962-0718

Duke Scientific Corporation 1135D SAN ANTONIO ROAD PALO ALTO, CALIF. 94303

LABORATORY SERVICE CENTER

(Equipment, Materials, Services, Instruments for Leasing). Maximum space — 4 inches per advertisement. Column width, 2-3/16″; two column width, 4-9/16″. Artwork accepted. No combination of directory rates with ROP advertising. Rates based on number of inches used within 12 months from first date of first insertion.
Per inch: 1″ — $165;
12″ — $160; 24″ — $155;
36″ — $150; 48″ — $145.

CALL OR WRITE JANE GATENBY

ANALYTICAL CHEMISTRY
500 Post Road East
P.O. Box 231
Westport, CT 06880
203-226-7131
FAX: 203-454-9939

HELP WANTED ADS

ROP display at ROP rates. Rate based on number of insertions within contract year. Cannot be combined for frequency.

Unit	1-Ti	6-Ti	12-Ti
1″ (25 mm)	$190	$170	$160
	24-Ti	48-Ti	72-Ti
	$150	$140	$130

ANALYTICAL CHEMISTRY
500 Post Road East
P.O. Box 231
Westport, CT 06880
203-226-7131/FAX: 203-454-9939

FREE DATA, FAST

To quickly amass data on all of the products you need, consult the Lab Data Service section on our *Analytical Chemistry* reader reply card insert.

ANALYTICAL APPROACH

The contribution of an alpaca yarn dyed with *Relbunium* from the Antunez de Mayolo collection by Max Saltzman, Laboratory for Historic Colorants, University of California, is gratefully acknowledged. Thanks are due to K. Antunez de Mayolo for some thought-provoking conversation, and to R. Wolfe, Alliance Imports, Sacramento, for contribution of some dyes.

This research was supported in part by state and federal funds appropriated to the Ohio Agricultural Research and Development Center (No. 121-90).

References

(1) Schweppe, H. In *Historic Textile and Paper Materials: Conservation and Characterization*; Needles, H. L.; Zeronian, S. H., Eds.; American Chemical Society: Washington, DC, 1986; pp. 153–74.
(2) Saltzman, M. In *Archaeological Chemistry II*; Carter, G. F., Ed.; American Chemical Society: Washington, DC, 1978; pp. 172–85.
(3) Abrahams, D. H.; Edelstein, S. M. *Am. Dyest. Rep.* **1964,** *53*, 19–25.
(4) Carlsson, D. J.; Wiles, D. M. In *Applied Fibre Science*; Happey, F., Ed.; Academic Press: New York, 1978, pp. 271–324.
(5) Grieble, D. L.; Gardner, S. A. *Text. Chem. Col.* **1989,** *21*, 11–13.
(6) Nelson, M. L.; O'Conner, R. T. *J. Appl. Polym. Sci.* **1964,** *3*, 1325–41.
(7) Kleinert, T. N. *Holzforschung* **1972,** *26*, 46–51.
(8) Lang, P. L.; Katon, J. E.; O'Keefe, J. F.; Schiering, D. W. *Microchem. J.* **1986,** *34*, 319–31.
(9) Katon, J. E.; Lang, P. L.; Schiering, D. W.; O'Keefe, J. F. In *The Design, Sample Handling, and Application of Infrared Microscopes*; Roush, P. B., Ed.; American Society for Testing and Materials: Philadelphia, 1987, ASTM STP 949; pp. 49–63.
(10) Sommer, A. J.; Martoglio, P. A.; Katon, J. E. *Appl. Spectrosc.*, in press.
(11) Feltham, J. *Peruvian Textiles*; Shire Ethnography: Aylesburg, Bucks, U.K., 1989.
(12) Gayton, A. H. *Kroeber Anthropological Society* **1961,** *25*, 111–28.
(13) Paul, A.; Niles, S. *Textile Museum Journal* **1985,** *23*, 5–15.
(14) Antunez de Mayolo, K. K. *J. Soc. Econom. Botany* **1989,** *43*, 5–15.
(15) Fester, G. A. *Dyestuffs* **1954,** *4*, 238–44.
(16) Jakes, K. A. In *Paracas Art and Architecture: Object and Context in South Coastal Peru*; Paul, A., Ed.; University of Iowa Press: Iowa City, in press.
(17) Jakes, K. A.; Katon, J. E.; Martoglio, P.A. In *Archaeometry 90: Proceedings of the 27th International Symposium on Archaeometry*; Pernicka, E.; Wagner, G., Eds.; Berkhauser Verlag: Switzerland, in press.

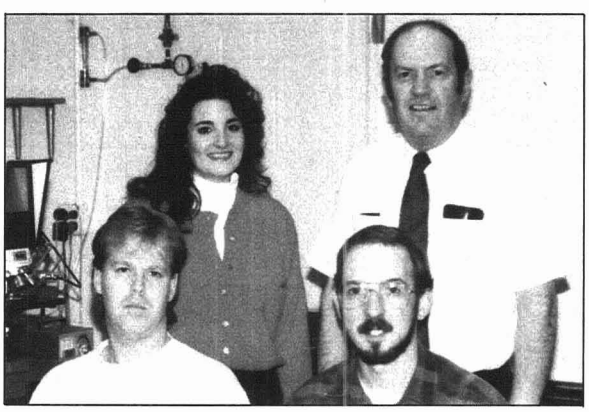

Pamela A. Martoglio (upper left) received a B.A. degree from Illinois Wesleyan University in 1987. She is currently a Ph.D. student in analytical chemistry at Miami University, working in the Molecular Microspectroscopy Laboratory (MML) and studying practical applications of IR and visible microspectroscopies.

J. E. Katon (upper right), professor of chemistry and director of the MML at Miami University, holds a B.A. degree from Bowling Green State University, an M.S degree from Kansas State University, and a Ph.D. from the University of Maryland. He joined Miami University in 1968. He is interested in the analytical and physical chemistry applications of IR and Raman spectroscopies.

André J. Sommer (lower right) received a B.S. degree from Delaware Valley College and an M.S. degree and Ph.D. from Lehigh University. In 1986 he joined the MML and is assistant director of the laboratory. His research interests are centered around the development and applications of IR and Raman microspectroscopies.

Steven P. Bouffard (lower left) received a B.S. degree in chemistry from Loyola Marymount University in 1990 and is currently in the Ph.D. program at Miami University. His undergraduate research involved the characterization of furniture finishes using IR microspectroscopy.

Kathryn A. Jakes is associate professor in the Textiles and Clothing Department, College of Human Ecology, at The Ohio State University. She holds a B.S. degree from the University of Illinois, an M.S. degree from the University of Maryland, and a Ph.D. in textile and polymer science from Clemson University. Her research focuses on the study of polymeric materials.

INDEX TO ADVERTISERS IN THIS ISSUE

CIRCLE INQUIRY NO.	ADVERTISERS	PAGE NO.
16	*Bacharach Coleman Instruments Skutski & Associates, Inc.	1122A
14	Baird Corporation W. J. Hearn & Company, Inc.	1117A
18	*J.T. Baker, Inc. Stiegler, Wells & Brunswick, Inc.	1084A
20	*Bio-Rad Digilab Division Digiart	OBC
30	*Dialog Information Services, Inc. HL&S Partners, Inc.	1112A
28	*Dionex Corporation Dionex Advertising & Design	IFC
32	*EM Science Tallant, LaPointe & Partners, Inc.	1115A
50	*Gilson Medical Electronics, Inc	1083A
51	**Gilson Medical Electronics, SA	1083A
70	Jandel Scientific	1092A
92	*Malvern Instruments, Ltd.	1111A
88	*Mattson Instruments, Inc. Cunningham & Welch Design Group	1093A
86	*Mettler Instrument Corporation Gilbert, Whitney & Johns, Inc.	1095A
90	*Millipore Corporation Mintz & Hoke, Inc.	1121A
95	*Nicolet Analytical Instruments	1089A
114	*Parr Instrument Company FBA Marketing/Communications	1118A
111, 112	Perkin-Elmer Corporation Keiler Advertising	1091A
127	*Sartorius Instruments Dunlap, Schulze & Associates, Inc.	1086A–1087A
130	*SGE Arden Advertising Agency	1094A
125	*Swagelok Company Falls Advertising Company	1096A
140	*Varian Lanig Associates	1098A
142	VG Masslab Deloittes Advertising & Marketing	1105A
146	Whatman, Inc. GrossTownsendFrankHoffman, Inc.	1100A

Directory section, see page 1128A.

** See ad in ACS Laboratory Guide.*

*** Company so marked has advertisement in Foreign Regional edition only.*

Advertising Management for the American Chemical Society Publications

CENTCOM, LTD

President
James A. Byrne
Executive Vice President
Benjamin W. Jones
Clay S. Holden, *Vice President*
Robert L. Voepel, *Vice President*
Joseph P. Stenza, *Production Director*

500 Post Road East
P.O. Box 231
Westport, Connecticut 06880
(Area Code 203) 226-7131
Telex No.643310
FAX: 203-454-9939

ADVERTISING SALES MANAGER
Bruce E. Poorman

ADVERTISING PRODUCTION MANAGER
Jane F. Gatenby

SALES REPRESENTATIVES

Philadelphia, PA . . . CENTCOM, LTD., GSB Building, Suite 405, 1 Belmont Avenue, Bala Cynwyd, Pa. 19004. Telephone: 215-667-9666, FAX: 215-667-9353.

New York/New Jersey . . . John F. Raftery, CENTCOM, LTD., Schoolhouse Plaza, 720 King Georges Post Road, Fords, NJ 08863, Telephone: 201-738-8200

Westport, CT . . . Edward M. Black, CENTCOM, LTD., 500 Post Road East, P.O. Box 231, Westport, Ct. 06880. Telephone: 203-226-7131, Telex 643310, FAX: 203-454-9939

Cleveland, OH . . . Bruce E. Poorman, John C. Guyot, CENTCOM, LTD., 325 Front St., Suite 2, Berea, Ohio 44017. Telephone: 216-234-1333, FAX: 216-234-3425

Chicago, IL . . . Michael J. Pak, CENTCOM, LTD., 540 Frontage Rd., Northfield, Ill. 60093. Telephone: 708-441-6383, FAX: 708-441-6382

Houston, TX . . . Michael J. Pak, CENTCOM, LTD. Telephone: 708-441-6383

San Francisco, CA . . . Paul M. Butts, CENTCOM, LTD., Suite 1070, 2672 Bayshore Frontage Road, Mountain View, CA 94043. Telephone: 415-969-4604

Los Angeles, CA . . . Clay S. Holden, CENTCOM, LTD., Newton Pacific Center, 3142 Pacific Coast Highway, Suite 200, Torrance, CA 90505. Telephone: 213-325-1903

Boston, MA . . . Edward M. Black, CENTCOM, LTD. Telephone: 203-226-7131

Atlanta, GA . . . John C. Guyot, CENTCOM, LTD. Telephone: 216-234-1333

Denver, CO . . . Paul M. Butts, CENTCOM, LTD. Telephone: 415-969-4604

United Kingdom
Reading, England . . . Malcolm Thiele, Technomedia Ltd., Wood Cottage, Shurlock Row, Reading RG10 OQE, Berkshire, England. Telephone: 073-434-3302, Telex #848800, FAX: 073-434-3848
Lancashire, England . . . Technomedia Ltd., c/o Meconomics Ltd., Meconomics House, 31 Old Street, Ashton Under Lyne, Lancashire, England. Telephone: 061-308-3025

Continental Europe . . . Andre Jamar, International Communications, Inc., Rue Mallar 1, 4800 Verviers, Belgium. Telephone: (087) 22-53-85, FAX: (087) 23-03-29

Tokyo, Japan . . . Sumio Oka, International Media Representatives Ltd., Room 100, 21 Bldg., 2-2-22 Okusawa, Setagaya-ku, Tokyo 158 Japan. Telephone: 502-0656, Telex #22633, FAX: 5706-7349

JOURNAL OF CHEMICAL AND ENGINEERING DATA

Get A World Of Precise, Accurate Data In This International, Quarterly Journal

Multidisciplinary in nature and international in scope, the *Journal of Chemical and Engineering Data* (*JCED*) features contributions by distinguished physicists, chemists, chemical engineers, mechanical engineers, biological scientists, and applied mathematicians from the world over. Their expert reports represent numerical data bases for private technical information systems, particularly in industry, that will broaden your scientific horizons and improve the quality of your work.

This unique journal offers you precise, accurate data on physical, thermodynamic and transport properties of well-defined materials. It also keeps you informed about the latest international standards on symbols, terminology and units of measurement for reporting data properly.

You'll find numerical property data measurements on:

- pure substances of defined purity
- well-defined gaseous, liquid and solid mixtures
- semi-empirical and theoretical correlations useful in interpolating, extrapolating and predicting properties of scientific and technological importance
- new substances — the physical and spectral properties of inorganic, organic, and biochemical substances and other complex substances prepared by established synthetic procedures that may have major scientific and technological applications

Editor
Bruno J. Zwolinski,
Texas A&M Univ.

Associate Editors
Henry V. Kehiaian,
Univ. of Paris, France

Randolph C. Wilhoit,
Texas A&M Univ.

1990 SUBSCRIPTION INFORMATION

Volume 35
4 Issues Per Year

		U.S.	Canada and Mexico	Europe (Air Service Included)	All Other Countries (Air Service Included)
ACS Members	1 year	$ 30	$ 35	$ 37	$ 40
	2 years	$ 54	$ 64	$ 68	$ 74
Nonmembers	1 year	$207	$212	$214	$217
Supplementary Material on Microfiche		$ 12	$ 16	$ 16	$ 16

Member subscription rates are for personal use only.
For nonmember rates in Japan, contact Maruzen Co., Ltd.

Journal subscriptions start January 1990 and are based on a calendar year.

Address your orders or inquiries to:
American Chemical Society
Sales and Distribution Department
1155 Sixteenth Street, N.W.
Washington, DC 20036

Toll free (800) 227-5558
Outside U.S. (202) 872-4363
Telex: 440159 ACSPUI or
892582 ACSPUBS
Fax: (202) 872-4615

This publication is available on microfilm, microfiche, and electronically through Chemical Journals Online on STN International.

Analytical CHEMISTRY

EDITOR: **GEORGE H. MORRISON**

ASSOCIATE EDITORS: **Catherine C. Fenselau, Georges Guiochon, Walter C. Herlihy, Robert A. Osteryoung, Edward S. Yeung**

Editorial Headquarters

1155 Sixteenth St., N.W.
Washington, DC 20036
Phone: 202-872-4570
Telefax: 202-872-4574

Managing Editor: Sharon G. Boots

Assistant Managing Editor: Mary Warner

Associate Editor: Louise Voress

Assistant Editors: Jane K. Baker, Grace K. Lee, Alan R. Newman

Editorial Assistant: Felicia Wach

Contributing Editor: Marcia Vogel

Director, Operational Support: C. Michael Phillippe

Head, Production Department: Leroy L. Corcoran

Art Director: Alan Kahan

Designers: Amy Meyer Phifer, Robert Sargent

Production Editor: Elizabeth E. Wood

Circulation: David Schulbaum

Editorial Assistant, LabGuide: Joanne Mullican

Journals Dept., Columbus, Ohio

Associate Head: Marianne Brogan

Journals Editing Manager: Joseph E. Yurvati

Senior Associate Editor: Rodney L. Temos

Advisory Board: Bernard J. Bulkin, Michael S. Epstein, Renaat Gijbels, William S. Hancock, Thomas L. Isenhour, James W. Jorgenson, Peter C. Jurs, Alan G. Marshall, Lawrence A. Pachla, John F. Rabolt, Debra R. Rolison, Ralph E. Sturgeon, Shigeru Terabe, George S. Wilson, Mary J. Wirth, Richard N. Zare
Ex Officio: Sam P. Perone

Instrumentation Advisory Panel: Daniel W. Armstrong, Bruce Chase, Thomas L. Chester, R. Graham Cooks, L. J. Cline Love, Sanford P. Markey, Brenda R. Shaw, Gary W. Small, R. Mark Wightman

Published by the
AMERICAN CHEMICAL SOCIETY
1155 16th Street, N.W.
Washington, DC 20036

Publications Division

Director: Robert H. Marks

Journals: Charles R. Bertsch

Special Publications: Randall E. Wedin

Manuscript requirements are published in the January 1, 1990 issue, page 89. Manuscripts for publication (4 copies) should be submitted to ANALYTICAL CHEMISTRY at the ACS Washington address.

The American Chemical Society and its editors assume no responsibility for the statements and opinions advanced by contributors. Views expressed in the editorials are those of the editors and do not necessarily represent the official position of the American Chemical Society.

AUTHOR INDEX

Amankwa, L., 2270
Armstrong, N. R., 2357

Bartsch, R. A., 2283
Beck, S., 2258
Berman, S. S., 2370
Blough, N. V., 2275
Brina, R., 2357

Cantwell, F. F., 2270
Cattrall, R. W., 2339
Claessens, H. A., 2288, 2296
Colby, S. M., 2400
Collins, G. E., 2357
Cotter, R. J., 2388
Cramers, C. A., 2288, 2296
Crouch, S. R., 2365

de Haan, J. W., 2288, 2296
De Marco, R., 2339
Desiderio, D. M., 2395
de Vries, M. S., 2385
Donaghay, P. L., 2408
Du, H. S., 2412

Fenselau, C., 2388, 2391

García Pinto, C., 2405
Giddings, J. C., 2306
Goo, M.-J., 2283
Guiochon, G., 2330

Hamilton, I. C., 2339
Harris, J. M., 2351
Hasan, M. N., 2318
Hayashita, T., 2283
Hernández Méndez, J., 2405
Hetem, M. J. J., 2288, 2296
Hughes, J. E., 2408
Hunziker, H. E., 2385

Imasaka, T., 2404
Ishibashi, N., 2404

Johnson, K. M., 2408
Jones, J. R., 2300
Jurs, P. C., 2318, 2323

Kieber, D. J., 2275
Kim, H., 2365
Kim, J. S., 2283
Kinkel, J. N., 2288, 2296
Köster, H., 2258
Krzykawski, J., 2283
Kusmierz, J. J., 2395

Lee, J. C., 2283
Lee, J. H., 2381
Lee, P. A., 2357
Leiner, M. J. P., 2377
Li, R., 2414
Liesegang, J., 2339
Luong, V., 2370
Lyne, P. D., 2347

Ma, Z., 2330
Moreno-Bondi, M. C., 2377
Moreno Cordero, B., 2405
Murphy, C. M., 2391

Nakagawa, H., 2404
Nyberg, G. L., 2339

Okazaki, T., 2404
O'Neill, R. D., 2347
Orlando, R., 2388

Parcher, J. F., 2313
Pérez Pavón, J. L., 2405
Phillips, G. R., 2351
Purnell, J. H., 2300

Reilly, J. P., 2400

Saperstein, D. D., 2385
Schaffar, B. P. H., 2377
Selim, S. A., 2365
Sieburth, J. M., 2408
Song, H., 2313
Stanton, D. T., 2323
Stewart, M., 2400
Sturgeon, R. E., 2370
Sumrada, R., 2395

Tang, I. N., 2381

van de Ven, L. J. M., 2288, 2296
Vestling, M. M., 2391

Wai, C. M., 2412
Wang, J., 2414
Weinstein-Lloyd, J. B., 2381
Wendt, H. R., 2385
Wijnen, P. W. J. G., 2296
Willie, S. N., 2370
Wolfbeis, O. S., 2377

Zabik, M. J., 2365

PERSPECTIVE: ANALYTICAL BIOTECHNOLOGY

Applications of Dioxetane Chemiluminescent Probes to Molecular Biology

Stephan Beck*[1] and Hubert Köster[2]

MilliGen/Biosearch, 186 Middlesex Turnpike, Burlington, Massachusetts 01803

DNA probes and synthetic oligonucleotides in general present one of the key tools in modern molecular biology research and increasingly also in commercial applications. Along with the many applications that have been developed for and with DNA probes, faster and more sensitive detection methods are being developed. One of the most promising recent developments presents a method based on enzymatically triggered chemiluminescence. Details of this chemistry along with applications in molecular biology and immunology will be discussed and compared to conventional methods.

INTRODUCTION

Over the last 10 years the use of DNA probes in molecular biology has increased tremendously (*21*). The term DNA probe, sometimes used synonymously with DNA primer and oligodeoxyribonucleotide, is a functional description for synthetic or natural occurring DNA molecules that are used to identify the presence or absence of a specific target DNA within a given DNA mixture. The term DNA primer is normally used in the context of extension (e.g. DNA sequencing) and amplification reactions (e.g. polymerase chain reaction, PCR) and more recently, the term oligodeoxynucleotide is increasingly being used in the context of antisense DNA/RNA. In basic research, DNA probes are employed e.g. for recombinant library screening, DNA mapping, in situ hybridization, DNA sequencing and other methods (*1–4, 21*). In clinical diagnostics DNA probes are used, e.g., for the identification of pathogens (bacteria, viruses) and certain forms of cancer and for the diagnosis of genetic disorders, and more recently, DNA probes are also being used in a method called "fingerprinting", e.g. to provide evidence in the field of forensic science (*1–4, 21*). Despite the quite different applications, the experimental procedure for most DNA probe assays is very similar. Under appropriate conditions the DNA probe will hybridize via hydrogen bonding according to Watson–Crick base pairing to the complementary target DNA (*1*). After the free, unhybridized probe is removed, the DNA hybrid (target DNA with bound probe) can be visualized by a variety of direct and indirect detection methods using radioactive, colorimetric, or luminescent labels (*3, 4, 21*). Table I compares some of the detection methods currently used for DNA probe assays. The detection limit of each method can vary by several orders of magnitude depending upon the assay and the experimental conditions.

This review article will emphasize on the current status of development of chemiluminescent detection methods, and in particular, it will focus on the chemistry and application of stabilized, enzyme triggerable 1,2-dioxetanes.

Luminescence is defined as the emission of electromagnetic radiation (in the form of ultraviolet, visible, or infrared light) from atoms or molecules as a result of the transition of an electronically excited state to a lower energy state. Depending on the nature of the luminescent reaction one distinguishes between chemiluminescence, bioluminescence, thermoluminescence, electroluminescence, photoluminescence (fluorescence and phosphorescence), and others. Known as the glow of fireflies (or other living organisms), bioluminescence probably presents the most spectacular subgroup.

The phenomenon of chemiluminescence, on which we focus here, was named and first described by Eilhard Wiedemann in 1888 as "light emission occurring as a result of chemical processes" (*9*). For a detailed review on the history of chemiluminescence please see ref 10.

CHEMICAL AND PHYSICAL PROPERTIES OF 1,2-DIOXETANES

Comparison with Other Chemiluminescent Systems. Several different systems applicable for chemiluminescent detection in bioassays have been described. The most frequently used systems (Figure 1) are based on luciferin, luminol/isoluminol, acridinium ester, and oxalate ester. As these systems have been reviewed recently (*11–14*), they will be briefly mentioned here only for comparative reasons.

In the luciferin/luciferase system the enzyme luciferase catalyzes the oxidation of D-luciferin **11** in the presence of ATP, Mg^{2+}, and O_2 to generate oxyluciferin **13** and light via a high-energy 1,2-dioxetanone intermediate **12**. Horseradish peroxidase catalyzes the oxidation of luminol **1** in the presence of hydrogen peroxide, forming a highly reactive endoperoxide which then decomposes via an electronically excited 3-aminophthalate dianion and emitting light on its return to the ground state. These two and the acridinium and oxalate ester systems are in use for quite a while. Despite many improvements and modifications, their usage is still limited. In many bioassays and for monitoring reactions in biochemistry and molecular biology, the use of radioactive detection is still in wide use. There are several reasons for this. Sometimes the sensitivity is not sufficient. Other reasons can be found in the relative complexity of the systems as several components need to be present; it turned out that optimization is technically difficult and too many additives can increase the background level to an unacceptable high extend, thus influencing the signal to noise ratio in an unfavourable way.

[1] Present address: Imperial Cancer Research Fund, 44 Lincoln's Inn Fields, London WC2A 3PX, England.
[2] Present address: 1640 Monument St., Concord, MA 01742.

0003-2700/90/0362-2258$02.50/0 © 1990 American Chemical Society

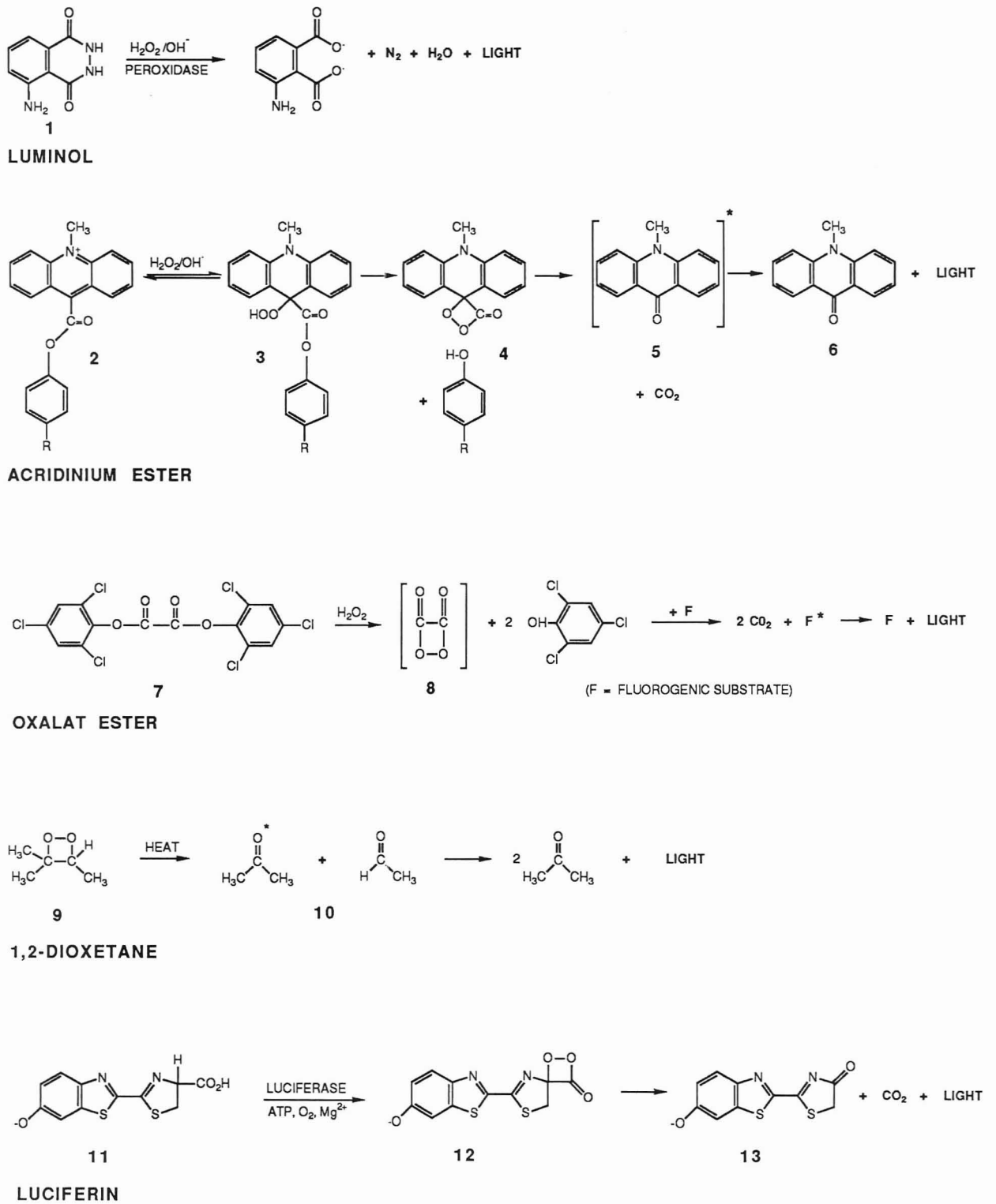

Figure 1. Overview of different chemiluminescent systems (*10*, *13*).

Luminol **1** is activated by hydrogen peroxide, alkali, and horseradish peroxidase. To increase the chemiluminescent efficiency various enhancers have been proposed for the luminol system (*14*). Oxalate esters **7** also need hydrogen peroxide and a fluorescent substance (e.g. fluorescein, anthracene) for enhancement. The oxalate ester chemiluminescence is very efficient in organic solvents; most bioassays, however, have to be performed in aqueous medium. In such an environment the quantum yield is significantly reduced. Acridinium esters **2** are again activated with hydrogen peroxide and alkali. Here the addition of a separate enhancer can be avoided as the generated acridone derivative **5** itself is fluorescent. The luciferin/luciferase system has also been adopted for chemiluminescent bioassays. Despite the enormous efficiency of this system its utility is limited due to its complexity and instability. The chemical sensitivity of the enzyme also makes it difficult to implement it into existing bioassays e.g. by covalent attachment to detector molecules. This problem has been addressed by a recent development of a detection system based on the quantification of alkaline phosphatase using D-luciferin-*O*-phosphate (*100*, *101*).

It is an additional problem that in most cases the light is generated in a "burst" or "flash" (Figure 2), which needs sophisticated instrumentation if results with sufficient accuracy and reproducibility are to be achieved. 1,2-Dioxetanes on the other hand until recently could not be implemented

Table I. Comparison of DNA Probe Detection Methods[a]

detection method	label	substrate	detection mode	detection limit for label, mol	detection limit in probe assay, mol	ref
radioactivity	^{32}P		scintillation counter	5×10^{-17}	5×10^{-17}	*15*, 20, 26, 27, 35
colorimetric	HRP	OPD	photometer	1×10^{-16}	1×10^{-16}	*15*
staining	AP	NBT/BCIP	photometer	2×10^{-16}	5×10^{-16}	*15*, 17, 18, 22, 23, 25, 28, 29
	AP	NPP	photometer	5×10^{-15}	5×10^{-15}	*15*
fluorescence	fluorescein		fluorometer	2×10^{-14}	5×10^{-13}	*15*, 25, 30, 31, 32
	rhodamine		fluorometer	5×10^{-15}	1×10^{-13}	*15*, 30, 31
	Texas Red		fluorometer	2×10^{-14}	1×10^{-13}	*15*
	AP	MUBP	fluorometer	8×10^{-20}	1×10^{-19}	*16*
chemiluminescence		isoluminol	luminometer	1×10^{-15}	1×10^{-13}	*15*
		acridinium ester	luminometer	2×10^{-18}	2×10^{-17}	*52*, 51
	HRP	luminol and enhancer	luminometer	5×10^{-17}	5×10^{-17}	*15*, 14, 20, 33
	AP	D-luciferin-*o*-phosphate	luminometer	5×10^{-20}	1×10^{-19}	*16*, 11, 100, 101
	AP	1,2-dioxetane	luminometer film	1×10^{-20}	1×10^{-19}	*52*, 16, 18, 19, 24, 34

[a] The given detection limits were taken from the corresponding, italicized reference. Key: AP, alkaline phosphatase; BCIP, 5-bromo-4-chloro-3-indolyl phosphate; HRP, horseradish peroxidase; NBT, nitro blue tetrazolium; NPP, *p*-nitrophenyl phosphate; OPD, *o*-phenyldiamine. Reprinted in modified form with permission from ref 52.

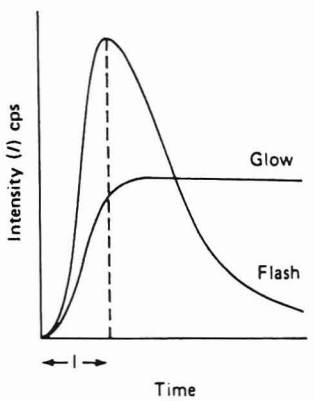

Figure 2. Different light generating kinetics of luminescent reactions. Reprinted with permission from ref 10. Copyright 1988 Verlagsgemeinschaft.

into the design of bioassays because they either were thermally too labile (*70*) or, if sufficiently stable, could not be activated under conditions compatible with the properties of bioassays.

Recently, however, stable 1,2-dioxetane derivatives have been designed that can be efficiently activated by chemical and enzymatic reactions and also generate light with high quantum yield (*5–8*). Of particular importance is the use of enzymes for the triggering of the chemiluminescence. In this case due to the high turn over rate a tremendous signal amplification is observed and in addition to this the light is produced in a "glowing" mode so that the signal very often persists for many hours or even days. Hence simple photomultiplier tube-based instrumentation can be employed.

The Phenomenon of Chemiluminescence. Exothermic chemical reactions generally release energy in the form of vibrational or rotational excitation or heat. In chemiluminescent reactions, however, the electronically excited state is reached by a chemical reaction, and it is light instead of heat that is generated (for a recent detailed discussion of chemiluminescence see ref 10). In most chemiluminescent reactions the source of the energy is the cleavage of an energy-rich bond such as that of peroxides, hydroperoxides, 1,2-dioxetanes, or dioxytenones (Figure 1). The decomposition of these metastable compounds can be triggered by chemical or enzymatic processes and yields one of the reaction products in a singlet or triplet electronic excited state. During the transition of these excited intermediates to the electronic ground state light is emitted. This process is also known as *direct chemiluminescence*. However, the energy of the excited intermediate could be transferred to a fluorgenic or fluorescent substrate forming an excited acceptor, which in turn reaches the ground state by the emission of a photon. This process is called *indirect, energy transfer* or *sensitized chemiluminescence* (Figure 3). The overall quantum yield (Φ_{CL}), i.e. the total number of photons emitted per number of molecules reacting, is described by the following equation: The term (Φ_{CE}) gives

$$\Phi_{CL} = \Phi_{CE} + \Phi_F + \Phi_{ET}$$

the yield of the excited-state molecules, i.e. the fraction of molecules going through the chemiluminescent pathway actually producing an excited-state intermediate (chemiexcitation). The term Φ_F describes the excited-state quantum yield or the fraction of excited state intermediates actually emitting a photon (quantum yield of fluorescence or phos-

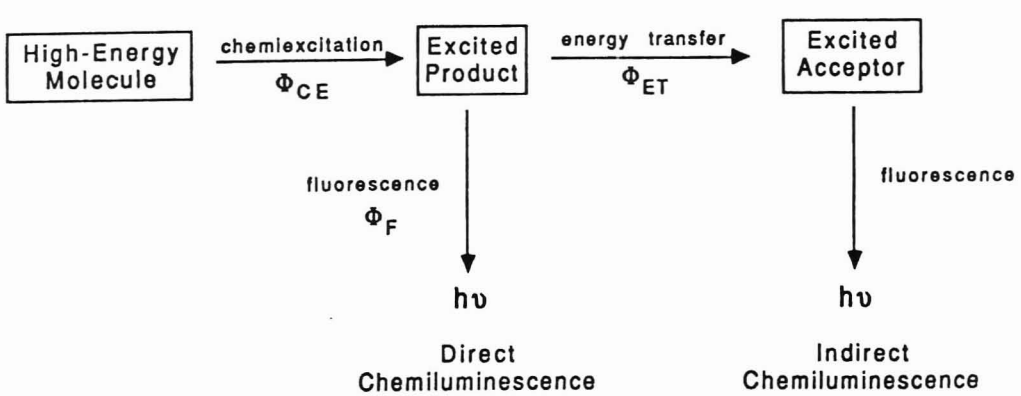

Figure 3. Direct and indirect chemiluminescence (*59*, *79*).

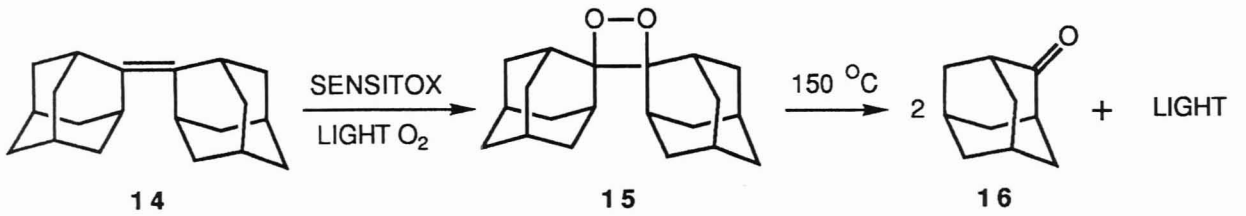

Figure 4. Most stable 1,2-dioxetane synthesized so far. SENSITOX: polymer bound Rose Bengal used as a photosensitizer for photooxygenation reactions (Hydron Laboratories, Inc., New Brunswick, NJ) (*77*, *78*).

phorescence) and the term Φ_{ET} describes the yield of the excited-state acceptor molecules resulting from the intermolecular energy transfer pathway.

In summary, for a reaction to be chemiluminescent, the chemical reaction has to be sufficiently exothermic to reach an electronically excited state and the chemical structure must allow the energy to be channeled to form an electronically excited state and must be capable of losing the energy by emitting a photon or transfering the energy to a fluorgenic/fluorescent molecule.

Stability and Reactivity of 1,2-Dioxetanes. Since the first report of the chemical (*71*) and photochemical (*72–74*) synthesis of 1,2-dioxetanes, a considerable number of derivatives have been synthesized that exhibit a wide range of thermal stabilities (for review see refs 75 and 76). Some are extremely unstable as would be chemically expected from peroxides forced into a four-membered ring structure. The first chemically synthesized 1,2-dioxetane, 3,3,4-trimethyl-1,2-dioxetane (**9**) (Figure 1 and ref 71), decomposes rapidly at room temperature. Others exert a remarkable thermostability. The most thermostable 1,2-dioxetanes described so far are derived from the sterically hindered adamantylidenadamantane (**14**) (Figure 4 and refs 77 and 78). The activation energy for decomposition is 37 kcal/mol and the half-life at 20 °C is more than 20 years. Luminescence could be triggered here only with heat (thermoluminescence) and thus the utility of these compounds for bioassays is limited; they have been, however, used as labels for a thermoluminescent immunoassay (*50*).

The reactivity and thermostability are governed by the chemical structure of the 1,2-dioxetanes and the mechanism by which the high-energy peroxide bond is cleaved. Steric hindrance at the dioxetane ring is certainly a stabilizing factor. During decomposition of the 1,2-dioxetanes the O–O bond is stretched, and while bending the C–C bond serves as a hinge which brings the substituents, attached to the C1 and C2 carbon atoms nearer together. If these substituents are adamantyl and/or aryl moieties, their opposing hydrogen atoms could intertwine and further add to stabilizing the high energy intemediates (*79*). For the decomposition two competing mechanisms have been proposed (Figure 5). A stepwise pathway involving homolysis of the O–O bond under formation of a biradical has been suggested for the decomposition of stable 1,2-dioxetanes requiring about 25–37 kcal/mol (*80*). The alternative mechanism assumes a concerted pathway involving an intramolecular electron transfer (*81–88*) also called CIEEL *chemically initiated electron exchange luminescence*. This mechanism is likely for 1,2-dioxetanes bearing substituents with low oxidation potential such as aryl–O^-. In this case the cleavage of the O–O bond is initiated by first transferring an electron from the oxidizable functionality e.g. phenoxide moiety to the antibonding orbital σ^* of the peroxide bond. Breakage of the O–O bond with concomitant formation of the two carbonyl species produces one

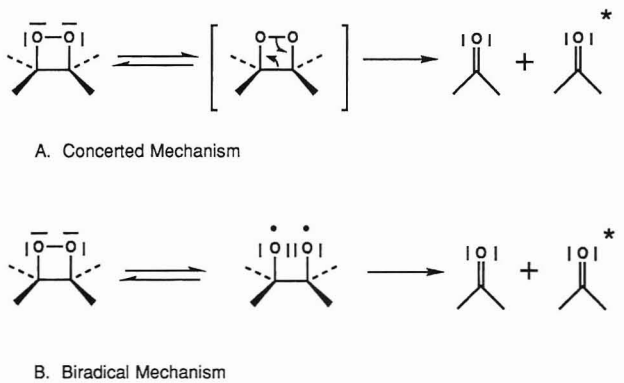

Figure 5. Mechanism of 1,2-dioxetane decomposition.

in the electronically excited state. The chemiluminescent efficiency is influenced by the mechanism of decomposition of the O–O bond (chemiexcitation Φ_{CE}) and the quantum yield of fluorescence (Φ_F) of the carbonyl cleavage products generated. A biradical mechanism generally produces low efficiency of chemiluminescence. In the case of the thermal decomposition of 3,3,4-trimethyl-1,2-dioxetane (**9**) and bis-(adamantyl)-1,2-dioxetane (**15**) the overall quantum yields (Φ_{CL}) are very low due to the biradical nature of the mechanism and the weak fluorescent properties (Φ_F) of the carbonyl species generated. In contrast, 1,2-dioxetane derivatives, which decompose via intramolecular electron transfer, generally produce chemiluminescence with high quantum yield. An observation made in 1982 (*89*) pointed into the right direction for the design of stable 1,2-dioxetanes generating chemiluminescence with high efficiency. It could be shown that 1,2-dioxetanes carrying a phenolic substituent produce chemiluminescence when triggered by base in organic solvents. Deprotonation to the peroxide-substituted species destabilized the 1,2-dioxetane to a dramatic extend: it decomposes 5.7×10^6 times faster than the protonated form.

Design of Highly Efficient and Stable 1,2-Dioxetanes. From these and other observations (see above) concerning the optimal structure of a stable but chemically or enzymatically triggerable 1,2-dioxetane, the following became clear: One carbon atom of the dioxetane ring carries an adamantyl moiety providing stability via sterical hindrance without interfering with the fluorescent signal (very low Φ_F, ref 6); the other carbon atom bears a fluorgenic phenolic substituent which is chemically stable in the protonated or protected form and can be activated by producing the phenoxide anion which in turn generates highly efficient chemiluminescence via the concerted electron transfer mechanism. Indirect chemiluminescence has also been observed in which an intermolecular electron transfer between a peroxide and a fluorescent hydrocarbon took place (*91*, *92*).

Figure 6 depicts some of the most interesting 1,2-dioxetanes. Compound **17** is triggerable by fluoride ions (*6*), **20** can be

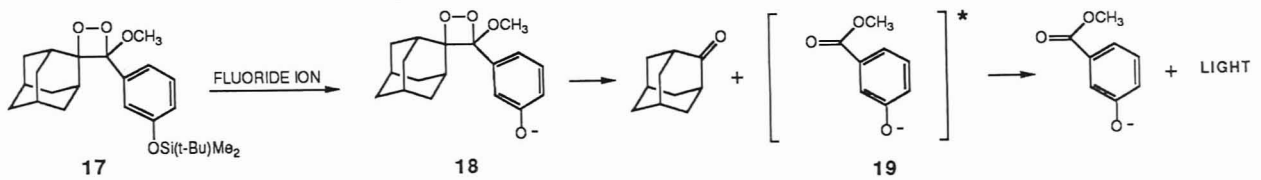

17 18 19

Thermal Stability

E_a = 28.4 kcal/mol
t(1/2) = 3.8 years at 25 °C

Triggering with Fluoride Ions

Solvent	ΦCL	ΦF	ΦCE
MeCN	0.094	0.21	0.45
DMSO	0.25	0.44	0.57

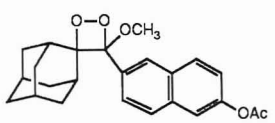

20

Thermal Stability

E_a = 32.5 kcal/mol
t(1/2) = 18.5 years at 25 °C

Triggering with Aryl Esterase (Tris buffer)

ΦCL = 1.6×10^{-6}
ΦF = 0.55
ΦCE = 3.0×10^{-6}

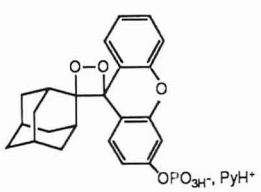

21

Thermal Stability

E_a = 30.7 kcal/mol
t(1/2 = 12.7 years at 25 °C

Triggering with Alkaline Phosphatase (221 buffer)

ΦCL = 1.4×10^{-6}
ΦF = 0.45
ΦCE = 3.0×10^{-6}

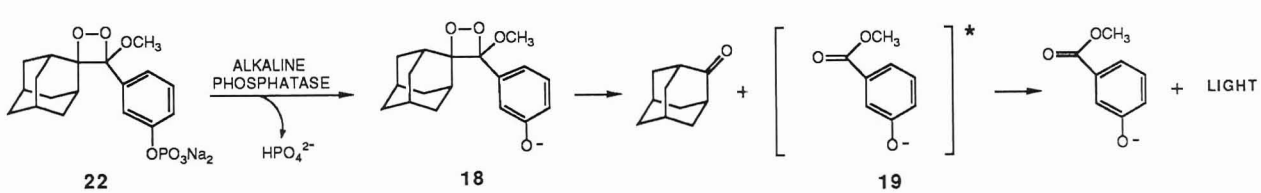

22 18 19

Thermal Stability

E_a = 32.5 kcal/mol
t(1/2) = 19 years at 25 °C

Triggering with Alkaline Phosphatase (221 buffer)

ΦCL = 1.3×10^{-5}
ΦCL = 4.8×10^{-3} (plus enhancer **28**)

Figure 6. Various 1,2-dioxetane derivatives (*5–7*, *46*, *90*): 221 buffer, 2-amino-2-methyl-1-propanol, 0.8 mM $Mg(OAc)_2$ pH 9.6.

either activated by hydroxide ions or activated enzymatically using aryl esterase (*5*), and **21** (*7*) and **22** (*90*) are both triggered enzymatically by alkaline phosphatase. The theme can be varied easily as shown in Figure 7 describing different analogues of **22** which all generate the same electronically excited species **19**, however, using different enzymes to triger chemiluminescence (*59*).

It is interesting to note, however, that there is one structural feature of 1,2-dioxetanes that significantly influences the efficiency (quantum yield Φ_{CL}), the emission wavelength of the electronically excited decomposition fragment, the rate of decomposition, and the rate of light release. It has been shown that the position of the trigger function on the aryl ring relative to the attachment point to the dioxetane ring is of critical importance: very high singlet chemiexcitation efficiencies (Φ_{CE}) are observed when the trigger function on the aryl moiety is positioned meta rather than para to the dioxetane ring (*6*). This has been confirmed in a recent study in which various "odd" and "even" substituted naphthyl derivatives of 1,2-dioxetanes have been synthesized and investigated (*93*). AMI molecular orbital calculations revealed for this system that the largest amount of charge can be transferred from a donor (e.g. the aryl–O^-anion) to an acceptor (the peroxide oxygen atom) if a meta ("odd") rather than para ("even") relationship exists (Figure 8). Odd, **23** and **24**, and even, **20**, naphthyl dioxetane derivatives (Figures 6 and 8) showed completely different luminescent kinetics. The naphthoxide anion of **23** and **24** produced either by base from **23** or by alkaline phosphatase from **24** generated extended chemiluminescence ("glow") with a half-life of about 30 min, while **20** gave a "flash"-like emission of light (Figure 2) after triggering with base with a half-life of only 15 s under otherwise comparable conditions. As the base-induced ester cleavage kinetics of **20** and **23** are apparently very similar if

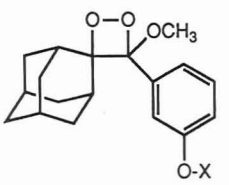

Substituent X	Enzyme
PO_3Na_2 (**22**)	Alkaline Phosphatase
Ac (**25**)	Aryl Esterase
SO_3Na	Sulfatase
H	Urease/Urea
β-Galactoside	β-Galactosidase

Figure 7. Enzyme triggerable derivatives of **18** (*59*, *79*).

not the same, the extended emission of the "odd" isomer **23**/**24** must be caused by an extended lifetime of the dioxetane anion **27**, while in the "even" or conjugated isomer **20** charge transfer and thus decomposition can apparently occur very rapidly (*93*). Basically the same contrasting results have been obtained in the case of phenoxy-substituted dioxetane derivatives **18**, **22**, and **25** (*93*, *94*, *6*) although in the latter case the *m*-**17** and *p*-*tert*-butyldimethylsilylphenyl ether dioxetane derivatives were compared after triggering with fluoride ions. Here it has been shown that the higher chemiluminescent quantum yield (Φ_{CL}) is not due to an increase in the fluorescent quantum yield (Φ_F) but that the chemiexcitation quantum yield (Φ_{CE}) is tremendously increased (*6*). Although the phenomenon is not quite understood today, it is likely that orbital symmetry and spin coupling greatly influence the charge transfer process in these derivatives. It could have wide ranging implications that also the emission spectra observed upon dioxetane decomposition are considerably different. Base hydrolysis of the acetate **23** generated green light emission at 555 nm, while base hydrolysis of the acetate **20** resulted in the emission of blue light at 495 nm. It is noteworthy that enzymatic hydrolysis of **23** using carboxylesterase in the presence of 0.1% BSA at pH 8 results in a "blue shift" to 530 nm (from 555 nm) as expected from having the chemiexcitation and light emission taking place in a hydrophobic environment (*93*).

Properties of Optimal Chemiluminescent Substrate. Today's most optimal configuration of a chemiluminescent substrate for the design of bioassays is the thermally stable dioxetane **22**, 3-(2′-spiroadamantane)-4-methoxy-4-(3″-phosphoryl)phenyl-1,2-dioxetane (Figures 6 and 7). This assay is based on the ultrasensitive, nonradioactive detection of alkaline phosphatase. As most of the current applications have been using this substrate, the properties of this unique compound will be discussed in more detail.

1,2-Dioxetane **22** is a very stable compound. The activation energy for its thermal decomposition is 32.5 kcal/mol and the half-life could be calculated to be 19 years at 25 °C (*59*). Due to the stability of the phosphate ester bond under a variety of chemical conditions, the nonenzymatic hydrolysis is extremely slow; i.e. the phosphate group is a highly efficient protecting group for the phenolic OH function. The half-life of the thermal decomposition in H_2O (activation energy 21.5 kcal/mol) is 142 h; in carbonate buffer at pH 12.0 it increases to 6214 h at 30 °C (*47*). This means that the luminescence background is very low. There seems to be no decomposition in the solid state at 4 °C. **22** is an excellent substrate for alkaline phosphatase; upon cleavage of the phosphate bond to give **18** (Figure 6) the 1,2-dioxetane structure becomes destabilized and decomposes rapidly. The total light emission is linearly dependent on the dioxetane and independent of enzyme concentration; i.e. the rate limiting step is apparently not the dephosphorylation of **22** but the decomposition of the dioxetane anion **18**. In the presence of excess **22** the light intensity, however, is a function of enzyme concentration and therefore allows for directly measuring the quantity of the enzyme (Figure 9). The 1,2-dioxetane anion **18** is moderately stable having a half-life between 2 and 30 min depending on the environment (*47*). The overall kinetics of the light emission is a two-step process. In the first step when substrate **22** is in excess, dephosphorylation proceeds in a constant rate depending on enzyme concentration. The anion **18** then decomposes with a finite half-life (second step). Due to the constant production of the slowly decomposing **18**, there is a lag phase. After a while the overall chemiluminescent reaction has reached a plateau (steady state). Thus the kinetics

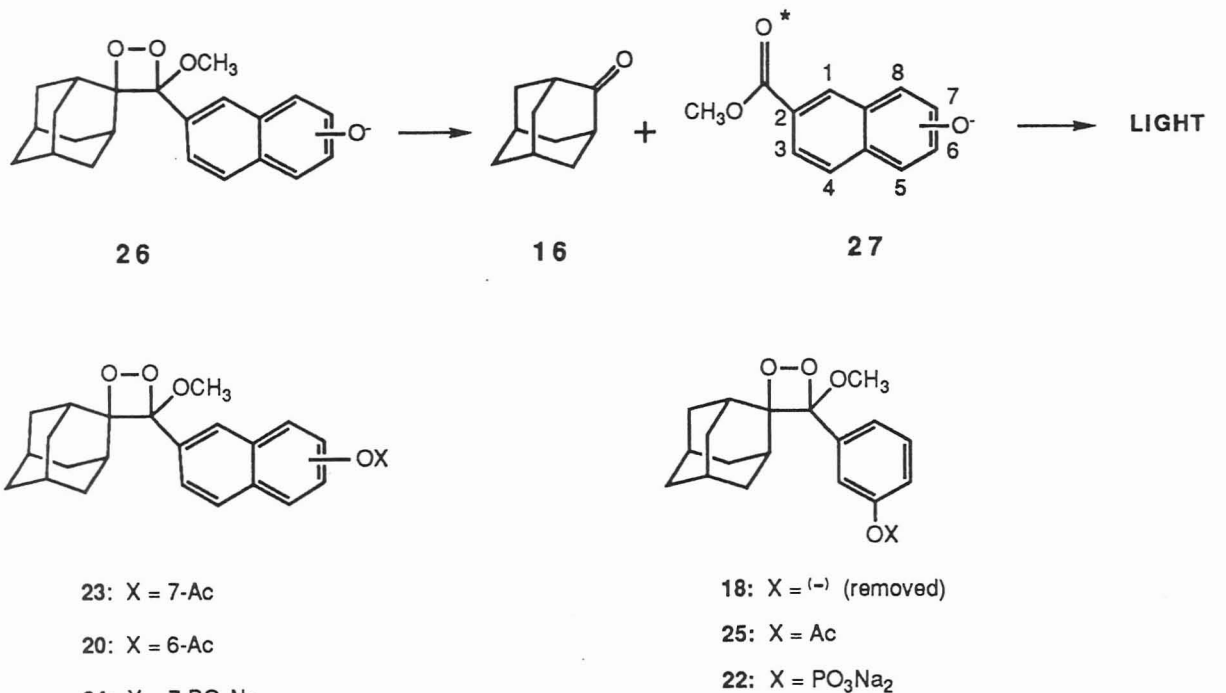

Figure 8. "Odd" and "even" substituted phenyl/naphthyl 1,2-dioxetane derivatives (*59*, *79*, *93*).

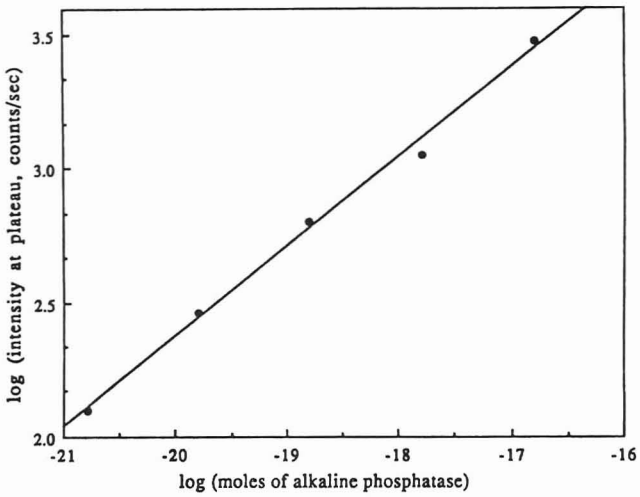

Figure 9. Correlation of alkaline phosphatase concentration versus chemiluminescence. Reprinted with permission of ref 46.

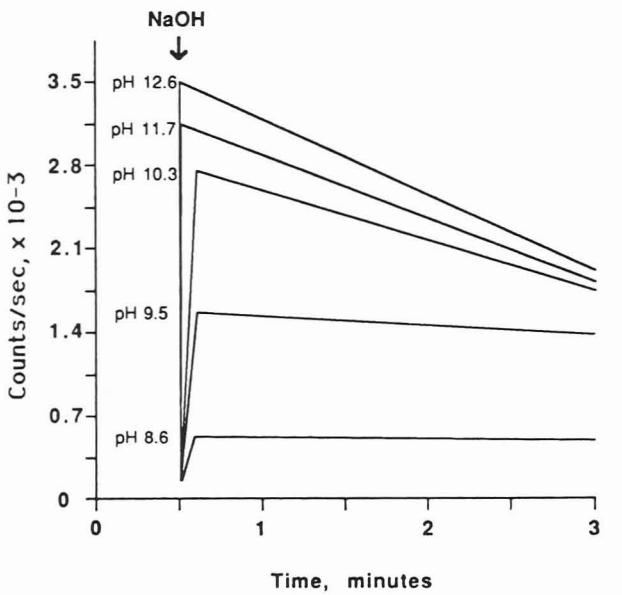

Figure 10. Influence of pH on the luminescence intensity of **22**. Reprinted with permission of ref 47.

is similar to the "glow" curve in Figure 2. The observed light emission maximum is at 470 nm. The pH optimum is at pH 9.0 and reflects the properties of the enzyme. However, the pH dependence of the light emitting process is different. The chemiluminescent emitting moiety is the methyl *m*-oxybenzoate anion **19** which has a pK_a of approximately 9.0. As the charge transfer process is extremely slow from the protonated form, it follows that acceleration of the rate-limiting step should be possible by increasing the pH. This is indeed the case (Figure 10 and ref 47). It is also obvious that the intensity of emission is considerably higher if the pH is above the pK_a of the anion *19*. If the pH optimum of an enzyme is far below the pK_a of the anion **19** as is the case for e.g. β-D-galactosidase with a pH optimum of 7.3 where the two reactions are decoupled, the enzymatic step can be done virtually without generating light. By addition of base, the light-producing process can be initiated. "Switching the light on and off" is also possible with the system consisting of **22** and alkaline phosphatase by simply changing between pH 9.5 and 7.0 (*47*).

Enhancement of the Chemiluminescent Efficiency. In addition to the amplification of chemiluminescence intensity via enzymatic catalysis (turn over), it was found that water-soluble macromolecules such as BSA (bovine serum albumin) (*47*) and aqueous micelles formed from a modified fluorescein

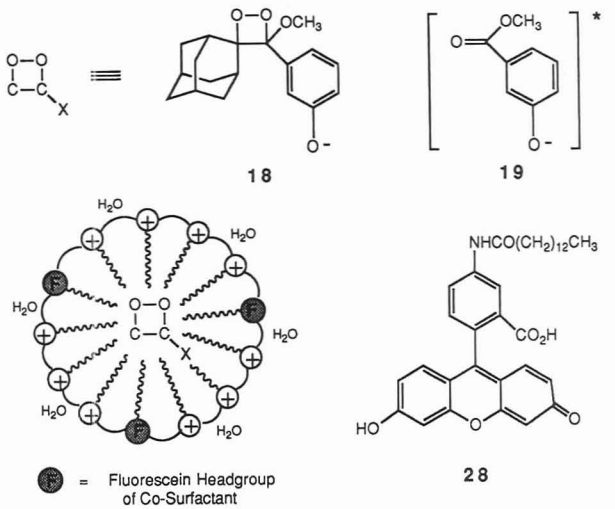

Conditions	Φ_{CL} (x 10^2)	$t_{(1/2)}$ (min) **18**	K_M (M)	k_{cat} (sec^{-1})
Fluorescent Micelles	0.48	36.9	1.3×10^{-4}	4.1×10^3
Homogeneous Fluorescein	0.026	3.27	1.2×10^{-4}	4.2×10^3
Buffer only	0.0013	3.08	1.2×10^{-4}	4.2×10^3

Figure 11. Enhanced chemiluminescence mediated by the interaction of **22** or **18/19** with micelles generated from CTAB (cetyltrimethylammonium bromide) and **28** (*46*, *106*).

molecule as cosurfactant *28* and CTAB (cetyltrimethylammonium bromide) as shown in Figure 11 (*46*, *59*) can result in a 3–400-fold signal enhancement. Although the true mechanism for this phenomenon is not known (it could also involve *indirect chemiluminescence*), one can speculate that either by means of hydrophobic "pockets" in the BSA molecule or by the micellar structure which will keep the anion **18/19** in a hydrophobic environment **18/19** is stabilized at the same time. That a hydrophobic interaction actually takes place could be shown by a "blue shift" of about 10 nm (*47*). This hydrophobic interaction of **18/19** is favored due to the greater lipophilicity of **18/19** compared to **22** which in turn is quite hydrophilic and therefore has good solubility in aqueous buffers necessary for the enzymatic trigger reaction. The stabilization could simply be due to the exclusion of water molecules, as placing **18/19** into a hydrophobic environment protects the anion **18/19** from being protonated. It is known that in the case were the actual emitter is a charge transfer excited state, the charge transfer process can be efficiently quenched in aqueous media via proton transfer.

Another interesting and versatile way of signal enhancement has recently been proposed (*59*) for the 1,2-dioxetane system utilizing energy transfer to tethered fluorescers such as **29** and **30**. A similar approach was used within the luminol system quite a while ago (*95*). Structures of **29** and **30** and quantum yields (Φ_{CL}) are shown in Figure 12.

Under optimal conditions using the enhancer **28** described in Figure 11, 0.0016 amol of alkaline phosphatase in 100 μL of buffer can be unequivocally detected (Figure 13 and ref 59). To optimize the system one has to take into consideration that the chemiluminescent efficiency of this system can be influenced negatively by dipole–dipole interactions with the solvent and proton transfer in polar, protic media which are required for biological compatibility. It has been shown that chemiexcitation efficiency is higher in a nonaqueous environment. Inhibitors of the trigger enzyme such as sodium dodecyl sulfate (SDS) could cause an irreversible decrease in signal intensity. Many dioxetanes are known to be destroyed via nonluminescent pathways by amines (*96*) and metal ions (*97*, *98*). It should be emphasized that for assays in solution the presence

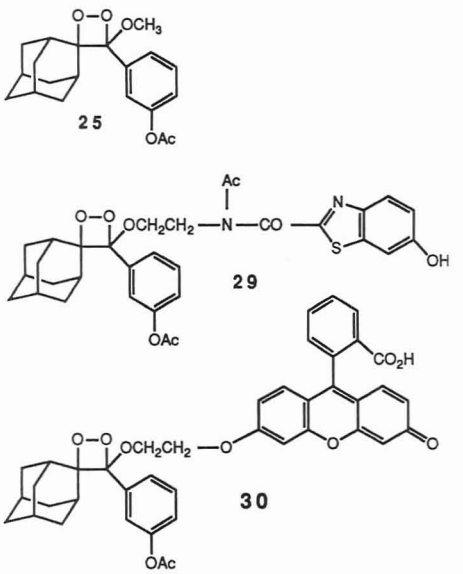

Triggering Conditions		Chemiluminescent Quantum Yields (x 10^2) 25	29	30
Enzymatic:	Aryl Esterase, pH 9.2	0.0012	0.29	0.39
Chemical:	Aqueous NaOH	0.00084	0.20	0.38
Chemical:	Aqueous CTAB, NaOH	0.017	2.2	1.4
Chemical:	DMSO, Fluoride	25	49	- - -

Figure 12. Enhanced chemiluminescence through intramolecular energy transfer to fluorescers tethered to **25** (*107*).

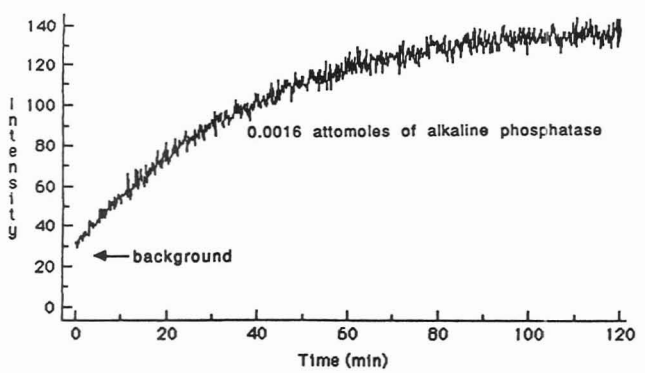

Figure 13. Ultrasensitive detection of alkaline phosphatase in 100 μL of 221 buffer containing **22**, enhancer composed from CTAB micelles, and **28**. Reprinted with permission of refs 46 and 106.

of stabilizing molecules (so-called enhancers), such as BSA or micelles formed from CTAB and **28**, is important to obtain high quantum yields, possibly due to either protection of the anionic species **18**/**19** against amines present in the buffer or protonation caused by the aqueous environment and/or indirect chemiluminescence.

The situation seems to be different when chemiluminescent reactions are being performed on membrane surfaces, which is the case in many applications involving blotting and hybridization steps. The hydrophobic interaction between the anion **18**/**19** and the membrane seems to have a stabilizing effect. It could be shown recently that there is indeed a hydrophobic interaction between the dioxetane substrate and the membrane (*99*). A hypochromic shift from 470 to 460 nm was observed in comparing the chemiluminescent reaction of **22** in solution or on a nylon membrane respectively (Figure 14). The solid line shows the chemiluminescent spectrum obtained on a nylon membrane, while the dotted line represents the results in solution. It has also to be considered that somewhat trapping or immobilizing the substrate **22** or **18**/**19**

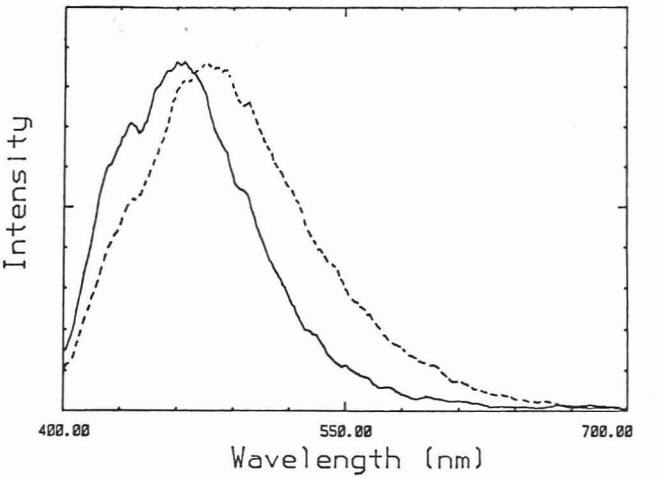

Figure 14. Chemiluminescence spectra obtained by triggering **22** with alkaline phosphatase. The dotted line represents the result obtained in solution (140 fmol of alkaline phosphatase labeled probe in 3 mL of 0.05 M bicarbonate/carbonate buffer pH 9.5, 1 mM $MgCl_2$) at room temperature. The solid line shows the luminescence resulting from 140 fmol of alkaline phosphatase labeled probe immobilized on a nylon membrane and incubated for 5 min with 0.4 mM **22** in the same buffer as described above. Both spectra represent the integration of five consecutive scans in a Spex Fluorlog fluorometer. Reprinted with permission of ref 99.

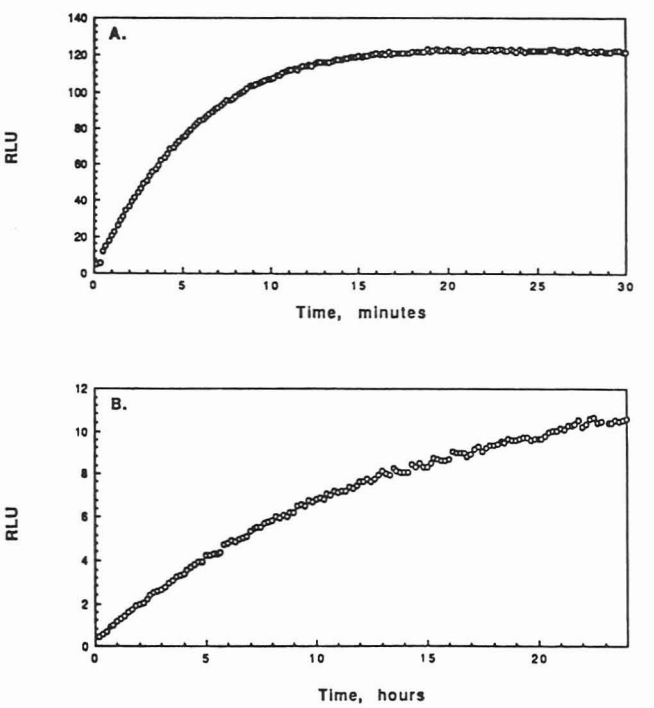

Figure 15. Kinetics of light emission of **22** triggered by alkaline phosphatase in solution and on a nylon membrane: Panel A, chemiluminescence from 0.5 mL of 0.4 mM **22** in buffer (see legend Figure 14) and 14 fmol of alkaline phosphatase labeled probe. The emitted light was measured in a Turner Model 20E luminometer. Panel B, 14 fmol of alkaline phosphatase labeled probe was immobilized on a nylon membrane disk of 6 mm diameter and incubated for 5 min with 0.4 mM **22** in buffer (see legend to Figure 14) in a heat-sealed plastic bag directly placed on the luminometer multiplier window of the Turner luminometer. RLU = relative light units. Reprinted with permission from ref 99.

on the surface of the membrane influences the kinetics of the enzymatic dephosphorylation. As in most applications alkaline phosphatase is attached to other high molecular weight target molecules, and it would not be surprising that the kinetics are much slower on a membrane surface compared to reactions in solution. This, in fact, has been shown to be the case (ref 99 and Figure 15). The upper panel shows the results with

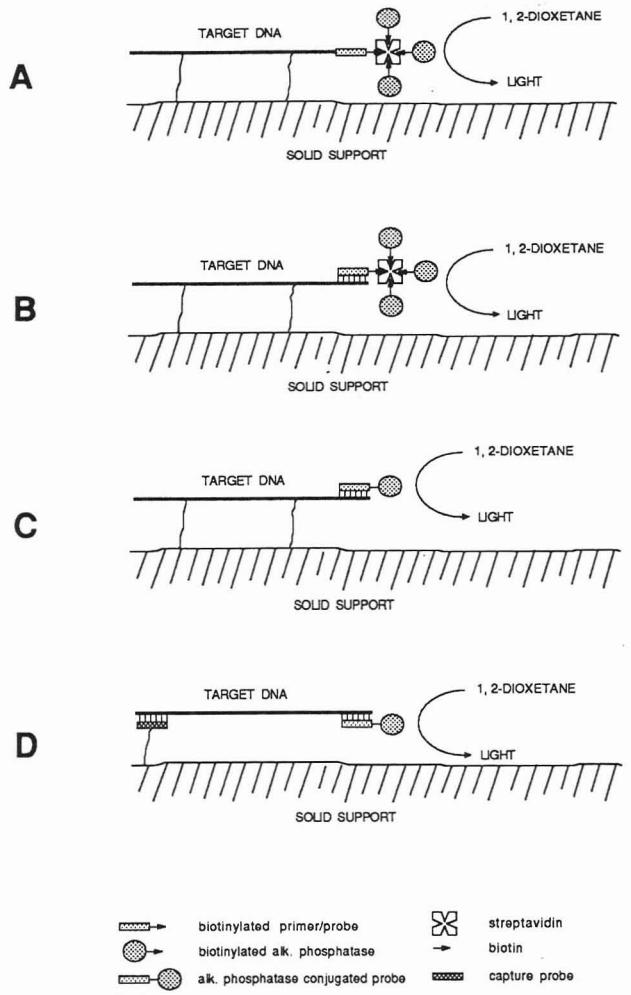

Figure 16. Schematic diagram of different strategies (A–D) for the chemiluminescent detection of DNA.

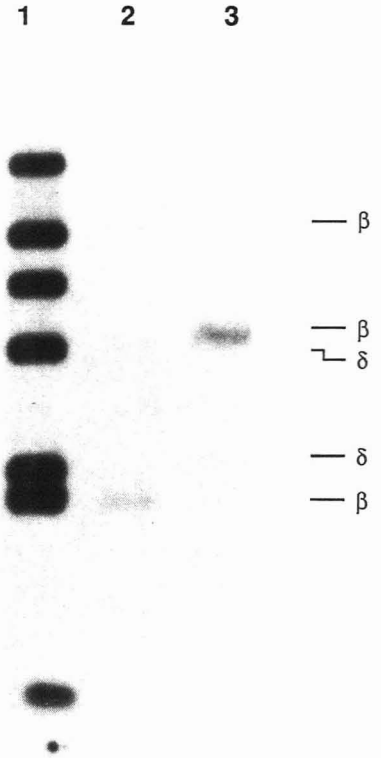

Figure 17. Chemiluminescent detection of human, single-copy globin genes by Southern blot analysis: lane 1, lambda Hind III marker; lane 2, 2 μg of human diploid fibroblast DNA digested with BamH I; lane 3, 2 μg of human diploid fibroblast DNA digested with Pst I. Exposure time was 5 min. For experimental details see ref 58. Reprinted with permission from ref 58. Copyright 1990, Life Technologies, Inc.

22 in solution; in the lower panel the alkaline phosphatase labeled probe was immobilized on a nylon membrane. The half-life of **18**/**19** on the membrane was estimated to be approximately 4 h compared to 2–30 min in carbonate buffer (*99*).

APPLICATIONS

Despite the fact that enzyme cleavable dioxetanes have only been first described in 1987 (*7*), they have already found widespread application in molecular biology, immunology, and biotechnology. Figure 16 outlines four of the most commonly used strategies for chemiluminescent detection involving DNA probes. In strategies A and B, the catalyzing enzyme is attached to biotinylated primers A or probes B (*29*, *37–39*) via a streptavidin bridge (*40*). In strategy C, the enzyme is directly conjugated to the probe (*15*, *17*, *22*, *23*). Strategy D, also known as sandwich hybridization (*55*), involves the use of two DNA probes. One probe is unlabeled and captures the target DNA and the labelled probe follows either the scheme of strategy B or C. The target DNA or, as in the case of strategy D, the capture probe usually is immobilized at one or multiple positions to a solid support such as membranes, beads, or microtiter plates. At this point it should be mentioned that instead of the described biotin/streptavidin system, one can probably also use the digoxigenin system (*103*). In the following, individual applications utilizing chemiluminescent DNA probes are reviewed and potential future applications are discussed.

Southern Blots. The method of Southern blotting (*26*) is widely used in molecular biology research for the identification of genes and other DNA fragments. The method usually involves the electrophoretic separation of restricted, genomic DNA, transfer of the resulting band pattern onto a membrane and subsequent hybridization of the membrane with a labeled probe. In the case of single copy genes (1–10) $\times 10^5$ molecules or (0.16–1.6) $\times 10^{-18}$ mol of target DNA need to be detected. In the past, mostly ^{32}P labeled probes have been used which have shown to give sufficient sensitivity. However, besides the hazards associated with radioactivity, the exposure times can be up to several days. The high turnover rate (4.1×10^3 molecules s^{-1}) of the phosphatase/dioxetane system (*79*) has shown to give comparable sensitivity in considerably reduced exposure time (*34*, *57*, *58*). Figure 17 shows a single copy gene Southern blot of human genomic DNA which was hybridized with a biotinylated probe for human β-globin according to strategy B (*58*).

DNA Fingerprinting. Genomic DNA of higher organisms contains so-called hypervariable minisatallite regions. These regions consist of short, tandemly organized DNA repeats that differ from one individual to another by their copy number, resulting in a high allelic variation. Digestion of genomic DNA with appropriate endonucleases generates, depending on the copy number, variable length fragments which, after hybridization with a minisatallite probe, reveal a distinct fingerprint of a given individual (*60*). The experimental procedure and the required sensitivity are similar to the ones described above for Southern blotting. To date, DNA fingerprinting has been applied in forensic science, paternity testing, population biology, linkage analysis, and others (*61*). Figure 18 shows examples of a single and a multilocus DNA fingerprint obtained by using the phosphatase/dioxetane detection system according to strategy C (*69*).

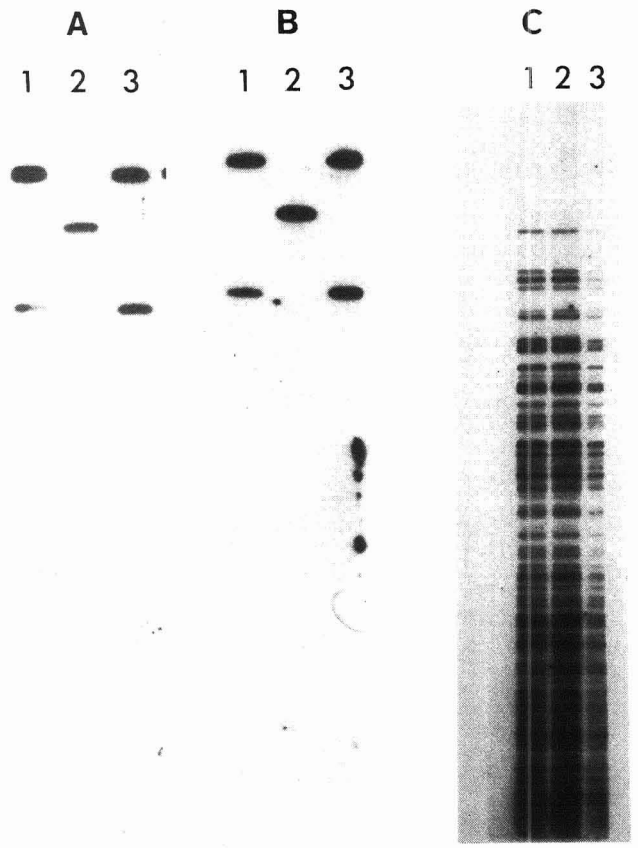

Figure 18. Chemiluminescent detected DNA fingerprinting. Comparison of a single locus DNA fingerprint after radioactive (^{32}P) (A) and chemiluminescent (1,2-dioxetanes) (B) detection. Two micrograms of Hinf I digested genomic DNA was analyzed per lane. Lanes 1 and 3 are from the same individual. Lane 2 shows one band only due to the small size of the second allele. Part C shows chemiluminescent detected multilocus DNA fingerprint. Hinf I (6, 4, and 2 μg) digested genomic DNA from one individual were analyzed in lanes 1–3, respectively. For experimental details see ref 69. Reprinted with permission from ref 69.

DNA Sequencing. The knowledge of the exact nucleotide sequence of a gene or eventually of entire genomes provides, of course, the ultimate genetic information. Recently, serious efforts have been started to entirely map and sequence the ~3 billion base pairs of the human genome. In order to make this project feasible, it is expected that the speed of the current DNA sequencing technology (*36*) will have to increase about 100 times over the next 10–15 years. One particular improvement presents the development of faster and more sensitive detection chemistries. The application of the phosphatase/dioxetane system for chemiluminescent detected DNA sequencing has been shown to give high sensitivity and considerably faster detection times than radioactive systems (*19*, *99*, *102*). Chemically (*54*) or enzymatic (*41*) generated DNA sequencing reaction products are separated by high resolution, denaturing polyacrylamide gel electrophoresis before being transferred onto a solid support, usually a nylon membrane for the chemiluminescent detection. Figure 19 (*102*) shows an example of such a chemiluminescent detected DNA sequence band pattern (according to strategy A) for standard dideoxy sequencing using a 5′-biotinylated primer and direct blotting electrophoresis (DBE) (*56*). Figure 20 (*104*) shows another example but for multiplex DNA sequencing (*42*) and using a 5′-biotinylated probe according to strategy B. Multiplex differs from standard DNA sequencing in a way that "n" numbers of clones can be pooled and processed in parallel throughout the sequencing procedure until they are demultiplexed or depooled again for the band analysis by specific hybridization. In both cases the image was captured by exposure to an X-ray film.

Table II. List of 1,2-Dioxetane Based DNA Probe Assays

organism	ref
Neisseria gonorrhoeae (tetM)	62
Chlamydia trachomatis	24
Hepatitis B	53, 18
Herpes Simplex	63

Table III. List of 1,2-Dioxetane Based Immunoassays

target molecule	ref
carcinoembrionic antigen (CEA)	50
α-fetoprotein (AFP)	48
human chorionic gonadotropin (β-hCG)	8
thyrotropin (TSH)	49
human luteinizing hormone (hLH)	8

DNA Probe Assays. Obviously, all of the above mentioned applications are DNA probe assays in one way or the other. However, the term DNA probe assay usually refers to clinical and industrial (e.g. food and beverage) applications in which DNA probes are used to detect pathogenic organisms (*21*). The experimental procedure has been adapted for processing multiple samples in parallel using dot blot and microtiter plate assays. Table II shows the growing list of organisms for which a chemiluminescent probe assay using the phosphatase/dioxetane system has already been developed. These assays follow the generalized detection schemes shown in Figure 10B–D.

Another variant of a DNA probe assay represents the method of in situ hybridization. This method allows the detection and study of nucleic acid sequences within their natural environment such as cells or biological tissue (*64*). The application of the phosphatase/dioxetane system for in situ hybridization is just emerging. To date, it has only been used to monitor the time course of cell infection with the Herpes Simplex virus (HSV 1) (*63*).

Immunoassays. Immunoassays usually do not involve DNA probes and therefore do not follow any of the strategies shown in Figure 10. However, since 1,2-dioxetanes present a very sensitive substrate also for immunoassays (*45–47*), this application was included in this review. The most common strategy for immunoassays is called ELISA (enzyme linked immunosorbent assay) in which antibodies, labeled e.g. with an enzyme, are used in various experimental configurations for the identification and quantification of biologically important molecules. Since the introduction of the first chemiluminescent immunoassay in 1976 (*43*) literally hundreds of modifications and applications have been described (*44*). Today, the major application of immunoassays is in the area of clinical diagnostics. Table III presents examples of immunoassays in which 1,2-dioxetanes were used and compared to other chemiluminescent or colorimetric substrates. The result revealed a 4–67-fold improvement in sensitivity for the dioxetane substrate depending on assay and experimental conditions.

Future Applications. As already indicated in the immunoassay section, the application of the phosphatase/dioxetane system is certainly not limited only to the use in combination with DNA probes. Besides the immunoassays, a similar need for fast and sensitive detection methods exists for proteins, e.g. in the areas of Western blotting and protein sequencing. A variety of new applications can be expected to grow rapidly along with the development of more versatile chemistries as discussed in the chapter on chemical and physical properties of 1,2-dioxetanes. A start in this direction presents, firstly, the development of modified 1,2-dioxetanes which can be triggered also by other enzymes than alkaline

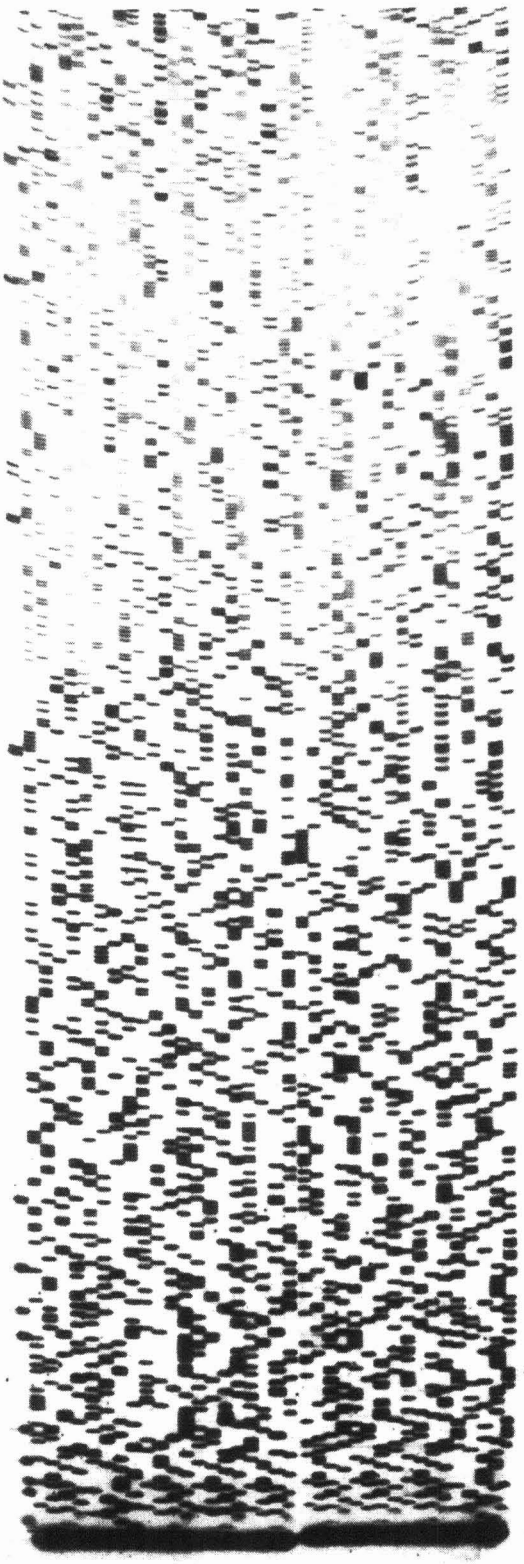

Figure 19. Standard DNA sequencing using chemiluminescent detection. The conditions included single-stranded template DNA, 5′-biotinylated primer, sequenase, manganese buffer, direct blotting electrophoresis (DBE), phosphatase/dioxetane detection, and 1-h exposure time. For more experimental details see ref 102. Reprinted with permission from ref 102.

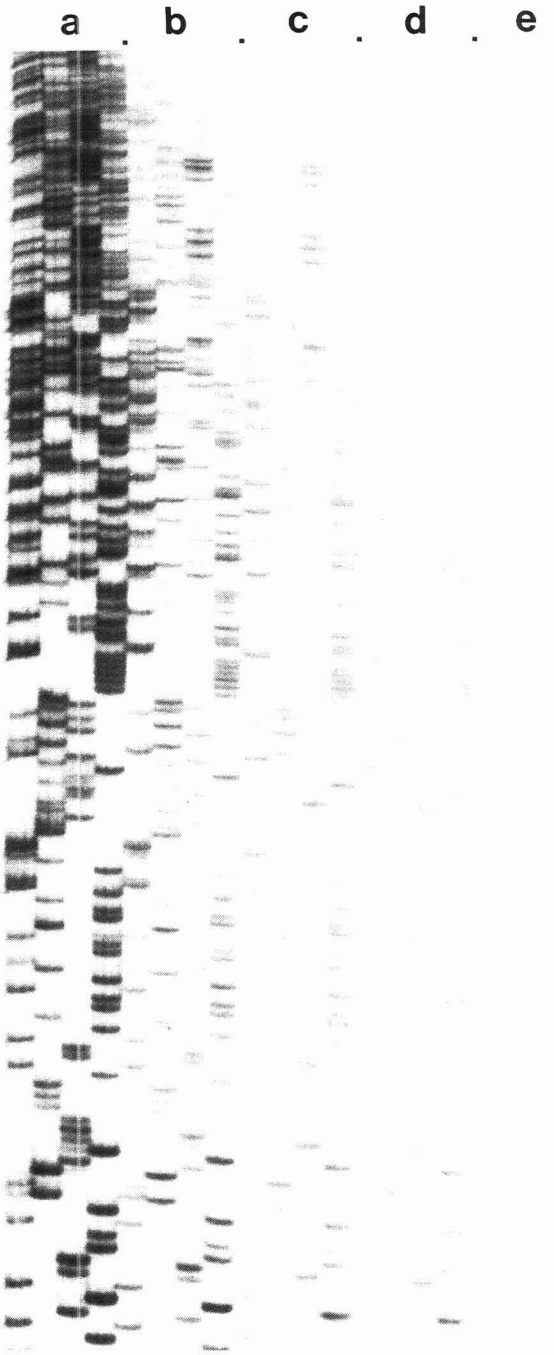

Figure 20. Multiplex DNA sequencing using chemiluminescent detection. The conditions included double stranded template DNA, Taq DNA polymerase, 5′-biotinylated probe, phosphatase/dioxetane detection, and 1 min exposure time. The multiplex conditions were as follows: 1 clone (a), pool of 2 clones (b), pool of 5 clones (c), pool of 10 clones (d), and pool of 20 clones (e).

phosphatase, such as aryl esterase, sulfatase, urease, and β-galactosidase (Figure 7 and refs 8, 59, and 79). Secondly, the fact that different isomeric trigger functions on the aryl ring generate light at different wavelengths can be used to design "multichannel" bioassays. Different trigger modes (e.g. different enzymes and/or chemistries) on the aryl- and/or naphthyl dioxetane isomers could be utilized to design multiplex nonradioactive bioassay systems. Another area that potentially will have a large impact on future applications and throughput lays in the further and new development of automated detection equipment, such as luminometers (*65*, *105*) and light-sensitive cameras (*66*), which can image the signal directly off a membrane (*19*, *67*, *68*).

CONCLUSION

This review clearly shows that chemiluminescent detection and in particular the phosphatase/dioxetane system presents a viable alternative to radioactive, colorimetric, and fluorescent detection of DNA probes and other applications. In terms of sensitivity, Table I and the presented application data all indicate that the sensitivity of this system is equal to or superior to conventional detection methods. In terms of han-

dling, this technology is, with respect to radioactive and fluorescent technologies, currently a little more labor intensive. However, this is compensated by a much shorter exposure time resulting in an overall shorter detection time except for the fluorescent detection. Finally, one should also keep in mind that this technology is only a couple of years old and there are many areas that still can be improved.

In summary, the advantages of this ultrasensitive detection system are as follows: (1) sensitivity similar or greater than radioactive detection using radioisotopes such as ^{32}P and ^{35}S; (2) elimination of complex chemiluminescent systems involving hydrogen peroxide to generate the peroxy intermediate and extensive optimization of the different additives necessary to generate high quantum yield; (3) stable substrates that can be directly activated, thus simplifying operation and optimization; (4) easy detection using standard and nonsophisticated equipment such as X-ray films or instant Polaroid films to generate a hardcopy of the experimental results or simple luminometers employing a photomultiplier tube in the photon counting mode; (5) low background and a wide linear range; (6) no radiation hazards; (7) relatively inexpensive reagents and equipment; (8) versatility, reactions can be conducted in solution, on latex beads, in microtiter plate wells, and on surfaces such as membranes.

ACKNOWLEDGMENT

We thank especially Dr. Paul Schaap for many helpful discussions and comments. We thank Drs. Hashem Akhavan-Tafti, Irena Bronstein, Renuka DeSilva, Allen Giles, Ed Jablonski, Fritz Pohl, Peter Richterich, Nancy Sasavage, Paul Schaap, and Mickey Urdea for providing results prior to publication. We are also grateful to Peggy Simpson for assistance in preparing the manuscript.

Registry No. 1,2-Dioxetane, 6788-84-7.

LITERATURE CITED

(1) Meinkoth, J.; Wahl, G. *Anal. Biochem.* **1984**, *138*, 267–284.
(2) Hames, B. D., Higgins, S. J., Eds. *Nucleic Acid Hybridization: a Practical Approach*; IRL Press: Oxford, 1985.
(3) Keller, G. H., Manak, M. M., Eds. *DNA Probes*; Stockton Press: New York, 1989.
(4) Symons, R. H., Ed. *Nucleic Acids Probes*; CRC press: Boca Raton, FL, 1989.
(5) Schaap, A. P.; Handley, R. S.; Giri, B. P. *Tetrahedron Lett.* **1987**, *28*, 935–938.
(6) Schaap, A. P.; Chen, T.-S.; Handley, R. S.; Desilva, R.; Giri, B. P. *Tetrahedron Lett.* **1987**, *28*, 1155–1158.
(7) Schaap, A. P.; Sandison, M. D.; Handley, R. S. *Tetrahedron Lett.* **1987**, *28*, 1159–1162.
(8) Bronstein, I.; Edwards, B.; Voyta, J. C. *J. Biolumin. Chemilumin.* **1989**, *4*, 99–111.
(9) Wiedeman, E. *Ann. Phys. Chem.* **1888**, *34*, 446–463.
(10) Campbell, A. K. *Chemiluminescence*; VCH Verlagsgemeinschaft: Weinheim, 1988.
(11) Gould, S. J.; Subramani S. *Anal. Biochem.* **1988**, *175*, 5–13.
(12) Kricka, L. J. *Anal. Biochem.* **1988**, *175*, 14–21.
(13) DeLuca, M. A., McElroy, W. D., Eds. *Methods in Enzymology*; Academic Press: Orlando FL, 1986; Vol. 133, p 133.
(14) Thorpe, G. H. G. and Kricka, L. J. *Methods Enzymol.* **1986**, *133*, 331–353.
(15) Urdea, M. S.; Warner, B. D.; Running, J. A.; Stempien, M.; Clyne, J. M.; Horn, T. *Nucl. Acids Res.* **1988**, *16*, 4937–4956.
(16) Ibanez, E. C.; Jablonski, E. G. *Abstracts of Fourth San Diego Conference on Nucleic Acid Applications* **1989**, 18.
(17) Murakami, A.; Tada, J.; Yamagata, K.; Takano, J. *Nucl. Acids Res.* **1989**, *17*, 5587–5595.
(18) Bronstein, I., Voyta, J. C. and Edwards, B. *Anal. Biochem.* **1989**, *180*, 95–98.
(19) Beck, S.; O'Keeffe, T.; Coull, J. M.; Köster, H. *Nucl. Acids Res.* **1989**, *17*, 5115–5123.
(20) Leong, M. M. L., Milstein, C. and Pannell, R. *J. Histochem. Cytochem.* **1986**, *34*, 1645–1650.
(21) Matthews, J. A. and Kricka, L. J. *Anal. Biochem.* **1988**, *169*, 1–25.
(22) Jablonski, E. G., Moomaw, E. W.; Tullis, R. H.; Ruth, J. I. *Nucl. Acids Res.* **1986**, *14*, 6115–6128.
(23) Ghosh, S. S.; Kao, P. M.; Kwoh, D. Y. *Anal. Biochem.* **1989**, *178*, 43–51.
(24) Clyne, J. M.; Running, J. A.; Stempien, M.; Stephens, R. S.; Akhaven-Tafti, H.; Schaap, A. P.; Urdea, M. S. *J. Biolumin. Chemilumin.* **1989**, *4*, 357–366.
(25) Haralambidis, J.; Angus, K.; Pownall, S.; Duncan, L.; Chai, M.; Tregear, G. H. *Nucl. Acids Res.* **1990**, *18*, 501–505.
(26) Southern, E. M. *J. Mol. Biol.* **1975**, *98*, 503–517.
(27) Collins, M. L.; Hunsaker, W. R. *Anal. Biochem.* **1985**, *151*, 211–224.
(28) Leary, J. J.; Brigati, D. J.; Ward, D. C. *Proc. Natl. Acad. Sci. U.S.A.* **1983**, *80*, 4045–4049.
(29) Kumar, A.; Tchen, P.; Roullet, F.; Cohen, J. *Anal. Biochem.* **1988**, *169*, 376–382.
(30) Cardullo, R. A.; Agrawal, S.; Flores, C.; Zamecnik, P. C.; Wolf, D. E. *Proc. Natl. Acad. Sci. U.S.A.* **1988**, *85*, 8790–8794.
(31) Chehab, F. F.; Kan, Y. W. *Proc. Natl. Sci. U.S.A.* **1989**, *86*, 9178–9182.
(32) Lichter, P.; Tang, C.-J. C.; Call, K.; Hermanson, G.; Evans, G. A.; Housman, D.; Ward, D. C. *Science* **1990**, *247*, 64–69.
(33) Pollard-Knight, D.; Read, Ch. A.; Downes, M. J.; Howard, L. A.; Leadbetter, M. R.; Pheby, S. A.; McNaughton, E.; Syms, A.; Brady, M. A. W. *Anal. Biochem.* **1990**, *185*, 84–89.
(34) Pollard-Knight, D.; Simmonds, A. C.; Schaap, A. P.; Akhavan, H.; Brady, M. A. W. *Anal. Biochem.* **1990**, *185*, 353–358.
(35) Feinberg, A. P.; Vogelstein, B. *Anal. Biochem.* **1983**, *132*, 6–13.
(36) Trainor, G. L. *Anal. Chem.* **1990**, *62*, 418–426.
(37) Wachter, L.; Jablonski, J.-A.; Ramachandran, K. L. *Nucl. Acids Res.* **1986**, *14*, 7985–7994.
(38) Coull, J. M.; Weith, H. L.; Bischoff, R. *Tetrahedron Lett.* **1986**, *27*, 3991–3994.
(39) Agrawal, S.; Christodoulou, C.; Gait, M. J. *Nucl. Acids Res.* **1986**, *14*, 6227–6245.
(40) Wilchek, M.; Bayer, E. A. *Anal. Biochem.* **1988**, *171*, 1–32.
(41) Sanger, F.; Nicklen, S.; Coulson, A. R. *Proc. Natl. Acad. Sci. U.S.A.* **1977**, *74*, 5463–5467.
(42) Church, G. M.; Kieffer-Higgins, S. *Science* **1988**, *240*, 185–188.
(43) Schroeder, H. R.; Vogelhut, P. O.; Carrico, R. J.; Boguslaski, R. C.; Buckler, R. T. *Anal. Chem.* **1976**, *48*, 1933–1937.
(44) Schölmerich, J.; Andreesen, R., Kapp, A., Ernst, M, Woods, W. G., Eds. *Bioluminescence and Chemiluminescence: New Perspectives*; John Wiley & Sons: Chichester, 1987.
(45) Bronstein, I.; Kricka, L. J. *J. Clin. Lab. Anal.* **1989**, *3*, 316–322.
(46) Schaap, A. P.; Akhavan, H.; Romano, L. J. *Clin. Chem.* **1989**, *35*, 1863–1864.
(47) Bronstein, I. *Luminescence Immunoassays and Molecular Applications*; van Dyke, K., Ed.; CRC Press, Inc.: Boca Raton, FL, 1990; pp 255–272.
(48) Thorpe, G. H. G.; Bronstein, I.; Kricka, L. J.; Edwards, B.; Voyta, J. C. *Clin. Chem.* **1989**, *35*, 2319–2321.
(49) Bronstein, I.; Voyta, J. C.; Thorpe, G. H. G.; Kricka, L. J.; Armstrong, G. *Clin. Chem.* **1989**, *35*, 1441–1446.
(50) Hummelen, J. C.; Luider, T. M.; Wynberg, H. *Methods Enzymol.* **1986**, *133*, 531–557.
(51) Septak, M. *J. Biolumin. Chemilumin.* **1988**, *2*, 258.
(52) Urdea, M. S. Personal communication.
(53) Urdea, M. S.; Kolberg, J.; Warner, B. D.; Horn, T.; Clyne, J.; Ku, L.; Running, J. A. *Luminescence Immunoassays and Molecular Applications*; van Dyke, Knox, Ed.; CRC Press, Inc.: Boca Raton, FL, 1990.
(54) Maxam, A. M.; Gilbert, W. *Proc. Natl. Acad. Sci. U.S.A.* **1977**, *74*, 560–564.
(55) Dunn, A. R.; Hassell, J. A. *Cell* **1977**, *12*, 23–36.
(56) Beck, S.; Pohl, F. M. *Embo J.* **1984**, *3*, 2905–2909.
(57) Bronstein, I.; Voyta, J. C.; Lazzari, K. G.; Murphy, O.; Edwards, B.; Kricka, L. J. *Biotechniques* **1990**, *8*, 310–314.
(58) Carlson, D. P.; Superko, C.; Mackey, J.; Gaskill, M. E.; Hansen, P. *Focus* **1990**, *12*, 9–12.
(59) Schaap, A. P.; Akhavan, H.; Romano, L. J. *Abstracts of Fourth San Diego Conference on Nucleic Acid Applications* **1989**, 9.
(60) Jeffreys, A. J.; Wilson, V.; Thein, S. L. *Nature* **1985**, *314*, 67–73.
(61) Cawood, A. H. *Clin. Chem.* **1989**, *35*, 1832–1837.
(62) Sanchez-Pescador, R.; Running, J. A.; Stempien, M. M.; Urdea, M. S. *Antimicrob. Agents Chemother.* **1989**, *33*, 1813–1815.
(63) Bronstein, I.; Voyta, J. C. *Clin, Chem.* **1989**, *35*, 1856–1857.
(64) Gowans, E. J.; Jilbert, A. R.; Burrell, C. J. *Nucleic Acids Probes*; Symons, R. H., Ed.; CRC Press: Boca Raton, FL, 1989.
(65) Jago, P. H.; Simpson, W. J. Denyer, S. P.; Evans, A. W.; Griffiths, M. W.; Hammond, J. R. M.; Ingram, T. P.; Lacey, R. F.; Macey, N. W.; McCarthy, B. J.; Salusbury, T. T.; Senior, P. S.; Sidorowicz, S.; Smither, R.; Stanfield, G.; Stanley, P. E. *J. Biolumin. Chemilumin.* **1989**, *3*, 131–145.
(66) Epperson, P. M.; Sweedler, J. V.; Bilhorn, R. B.; Sims, G. R.; Denton, M. B. *Anal. Chem.* **1988**, *60*, 327A–335A.
(67) Leaback, D. H.; Haggart, R. *J. Biolumin. Chemilumin.* **1989**, *4*, 512–522.
(68) Karger, A., Ives, J. T., Weiss, R. B., Harris, J. M. and Gesteland, R. F. *Proc. SPIE—Int. Soc. Photoopt. Instrum. Eng.* in press.
(69) Giles, A. F.; Booth, K. J.; Parker, J. R.; Garman, A. J.; Carrick, D. T.; Akhavan, H.; Schaap, A. P.; *Proceedings of the International Society for Forensic Haemogenetics*; Springer-Verlag, in press.
(70) McCapra, F. *Q. Rev.* **1970**, 485–510.
(71) Kopecky, K. R.; Mumford, C. *Can. J. Chem.* **1969**, *47*, 709–711.
(72) Bartlett P. D.; Mendenhall, G. D.; Schaap, A. P. *Ann. N. Y. Acad. Sci.* **1970**, *171*, 79–87.
(73) Bartlett, P. D.; Schaap, A. P. *J. Am. Chem. Soc.* **1970**, *92*, 3223–3225.
(74) Mazur, S.; Foote, C. S. *J. Am. Chem. Soc.* **1970**, *92*, 3225–3226.
(75) Adam, W. *The Chemistry of Functional Groups*; John Wiley: New York, 1983; Chapter 24.
(76) Wilson, T., *Singlet Oxygen*; CRC Press: Boca Raton, FL, 1985; Vol II, Chapter Two.

(77) Wieringa, J. H.; Stratling, J.; Wynberg, H.; Adams, W. *Tetrahedron Lett.* **1972**, 169–172.
(78) Schuster, G. B.; Turro, N. J.; Steinmetzer, H.-C.; Schaap, A. P.; Faler, G.; Adam, W.; Lui, J. C. *J. Am. Chem. Soc.* **1975**, *97*, 7110–7118.
(79) Schaap, A. P. Personal communication.
(80) Richardson, W. H.; Montgomery, G. C.; Yelvington, M. B.; O'Neal, H. E. *J. Am. Chem. Soc* **1974**, *96*, 7525–7532.
(81) Koo, J.-Y.; Schuster, G. B. *J. Am. Chem. Soc.* **1977**, *99*, 6107–6109.
(82) Schuster, G. B.; Dixon, B.; Koo, J.-Y.; Schmidt, S. P.; Smith, J. P. *Photochem. Photobiol.* **1979**, *30*, 17–26.
(83) Handley, R. S.; Stern, A. J.; Schaap, A. P. *Tetrahedron Lett.* **1985**, 3183–3186.
(84) Schaap, A. P.; Gagnon, S. D.; Zaklika, K. A. *Tetrahedron Lett.* **1982**, 2943–2946.
(85) Lee, C.; Singer, L. A. *J. Am. Chem. Soc.* **1980**, *102*, 3823–3929.
(86) McCapra, F.; Beheshti, I.; Burford, A.; Hann, R. A.; Zaklika, K. A. *J. Chem. Soc., Chem. Commun.* **1977**, 944–946.
(87) McCapra, F. *J. Chem. Soc., Chem. Commun.* **1968**, 155–156.
(88) Turro, N. J.; Lechtken, P.; Schuster, G.; Orell, J.; Steinmetzer, H.-C.; Adam, W. *J. Am. Chem. Soc.* **1974**, *96*, 1627–1629.
(89) Schaap, A. P.; Gagnon, S. D. *J. Amer. Chem. Soc.* **1982**, *104*, 3504–3506.
(90) Schaap, A. P. *Photochem. Photobiol.* **1988**, *47S*, 50.
(91) Schuster, G. B.; Schmidt, S. P. *Adv. Phys. Org. Chem.* **1982**, *18*, 187–238.
(92) Adam, W.; Cueto, O. J. *J. Am. Chem. Soc.* **1979**, *101*, 6511–6515.
(93) Edwards, B.; Sparks, A.; Voyta, J. C.; Bronstein, I. *J. Biolumin. Chemilumin.* **1990**, *5*, 1–4.
(94) Bronstein, I.; Voyta, J. V.; Edwards, B. *J. Biolumin. Chemilumin.* **1988**, *2*, 186.
(95) Ribi, M. A.; Wei, C. C.; White, E. H. *Tetrahedron* **1972**, *28*, 481–492.
(96) Wilson, T. *Int. Rev. Sci.: Phys. Chem., Ser. Two* **1976**, *9*, 265–322.
(97) Wilson, T.; Landis, M. E.; Baumstark, A. L.; Bartlett, P. D. *J. Am. Chem. Soc.* **1973**, *95*, 4765–4766.
(98) Bartlett, P. D.; Baumstark, A. L.; Landis, M. E. *J. Am. Chem. Soc.* **1974**, *96*, 5557–5558.
(99) Tizard, R.; Cate, R. L.; Ramachandran, K. L.; Wysk, M.; Voyta, J. C.; Murphy, O. J.; Bronstein, I. *Proc. Natl. Acad. Sci. U.S.A.* **1990**, *87*, 4514–4518.
(100) Hauber, R.; Geiger, R. *J. Clin. Chem. Clin. Biochem.* **1987**, *25*, 511–514.
(101) Hauber, R.; Geiger, R. *Nucl. Acids Res.* **1988**, *16*, 1213.
(102) Richterich, P. Thesis, Universität Konstanz, FRG, 1990.
(103) *Genius: non-radioactive DNA labeling and detection kit, Application Manual*; Boehringer: Mannheim, 1989.
(104) Kissinger, C.; Dunne, T.; Beck, S.; Köster, H. Unpublished results.
(105) Bronstein, I.; Kricka, L. J. *Am. Clin. Lab.* Jan/Feb **1990**, 33–37.
(106) Schaap, A. P.; Akhavan-Tafti, H. Personal communication.
(107) Schaap, A. P.; Akhavan-Tafti, H.; DeSilva, R. Personal communication.

ARTICLES

Dissociation of Tetrahexylammonium Picrate Ion Pairs Adsorbed at the Chloroform–Water Interface

Lawrence Amankwa and Frederick F. Cantwell*

Department of Chemistry, University of Alberta, Edmonton, Alberta, Canada T6G 2G2

Two membrane phase separators, made of porous Teflon and of paper, are used to measure isotherms for adsorption of tetrahexylammonium picrate (QP) at the chloroform–water interface in a rapidly stirred liquid–liquid dispersion. The ion-pair species QP and the cation Q^+ are both surface-active but the picrate anion P^- is not. In the presence of a large excess of P^- dissociation of the adsorbed species QP is suppressed. Its adsorption follows a Langmuir isotherm. Without a large excess of P^- present, the adsorbed QP dissociates appreciably on the interface. The ion-pair dissociation constant is $K_{Dis,QP} = (1.2 \pm 0.1) \times 10^{-5}$ mol/L. Aspects that are peculiar to ion-pair dissociation at an interface, as opposed to ion-pair dissociation in bulk solution, are discussed and quantified. These include competitive adsorption between Q^+ and QP as well as the presence of an electric charge on the interface as a result of adsorbed Q^+.

Experiments employing a rapid-stir apparatus with a porous Teflon membrane phase separator previously have been used to measure adsorption isotherms for ion pairs at the chloroform–water interface. Langmuir adsorption isotherms have been observed for interfacial adsorption of ion pairs formed between cationic metal–ligand complexes and simple anions (*1*) and for the ion pair tetrahexylammonium bromothymol blue (QHB) (*2*). For the latter system not only does the ion pair adsorb but also both the constituent ions, Q^+ and HB^-, adsorb. Competitive adsorption between HB^- and QHB was characterized. Analytically, bromothymol blue is an important reagent anion used in the photometric determination of cations by ion-pair extraction (*3*).

An even more important reagent for this purpose is picrate, P^- (*3*, *4*). Picrate differs from bromothymol blue in that it does not adsorb at the chloroform–water interface. In the present paper it is shown that this difference leads to a significant difference in the properties of interfacially adsorbed tetrahexylammonium picrate ion pair (QP) compared to QHB in the same concentration range. Adsorbed QP is involved in a dissociation equilibrium into Q^+, which is adsorbed, and P^-, which is in the aqueous phase. Use of a paper membrane phase separator allows direct measurement of the concentration of P^- in the aqueous phase during stirring. The ion-pair dissociation of QP at the interface is quantitatively characterized.

0003-2700/90/0362-2270$02.50/0 © 1990 American Chemical Society

EXPERIMENTAL SECTION

Reagents. Water was demineralized, distilled, and finally distilled over alkaline permanganate. Aqueous phosphate buffer at pH 6.5 was prepared from sodium hydrogen phosphate and sodium dihydrogen phosphate at an ionic strength of 0.050. Reagent grade chloroform was washed with water shortly before use. A 1×10^{-3} M solution of reagent grade tetrahexylammonium bromide (Eastman Kodak Co., Rochester, NY) was prepared in chloroform. Reagent grade picric acid (Matheson, Coleman and Bell, Ltd.) was used as received to prepare a 1×10^{-3} M aqueous solution in pH 6.5 phosphate buffer. Chloroform solutions of the ion-pair QP were prepared in the concentration range 2.0×10^{-6} to 2.0×10^{-4} M as follows: An aqueous solution of QBr and an aqueous solution of pH 6.5 picric acid, containing at least a 5-fold stoichiometric excess of picric acid, were pipetted into a separatory funnel containing 60 mL of chloroform. After the funnel was shaken for about 5 min and the phases allowed to separate, the chloroform extract was transferred into a second separatory funnel and washed with 20 mL of fresh aqueous buffer. The chloroform phase was then transferred into a 100-mL volumetric flask and diluted to volume with chloroform.

Apparatus. The rapid-stir extraction apparatus incorporating the porous membrane phase separator and photometric detector interfaced to an IBM-XT microcomputer has previously been described in detail (*2, 5*). A porous Teflon membrane was used as a phase separator when the chloroform phase was being monitored and a paper membrane was used when the aqueous phase was being monitored. In all experiments 100.0 mL of both of the chloroform and aqueous phases were combined in the rapid-stir cell at 20 ± 1 °C. Stirring was at a constant speed of 2300 rpm and the pumping rate was 1.0 mL/min.

In some experiments absorbance of the separated phase was measured by flowing it through the on-line spectrophotometer, while in other experiments absorbance was measured on a collected portion of the separated phase in a Model 8451A diode array spectrophotometer (Hewlett-Packard). Measurements of pH were made with an Accumet Model 525 pH meter (Fisher Scientific) with a combination electrode. Interfacial tensions between previously equilibrated chloroform and aqueous solutions were made by the drop-volume technique as previously described (*2*).

Liquid–Liquid Distribution. The distribution isotherm for tetrahexylammonium, added as tetrahexylammonium bromide, QBr, between chloroform and aqueous bulk-liquid phases was measured by a batch equilibration experiment, as previously described (*2*).

Interfacial Adsorption. Interfacial adsorption isotherms between the chloroform–water interface and the bulk-liquid phases were measured for tetrahexylammonium and for the ion-pair QP using the rapid-stir cell. Details of the measurement of the adsorption isotherm for tetrahexylammonium have previously been presented (*2*). For QP, interfacial adsorption was measured as follows: A pH 6.5 aqueous buffer and a chloroform solution of QP were combined and stirred to achieve distribution equilibrium. While stirring, and with the aid of the Teflon membrane phase separator, the concentration of QP was measured in the chloroform phase using the absorbance at 372 nm. The stirrer was then shut off and, after the phases completely coalesced, the concentration of QP was again measured in the chloroform phase. The amount of QP adsorbed at the interface was calculated from the difference in concentrations with the stirrer off and on. Repeating the experiment with different initial concentrations of QP yields the adsorption isotherm.

In a second set of experiments, to demonstrate the effect of NaP on adsorption of QP, the procedure was repeated but with excess NaP added to the aqueous phase.

In a third set of experiments, the procedure was again repeated, without added NaP, but using the paper phase separating membrane instead of the Teflon one and measuring the absorbance of picrate ion in the aqueous phase at 362 nm.

RESULTS AND DISCUSSION

Distribution of Q^+. Both the liquid–liquid distribution and the interfacial adsorption previously have been studied for tetrahexylammonium bromide (*2*). The species adsorbed at the interface is the cation Q^+ with electroneutrality near the positively charged interface provided by an equivalent surface excess of negative charge in the diffuse part of the electrical double layer in the aqueous phase (*6, 7*).

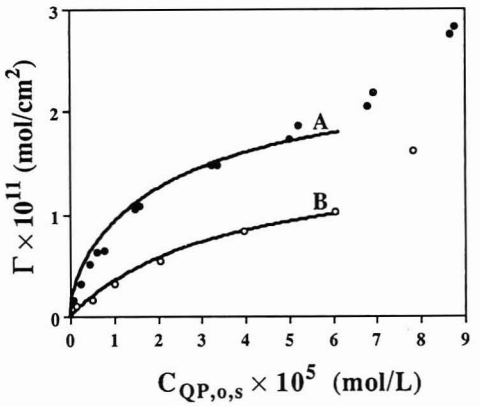

Figure 1. Adsorption isotherms for tetrahexylammonium picrate at the chloroform–aqueous interface. Points are experimental. Curve A is in absence of added NaP, line calculated with eq 10. Curve B is in presence of 4.0×10^{-4} M NaP, line calculated with eq 4. Constants used: $K_{QP} = 2.75 \times 10^4$, $\Gamma_{QP,SAT} = 1.60 \times 10^{-11}$, $K_{Dis,QP} = 1.2 \times 10^{-5}$. Only data up to $C_{QP,o,s} \approx 6 \times 10^{-5}$ M are of interest.

Distribution of P^-. In aqueous solution at pH 6.5 picric acid is fully dissociated to picrate ion. Previous studies have shown that NaP does not extract into chloroform (*8*). Furthermore, neither P^- nor NaP adsorbs at the chloroform–water interface. This is revealed both by the fact that the concentration of P^- in the aqueous phase is the same whether the stirrer is on or off and by the fact that the "Gibbs isotherm", which is a plot of interfacial tension versus the logarithm of the concentration of sodium picrate (not shown) (*9*), is essentially horizontal (slope 0.15 ± 0.06).

Distribution of QP. The ion-pair extraction constant for QP between chloroform and water is about 4×10^{10} (*10–12*), so that there is virtually none of this component present in the aqueous phase at the concentrations employed in this work. Also at these concentrations, dimerization and higher aggregation of the ion pair in chloroform are negligible (*3, 12*). The dissociation constant of QP in chloroform has not been measured but is expected to be about 10^{-7} (*2, 3, 13, 14*). Thus, dissociation of QP in chloroform may or may not occur to some extent at concentrations as low as 10^{-6} M. However, since concentrations of tetrahexylammonium picrate in chloroform were measured spectrophotometrically against a calibration curve of absorbance versus concentration, the measured concentrations are correct, independent of whether any ion-pair dissociation occurs in chloroform. (Incidently, the calibration curve was linear with zero intercept.)

The total moles of tetrahexylammonium adsorbed at the interface, n_{ADS}, is calculated from the expression

$$n_{ADS} = (C_{QP,o,ns}V_o) - (C_{QP,o,s}V_o) \quad (1)$$

where $C_{QP,o}$ is the analytical concentration of tetrahexylammonium picrate in the chloroform phase, V_o is the volume of the chloroform phase, and the subscripts "s" and "ns" refer to "stirring" and "no-stirring", respectively.

Two interfacial adsorption isotherms for tetrahexylammonium picrate are shown in Figure 1. These isotherms are plots of Γ versus $C_{QP,o,s}$. Interfacial concentration (i.e. surface excess) in units mol·cm^{-2} is given by

$$\Gamma = n_{ADS}/A \quad (2)$$

The interfacial area, A, has the value 3.9×10^{-4} cm^2, as measured in this apparatus at 2300 rpm (*2*). Curve A in Figure 1 was measured with no excess sodium picrate (NaP) added to the aqueous phase while curve B was measured with 4.0×10^{-4} M NaP added to the aqueous phase.

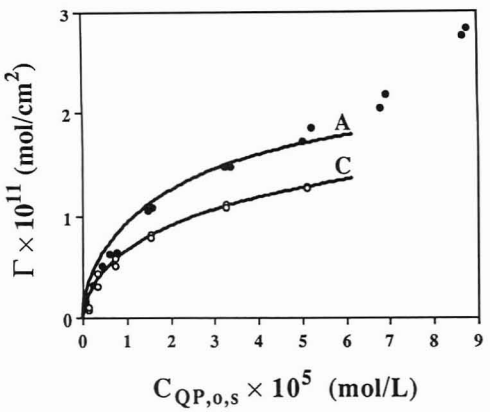

Figure 2. Adsorption of tetrahexylammonium picrate in the absence of added NaP. Curve A is the identical adsorption isotherm as curve A in Figure 1. Curve C is a plot of Γ_Q calculated from experimental values of $[P^-]_a$ using eq 6. Solid line in curve C is empirical fit. Only data up to $C_{QP,o,s} \approx 6 \times 10^{-5}$ M are of interest.

Briefly, these adsorption isotherms involve the adsorption of the species QP from chloroform onto the interface and the partial dissociation of this adsorbed ion-pair according to the reaction

$$(QP)_i \rightleftharpoons (Q^+)_i + (P^-)_a \quad (3)$$

in which the surface-active cation Q^+ is adsorbed at the interface but the non-surface-active anion P^- enters the aqueous phase. Addition of sodium picrate to the aqueous phase shifts the equilibrium in eq 3 to the left, suppressing the ion-pair dissociation (Le Chatelier's principle). A picrate concentration of 4.0×10^{-4} M is sufficient to quantitatively suppress ion-pair dissociation so that curve B in Figure 1 is the adsorption isotherm for the species QP, alone. The details and justification for this model are presented below.

The data in curve B, up to about $C_{QP,o,s} = 6 \times 10^{-5}$ M, conform to the Langmuir adsorption equation (*6*)

$$\Gamma_{QP}(\text{curve B}) = \frac{\Gamma_{QP,SAT} K_{QP} C_{QP,o,s}}{1 + K_{QP} C_{QP,o,s}} \quad (4)$$

in which Γ_{QP}(curve B) is the surface excess of the species QP, $\Gamma_{QP,SAT}$ is the surface excess at monolayer saturation by the species QP, and K_{QP} is the equilibrium constant in L/mol for the adsorption of the species QP. It can be demonstrated that the data in curve B up to about $C_{QP,o,s} = 6 \times 10^{-5}$ M conform to Langmuir behavior by the fact that a plot of $C_{QP,o,s}(\Gamma_{QP}\text{(curve B)})^{-1}$ versus $C_{QP,o,s}$ is linear for the first six data points (*8*). The line has a slope of $(0.62 \pm 0.10) \times 10^{11}$ cm^2/mol and an intercept of $(2.3 \pm 0.3) \times 10^6$ cm^2/L. The value of K_{QP} is calculated from the ratio slope/intercept to be $(2.7 \pm 0.6) \times 10^4$ L/mol and the value of $\Gamma_{QP,SAT}$ is calculated from (slope)$^{-1}$ to be $(1.6 \pm 0.3) \times 10^{-11}$ mol/cm^2.

The solid line in curve B of Figure 1 was calculated via eq 4 using the above reported values of K_{QP} and $\Gamma_{QP,SAT}$. The data up to $C_{QP,o,s} \approx 6 \times 10^{-5}$ M are well represented by the line, but above that concentration the data (seventh point) exhibit a marked upward deviation from Langmuir behavior. The general shape of the overall isotherm is a familiar one, having been designated as a type II BET isotherm in gas–solid adsorption (*15*) and as a type L3 or perhaps L4 isotherm in liquid–solid adsorption (*16–19*). Nearly always, this type of upward deviation from Langmuir behavior is the result of interactions between adsorbed solute molecules coming into play when they become crowded together as monolayer coverage is approached (*15*, *16*). Specifically, it may be due to reorientation of the molecules which allows tighter packing or to multilayer formation (*18–20*). In the present case, where we are interested in studying dissociation of the ion-pair QP, we shall deal only with data in the Langmuir region, at $C_{QP,o,s} \lesssim 6 \times 10^{-5}$ M, in order to avoid complications introduced by interactions between ion pairs on the interface.

Comparing curves A and B in Figure 1, it is proposed that the difference between these two curves is due mainly to dissociation of QP via eq 3. This proposition can be tested by measuring the concentration of picrate ion in the aqueous phase. In the absence of added NaP, it is found that there is no P^- in the aqueous phase with the stirrer turned off but that P^- appears in the aqueous phase when the stirrer is turned on (curve C, Figure 2). This evidence confirms the occurrence of ion-pair dissociation at the interface.

A further question is whether the dissociation shown in eq 3 can be quantitatively expressed in terms of the equilibrium dissociation quotient predicted from the law of mass action

$$K_{Dis,QP} = \Gamma_Q [P]_a / \Gamma_{QP} \quad (5)$$

in which $[P^-]_a$ is the picrate ion concentration in the aqueous phase and Γ_Q is the surface excess of the adsorbed species Q^+. By analogy with ion-pair dissociation in solution, it might seem that the value of Γ_{QP} to be used in eq 5 when no excess picrate is present should be equal to Γ_{QP} (curve B) from eq 4, obtained in the presence of a large excess of P^-. However, this reasoning is not necessarily correct for species adsorbed at the interface. For example, it has clearly been demonstrated for the ion-pair tetrahexylammonium bromothymol blue (QHB) that both of the Langmuir adsorption parameters ($\Gamma_{QHB,SAT}$ and K_{QHB}) are decreased by the presence of an excess of one of the constituent ions (e.g. HB^-) as a result both of competitive adsorption and of changes in the chemical character of the interface (*2*). Also, it has been found in the picrate system that addition of a large excess of tetraalkylammonium bromide quantitatively prevents adsorption of the tetraalkylammonium picrate ion pair because of adsorption of Q^+ (*21*).

Therefore, in the current system it is anticipated that the presence of adsorbed Q^+, which is present as a result of dissociation of adsorbed QP, might reduce $\Gamma_{QP,SAT}$ and K_{QP} for the remaining undissociated QP to values lower than those measured for curve B. If this happens then Γ_{QP} to be used in eq 5, when no excess picrate is present, will not be equal to Γ_{QP} (curve B) obtained in the presence of a large excess of picrate. In any event, whether or not this is true, the correct value of Γ_{QP} to be used in eq 5 can be obtained in the following manner. First, from the stoichiometry of eq 3 it is seen that in the absence of added P^-

$$\Gamma_Q = [P^-]_a V_a / A \quad (6)$$

Shown as curve C in Figure 2 is a plot of $[P^-]_a V_a A^{-1}$ versus $C_{QP,o,s}$. Curve A in Figure 2 is the same as Curve A in Figure 1. Next, according to the proposed model

$$\Gamma(\text{curve A}) = \Gamma_{QP} + \Gamma_Q \quad (7)$$

Therefore, Γ_{QP} can be calculated by rearranging eq 7 and substituting for Γ_Q from eq 6

$$\Gamma_{QP} = \Gamma(\text{curve A}) - [P^-]_a V_a / A \quad (8)$$

A plot of Γ_{QP} obtained from eq 8 versus Γ_{QP} (curve B) obtained from eq 4 is approximately linear with zero intercept but, instead of having a slope of 1, it has a slope of 0.52 ± 0.04. While the linearity of this plot is fortuitous, the fact that the values of Γ_{QP} from eq 8 fall well below the Langmuir values of Γ_{QP} (curve B) demonstrates that the adsorbed Q^+, arising from dissociation of the ion pair, does in fact decrease $\Gamma_{QP,SAT}$ and/or K_{QP} to values below those that they have in curve B. Furthermore, the magnitude of this effect is in the range that would be predicted by analogy with the QHB system (*2*) for the values of Γ_Q involved. The alternative explanation, that either the Teflon membrane or the paper membrane might not be measuring the true bulk-phase equilibrium concen-

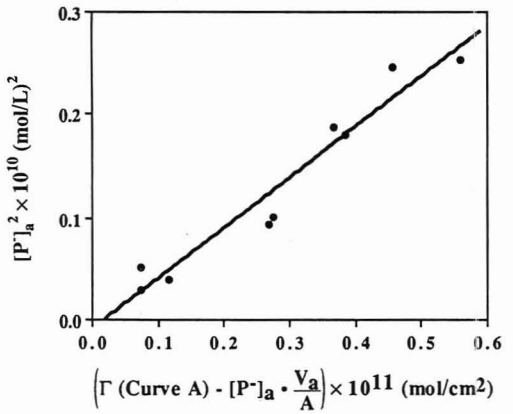

Figure 3. Plot based on eq 9 to evaluate the ion-pair dissociation quotient $K_{Dis,QP}$. The points are experimental and the line is from linear regression.

tration, has already been ruled out (*22*). Thus, the important conclusion here is that the values of Γ_{QP} to be used in eq 5 to fit the data in curve A should be calculated with eq 8 rather than being calculated with eq 4.

Combining eq 5, 6, and 7 and rearranging yields the expression

$$[P^-]_a^2 = K_{Dis,QP}\frac{A}{V_a}\left(\Gamma(\text{curve A}) - [P^-]_a\frac{V_a}{A}\right) \quad (9)$$

Shown in Figure 3 is a plot of this equation with the data taken from curves A and C. The points are calculated at values corresponding to the data points in curve A. The solid line in Figure 3 is the linear regression line. The fact that this plot has a zero intercept ($-0.9 \pm 1.5) \times 10^{-2}$ and is linear ($r = 0.97$) validates eq 5 with $K_{Dis,QP}$ as a constant. From the slope of this line (0.49 ± 0.05) the interfacial ion-pair dissociation quotient is found to be $K_{Dis,QP} = (1.2 \pm 0.1) \times 10^{-5}$ mol/L. The scatter of the points in Figure 3 reflects, among other things, the fact that the term (Γ(curve A) $- [P^-]_a V_a/A$) is the difference between numbers of similar magnitude and also the fact that $[P^-]_a^2$ is the square of a measured concentration.

It can be calculated from eq 5, and it can be observed graphically from the closeness of curves A and C in Figure 2, that in the absence of added excess P^- adsorbed tetrahexylammonium picrate is extensively dissociated at surface concentrations below about 2×10^{-11} mol/cm^2 (i.e. below $C_{QP,o,s} \approx 6 \times 10^{-5}$ M at the present stirring rate). Furthermore it can also be calculated from eq 5 that in the presence of 4.0×10^{-4} M excess P^- dissociation of adsorbed QP is never greater than about 3%, justifying the assumption that the isotherm in curve B is that of the ion-pair only.

It should be noted that the evaluations of Γ_{QP}, Γ_Q, $[P^-]_a$, and $K_{Dis,QP}$, described above, utilized data only from curves A and C and did not employ curve B. Nevertheless, it is worthwhile trying to express curve A in terms of curve B in order to develop an expression relating curve A to the solution concentration, $C_{QP,o,s}$. The key to doing this is the relationship between Γ_{QP} and Γ_{QP} (curve B) which is emperically expressed by the slope of a plot of these two quantities, i.e. 0.52 (see above). Combining this relationship with eqs 5, 6, and 7 gives the expression

$$\Gamma(\text{curve A}) = 0.52\Gamma_{QP}(\text{curve B}) + \left(K_{Dis,QP}\frac{V_a}{A}(0.52)\Gamma_{QP}(\text{curve B})\right)^{1/2} \quad (10)$$

in which Γ_{QP}(curve B) is calculated via the Langmuir equation, eq 4. The line in curve A in Figures 1 and 2 was calculated by using eq 10. The agreement between the points and the calculated line is within experimental error, considering that the relative uncertainty in the calculated line is about 10% and that in the points is about the same.

Table I. Parameters Related to Electrical Double Layer Theory and to the Thermodynamic Ion-Pair Dissociation Constant (See Text for Details)

$10^5 C_{QP,o,s}$, mol/L	c_x,[a] (mol/L)	Ψ_0, V	Ψ_x, V	$\gamma_{P,x}$[b]	$\gamma_{P,x}^2 \exp(+F\Psi_x/RT)$
0.250	0.064	0.0059	0.0021	0.74	0.60
0.450	0.069	0.0083	0.0030	0.73	0.60
0.594	0.073	0.0096	0.0034	0.73	0.61
0.775	0.076	0.0110	0.0039	0.72	0.61
1.463	0.086	0.0149	0.0053	0.71	0.62
1.575	0.087	0.0154	0.0055	0.71	0.62
3.225	0.101	0.0206	0.0074	0.69	0.63
3.375	0.102	0.0209	0.0075	0.69	0.63
5.00	0.111	0.0241	0.0086	0.68	0.64
5.20	0.112	0.0244	0.0087	0.68	0.64

[a] Ionic strength of the bulk aqueous phase is $c_a = 0.050$. [b] Ionic activity coefficient in the bulk aqueous phase is $\gamma_{P,a} = 0.77$ from D–H limiting law.

Effect of Interfacial Charge. When surface-active ions are adsorbed at a liquid–liquid interface, an electrical potential difference is developed between the charge-surface containing the charges of these ions and the bulk aqueous solution (*6*). The existence of a potential can be demonstrated by microelectrophoresis (*23*) or potentiometry (*24*). In the simplest case, the interfacial potential, ψ_0, can be calculated from Γ_Q by using the Gouy–Chapman equation to describe the "electrical double layer" (*6*, *25*, *26*). As a consequence of this potential, ions, including P^-, have a different concentration in the aqueous phase near the interface than they have in the bulk aqueous phase, and the degree of this difference is greater at higher potentials. For this reason one might have expected that $K_{Dis,QP}$ in eq 5 would not have been a constant. However, it is shown below that at the low potentials involved a constant value for $K_{Dis,QP}$ is consistent with theory.

The thermodynamic dissociation constant of QP at the interface is

$$K^\circ_{Dis,QP} = \frac{a_{Q,i}a_{P,x}}{a_{QP,i}} = \frac{\Gamma_Q[P^-]_x\gamma_{P,x}^2}{\Gamma_{QP}} \quad (11)$$

where $[P^-]_x$ is the molar concentration of picrate in the aqueous phase at a distance x-cm away from the charge surface and $\gamma_{P,x}$ is the ionic activity coefficient of picrate ion at distance x. It is assumed in eq 11 that $\gamma_{Q,x}$ for the adsorbed ion Q^+, which protrudes into the aqueous phase, is also equal to $\gamma_{P,x}$ and that $\gamma_{QP,x}$ for the adsorbed neutral ion pair is equal to 1. The distance x is the location of the plane of closest approach to the charge surface by nonpaired picrate ions. It is taken to be the sum of the radius of the Q^+ ion (9 Å) and the radius of the hydrated P^- ion (5 Å), on the assumption that ions closer than a hydrated radius will be ion paired with Q^+. Ionic radii were measured from space-filling molecular models.

The charge-surface of Q^+ ions is probably located at or very close to the chloroform–water interface. This is because Q^+ is spherically symmetrical, unlike ions such as dodecyltrimethylammonium for which the charge surface is said to be located a few angstrom units away from the interface (*6*, *25*, *26*).

At the low ψ_0 and ionic strength involved the Debye–Hückel approximation can be used to simplify the Gouy–Chapman equation (*27*). The interfacial potential is given by the expression

$$\psi_0 \approx (4.39 \times 10^3)F\Gamma_Q c_a^{-1/2} \quad (12)$$

in which F is the Faraday constant and c_a is the ionic strength

in the bulk aqueous solution (i.e. 0.050). The potential at distance x is given by

$$\psi_x \approx \psi_0 \exp((-3.29 \times 10^7)c^{1/2}x) \quad (13)$$

in which $x = 14. \times 10^{-8}$ cm, as discussed above. The concentration of P^- at x is related to its measured concentration in bulk solution by the Boltzmann equation

$$[P^-]_x = [P^-]_a \exp\left(+\frac{F\psi_x}{RT}\right) \quad (14)$$

Substituting for $[P^-]_x$ in eq 11 from eq 14 yields

$$K^\circ_{Dis,QP} = \frac{\Gamma_Q[P^-]_a}{\Gamma_{QP}}\gamma_{P,x}^2 \exp\left(+\frac{F\psi_x}{RT}\right) \quad (15)$$

from which it is seen by comparison with eq 5 that

$$K_{Dis,QP} = K^\circ_{Dis,QP}\left[\gamma_{P,x}^2 \exp\left(+\frac{F\psi_x}{RT}\right)\right]^{-1} \quad (16)$$

For consistency the ionic activity coefficient should be calculated from the Debye–Hückel limiting law (*28*)

$$\gamma_{P,x} = \text{antilog}\ (-0.51c_x^{1/2}) \quad (17)$$

since the Debye–Hückel approximation was used in deriving eqs 12–14. The ionic strength, c_x, at distance x includes contributions from Na^+, $H_2PO_4^-$, and HPO_4^{2-} ions, all of whose concentrations at x are different from those in bulk solution but can be calculated via the appropriate forms of the Boltzmann equation (*27*) and from the Q^+ ion. The concentration of Q^+ at x was calculated as $(\Gamma_Q x^{-1}10^3)$ mol/L.

Shown in Table I are the values of c_x, ψ_0, ψ_x, $\gamma_{P,x}$, and $\gamma_{P,x}^2 \exp(+F\psi_x/RT)$, calculated to correspond with the data points in Figure 3. Two features of this table should be noted. The first is that, as a result of the small surface-charge densities, the interfacial potentials are small. The second is that the quantity $\gamma_{P,x}^2 \exp(+F\psi_x/RT)$ is essentially constant (0.62 ± 0.01). The constancy of this term explains why the dissociation quotient, $K_{Dis,QP}$, in concentration units, turns out to be a constant. It is the quotient of two constants, $K^\circ_{Dis,QP}$ and $\gamma_{P,x}^2 \exp(+F\psi_x/RT)$ as seen in eq 16.

Other Considerations. Interfacial tension or pressure measurements (*29–31*) and zeta potential measurements (*23*) have previously been used as qualitative evidence to suggest that ions adsorbed at the liquid–liquid interface undergo some ion-pair formation with counterions from solution. The present work provides an alternative experimental approach in which a large ratio of interfacial area to bulk solution volume is employed. It provides direct measurement of concentrations in both bulk phases and indirect measurement of the amount of solute adsorbed at the interface. Interfacial equilibria are readily evaluated quantitatively, making this an attractive alternative or complementary approach to conventional surface chemical techniques.

The analytical consequences of the dissociation of interfacially adsorbed ion pairs are similar to those described for the ion pair tetrahexylammonium bromothymol blue (*2*) because the effect of a varying, low excess reagent concentration of P^- in the aqueous phase on the amount of cationic component adsorbed is similar to the effect of HB^- concentration, though for a different chemical reason; picrate affects the degree of dissociation while HB^- exercises its effect by competitive adsorption. Two analytical techniques in which immiscible liquid phases are used under conditions where the ratio of interfacial area to bulk liquid volume is large are segmented flow (e.g. solvent extraction/flow injection analysis (*4*)) and liquid–liquid partition chromatography (e.g. "extraction chromatography" (*32*)). The latter is popular in radioanalytical chemistry. An insufficient excess of reagent ion could lead to a nonlinear calibration curve in the former technique and to asymmetric chromatographic peaks in the latter technique.

LITERATURE CITED

(1) Watarai, H. *Talanta* **1985**, *32*, 817–820.
(2) Amankwa, L.; Cantwell, F. F. *Can. J. Chem.*, in press.
(3) Schill, G. In *Ion Exchange and Solvent Extraction*; Marinsky, J. A., Marcus, Y., Eds.; Marcel Dekker: New York, 1974; Vol. 6, Chapter 1.
(4) Fossey, L.; Cantwell, F. F. *Anal. Chem.* **1982**, *54*, 1693–1697.
(5) Amankwa, L.; Cantwell, F. F. *Anal. Chem.* **1989**, *61*, 1036–1040.
(6) Davies, J. T.; Rideal, E. K. *Interfacial Phenomena*; Academic Press: New York, 1961; Chapters 2, 4, 5.
(7) Scibona, G.; Danesi, P. R.; Fabiani, C. In *Ion Exchange and Solvent Extraction*; Marinski, J. A., Marcus, Y., Eds.; Marcel Dekker: New York 1981, Vol. 8, Chapter 2.
(8) Mohammed, H. Y.; Cantwell, F. F. *Anal. Chem.* **1979**, *51*, 1006–1012.
(9) Hiementz, P. C. *Principles of Colloid and Surface Chemistry*; Marcel Dekker: New York, 1986; Chapter 7.
(10) Modin, R.; Schill, G. *Acta Pharm. Suec.* **1967**, *4*, 301–326.
(11) Motomizu, S.; Shoichi, H.; Kyoji, T. *Bunseki Kagaku* **1983**, *32*, 648–653.
(12) Gustavii, K. *Acta Pharm. Suec.* **1967**, *4*, 233–246.
(13) Kraus, C. A. *J. Phys. Chem.* **1956**, *60*, 129–141.
(14) Fuoss, R. M.; Kraus, C. A. *J. Am. Chem. Soc.* **1933**, *55*, 1019–1028.
(15) Brunauer, S.; Emmett, P. H.; Teller, E. *J. Am. Chem. Soc.* **1938**, *60*, 309–319.
(16) Giles, C. H.; MacEwan, T. H.; Nakhwa, S. N.; Smith, D. *J. Chem. Soc.* **1960**, 3973–3993.
(17) Giles, C. H.; Smith, D.; Huitson, A. *J. Colloid Interface Sci.* **1974**, *47*, 755–765.
(18) Clunie, J. S.; Ingram, B. T. In *Adsorption from Solution at the Solid/Liquid Interface*; Parfitt, G. D., Rochester, C. H., Eds.; Academic Press: Toronto, 1983; Chapter 3.
(19) Parfitt, G. D.; Rochester, C. H. In *Adsorption from Solution at the Liquid/Solid Interface*; Parfitt, G. D., Rochester, C. H., Eds.; Academic Press: Toronto, 1983; Chapter 1.
(20) Kipling, J. J. *Adsorption from Solutions of Non-Electrolytes*; Academic Press: New York, 1965; Chapter 12.
(21) Cantwell, F. F. Unpublished results.
(22) Persaud, G.; Tian, X.-M.; Cantwell, F. F. *Anal. Chem.* **1987**, *59*, 2–7.
(23) Anderson, P. J. *Trans. Faraday Soc.* **1959**, *55*, 1421–1429.
(24) Scibona, G.; Mantella, L.; Danesi, P. R. *Anal. Chem.* **1970**, *42*, 844–848.
(25) Davies, J. T. *Proc. R. Soc. London, A* **1951**, *A208*. 224–247.
(26) Haydon, D. A.; Taylor, F. H. *Philos. Trans. R. Soc. London, A* **1960**, *252A*, 225–248.
(27) Hiementz, P. C. *Principles of Colloid and Surface Chemistry*; Marcel Dekker: New York, 1986; Chapter 12.
(28) Bates, R. G. *Determination of pH*; John Wiley: Toronto, 1973; Chapter 1.
(29) Tamaki, K. *Bull. Chem. Soc. Jpn.* **1967**, *40*, 38–41.
(30) Scibona, G.; Danesi, P. R.; Conte, A.; Scuppa, B. *J. Colloid Interface Sci.* **1971**, *35*, 631–635.
(31) Pizzichini, M.; Chiarizia, R.; Danesi, P. R. *J. Inorg. Nucl. Chem.* **1978**, *40*, 669–671.
(32) Braun, T., Ghersini, G., Eds. *Extraction Chromatography*; Elsevier: Amsterdam, 1975.

RECEIVED for review April 25, 1990. Accepted June 29, 1990. This work was supported by the National Sciences and Engineering Research Council of Canada and by the University of Alberta.

Determination of Carbon-Centered Radicals in Aqueous Solution by Liquid Chromatography with Fluorescence Detection

David J. Kieber and Neil V. Blough*

Chemistry Department, Woods Hole Oceanographic Institution, Woods Hole, Massachusetts 02543

A simple method to detect subnanomolar to micromolar levels of photochemically generated carbon-centered radicals in aqueous solutions has been developed and optimized. This method is based on the efficient trapping of radicals by a water-soluble amino nitroxide, followed by derivatization of the trapped products with fluorescamine to produce highly fluorescent adducts. These adducts can be separated by reversed-phase high-performance liquid chromatography and detected fluorometrically. The fluorescent derivatives are stable over a period of days. The detection limit, primarily determined by reagent interferences, ranged from 0.3 to 1 nM per analyte for a 500-μL injection at a signal-to-noise ratio of two. The precision of the method for the determination of adduct concentrations in the 1–10 nM range varied from 2.4 to 8.4% relative standard deviation ($n = 6$). A direct comparison with electron paramagnetic resonance spectroscopy/spin trapping illustrates the advantages of our technique. One important feature of the method is that it permits the simultaneous detection of an array of radicals, as demonstrated through the study of the photochemical production of radicals in a variety of natural water samples and in Suwannee River fulvic acid.

INTRODUCTION

The lack of methods with which to detect and identify very low concentrations of free radicals in condensed phases presents a major hurdle to our understanding of the impact of these highly reactive species on numerous chemical (*1*, *2*), environmental (*3*), biological (*4*, *5*), and toxicological (*6*) processes. Direct detection of radicals by electron paramagnetic resonance (EPR) or optical spectroscopies is generally not possible at the commonly encountered low, steady-state levels of these species. More often, radicals are detected indirectly by employing radical traps or scavengers which react rapidly with transient radicals to form stable or persistent products. The accumulation of products (or loss of trap) thus acts to integrate the radical "signal".

Spin trapping is one of the most often used indirect methods of radical detection (*7*, *8*). In this method, radicals are scavenged by nitrones or nitroso compounds (spin traps) to produce persistent nitroxyl radicals (spin adducts); the pattern and magnitude of the hyperfine splittings obtained from the EPR spectrum of the spin adduct can be used in some instances to identify the structure of the trapped radical. While often successfully employed, this approach is subject to a number of limitations and potential artifacts, including (1) spin adduct instability (*9–11*), (2) the artifactual production of spin adducts (*12*), (3) the need for high concentrations of spin traps to scavenge some radicals due to low rate constants for the trapping reaction (*13*), and (4) the inability to resolve mixtures of structurally similar spin adducts by EPR because of indistinguishable g values and/or hyperfine splitting constants (*7–9*). Better selectivity may be achieved through use of high-performance liquid chromatography (HPLC) combined with EPR detection to separate and identify individual spin adducts (*14*, *15*). However, spin adduct instability can make extraction, separation, and structural identification difficult, if not infeasible, in many cases.

As compared to spin traps, the stable di-*tert*-alkyl nitroxides offer some distinct advantages as free radical traps. First, rate constants for reaction of nitroxides with radicals ($\sim 10^8$–10^9 M^{-1} s^{-1} (*16–18*)) are generally at least an order of magnitude higher than those for spin traps ($\sim 10^6$–10^7 M^{-1} s^{-1} (*19*)). Thus for an equivalent trapping efficiency, much lower concentrations of nitroxides can be employed. Second, the reaction of nitroxides with most carbon-centered radicals leads to the formation of stable alkoxyamine products, allowing for the isolation and identification of an important class of radical intermediates (*18*). Third, while the aliphatic nitroxides do not react with peroxy radicals (*20*, *21*), superoxide and the hydroxyl radical can be detected through the addition of appropriate compounds (*22*, *23*). Fourth, the sensitivity of radical detection can be substantially improved by covalently linking the nitroxide to a fluorophore (*24–26*). When coupled to the nitroxide, the fluorescence yield of the fluorophore is very low owing to efficient intramolecular quenching of the fluorophore by the nitroxide. However, conversion of the nitroxide to a diamagnetic product through radical (or redox) reactions produces greatly enhanced fluorescence that can be used as a very sensitive measure of radical scavenging.

On the basis of this property of enhanced fluorescence, we recently developed a highly sensitive HPLC method for the determination of photochemically generated carbon-centered radicals in aqueous solution (*27*). In this method, a water-soluble amino nitroxide (3-(aminomethyl)-2,2,5,5-tetramethyl-1-pyrrolidinyloxy free radical, 3-AMP) is used to trap carbon-centered radicals (Figure 1). Products are subsequently reacted with fluorescamine to produce highly fluorescent alkoxyamine– and hydroxylamine–fluorescamine adducts (AFl and HFl adducts, respectively). Adducts are separated by reversed-phase HPLC and detected fluorometrically (*27*).

Here we present results on the optimization of this method for the detection of very low levels of carbon-centered radicals in aqueous media. Advantages and drawbacks of this technique and potential applications of this approach are discussed.

EXPERIMENTAL SECTION

Chemicals. Boric acid, ketones, 5,5-dimethylpyrroline 1-oxide (DMPO), and 3-AMP were purchased from Aldrich. Sodium dithionite was obtained from Fluka. Amino acids, α-keto acids, nucleotide bases, buffer salts, and fluorescamine were from Sigma. All chemicals were of the highest purity available and, except where noted, were used without further purification. Distilled-in-glass grade solvents were obtained from Burdick and Jackson.

* To whom correspondence should be addressed.

0003-2700/90/0362-2275$02.50/0 © 1990 American Chemical Society

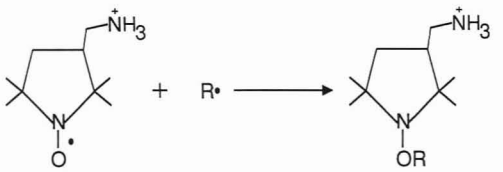

Figure 1. Reaction scheme employed to trap carbon-centered radicals in aqueous solution. The 3-AMP reacts rapidly with carbon-centered radicals (R•) to form stable alkoxyamines or, for reducing radicals, the hydroxylamine (R = H).

The DMPO was purified with activated charcoal (*28*).

A 5 mM stock solution of fluorescamine in acetonitrile was prepared daily and stored in the dark at 20 °C. Stock solutions of purified 3-AMP (vide infra) in sodium borate buffer (pH 8.1, 0.2 M) were stored at 4 °C. Water used in all experiments was from a Millipore Milli Q system.

Suwannee River fulvic acid was obtained from the U.S. Geological Survey, Denver, and used as received. A stock solution (15 mg/L) was prepared by dissolving the fulvic acid into 0.2 M borate buffer (pH 8.1).

The sodium acetate buffer used in the HPLC mobile phase was prepared by adding glacial acetic acid to Milli Q water and adjusting the pH with sodium hydroxide pellets. Carbonate buffer was prepared by adjusting the pH of a 50 mM potassium bicarbonate solution with concentrated HCl.

Purification of 3-AMP. The 3-AMP was purified by a solid phase extraction procedure, which employed a Waters C_{18} Sep-Pak (SP) to remove traces of diamagnetic amine impurities that produced a fluorescent background upon coupling with fluorescamine.

The SP was rinsed sequentially with 20 mL of water, 10 mL of methanol, and 30 mL of water. A 2-mL aliquot of 3-AMP in water (~10 mM) was then loaded onto the SP and rinsed with 24 mL of water. The 3-AMP was eluted with 5 mL of 20% methanol in water and the first 4 mL was saved. This entire procedure was repeated until 10–20 mL of eluate was collected. The combined eluate was roto-evaporated to dryness at 50 °C. The 3-AMP was redissolved in 0.2 M borate buffer (pH 8.1) and its purity determined by HPLC. This extraction procedure removed most of the contaminants that eluted after the 3-AMP–fluorescamine peak. However, hydrophilic interferences such as the hydroxylamine were not removed.

The concentration of the stock 3-AMP solution (~10 mM) was determined on diluted samples by comparing the area obtained by double integration of the EPR signal with that obtained from a standard curve of area versus concentration determined for aqueous solutions of 3-carboxy-2,2,5,5-tetramethyl-1-pyrrolidinyloxy free radical (Aldrich).

Apparatus. The HPLC consisted of an Eldex Model B-100-S single piston pump followed by a Gilson Model 811B dynamic mixer, a 0–5000 psi pressure gauge (C and H Sales), a Valco Model C10W injection valve, and a RCM 8 × 10 cm Waters radial compression module containing a 0.5 × 10 cm Nova-PAK column with 4-μm reversed-phase (C_{18}) packing; 0.5-μm filters were placed after the pump and injector. A Hitachi Model F1000 fluorescence detector (Tokyo) set at 390 nm (excitation, 15 nm band-pass) and 480 nm (emission, 15 nm band-pass) was connected to an ELAB PC-based data collection system (OMS Tech). Unless noted, HPLC injections were through a 100-μL sample loop. In some cases, as a comparison, samples were also injected into the chromatograph via a 0.2 × 5.5 cm i.d. enrichment column (Upchurch) with 40-μm C_{18} packing. The mobile phase composition was controlled by an ELAB low-pressure gradient system. Chromatographic separations were at room temperature and at a flow rate of 1.3 mL/min.

The mobile phase used for isocratic elutions consisted of 35% sodium acetate (50 mM, pH 4.0)/65% methanol (v/v). For standard gradient elutions, the mobile phase composition was (A) 60% sodium acetate (50 mM, pH 4.0)/40% methanol (v/v) and (B) methanol, and the gradient used was 0% B for 5 min, 0 to 35% B from 5 to 10 min, 35 to 65% B from 10 to 26 min, 65 to 0% B in 1 min, and 0% B for 13 min. The gradient used for the separation of amino acid or natural water samples was 0 to 48% B in 15 min, isocratic at 48% B for 4 min, 48 to 0% B in 10 min, and isocratic at 0% B for 10 min, with (A) 55% 50 mM potassium carbonate (pH 7.0)/45% methanol (v/v), and (B) methanol.

A Bruker/IBM ER 200D-SRC EPR spectrometer was employed to obtain spin concentration. Samples were drawn into 50-μL calibrated capillaries, which were then sealed at the top and bottom and placed within standard 3 mm i.d. quartz EPR tubes. Standard instrument settings were as follows: frequency, 9.77 GHz; power, 10 mW; and modulation amplitude, 1.6 G. Nitroxide loss was calculated from the decrease in peak amplitudes, since line widths were identical for all samples.

Excitation and emission spectra were collected with a SLM-Aminco SPF-500 spectrofluorometer using a 2 nm band-pass for both the excitation and emission wavelengths. Samples were thermostated at 20 °C. Spectra were corrected for instrumental response and integrated with correction factors and software provided by the manufacturer with some modifications (*25*).

Irradiation Conditions. Alkoxyamines and the hydroxylamine were generated by the photolysis of ketones or α-keto acids in the presence of micromolar concentrations of 3-AMP in 0.2 M, pH 8.1 borate buffer (hereafter denoted as standard buffer); natural water samples and the fulvic acid (buffered to pH 8.1) were treated in a similar fashion. Samples in a 1-cm quartz cell were irradiated with a 300-W xenon lamp (Varian Model PS300-1). The light was first filtered through 22 cm of Milli Q water and then passed through either a ≥275 nm Pyrex filter (50% transmission at 305 nm; ketones, α-keto acids) or a ≥295 nm Pyrex filter (50% transmission at 335 nm; natural water samples and fulvic acids). Unless noted, the light intensity at the cell as determined with a YSI Model 65A radiometer was 140 and 160 mW/cm^2 with the 295- and 275-nm filter, respectively. Prior to irradiation, samples were deoxygenated for 5 min with N_2 (99.999% purity, Union Carbide) or Ar (99.995% purity) that had been passed through an oxygen trap (Alltech). The cell headspace was continuously purged with either N_2 or Ar during sample irradiation.

Derivatization Procedure. The standard procedure entailed the addition of a 200-μL aliquot of the stock fluorescamine solution to 1 mL of sample within an all-Teflon vial, which was then stirred vigorously on a vortex mixer. The reaction time was 1 min at room temperature and at pH 8.1.

The derivatization procedure was optimized with respect to the fluorescamine concentration and reaction pH. The dependence of the fluorophore yield on fluorescamine concentration was determined for the alkoxyamine of the acetyl radical formed by the photolysis of 330 μM pyruvate in standard buffer containing 5.1, 14.5, or 65.3 μM 3-AMP. The alkoxyamine concentration was held constant at 0.7 μM while the fluorescamine concentration was varied from 6 to 1200 μM, depending on the concentration of 3-AMP in the solution. The dependence of fluorophore yield on fluorescamine concentration was also determined for the alkoxyamine derivatives of radicals 4 through 9 (Table I) in the presence of 5.1 μM 3-AMP.

The dependence of fluorophore yields on reaction pH was similarly determined for the alkoxyamines of radicals 4 through 12 (Table I). The standard buffer containing 10 μM 3-AMP and 300–400 μM 3,3-dimethyl-2-butanone, 3-pentanone, 3-methyl-2-butanone, α-ketovalerate, α-ketocaproate, acetone, and β-phenylpyruvate was irradiated for 10 min to generate alkoxyamines in the 0.1–0.5 μM range. Aliquots of this solution were adjusted to a pH between 5.1 and 11.0 by addition of a strong borate buffer of the appropriate pH. The pH-adjusted solutions were then derivatized by the standard procedure, and fluorophore yields were determined by HPLC.

To determine the stability of hydroxylamine, it was first formed by the substoichiometric addition of dithionite to a deoxygenated solution of 3-AMP (33 μM) in standard buffer at 20 °C. This solution was stored under aerated or deaerated conditions and aliquots were withdrawn periodically to determine the hydroxylamine concentration following derivatization. The stability of the HFl adduct was also determined by measuring its loss upon storage under aerated conditions in standard buffer containing excess fluorescamine. To determine the stability of the AFl adducts, the alkoxyamines were first formed by irradiating deoxygenated standard buffer containing 9.3 μM 3-AMP and 300–500 μM 3-methyl-2-butanone, 3,3-dimethyl-2-butanone, 3-pentanone, α-ketovalerate, α-ketoadipate, α-ketocaproate, acetone,

Table I. List of Primary Radicals (R•) Expected from the Norrish Type I Photochemical Cleavage of α-Keto Acids (at pH > pK_a) and Ketones in Aqueous Solution[a]

precursor	R•	precursor	R•
β-hydroxypyruvate	(1) $CO_2^{\bullet-}$ (2) $H_2C(OH)\dot{C}O$	β-phenylpyruvate	(1) $CO_2^{\bullet-}$ (11) $C_6H_5\dot{C}H_2$
α-ketoadipate	(1) $CO_2^{\bullet-}$ (3) $^-O_2C(CH_2)_2\dot{C}O$	acetone	(6) $\dot{C}H_3$ (4) $CH_3\dot{C}O$
pyruvate	(1) $CO_2^{\bullet-}$ (4) $CH_3\dot{C}O$	2-butanone	(9) $CH_3\dot{C}H_2$ (4) $CH_3\dot{C}O$
α-ketobutyrate	(1) $CO_2^{\bullet-}$ (5) $CH_3CH_2\dot{C}O$	3-pentanone	(9) $CH_3\dot{C}H_2$ (5) $CH_3CH_2\dot{C}O$
α-ketovalerate	(1) $CO_2^{\bullet-}$ (7) $CH_3(CH_2)_2\dot{C}O$	3-methyl-2-butanone	(10) $(CH_3)_2\dot{C}H$ (4) $CH_3\dot{C}O$
α-ketocaproate	(1) $CO_2^{\bullet-}$ (8) $CH_3(CH_2)_3\dot{C}O$	3,3-dimethyl-2-butanone	(12) $(CH_3)_3\dot{C}$ (4) CH_3CO

[a] The $CO_2^{\bullet-}$ radical reduces 3-AMP to the hydroxylamine.

and β-phenylpyruvate. Fluorescamine was then added to form the AFl adducts, which ranged in concentration from 0.2 to 1.3 μM. This solution was stored in the dark at 4 °C, and 100-μL aliquots were analyzed by HPLC periodically over a period of 4 weeks. Prior to sample analysis by HPLC, the fluorometer was calibrated with a standard solution of quinine sulfate in 0.1 N H_2SO_4.

Apparent Fluorescence Quantum Yield Determinations. A solution of 15.1 μM 3-AMP in standard buffer was derivatized according to the standard procedure, yielding the fluorescamine derivative of 3-AMP in 17% acetonitrile/83% borate buffer (v/v). The apparent fluorescence quantum yield of the 3-AMP–fluorescamine adduct was determined before and after its reduction with dithionite (vide infra). Quantum yields were calculated with respect to quinine sulfate as previously described (*25*).

Dithionite Titrations. The 3-AMP–fluorescamine adduct was reduced to the corresponding HFl adduct by the stepwise addition of a deoxygenated solution of dithionite in standard buffer. After each dithionite addition, an EPR spectrum and fluorescence excitation and emission spectra were recorded. Complete reduction of 3-AMP–fluorescamine to the HFl adduct was verified by EPR.

Determination of Adduct Concentration. The standard buffer containing a ketone or α-keto acid (300–400 μM) and 7.3 μM 3-AMP was irradiated for specific time intervals ranging from 0.5 to 25 min to produce differing levels of 3-AMP loss and adduct formation. Adduct concentrations were calibrated by comparing the loss of 3-AMP as monitored by EPR with the increase in fluorescence area of the HPLC peaks corresponding to the adducts that formed (*27*).

Once alkoxyamine concentrations were determined as described above, they were used as standards to quantify adduct concentrations in the picomolar to nanomolar range (where calibration by EPR was not possible). Calibration curves in the nanomolar range were generated by dilution of the micromolar standards and plotting fluorescence area as a function of adduct concentration.

Comparison to Spin Trapping. Standard buffer containing 500 μM pyruvate and either 500 μM DMPO or 50 μM 3-AMP was irradiated under deoxygenated conditions for 2–18 min. For samples containing DMPO, aliquots were withdrawn with 50-μL calibrated capillaries and the acquisition of the EPR spectrum for each aliquot was initiated 40 s after irradiation. EPR settings were as follows: frequency, 9.77 GHz; power, 10 mW; modulation amplitude, 1.0 G; time constant, 0.16 s; scan range, 100 G; and scan time, 200 s. Spin adduct concentrations were obtained by the same procedure employed for the standardization of 3-AMP. Samples containing 3-AMP were derivatized according to the standard procedure and separated by isocratic elution.

Sampling Procedure. Natural water samples were collected in 2-L acid-washed reagent bottles with Teflon-lined caps. Prior to sample collection, glassware was washed overnight in 10% HNO_3 and then copiously rinsed with water and sample. After collection, samples were filtered through 0.22-μm Nylon 66 filters (MicronSep) and stored at 4 °C until analyzed. Immediately prior to an irradiation, the pH of the natural water sample was adjusted to pH ~8 by a small addition of 0.2 M borate (pH 8.1).

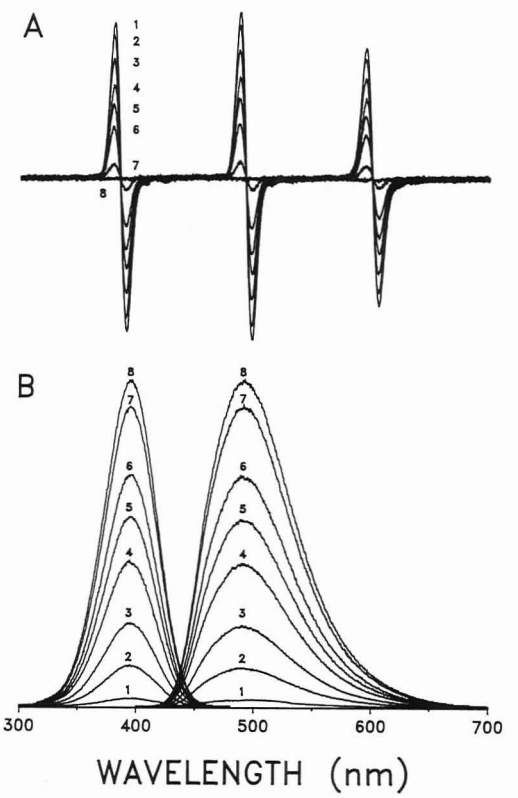

Figure 2. Anaerobic reduction of the 3-AMP–fluorescamine adduct to the HFl adduct by dithionite. Dithionite was added in stepwise additions increasing in concentration from 1 to 8. The EPR spectra show the spin loss of the paramagnetic 3-AMP–fluorescamine adduct upon reduction (A) while the excitation and emission spectra (B) show the concomitant increase in fluorescence yield due to hydroxylamine formation.

RESULTS

Fluorescence Properties of Fluorescamine Adducts. Unlike other primary amines, 3-AMP reacts with fluorescamine (*29*, *30*) to form a product with a low apparent quantum yield of fluorescence ($\Phi_f \pm \sigma = 0.0017 \pm 0.0003$), due to the efficient intramolecular quenching of the excited singlet state of this fluorophore by the nitroxide moiety (*24*, *25*). Reduction of the nitroxide to the diamagnetic hydroxylamine (the HFl adduct) with dithionite leads to a fluorescence yield increase that is directly proportional to the loss of the nitroxide spin (Figure 2A), leaving the line widths of the excitation and emission spectra unaltered (Figure 2B). Complete reduction of the 3-AMP adduct to the hydroxylamine produces an ~ 50-fold increase in fluorescence yield ($\Phi_f \pm \sigma = 0.080 \pm 0.001$). Fluorescence quantum yields reported here are estimates, since

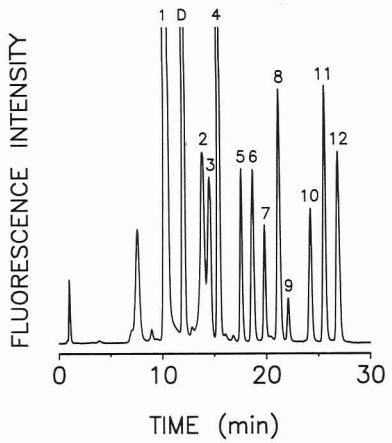

Figure 3. Chromatogram showing the standard gradient separation of a mixture of AFl adducts. Peak assignments refer to the AFl adducts of the radicals listed in Table I. Concentrations of the AFl adducts ranged from 69 nM (peak 9) to 528 nM (peak 4), while concentrations of the HFl (peak 1) and 3-AMP–fluorescamine (peak D) adducts were 2.5 and 520 μM, respectively.

these solutions contain fluorescamine hydrolysis products with a constant, but unknown absorbance contribution. We are currently determining the fluorescence quantum yield for the purified fluorescamine derivative of 3-AMP, as well as for the fluorescamine derivatives of other amine-substituted nitroxides.

Estimates of Φ_f for the AFl adducts obtained by comparison to the HFl adduct (*27*) are even higher, ranging from 0.16 to 0.20. These values agree reasonably well with reported values of Φ_f in ethanol (*30*) for the fluorescamine adducts of various primary amines such as butylamine (Φ_f = 0.23) and benzylamine (Φ_f = 0.27).

HPLC Separation of HFl and AFl Adducts. We showed previously that 3-AMP efficiently scavenges carbon-centered radicals to form alkoxyamines or the hydroxylamine. The AFl and HFl adducts, obtained by derivatization with fluorescamine, can be separated and identified by reverse-phase HPLC using isocratic elution and fluorometric detection (*27*). Under the conditions reported here, we are now able to resolve and sensitively detect a significantly more complex array of AFl adducts having substantially different capacity factors (Figure 3). Where possible, these AFl adducts were assigned directly through intercomparison of the elution patterns of adducts formed from the photolysis of individual ketones or α-keto acids (*27*). For example, photolysis of 3-pentanone or 2-butanone gives rise to a common product which was assigned as the ethyl radical adduct (Table I). Where direct intercomparisons were not possible, adducts were assigned on the basis of known or expected photochemistry and the chromatographic elution characteristics of the AFl adducts (e.g., polar vs nonpolar).

No fluorescent products were formed when either aerated or deaerated solutions of 3-AMP alone were irradiated. When aerated solutions of ketones or α-keto acids were irradiated in the presence of low concentrations of 3-AMP ($\sim$10 μM), no AFl or HFl products corresponding to the radicals listed in Table I were detected, consistent with an efficient scavenging of the primary radicals by oxygen to form oxygen-centered radicals that are unreactive with 3-AMP (*20*, *21*). However, small amounts of an unknown species eluting near the void volume was detected. We are currently investigating the nature of this unknown. All dark controls, with and without added α-keto acids or ketones, also showed no evidence for the formation of fluorescent products. No fluorescent products were detected when solutions of the aliphatic ketones were irradiated in the presence of 3-AMP at wavelengths >350 nm.

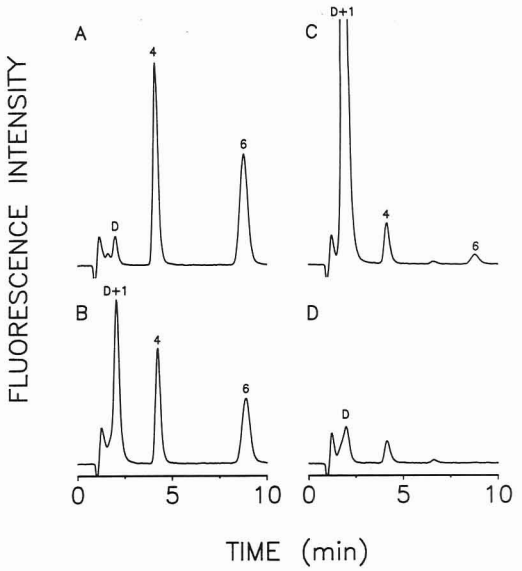

Figure 4. Effect of added methanol on the photolysis of acetone. Chromatograms A through D show the isocratic separation of the fluorescamine adducts produced by irradiation (≥275 nm) of the standard buffer containing 330 μM acetone and 17 μM 3-AMP in the presence and absence of methanol: (A) acetone and 3-AMP with no methanol added, (B) acetone and 3-AMP with 0.5 M methanol, (C) acetone and 3-AMP with 6.5 M methanol, and (D) 3-AMP and 6.5 M methanol with no acetone added. Peak assignments refer to the AFl adducts of the radicals listed in Table I; peak D is the fluorescamine derivative of 3-AMP. Under isocratic conditions, species 1 and D coeluted.

As a simple additional test of the method, we examined the influence of an added hydrogen atom donor, methanol, on the photolysis of an aqueous solution of acetone. The photolysis of acetone proceeds through a Norrish type I cleavage from the excited triplet state to form the acetyl and methyl radicals

$$^3[CH_3COCH_3] \rightarrow CH_3\dot{C}O + \dot{C}H_3 \quad (1)$$

In the presence of sufficient methanol, however, photoreduction of acetone to produce α-hydroxy radicals should occur (*31*)

$$^3[CH_3COCH_3] + CH_3OH \rightarrow CH_3\dot{C}OHCH_3 + \dot{C}H_2OH \quad (2)$$

Because α-hydroxy radicals reduce the nitroxide to the hydroxylamine (*32*, *33*), a change in products was anticipated. Consistent with expectations, the AFl adducts of the methyl and acetyl radicals decreased with increasing methanol concentrations concomitant with an increase in the concentration of the HFl adduct (Figure 4). The light control containing methanol and 3-AMP, but no acetone, showed no appreciable production of the HFl or AFl adducts.

Optimization of the Derivatization Procedure. Because fluorescamine rapidly hydrolyzes in aqueous solution to form nonfluorescent products, an excess of fluorescamine is required for optimal fluorophore formation (*30*). As shown in Figure 5, with decreasing 3-AMP concentrations, a higher molar ratio of fluorescamine to 3-AMP was needed to produce maximal fluorophore yields for the alkoxyamine derivative of the acetyl radical (0.7 μM). At the highest 3-AMP concentration tested, a 1.5-fold molar excess of fluorescamine was sufficient for maximal fluorescence, while at least an 8-fold molar excess of fluorescamine was required for optimal yields at the lowest 3-AMP concentration tested (5.1 μM). This same dependence was observed at 5.1 μM 3-AMP for the alkoxyamine derivatives of radicals 4 through 9 (Table I). Thus, with increasing concentrations of 3-AMP, a lower molar ratio of fluorescamine/3-AMP is needed to obtain optimal AFl and HFl yields.

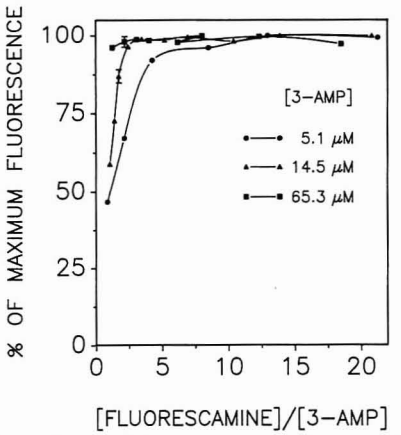

Figure 5. Dependence of the percentage of the maximum fluorescence of the AFI adduct of the acetyl radical (0.7 μM) on the molar ratio of fluorescamine to 3-AMP, determined for three concentrations of 3-AMP. Error bars denote σ (n = 3).

Fluorophore yields were highest and independent of pH in the range 7.5–9.5 for the reaction of fluorescamine with the alkoxyamines of radicals 4 through 12 (Table I). Outside this range, the yields decreased for all alkoxyamines tested. For example, at pH 5.1, yields were 35 to 55% less than the maximum. At pH >10, yields decreased by 10 to 30% for all alkoxyamines, presumably owing to an increased rate of fluorescamine hydrolysis (*30*). The observed pH optimal is similar to that measured for amino acids which show optimal fluorophore formation between pH 8 and 9 (*30*). However, one important difference is that the alkoxyamines are significantly more reactive toward fluorescamine at pH <8, possibly allowing for selective derivatization of the alkoxyamines in the presence of an excess of amino acids.

Optimization of Chromatographic Conditions. A study was conducted to determine if the AFI adducts could be concentrated on an enrichment column (EC). Samples were loaded onto the EC and then injected by back flushing the retained material off the EC and onto the analytical column. The volume of sample passed through the EC was varied from 10 to 5000 μL. Peak areas increased linearly with increasing sample volume, and identical recoveries were obtained for all the AFI adducts ($\bar{x} \pm \sigma = 100 \pm 3\%$) when equal volumes of sample were injected by means of a sample loop or the EC.

The degree of separation of the AFI adducts varied significantly depending on the pH of the buffer used in the mobile phase (Figure 6). Increasing the buffer pH from pH 3.0 to 4.2 resulted in a decrease in the capacity factor (k') of all AFI adducts tested. The largest change in k' was observed for the most highly retained species (e.g., the AFI adduct of the methyl radical) while only minor changes were seen for the more hydrophilic species (e.g., the AFI adduct of the acetyl radical). The best selectivity was achieved at lower values of pH where the largest differences in k' and best peak shapes were obtained. In this study, no decay of the AFI derivatives on the HPLC column was observed at any pH tested. In contrast, when trichloroacetic acid was used to buffer the pH of the mobile phase to <3, the fluorescamine derivatives of a series of primary amines were found to decay slowly on the column to form nonfluorescent products (*34*).

Under isocratic conditions at pH <4.2, each AFI adduct eluted as a single peak (Figure 6B). When the pH was ≥4.2, each adduct eluted as two partially resolved peaks (Figure 6C). Complete resolution of these peaks could not be achieved at pH ≥4.2. When eluate was collected from either the leading edge of the first peak of the methyl radical adduct (Figure 6C, retention time ~8 min) or the tailing edge of the second peak in this pair (Figure 6C, retention time ~9 min) and then reinjected into the chromatograph, a doublet peak was again

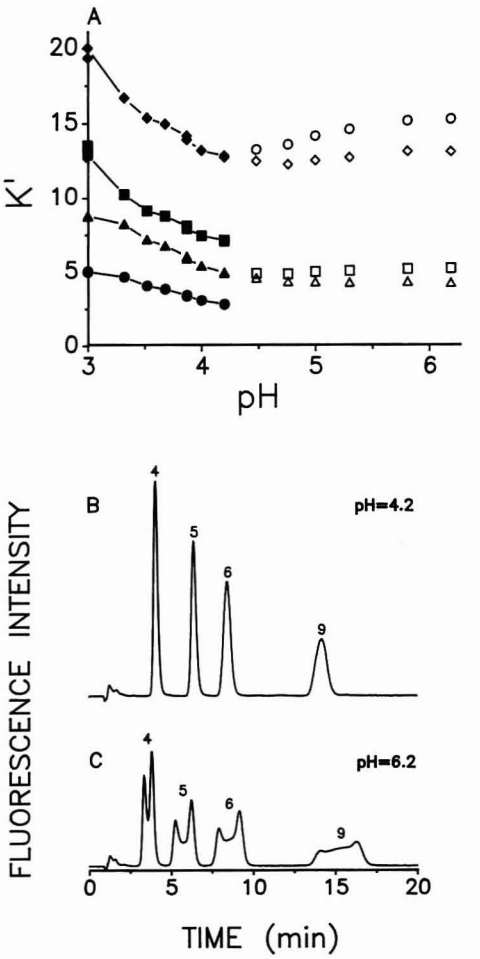

Figure 6. Effect of the acetate buffer pH on the isocratic separation of the AFI adducts. (A) Plot of the capacity factor (k') as a function of buffer pH for the adducts of the radicals: (4) $CH_3\dot{C}O$ (●), (5) $CH_3CH_2\dot{C}O$ (▲), (6) $\dot{C}H_3$ (■), and (9) $CH_3\dot{C}H_2$ (◆). Open symbols are given at pH >4.2 to denote the relative retention of the two partially separated peaks for the AFI adducts of (5) $CH_3CH_2\dot{C}O$ (△, □) and (9) $CH_3\dot{C}H_2$ (○, ◇). (B) Chromatogram showing the isocratic separation of the AFI adducts at a buffer pH of 4.2 and (C) separation of the same sample at pH 6.2. Peak assignments refer to the AFI adducts of the radicals listed in Table I; peak D is the fluorescamine derivative of 3-AMP.

observed with the same ratio in peak heights as seen in the original chromatogram (Figure 6C). This effect was also observed for the HFI adduct, which is known to form a single product upon chemical reduction of 3-AMP with either ascorbate or dithionite (*24*, *27*). Although the precise origin of this effect is unknown, the doublet peaks do not result from different fluorescamine products but rather appear to result from an interconversion between two different chromatographic forms of a single adduct that occurs on a time scale similar to the HPLC separation. This may result from interconversion between lactone and acid forms of the fluorescamine adducts. This effect was never observed when gradient elutions were employed.

Detection Limit. The detection limit (DL) was determined by comparing the peak height of individual AFI adducts (Figure 7, lower chromatogram), formed by derivatization of an alkoxyamine solution containing 10 μM 3-AMP, to the height of the background noise determined for a derivatized 10 μM 3-AMP blank (Figure 7, upper chromatogram). For a 500-μL injection, the DL for most adducts is approximately 0.3–0.5 nM at a signal-to-noise (S/N) ratio of roughly 2 (Figure 7, lower chromatogram). With use of an EC (5000-μL injection), the DL can be improved by an additional order of magnitude for adducts that do not coelute with 3-AMP or

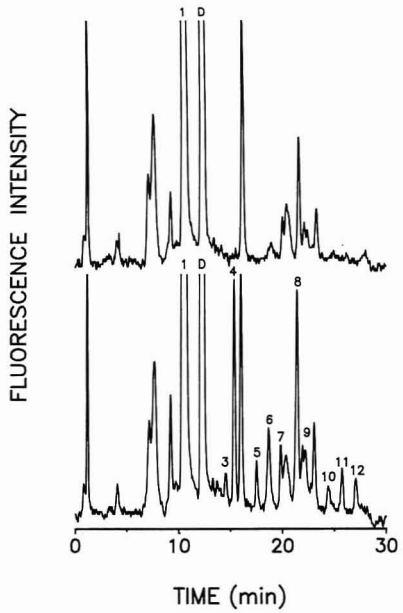

Figure 7. Detection of AFl adducts near the detection limit of the method. The upper chromatogram shows the gradient elution of a fluorescamine-derivatized 10 μM 3-AMP blank. The lower chromatogram shows the separation of a mixture of AFl adducts in the presence of 10 μM 3-AMP–fluorescamine. Peak assignments refer to the AFl adducts of the radicals listed in Table I; peak D is the fluorescamine derivative of 3-AMP. Concentrations of AFl adducts are (3) 0.6 nM, (4) 2.7 nM, (5) 0.6 nM, (6) 1.1 nM, (7) 0.3 nM, (8) 0.9 nM, (9) 0.4 nM, (10) 0.5 nM, (11) 0.6 nM, and (12) 0.4 nM. The injection volume was 640 μL.

amine contaminants. The DL for the AFl adducts of radicals 7 through 9 (Table I) is approximately 1 nM due to minor contaminants in the blank. We are currently examining other procedures to further purify the 3-AMP, which appears to be the major source of contamination. Nevertheless, the DL is 2 to 3 orders of magnitude lower than the DL of radical trapping methods employing EPR detection (vide infra).

Precision and Linearity. The precision of the method was determined for a solution of alkoxyamines that ranged in concentration from 4 to 27 nM. Six separate aliquots of this solution were derivatized with fluorescamine and the AFl adducts separated by the standard gradient elution. The percent relative standard deviation (%RSD) in the retention time for all the AFl adducts examined (3–12, Table I) was <1.5%, while the %RSD for the determination of adduct concentrations ranged from 2.3 to 8.4%.

The linearity was determined by measuring the fluorescence response for adduct concentrations ranging from 1 to 6000 nM (n = 14). The fluorescence response of all adducts (3–12, Table I) increased linearly with concentration. In all cases, $r^2 \geq 0.996$ and y intercepts were not significantly different from zero.

Stability of Hydroxylamine and Alkoxyamine Adducts. The stability of the hydroxylamine was highly dependent upon storage conditions. When stored under aerated conditions, the hydroxylamine was rapidly reoxidized (Figure 8). Reoxidation followed first-order kinetics with a half-life of 1.6 min. When the hydroxylamine was stored under deoxygenated conditions, no loss was observed during the first 40 min (Figure 8), and only 15% loss was observed over a period of 3 h. This slow oxidation may have resulted from traces of oxygen in the nitrogen resulting in low residual levels of O_2 ($\leq \sim 0.1$ ppm) in the sample. The HFl adduct showed markedly improved stability relative to the underivatized hydroxylamine when stored under aerated conditions (Figure 8). No reoxidation was observed for the first 20 min of storage followed by a loss of 1.1 μM h^{-1}.

In contrast, the AFl adducts were very stable. Concentrations of these adducts decreased by <1% after 1 day. After

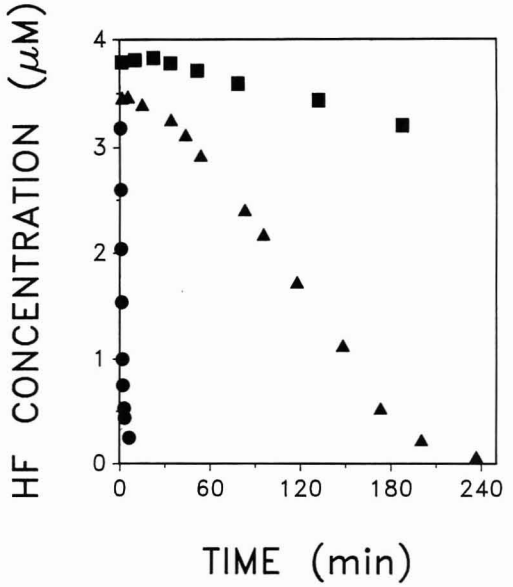

Figure 8. Stability of hydroxylamine under aerated (●) and deaerated (■) conditions, and the HFl adduct under aerated conditions (▲). The hydroxylamine stability was determined after aliquots were derivatized with fluorescamine employing the standard procedure.

1 month, the concentrations of the AFl adducts decreased by only 20%, except for the AFl adduct of radical 3 which showed a substantial loss (71%).

Reduction of the 3-AMP Fluorescamine Adduct. The 3-AMP–fluorescamine adduct was slowly reduced to the hydroxylamine in solutions containing excess fluorescamine. The initial rate of reduction was approximately 10 nM min^{-1} at a 3-AMP concentration of 88 μM. The 3-AMP–fluorescamine adduct was only reduced when solutions (stored in capped Teflon vials) were exposed to laboratory lighting. No reduction was observed when samples were stored in the dark. In general, the derivatization procedure employs excess fluorescamine, and thus care should be taken to perform the derivatization reaction in subdued lighting. The 3-AMP–fluorescamine adduct, purified by HPLC and then diluted into 20% acetonitrile/80% standard buffer, showed no evidence of reduction, indicating that this light-dependent process is associated with the fluorescamine hydrolysis products.

Potential Amine Interferences. The ubiquitous occurrence of amino acids in biological and environmental systems warranted a study of the elution pattern of the common primary amino acids as well as citrulline and ornithine. The fluorescamine derivatives of amino acids were separated by HPLC using the same carbonate mobile phase employed for the analysis of natural water samples (vide infra). Of the amino acids studied here, Gly, Ser, Thr, and Arg formed one major product eluting at the void volume (~1 min). Two products were observed for Ala, Val, Phe, Trp, Tyr, Asn, Gln, Asp, His, and Cit, while four products were detected for Lys and Orn, presumably owing to the presence of a second primary amine group in these compounds. These results are in general agreement with previous investigators who observed that amino acids form two products upon reaction with fluorescamine (*35*). One product has been identified as the lactone while the other corresponds to the free acid. However, three products were detected for Leu, Ile, Met, Cys, and Glu. The reason for this product distribution is unclear, except for Glu which may form two lactones.

With the exception of Tyr, Leu, and Phe, all of the fluorescamine adducts of the amino acids eluted ≤5 min, well before the HFl adduct which eluted at 7 min or the AFl adducts which eluted after 7 min. Only Tyr, Leu, and Phe showed the elution of one product (retention time of 7.5, 9, and 10 min, respectively) later than the HFl adduct.

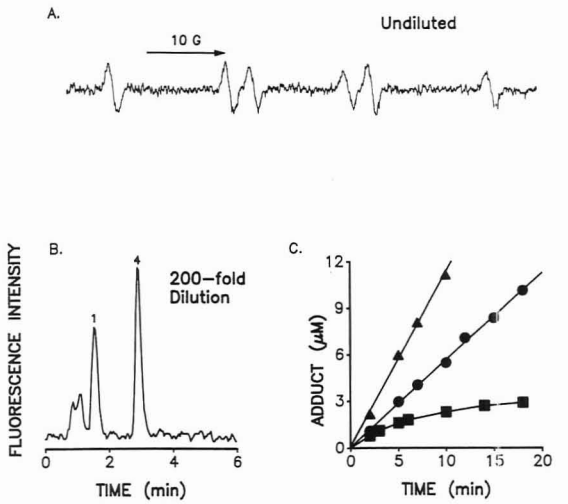

Figure 9. (A) EPR spectrum obtained after a 2-min irradiation of 500 μM pyruvate in the presence of 500 μM DMPO. EPR settings are given in the text. (B) Chromatogram of a 200-fold dilution of the fluorescamine derivatives of the hydroxylamine (peak 1) and the AFl adduct of the acetyl radical (peak 4) obtained after a 2-min irradiation of 500 μM pyruvate in the presence of 50 μM 3-AMP. (C) Dependence of the total adduct formation (i.e., sum of the acetyl and formyl radical adducts) on irradiation time for DMPO (■) and 3-AMP (▲). Also given is the AFl adduct yield of the acetyl radical (●).

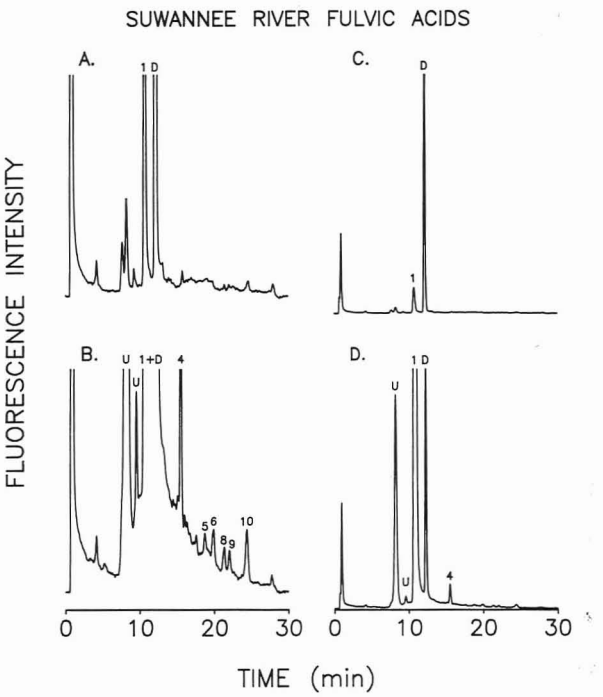

Figure 10. Chromatograms showing the production of free radicals due to the irradiation of a deoxygenated SRFA solution: (A) SRFA and 81 μM 3-AMP, dark control, and (B) SRFA and 81 μM 3-AMP, irradiated 30 min at a light intensity of 174 mW cm^{-2}. Panels C and D are rescaled chromatograms of A and B, respectively. Peak assignments refer to the AFl adducts of the radicals listed in Table I; peaks D and U are the fluorescamine derivatives of 3-AMP and the unknown 3-AMP adducts, respectively.

Therefore, other than for the very hydrophilic AFl adducts, amino acids should not interfere with the detection of the HFl or AFl adducts when the carbonate gradient is employed. In cases where interferences are observed, it should be possible to adjust the pH of the derivatization reaction to select for reaction with the alkoxyamines (vide supra). Potential interferences from peptides were not examined here, although they are known to react with fluorescamine over a wider pH range than observed for amino acids (*30*).

Unlike primary amines, the purine bases adenine and guanine, and the pyrimidine base cytosine did not form fluorescent products with fluorescamine at pH 8.1.

Comparison to Spin Trapping. To compare spin trapping to our method, deoxygenated samples containing 500 μM pyruvate and either 50 μM 3-AMP or 500 μM DMPO were irradiated under identical conditions. Results of this comparison after a 2-min irradiation are shown in Figure 9A for the EPR signal observed for the DMPO sample and in Figure 9B for the fluorescence signal observed for a 200-fold dilution of the derivatized 3-AMP sample; the dependence of adduct yields on irradiation time for the two methods is presented in Figure 9C.

These data clearly demonstrate the advantages of this method over spin trapping. First, after accounting for the 200-fold dilution, the S/N ratio obtained for the AFl adduct of the acetyl radical alone (Figure 9B, peak 4) is roughly 800-fold higher than that of the EPR signal (Figure 9A), which presumably reflects the sum of the signals arising from the spin adducts of the formyl and acetyl radicals. Assuming that the S/N for the EPR detection of the spin adducts could be improved 10-fold (e.g., use of a flat cell and/or increase in the modulation amplitude), the sensitivity of the 3-AMP method would remain about 2 orders of magnitude higher. Second, unlike the fluorescamine adducts, the concentration of spin adducts does not increase linearly with increasing irradiation time (Figure 9C) apparently due to loss of the spin adducts through disproportionation (*7*, *8*, *16*) or further radical reactions (*16*). Third, the initial spin adduct yield is approximately 3-fold lower than the initial fluorescamine adduct yield (Figure 9C) suggesting that even at the higher level of DMPO (500 μM) complete scavenging of the primary radicals by DMPO is not occurring. Finally, the chromatographic separation of the stable fluorescamine adducts allows for the unequivocal identification and quantification of individual radical species (Figure 9B,C). In contrast, the EPR spectra recorded for the DMPO samples appear to be a composite of signals arising from the acetyl and formyl radical spin adducts exhibiting very similar *g* values and hyperfine splitting constants.

Suwannee River Fulvic Acid. As a first demonstration of the potential of this technique to study free radical processes in natural waters, we examined a standard preparation of fulvic acid isolated from the Suwannee River (SRFA). Irradiation of the SRFA for 30 min under deoxygenated conditions resulted in the production of a variety of carbon-centered radicals (Figure 10), which we have tentatively identified based on their coelution with known adducts of the radicals listed in Table I. Adduct concentrations ranged from 6.5 nM for the pentanoyl adduct (peak 8) to 85.5 nM for the acetyl adduct (peak 4). Rescaling of the chromatogram (Figure 10B) to that shown in Figure 10D reveals that the predominant products are the one-electron reduction product, the hydroxylamine (2.8 μM, peak 1), and an unknown eluting at 8.2 min (0.7 μM, based on the acetyl response factor). These two products accounted for approximately 65% of the observed 3-AMP loss (5.4 μM). A large, broad band was also evident from 8 to 28 min in the chromatogram (Figure 10B). We suspect that this broad background may result from the tagging by 3-AMP of radical sites generated directly on the SRFA. We are currently investigating this possibility.

Analysis of Natural Water Samples. The application of this method to the analysis of natural waters is presented in Figure 11. While irradiation of high-purity laboratory water containing 3-AMP showed no production of products (Figure 11A), a variety of adducts were formed when natural water samples were irradiated (Figure 11, panels B–E). No adducts formed when samples were irradiated without added 3-AMP. The total radical adduct yields of the different water samples decreased in the order Cambridge tap water > pond water ≥

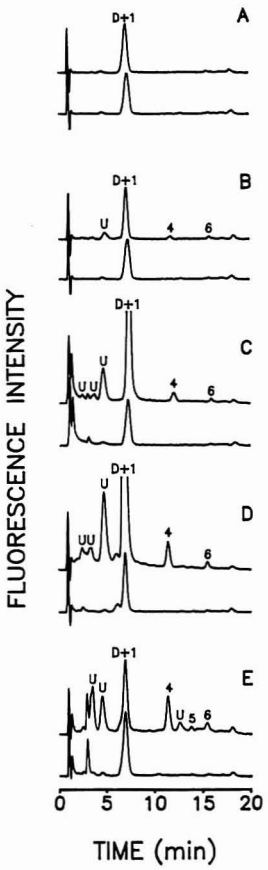

Figure 11. Chromatograms showing the gradient separation of AFI or HFI adducts of free radicals formed during the irradiation of a variety of natural water samples. The initial concentration of 3-AMP was 7.3 μM. The volume injected was 640 μL. In panels A through E, the lower chromatogram depicts the dark control and the upper chromatogram represents samples irradiated for 30.0 min. Panels represent the following: (A) distilled, deionized water (Milli Q water), (B) commercially bottled water, (C) Icehouse pond water (Woods Hole, MA), (D) Cambridge (MA) tap water and (E) rain collected in Woods Hole. Peak assignments refer to the fluorescamine derivatives of the radicals listed in Table I; peaks D and U are the fluorescamine derivatives of 3-AMP and the unknown 3-AMP adducts, respectively.

rain water > commercially bottled water.

Two radicals that were formed in all natural water samples examined were tentatively identified as $CH_3\dot{C}O$ (peak 4) and $\dot{C}H_3$ (peak 6) based on their coelution with standards. Hydroxylamine (quantified as the HFl adduct, peak 1), formed through reaction of 3-AMP with reducing radicals and/or photochemically generated reductants, was the major product detected in the Cambridge (MA) tap water and pond water. In contrast, little of this product was formed during the irradiation of rain and bottled water. The concentration of individual adducts produced by 30 min of irradiation was 60 nM or less. For example, the concentration of the $CH_3\dot{C}O$ radical adduct in rain water was 27 nM. While the photolytic production of carbon-centered radicals in natural waters has been postulated (*36*), these results provide the first evidence for the formation of these transient intermediates.

DISCUSSION

Fluorescamine is an ideal derivatization reagent for the hydroxylamine and alkoxyamines of 3-AMP since its reaction with primary amines is facile and since it does not react with the ammonium ion which can be a major interference in some biological and environmental samples. One drawback to fluorescamine, however, is that it reacts rapidly with other primary amines such as amino acids potentially resulting in high fluorescent backgrounds. This problem can be alleviated to some extent by the proper choice of the reaction pH or mobile phase.

However, the approach that we have outlined here should not be limited to only fluorescamine or to 3-AMP. Coupling strategies employing other functional groups should be feasible, possibly affording even better chromatographic selectivity or improved fluorescence characteristics. Development of coupling schemes that produce adducts having different chromatographic selectivities can also provide additional tests of the identity of the trapped radicals. Ultimately, positive identification of adducts should be achieved by mass spectral analysis of the isolated adducts or by combining microbore HPLC with mass spectrometry (LC/MS).

Drawbacks to the method include the following: (1) structural information is lost for radicals that are reducing with respect to the nitroxide (e.g., α-hydroxy radicals), (2) in aerated solutions, the nitroxide can be slowly regenerated from the alkoxyamines due to their reaction with peroxy radicals (*37*), and (3) the detection of oxygen-centered radicals such as $O_2^{\bullet-}$ and $^{\bullet}OH$ is likely to require the presence of additional compounds (*22*, *23*). Overall, however, this method is far simpler, more sensitive, and less prone to artifacts than current techniques for the detection and identification of carbon-centered radicals in aqueous solution. In addition, the method, in principle, does not require the use of an EPR spectrometer and instead employs equipment and reagents that are relatively inexpensive, portable, and uncomplicated to use. These factors should make studies of radical processes available to the broader scientific community.

While only a few applications of the method were illustrated here, this approach should prove useful for examining a variety of radical processes that occur in biological and chemical systems. As one example, the coupling sequence described in this work should allow for the fluorescence tagging of radical centers generated in macromolecules such as DNA by irradiation (*38*) or chemical reaction. The method should also be ideally suited for chromatographic applications employing postcolumn photochemical detection (*39*).

LITERATURE CITED

(1) Davidson, R. S. *Adv. Phys. Org. Chem.* **1983**, *19*, 1–130.
(2) Denisov, E. T.; Khudyakov, I. V. *Chem. Rev.* **1987**, *87*, 1313–1357.
(3) Mill, T.; Hendry, D. G.; Richardson, H. *Science* **1980**, *207*, 886–887.
(4) Burton, G. W.; Ingold, K. U. *Acc. Chem. Res.* **1986**, *19*, 194–201.
(5) Porter, N. A. *Acc. Chem. Res.* **1986**, *19*, 262–268.
(6) Mason, R. P. *Spin Labelling in Pharmacology*; Academic Press: New York, **1984**; pp 87–129.
(7) Janzen, E. G. *Acc. Chem. Res.* **1971**, *4*, 31–40.
(8) Perkins, M. J. *Adv. Phys. Org. Chem.* **1980**, *17*, 1–64.
(9) Janzen, E. G. *Methods Enzymol.* **1984**, *105*, 188–198.
(10) Samuni, A.; Krishna, C. M.; Riesz, P.; Finkelstein, E.; Russo, A. *Free Radicals Biol. Med.* **1989**, *6*, 141–148.
(11) Samuni, A. Y.; Samuni, A.; Swartz, H. M. *Free Radicals Biol. Med.* **1989**, *6*, 179–183.
(12) Finkelstein, E.; Rosen, G. M.; Rauckman, E. J.; Paxton, J. *Mol. Pharm.* **1979**, *16*, 676–685.
(13) Finkelstein, E.; Rosen, G. M.; Rauckman, E. J. *J. Am. Chem. Soc.* **1980**, *102*, 4994–4999.
(14) Rokushika, S.; Taniguchi, H.; Hatano, H. *Anal. Lett.* **1975**, *8*, 205–213.
(15) Makino, K.; Moriya, F.; Hatano, H. *J. Chromatogr.* **1985**, *332*, 71–106.
(16) Ingold, K. U. *Landolt-Bornstein, Numerical Data and Functional Relationships in Science and Technology, Vol. 13, Subvol. C, Radical Reaction Rates in Solution*; Springer-Verlag: New York, 1983; pp 166–270.
(17) Chateauneuf, J.; Lusztyk, J.; Ingold, K. U. *J. Org. Chem.* **1988**, *53*, 1629–1632.
(18) Beckwith, A. L. J.; Bowry, V. W.; Moad, G. *J. Org. Chem.* **1988**, *53*, 1632–1641.
(19) Schmid, P.; Ingold, K. U. *J. Am. Chem. Soc.* **1978**, *100*, 2493–2500.
(20) Brownlie, I. T.; Ingold, K. U. *Can. J. Chem.* **1967**, *45*, 2427–2432.
(21) Blough, N. V. *Environ. Sci. Technol.* **1988**, *22*, 77–82.
(22) Finkelstein, E.; Rosen, G. M.; Rauckman, E. J. *Biochim. Biophys. Acta* **1984**, *802*, 90–98.
(23) Rosen, G. M.; Freeman, B. A. *Proc. Natl. Acad. Sci. U.S.A.* **1984**, *81*, 7269–7273.
(24) Blough, N. V.; Simpson, D. J. *J. Am. Chem. Soc.* **1988**, *110*, 1915–1917.
(25) Green, S. A.; Simpson, D. J.; Zhou, G.; Ho, P. S.; Blough, N. V. *J. Am. Chem. Soc.*, in press.

(26) Gerlock, J. L.; Zacmanidis, P. J.; Bauer, D. R.; Simpson, D. J.; Blough, N. V.; Salmeen, I. T. *Free Radical Res. Commun.* **1990**, *10*, 119–121.
(27) Kieber, D. J.; Blough, N. V. *Free Radical Res. Commun* **1990**, *10*, 109–117.
(28) Buettner, G. R.; Oberley, L. W. *Biochim. Biophys. Res. Commun.* **1978**, *83*, 69–74.
(29) Undenfriend, S.; Stein, S.; Bohlen, P.; Dairman, W.; Leimgruber, W.; Weigele, M. *Science* **1972**, *178*, 871–872.
(30) DeBernardo, S.; Weigele, M.; Toome, V.; Manhart, K.; Leimgruber, W.; Bohlen, P.; Stein, S.; Udenfriend, S. *Arch. Biochem. Biophys.* **1974**, *163*, 390–399.
(31) Turro, N. J. *Modern Molecular Photochemistry*; Benjamin/Cummings: Menlow Park, CA, 1978; pp 363–368.
(32) Willson, R. L. *Trans. Faraday Soc.* **1971**, *67*, 3008–3019.
(33) Nigam, S.; Asmus, K.-D.; Willson, R. L. *J. Chem. Soc., Faraday Trans.* **1976**, *1*, 2324–2340.
(34) Ingles, D. L.; Gallimore, D. *J. Chromatogr.* **1985**, *325*, 346–352.
(35) McHugh, W.; Sandmann, R. A.; Haney, W. G.; Sood, S. P.; Wittmer, D. P. *J. Chromatogr.* **1976**, *124*, 376–380.
(36) Zafiriou, O. C.; Joussot-Dubien, J.; Zepp, R. G.; Zika, R. G. *Environ. Sci. Technol.* **1984**, *18*, 358A–371A.
(37) Klemchuk, P. P.; Gande, M. E. *Polym. Degrad. Stab.* **1988**, *22*, 241–274.
(38) Swarts, S. G.; Sevilla, M. D. *Radiat. Res.* **1987**, *112*, 21–35.
(39) Krull, I. S.; Lacourse, W. R. *Reaction Detection in Liquid Chromatography*; Marcel Dekker: New York, 1986; pp 303–352.

RECEIVED for review May 29, 1990. Accepted July 30, 1990. This work was supported by the Office of Naval Research under ONR Contract N00014-87-K-007 and Grant N00014-89-J-1260. This is contribution No. 7410 from the Woods Hole Oceanographic Institution.

Selective Sorption of Alkali-Metal Cations by Carboxylic Acid Resins Containing Acyclic or Cyclic Polyether Units

Takashi Hayashita, Mi-Ja Goo, Jong Chan Lee, Jong Seung Kim, Jan Krzykawski, and Richard A. Bartsch*

Department of Chemistry and Biochemistry, Texas Tech University, Lubbock, Texas 79409-1061

Novel ion-exchange resins have been prepared by condensation polymerization with formaldehyde in formic acid of three polyether carboxylic acids which possess two benzo group substituents. The selectivities and efficiencies of competitive alkali-metal cation sorption from aqueous solutions by these polyether carboxylic acid resins are strongly influenced by (1) the pH of the aqueous solution, (2) the acyclic or cyclic nature of the polyether unit, and (3) the conformational positioning of the carboxylic acid group in the resins derived from cyclic polyether (crown ether) compounds. Good sorption selectivity for Na^+ was observed for dibenzo-16-crown-5 resin 3 in which the pendant carboxylic acid group is oriented over the polyether cavity. Resin 3 was utilized as a stationary phase for selective column concentration of Na^+ from dilute aqueous solution.

INTRODUCTION

Synthetic macrocyclic multidentate ligands such as crown ethers are useful organic compounds for the separation of alkali-metal and alkaline-earth cations from aqueous solutions (*1*, *2*). These ligands have hydrophilic interior cavities and hydrophobic exteriors and form stable complexes by coordinating metal cations within their cavities. However, many of these macrocyclic compounds are quite expensive and some possess toxic properties (*3*). Both factors influence the potential of such macrocyclic compounds for practical applications in metal ion separations.

An attractive method to circumvent both problems is to incorporate the macrocyclic compound in a polymer network. Blasius and co-workers synthesized a series of crown ether resins by polycondensation reactions of dibenzo crown ethers with formaldehyde (*4*). These resins were used as stationary phases for the chromatographic separation of alkali-metal and alkaline-earth cations and their counteranions (*5*, *6*). Linear crown ether polymers derived from vinyl-type monomers have been prepared by Smid et al. (*7*, *8*) and later by Kimura et al. (*9*, *10*). Polymerization of azacrown ethers and cryptands has been reported by Blasius et al. (*11*, *12*) and by Gramain (*13*). All of these studies focused on the immobilization of neutral macrocyclic multidentate compounds. Hence the binding of metal cations was significantly affected by the identities of the requisite anions. This complication would be avoided if ion-exchange groups, which could control the sorption and desorption of metal cations, were incorporated into the crown ether resins.

In earlier investigations, we have utilized a series of dibenzo crown ethers with pendant ionizable groups for selective solvent extraction of alkali-metal cations (*14–21*). Polycondensation reactions of such crown ethers by a reported procedure (*22*) should be feasible. In the present study, we have synthesized new acyclic and cyclic polyether carboxylic acid resins **1**, **2**, and **3** and compared their competitive sorption behavior for alkali-metal cations from aqueous solutions with that for a commercial poly(methacrylic acid) ion-exchange resin. The results of this investigation are now reported together with an application of crown ether carboxylic acid resin **3** for selective column concentration of alkali-metal cations from dilute aqueous solution.

EXPERIMENTAL SECTION

Apparatus. ^1H NMR spectra were taken with an IBM AF-200 nuclear magnetic resonance spectrometer. IR spectra were taken with Perkin-Elmer Model 1600 or Nicolet MS-X infrared spectrophotometers. Concentrations of alkali-metal cations in the aqueous phases were determined with a Dionex Model 2000i ion chromatograph or with a Perkin-Elmer Model 5000 atomic absorption spectrophotometer. pH measurements were made with a Fisher Scientific Accumet Model 825MP pH meter and a Corning 7605 glass body combination electrode. A Burrell Model 25 wrist-action shaker was used to shake the aqueous solution–resin mixtures. To prevent metal contamination, all glassware was soaked in 5% HNO_3 solution for 24 h and rinsed with distilled, deionized water before use. Elemental analysis was performed

* To whom correspondence should be addressed.

0003-2700/90/0362-2283$02.50/0 © 1990 American Chemical Society

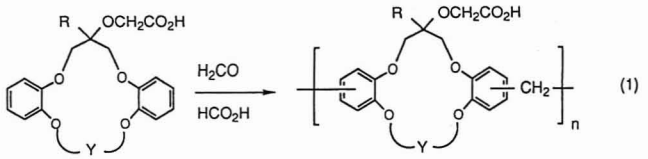

	Y		R	
4	$-CH_3$	CH_3-	-H	1
5	$-CH_2CH_2OCH_2CH_2-$		-H	2
6	$-CH_2CH_2OCH_2CH_2-$		$-C_3H_7$	3

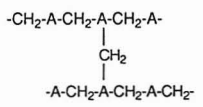

7

by Desert Analytics (Tucson, AZ) and Galbraith Laboratories (Knoxville, TN).

Reagents. *sym*-Dibenzo-16-crown-5-oxyacetic acid (**5**) was prepared by the reported method (*14*). *sym*-Ketodibenzo-16-crown-5 was synthesized by the reported procedure (*19*). Amberlite CG-50 ion exchange resin was obtained from Aldrich Chemical Co. LiOH, LiCl, NaCl, and KCl were purchased from Fisher Scientific Co. CsCl (99%) and RbCl (99%) were obtained from Morton Thiokol, Inc. (Alfa Products). Stock aqueous solutions of 0.50 M alkali-metal chlorides (NaCl, KCl, RbCl, and CsCl), 0.50 M LiCl, and 0.50 M LiOH were stored in polyethylene bottles. Sample solutions were prepared by mixing and diluting these stock solutions. Other inorganic and organic compounds were reagent-grade commercial products and were used as received. Purified water was prepared by passing distilled water through three Barnstead D8922 combination cartridges in series.

Preparation of 1,3-Bis(*o*-methoxyphenoxy)-2-propanol. To 16.39 g (132 mmol) of *o*-methoxyphenol in 1.8 L of H_2O–THF (1:1), 5.28 g (132 mmol) of NaOH was slowly added. The mixture was stirred and heated for 2 h at 80 °C under nitrogen and then cooled to 50 °C. Epichlorohydrin (6.11 g, 66 mmol) was added during 8 h with a syringe pump and stirring was continued at 50 °C for 2 days. After evaporation of the THF in vacuo, the residue was extracted with CH_2Cl_2. The CH_2Cl_2 extracts were washed with brine, dried over $MgSO_4$, and evaporated in vacuo. Chromatography of the residue on alumina with EtOAc as eluent gave 13.32 g (66%) of the title compound as a white solid with mp 69–71 °C: IR (deposit on NaCl plate) 3428 (OH), 1253, 1124 cm^{-1} (CO); ^1H NMR ($CDCl_3$) δ 3.72 (s, 1), 3.80 (s, 6), 4.15–4.25 (m, 4), 4.42 (pen, 1), 6.80–7.00 (m, 8). Anal. Calcd for $C_{17}H_{20}O_5$: C, 67.09; H, 6.62. Found: C, 67.24; H, 6.73.

Preparation of 1,3-Bis(*o*-methoxyphenoxy)-2-propoxyacetic Acid (4). The protecting mineral oil was removed by washing KH (28.32 g of 35% dispersion in mineral oil, 0.24 mol) with dry pentane under nitrogen and dry THF (200 mL) was added. A solution of 1,3-bis(*o*-methoxyphenoxy)-2-propanol (12.0 g, 39 mmol) in 100 mL of dry THF was added dropwise and the reaction mixture was stirred for 1 h at room temperature. A solution of bromoacetic acid (5.42 g, 78 mmol) in 125 mL of dry THF was added dropwise during 3 h and the reaction mixture was stirred at room temperature for 1 day. Water (5 mL) was carefully added to decompose the unreacted KH. The reaction mixture was filtered and the filtrate was evaporated in vacuo. The residue was dissolved in H_2O (200 mL) and acidified to pH <1 with concentrated HCl. The precipitated oil was decanted and washed with H_2O (two 100 mL portions). The resulting sticky oil was dissolved in CH_2Cl_2 and the solution was washed with H_2O, dried over $MgSO_4$, and evaporated in vacuo to form a residue which upon recrystallization from acetone–hexane gave 9.50 g (67%) of **4** as a white solid with mp 82–84 °C: IR (deposit on NaCl plate) 3357 (COOH), 1762 (C=O), 1255, 1124 cm^{-1} (CO); ^1H NMR ($CDCl_3$) δ 3.85 (s, 6), 4.05–4.35 (m, 5), 4.48 (s, 2), 6.75–7.05 (m, 8). Anal. Calcd for $C_{19}H_{22}O_7$: C, 62.97; H, 6.12. Found: C, 62.87; H, 6.30.

Preparation of *sym*-(Hydroxy)(propyl)dibenzo-16-crown-5. Under nitrogen, 0.70 g (30.6 mmol) of magnesium turnings was added to 3.79 g (30.6 mmol) of 1-bromopropane in 150 mL of refluxing THF and refluxing was continued until the magnesium had dissolved. The solution was cooled in an ice bath and 5.30 g (15.4 mmol) of *sym*-ketodibenzo-16-crown-5 dissolved in 80 mL of THF was added. The reaction solution was refluxed for 4 h and then stirred overnight at room temperature. The reaction mixture was cooled in an ice bath and 100 mL of 5% NH_4Cl solution was slowly added to quench the reaction. After the mixture was stirred for 30 min at room temperature, the THF was evaporated in vacuo. The residue was extracted with CH_2Cl_2 and the extract was dried over $MgSO_4$ and evaporated in vacuo. The resulting solid was recrystallized from Et_2O (350 mL) to give 5.00 g (84%) of white solid with mp 120–121 °C: IR (deposit on NaCl plate) 3449 (OH), 1254, 1046 cm^{-1} (CO); ^1H NMR ($CDCl_3$) δ 0.99 (t, 3), 1.45–1.65 (m, 2), 1.80–1.90 (m, 2), 3.22 (s, 1), 3.80–4.30 (m, 12), 6.80–7.00 (m, 8). Anal. Calcd for $C_{22}H_{28}O_6$: C, 68.02; H, 7.27. Found: C, 67.62; H, 7.08.

Preparation of *sym*-(Propyl)dibenzo-16-crown-5-oxyacetic Acid (6). The protecting mineral oil was removed from KH (14.16 g of 35% dispersion in mineral oil, 0.12 mol) by washing with dry pentane under nitrogen and 40 mL of dry THF was added. A solution of *sym*-(hydroxy)(propyl)dibenzo-16-crown-5 (8.00 g, 20.6 mmol) in 60 mL of THF was added dropwise and the mixture was stirred for 1 h. Bromoacetic acid (5.72 g, 41.2 mmol) in 40 mL of THF was added dropwise and the reaction mixture was stirred overnight at room temperature and then refluxed for 30 min. After the reaction mixture cooled, ice and water were carefully added to destroy the excess KH and the THF was evaporated in vacuo. The residue was acidified to pH 1 with 6 N HCl and extracted with CH_2Cl_2. The CH_2Cl_2 solution was washed with 5% HCl, dried over $MgSO_4$, and evaporated in vacuo to give 8.55 g (93%) of **6** as a white solid with mp 153–154 °C: IR (deposit on NaCl plate) 3357 (COOH), 1746 (C=O), 1256, 1124 cm^{-1} (CO); ^1H NMR ($CDCl_3$) δ 1.06 (t, 3), 1.50–1.60 (m, 2), 1.90–2.00 (m, 2), 3.70–4.20 (m, 10), 4.60 (d, 2), 4.85 (s, 2), 6.60–7.00 (m, 8). Anal. Calcd for $C_{24}H_{30}O_8$; C, 64.57; H, 6.77. Found: C, 64.58; H, 6.78.

Preparation of Polyether Carboxylic Acid Resins 1–3. Resins **1–3** were synthesized by condensation polymerization of the dibenzo polyether carboxylic acid monomers **4–6**, respectively, with formaldehyde in formic acid (*22*). The monomer (12 mmol) was dissolved in a solution of formic acid (200 mL) and formaldehyde (37% aqueous solution, 200 mL for **1** and 100 mL for **2** and **3**). The mixture was refluxed for 24 h and cooled. The precipitate was collected, washed with formic acid and then water, and dried at 80 °C. The resin was ground and used in powder form (finer than 100 mesh). Resin **1** was obtained in 48% yield: IR (KBr) 3448 (COOH), 1755 (C=O), 1278, 1090 cm^{-1} (CO). Anal. Calcd according to **7**: C, 64.49; H, 5.89. Found: C, 64.36; H, 5.64. Resin **2** was formed in 93% yield: IR (KBr) 3448 (COOH), 1735 (C=O), 1282, 1129 cm^{-1} (CO). Anal. Calcd according to **7**·$2H_2O$: C, 62.73; H, 5.86. Found: C, 62.63; H, 5.54. Resin **3** was produced in 72% yield: IR (KBr) 3448 (COOH), 1735 (C=O), 1282, 1104 cm^{-1} (CO). Anal. Calcd according to **7**·$2H_2O$: C, 64.79; H, 6.63. Found: C, 64.75; H, 6.44. Although we have experienced no physiological problems in handling resins **2** and **3** or their crown ether alcohol or carboxylic acid precursors, care should always be exercised in working with cyclic polyether compounds (*3*).

Ion-Exchange Capacities of Resins 1–3. The ion-exchange capacity of a resin was determined by Na^+ sorption. A 5.0-mL sample solution (aqueous or 80% methanol) containing 0.080 M NaOH and 0.00–0.60 M NaCl was shaken with 0.050 g of the resin for 3.0 h in a 30-mL separatory funnel at room temperature (21–23 °C). After filtration with a sintered glass filter funnel, the resin was washed with 100 mL of water and dried. Of the dried resin, a 0.010-g sample was shaken with 5.0 mL of 0.10 M HCl solution for 1.0 h to strip the Na^+ from the resin into an aqueous solution for analysis by atomic absorption spectrophotometry.

Procedure. An aqueous solution of alkali-metal chlorides with hydroxides for pH adjustment (5.0 mL, 0.10 M in each) and 0.050 g of the resin were shaken for 3.0 h in a 30-mL separatory funnel at room temperature (21–23 °C) with a Burrell wrist-action shaker. The aqueous phase was filtered with a sintered glass filter funnel (15 mL, medium porosity) and the equilibrium pH of the aqueous phase was measured. The resin was washed with 100 mL of water and dried. Of the dried resin, a 0.020-g sample was shaken with 5.0 mL of 0.10 M HCl solution for 1.0 h to strip the alkali-metal cations from the resin into an aqueous solution for analysis by

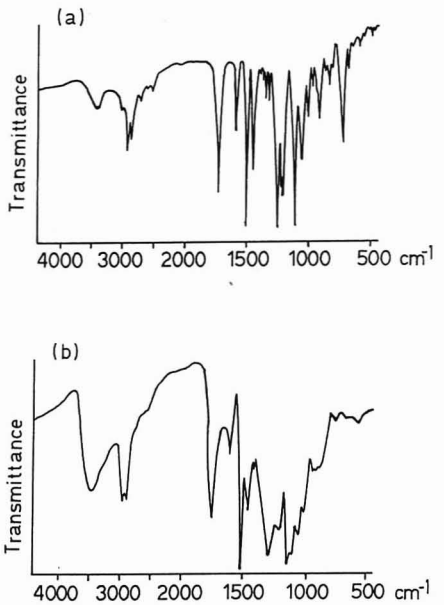

Figure 1. Infrared spectra for (a) crown ether carboxylic acid **5** and (b) crown ether carboxylic acid resin **2**.

ion chromatography. When water was substituted as the stripping solution, no detectable concentrations of alkali-metal cations were evident in the chromatographic analysis.

RESULTS AND DISCUSSION

Characterization of Polyether Carboxylic Acid Resins. Polyether carboxylic acid resins **1–3** were prepared by condensation polymerization of the corresponding acyclic or cyclic polyether carboxylic acids with formaldehyde in formic acid (eq 1). A comparison of the infrared spectra for crown ether carboxylic acid **5** and the corresponding crown ether carboxylic acid resin **2** is presented in Figure 1. Although the spectrum for the polymer shows broadening in comparison with that of the monomer, no differences in absorption peaks are observed. This demonstrates the absence of monomer decomposition during synthesis of the resin. Similar infrared spectra were observed for polyether carboxylic acid resins **1–3** (see Experimental Section).

Structural representations **1–3** imply polymers with no cross-linking. This is most certainly an oversimplification since some level of cross-linking is anticipated (*4*). A possible structure for the partially cross-linked resins is given by **7** in which A is the polyether carboxylic acid unit in the resin. Elemental analysis results for resin **1** agree with this formulation. For resins **2** and **3**, the elemental analysis results are consistent with that for **7** as a dihydrate (see Experimental Section).

The ion exchange capacities of resins **1–3** were evaluated from the maximum sorption of Na^+ by the resins. To determine the maximum value, Na^+ sorption by each resin was investigated for different Na^+ concentrations in both aqueous and 80% methanol solutions. In each solution the hydroxide ion concentration was adjusted to 0.080 M to maintain a high pH condition. Results are presented in Table I.

In the sorption from aqueous solutions (entries 1 and 2), Na^+ sorption by acyclic polyether carboxylic acid resin **1** remained constant when the initial Na^+ concentration was increased from 0.080 to 0.58 M. For the cyclic polyether carboxylic acid resins **2** and **3**, slightly enhanced (<10%) sorption was noted at the higher Na^+ concentration. On the other hand, Na^+ sorption from 80% methanol solutions was unaffected as the initial Na^+ concentration was varied from 0.080 to 0.68 M for all three resins (entries 3–7). The effective ion-exchange capacities for polyether carboxylic acid resins 1–3 as assessed by Na^+ sorption from 80% methanol solutions

Table I. Sorption of Na^+ by Polyether Carboxylic Acid Resins 1–3[a]

entry	[Na^+],[b] M	[methanol], vol %	sorption of Na^+ by resin, mmol/g 1	2	3
1	0.080	0	2.11	1.65	1.41
2	0.58	0	2.11	1.75	1.46
3	0.080	80	2.08	1.82	1.41
4	0.18	80	2.13	1.79	1.48
5	0.28	80	2.06	1.80	1.42
6	0.48	80	2.14	1.84	1.45
7	0.68	80	2.09	1.82	1.43

[a] The sample solution was an aqueous or 80% methanol solution containing 0.080 M NaOH and 0.00–0.60 M NaCl. [b] Initial Na^+ concentration in the sample solution.

are 2.10 ± 0.03, 1.81 ± 0.02, and 1.44 ± 0.03 mmol/g, respectively. The theoretical ion exchange capacities calculated for resins **1–3** according to formula **7** are 2.66, 2.39, and 2.17 mmol/g. Thus the effective ion-exchange capacities are somewhat lower than the theoretical values. Probably this is attributable to steric hindrance for metal ion adsorption in certain portions of the resin structures.

Alkali-Metal Cation Adsorption by Polyether Carboxylic Acid Resins. In our studies of alkali-metal cation solvent extraction by crown ether carboxylic acids, competitive extraction behavior was investigated since the efficiencies and selectivity orders for competitive extractions are often quite different from extrapolations based upon the results of single ion extractions (*15–20*). Also, competitive extraction more closely resembles actual metal separation systems. In the present study, competitive sorption behavior of alkali-metal cations was investigated.

An aqueous solution of the five alkali-metal cations (0.10 M in each) as the chlorides and hydroxides was shaken with the polyether carboxylic acid resin. In control experiments conducted with resin **2**, no significant variation in sorption was noted for shaking times which ranged from 1.0 to 12.0 h. Compared wih the equilibrium values, more than 85% of sorption was observed after a shaking time of 5.0 min. The resin was filtered, washed with water, and dried. Of the dried resin a portion was shaken with 0.10 M HCl to strip the alkali-metal cations from the resin into aqueous solution for analysis by ion chromatography. In control experiments conducted with resin **2**, times which ranged from 0.5 to 120 min gave complete stripping. Also no significant difference was noted when the stripping solution concentration was varied from 0.05 to 1.0 M HCl. These experiments demonstrate that both alkali-metal cation sorption and stripping are rapid.

For comparison with a commercially available carboxylic acid ion-exchange resin, alkali-metal cation sorption by Amberlite CG-50, a poly(methacrylic acid) resin, was investigated. By use of the method described above but with Li^+ instead of Na^+, the effective ion-exchange capacity of this weak acid ion exchange resin was determined to be 8.71 ± 0.05 mmol/g. Results for the competitive sorption of alkali-metal cations by Amberlite CG-50 resin as a function of pH of the aqueous solution are shown in Figure 2. The alkali-metal cation sorption by the resin phase at equilibrium with aqueous solutions which were 0.10 M in each of the five alkali-metal cations is the ordinate and the equilibrium aqueous phase pH is the abscissa. For each of the alkali-metal cations the degree of sorption is enhanced in the pH of the aqueous phase increased. This demonstrates that the ion-exchange sorption of alkali-metal cations is facilitated by deprotonation of the carboxylic acid groups in the resin. When pH >7 the sorption selectivity is $Li^+ > Na^+ > K^+, Rb^+, Cs^+$. The maximum

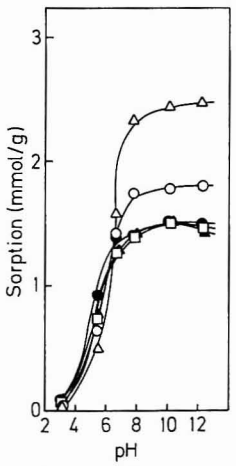

Figure 2. Sorption of alkali-metal cations by Amberlite CG-50 ion exchange resin vs the equilibrium pH of the aqueous phase: (△) Li^+, (○) Na^+, (□) K^+, (▲) Rb^+, (●) Cs^+.

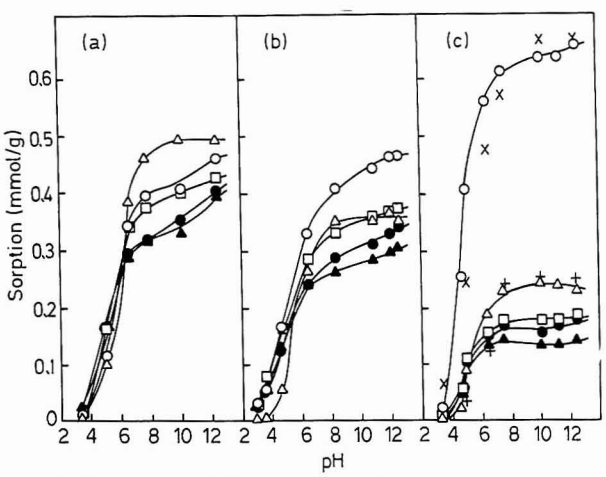

Figure 3. Sorption of alkali-metal cations by the polyether carboxylic acid resin vs the equilibrium pH of the aqueous phase for (a) **1**, (b) **2**, (c) **3**: (△) Li^+, (○) Na^+, (□) K^+, (▲) Rb^+, (●) Cs^+. Reproducibility of results for a second preparation of **3** is shown as (+) Li^+ and (×) Na^+.

combined metal ion loading (based upon the effective ion-exchange capacity) for the resin is 99% at pH 12.5.

Results for competitive alkali-metal cation sorption by polyether carboxylic acid resins **1**–**3** are presented in parts a–c of Figure 3, respectively. The relationship between alkali-metal cation sorption by resins **1**–**3** and the equilibrium pH of the aqueous alkali-metal cation solution (0.10 M in each) is similar to that observed for Amberlite CG-50 resin (Figure 2). The maximum combined metal ion loadings for resins **1**–**3** at pH 12.5 (based upon the effective ion-exchange capacities) are 100, 100, and 95%, respectively.

Significant differences in sorption selectivities are observed between the acyclic polyether carboxylic acid resin **1** and the cyclic polyether carboxylic acid resins **2** and **3** (Figures 3 and 4). In the pH region of 7–12.5 the sorption selectively for **1** is $Li^+ > Na^+ > K^+ > Rb^+$, Cs^+, closely resembling that obtained with Amberlite CG-50 resin which contains carboxylic acid groups, but no ether linkages. On the other hand, the sorption selectivities for cyclic polyether carboxylic acid resins **2** and **3** are $Na^+ > Li^+$, $K^+ > Cs^+ > Rb^+$ and $Na^+ \gg Li^+ > K^+$, $Cs^+ > Rb^+$, respectively. Clearly the sorption selectivity is influenced by the presence of cyclic polyether (crown ether) rings in the resin. Thus the sorption selectivity for Li^+ shown by the acyclic polyether carboxylic acid resin **1** changes to Na^+ sorption selectivity for the crown ether carboxylic acid resins **2** and **3**. From an examination of Corey–Pauling–Kortun (CPK) space-filling models, the cavity diameter of dibenzo-16-crown-5 is estimated to be 2.0–2.4 Å.

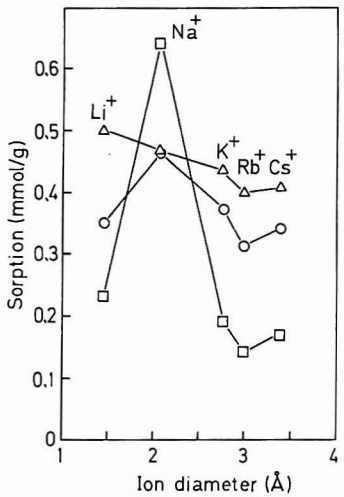

Figure 4. Sorption of alkali-metal cations by the polyether carboxylic acid resin at pH 12–13 vs the diameter of the alkali-metal cations: (△) resin **1**, (○) resin **2**, (□) resin **3**.

The ionic diameters of the alkali-metal cations are as follows: Li^+, 1.48 Å; Na^+, 2.04 Å; K^+, 2.76 Å; Rb^+, 2.98 Å; Cs^+, 3.40 Å (*23*). Based upon the relationship between the relative diameters of the metal ions and the polyether cavity in resins **2** and **3**, selectivity for Na^+ sorption would be predicted.

The reproducibility of sorption behavior for the polyether carboxylic acid resins was probed for resin **3**. A different batch of monomer **6** was prepared and polymerized as before with formaldehyde and formic acid to produce a second batch of crown ether carboxylic acid resin **3**. Alkali-metal cation sorption by the new preparation of resin **3** was evaluated as before. The Na^+ (×) and Li^+ (+) sorption results are shown in Figure 3c and establish good reproducibility of the sorption behavior for two independent preparations of crown ether carboxylic acid resin **3**.

Although both crown ether carboxylic acid resins **2** and **3** are selective for Na^+ as would be predicted for the polyether ring size, it is evident that the Na^+ sorption selectivity of **3**, in which a propyl group is attached to the same carbon of the crown ether ring as the pendant carboxylic acid group, is much higher than that of **2**. Examination of CPK space-filling models reveals that when the propyl chain in **3** points away from the polar crown ether ring, the carboxylic acid group is oriented directly over the crown ether cavity. Such preorganization of the binding site (*24*) is also suggested by the ^1H NMR spectrum of monomer **6** from which resin **3** is prepared. The diastereomeric methylene group protons on the three-carbon bridge of **6** appear as an AB quartet, which demonstrates that the conformation of that portion of the polyether ring is locked on the NMR time scale. The corresponding methylene group protons on the three-carbon bridges in monomers **4** and **5**, from which resins **1** and **2**, respectively, are prepared do not appear as AB quartets.

The high Na^+ selectivity observed for crown ether resin **3** is attributed to preorganization of the pendant carboxylic acid group. This is the first instance in which the conformational positioning of the ion-exchange group in the resin has shown an important influence on metal ion recognition.

Selective Column Concentration of Alkali-Metal Cations. The rapid sorption and desorption of alkali-metal cations from polyether carboxylic acid resins **1**–**3** suggests that such resins could be utilized as stationary phases for column chromatographic concentration of alkali-metal cations from aqueous solutions.

As a preliminary study of this potential application, column concentration of alkali-metal cations from dilute aqueous solution was investigated with crown ether carboxylic acid resin **3**. An aqueous solution (1.00 L, pH = 10.2) with the

Table II. Column Concentration of Alkali-Metal Cations by Crown Ether Carboxylic Acid Resin 3[a]

alkali-metal cation	concn factor (CF)	recovery, %	loading, mmol/g	loading for batch treatment,[b] mmol/g
Li^+	49	25	0.15	0.24
Na^+	157	79	0.47	0.61
K^+	54	27	0.16	0.17
Rb^+	43	22	0.13	0.13
Cs^+	48	24	0.14	0.15

[a] From an aqueous solution of the five alkali-metal cations (6.00×10^{-5} M in each) at pH 10.2. [b] At equilibrium pH = 10.0.

concentration for each of the five alkali-metal cations at 6.00×10^{-5} M was eluted through a 0.42 cm i.d. column of resin **3** (0.10 g) at a flow rate of 8.0 mL/min. At the same flow rate, the column was then washed with 100 mL of water and stripped with 5.00 mL of 0.10 M HCl. The stripping solution was analyzed by ion chromatography. The results are recorded in Table II in which the concentration factor (CF) is defined as

$$CF = \frac{\text{concn of } M^+ \text{ in the stripping solution}}{\text{initial concn of } M^+ \text{ in the sample solution}} \quad (2)$$

The concentration factor of 157 for Na^+ was much higher than those of 43–54 for the other alkali-metal cations. For a single passage of the sample solution through the column of resin **3**, the recovery of Na^+ was 79%. No detectable alkali-metal cation concentrations were observed in a second 5.00 mL of stripping solution.

The alkali-metal cation loadings observed for the column treatment are similar to those for the batch treatment (compare the last two columns in Table II), which demonstrates that selective sorption also occurs from dilute aqueous solution. Thus effective column concentration of a desired metal cation can be attained in this type of system. Such selective column concentration would be useful not only for the enhancement of analytical detection limits but also for the recovery of target metal cations, such as radioactive Cs^+.

CONCLUSIONS

Sorption selectivity for alkali-metal cations by cyclic polyether (crown ether) carboxylic acid resins is controlled by the relationship between the crown ether and metal ion diameters. Thus resins **2** and **3** which are based upon dibenzo-16-crown-5 units exhibit sorption selectivity for Na^+. However the much higher Na^+ sorption selectivity of **3** is attributed to conformational positioning of the pendant carboxylic acid group over the crown ether cavity. Hence, not only the nature of the crown ether backbone but also the location of the ion-exchange group plays an important role in cation sorption.

Since the sorption and desorption of alkali-metal cations by polyether carboxylic acid resins **1**–**3** are rapid, such resins have potential for use as stationary phases for column chromatographic concentration of alkali-metal cations from aqueous solutions. Thus crown ether carboxylic acid resin **3** was shown to provide efficient and selective concentration of Na^+ from a dilute solution of five alkali-metal cations.

LITERATURE CITED

(1) Pedersen, C. J. *J. Am. Chem. Soc.* **1967**, *89*, 7017–7036.
(2) Izatt, R. M.; Bradshaw, J. S.; Nielsen, S. A.; Lamb, J. D.; Christensen, J. J.; Sen, D. *Chem. Rev.* **1985**, *85*, 271–339.
(3) Hiraoka, M. *Crown Compounds: Their Characteristics and Applications*; Elsevier: New York, 1982; pp 265–272.
(4) Blasius, E.; Adrian, W.; Janzen, K.-P.; Kalutke, G. J. *J. Chromatogr.* **1974**, *96*, 89–97.
(5) Blasius, E.; Maurer, P. G. *J. Chromatogr.* **1976**, *125*, 511–516.
(6) Blasius, E.; Janzen, K.-P.; Adrian, W.; Klein, W.; Klotz, H.; Luxenburger, H.; Mernke, E.; Nguyen, V. B.; Nguyen-Tien, T.; Rausch, R.; Stockemer, J.; Toussaint, A. *Talanta* **1980**, *27*, 127–141.
(7) Kopolow, S.; Hogen Esch, T. E.; Smid, J. *Macromolecules* **1971**, *4*, 359–360.
(8) Kopolow, S.; Hogen Esch, T. E.; Smid, J. *Macromolecules* **1973**, *6*, 133–142.
(9) Kimura, K.; Maeda, T.; Shono, T. *Anal. Lett.* **1978**, *A11*, 821–827.
(10) Kimura, K.; Maeda, T.; Tamura, H.; Shono, T. *J. Electroanal. Chem. Interfacial Electrochem.* **1979**, *95*, 91–101.
(11) Blasius, E.; Maurer, P. G. *Makromol. Chem.* **1977**, *178*, 649–657.
(12) Blasius, E.; Janzen, K.-P.; Keller, M.; Lander, H.; Nguyen-Tien, T.; Schoten, G. *Talanta* **1980**, *27*, 107–126.
(13) Gramain, P. H. *Recent Developments in Ion Exchange*; Williams, P. A., Hudson, M. J., Eds.; Elsevier Applied Science: New York, 1987; pp 300–314.
(14) Bartsch, R. A.; Heo, G. S.; Kang, S. I.; Liu, Y.; Strzelbicki, J. *J. Org. Chem.* **1982**, *47*, 457–460.
(15) Strzelbicki, J.; Bartsch, R. A. *Anal. Chem.* **1981**, *53*, 1984–1989.
(16) Strzelbicki, J.; Bartsch, R. A. *Anal. Chem.* **1981**, *53*, 2251–2253.
(17) Charewicz, W. A.; Heo, G. S.; Bartsch, R. A. *Anal. Chem.* **1982**, *54*, 2094–2097.
(18) Charewicz, W. A.; Bartsch, R. A. *Anal. Chem.* **1982**, *54*, 2300–2303.
(19) Bartsch, R. A.; Liu, Y.; Kang, S. I.; Son, B.; Heo, G. S.; Hipes, P. G.; Bills, L. J. *J. Org. Chem.* **1983**, *48*, 4864–4869.
(20) Pugia, M. J.; Ndip, G.; Lee, H. K.; Yang, I.; Bartsch, R. A. *Anal. Chem.* **1986**, *58*, 2723–2726.
(21) Walkowiak, W.; Charewicz, W. A.; Kang, S. I.; Yang, I.-W.; Pugia, M. J.; Bartsch, R. A. *Anal. Chem.*, in press.
(22) Hayashita, T.; Oka, H.; Noguchi, H.; Igawa, M. *Anal. Sci.* **1989**, *5*, 101–103. Hayashita, T.; Noguchi, H.; Oka, H.; Igawa, M.; Takagi, M. *J. Appl. Polym. Sci.* **1990**, *39*, 561–569.
(23) McBride; D. W.; Izatt, R. M., Lamb, J. D.; Christensen, J. J. *Inclusion Compounds*; Atwood, J. L., Davies, J. E. D., McNicol, D. D., Eds.; Academic Press: New York, 1984; Vol. 3, p 586.
(24) Cram, D. J. *Angew. Chem., Int. Ed. Engl.* **1986**, *25*, 1039–1057.

RECEIVED for review June 18, 1990. Accepted July 30, 1990. This research was supported by the Division of Chemical Sciences of the Office of Basic Energy Sciences of the U.S. Department of Energy (Grant DE-FG05-88ER13832) and the Advanced Technology Program of the State of Texas.

Influence of Alkyl Chain Length on the Stability of *n*-Alkyl-Modified Reversed Phases. 1. Chromatographic and Physical Analysis

Martin J. J. Hetem,*[1] Jan W. de Haan, Henk A. Claessens, Leo J. M. van de Ven, and Carel A. Cramers

Laboratory of Instrumental Analysis, Eindhoven University of Technology, P.O. Box 513, 5600 MB Eindhoven, The Netherlands

Joachim N. Kinkel

E. Merck, Frankfurterstrasse 250, D-6100 Darmstadt 1, West Germany

The influence of the ligand alkyl chain length, chemically bonded at the surface of a silica substrate, on stationary phase stability in liquid chromatography practice is reviewed. Several factors affecting long-term stability of modern reversed-phase high-performance liquid chromatography (RP-HPLC) phases are considered and their individual contributions are evaluated in this paper and the following paper in this issue. The stationary phases under study were identically modified on the same batch of silica substrate to eliminate differences in substrate properties and synthesis conditions. Modifications with ligand alkyl chain length between C_1 and C_{18} were performed such that an approximately equal ligand density was obtained for the seven RP-HPLC phases studied. These *n*-alkyldimethylsiloxysilane bonded phases were exposed to simulated aging experiments. A subsequent chromatographic characterization regarding changes in capacity, lipophilic and polar selectivity, and silica degradation related separation performance was carried out. Comparison with results determined by other characterization methods, like bulk analysis, elemental analysis, and solid-state ^{29}Si cross-polarization magic angle spinning NMR revealed that with longer *n*-alkyl ligands gradually better substrate shielding properties were obtained. The ligand alkyl chain length affects the stability of reversed phases to a large extent. Short ligand modified phases changed drastically using relatively aggressive eluents. Organic modifier rich eluents combined with longer ligand modified phases are preferable for a longer lifetime of RP-HPLC columns, especially when aggressive eluents are used.

INTRODUCTION

Modified silica-based packings most commonly used as reversed phases in high-performance liquid chromatography (RP-HPLC) are *n*-octyl and *n*-octadecyl bonded phases. Usually commercially available RP-HPLC phases are synthesised with monofunctional reagents like *n*-alkyldimethylmonochlorosilane, to prevent additional hydroxyl groups due to hydrolysis of remaining Si–Cl groups when di- and trifunctional silanes are used (*2*, *3*). Most RP-HPLC separations in laboratory practice are performed with *n*-octadecyl modified silica substrates. These phases are better defined than the corresponding di- and trifunctional modifications and have the advantage of a large stationary phase volume and the possibility of adequate selectivity for the separation of many organic compounds. Until recently, only separations of large organic molecules with molecular weights between 1000 and 10000 were carried out on short alkyl ligand phases, e.g. *n*-butyldimethylsiloxysilane modified silica. With the better understanding of the phenomenon "selectivity" in modern RP-HPLC practice (*4–8*) and the need for sophisticated and tailor made solutions of separation problems in the last years, the interest in stationary phases with various alkyl chain length ligands has grown (*2*, *9–13*). With the introduction of commercially available expert systems in HPLC (*14*), the popularity of all kinds of stationary phases with different selectivity will probably increase even more. Furthermore, introduction of silica substrates with a very large specific surface area (>500 $m^2\ g^{-1}$) will promote the application of short alkyl ligand bonded phases. However, relatively high ligand surface concentrations and superior substrate shielding properties by secondary groups (e.g. isopropyl) or multidentate surface attachments, with varying numbers of chemical bonds with the surface, are needed (*3*, *15*). The alkyl chain length and alkyl surface concentration are two critical parameters that determine the hydrophobicity of a packing material and thence retention and selectivity characteristics (*9*, *10*). However, the same two parameters also affect the useful lifetime of RP-HPLC columns to a large extent. Long-term stability of chemically bonded stationary phases in laboratory practice is limited by hydrolysis and dissolution of the ligands from the silica surface and of the silica substrate itself, especially when aggressive eluents or conditions are used (*3*, *15*). Although hydrolysis is a slow process, in practice, a stationary phase alters after a period of intensive use. This can be observed by changes in capacity factors, selectivity, and separation performance (*3*, *16*). Although these changes can be determined, the factors causing the process of stationary phase degradation are not completely clear. The influence of ligands anchored at the silica surface, their functionality, chain length, and surface concentration on the process of hydrolysis, has been partially reported previously (*3*, *15–19*). However, the specific effect of the ligand alkyl chain length of chemically bonded phases on stability and ligand and/or substrate hydrolysis and dissolution has not yet been systematically studied. In this and the subsequent paper (*1*), the emphasis is on the process of stationary phase deterioration, correlated with the shielding effect by the anchored ligands at the silica surface. At the same time the influence of various eluents on this process was studied. Combined with chromatographic data, factors affecting stationary phase aging in laboratory practice are reviewed.

The stability of seven RP-HPLC stationary phases modified on the same batch of silica substrate with various *n*-alkyl ligands between *n*-C_1 and *n*-C_{18} was studied by controlled aging of these phases under simulated routine use conditions.

[1] Present address: G.E. Plastics Europe, 1 Plasticlaan, P.O. Box 117, 4600 AC Bergen op Zoom, The Netherlands.

0003-2700/90/0362-2288$02.50/0 © 1990 American Chemical Society

The silica substrate used for modification possessed a very large specific surface area (S_{BET} = 579 $m^2 g^{-1}$). Modification of this silica substrate was performed such that an approximately equal ligand density was obtained for all seven phases. After the modified phases were subjected to artificial aging, changes were investigated in detail by chromatography, analysis of various bulk properties, elemental analysis, and high-resolution solid-state ^{29}Si NMR. In this way, the influence of the *n*-alkyl chain length on the stability and the resistance toward hydrolysis of the stationary phases under study could be determined.

EXPERIMENTAL SECTION

Materials. The test components used for chromatographic characterization were all reference grade. *n*-Alkylbenzenes (test mixture 1) were benzene, methylbenzene, ethylbenzene, *n*-propylbenzene and *n*-butylbenzene (Pierce Chemical Corp., Rockford, IL). *n*-Alkyl aryl ketones (test mixture 2) used as test compounds were ethanophenone, *n*-propanophenone, *n*-butanophenone, *n*-hexanophenone, and *n*-octanophenone (Pierce). *p*-Hydroxybenzoic acid *n*-alkyl esters (test mixture 3) were methyl *p*-hydroxybenzoate, ethyl *p*-hydroxybenzoate, *n*-propyl *p*-hydroxybenzoate, and *n*-butyl *p*-hydroxybenzoate (Sigma Chemical Co., St. Louis, MO). All other solvents and chemicals were analytical reagent grade (E. Merck, Darmstadt, F.R.G.). The deionized water exhibited a specific electric resistance >10 $M\Omega \cdot cm^{-1}$. (Milli-Q System, Millipore Corp., Bedford, MA). All eluents were freshly prepared and filtered over 0.22-μm membrane filters (Millipore) prior to use.

Chromatography. The *n*-alkyldimethylsiloxysilane bonded phases were all prepared on the same experimental spherical silica (d_p = 5 μm, S_{BET} = 579 $m^2 g^{-1}$, research sample, E. Merck) to eliminate substrate-dependent effects on the stability of the phases under study. The silica modification with methyl-, ethyl-, *n*-butyl-, *n*-hexyl-, *n*-octyl-, and *n*-dodecyldimethylmonochlorosilane was catalyzed with 2,6-lutidine to accelerate the kinetics of the silanization reaction. The modification with octadecyldimethylmonochlorosilane was catalyzed with imidazole (*20*, *21*) in order to obtain a maximal ligand surface concentration. Still, the coverage was somewhat lower; see Table II. The seven *n*-alkyldimethylsilane-modified bonded phases were prepared at the R&D Chromatography Department of E. Merck, according to the optimized procedures reported earlier (*20*). Approximately 30 g of material was synthesized for each of the reversed phases. From each stationary phase seven identical columns (100 mm, 4 mm i.d.) (Knauer, Bad Homburg, F.R.G.) were packed according to a standard packing procedure. Due to the packing procedure, it was difficult to control variations in column efficiency. Variations up to 50% were measured between apparently identical columns. Regarding the objectives of the present study, the test procedures were focused on uniform capacity factors and selectivities of all columns packed with identical reversed phases. The test criterion was a deviation of ±10%, close to the analytical reproducibility. After this chromatographic test six columns were placed in an apparatus for simulated routine use experiments. The procedure and equipment for these experiments are discussed and described earlier (*3*, *6*). Only the pulse damping system was modified with addition of a pulse damper (Waters, Millipore), a 3 m × 0.10 mm i.d. capillary and a permanent 0.2-μm filter in series to ensure a more constant flow through the columns during the aging experiments. The basic and acidic aqueous and aqueous–methanol buffers used as eluents for simulated routine use experiments are listed in Table I. Before and after the aging experiments, the columns were subjected to a chromatographic characterization, derived from retention models proposed earlier by Jandera (*5*, *6*, *22*). The aging experiment with eluent 4 appeared to be too destructive; therefore a subsequent chromatographic characterization was not meaningful. In an earlier study it was shown that eluent 4 was destructive due to the absence of the protecting organic modifier (*3*). In this study three series of homologues, *n*-alkylbenzenes, *n*-alkyl aryl ketones, and *p*-hydroxybenzoic acid *n*-alkyl esters, at suitable eluent composition were used. Chromatograms of the test mixtures were collected at minimal 4 different eluent compositions. By multiple linear regression of the logarithms of the capacity factors of a homologous series at suitable eluent compositions, a set of characteristic parameters can be derived (*3*, *6*, *22*)

Table I. Eluent Compositions of the Experiments for Simulating Routine Use[a]

aging expt no.	buffer	pH	vol fraction of methanol in eluent	ion pairing agent, concn 5 mmol
1	0.05 M phosphate	3.0	0	
2	0.05 M phosphate	3.0	0.5	
3	0.05 M phosphate	3.0	0.5	hexylsulfonate
4	0.05 M carbonate	8.4	0	
5	0.05 M carbonate	8.4	0.5	
6	0.05 M carbonate	8.4	0.5	triethylamine

[a] Each column was purged by 7000 column volumes of a typical eluent; flow rate 0.5 mL/min; time 240 h; ambient temperature.

$$\log k' = a_0 + a_1 n_c - x(m_0 + m_1 n_c) \quad (1)$$

further

$$p = m_1/a_1 \text{ and } q = m_0 - p a_0 \quad (2a,b)$$

where x is the volume fraction of organic modifier in a binary eluent with water and n_c is the incremental carbon number of a homologous series of components. The characteristic parameters to be determined with regression are a_0, a_1, m_0, m_1, p, and q. The validity of this regression has been shown before (*3*, *16*). Good correlation coefficients (r > 0.995) were obtained for eluent compositions containing 50% to 90% (v/v) methanol as modifier for all stationary phases in this study. The parameters m_0 and q in eqs 1 and 2b, respectively, characterize contributions to the selectivity (*6*): m_0 denotes mainly nonspecific, lipophilic selectivity and q represents specific, polar selectivity, as discussed extensively earlier (*3*).

The chromatographic characterization experiments of the stationary phases were performed with a Model 100A pump (Beckmann Instruments, Berkeley, CA), a Model CV-6-VHPa-N60 injection valve equipped with a 20-μL loop (Valco, Houston, TX), and a Model LC-3 variable-wavelength UV detector (Pye Unicam, Cambridge, U.K.) operated at suitable wavelengths for an optimal response: test mixture 1, 261 nm; test mixture 2, 241 nm; and test mixture 3, 257 nm. Typically, injections of 5–10 μL of the test mixtures were performed. The detector signal was sampled at 10 Hz and integrated with a Nelson 3000 data system (Nelson Analytical, Cupertino, CA).

Solid-State ^{29}Si NMR Measurements. The solid-state ^{29}Si NMR spectra were obtained on a Bruker CXP-300 Fourier transform nuclear magnetic resonance spectrometer at 59.63 MHz. Representative samples of 160–240 mg were spun at ca. 3.5 kHz using 7 mm o.d. aluminum oxide and zirconium oxide rotors of the Bruker double-bearing type. ^{29}Si Bloch decay magic angle spinning (MAS) NMR spectra of the original silica substrate were obtained with a pulse interval time of 90 s. If interval times exceed 5 times the T_1 relaxation time, the signal areas measured with this technique represent the relative amounts of silicon nuclei of different nature in the sample. Typically 1000 FIDs (free induction decays) with an acquisition time of 10 ms were accumulated in 1K data points and zero-filled to 8K prior to Fourier transformation. A line broadening of 10 Hz prior to zero-filling was used. ^{29}Si cross-polarization magic angle spinning (CP-MAS) NMR spectra of all modified stationary phases prior to and after aging experiments were obtained with a cross-polarization contact time of 6 ms. The pulse interval time was 1 s. Typically, 2000 FIDs with an acquisition time of 10 ms were accumulated in 1K data points and zero-filled to 8K prior to Fourier transformation. The line broadening used was 15 Hz prior to zero-filling and Fourier transformation. The spectral width for all spectra was 15 kHz.

^{29}Si CP-MAS NMR experiments with variable contacts of trimethylsiloxysilane silica (Si–C_1) before and after several aging experiments showed consistent CP characteristics. This pertains to all siliceous moieties at the silica surface. Different results were found for different signals in the ^{29}Si NMR spectrum. Thence, quantification of siliceous moieties at the surface with ^{29}Si CP-

Table II. Bulk Properties Prior to Aging of the Bare Substrate and the *n*-Alkyldimethylsiloxysilane Modified Phases Studied Here[a]

stationary phase	specific surface area, S_{BET}, $m^2\ g^{-1}$	mean pore size, nm	pore volume, $cm^3\ g^{-1}$	carbon content P_C, % (w/w)	ligand surface density, α_1 (see ref 2, eq 1), $\mu mol\ m^{-2}$
bare silica	579	6.0	0.82		
Si–C_1	522	5.7	0.68	6.69	2.67
Si–C_2	428	5.4	0.58	7.59	3.15
Si–C_4	410	5.2	0.53	10.53	3.03
Si–C_6	396	5.8	0.48	12.01	2.63
Si–C_8	345	4.8	0.41	13.96	2.50
Si–C_{12}	299	5.2	0.39	18.78	2.58
Si–C_{18}	357	5.4	0.48	18.06	1.69

[a] Mean particle size, $d_p = 5 \pm 1.3\ \mu m$.

MAS NMR can be performed with a single contact time but with specific correction factors for different ^{29}Si NMR absorptions (*23*).

Bulk Analysis. Surface area, pore size distribution, and pore volume were measured by the conventional Brunauer–Emmett–Teller (BET) method. The measurements were performed at the R&D Chromatography Department of E. Merck.

The bare silica and the derived modified phases were measured before the simulated aging experiments, results are listed in Table II. The measured drop in S_{BET} upon modification was in part caused by the increased density of the modified phases due to the added weight of the anchored ligands at the surface. Secondly, anchored ligands occupy part of the adsorption places. Hence, interpretation of the S_{BET} data will be rather complicated. The pore size and pore volume data are more clear.

After aging experiments only a selected group of stationary phases was submitted for BET measurements. The deviation of the surface area measurements varied by as much as 10–15%. The carbon contents of the modified stationary phases prior to and after each aging experiment were obtained with a Perkin-Elmer Model 240 Analyzer (Perkin-Elmer, Norwalk, CT). Tungsten oxide was added to the modified silica as a catalyst. The samples were periodically compared with materials of standard quality. The reproducibility of the elemental analysis measurements was within the 5% range. The carbon content, P_C, and the ligand surface concentration, α_1, calculated according to eq 1 (*3*), of the starting materials are listed in Table II.

RESULTS AND DISCUSSION

Chromatography. Fundamental chromatographic characterization of the *n*-alkyl modified reversed phases in this study was performed with three sets of homologous series of components with different molecular residues. The selectivity of a typical separation system can be described by the parameters m_0 for lipophilic and q for polar selectivity (see formulas 1 and 2b, respectively). The values of m_0 and q depend on the applied stationary phase, the type of organic modifier in the eluent, and the test solutes. The hydrophobic and hydrophilic properties of a stationary phase depend not only on the ratio of the number of $\mu mol\ m^{-2}$ of ligands and residual silanol but also on the accessibility and type of silanol groups and the shielding factor of the ligands to that. Moreover, the distribution of the silanols and ligands across the silica surface may play an important role. Therefore it is difficult to give a completely satisfying explanation of the results when the test solutes carry both hydrophobic and hydrophilic functionalities. This is even true for the alkylbenzenes, applied to test the hydrophobicity of the stationary phases, where the benzene part is polarizable and probably interacts with the silanol groups present. Nevertheless, the presence of benzene was necessary in our experiment due to the detection limitations of the equipment. The lipophilic selectivity as a function of the *n*-alkyl chain length of the ligands for the test mixtures is depicted in Figure 1. As expected, increasing m_0 values as a function of longer *n*-alkyl ligands were determined for *n*-alkylbenzene test mixture, showing large lipophilic interactions/contribution during the elution. In contrast the m_0 values determined for the phenyl ketones and for the *p*-hydroxybenzoates showed less lipophilic interaction with the modified phases under study and a more or less capricious course, which can be attributed to the mixed retention mechanism discussed above. Thence, changes in lipophilic selectivity of a stationary phase may be monitored best by the *n*-alkylbenzene mixture.

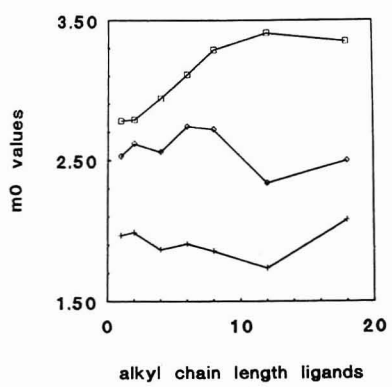

Figure 1. Chromatographically determined m_0 values (lipophilic selectivity) versus the ligand alkyl chain length of the reversed phases under study, before aging experiments: (□) *n*-alkylbenzenes, (+) aryl *n*-alkyl ketones, (◇) *p*-hydroxybenzoic acid *n*-alkyl esters. The lines drawn exhibit only an illustrative value.

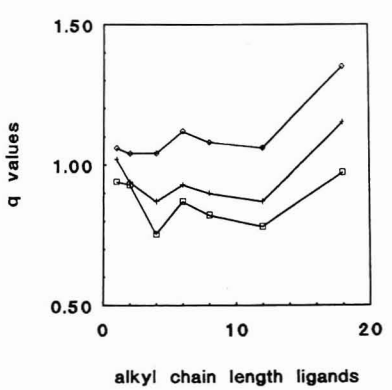

Figure 2. Chromatographically determined q values (polar selectivity) versus the ligand alkyl chain length of the reversed phases under study, before aging experiments: (□) *n*-alkylbenzenes, (+) aryl *n*-alkyl ketones, (◇) *p*-hydroxybenzoic acid *n*-alkyl esters. The lines drawn exhibit only an illustrative value.

The influence of the ligand alkyl chain length on the polar selectivity, q, for the three test mixtures is shown in Figure 2. With the exception of the C_{18}-reversed phase, which showed a smaller ligand density, the q values for the *p*-hydroxybenzoates were found constant to a certain amount. Due to the more or less equal ligand concentrations at the silica surface (except for the octadecyl bonded phase), the polar interactions between the *p*-hydroxybenzoate and the residual silanol groups at the surface are shown to be equal to a certain

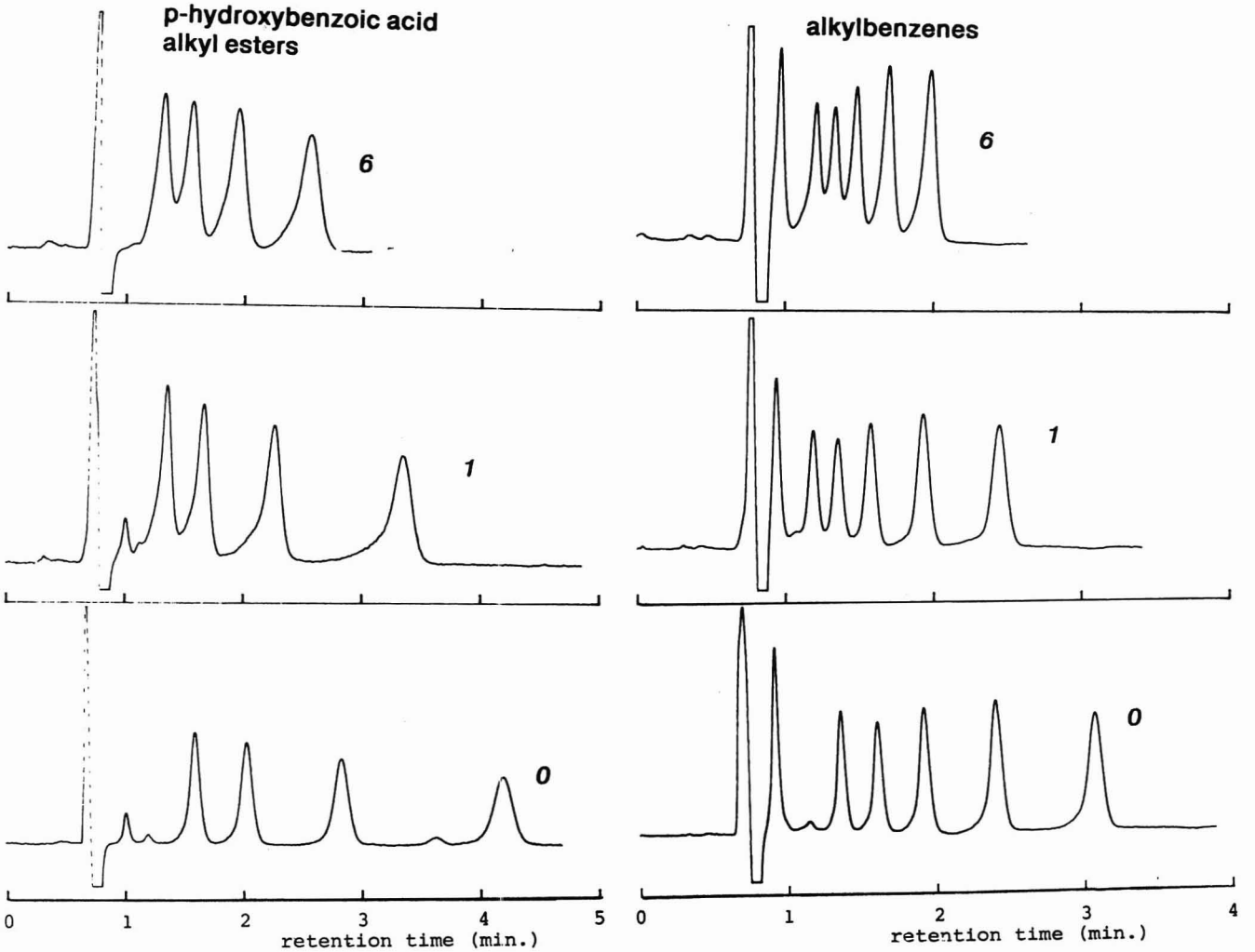

Figure 3. Chromatograms of the *p*-hydroxybenzoic acid *n*-alkyl ester (left) and the *n*-alkylbenzene (right) test mixtures eluted on *n*-butyldimethylsiloxysilane modified phase before and after aging experiments 1 and 6. Chromatographic test conditions were as follows: methanol–water (80:20 (v/v)); flow rate, 1.0 mL/min; UV detection, test mixture 1, 261 nm; test mixture 3, 257 nm.

extent. The values of q for the other two test mixtures were smaller but showed an identical course as the q values for the *p*-hydroxybenzoates. Changes in this type of selectivity may be monitored best by the *p*-hydroxybenzoic acid *n*-alkyl esters.

The effect of long-term exposure to relatively aggressive eluents on the performance of a stationary phase can be illustrated by chromatography. As an example Figure 3 depicts the chromatograms of the *n*-alkylbenzene and the *p*-hydroxybenzoic acid *n*-alkyl ester test mixtures eluted on the *n*-butyldimethylsilane modified phase before and after aging experiments 1 and 6. From the set of chromatograms collected of each combination of stationary phase, mobile phase, and test mixture, the capacity factors were calculated. Subsequently, typical diagrams of log k' versus the volume fraction methanol (x) in the test eluent and the incremental carbon number of the components of the homologous series (n_C) for each stationary phase could be derived, as was outlined previously (*3*). The values of m_0 (*n*-alkylbenzenes) were determined by multiple linear regression from these diagrams, eq 1, before and after each aging experiment. These m_0 values for the stationary phases under study are listed in Table III. As in earlier studies (*3*, *19*) a good correlation was found between the lipophilic selectivity m_0 and a_0 (*n*-alkylbenzenes). The latter represents the logarithm of the capacity factor of the homologue residue extrapolated for pure water as the eluent and is strongly related to the amount of bonded ligands present at the surface.

For the short ligand phases considerable changes in lipophilic selectivity were determined, especially with the high pH used in aging experiments 5 and 6. Chromatographic characterization of the Si–C_1 phase after these aging experiments was impossible; all components eluted shortly after the dead time. The drop in capacity factors (a_0 values) and lipophilic selectivity is related to intensive stripping of the anchored ligands from the silica surface. A gradually smaller decrease in lipophilic selectivity caused in the aging experiments was determined for phases containing longer alkyl chain lengths. From these data it can be concluded that shielding of the silica substrate surface depends largely on the ligand alkyl chain length. Short alkyl ligands showed inferior shielding properties in some of the aging experiments per-

Table III. Lipophilic Selectivity, the m_0 (*n*-alkylbenzenes) Value Determined by Chromatographic Characterization for the Reversed Phases under Study, before and after Each Aging Experiment[a]

aging expt no.	m_0 for *n*-alkyldimethylsiloxysilane phases						
	Si–C_1	Si–C_2	Si–C_4	Si–C_6	Si–C_8	Si–C_{12}	Si–C_{18}
0	2.78	2.79	2.94	3.11	3.29	3.41	3.35
1		1.69	2.53	3.14	3.32	3.44	3.21
2	2.79	2.70	2.93	3.18	3.34	3.42	3.46
3	2.68	2.69	2.78	3.14	3.01	3.14	3.36
5		2.55	2.72	2.57	2.94	3.05	3.20
6		1.35	2.09	2.47	2.88	3.01	3.14

[a] The experimental conditions of the aging experiments are outlined in Table I. Experiment 0 denotes the stationary phase after packing/chromatographic characterization.

Table IV. Polar Selectivity, the q (p-Hydroxybenzoates) Values Determined by Chromatographic Characterization for the Reversed Phases under Study, before and after Each Aging Experiment[a]

aging expt no.	q for n-alkyldimethylsiloxysilane phases						
	Si–C_1	Si–C_2[b]	Si–C_4	Si–C_6	Si–C_8	Si–C_{12}	Si–C_{18}
0	1.06	1.04 (0.94)	1.04	1.12	1.08	1.09	1.35
1		(1.23)	1.05	1.04	1.15	1.11	1.32
2	1.11	(0.90)	0.98	1.01	1.02	1.09	1.24
3	1.19	(0.95)	1.34	1.13	1.23	1.24	1.36
5		(1.52)	1.36	1.39	1.66	1.24	1.41
6		(1.48)	1.38	1.28	1.79	1.51	1.39

[a] The experimental conditions of the aging experiments are outlined in Table I. Experiment 0 denotes the stationary phase after packing/chromatographic characterization. [b] For the Si–C_2 phase the q (p-hydroxybenzoates) values were not determined after the aging experiments. Instead, the values of q (phenyl ketones) are listed in parentheses.

formed in this study. In earlier studies, we noticed also a great influence of the ligand surface concentration on the stability of modified phases (*3*, *16*). In this study we concentrated on the role of the alkyl chain length in this respect. In the frame work of the experimental conditions it can be concluded that the minimum chain length of octyl ligands might be necessary to prevent monofunctionally n-alkylsilane modified stationary phases from deterioration. The q values of the p-hydroxybenzoates presented in Table IV support the conclusion that a substantial amount of the short ligands was hydrolyzed and dissolved from the silica surface. With decreasing m_0 (n-alkylbenzenes) values for these stationary phases the q (p-hydroxybenzoates) values increased. This indicates larger polar interactions between the p-hydroxybenzoates and the silica surfaces. The increased polar interactions can be explained by an increasing amount of silanol groups formed at the surface by hydrolysis of ligands and of silica.

Aging experiment 4 was found too destructive for subsequent chromatographic testing. Deterioration of the packed bed inside the column caused chromatograms with doubled peaks and bad peak shapes. However, the collapse of the particle bed may be independent of the chemical changes at the stationary phase surface; see the NMR section (below).

Bulk analysis and solid-state NMR measurements on the stationary phases after aging experiment 4 were still possible.

Solid-State ^{29}Si NMR. The structures of siliceous moieties at the surface of the silica gel before and after modification, their notations, and typical ^{29}Si chemical shifts were presented earlier (*3*). The ^{29}Si MAS NMR spectrum, together with the deconvoluted signal areas, of the experimental silica substrate yield a silanol content of 43.9%. This points to an extraordinarily large specific surface area of the silica gel. By dividing the relative silanol content by the measured surface area (S_{BET}), one can estimate the silanol density at the silica surface, here 0.076 (content × g m^{-2}). This density was smaller than that reported for Hypersil and a Nucleosil silica earlier (*3*): 0.092 (content × g m^{-2}). We assume the geometry of the pore surface of the silica affects the density of the silanol groups. The small average pore size of 6 nm combined with the large surface area may point to an open silica structure with relatively thin pore walls/boundaries. Such an open structure increases the presence of siloxane groups at the pore surface, decreasing the silanol density. Of the total amount of silanol groups only 7.1% relative were geminal silanols, dihydroxysiloxanes (Q^2), and 92.9% relative were vicinal and/or "lone" silanol groups, hydroxysiloxanes (Q^3). Caused by the relatively low silanol density most of the hydroxysiloxanes will be "lone" silanol groups.

Before and after the aging experiments ^{29}Si CP-MAS NMR spectra were obtained. Figures 4, 5, and 6 show these spectra for Si–C_1, Si–C_2, and Si–C_{12} phases, respectively. The trimethylsiloxysilane bonded phase showed an almost total loss of ligands after aging experiments 1, 4, 5, and 6. Concomitantly, the relative amount of hydroxysiloxanes was increased. Especially after aging experiment 1, a pronounced amount of geminal silanol groups was determined. Secondly, we observed, that after the aging experiments with high pH eluents, the trimethylsiloxysilane ligands were stripped from the surface and parallel or subsequently the silica substrate was hydrolzyed and dissolved as well. Dissolution of the substrate caused a drop in surface area and subsequently a decreased amount of silanol groups relative to the nonaged trimethylsiloxysilane phase. A diminished surface area can be detected indirectly with ^{29}Si CP-MAS NMR by a decrease in total signal area and consequently a worse signal to noise ratio. Here, after aging experiments 4 to 6 the amount of silanol groups did not increase to the same extent as the decrease in trimethylsiloxysilane groups, indicating that substrate dissolution took place also. The spectra of the other two modified phases, Si–C_2 and Si–C_{12}, show again that the resistance toward ligand dissolution is generally superior with longer alkyl chain length ligands. With the Si–C_2 phase still only small amounts of ethyldimethylsilanes were detected after aging experiments 1, 4, and 6. On the other hand, the amounts of ligands anchored at the surface after aging experiment 5 were about half that of the nonaged phase.

The shielding effect of the anchored ligands and the dissolution of the substrate with some of the eluents is illustrated by comparison of the amounts of siliceous moieties present at the surface after a particular aging experiment, relative to their amounts at the nonaged silica surface. A comparison of the amount of ligands (M^1) and the total amount of silanol (Q^2 and Q^3) of all stationary phases after aging experiment 1, relative to the nonaged phases, is depicted in Figure 7. With short alkyl ligand modified phases large amounts, up to approximately 90%, of alkyldimethylsiloxysilanes were stripped from the surface by the low pH aqueous phosphate buffer. However, only a part of these dissolved ligands were replaced by silanol groups. The resulting vacancies at the silica surface were either condensed with formation of siloxane bridges or hydrolyzed/dissolved from the substrate resulting in less surface area. The substrate shielding effect by the long alkyl ligands was obvious. The n-octyl, n-dodecyl, and n-octadecyl ligands showed almost no significant reduction of the amount of anchored ligands and/or increased amount of silanol groups.

A similar graph for the effect of the simulated routine use experiment with the low pH aqueous–methanol phosphate buffer, aging experiment 2, is depicted in Figure 8. Here, only relatively small fluctuations in ligand and silanol amounts were observed. The ligand shielding seemed independent of the alkyl chain length. Even the total amount of siliceous moieties remained constant. No intensive substrate hydrolysis or silanol condensation was detected. In sharp contrast, all high pH carbonate buffer eluents changed the substrate surface of the short alkyl ligand modified phases drastically; see Figure 9. Well advanced surface degradation by stripped ligands and dissolved silica was observed. Large amounts of both

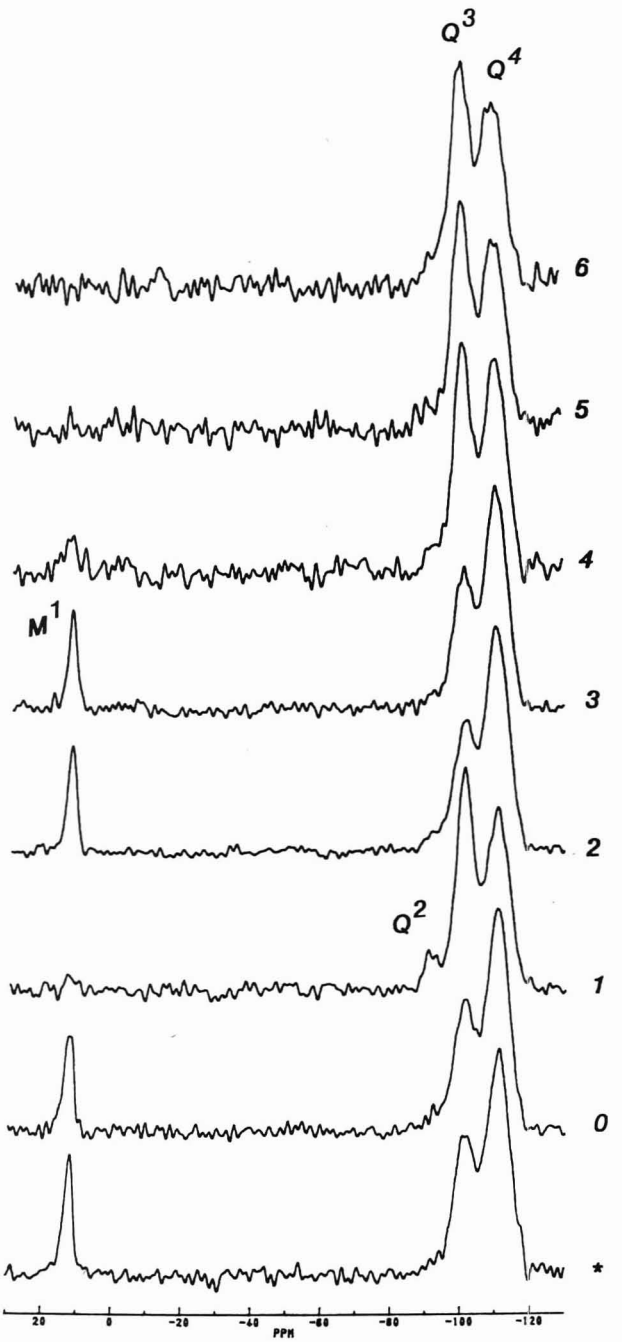

Figure 4. ^{29}Si CP-MAS NMR spectra of trimethylsiloxysilane modified silica (Si–C_1), before and after the aging experiments. The numbers indicate the typical aging experiments as outlined in Table I. Asterisk denotes the original stationary phase; 0, refers to the stationary phase after packing.

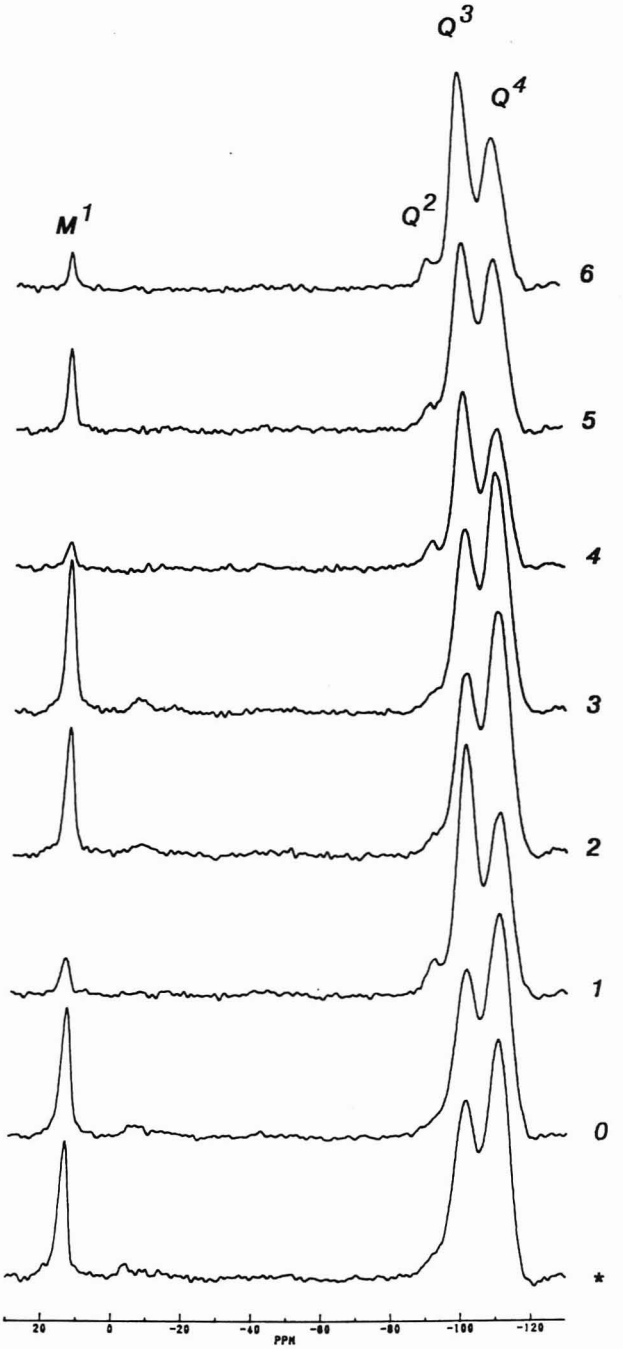

Figure 5. ^{29}Si CP-MAS NMR spectra of ethyldimethylsiloxysilane-modified silica (Si–C_2), before and after the aging experiments. The numbers indicate the typical aging experiments as outlined in Table I. Asterisk denotes the original stationary phase; 0 refers to the stationary phase after packing.

ligand silanes and hydroxysiloxanes disappeared from the surface. Only a small part of the silanol groups condensed to siloxane bridges, the major amount of silanol groups apparently dissolved in the aggressive buffer eluents. A worse signal to noise ratio of the Si–C_1 phases after high pH aging experiments indicated already a diminishing silica surface; see Figure 4. From the previous graphs it is clear that ligand hydrolysis was affected by the type of eluent used for the aging experiment.

The eluents used for the routine use simulations in this study can be ranked in order of increasing hydrolysis of ligands and silica: $2 \rightarrow 3 \rightarrow 5 \rightarrow 1 \rightarrow 6 \rightarrow 4$.

With the high pH eluents a large degree of ligand stripping, due to hydrolysis and dissolution, was observed, especially for short ligand phases. Addition of methanol (50% (v/v)) to the high pH buffer eluent only reduced the hydrolysis of long ligand modified silica (n-alkyl chain length > n-octyl), probably due to solvatation of the long ligands by the organic modifier. For low pH buffered eluents, the addition of methanol reduced the hydrolysis of short ligands drastically. Long alkyl chain ligands were much less affected by low pH eluents.

Bulk Analysis. The carbon content after three different aging experiments for all modified phases relative to that of the originate phase is depicted in Figure 10. The longer alkyl ligands inhibited dissolution of surface-anchored n-alkyldimethylsiloxysilanes by aggressive eluents. These curves reflect the ligand length and concentration at the silica surface. As such, the shape of the curves was similar to the ^{29}Si CP-MAS NMR measured relative ligand content depicted in Figures 7 to 9. However, in contrast with the results of the solid-state ^{29}Si NMR measurements, here we observed substantial

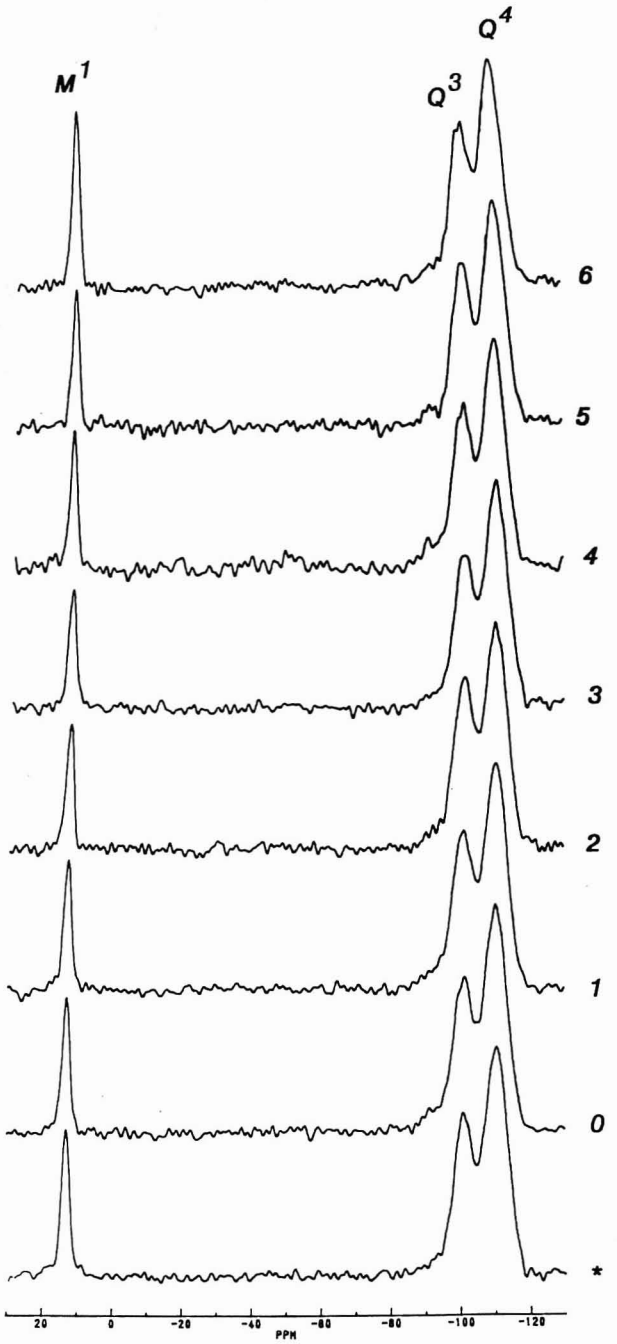

Figure 6. ^{29}Si CP-MAS NMR spectra of dodecyldimethylsilane modified silica (Si–C_{12}), before and after the aging experiments. The numbers indicate the typical aging experiments as outlined in Table I. Asterisk denotes the original stationary phase; 0 refers to the stationary phase after packing.

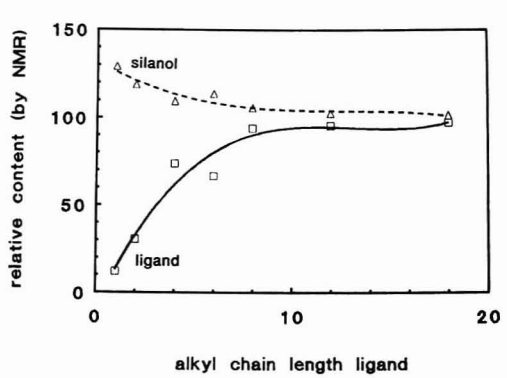

Figure 7. Percentage ligand, M^1 (□), and total silanol Q^3 and Q^2 (△), present after aging experiment 1, relative to the originate reversed phases. Measured by ^{29}Si CP-MAS NMR.

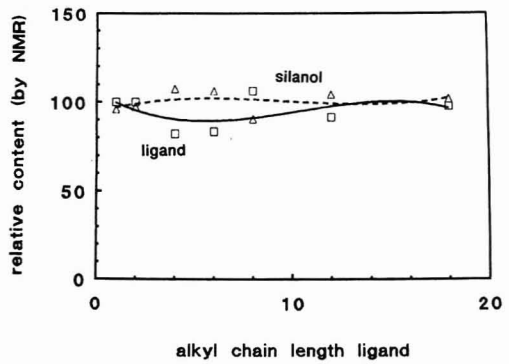

Figure 8. Percentage ligand, M^1 (□), and total silanol, Q^3 and Q^2 (△), present after aging experiment 2, relative to the originate reversed phases. Measured by ^{29}Si CP-MAS NMR.

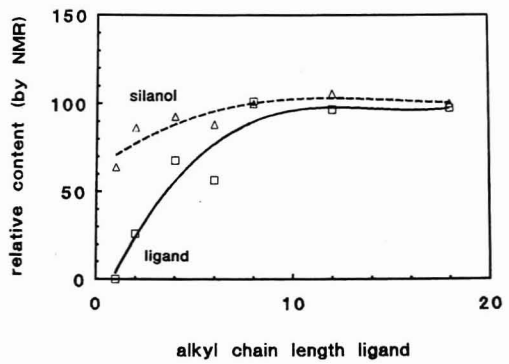

Figure 9. Percentage ligand, M^1 (□), and total silanol, Q^3 and Q^2 (△), present after aging experiment 6, relative to the originate reversed phases. Measured by ^{29}Si CP-MAS NMR.

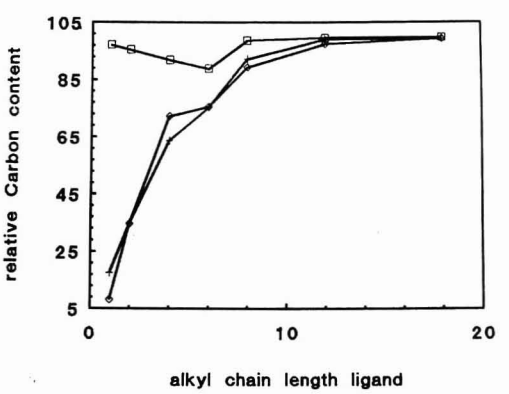

Figure 10. Carbon content relative to the originate reversed phases after aging experiment 1 (+), 2 (□), and 6 (◇). Measured with elemental analysis. The lines drawn exhibit only an illustrative value.

changes in the carbon content for the *n*-octyl bonded phase after aging experiments 1 and 6. After aging experiment 6 in total 12% of the carbon was removed from the silica substrate. Results of the BET measurements of a selected group of stationary phases before and after a specific aging experiment are listed in Table V. This table reports two specific area values: S_{BET} measured and the for the ligand content corrected value. The mass of the ligands affects the density of the substrate. Major changes in substrate properties were determined from the values of the pore size and pore diameter. As expected, increased pore size and pore volume were noticed for short ligand phases after aging experiments with high pH buffer solutions and low pH aqueous buffer solutions, indicating severe substrate hydrolysis. Changes in pore size and pore volume decreased gradually with longer alkyl chain length of the ligands. Although only a selected amount of BET measurements were performed, it can be concluded that longer alkyl ligands isolated the silica surface better from substrate

Table V. Bulk Properties before and after Aging Experiments of the *n*-Alkyldimethylsiloxysilane Modified Phases Studied Here[a]

stat phase/ aging expt	specific surface area, S_{BET}, $m^2\ g^{-1}$	mean pore size, nm	pore volume, $cm^3\ g^{-1}$	carbon content P_C, % (w/w)	spec surface area, corrtd for ligand content, $m^2\ g^{-1}$
Si–C_1					
*	522	5.7	0.68	6.69	592
4	482	9.2	1.10	0.87	488
Si–C_2					
*	428	5.4	0.58	7.59	487
2	448	5.5	0.63	7.11	505
4	417	8.4	1.14	2.58	434
5	517	6.2	0.82	4.38	558
6	570	6.8	0.92	2.31	593
Si–C_4					
*	410	5.2	0.48	10.53	484
2	470	4.9	0.58	10.29	547
4	289	8.3	0.60	9.97	335
6	630	5.6	0.88	6.92	699
Si–C_{12}					
*	299	5.2	0.39	18.78	375
2	300	5.5	0.41	18.38	375
5	232	6.9	0.40	18.00	288
Si–C_{18}					
*	357	5.4	0.48	18.06	441
5	314	5.4	0.40	17.98	387

[a] The experimental conditions of the aging experiments are outlined in Table I. Experiment * denotes the original stationary phase.

hydrolysis by aggressive eluents.

The alternating changes in measured and corrected specific surface areas for short ligand modified silica were indistinct. It may well be that substrate degradation into small subcolloidal level (<1–3 nm) silica/silicate particles occurred, enlarging the specific surface area. The short *n*-alkyl bonded phases showed an enlarged surface area after aging experiments 5 and 6. Presumably, silica hydrolysis and dissolution resulted in small dissolved silica particles and coarsened pore surfaces (*1*).

On the other hand, direct silica dissolution results in a smaller specific surface area. Aging experiment 4 reduced the specific surface area drastically due to severe silica dissolution. However, both hydrolysis and subsequent dissolution processes resulted in a significant larger pore size and pore volume.

CONCLUSIONS

The trimethylsiloxysilane, ethyl-, *n*-butyl-, and *n*-hexyldimethylsiloxysilane silica phases show a rather poor resistance toward ligand hydrolysis and dissolution when aggressive low and high pH buffer solutions are used as eluent. The stability of these reversed phases increases gradually with longer alkyl chain length of the ligands. This is confirmed by our chromatographic characterization method, the ^{29}Si CP-MAS NMR measurements, and the elemental analysis of the stationary phases after aging. The longer alkyl ligands inhibit the attack of the surface by aggressive buffer solutions, under the experimental conditions and time schedule here.

Even if other stationary phase properties will affect the stability of modified stationary phases as well, see refs 3 and 15–19, the ligand alkyl chain length seems of major influence. Short *n*-alkyldimethylsilane ligand modified silicas will deteriorate when low or high pH buffer solutions are used as an eluent in practice, even over a short period of time.

Due to better solvatation of the ligands by organic modifiers, e.g. methanol, longer ligands presumably are more effective in shielding the substrate. Consequently, severe degradation of the stationary phases is inhibited to a large extent. Thence, as experienced from daily chromatographic practice, organic modifier rich eluents combined with longer alkyl chain length modifications are preferable for a longer lifetime of the RP-HPLC columns. Concurrent hydrolysis and dissolution of silica and ligands (*1*) affects the chromatographic performance and alters the selectivity of reversed-phase columns. Changed capacity factors and lipophilic selectivity indicate that these processes are going on, causing increased specific polar interactions. For sensitive compounds large shifts in retention data may be observed, spoiling the easy life of the LC chromatographer and his data system.

As illustrated in this study a set of selective test components, like the homologous series of *n*-alkylbenzenes and *p*-hydroxybenzoic acid *n*-alkyl esters, can be used to adequately examine the actual status of the RP-HPLC column. The derived parameters m_0 and q adapted by an expert (or expert system) can easily be used to correct the eluent composition for a typical separation. The values for m_0 and q also support the decision about the practical useful lifetime of a typical RP-HPLC column. In an accompanying, subsequent paper some of the important interactions between the RP-HPLC phases and the eluents will be reported in some detail. This pertains in particular to the dissolution of the substrate into mixtures of water and methanol at pH >12, selected to mimic the situation prevailing in RP-HPLC using basic eluents.

ACKNOWLEDGMENT

We thank Mr. R. Goossens and Miss M. Roelofs for their practical assistance and Mr. H. Eding for the elemental analysis measurements of the stationary phases.

LITERATURE CITED

(1) Hetem, M.; de Haan, J.; Claessens, H.; Wijnen, P.; van de Ven, L.; Kinkel, J.; Cramers, C. *Anal. Chem.*, following paper in this issue.
(2) Roumeliotis, P.; Unger, K. K. *J. Chromatogr.* **1978**, *149*, 211–224.
(3) Hetem, M.; van de Ven, L.; de Haan, J.; Cramers, C.; Albert, K.; Bayer, E. *J. Chromatogr.* **1989**, *479*, 269–295.
(4) Schoenmakers, P. J. *Optimization of chromatographic selectivity*; Elsevier: Amsterdam, 1986; p 31 ff, p 116 ff.
(5) Jandera, P. *Chromatographia* **1984**, *19*, 101–112.
(6) Jandera, P. *J. Chromatogr.* **1984**, *314*, 13–36.
(7) Dill, K. A. *J. Phys. Chem.* **1987**, *91*, 1980–1988.
(8) Coenegracht, P.; Metting, H.; Smilde, A.; Coenegracht-Lamers, P. *Chromatographia* **1989**, *27*, 135–141.
(9) Berendsen, G. E. Ph.D. Thesis, 1980, Delft, NL.
(10) Lork, K. D.; Unger, K. K. *Chromatographia* **1988**, *26*, 115–119.
(11) Morel, D.; Tabor, T.; Serpinet, J.; Claudy, P.; Letoffe, J. *J. Chromatogr.* **1987**, *395*, 37–84.
(12) Gilpin, R. K.; Gangoda, M. E. *Anal. Chem.* **1984**, *56*, 1470–1473.

(13) Pfleiderer, B.; Albert, K.; Lork, K.; Unger, K.; Bruckner, H.; Bayer, E. *Angew. Chem.* **1989**, *101*, 336-340.
(14) Goulder, D.; et al. ESPRIT Project 1570 *Chromatographia*, **1988**, *26*, 237-244.
(15) Kirkland, J. J.; Glajch, J. L.; Farlee, R. D. *Anal. Chem.* **1989**, *61*, 1-11.
(16) Claessens, H. A.; de Haan, J. W.; van de Ven, L. J. M.; de Bruyn, P. C.; Cramers, C. A. *J. Chromatogr.* **1988**, *436*, 345-365.
(17) Sagliano, N., Jr.; Hartwick, R. A.; Patterson, R. E.; Woods, B. A.; Bass, J. L.; Miller, N. T. *J. Chromatogr.* **1988**, *458*, 225-240.
(18) Kohler, J.; Chase, D. B.; Farlee, R. D.; Vega, A. J.; Kirkland, J. J. *J. Chromatogr.* **1986**, *352*, 275-305.
(19) Hetem, M.; de Haan, J.; Claessens, H.; Mussche, Ph.; Cramers, C. *Chromatographia* **1990**, *29*, 473-481.
(20) Kinkel, J. N.; Unger, K. K. *J. Chromatogr.* **1984**, *316*, 193-200.
(21) Bayer, E.; Paulus, A.; Peters, B.; Laup, G.; Reiners, J.; Albert, K. *J. Chromatogr.* **1986**, *364*, 25-37.
(22) Jandera, P. *J. Chromatogr.* **1986**, *352*, 91-110.
(23) Zhang, M.; Maciel, G. E. *Anal. Chem.* **1989**, *61*, 2579-2582.

RECEIVED for review March 21, 1990. Accepted July 16, 1990. These investigations were supported by the Netherlands Foundation for Chemical Research (SON) with financial aid from the Netherlands Organization for Scientific Research (NWO) under Grant 700-344-009.

Influence of Alkyl Chain Length on the Stability of *n*-Alkyl-Modified Reversed Phases. 2. Model Dissolution Study

Martin J. J. Hetem,*[1] Jan W. de Haan, Henk A. Claessens, Leo J. M. van de Ven, and Carel A. Cramers

Laboratory of Instrumental Analysis, Eindhoven University of Technology, P.O. Box 513, 5600 MB Eindhoven, The Netherlands

Peter W. J. G. Wijnen

Laboratory of Inorganic Chemistry, Eindhoven University of Technology, P.O. Box 513, 5600 MB Eindhoven, The Netherlands

Joachim N. Kinkel

E. Merck, Frankfurterstrasse 250, D-6100 Darmstadt 1, West Germany

A direct, in situ study of the hydrolysis and dissolution of various *n*-alkyl modified phases was performed with ^{29}Si magic angle spinning NMR spectrometry as a model for stationary phase aging in laboratory practice. With this study, the substantial effect of the ligand length on the dissolution reaction of the alkyl modified phases under aggressive eluent conditions is confirmed. As expected, longer *n*-alkyl ligands gradually show better substrate shielding properties. Above a certain critical ligand length, shielding by longer ligands inhibit the dissolution rate drastically by affecting the hydrolysis and dissolution processes. The type of solvent system used, in liquid chromatography practice or for dissolution studies as reported here, mainly affects the proportions of dissolved silicates in the eluent. On the basis of this in situ dissolution study a model for ligand and substrate hydrolysis and dissolution with the involved reactions is presented.

INTRODUCTION

In the foregoing, accompanying paper it is made clear that one of the most important reasons for instability of stationary phases for reversed-phase high-performance liquid chromatography (RP-HPLC) is concerned with unwanted chemical interactions between the mobile phase and the stationary phase (*1*). A similar conclusion was drawn in earlier pubications from this (*2*, *3*) and other (*4*) laboratories. Although hydrolysis and dissolution are rather slow processes in LC practice, the RP-HPLC phase deteriorates after a period of intensive use. This is observed by changes in capacity factors, selectivity, and column efficiency.

[1] Present address: G.E. Plastics Europe, 1 Plasticlaan, P.O. Box 117, 4600 AC Bergen op Zoom, The Netherlands.

There are only a few techniques that enable in situ studies of such reversed-phase dissolution. ^{29}Si NMR may provide useful details concerning the molecular structures of species leaving the substrate surface and forming intermediate and final reaction products (*5-8*). To the best of our knowledge, these studies have been confined to silica gel only, e.g. the substrate part of the stationary phases for RP-HPLC. This prompted us to perform a ^{29}Si NMR study of the dissolution characteristics of several phases for RP-HPLC, investigated in the accompanying paper (*1*). The stationary phases under study were modified on the same batch of silica substrate using various ligands of increasing *n*-alkyl chain length.

With this study, information on the substantial effect of the ligand alkyl chain length on the various dissolution reactions was obtained. Thence, this paper emphasizes the process of stationary phase deterioration, correlated with the shielding effect of the anchored ligands at the silica surface. The influence of the eluent composition is also considered.

EXPERIMENTAL SECTION

The synthesis and physical characterization of the RP-HPLC phases with varying *n*-alkyl chain length are described in the accompanying paper (*1*).

Preparation of Solutions. The dissolutions of the reversed phases or the native silica were performed by adding ca. 350 μL of a 6 M solution of sodium hydroxide in methanol-water (50:50 (v/v)) to approximately 70 mg of stationary phase (this amount was corrected for the ligand content) in a zirconium oxide rotor of the Bruker double air bearing type. In this way a well mixed suspension of Na_2O-SiO_2 with an overall, molar composition of 1:1 was obtained. Similar dissolutions were performed in a 2 M aqueous sodium hydroxide solution in order to obtain an overall, molar composition of 1:3 Na_2O-SiO_2. The well-mixed suspension was introduced into the solid-state NMR spectrometer as quickly as possible.

^{29}Si NMR Measurements. The ^{29}Si NMR spectra were obtained on a Bruker CXP Fourier transform nuclear magnetic

0003-2700/90/0362-2296$02.50/0 © 1990 American Chemical Society

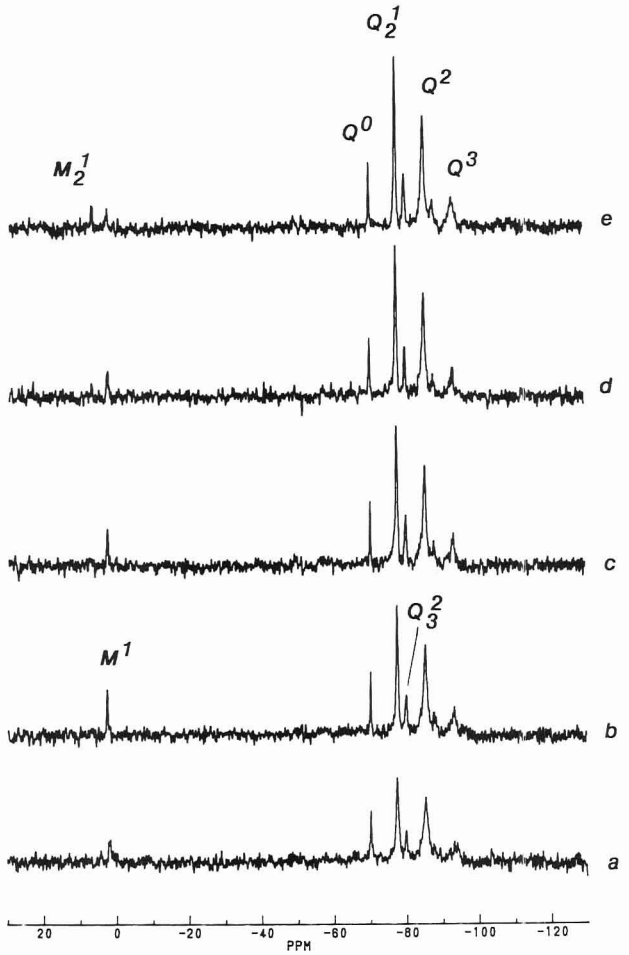

Figure 1. Dissolution of Si–C_4 in an aqueous–methanol–sodium hydroxide solution observed with ^{29}Si MAS NMR after (a) 0.5, (b) 1.5, (c) 3, (d) 6, and (e) 15 h: molar ratio, 1:1 Na_2O–SiO_2; methanol content, 50% (v/v).

resonance spectrometer at 59.63 MHz. The dissolution studies were performed with magic angle spinning (MAS) NMR to average any chemical shift anisotropies, which might occur in viscous fluids. The well-mixed suspensions were introduced in the zirconium oxide rotor with an outside diameter of 7 mm. The spin frequency used was ca. 1.5 kHz. The spectra were collected at ambient temperature and atmospheric pressure. A 45° flip angle ^{29}Si pulse was applied for excitation. Typically, a series of 30 sequential blocks of 360 accumulated FIDs (free induction decays) with 50 ms acquisition time and 5 s pulse decay were collected in 1K data points each and zero-filled to 8K prior to Fourier transformation. A line broadening of 15 to 25 Hz prior to zero-filling was applied.

RESULTS AND DISCUSSION

The molar Na_2O/SiO_2 ratios applied for dissolution of chemically bonded phases in aqueous–methanol or plain aqueous systems were selected for practical reasons. The relatively high sodium content ensured hydrolysis and dissolution of the modified silicas within a reasonable time. With the simulated aging experiments 1 L of low pH buffer (pH = 3.0) or high pH buffer (pH = 8.4) was recycled. Thence, possible saturation of the eluent with dissolved ligands and/or silica could occur, reducing the aging effect of the experiments. In RP-HPLC practice, chromatographers commonly use freshly prepared eluents. We will return to this point later.

The reactions involved in the dissolution of the *n*-alkyldimethylsiloxysilane bonded silica substrate were observed with ^{29}Si MAS NMR, by sequential blocks of accumulated acquisitions. Each block represents 30 min of reaction time; see Figure 1. The ^{29}Si NMR spectra of the silica solution exhibited several resonances corresponding to different environments of the ^{29}Si nuclei. These spectra yield also the

Table I. Most Relevant Dissolved Silane/Siloxane Species, Their Functionality, Notation, and Typical ^{29}Si NMR Chemical Shift in the Aqueous–Methanol–Sodium Hydroxide Solution and the Aqueous–Sodium Hydroxide Solution.[a]

silane/siloxane species in solution	chemical (spectral) function	topological (network) function	code	typical chemical shift (ppm downfield from TMS)	
				H_2O–MeOH	H_2O
n-alkyldimethylhydroxysilane	M	0	M^0	+16	+15
n-alkyldimethylsiloxysilane, dimer[b]	M	1	M_2^1	+7	
n-alkyldimethylsiloxysilane	M	1	M^1	+3	
tetrahydroxysiloxane	Q	0	Q^0	−70.4	−71.9
trihydroxysiloxane, dimer[b]	Q	1	Q_2^1	−77.9	−79.9
dihydroxysiloxane, cyclic trimer[b]	Q	2	Q_3^2	−80.3	−81.6
dihydroxysiloxane	Q	2	Q^2	−85.4	−88.4
hydroxysiloxane	Q	3	Q^3	−93.7	−96.9
tetrasiloxysilane	Q	4	Q^4		−106

[a] If not mentioned, the species are part of small oligomers. [b] The subscript refers to the number of particular sites within a dissolved silicate species. In the nomenclature these silicates are also referred to as one species: M_2^1, 1,2-di-*n*-alkyltetramethyldisiloxane; Q_2^1, hexahydroxydisiloxane; Q_3^2, hexahydroxycyclotrisiloxane.

proportions of mono- and tetrafunctional silicon atoms in the solution. The silicon atoms are denoted by M^n (n = 0, 1) and Q^n (n = 0, 1, 2, 3, 4). This nomenclature was introduced by Engelhardt et al. (*6*). The chemical shifts of resonance peaks in the ^{29}Si NMR spectra of aqueous–methanol or aqueous–sodium hydroxide silicate solutions are presented in Table I. The ^{29}Si NMR chemical shifts of quaternary siloxanes are in agreement with previous assignments for dissolution/solvation of aqueous silica gel systems (*5*, *9*). The M^0 and M_2^1 ^{29}Si NMR chemical shifts were derived from trimethylethoxysilane and hexamethyldisiloxane, respectively (*9*). The ^{29}Si NMR chemical shift assignment of the oligomeric *n*-alkyldimethylsiloxysilane M^1 should be considered as preliminary. Shielding by chemical bonding to an oligomeric silicate species in solution could be responsible for a shift of approximately 4 ppm to higher field. This ligand attached silicate species was formed by direct dissolution of oligomeric silicates species from the silica gel.

Silica can be dissolved in highly alkaline media (pH >11), where the hydroxyl anion is considered to be a catalyst (*5*, *10*). As such, silica dissolves in the form of monomeric tetrahydroxysiloxane, $Si(OH)_4$ (Q^0). Presumably, formation of monomeric silicate anions in the solution leads to oligomerization of the monomers to hexahydroxydisiloxanes (Q_2^1), hexahydroxycyclotrisiloxanes (Q_3^2), polymeric dihydroxysiloxanes (Q^2), and polymeric hydroxysiloxanes (Q^3). Only recently, chemical exchange between various dissolved silicates (e.g. between Q^0 monomer and Q_2^1 dimer or Q_3^2 trimer) was demonstrated elegantly by Knight et al. (*7*).

In the present study, ^{29}Si NMR spectra of the dissolution and subsequent reactions of the *n*-butyldimethylsiloxysilane modified silica substrate (Figure 1) revealed a fast dissolution of the reversed-phase material with formation of monomeric tetrahydroxysiloxane followed by oligomerization to polymeric silicate species. The tetrahydroxysiloxane Q^0 level in the

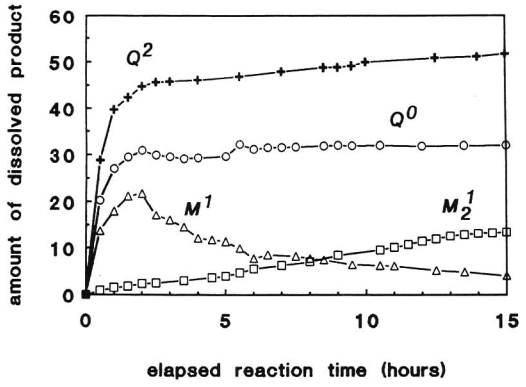

Figure 2. Curves of the relative signal intensities observed with ^{29}Si MAS NMR of several dissolved products from Si–C_4 in the aqueous–methanol–sodium hydroxide solution with elapsed reaction time: molar ratio, 1:1 Na_2O–SiO_2; methanol content, 50% (v/v).

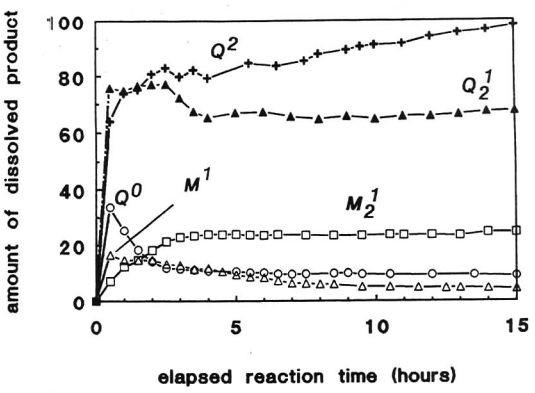

Figure 3. Curves of the relative signal intensities observed with ^{29}Si MAS NMR of several dissolved products from Si–C_1 in the aqueous–methanol–sodium hydroxide solution with elapsed reaction time: molar ratio 1:1 Na_2O–SiO_2; methanol content, 50% (v/v).

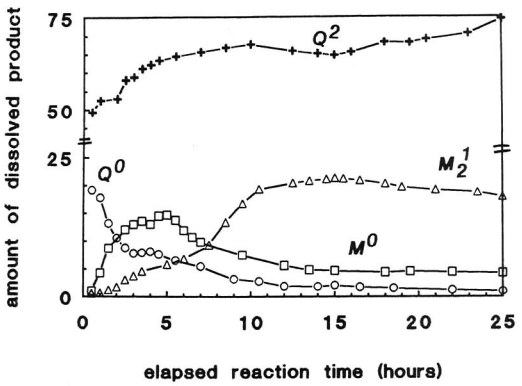

Figure 4. Curves of the relative signal intensities observed with ^{29}Si MAS NMR of several dissolved products from the Si–C_{18} phase in the aqueous–methanol–sodium hydroxide solution with elapsed reaction time: molar ratio, 1:1 Na_2O–SiO_2; methanol content, 50% (v/v).

methanol–water solution seemed to be rather low compared with results of silica dissolution studies published (*5*, *11*). Possibly, the subsequent oligomerization reaction proceeded relatively fast compared with the monomer dissolution under our experimental conditions. Already after half an hour substantial amounts of various oligomers were determined. An equilibrium was reached after approximately 2 h. The ratios of the various dissolved silicates remained almost constant with time, only the signal areas of the oligomers increased slightly.

After 1 h a significant amount of *n*-butyldimethylsiloxysilane (M^1), as part of small oligomer species was detected in the solution. After approximately 2 h this started to decrease. It turned out that a secondary product, a di-*n*-butyltetramethyldisiloxane dimer (M_2^1), was formed by continued hydrolysis and condensation. The reactions can be summarized in the following scheme (for nomenclature, see Table I):

(1A) Dissolution of silica substrate, hydrolysis of siloxane bonds

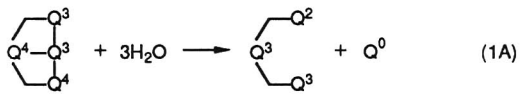

(1A)

(1B) Oligomerization

$$2Q^0 \rightarrow Q_2^1 + H_2O;\ Q_2^1 + Q^0 \rightarrow Q^1Q^2Q^1 + H_2O, \text{ etc.} \quad (1B)$$

(2A) Hydrolysis of silica to silane bonds

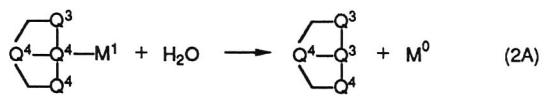

(2A)

(2B) Dimerization of silane

$$2M^0 \rightarrow M_2^1 + H_2O \quad (2B)$$

(3A) Oligomeric dissolution of silica, e.g.

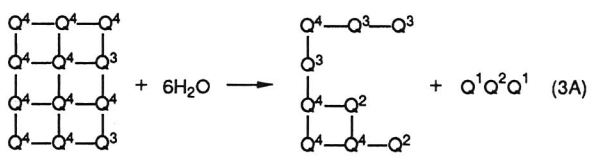

(3A)

(3B) Oligomeric dissolution of silane-bonded silica, e.g.

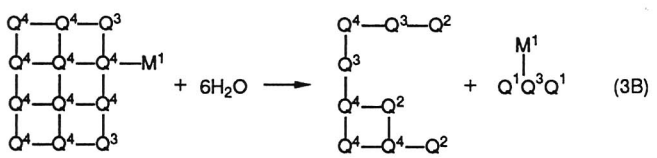

(3B)

Figure 2 depicts curves of the signal intensities of several dissolved products from Si–C_4 in the aqueous–methanol solution with elapsed reaction time.

Very similar spectra as for Si–C_4 were obtained from the dissolution of the trimethylsiloxysilane bonded silica (Si–C_1) in the aqueous–methanol solution under the same conditions as above. In this case, however, both dissolved ligand–silicates M^1 and M_2^1 were formed directly from the start (see Figure 3). An equilibrium between these two dissolved species was attained after about 2 h. Up to *n*-hexyldimethylsiloxysilane modified silica analogous ligand–silicates were observed upon dissolution.

The ^{29}Si NMR spectra following the dissolution of the *n*-octadecyldimethylsiloxysilane bonded phase in the aqueous–methanol solution revealed a rather similar pattern. Figure 4 depicts curves of the signal intensities of several dissolved products with Si–C_{18} in the aqueous–methanol solution with elapsed reaction time. The dissolution rate of tetrahydroxysiloxane monomer was clearly decreased by the longer octadecyl ligands attached to the silica surface.

The dissolution characteristics of the native silica in the aqueous–methanol–sodium hydroxide solution are depicted in Figure 5. The equilibrium was attained rapidly. The proportions of dissolved silicates agreed with those of the short alkyl ligand modified phases, only the amount of dissolved monomer silicates observed was much less. Major concurrent dissolution of small oligomeric silicate species (reaction 1B) probably affected the monomer content by chemical exchange with already dissolved monomeric silicates (*7*).

Dissolution studies of other *n*-octadecyl modified silicas revealed that the proportions of dissolved silicates depended primarily on the hydrolysis and dissolution rate of tetra-

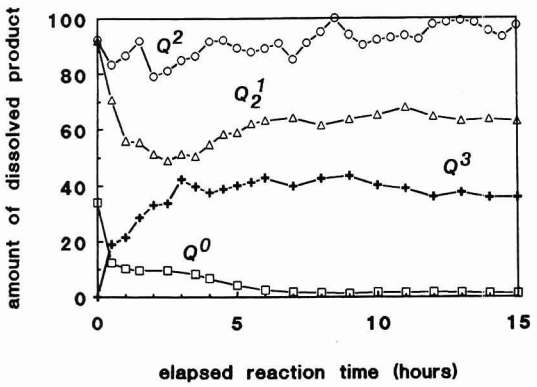

Figure 5. Curves of the relative signal intensities observed with ^{29}Si MAS NMR of several dissolved products from the native silica in the aqueous–methanol–sodium hydroxide solution with elapsed reaction time: molar ratio 1:1 Na_2O–SiO_2; methanol content, 50% (v/v).

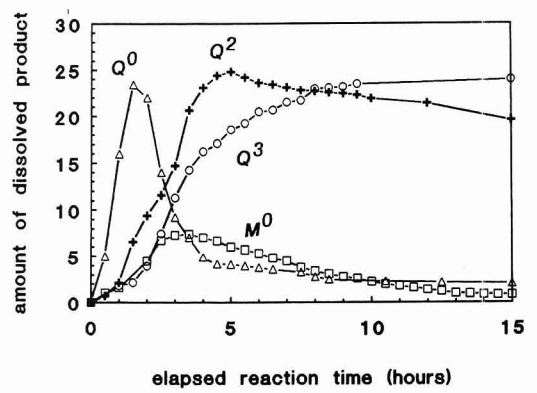

Figure 6. Curves of the relative signal intensities observed with ^{29}Si MAS NMR of several relevant dissolved silicates and ligand attached silicates from Si–C_4 in the aqueous–sodium hydroxide solution with elapsed reaction time: molar ratio, 1:3 Na_2O–SiO_2.

hydroxysiloxanes, Q^0. Furthermore, the proportions of the oligomeric silicates in particular were affected by the type of solvent used for dissolution studies as is the case with silica substrates (*5*, *11*).

As an example of this sensitivity toward solvents, the course of the dissolution of the *n*-butyldimethylsiloxysilane modified silica in an aqueous, no modifier added, sodium hydroxide solution with a molar composition of 1:3 Na_2O:SiO_2 are depicted in Figure 6. Almost equal spectra were collected from the dissolution of Si–C_1 and Si–C_{12} under these conditions. Due to a smaller sodium hydroxide content, the hydrolysis and dissolution of monomeric silicate started more slowly. The smaller oligomerization rate at the start of the experiment allowed a higher content of tetrahydroxysiloxane to be formed in the aqueous solution. Substantial amounts of *n*-alkyldimethylhydroxysilanes were observed with the dissolution in the aqueous buffer solution (pH >12) of the modified silicas. Condensation of this monomer to dimeric silicate was not detected. Presumably, oligomerization with large silicate oligomers results in less mobile ligands, that are hardly detectable.

Comparison of the different dissolution reactions yields the following. It can be concluded that the apparent detachment of short ligands from the modified silica surface was in fact caused by hydrolysis and dissolution of the underlying substrate silica; see reaction 3B. Thence, we conclude that with advanced monomer dissolution small oligomeric silicate species were concurrently dissolved with monomeric silicates in our aqueous–methanol solvent system.

This concurrent dissociation of oligomeric silicates could be influenced by the open structure of the silica gel studied here. The rather thin pore walls/boundaries could enhance

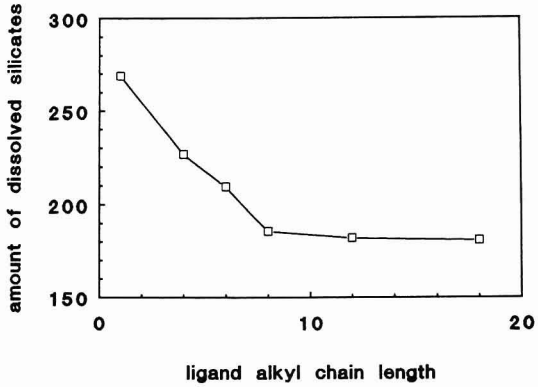

Figure 7. Total amount of dissolved silicates determined by ^{29}Si MAS NMR after 15 h of reaction time for the *n*-alkyl modified phases in an aqueous–methanol–sodium hydroxide solution: molar ratio, 1:1 Na_2O–SiO_2; methanol content, 50% (v/v).

dissolution of small silicate pieces.

A different situation prevails for the longer chain modified silicas. Fast oligomerization of the monomeric silicate reduced the amount of monomer and subsequent products of reaction 1B in the solution to a very small value. As a result relatively more polymeric dihydroxysiloxanes, Q^2, and hydroxysiloxanes, Q^3, were observed after 15 h of dissolution of silica substrate modified with the octadecyl ligand. Here again, an equilibrium for the dissolved silicates was attained after approximately 2 h.

In fair agreement with all other evidence produced in this study, the amount of dissolved ligand–silicates were relatively small for longer ligands. Furthermore, the removal of longer ligands from the silica surface occurred mainly by direct hydrolysis to form *n*-octadecyldimethylhydroxysilanes, M^0. Subsequent condensation with other dissolved monomeric silicates resulted in di-*n*-octadecyltetramethyldisiloxane dimers, M_2^1, reaction 2B. Presumably, steric hindrance and boundaries caused by van der Waals interactions between neighboring ligands inhibited direct dissolution of small ligand–silicate oligomeric species from the silica surface. It seemed that dissolution of oligomeric silicate species was reduced likewise. Analogous dissolution behavior was observed for the Si–C_8 and Si–C_{12} phases.

The total amount of dissolved silicate species determined after Si–C_1, Si–C_4, and Si–C_6 dissolution in the aqueous–methanol–sodium hydroxide solution was significantly higher than after Si–C_8, Si–C_{12}, and Si–C_{18} dissolution with a corresponding amount of stationary phase under identical conditions; see Figure 7. The *n*-octyldimethylsiloxysilane phase obviously possessed a kind of critical ligand chain length for dissolution of the modified silicas.

The translation of the dissolution studies described here to the aging of RP-HPLC stationary phases can be made as follows. The model dissolution studies were performed as a batch process in limited volume rotors (350 μL) with rather high pH solvents (pH >12). The relatively high sodium content ensured hydrolysis and dissolution of the modified silicas within a reasonable time. In this small volume under the experimental conditions, saturation of the solvent may well affect the further dissolution of the reversed-phase materials. A comparison of dissolution and stationary phase hydrolysis in daily chromatography practice is subject to certain restrictions. The oligomerization reactions observed in the sodium hydroxide solution may be promoted as a consequence of a high concentration of the primary dissolution products. Probably, when freshly prepared eluents are used, only hydrolysis and dissolution of ligands and silica without subsequent oligomerization will be the main causes of stationary phase degradation. Thence, the primary dissolution reactions observed with ^{29}Si NMR spectroscopy here reflect

the main course of the dissolution process that occurs under RP-HPLC conditions in practice. Factors affecting this process should be considered for stationary phase hydrolysis and dissolution.

CONCLUSIONS

Two fundamentally different ligand dissolution processes are observed in an aqueous–methanol solution. Short alkyl ligand modified silica gels degrade by concurrent dissolution of monomeric tetrahydroxysiloxane (reaction 1A) and small oligomeric silicate particles of subcolloidal level (<1–3 nm) (5). The process of oligomer dissolution (reactions 3A and 3B) enhances the degradation rate of short alkyl modified silicas drastically.

Longer alkyl ligand modified silicas degrade mainly by monomeric dissolution of silica (reaction 1A). Surface attached ligands are hydrolyzed and dissolved as *n*-alkyldimethylhydroxysilanes (reaction 2A).

The use of water as a solvent promotes monomeric dissolution, also with short alkyl ligand modified silicas.

The *n*-octyl bonded phase exhibits the critical ligand alkyl chain length upon modification of the silica substrate used in this study, with respect to direct oligomer dissolution in aqueous–methanol solvents.

For short alkyl ligand bonded phases multidentate surface attachment will not prevent dissolution of the ligands, due to oligomer dissolution. Polymer coated stationary phases or neighbor attached silanes, cross-linked across the silica surface may prevent severe dissolution of the short ligands by oligomer dissolution. Specific surface shielding groups (e.g. pre- or end-capping with trimethylsiloxysilanes) may contribute also to prevent degradation of the stationary phases. Longer *n*-alkyl ligands with large enough surface concentration should be preferred with aggressive eluents. Preliminary experiments involving dissolution of bi- and trifunctionally derivatized silicas ("polymeric") indicate that product ratios are formed, considerably different from those of the monofunctional phases.

LITERATURE CITED

(1) Hetem, M.; de Haan, J.; Claessens, H.; van de Ven, L.; Kinkel, J.; Cramers, C. *Anal. Chem.*, preceding paper in this issue.
(2) Hetem, M.; van de Ven, L.; de Haan, J.; Cramers, C.; Albert, K.; Bayer, E. *J. Chromatogr.* **1989**, *479*, 269–295.
(3) Claessens, H. A.; de Haan, J. W.; van de Ven, L. J. M.; de Bruijn, P. C.; Cramers, C. A. *J. Chromatogr.* **1988**, *436*, 345–365.
(4) Kirkland, J. J.; Glajch, J. L.; Farlee, R. D. *Anal. Chem.* **1989**, *61*, 1–11.
(5) Wijnen, P.; Beelen, T.; de Haan, J.; Rummens, C.; van de Ven, L.; van Santen, R. *J. Non-Cryst. Solids* **1988**, *109*, 84–94.
(6) Engelhardt, G.; Zeigan, D.; Jancke, H.; Hoebbel, D.; Wieker, W. *Z. Anorg. Allg. Chem.* **1975**, *418*, 17–28.
(7) Knight, C.; Kirkpatrick, R.; Oldfield, E. *J. Magn. Res.* **1988**, *78*, 31–37.
(8) Kinrade, S. D.; Swaddle, T. W. *J. Am. Chem. Soc.* **1986**, *108*, 7159–7165.
(9) Engelhardt, G.; Jancke, H.; Mägi, M.; Pehk, T.; Lippmaa, E. *J. Organomet. Chem.* **1971**, *28*, 293–300.
(10) Iler, R. K. *The Chemistry of Silica*; Wiley: New York, 1979.
(11) Wijnen, P.; Beelen, T.; de Haan, J.; van de Ven, L.; van Santen, R. *Colloids Surf.* **1990**, *45*, 255–268.

RECEIVED for review March 21, 1990. Accepted July 16, 1990. These investigations were supported by the Netherlands Foundation for Chemical Research (SON) with financial aid from the Netherlands Organization for Scientific Research (NWO) under Grant 700-344-009.

Prediction of Retention Times in Serially Linked Open-Tubular Gas Chromatographic Columns and Optimization of Column Lengths

Jeffrey R. Jones and J. Howard Purnell*

Department of Chemistry, University College of Swansea, Singleton Park, Swansea SA2 8PP, Wales, U.K.

The serial gas chromatographic theory, first advanced and then further developed by Purnell and Williams, is used to optimize the analysis of a nine-component phenol mixture by use of linked capillary columns. The capacity factors of sample components with the system serially coupled in either mode, column A/column B or column B/column A, and of different relative length, are shown to agree essentially exactly with those predicted by theory. The window analysis procedure devised by Laub and Purnell is then used to calculate the relative and overall length of the columns required to achieve base-line resolution. The experimental chromatograms are shown to correspond precisely to prediction. When the methodology is applied generally, it is shown that the requisite data can be determined easily and rapidly and the subsequent calculations can be carried out via an equally simple computer program. The consequent techniques and procedures should help the development of serial-coupled open-tubular column chromatography (SCOTCH).

INTRODUCTION

Early interest in the analytical use of serially linked gas chromatographic columns led to the observation that retentions of mixture components were not simple averages of the values for the individual columns and, further, depended also on the column sequence. This work was reviewed in detail in the pioneering study of Hildebrand and Reilley (*1*) who, in 1965, developed an approximate theory adequate to explain the above effects, although it failed quantitatively in most cases of application. Interest in the topic then waned, except for the brief studies by Buys and Smuts (*2*) and Krupcik, Guiochon, and Schmitter (*3*). However, the potential of linked capillaries attracted fresh interest (*4*, *5*) in the early 1980s; unfortunately, the inadequate theoretical basis available led to failure to account for retention variation, and therefore column optimization for particular analyses also failed.

In 1984, Purnell and Williams (*6*) returned to the theoretical problem and, in a series of subsequent papers (*7–12*), generated the general theory and consequent optimization procedure for serial-column analyses. They showed, using packed columns, both that the theory was valid and that simple procedures could be devised to permit the accurate prediction of retentions with serial columns. In addition, they showed how the window diagram procedure devised by Laub and Purnell (*13–16*) could be used to evaluate very precisely the relative and total column lengths required to provide optimized separations.

0003-2700/90/0362-2300$02.50/0 © 1990 American Chemical Society

Since the theory is equally applicable to all forms of gas chromatography, they chose to carry out their studies with packed columns for reasons of economy. They pointed out, however, that only in certain special and rather unusual circumstances would a serially coupled packed system provide a more convenient solution than would a single packed GLC column containing mechanically mixed packings.

In contrast, mixed substrate capillaries present a number of difficulties and, without much doubt, the serial column solution is, in this case, the more convenient. Accordingly, we present here the first study of a linked capillary system in which our approach is applied to the optimization of an analytical problem. The theory and procedures are fully tested and validated and the results enable the full exploitation of isothermal or multitemperature linked GC capillary systems.

THEORY

For two columns of any kind, operated serially, the total time of transport (t_R) of any material injected is, self-evidently, the sum of the times spent in the front (F) and back (B) columns

$$t_R = t_{RF} + t_{RB} \tag{1}$$

For a chromatographic system, introducing capacity factors ($k' = K_R V_l / V_M$), where K_R is the partition coefficient, V_l is the volume of solvent, and V_M is the column free volume or dead volume, the overall retention time with the serial system (t_R) is thus

$$t_R = (t_{dF} + t_{dB})(1 + k') = t_{dF}(1 + k_F') + t_{dB}(1 + k_B') \tag{2}$$

where k' represents the appropriate capacity factor for some eluate and t_d represents the dead time (time of elution of unretained sample) for the column. Introducing the function

$$P = t_{dF}/t_{dB} \tag{3}$$

eq 2 then rearranges to

$$k' = \left[\frac{Pk_F' + k_B'}{P + 1}\right] \tag{4}$$

Equation 4 is valid for any kind of serial system for which the retentive property is describable in terms of capacity factors or their analogues. Thus, in order to predict k' for all sample components, with any combination of column lengths (L_F and L_B), we need only to measure k_F' and k_B' with individual test columns and determine P for the combination. The latter task is not straightforward in gas chromatography, however, because of the gas compressibility effect. Where the carrier is an incompressible fluid, of course, P will be directly calculable from the same data as will provide k_F' and k_B'.

Hildebrand and Reilley (*1*) emphasized the usefulness of the function R_F, which they termed the resistance to flow, and which is defined by

$$R_F = \frac{[p_i^2 - p_o^2]}{p_o u_o} = \frac{2\epsilon\eta L}{B_o} \tag{5}$$

where p_i and p_o are the column inlet and outlet pressures, u_o is the gas velocity at the outlet, L is column length, ϵ and B_o are the porosity and specific permeability of the bed, and η is the fluid viscosity. Equation 5 is a form of D'Arcy's law.

Since the product of pressure (p) and velocity (u) at any point in the column (pu) is constant for a column of uniform free cross-section, $p_o u_o = \bar{p}\bar{u}$ (the column average values)

$$\bar{u} = \frac{[p_i^2 - p_o^2]}{\bar{p}R_F} = \frac{j[p_i^2 - p_o^2]}{p_o R_F}$$

where j is the James–Martin compressibility factor

$$j = \frac{3}{2}p_o\left[\frac{(p_i^2 - p_o^2)}{(p_i^3 - p_o^3)}\right]$$

Since $t_d = L/\bar{u}$

$$t_d = \frac{2LR_F}{3}\left[\frac{(p_i^3 - p_o^3)}{(p_i^2 - p_o^2)^2}\right] \tag{6}$$

This is the general equation for the dead time in any gaseous column system where the ideal gas approximation applies and a plot of t_d against the bracketed pressure function should be linear and of slope ($2LR_F/3$). With L known, R_F can thus be evaluated on the basis of a few, simple, pressure dead time measurements which, given knowledge of fully corrected volumetric flow rates (F_c) at the column temperature (T_c), also provide values of V_M, the total column free volume since

$$V_M = jF_c t_d$$

For a serial column pair of columns F/B, the front column operates between p_i and p, the junction pressure, and the back column between p and p_o. For the front column, from eq 5 we have

$$R_{FF} = \frac{p_i^2 - p^2}{pu}$$

but, since the column can be assumed to have constant free cross-sectional area (A_F), $u = F/A_F$, where F is the column temperature flow rate at the junction. Hence

$$pF = \frac{A_F}{R_{FF}}(p_i^2 - p^2)$$

Correspondingly, for the back column, $u_o = F_c/A_B$ and

$$p_o F_c = \frac{A_B}{R_{FB}}(p^2 - p_o^2)$$

Since the mass flow rate is constant throughout the whole system, so too is the product pF. Thus

$$\frac{A_F}{R_{FF}}(p_i^2 - p^2) = \frac{A_B}{R_{FB}}(p^2 - p_o^2)$$

Finally, $A = V_M/L$, so that

$$\frac{V_{MF}}{L_F R_{FF}}(p_i^2 - p^2) = \frac{V_{MB}}{L_B R_{FB}}(p^2 - p_o^2) \tag{7}$$

Rearrangement of eq 7 yields an expression for the junction pressure, p, thus

$$p^2 = \left[\frac{p_i^2 - l_F[p_i^2 - (V_{MB}R_{FF}/V_{MF}R_{FB})p_o^2]}{1 - l_F\,[1 - (V_{MB}R_{FF}/V_{MF}R_{FB})]}\right] \tag{8}$$

where l_F is the length fraction of the front column ($L_F/L_F + L_B$).

Returning to eq 6 we have, for the serial pair

$$t_{dF} = \frac{2L_F R_{FF}}{3}\left[\frac{(p_i^3 - p^3)}{(p_i^2 - p^2)^2}\right]$$

and

$$t_{dB} = \frac{2L_B R_{FB}}{3}\left[\frac{(p^3 - p_o^3)}{(p^2 - p_o^2)^2}\right]$$

Substituting for $(p_i^2 - p^2)^2$ in the expression for t_{dF} and then dividing by that for t_{dB} gives the equation for P

$$P = \left[\frac{L_B R_{FB}}{L_F R_{FF}}\right]\left[\frac{V_{MF}}{V_{MB}}\right]^2\left[\frac{p_i^3 - p^3}{p^3 - p_o^3}\right] \tag{9}$$

So, if we now fix on some values of p_i, p_o, L_F, and L_B, since we know the relevant R_F and V_M for the individual columns, we are able, via eq 8, to calculate p, which then via eq 9 gives us P. Individual values of k' can then be calculated for all components via eq 4. Within the limitations of the ideal gas assumption, we can thus accurately predict retention data for serial columns from the data for individual columns.

Calculating Column Lengths for Optimizing Separations. Only when pressure drops or relative column lengths (e.g. L_F/L_B) are trivial will capacity factors be linear in l_F. This situation will not occur often in practice. Thus, an ability to calculate k' for components in the serial system only occasionally permits immediate calculation of l_F. To do this we need to develop the theory further.

Let us postulate that there is some quantity f_F ($f_F + f_B = 1$) which linearly relates k' for a given component with the serial system to the relevant values for the individual columns, viz.

$$k' = f_F k_F' + f_B k_B' \tag{10}$$

Combining this with eq 4 yields

$$f_F = P/(P + 1) \text{ or } P = f_F/(1 - f_F) \tag{11}$$

Rearranging eq 9 then gives us

$$p^3 = \left[\frac{p_i^3 + P\gamma p_o^3}{1 + P\gamma}\right] \tag{12}$$

where

$$\gamma = \left[\frac{L_F R_{FF}}{L_B R_{FB}}\right]\left[\frac{V_{MB}}{V_{MF}}\right]^2 = \left[\frac{\bar{R}_{FF}}{\bar{R}_{FB}}\right]\left[\frac{\bar{V}_{MB}}{\bar{V}_{MF}}\right]^2 \tag{13}$$

where the over-bar symbol indicates the value per unit length of column. Substituting for P in eq 12 from 11 gives

$$p^3 = \left[\frac{p_i^3 - f_F(p_i^3 - \gamma p_o^3)}{1 - f_F(1 - \gamma)}\right] \tag{14}$$

so that we may calculate the relevant value of p for any values of f_F, p_i, p_o, and γ. We can also rearrange eq 8 to give

$$l_F^{-1} = \left[\frac{\bar{R}_{FF}\bar{V}_{MB}}{\bar{R}_{FB}\bar{V}_{MF}}\left[\frac{(p^2 - p_o^2)}{(p_i^2 - p^2)}\right] + 1\right] \tag{15}$$

hence, we are now in a position to calculate l_F for any value of f_F at known p_i, p_o, and γ.

Since k' for the serial system is linear in f_F, we are able to construct a plot of k' over the range $f_F = 0$–1 simply by connecting the k' values for each sample component with the individual test columns. Such plots can be used to calculate relative retentions (α) for use with f_F in the window diagram procedure developed by us previously. The value of f_F at the maximum window height can be employed to calculate the optimum l_F. From an assessment of bandwidths/carrier velocity relationships determined in the test experiments, we can calculate the theoretical plate height attainable. Finally, via the well-known equation (*17*), which provides a value of the number of theoretical plates required for base-line separation of all components

$$N_{req} = 36\left[\frac{\alpha}{\alpha - 1}\right]^2\left[\frac{1 + k'}{k'}\right]^2 \tag{16}$$

we may also calculate the total length ($L_F + L_B$) of the serial column required for the full (base-line) resolution of the sample mixture, since the optimum window maximum provides the necessary values of α_{min} and k' relating to the most difficult pair to separate.

EXPERIMENTAL SECTION

The nine phenols comprising the analytical sample used here were obtained from Aldrich Chemical Co., Inc., and were of minimum 97% purity. The capillary columns, purchased from S.G.E. Inc., were each of 0.33 mm i.d. and 12 m length. Both contained bonded substrates, one (BP1) having the nonpolar dimethyl polysiloxane, the other (BP20), the most polar in the range, having poly(ethylene glycol).

Columns were connected to the injector and detector with 0.5 mm i.d. graphite ferrules fitted into 3 mm stainless steel unions (Hewlett-Packard). For serial linking, the column ends were first cut square with a silicon wafer knife, and then butt-joined inside a graphite zero-volume fitting which was encased in a double-threaded stainless steel union. As the end nuts were tightened, the graphite ferrule compressed to secure the column ends with a clean interface. Careful technique allowed the connecting union to be reused indefinitely.

The gas chromatograph was a Hewlett-Packard Model 5890 fitted with a flame ionization detector and was used in conjunction with a Hewlett-Packard 3390A reporting integrator. Helium was the carrier gas and a split ratio of 100:1 was employed at the injector. The flame ionization detector (FID) was supplied with hydrogen/air as combustion gas and nitrogen, at 30 mL min^{-1}, as make-up gas. The helium gas passed through two in-line filters, one for water and the other for oxygen removal.

Prior to use, the solid sample components were dissolved to ca. 0.01 M in AnalaR grade *n*-pentane. They were injected, alone or in mixture, by use of a graduated 1.0-μL glass syringe (S.G.E.), the usual sample volume being 0.04 μL. Dead times (volumes) were determined by methane elution; the high column temperature and low intrinsic retention ensured that this was a valid procedure.

Flow rates were determined with a bubble meter prior to, and after, the elution of samples. Numerous measurements were made and averaged before correction for water vapor pressure and recalculation to column temperature (F_c).

Because of the importance of obtaining the highest possible accuracy in the determination of column pressures on account of the relatively low inlet pressures that apply in capillary work, the inlet end of the system was fitted both with a pressure gauge and a mercury manometer for accurate calibration of the gauge. The outlet pressure was measured with a Negretti and Zambra precision barometer (M/9714).

Preliminary experiments, and manufacturer's information, indicated that a column temperature of 125 °C would provide reasonable retention times. Thus, prior to the study, both columns were purged overnight at 180 °C to remove any possible volatile contaminants and, subsequently, maintained permanently at 125 °C. For analysis, the injector and detector temperatures were maintained at 225 and 250 °C, respectively.

RESULTS

Evaluation of R_F and V_M. Figure 1 illustrates plots of t_d against $(p_i^3 - p_o^3)/(p_i^2 - p_o^2)^2$ for both the BP1 and BP20 columns. The linearity is excellent, which confirms that helium at this moderately high temperature shows ideal gas behavior. The relevant slopes ($2LR_F/3$) yield the values of R_F (BP1 = 2.36×10^5 N s m^{-3}; BP20 = 2.88×10^5 N s m^{-3}). The numerous data for t_d, in association with the relevant values of j and F_c, allow calculation of V_M for each column. The average values, derived from determinations at 15 inlet pressures (flow rates) in the range 2–13 psi (gauge) for the two columns were found to be BP1 1.95 mL and BP20 2.09 mL; the standard deviation was 1% in each case.

We earlier emphasized the need for accurate pressure determination, essentially because of the reduced accuracy of mechanical gauges at the relatively low inlet pressures typical of capillary operation and the complexity of the pressure function of eq 6 and later equations. It is worthwhile to illustrate this feature in detail even though it may be argued to be peculiar to the equipment used here. Table I lists the gauge and manometer pressures registered in test experiments with the BP1 column.

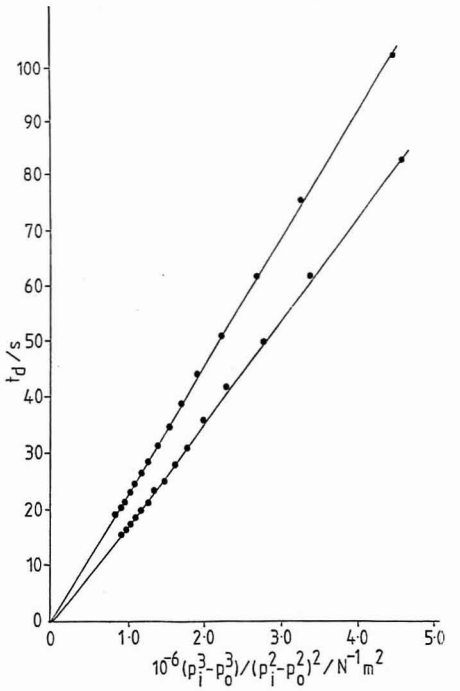

Figure 1. Plots of t_d against $(p_i^3 - p_o^3)/(p_i^2 - p_o^2)^2$ for the columns: upper line, BP20; lower, BP1; carrier gas, helium; column temperature, 125 °C.

Table I. Pressure Gauge Calibration Data

gauge pressure, psi	manometer pressure, psi	gauge pressure, psi	manometer pressure, psi
2.90	2.42	7.98	7.98
3.63	3.32	8.70	8.76
4.35	4.06	9.43	9.43
5.07	4.94	10.2	10.2
5.80	5.68	10.9	10.9
6.53	6.48	11.6	11.6
7.25	7.25	12.3	12.3

We see that, at the lowest pressures, the gauge consistently recorded too high a value. The discrepancy progressively diminished with increasing pressure until, above about 7 psi, the error was essentially nil. Since p_i includes also the atmospheric value (p_o), even the worst error illustrated might appear acceptably small; in fact, the form of the pressure function of eq 6, for instance, is such that this is not true. Figure 2 illustrates the plot of t_d against $(p_i^3 - p_o^3)/(p_i^2 - p_o^2)^2$ resulting from using the gauge derived rather than the correct values of p_i. We see a very pronounced curvature which increases as we go to lower p_i (longer retention). We can illustrate the extent of the problem arithmetically by reference to the lowest p_i datum. The uncorrected gauge pressure (see Table I) of 2.90 psi, with p_o = 14.55 psi gives p_i = 17.45 psi; the correct value is 16.97 psi. The discrepancy is thus, only, 2.8%. However, the corresponding values of the pressure function of eq 6 are 3.76×10^{-5} and 4.49×10^{-5} m^2 N^{-1}, a discrepancy now of 16.3%. It is therefore crucially important that p_i be determined to better than 1% if eq 6 is to be properly tested for validity and subsequent use to evaluate R_F in any attempt to use relatively short linked capillaries in practice.

Capacity Factors (k'). The capacity factors of the various sample components were determined by replicate elutions of both individual components and selected mixtures. The same values were derived either way and the final average values are listed in Table II.

Column BP1, as expected from its nonpolar nature, provided low retention of the polar solutes and little if any separation of components 7 and 8 (α = 1) and 2 and 9 ($\alpha \simeq 1$).

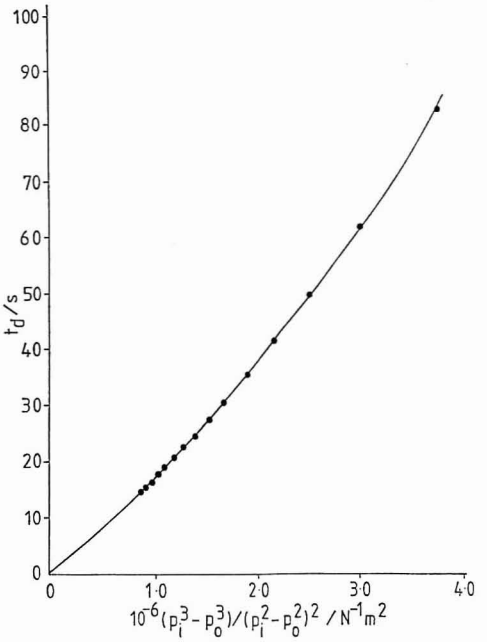

Figure 2. Plot of t_d for column BP1 against pressure function as in Figure 1 but using gauge recorded pressures instead of correct, calibrated values.

Table II. Capacity Factors (k') for Elution from 12-m Columns of BP1 and BP20 of Named Sample Components by helium at 125 °C

	component	bp, °C	k' BP1	k' BP20
1	2,3-dimethylphenol	217	2.54	50.8
2	2,4-dimethylphenol	212	2.18	37.8
3	2,6-dimethylphenol	203	1.79	16.9
4	3,4-dimethylphenol	227	2.75	68.6
5	3,5-dimethylphenol	222	2.39	56.7
6	*o*-cresol	191	1.26	26.7
7	*m*-cresol	203	1.47	39.0
8	*p*-cresol	202	1.47	37.8
9	2,6-dichlorophenol	219	2.19	40.6

Thus these pairs would not be separated on any realistic length of column. Column BP20, on the other hand, provided high retentions but now components 2 and 8 have identical measured k' with, in addition, poor resolution of this pair and components 7 and 9. Since α is essentially unity, components 2 and 8 could not be resolved at any realistic column length. Actual chromatograms of the full mixture with the individual columns are shown in Figures 3 and 4. Since the pairs that cannot be resolved are different in the two cases, a serial solution to the problem is feasible.

Prediction of k' for the Linked Columns. We can now test the validity of the theory by comparing the calculated k' with those measured experimentally when the two test columns are linked serially in the alternative modes: BP1-(F)/BP20(B) and BP20(F)/BP1(B). For this comparison we fix on a value of p_i that will provide an acceptable theoretical plate height, and in concert with the values of R_F and V_M already listed, knowing that l_F = 0.5, and also measuring the prevailing value of p_o, we can calculate p, P, and, thence, k' via the relevant equations. In this illustration we chose p_i = 19.93 psi, which, with p_o = 14.99 psi yielded the data listed in Table III.

The agreement of calculated and experimental values of k' for the linked columns, in either mode, is essentially exact which confirms the validity of the theory.

Parenthetically, it is worth pointing out that the foregoing is an excellent illustration of the inadequacy of the "practical"

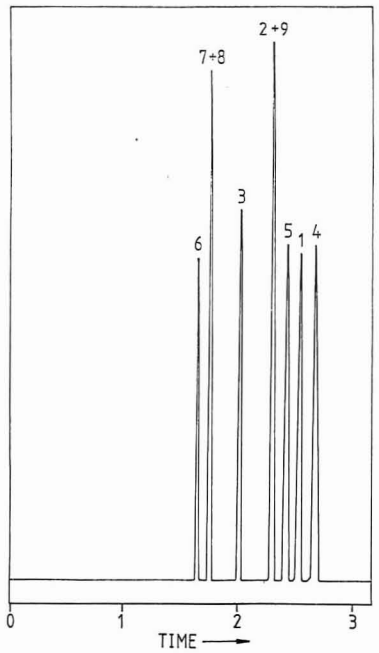

Figure 3. Chromatogram of nine-component phenol (see Table II) mixture with 12-m column BP1 at 125 °C: carrier gas, helium; time in min.

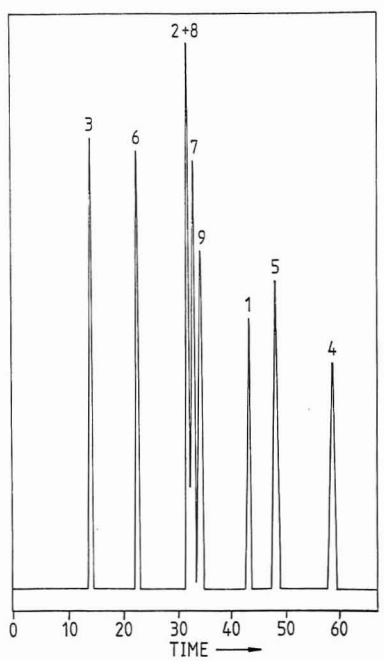

Figure 4. Chromatogram of nine-component phenol mixture with 12-m column BP20 at 125 °C: carrier gas, helium; time in min.

approach of simply linking different columns together in search of an analytical solution. In either mode, as Table III shows, components 2 and 7, although separable on the individual columns, cannot be separated at any column length of the serial system.

Optimizing the Separation. The experimental capacity factors of Table II provide us with sets of the coefficients of f_F and f_B in eq 9 so that k' may be calculated for each sample component over the range $f_F = 0$ to 1. For example, for *m*- and *p*-cresols we have

$$k'(m) = 1.47f_{BP1} + 39.0f_{BP20}$$

$$k'(p) = 1.47f_{BP1} + 37.8f_{BP20}$$

From these, and the corresponding equations for the other components, we can calculate k' as a function of f_{BP1}, for instance, over the range 0–1, as an alternative to graphical

Table III. Test of Prediction of k' for Serially Linked BP1 and BP20 (each 12 m; $l_F = 0.50$) Columns, Elution by Helium at 125 °C

component	mode: BP1(F)/BP20(B) p = 17.79 psi; P = 1.074		mode: BP20(F)/BP1(B) p = 17.47 psi; P = 1.239	
	k'_{exp}	k'_{calc}	k'_{exp}	k'_{calc}
1	25.8	25.8	29.2	29.2
2	19.4	19.3	21.8	21.9
3	9.03	9.06	10.1	10.1
4	34.6	34.5	38.9	39.2
5	28.6	28.6	32.2	32.4
6	13.5	13.5	15.3	15.4
7	19.4	19.5	21.8	22.2
8	18.7	18.9	21.5	21.5
9	21.1	20.7	23.6	23.4

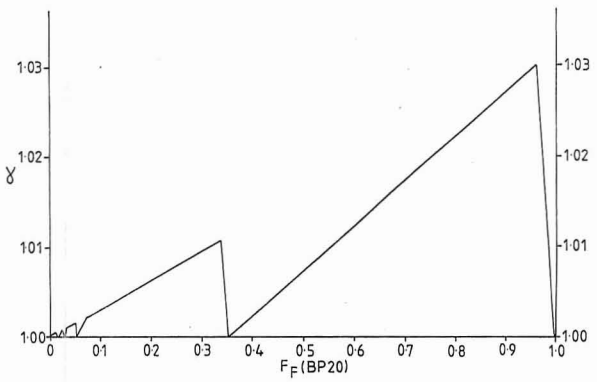

Figure 5. Window diagram for phenolic mixture plotted as relative retention (α) against f_F. F = BP20.

evaluation. These values then allow us to calculate the relative $\alpha(k_2'/k_1')$ for all pairs in the mixture. The majority of such values can be ignored since values greater than about 1.1 present no great separation difficulty. We can then plot the remaining values of α against f_F (BP20 = F) to provide the window diagram that is shown in Figure 5. This diagram represents the envelope of all values of the minimum α of the set. We see immediately that there are only two windows and that one is very much more useful than the other, viz. that at $f_{BP20} = 0.96$ with a minimum α of 1.030. The most difficult separation relates to components 2 and 8 and so, as reference to Table II shows, the relevant limiting k' is ca. 35. Thus, using eq 16, we find that the theoretical plate requirement is 44 800 for base-line separation.

We now choose a value of p_i that will provide a theoretical plate height (H) close to the minimum on a van Deemter plot and, knowing p_o, f_F (in either mode, 0.96 or 0.04), and γ, calculate p via eq 14. We then have all the necessary information to evaluate l_F via eq 15. We find

Mode: BP20(F)/BP1(B); $l_F = 0.9520$

BP1(F)/BP20(B); $l_F = 0.0365$

It remains only to ascertain the total column length. During the t_d and k' measuring sequence, values of H were gathered as a matter of course. We found that both columns gave H_{min} = 0.052 cm at the value p_i = 19.93 psi, with p_o at 14.99 psi. So knowing N_{req}, we calculate $L_F + L_B$ = 23.35 m. The column lengths in the alternative modes are, thus

Mode: BP20(F)/BP1(B); L_{BP20} = 22.23 m, L_{BP1} = 1.12 m;

p = 15.23 psi, P = 24.64

BP1(F)/BP20(B); L_{BP1} = 0.852 m, L_{BP20} = 22.49 m;

p = 19.79 psi, P = 0.041

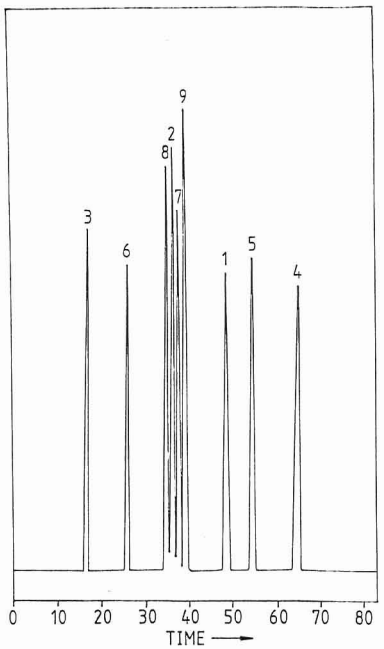

Figure 6. Window diagram optimized separation of phenolic mixture with serially coupled columns; F = BP20, B = BP1. Total and relative lengths as cited in text.

Table IV. Comparison of Experimental and Calculated k' for the Optimized Separation of Phenols with the Serial BP20(F)/BP1(B) Column System: I_{BP20} = 0.952, L_{BP20} = 22.23 m, L_{BP1} = 1.12 m

component	k'_{exp}	k'_{calc}	$\Delta k'$, %
1	48.8	48.9	−0.14
2	36.7	36.4	+0.76
3	16.2	16.3	−0.93
4	65.8	66.0	−0.32
5	54.8	54.6	+0.31
6	25.8	25.7	+0.46
7	37.8	37.5	+0.66
8	35.9	36.3	−1.25
9	39.4	39.1	+1.16

Because f_{BP20} is so close to unity, it happens that no great error would be introduced in the example by equating f_F and l_F. At more central values of f_F such an approximation would introduce gross error.

Since the window is shared by both modes, the chromatogram that will be obtained with either is exactly the same, although the relative column lengths in the modes are different. For reasons that we will develop elsewhere, as a general (though not universal) rule, the mode that has the longer column in front is the better choice. We show in Figure 6 the optimized chromatogram obtained here in the BP20(F)/BP1(B) mode; the prediction of an essentially base-line separation is fulfilled. Finally, in Table IV we confirm the accuracy of prediction of the relevant k'.

DISCUSSION

Prior to this study, attempts to work with linked capillary columns have either entirely or, at least very largely, involved eventual reversion to empirical solutions of analytical problems. This has resulted either from a failure to appreciate that the necessary detailed theoretical background and procedures exist or from reliance on approximate theories that fail when applied in practice. It is clear that this is unnecessary since, as we have shown here, not only can capacity factors (or other measures of retention) be accurately predicted on the basis of a relatively small number of simple measurements but the optimization of relative and overall column lengths can also be rapidly ascertained from the same data via the window diagram procedure. Thus, in all essentials, the problem of operating serially linked columns is fully resolved.

It may be held that the procedure is cumbersome, involving as it does a substantial amount of calculation. This too is erroneous since the kinds of calculations involved are mathematically trivial and can all be performed via an extremely simple computer program which can, additionally (*18*), provide illustrative print-out, such as the window diagram illustrated earlier, and, if desired, the projected optimized chromatogram.

It has been suggested to us in discussion that practitioners might show great reluctance to segment capillary columns due to their very considerable cost. This view is, in fact, impractical, as we can illustrate. First, a cursory inspection of the basic k' data of Table II might have suggested that the two 12-m test columns, linked together, would have provided the desired separation. However, as we showed earlier, this is not the case. Secondly, in practice, *usable* windows are few and diminish in utility (α_{min}) with increasing mixture complexity. For example, if we refer to Figure 5, we see that the second best window gives an α_{min} of about 1.01, which would demand almost 400 000 theoretical plates for base-line separation of the mixture; that is, a column system of some 200 m in length. In fact, there are many values of f_F within the higher window that offer better prospects than does the second window, i.e., any value of f_F greater than about 0.6 in which region α_{min} increases linearly toward the window maximum. One possibility that would retain the integrity of the original 12-m columns, for instance, would be to link two 12-m lengths of BP20 with one of BP1. This would give $f_F \simeq 0.7$ at which point $\alpha_{min} \simeq 1.0175$, which defines a theoretical plate demand of ca. 130 000, i.e. a combined column length of ca. 70 m, or six column units. In the example given here, three units were needed for optimization, two of BP20 and one of BP1. Little was lost from the former while 10.5 of the latter was left for alternative use. In the present instance, at least, the solution devised was both analytically and financially optimized. If the final objective is to optimize the speed of analysis as well, a procedure requiring use of excessive column length at much higher gas velocity than u_{min}, there is, of course, some latitude to employ integral sections in the appropriate length ratio. In either event, the efficiency with which column sections can be joined suggests that purchase of very long lengths of tubular columns is unnecessary.

Alternatively, of course, excess column length can be traded for faster elution by elevation of the temperature of the more retentive column since the theory and procedures described apply just as well to dual temperature systems as to isothermal systems. The dual temperature approach, in addition, is evidently as relevant to packed as to capillary columns, in contrast to the example presented here.

ACKNOWLEDGMENT

We are grateful to R. J. Laub for helpful advice.

LITERATURE CITED

(1) Hildebrand, G. P.; Reilley, C. N. *Anal. Chem.* **1964**, *36*, 47.
(2) Buys, T. S.; Smuts, T. W. *HRC CC, J. High Resolut. Chromatogr. Chromatogr. Commun.* **1980**, *3*, 461.
(3) Krupcik, J.; Guiochon, G.; Schmitter, J. M. *J. Chromatogr.* **1981**, *213*, 189.
(4) Ingraham, D. F.; Shoemaker, C. F.; Jennings, W. *J. Chromatogr.* **1982**, *239*, 39.
(5) Mayfield, H. T.; Chesler, S. N. *HRC CC, J. High Resolut. Chromatogr. Chromatogr. Commun.* **1985**, *8*, 595.
(6) Purnell, J. H.; Williams, P. S. *HRC CC, J. High Resolut. Chromatogr. Chromatogr. Commun.* **1983**, *6*, 569.
(7) Purnell, J. H.; Williams, P. S. *J. Chromatogr.* **1984**, *292*, 197.
(8) Purnell, J. H.; Williams, P. S. *J. Chromatogr.* **1985**, *321*, 249.
(9) Purnell, J. H.; Rodriguez, M.; Williams, P. S. *J. Chromatogr.* **1985**, *323*, 402.
(10) Purnell, J. H.; Williams, P. S. *J. Chromatogr.* **1985**, *325*, 1.

(11) Purnell, J. H.; Rodriguez, M.; Williams, P. S. J. Chromatogr. 1986, 358, 39.
(12) Purnell, J. H.; Jones, J. R.; Wattan, M. H. J. Chromatogr. 1987, 399, 99.
(13) Laub, R. J.; Purnell, J. H. J. Chromatogr. 1975, 112, 71.
(14) Laub, R. J.; Purnell, J. H. Anal. Chem. 1976, 48, 799.
(15) Laub, R. J.; Purnell, J. H. Anal. Chem. 1976, 48, 1720.
(16) Laub, R. J.; Purnell, J. H.; Williams, P. S. J. Chromatogr. 1977, 134, 249.
(17) Purnell, J. H. J. Chem. Soc. 1960, 1268.
(18) Laub, R. J. J. Liq. Chromatogr. 1984, 7, 647.

RECEIVED for review April 3, 1990. Accepted July 18, 1990.

Hydrodynamic Relaxation and Sample Concentration in Field–Flow Fractionation Using Permeable Wall Elements

J. Calvin Giddings

Field-Flow Fractionation Research Center, Department of Chemistry, University of Utah, Salt Lake City, Utah 84112

The advantages of hydrodynamic relaxation in field–flow fractionation, in which an injected sample is driven rapidly toward its equilibrium distribution by flow, are described relative to conventional field-driven relaxation. A new concept for achieving hydrodynamic relaxation, based on the use of permeable wall elements (or frit elements) embedded in the channel walls, is introduced. Here an auxiliary substream of carrier fluid, permeating uniformly into the FFF channel near the inlet, drives the sample, entrained in its own substream, close to its equilibrium configuration. Such frit elements can also be used to enrich the sample at the outlet. Equations are derived and plots are provided for the position of the splitting plane dividing the two substreams; this position defines the strength of the hydrodynamic relaxation. Variations in shear through these frit-modified end regions are also formulated and plotted. The effects of frit elements on band broadening are discussed. It is concluded that permeable wall elements in many configurations may be broadly applicable to FFF and related methods for improved sample introduction, increased separation speed, reduced risk of sample adhesion to the wall, improved flow stability, and sample enrichment.

In virtually any kind of field–flow fractionation (FFF) process, a relaxation step must be carried out in the FFF channel prior to the beginning of effective separation (*1–3*). In the relaxation process, sample material that is distributed widely over the streamlines entering the channel is forced into narrow cross-sectional distributions from which separation is possible. Normally, a sample is driven close to one wall (the accumulation wall) of the channel during relaxation by the same external field or gradient that is used to implement FFF separation. In most cases the axial flow is halted, as relaxation takes place in order to control band distortion and broadening. This so-called *stopflow procedure* sometimes leads to flow instabilities accompanied by baseline shifts and provides a window of vulnerability in which sample particles are most susceptible to adhesion to the channel wall. It also increases run time. Consequently, means have been pursued recently for introducing samples into FFF channels without stop flow operation (*4, 5*).

One of the concepts developed and implemented in this laboratory for avoiding stop flow operation makes use of *hydrodynamic relaxation*, a process in which sample material is driven close to its equilibrium position rapidly by the manipulation of flow rather than by sluggish field-driven transport in the channel (*5, 6*). In the above-mentioned studies, hydrodynamic relaxation was proposed and carried out by using a flow splitter at the inlet end of the FFF channel. Manipulation of the flow rates of the incoming flow streams entering above and below the splitter make it possible to drive the sample, contained exclusively in the substream emerging from below the splitter, close to the accumulation wall of the channel, a position from which separation can quickly commence.

A second flow splitter can be used at the outlet of the channel to concentrate the component materials for enhanced detection (*6*). It was shown earlier that an outlet flow splitter was capable of stripping off the bulk of the liquid flowing above the sample layers in the channel, thus leaving the sample in a more concentrated form for detection and collection (*7*).

There are several disadvantages associated with the use of flow splitters in FFF systems for the above purposes. First, for proper operation these splitters must be suspended evenly across the several centimeters wide gap of the thin channel; unevenness amounting to a few tens of micrometers would noticeably distort the hydrodynamic relaxation process. A second difficulty is that the introduction of a flow splitter and the two associated flow spaces on either side of the splitter—three layers in all—is very often inconsistent with the utilization of very thin (e.g. 100–200 μm) high-performance channels. Third, since the flow stream into which the sample is introduced must traverse the narrow gap on one side of the splitter where the thickness is only a fraction (usually approximately one-third) of that of the full channel, there is an enhanced risk that larger particles in the sample, whether part of the sample or part of an impurity, will clog all or part of the stream path needed for sample introduction. Fourth, at high flow rates the abrupt change in flow direction at the splitter edges may introduce eddy currents in the fluid capable of disrupting the distribution of components near the inlet and outlet.

The purpose of this report is to describe a new and more promising channel configuration capable of achieving hydrodynamic relaxation and sample concentration. This method entails utilizing a special element of permeable wall material (a "frit element") at one or both ends of the channel, through which flow can be freely and independently introduced into the channel or withdrawn from the channel depending upon needs. The frit element will normally be embedded smoothly in one of the channel walls, thus replacing a small area of the usual wall material. The flow substream or substreams entering or departing through the special element(s) are generally complemented by independently con-

0003-2700/90/0362-2306$02.50/0 © 1990 American Chemical Society

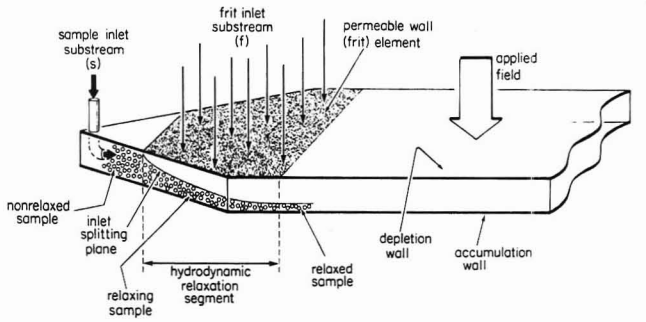

Figure 1. Diagram showing one possible configuration of a permeable wall (frit) element at the inlet of the FFF channel. By permeating the frit inlet substream through the frit element, the sample-containing substream is driven toward the accumulation wall, thus bringing about hydrodynamic relaxation.

trolled flow streams (the sample substreams) carrying sample material into or out of the FFF channel. The *frit inlet substream* is introduced into the channel through the inlet frit element in such a way as to compress the *sample inlet substream* against one wall (generally the accumulation wall). The *frit outlet substream* and the associated outlet frit element are similarly positioned to strip carrier liquid away from the sample at the outlet, leaving the sample material concentrated in the *sample outlet substream*. To function in these roles, such frit elements must generally constitute part of the depletion wall of the channel, which is the wall opposite the accumulation wall where the sample is concentrated. Their use should make it possible to achieve both hydrodynamic relaxation and sample enrichment without any of the disadvantages noted above for flow splitters.

Hydrodynamic relaxation achieved by the use of a permeable wall element at the inlet is illustrated in Figure 1. The sample pulse is introduced into a carrier stream (substream s) that enters the inlet end of the FFF channel. A second substream (f), usually of larger flow rate than the first, is introduced through the permeable wall element, a segment of the depletion wall generally extending across the full breadth of the channel but being only a small fraction of its length. Flow stream f percolates into the channel across the permeable wall element, thereby displacing feed stream s downward toward the accumulation wall. This compression is indicated in Figure 1 by the downward displacement of the inlet splitting plane, the stream plane that divides the fluid elements entering in substreams s an f. The sample material remains below the splitting plane (except for a generally negligible amount displaced across the plane by diffusional transport) and is thereby compressed to the vicinity of the accumulation wall by the unique configuration of merging flows. The sample compression process is referred to as hydrodynamic relaxation.

As shown in Figure 1, the permeable wall or frit element used for hydrodynamic relaxation is located close to the inlet. It may extend over all or part of the triangular endpiece normally utilized as a part of the FFF channel structure. In other cases it can be positioned partially or entirely beyond the triangular endpiece. Several possible configurations of the frit element used at the inlet are shown in Figure 2. Special shapes can be used (as in Figure 2d) to reduce end or edge effects or otherwise control the details of channel flow.

The achievement of hydrodynamic relaxation by a permeable wall element at the inlet is expected to be applicable to virtually all forms of FFF including sedimentation FFF, thermal FFF, electrical FFF, and flow FFF in both steric and normal modes of operation. It is expected to be particularly convenient for flow FFF, for which the depletion wall is generally permeable (made up of permeable frit material) to begin with. A liquid feed chamber usually extends along

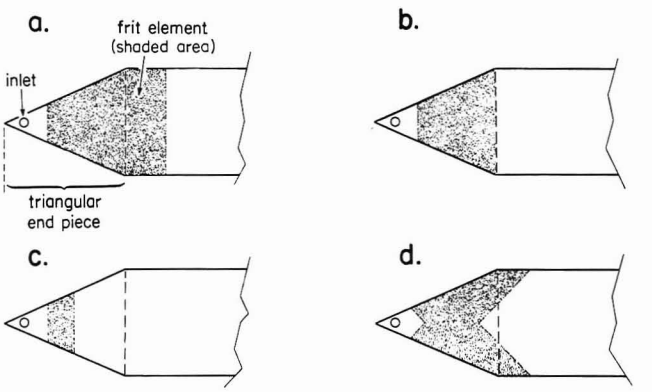

Figure 2. Various configurations of inlet frit elements.

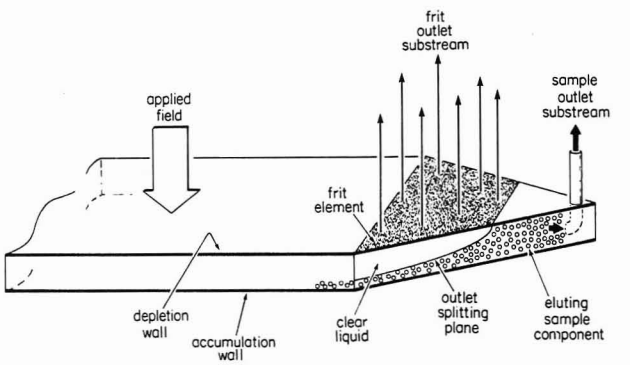

Figure 3. Use of an outlet frit element to withdraw clear (sample-free) liquid flowing above the sample components lying close to the accumulation wall. Removal of the clear liquid leads to sample concentration.

the length of the permeable wall on its reverse side to distribute incoming liquid uniformly over the permeable wall area. All that is needed is to isolate by a sealing arrangement a small feed chamber above the area selected to be the permeable wall element. Fluid substream f is then fed into this isolated chamber and through the permeable wall element; the seals prevent this stream from intermixing with the normal crossflow stream entering through the frit further along the length of the channel. Thus, while the permeable wall may be continuous, it can be divided into functional elements by flow control. Generally the permeation rate per unit area of frit will be much higher for the permeable wall element than for the normal depletion wall downstream, necessitating the proposed isolation of the two.

A permeable wall element similar to that described above can be used at the outlet to enrich the sample. This use is illustrated in Figure 3. Here one uses the permeable wall element to skim off the "clear" (sample-free) carrier liquid flowing above the atmosphere of sample particles or molecules. If not removed by some such means, this carrier mixes with the sample at the outlet and leads to considerable sample dilution. As before, the gentle flow conditions provided by a permeable wall element (preferably of uniform permeability) can systematically withdraw all the fluid above an outlet splitting plane whose initial position is determined by the ratio of the volumetric flow rates of the two outlet substreams.

THEORY

Hydrodynamic Relaxation. It is assumed here that the permeable wall element (frit) at the inlet end is a segment of the depletion wall that extends over the breadth of the channel (reduced from the full breadth b in the inlet triangular endpiece), commencing at axial position z_1 and extending to position z_2. The total frit area, A_f, can be imagined to consist of thin strips of area dA, as illustrated in Figure 4. A substream of flow rate $\dot{V}_f$ is assumed to permeate uniformly

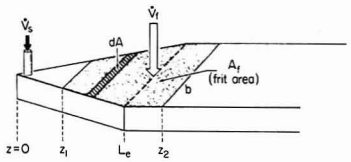

Figure 4. Frit inlet system showing flow rates, coordinate positions, and area elements referred to in the text.

through the frit area and into the channel. As fluid enters the channel through the frit, it joins other fluid elements flowing down the channel axis. Thus the channel flow rate $\dot{V}$ increases from point z_1 to z_2 as new elements of fluid enter the stream. (It is assumed here that any fluid losses, such as those that may exit a permeable accumulation wall, are negligible in the inlet region extending from $z = 0$ to $z = z_2$.) At any axial position z the channel flow rate will equal

$$\dot{V}(z) = \dot{V}_s + \dot{V}_f \frac{A(z)}{A_f} \tag{1}$$

where $\dot{V}_s$ is the flow rate of the sample stream and $A(z)$ is the frit area exposed up to position z. Equation 1 is independent of the shape of the frit element.

As noted earlier, the inlet splitting plane is defined as the plane dividing fluid entering through the frit from fluid in the sample stream. The two streams are assumed to merge smoothly without turbulence, with the frit stream gradually displacing the sample stream further toward the accumulation wall as the frit stream accumulates strength from z_1 to z_2 (see Figure 1). For simplicity we assume that the inlet splitting plane is flat although in reality it will bulge up slightly in the center due to end effects. We assume also that the flow profile is parabolic across the channel thickness despite small disturbances due to crossflow and that the flow velocity is constant across the breadth at any position z despite some nonuniformities introduced by edge and end effects.

At any axial position z, the elevation $x_s(z)$ of the inlet splitting plane above the accumulation wall will be determined by the relative flow rates of the sample stream ($\dot{V}_s$) that must be accommodated below the splitting plane and the cumulative frit stream ($\dot{V}_f A(z)/A_f$) that flows above the splitting plane. Therefore the splitting plane elevation x_s is determined by the expression

$$\frac{\int_0^{x_s} v(x, z)\, dx}{\int_0^{w} v(x, z)\, dx} = \frac{\dot{V}_s}{\dot{V}_s + \dot{V}_f A(z)/A_f} \tag{2}$$

where $v(x, z)$ is the local flow velocity at elevation x and axial position z and w is the channel thickness. The parabolic flow condition is described by

$$v(x, z) = 6\langle v(z)\rangle\left(\frac{x}{w} - \frac{x^2}{w^2}\right) \tag{3}$$

where the triangular brackets represent an averaging (of local velocity v) over the flow cross section at position z. When eq 3 is substituted into eq 2 and the integration performed, we obtain

$$3\left(\frac{x_s}{w}\right)^2 - 2\left(\frac{x_s}{w}\right)^3 = \left(1 + \frac{\dot{V}_f}{\dot{V}_s}\frac{A(z)}{A_f}\right)^{-1} \tag{4}$$

an expression giving the relationship between splitting plane position x_s (relative to w) and the progress of fluid through the frit segment of the channel as expressed by $A(z)/A_f$. A plot of x_s/w versus $A(z)/A_f$ for different flow rate ratios $\dot{V}_f/\dot{V}_s$ is shown in Figure 5.

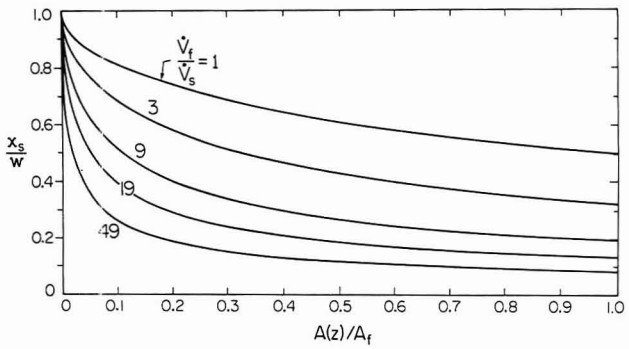

Figure 5. Relative height of the splitting plane above the accumulation wall at different positions that correspond to specific values of the fraction $A(z)/A_f$ of the frit area upstream of that coordinate position.

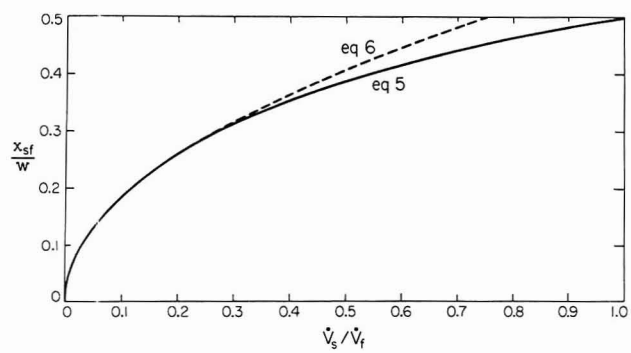

Figure 6. Final value of the relative position of the splitting plane as a function of the ratio of the sample inlet substream and the frit inlet substream according to eqs 5 and 6.

At the downstream end of the frit segment of the channel, hydrodynamic relaxation will be essentially completed. Its effectiveness can be judged in part by the degree of depression of the splitting plane (i.e., the smallness of x_s/w) at this point. The final position of the splitting plane, x_{sf}, is given by eq 4 with $A(z)/A_f$ equal to unity. With minor rearrangement this gives

$$3\left(\frac{x_{sf}}{w}\right)^2 - 2\left(\frac{x_{sf}}{w}\right)^3 = \frac{\dot{V}_s}{\dot{V}_s + \dot{V}_f} = f_s \tag{5}$$

where f_s is the fraction of total channel flow rate $\dot{V}$ entering through the sample substream. When $\dot{V}_f \gg \dot{V}_s$ ($f_s \ll 1$) and therefore $w \gg x_{sf}$, eq 5 can be approximated by

$$\frac{x_{sf}}{w} = \left(\frac{\dot{V}_s}{3\dot{V}_f}\right)^{1/2} \tag{6}$$

which yields x_{sf}/w within 5% of the value from eq 5 up to $x_{sf}/w = 0.35$. (The similar approximation $(x_{sf}/w) = (f_s/3)^{1/2}$ also works well for small f_s values.)

Plots of eqs 5 and 6 are shown in Figure 6. It is clear from these plots that very small values of the flow ratio $\dot{V}_s/\dot{V}_f$ are needed to depress the splitting plane toward the accumulation wall to within 10–20% of w. Specifically, $\dot{V}_s/\dot{V}_f$ equals 0.0288 and 0.116 for x_{sf}/w values of 0.1 and 0.2, respectively.

Shear Effects. One of the advantages mentioned earlier for stopless flow injection is the continued application of flow and consequently of shear in the FFF channel. Hydrodynamic lift forces (*8–11*), which become greater with increasing shear rate, provide the simplest possible mechanism for keeping particles removed from the attractive forces of the wall and thus mobilized for separation and recovery (*12*). The range of particle diameters immune from wall adsorption is expected to increase with the shear rate. However, exceedingly fragile species can be degraded by shear, which must then have an upper bound to maintain sample integrity. In either case it

is useful to evaluate the shear in the end regions of FFF channels where rapid variations in shear rate are normally encountered. The frit inlet (or outlet) system has the advantage of leveling out these strong variations (see later).

The shear rate, $s = dv/dx$, can be obtained as a derivative of eq 3

$$s = \frac{6\langle v\rangle}{w} - \frac{12\langle v\rangle x}{w^2} \tag{7}$$

At the wall ($x = 0$) where s is maximal

$$s_0 = 6\langle v\rangle/w \tag{8}$$

Since $\langle v\rangle = \dot{V}/b_e w$, we have

$$s_0 = 6\dot{V}/w^2 b_e \tag{9}$$

where $b_e \equiv b_e(z)$ is the variable breadth of the channel end regions. In view of eq 1, s_0 becomes

$$s_0 = \frac{6}{w^2 b_e}\left(\dot{V}_s + \dot{V}_f \frac{A(z)}{A_f}\right) \tag{10}$$

For a triangular channel endpiece, $b_e = \beta_z$, where constant β is the channel breadth b divided by the length L_e of the endpiece (see Figure 4). It is simplest if the frit element is confined to the triangular endpiece and begins and ends along straight boundary lines at z_1 and z_2, respectively. Examples of such frit elements are shown in parts b and c of Figure 2. For such elements

$$A(z) = \int_{z_1}^{z} b_e\, dz = \frac{\beta}{2}(z^2 - z_1^2) \tag{11}$$

and

$$\frac{A(z)}{A_f} = \frac{z^2 - z_1^2}{z_2^2 - z_1^2} \tag{12}$$

Equation 12 is valid for $z_1 \le z \le z_2$; the area ratio of eq 12 is zero for $z < z_1$. With eq 12 and $b_e = \beta_z$, eq 10 becomes

$$s_0 = \frac{6L_e}{w^2 b}\left[\frac{1}{z}\left(\dot{V}_s - \dot{V}_f \frac{z_1^2}{z_2^2 - z_1^2}\right) + z\frac{\dot{V}_f}{z_2^2 - z_1^2}\right] \tag{13}$$

in the range from z_1 to z_2 and

$$s_0 = \frac{6L_e\dot{V}_s}{w^2 bz} \tag{14}$$

for $z < z_1$. If $L_e > z_2$, then s_0 in the space between z_2 and L_e becomes

$$s_0 = \frac{6L_e(\dot{V}_s + \dot{V}_f)}{w^2 bz} = \frac{6L_e\dot{V}}{w^2 bz} \tag{15}$$

which reduces to $s_0 = 6\dot{V}/w^2 b$ at the end of the triangular endpiece and remains at that level throughout the main channel until the point where the outlet endpiece is encountered. (The above s_0 equation applies also to the outlet if z is measured back from the outlet tip.)

It is instructive to apply these equations to an example. We assume a triangular endpiece with $L_e = b = 2$ cm, $z_1 = 0.5$ cm, $z_2 = 1.5$ cm, and $w = 0.0254$ cm. The flow rates, $\dot{V}_s$, $\dot{V}_f$, and $\dot{V}$, are assumed to be 0.05, 0.95, and 1.0 mL/min, respectively ($f_s = 0.05$). The results are plotted in Figure 7. The shear rate at the wall, s_0, experiences four different trends over four domains of flow. First of all, s_0 drops off hyperbolically with z as the channel tip widens out. At $z = z_1 = 0.5$ cm, the frit element is encountered and the incoming frit flow drives s_0 upward. The upward trend continues across the frit element. At the end of the frit, $z = z_2 = 1.5$ cm, the fluid moves into the final segment of the triangular endpiece. Here s_0 drops

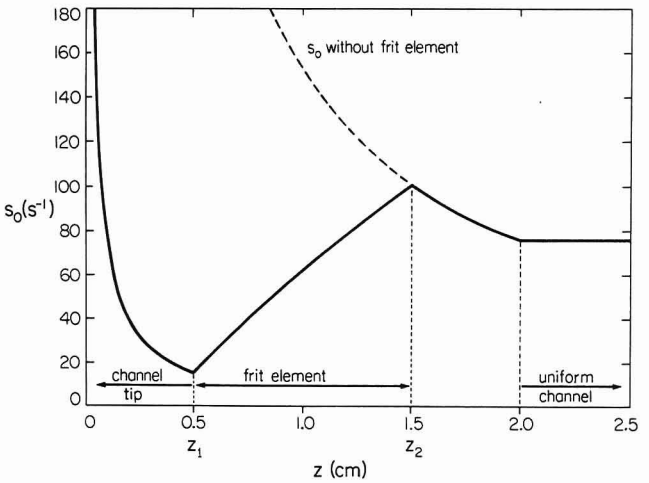

Figure 7. Variation of the maximum shear rate (the value at the wall being s_0) with distance z through a triangular endpiece of length 2.0 cm with the frit element extending across the breadth of the inlet from $z = 0.5$ to $z = 1.5$ cm. Breadth $b = 2$ cm. The flow rates are $\dot{V}_s = 0.05$ and $\dot{V}_f = 0.95$ mL/min. The dashed line and its extension to the right pertain to a normal channel without a frit inlet.

off again because the channel is still becoming broader, but there is no offsetting influx of fresh carrier. At the end of the triangular endpiece, $z = L_e = 2.0$ cm, the carrier fluid passes into the long uniform channel segment where separation is realized. Because of the uniform flow cross section and the constant flow rate, s_0 is constant throughout this main channel segment.

Figure 7 shows that the shear rate undergoes substantial variations through the inlet region. However, the variation, particularly on the upside, is much greater without a frit element, as shown by the dashed line. This line continues steeply upward and off the graph (in accordance with the hyperbolic dependency of eq 15) as one approaches the inlet tip. At 1 mm from the tip, s_0 has reached over 1500 s^{-1}, in comparison to 78 s^{-1} for the inlet with the frit element. While both curves, in theory, approach infinity as they move toward $z = 0$, the inlet tip can easily be modified to eliminate this severe increase. Thus the shear rate can be held within reasonable bounds everywhere in the FFF channel by the judicious placement of a frit element. Even the substantial dip in shear rate at $z = z_1$ can be considerably modified by moving z_1 back toward the inlet tip or by increasing $\dot{V}_s$. The s_0 profile could be further modified by using other frit geometries.

Whereas the shear rate could be limited to a relatively narrow range with a frit element, such is not the case with the normal triangular endpiece without this feature. We have already noted that the shear rate reaches extremely high values near the tip of such a normal inlet (or outlet). However, in many cases a more severe problem is encountered when the flow is stopped for relaxation. With stop flow operation, the entire curve collapses to the baseline and the system is deprived of any means of keeping particles away from the immediate vicinity of the wall in this time interval. By contrast, the stopless flow operation utilized with hydrodynamic relaxation maintains the same shear rate values throughout the injection process and the run itself.

We observe that the above equations for shear rate, like the previous equations describing the position of the splitting plane, are based on the assumptions of parabolic flow and of uniform flow over the channel breadth. These assumptions should be reasonably adhered to (except at the very tip of the channel), providing the span ($z_2 - z_1$) of the frit element is much greater than the channel thickness w and providing the angle of expanding flow at the channel tip is not too great.

Band Broadening. As is the case with most FFF and chromatographic systems, the broadening of component bands has a number of sources within and outside the separation channel or column. For the frit inlet FFF system, some sources of band broadening are virtually identical with those found in conventional FFF systems. This includes nonequilibrium effects, which generally dominate axial dispersion in FFF systems. However, some band-broadening contributions originating at the inlet and outlet ends are altered by the unique flow characteristics of the frit elements.

Band-broadening contributions can be expressed in terms of the increment in the time-based variance σ_t^2 made by the mechanism of interest. If the contributing σ_t^2 is known, then the unwanted increase in the plate height H can be calculated from

$$H = L\sigma_t^2/t_r^2 \tag{16}$$

where L is the FFF channel length and t_r is the retention time of the component under consideration (*13*).

For chromatographic and FFF systems alike, a component band will be somewhat broadened at the inlet before active separation commences. The inlet broadening can be measured by either time-based variance σ_t^2 or volume-based variance σ_V^2. In the case of the frit inlet system, the incoming band will gain some variance σ_V^2 in volume, as measured relative to the sample substream only, by the time hydrodynamic relaxation is completed at coordinate position z_2. The corresponding σ_t^2 is

$$\sigma_t^2 = \sigma_V^2/\dot{V}_s^2 \tag{17}$$

This is an important equation because it points to a unique compromise needed for the effective operation of a frit inlet system. (The same considerations apply to the split inlet configuration.) Specifically, the sample inlet flow rate $\dot{V}_s$ must be small compared to the total channel flow rate $\dot{V}$ in order to reduce the elevation of the inlet splitting plane and achieve effective hydrodynamic relaxation. However, the inverse dependence of σ_t on $\dot{V}_s$ shown in eq 17 makes it clear that the reduction in $\dot{V}_s$ must be limited in order to avoid unacceptable band broadening. It is obviously important to reduce σ_V^2 as much as possible to ease the constraints imposed on $\dot{V}_s$ by eq 17.

The exact calculation of σ_V^2 is difficult and will not be attempted here. In general, σ_V^2 contributions will increase in proportion to the square of the volume in which the elementary band-broadening steps take place, providing the sample material does not have time to approach equilibrium along the axis transverse to flow. Thus the key to reducing σ_V^2 is to eliminate all unnecessary volume in the sample inlet substream between the injection loop and the point of completion of hydrodynamic relaxation.

The inlet components whose volumes are subject to reduction are (i) the sample injection loop, (ii) the tubing connecting the loop to the channel, (iii) the channel inlet region up to the frit element at position z_1, and (iv) the region between z_1 and z_2 covered by the frit that lies below the splitting plane. The following considerations apply to these volume components.

1. The volume V_{inj} of the sample injection loop (typically 10–50 μL), which contributes $V_{inj}^2/12$ to σ_V^2, can be reduced to the minimum allowed by detector sensitivity and concentration effects. Normally, a highly concentrated sample contributes to overloading in FFF (*14*), but with frit inlet (or split inlet) injection there is a compensating dilution effect as the two streams merge together.

2. The volume of the tubing connecting the sample loop to the channel can be reduced by moving the injector closer to the channel, thus reducing the tube length. The diameter of the tube can generally be reduced below that normally used because the full inlet stream need not be pumped through this inlet. The extent of diameter reduction depends to some degree on the tolerance of sample components to shear effects.

3. The volume in the channel inlet region up to point z_1 is best reduced by moving the frit element as close as possible to the inlet tip of the channel.

4. The volume lying beneath the splitting plane between z_1 and z_2 can be reduced by using small frit elements, but care must be taken to maintain flow integrity if these elements are too greatly condensed in size. The volume beneath the splitting plane can obviously be reduced by decreasing the sample inlet flow rate $\dot{V}_s$, but this is offset by the gains in σ_t^2 expressed in eq 17.

Similar considerations apply if carrier fluid is skimmed away from the sample substream at the outlet. Again, each component of the outlet system, up to and including the detector, will contribute a σ_V^2 term to band broadening. Equation 17 still applies. This equation makes it clear, as before, that any contributing σ_V^2 terms are amplified by a reduced sample substream flow rate, whether outlet or inlet. Because these end effects are amplified by low sample flow rates, all extraneous volumes at the ends of channels, where such flow division is taking place, must be reduced to a minimum.

We have emphasized above that end effects are expected to become excessive if the flow rate $\dot{V}_s$ of the sample substreams is too severely reduced (see eq 17). However, with a given channel flow rate $\dot{V}$, if the sample substream flow rate is not adequately reduced, the elevation of the splitting plane remains high and hydrodynamic relaxation is only partially effective. Under these circumstances the completion of relaxation by ordinary field-driven transport under stopless flow conditions will contribute substantially to band broadening. Therefore, the magnitude of $\dot{V}_s$ relative to $\dot{V}$ or $\dot{V}_f$ must be set at a compromise level at which the overall plate height is minimal. (The channel flow rate $\dot{V}$ is itself subject to compromise in accordance with the long-standing principles governing FFF operation (*3*, *4*).)

DISCUSSION

The experimental implementation of hydrodynamic relaxation, both by the frit inlet system described here and by a split inlet configuration, will be reported in a forthcoming paper. However, the basic effectiveness of the frit inlet method for stopless flow operation is illustrated in Figure 8. Here a frit inlet element (z_1 = 0.2 cm and z_2 = 3.4 cm) has been incorporated in a flow FFF channel (L = 38.0 cm, L_e = 2.4 cm, b = 2.0 cm, and w = 220 μm) in order to realize hydrodynamic relaxation. Latex beads of nominal diameters 29, 15, 10, 7, and 5 μm were introduced into an aqueous stream without stop flow operation. In Figure 8a (left side), $\dot{V}_f = 0$ and thus there is no hydrodynamic relaxation. Clearly, there is no effective resolution in this case. Hydrodynamic relaxation is utilized in Figure 8b (right side) by adjusting flow rates to $\dot{V}_f$ = 3.9 mL/min and $\dot{V}_s$ = 0.4 mL/min (f_s = 0.09). Excellent resolution of the latex beads is found. The overall flows acting in the channel in the two cases ($\dot{V}$ = 4.3 mL/min and $\dot{V}_c$ = 5.7 mL/min) are virtually identical. The difference, making resolution possible, is the use of a substantial frit inlet substream and thus hydrodynamic relaxation in Figure 8b.

In describing the application of frit elements in FFF, we have implied that the inlet frit element must be imbedded in the depletion wall of the channel so that relaxation (in which particles are driven toward the accumulation wall) can be accomplished hydrodynamically without excessive band broadening. However, a more careful analysis shows that it is not the normal transport-based relaxation as such that causes band broadening in stopless flow injection but the fact that particles enter the channel simultaneously at many different altitudes above the accumulation wall. Therefore,

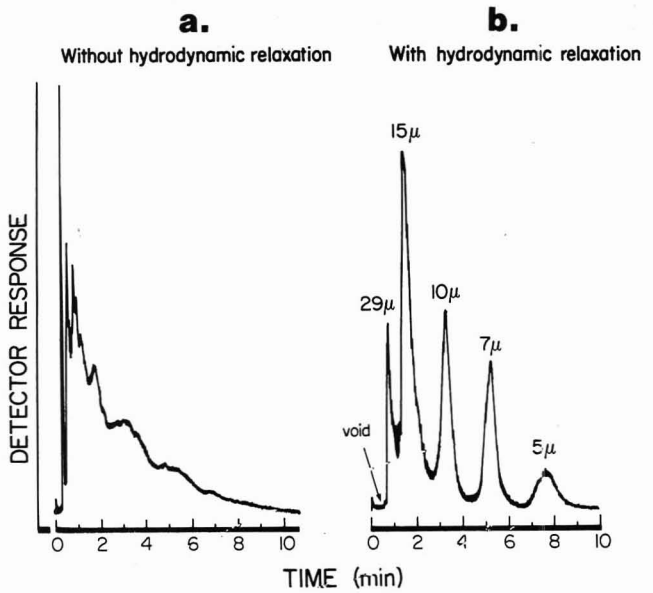

Figure 8. Comparison of two flow FFF runs carried out with identical channel flow conditions and stopless flow injection. The channel used for both runs is equipped with a frit inlet element, which was used to realize hydrodynamic relaxation in b but not in a (details in the text).

the relaxation process has many different beginning points, each leading to a different flow displacement down the channel in the course of relaxation. The different flow displacements caused by the different starting positions of particles are responsible for the excessive band broadening observed in stopless flow relaxation (*1*). This problem can be largely solved by confining all entering particles within a thin lamina occupying only a small fraction of the channel thickness. If, for example, the thin lamina containing the sample particles enters next to the depletion wall, as could be arranged by inserting the frit element into the accumulation wall, all particles would have to relax across the full thickness of the channel. However, band broadening would be limited by the fact that all particles of the same type would be following the same relaxation trajectory and would thus approach their equilibrium positions at about the same distance along the channel axis. A similar result would be achieved if the sample-containing lamina was confined to the central region of the channel, which could be accomplished by having frit elements in both walls near the inlet. Again, with narrow confinement, all relaxation trajectories would be the same and particles of the same type would arrive at the accumulation wall in a narrow band. Thus, in general, the excessive band broadening caused by stopless flow relaxation can be avoided if the relaxation trajectories are spatially coherent, differing only by small increments of distance from one another. Such coherence is made possible, as illustrated above, by various combinations of inlet frit elements.

It is expected that a frit element in the depletion wall will generally (but not always) be advantageous because the frit inlet substream then drives entering particles and molecules close to their equilibrium positions near the accumulation wall. In this case, separation based on differences in equilibrium migration rates commences immediately, thus speeding up the completion of separation.

We note that in some FFF processes different kinds of particles approach equilibrium at different channel walls. Thus in sedimentation FFF, particles denser than the carrier medium seek equilibrium at the outside wall and particles less dense than the medium approach equilibrium at the inside wall (*15*). Thus both walls act as accumulation walls for different sets of particles. It is obviously impossible to introduce the different particles simultaneously to their respective accumulation walls by hydrodynamic relaxation. However, different combinations of frit elements can be used to introduce all the particles in a thin lamina, which might be located near one of the walls or be positioned in the interior of the channel. This way, each particle type will approach its own equilibrium position coherently without excessive band broadening. Thus stopless flow injection is still feasible if the right combination of frit elements is used at the inlet end.

In general, frit elements substituted for part of the wall area of a thin flow tube or channel can, providing they are served by independently controlled flow streams, act to introduce (or withdraw) thin laminae of fluid into (or from) almost any desired part of the flow cross section. This is particularly promising for field–flow fractionation as we have seen above, but the concept is equally applicable to other separation systems where the control of fluid laminae is important. Thus in split-flow thin (SPLITT) separation cells, continuous separation (in the transport mode) is realized only after compressing the sample-containing substream into a thin flow lamina near one wall of the narrow channel (*16*, *17*). This compression is usually achieved by using an inlet flow splitter, but such splitters have the same disadvantages noted previously for FFF. The formation of the thin sample-containing lamina could be better controlled by using a frit inlet element in the wall opposite the desired position of the lamina. Even more versatility could be gained by placing frit inlet elements in both walls near the inlet, in which case the sample-containing lamina could be compressed into a thin film directly in the center of the channel or offset to any other desired location between channel walls. Frit elements could also be used at the outlet of the SPLITT cell to withdraw the desired fluid lamina providing they did not block the passage of particles too large to permeate through the pores of the frit.

An inlet frit element might also be used in some cases to improve the performance of capillary hydrodynamic chromatography (CHDC) operating under high shear conditions. In this variant, particles or polymer molecules are introduced into a narrow capillary in which, because of their different sizes, they have access to different cross sectional areas in the tube within which the fluid has different mean flow velocities. While particles normally diffuse freely across their accessible area, at high flow velocities shear-induced forces tend to drive each particle type to a specific equilibrium distribution in the tube (*18*, *19*). Band broadening in such a system is amplified because any given particle type that enters the tube is initially spread over its accessible flow cross section and the individual particles corresponding to that type are only slowly transported by the shear-induced forces to their equilibrium distributions. During the relaxation process, different particles of the same type are travelling at different velocities because they have entered the tube in different streamlines. This inequality in the velocities of like particles will broaden the particle band and lessen resolution. However, if all particles of the same type enter through the same thin flow filament, they experience equal or near-equal velocities during relaxation and this transient band-broadening effect should be much reduced. One way to achieve such coherence would be to use a short segment of a tube or capillary with a permeable wall immediately preceding the normal capillary tube. The sample substream would enter the inlet opening of this segment and a second substream permeating in through the porous wall would collimate the sample substream into a thin filament at the center of the tube. All like particles would then follow the same trajectories along the radial coordinate as they approached equilibrium, thus reducing band broadening.

CONCLUSIONS

Many separation methods that rely on flow in an empty tube or channel, such as FFF, SPLITT, and CHDC, can be

improved by methods that permit the rapid focusing of entering particle bands into small regions of the flow cross section. In FFF, such localization (in the form of relaxation) can often be achieved by the application of transverse driving forces, but by this approach the localization is relatively slow and substantial band broadening can occur before localization is complete. It is far better to induce the localization of the initial particle band hydrodynamically, that is, by flow transport, which can induce the necessary displacements almost instantaneously. The necessary flow transport can be induced by utilizing small areas of a permeable wall material through which one or more substreams can enter the flow duct at a controlled flow rate. Similar permeable wall or frit elements can be used to withdraw fluid from the outlet end of the channel and thus concentrate the sample or to deflect the streamlines near the outlet if desired for some other purpose. These frit elements provide maximum control over the positions of flow laminae in the tube or channel and are consistent with the use of very thin channels and the maintenance of continuous laminar flow.

ACKNOWLEDGMENT

I acknowledge the help of Mr. Min-Kuang Liu in producing the results shown in Figure 8 and Dr. Steve Williams for critically reading the manuscript.

GLOSSARY

A_f	frit area
$A(z)$	frit area to position z
b	channel breadth
f	frit inlet substream
f_s	fraction of total channel flow rate entering through sample substream
H	plate height
L	channel length
L_e	length of endpiece
s	sample inlet substream
s	shear rate
s_0	shear rate at wall
t_r	retention time
v	local flow velocity
$\langle v \rangle$	average local flow velocity
V_{inj}	volume of sample injection loop
$\dot{V}$	channel flow rate
$\dot{V}_f$	flow rate of frit inlet substream
$\dot{V}_s$	flow rate of sample inlet substream
w	channel thickness
x_s	splitting plane elevation
x_{sf}	final position of splitting plane
z_i	axial position on frit

Greek Characters

β	channel breadth b divided by length L_e of endpiece
σ_t^2	time-based variance
σ_V^2	volume-based variance

LITERATURE CITED

(1) Hovingh, M. E.; Thompson, G. E.; Giddings, J. C. *Anal. Chem.* **1970**, *42*, 195.
(2) Yang, F. J.; Myers, M. N.; Giddings, J. C. *Anal. Chem.* **1977**, *49*, 659.
(3) Giddings, J. C.; Myers, M. N.; Caldwell, K. D.; Fisher, S. R. *Methods of Biochemical Analysis*; Glick, D., Ed.; John Wiley: New York, 1980; Vol. 26, pp 79–136.
(4) Giddings, J. C. *Sep. Sci. Technol.* **1989**, *24*, 755.
(5) Lee, S.; Myers, M. N.; Giddings, J. C. *Anal. Chem.* **1989**, *61*, 2439.
(6) Giddings, J. C. *Anal. Chem.* **1985**, *57*, 945.
(7) Giddings, J. C.; Lin, H. C.; Caldwell, K. D.; Myers, M. N. *Sep. Sci. Technol.* **1983**, *18*, 293.
(8) Segrè, G.; Silberberg, A. *Nature* **1961**, *189*, 209.
(9) Saffman, P. G. *J. Fluid Mech.* **1965**, *22*, 385.
(10) Cox, R. G.; Brenner, H. *Chem. Eng. Sci.* **1968**, *23*, 147.
(11) Leal, L. G. *Annu. Rev. Fluid. Mech.* **1980**, *12*, 435.
(12) Giddings, J. C.; Chen, X.; Wahlund, K.-G.; Myers, M. N. *Anal. Chem.* **1987**, *59*, 1957.
(13) Giddings, J. C. *Dynamics of Chromatography*; Marcel Dekker: New York, 1965.
(14) Caldwell, K. D.; Brimhall, S. L.; Gao, Y.; Giddings, J. C. *J. Appl. Polym. Sci.* **1988**, *36*, 703.
(15) Jones, H. K.; Phelan, K.; Myers, M. N.; Giddings, J. C. *J. Colloid Interface Sci.* **1987**, *120*, 140.
(16) Giddings, J. C. *Sep. Sci. Technol.* **1985**, *20*, 749.
(17) Springston, S. R.; Myers, M. N.; Giddings, J. C. *Anal. Chem.* **1987**, *59*, 344.
(18) Tijssen, R.; Bos, J.; van Kreveld, M. E. *Anal. Chem.* **1986**, *58*, 3036.
(19) Afrornowitz, M. A.; Samaras, J. E. *Sep. Sci. Technol.* **1989**, *24*, 325.

RECEIVED for review July 16, 1990. Accepted July 20, 1990. This work was supported by Grant GM10851-32 from the National Institutes of Health.

Simultaneous Determination of Bruneaur–Emmett–Teller and Inverse Gas Chromatography Surface Areas of Solids

Hengchang Song and Jon F. Parcher*

Department of Chemistry, University of Mississippi, University, Mississippi 38677

Inverse gas chromatography, IGC, and mass spectrometric tracer pulse chromatography, MSTPC, were used concurrently to provide independent, but complementary, methods for the determination of adsorbent surface areas. Nitrogen at 77 K was used as the adsorbate in both procedures. The IGC technique involved the use of argon as the probe solute, whereas $^{15}N_2$ was used as the probe in the MSTPC method. The IGC method identifies the point of completion of a monolayer of adsorbed nitrogen and hence the surface area from the amount of adsorbed nitrogen required to change the primary retention mechanism for argon from gas–solid adsorption to gas–liquid partition in the adsorbed film of "liquid" nitrogen. The MSTPC method was used to determine the amount of nitrogen adsorbed. The experimentally measured adsorption isotherm data for N_2 at 77 K were fit to the classical BET equation to determine the surface area of different solids. The total surface area of the adsorbent in a packed GC, SFC, or HPLC column can be determined in situ, i.e., without unpacking or disturbing the column in any way. The two independent surface area measurements were carried out simultaneously on a given adsorbent to provide both theoretical and modelless values for the monolayer capacity. It was demonstrated that the IGC, MSTPC, and volumetrically measured surface areas (where available) agreed with an average relative deviation of <10% for a series of adsorbents including graphitized carbon blacks, silica, chemically bonded silicas, glass beads, and diatomaceous earth chromatographic adsorbents. In the case of the glass bead adsorbents, it was shown that the BET plot was not linear, whereas the IGC plots were linear and gave a more reliable surface area estimate. The method IGC was also used to determine the Henry's law constant of 0.10 atm for argon in liquid nitrogen at 77 K.

INTRODUCTION

Volumetric, gravimetric, and chromatographic methods have all been used successfully to determine the surface area of solids from the adsorption isotherms of nitrogen at 77 K by the classical BET (*1*) technique. Although the BET method is popular and useful for the measurement of surface areas, the theory does not represent an accurate adsorption model. There are several discrepancies in the model that have been discussed extensively in the literature (*2–4*). The major deficiencies in the model are the assumptions of (i) a planar, homogeneous surface and (ii) negligible solute–solute interactions in the adsorbed phase. The primary datum from the BET method is the monolayer capacity of an adsorbent, and this can be determined relatively accurately. However, this must be related to the surface area by a "size" parameter for the adsorbate. The accepted standard is nitrogen with an assumed size of 16 Å^2 at 77 K, although there is some controversy concerning the validity of this figure for all adsorbents.

Because of the uncertainties inherent in the BET method, several other procedures have been developed that do not depend upon a specific theoretical model for the estimation of the monolayer capacity of a solid adsorbent. One such technique was developed by Serpinet (*5*) in 1976. The method utilized inverse gas chromatography, IGC, to determine the monolayer capacity of *hydroxylated adsorbents for nonvolatile, high molecular weight "adsorbates"*. The method was based on the assumption that the dominant retention mechanism for a probe solute would change from adsorption to partition at the point of formation of a monolayer of stationary liquid phase as the liquid loading was varied from submonolayer to multilayer surface coverage. The monolayer capacity was determined graphically from the breakpoint in a plot of the retention volume of the probe solute versus the reciprocal of the weight of stationary liquid phase in each column. The size parameter, which could vary with orientation for the high molecular weight adsorbate, had to be determined from adsorption on well-characterized adsorbents. Another potential problem with this method is that the surface areas previously measured with nonvolatile, high molecular weight adsorbates have often been observed (*6, 7*) to be significantly lower than the surface area from BET measurements with nitrogen on the same adsorbent. Thus, the method must be limited to meso- and macroporous adsorbents with pores sizes (usually >60 Å) larger than the molecular size of the "adsorbates". One variant of this method eliminates the need for multiple columns but requires retention volume measurements for 8–10 temperatures above and below the melting transition of the liquid phase as well as prior knowledge of the value of the partition coefficient of the probe solute in the stationary liquid phase.

Although the modelless IGC methods avoid the theoretical problems of the BET method, the IGC methods also have the disadvantages and limitations already cited. An obvious solution to both the theoretical and practical problems of the BET and IGC methods would be the development of an IGC method using a small inert adsorbate (stationary liquid phase), such as nitrogen at 77 K.

Recently, mass spectrometric tracer pulse chromatography with labeled nitrogen as the probe was used to determine the BET surface areas of diverse adsorbates from nitrogen adsorption isotherms (*8*). It was observed in that investigation that the retention volume of argon varied with the amount of nitrogen adsorbed. It is the purpose of the present work to introduce an IGC method for the measurement of surface areas using argon as the probe solute with nitrogen at 77 K as the adsorbate. In this case, the BET and IGC measurements could be carried out simultaneously to yield both a theoretical value and a modelless value for the monolayer capacity of any adsorbent for nitrogen.

EXPERIMENTAL SECTION

The instrumentation and experimental procedures have been described in a previous publication (*8*). The experimental procedure was tracer pulse chromatography with a mass specific detector. Mixtures of nitrogen and helium with differing compositions were used as the carrier gas. A gaseous mixture of neon, argon, and labeled nitrogen, $^{15}N_2$, was injected with a gas sampling valve. The retention time of neon was used for the deadtime, t_0; the retention time of the labeled nitrogen was used to determine

0003-2700/90/0362-2313$02.50/0 © 1990 American Chemical Society

Table I. Description of Chromatographic Columns and Adsorbents

adsorbent material	particle size, μm	column dimens, mm	packing weight, mg
Carbopack A	180–250	100 × 3	150.0
Carbopack B	180–250	60 × 3	44.1
Carbopack C	150–180	400 × 3	831.3
silica	5	50 × 3	49.1
C_{18}-bonded silica	5	50 × 3	75.4
diol-bonded silica	5	50 × 3	40.3
cyano-bonded silica	5	50 × 3	59.6
glass beads	180–250	400 × 6.4	9320
Chromosorb P	180–250	300 × 3	304.2

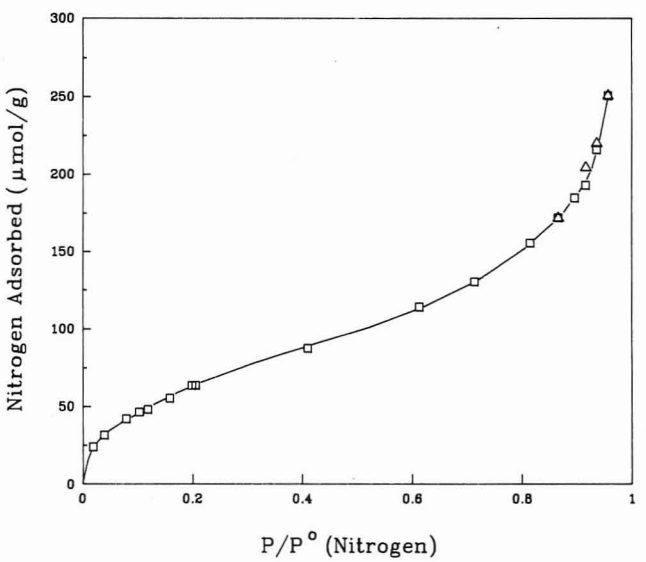

Figure 1. Adsorption isotherm of nitrogen on Chromosorb P at 77 K: (□) adsorption; (△) desorption.

the amount of nitrogen adsorbed, Γ; and the retention time of argon was used to calculate the retention volume of the IGC probe solute.

The surface area of the adsorbent was calculated from the linear form of the BET equation

$$\frac{P}{\Gamma(P^0 - P)} = \left(\frac{1}{C\Gamma_m}\right) + \frac{C-1}{C\Gamma_m}\left(\frac{P}{P^0}\right) \qquad (1)$$

where P and P^0 are the pressure of nitrogen in the column and the vapor pressure of liquid nitrogen at the column temperature, Γ_m is the monolayer capacity, and C is an empirical parameter that is related to the heat of adsorption and the shape of the isotherm in the region of monolayer formation.

The adsorbents used in the investigation are listed in Table I.

RESULTS AND DISCUSSION

Macroporous Adsorbent. The experimentally measured adsorption isotherm of nitrogen on Chromosorb P at 77 K is shown in Figure 1. The isotherm showed little or no hysteresis even at the highest pressures. The BET plot for this adsorbent was linear over the range $0.02 \leq P/P^0 \leq 0.40$ and gave a calculated surface area of 5.4 m^2/g.

Figure 2 shows the IGC retention volume data for argon on Chromosorb P as a function of the amount of nitrogen adsorbed, which was determined from the retention volume of the MSTPC probe, $^{15}N_2$. The plot shows two distinct regions corresponding to the two predominant retention mechanisms, e.g., adsorption and partition. From the BET plots for nitrogen, it was calculated that a monolayer of nitrogen was formed at about 56 μmol/g (marked with an arrow in the figure). At surface coverages of less than 56 μmol/g, the retention mechanism was predominantly adsorption of

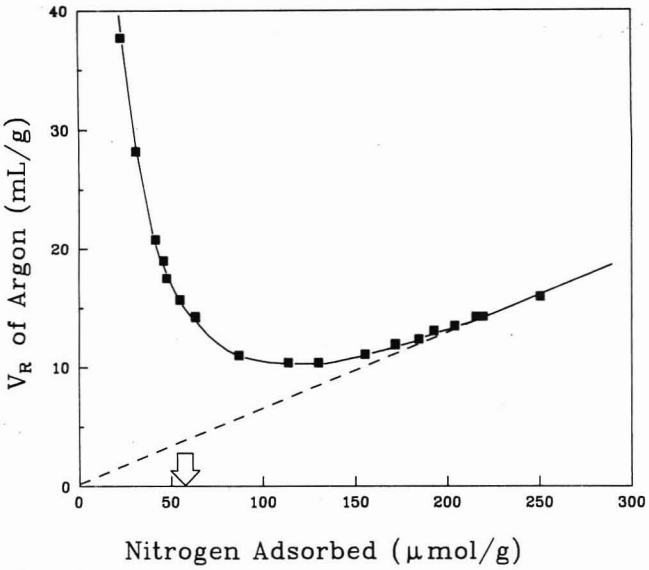

Figure 2. Retention volume of argon on Chromosorb P with preadsorbed nitrogen at 77 K: (■) experimental data; (– – –) Henry's law line for argon in N_2.

argon on the exposed solid surface. The retention volume decreased as the amount of adsorbed nitrogen increased because the nitrogen effectively blocked the surface for argon adsorption. At surface coverages higher than 150 μmol/g, the retention mechanism was primarily *partition of argon into the adsorbed, liquidlike layer of nitrogen*, i.e., simply gas–liquid partition chromatography with adsorbed nitrogen as the stationary liquid phase. The retention volume of argon increased directly with the amount of nitrogen adsorbed. Thus, the overall retention equation would have the form

$$V_{R_i} = K_{s_i} v \Gamma + K_{A_i}(1-\theta)A_s \begin{cases} K_{A_i} > 0 \text{ for } \theta < 1 \\ K_{A_i} = 0 \text{ for } \theta \geq 1 \end{cases} \qquad (2)$$

where K_s is the partition coefficient for solute i in liquid nitrogen, v is the molar volume of liquid nitrogen, K_A is the adsorption coefficient of solute i on the adsorbent, θ is the fractional surface coverage of the solid adsorbent by nitrogen, and A_s is the surface area of the adsorbent. The dashed line in the figure represents the calculated linear regression line for the data at the highest surface coverage (>200 μmol/g). The value of $K_{s_i} v = 64$ L/mol was determined from the slope of this line. No previous value for this solubility "parameter" was found in the literature. This type of solubility measurement would be difficult to achieve with classical volumetric or gravimetric procedures because the volatility of the solvent, N_2, *was greater than that of the solute*, Ar. In fact, 77 K is below the *melting* point of solid argon. This measurement can be performed chromatographically because of the inherent capability to operate in the "infinite dilution" region of the partition isotherm of argon in liquid nitrogen.

Several authors (*9–13*) have suggested that one way to determine the separate contributions to a complex retention mechanism was to plot the data in the form of reciprocals. That is, eq 2 can be rearranged to give

$$\frac{V_{R_i}}{\Gamma} - K_{s_i} v = \frac{-K_{A_i} A_s}{\Gamma_m} + K_{A_i} A_s \left\{\frac{1}{\Gamma}\right\} \qquad (3)$$

where $\Gamma_m = \Gamma/\theta$ is the monolayer capacity required for the surface area calculations. The full equation would only hold for the range $\Gamma \leq \Gamma_m$, i.e. $K_A = 0$ for $\Gamma \geq \Gamma_m$. The value of Γ_m can be determined from a plot of $\{V_{R_i}/\Gamma - K_{s_i} v\}$ vs $1/\Gamma$ for values of $\Gamma \leq \Gamma_m$. Such a plot is shown in Figure 3 for the Chromosorb P adsorbent. As is commonly observed, the plot was not perfectly linear at high values of $1/\Gamma$; however, linear

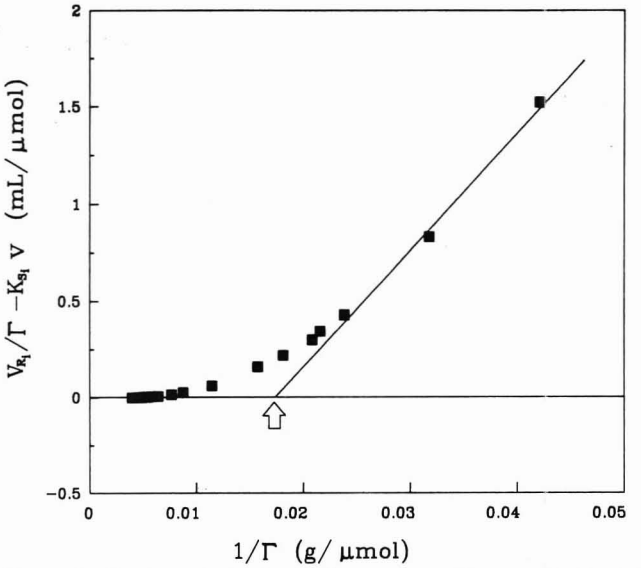

Figure 3. Reciprocal plot (eq 3) for argon on Chromosorb P: (■) experimental data; (—) linear regression results. The arrow shows the monolayer capacity calculated from the BET equation.

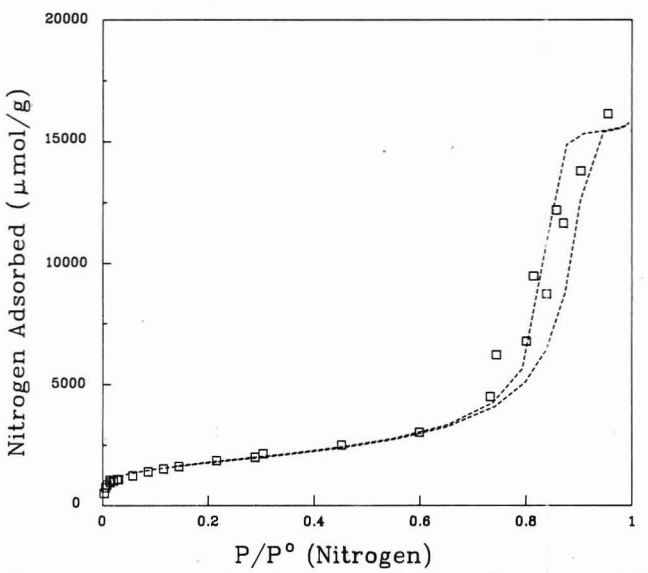

Figure 4. Adsorption isotherms of nitrogen on 5-μm silica at 77 K: (□) experimental data; (---) volumetric data (*14*).

regression of the data in the range $0.5 \leq \{V_{R_i}/\Gamma - K_{s_i}v\} \leq 2.0$ gave a value for Γ_m of 58.3 μmol/g at $\{V_{R_i}/\Gamma - K_{s_i}v\} = 0$ and a surface area of 5.6 m^2/g, which agreed with the BET value of 5.4 m^2/g. The value of Γ_m was determined from the intercept on the abscissa, rather than the ratio of the slope and ordinate intercept, in order to emphasize the graphic interpretation and empiricism of the analysis.

Mesoporous Adsorbents. The full adsorption isotherm of nitrogen on a 5 μm silica stationary phase over a range of relative pressures from 0.01 to 0.95 is shown in Figure 4, along with independently measured (*14*) volumetric data. The BET surface area was determined to be 148 m^2/g, and the volumetric measurements (*14*) gave values of 151 and 155 m^2/g for duplicate analyses. A significant hysteresis loop, which is characteristic of mesoporous adsorbents, was observed at the higher pressures. The MSTPC measurements were not reliable in this region due to the pressure drop across the column. A plot of the data in the form for IGC analysis is shown in Figure 5. Again, the plot was linear in the range $0.5 \leq \{V_{R_i}/\Gamma - K_{s_i}v\} \leq 2.0$, and the calculated surface area was 141 m^2/g, which is in agreement with the BET values. The IGC method provides an independent means for surface area measurement, which agrees with both chromatographic and

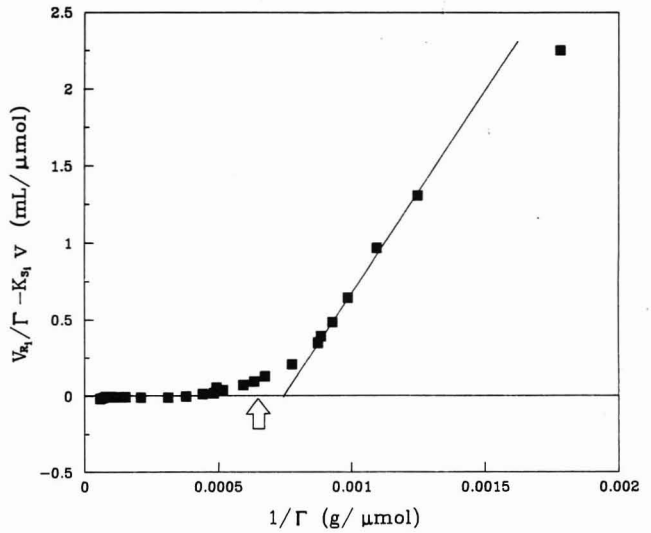

Figure 5. Reciprocal plot for argon on silica.

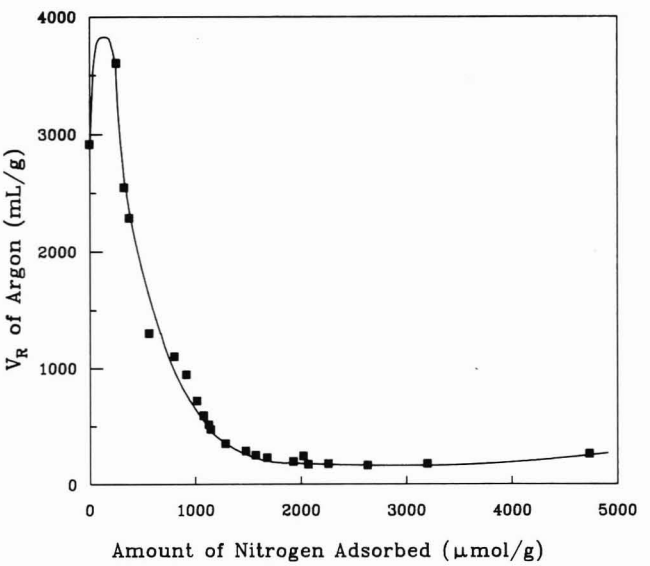

Figure 6. Retention volume of the IGC probe, argon, on silica.

static BET results well within the ±10% figure commonly cited for the uncertainty of the BET method (*2*).

The data plotted in the more common form of V_R(argon) vs Γ(nitrogen) on silica are illustrated in Figure 6 and show a maximum in the retention volume at very low surface coverage. Such maxima have been observed previously with both volatile (*15*, *16*) and nonvolatile (*17*, *18*) adsorbates on graphitized carbon black adsorbents. The postulated cause of the maximum is enhanced adsorption and retention at low surface coverages due to solute–adsorbate–adsorbent (three-body) interactions, which are completely neglected in the BET model as well as the retention model represented by eq 2.

Three chemically bonded stationary phases, e.g., diol-, cyano-, and octadecyl-bonded silica, were studied in the same manner. Figure 7 shows the retention volume data for argon on all four silica-based SFC adsorbents plotted in the form of the retention volume of argon as a function of the total amount of nitrogen adsorbed. The observed coincidence of the curves at high surface coverage confirms the supposition that the primary retention mechanism for the nitrogen-coated adsorbents was partition of argon into the adsorbed layer of condensed nitrogen. Thus, the retention volume of argon should be proportional to the amount of nitrogen adsorbed and *independent of the type of adsorbent* for multilayer adsorption of nitrogen. The straight line in Figure 7 had a measured slope of 66 L/mol, which gave a calculated Henry's law constant of 0.10 atm.

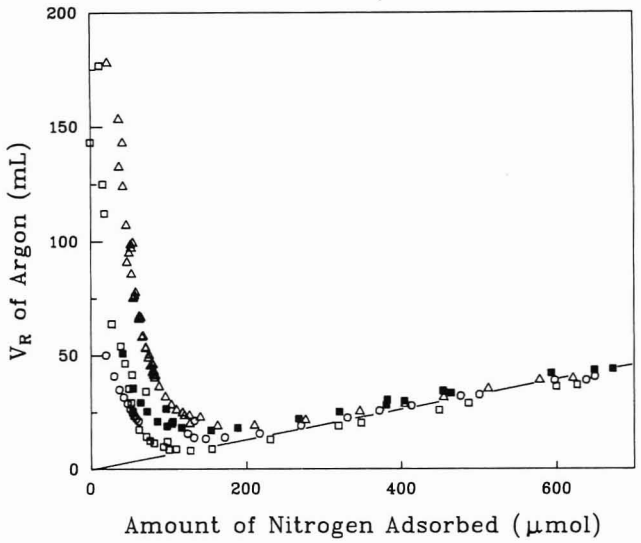

Figure 7. Retention volume of argon on silica-based adsorbents: (□) silica; (■) C_{18}-silica; (△) diol-silica; (○) cyano-silica; (—) linear regression for ≥300 μmol adsorbed.

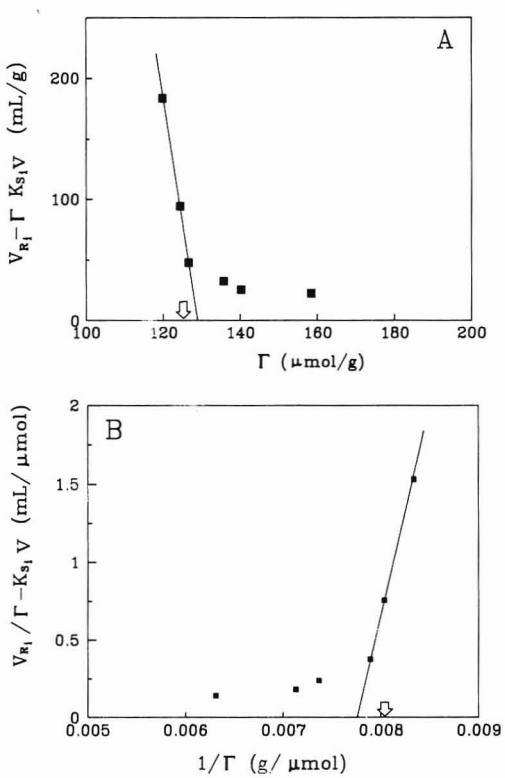

Figure 8. Retention volume (A) and reciprocal plot (B) of the IGC probe, argon, on Carbopack A.

The diol-bonded silica gave a chromatographic BET surface area of 241 m^2/g and an IGC surface area of 222 m^2/g. For the cyano-bonded silica the results were 112 and 122 m^2/g for the BET and IGC methods, respectively. Similar results, e.g., 94 and 106 m^2/g, were observed for the octadecyl-bonded silica. In this case, the same material had been determined by volumetric analysis to have a BET surface area of 89 and 98 m^2/g for duplicate analyses (*14*).

Nonporous Adsorbents. Similar experiments were carried out for three graphitized carbon black adsorbents, e.g., Carbopacks A, B, and C. The results for the retention volume of argon on Carbopack A and the IGC analysis are shown in Figure 8 for six relative pressures of nitrogen in the range $0.02 \leq P/P^0 \leq 0.20$. In this range the BET plot was linear with a calculated monolayer capacity of 124 μmol/g and surface area of 12.0 m^2/g (*8*). The retention volume of the argon probe

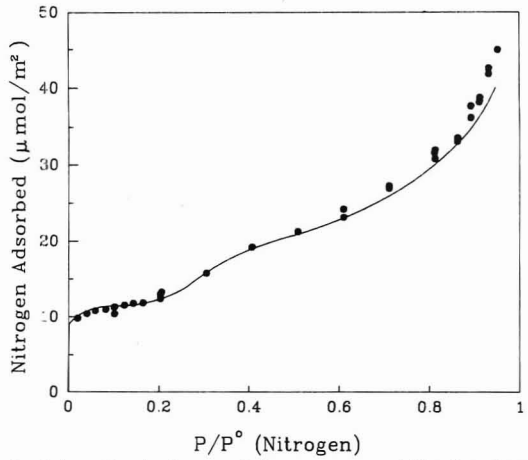

Figure 9. Adsorption isotherm of nitrogen on graphitized carbon black (Carbopack C) at 77 K: (●) experimental data; (—) Avgul and Kiselev (*19*).

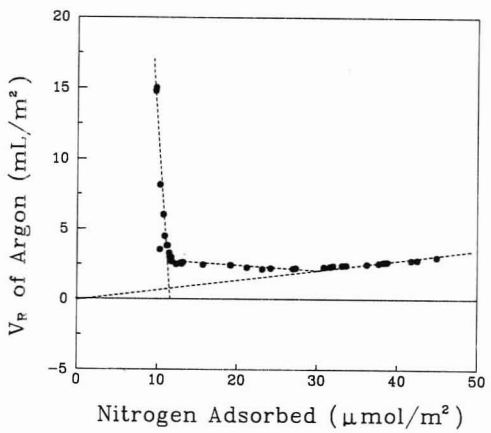

Figure 10. IGC plot for argon of Carbopack C with preadsorbed nitrogen.

decreased linearly with surface coverage for the lowest surface coverages, as shown in Figure 8A. This is in agreement with the retention volume equation for IGC probe i on a liquid-modified solid adsorbent. Extrapolation of the linear portion of the plot at low Θ to $V_{R_i} - K_{s_i} v\, \Gamma = 0$ gives the monolayer capacity. In this case, the calculated value was 129 μmol/g, which gave a surface area of 12.4 m^2/g. The reciprocal plot is shown as Figure 8B, and the surface area measured from regression of the data in this form gives the same value of 12.4 m^2/g.

The surface area for one batch of Carbopack B was also determined by the same method. The measured BET surface area was 80 m^2/g, whereas the ICG linear extrapolation produced a value of 82 m^2/g.

Carbopack C was investigated more extensively due to the popularity of this adsorbent. The adsorption isotherm of nitrogen is shown in Figure 9 along with previously measured data published by Avgul and Kiselev (*19*). The very sharp "knee" in the isotherm indicates the clean formation of a distinct monolayer of nitrogen at 9–10 μmol/m^2. The BET analysis gave a surface area of 9.1 m^2/g with a large *C* value of 340, also indicative of the sharp knee. The IGC analysis gave a surface area of 10.0 m^2/g, which agreed within 10% of the BET area.

The IGC plot for this adsorbent is shown in Figure 10 and clearly demonstrates a third type of retention mechanism in addition to adsorption on uncovered support and partition into the bulk liquid nitrogen. In the range 10–30 μmol/m^2 of nitrogen adsorbed, i.e., in the region of formation of the second and third layers of adsorbed nitrogen, the retention volume of argon was constant or diminished slightly with

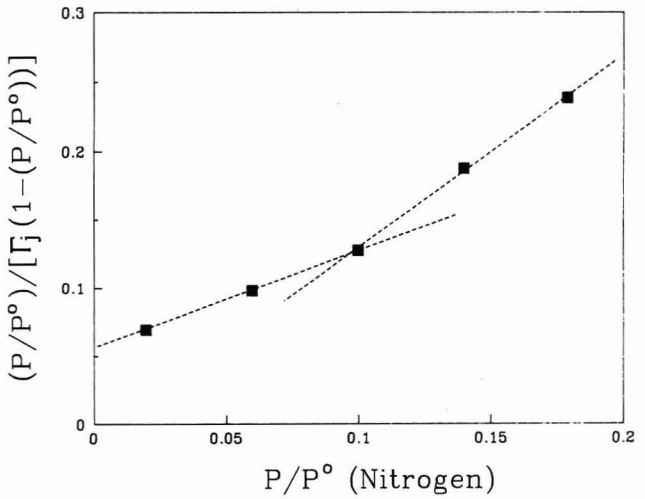

Figure 11. BET plot for nitrogen on glass beads at 77 K.

increasing amount of nitrogen adsorbed. This indicates that the solubility of argon in (or the adsorption of argon on) the second and third adsorbed layers was *slightly greater than* in the bulk liquid nitrogen. That is, another term would need to be added to eq 2 with a different K value for the presumably oriented second and third layers. The contribution of this mechanism would decrease with the amount of nitrogen adsorbed because the structured character of these layers was progressively destroyed until all of the adsorbed nitrogen acted as bulk liquid at high loadings. Thus, this exceptionally simple system, e.g., nitrogen/argon/carbon at 77 K, displays very complex retention mechanisms including cooperative and competitive gas–solid adsorption, gas–liquid partition, and an uncertain mechanism involving the interaction of argon with a very thin film of adsorbed nitrogen only two to three molecular diameters thick. The simple BET equation is not adequate for this system, and a full retention volume equation would require at least four terms, *two increasing with* Γ *(cooperative adsorption and partition) and the other two decreasing with* Γ *(competitive adsorption).* This type of complex retention mechanism has been observed for other "simple" systems involving volatile solutes and nonvolatile "adsorbates" on silica (*20*) and alumina (*21*).

The nitrogen isotherm was also measured for a batch of glass beads with a nominal surface area of 0.01–0.1 m^2/g. The BET plot for these beads is shown in Figure 11. The plot was not linear even over the nearly ideal range of $0.02 \leq P/P^0 \leq 0.2$, and the calculated surface areas ranged from 0.07 m^2/g at the high-pressure range to 0.12 m^2/g at the low-pressure range. On the other hand, the IGC plot (eq 2) was linear over the range $0.2 \leq \{V_{R_i}/\Gamma - K_{s_i}v\} \leq 2.0$ and gave a calculated surface area of 0.14 m^2/g. This is an example where the complementary IGC method provided an independent surface area measurement in a case where the classical BET analysis was unsatisfactory.

CONCLUSIONS

MSTPC and IGC methods can be combined to give two independent estimates of the amount of nitrogen or other adsorbate required to form a monolayer on a solid surface and thus the surface area of the solid. The MSTPC method produces a multipoint isotherm, which can be regressed to the BET model or used to determine the so-called "point B" of the isotherm. The IGC method measures the amount of adsorbate that must be adsorbed to change the retention mechanism for an IGC probe, such as argon, from adsorption on uncoated adsorbent surface to partition in "liquid" adsorbate when multilayer adsorption occurs. One method depends upon a theoretical model; the other method is empirical. The methods are independent, but complementary. In most cases, both methods give the same surface area within experimental uncertainty. However, in the case where one method is unreliable, the other method will usually provide a better estimate of the adsorbent surface area.

The advantages of this dual method over other chromatographic techniques for the measurement of solid surface areas are as follows:

The primary experimental data are retention times not peak areas. No detector calibration or blanks are required.

The experimental systems remain isothermal and isocratic (for a data point). The baseline and flow rate disturbances associated with adsorption (cooling) and desorption (heating) cycles and breakthrough curves are avoided.

The surface areas of adsorbents in packed HPLC, SFC, or GC columns can be measured in situ. A large pressure drop across a packed column will degrade the accuracy of the BET method but has little or no effect on the IGC measurements.

Any combination of adsorbates and probes could be used; however, nitrogen, argon, and krypton are the most convenient probes and adsorbates. Both methods, IGC and BET, measure only the monolayer capacity. An accurate size parameter for the probe adsorbate is required for the determination of surface areas.

The methods are fast, simple, and accurate. However, a mass-specific detection system and labeled isotopic solutes are required for the MSTPC procedure.

Registry No. Ar, 7440-37-1; N_2, 7727-37-9.

LITERATURE CITED

(1) Bruneaur, S.; Emmett, P. H.; Teller, E. *J. Am. Chem. Soc.* **1938**, *60*, 309.
(2) Gregg, S. J.; Sing, K. S. W. *Adsorption, Surface Area and Porosity*; Academic Press: New York, 1982.
(3) Ross, S.; Oliver, J. P. *On Physical Adsorption*; Interscience: New York, 1964.
(4) Steele, V. A. *The Interaction of Gases with Solid Surfaces*; Pergamon Press: New York, 1974.
(5) Serpinet, J. *J. Chromatogr.* **1976**, *119*, 483.
(6) Dyer, A.; Leigh, D.; Sharples, W. E. *J. Chromatogr.* **1976**, *118*, 319.
(7) Tremaine, P. R.; Wikjord, A. G.; LeBlanc, J. C. *Can. J. Chem.* **1982**, *60*, 2859.
(8) Song, H.; Strubinger, J. R.; Parcher, J. F. *J. Chromatogr.* **1990**, *518*, 319.
(9) Conder, J. R.; Locke, D. C.; Purnell, J. H. *J. Chromatogr.* **1969**, *73*, 700.
(10) Conder, J. R.; Young, C. L. *Physicochemical Measurements by Gas Chromatography*; Wiley-Interscience: New York, 1979.
(11) Komaita, T.; Naito, K.; Takei, S. *J. Chromatogr.* **1975**, *114*, 1.
(12) Naito, K.; Takei, S. *J. Chromatogr.* **1980**, *190*, 21.
(13) Moriguchi, S.; Takei, S. *J. Chromatogr.* **1985**, *350*, 15.
(14) Micromeritics, Inc., Atlanta, GA.
(15) Hyver, K. J.; Parcher, J. F. *Anal. Chem.* **1984**, *56*, 274.
(16) Parcher, J. F.; Johnson, D. M. *J. Chromatogr. Sci.* **1985**, *23*, 459.
(17) Bruner, F.; Ciccioli, P.; Crescentini, G.; Pistolesi, M. T. *Anal. Chem.* **1973**, *45*, 1851.
(18) Di Corcia, A.; Liberti, A. In *Advances in Chromatography*; Giddings, J. C., et al., Eds.; Marcel Dekker: New York, 1976; Chapter 7.
(19) Avgul, N. N.; Kiselev, A. V. In *Chemistry and Physics of Carbon*; Walker, P. L., Ed.; Marcel Dekker: New York, 1970.
(20) Naito, K.; Sagara, T.; Takei, S. *J. Chromatogr.* **1990**, *503*, 25.
(21) Naito, K.; Ohwada, N.; Moriguchi, S.; Takei, S. *J. Chromatogr.* **1985**, *330*, 193.

RECEIVED for review April 9, 1990. Accepted July 30, 1990. Acknowledgment is made to the National Science Foundation for support of this work.

Prediction of Gas and Liquid Chromatographic Retention Indices of Polyhalogenated Biphenyls

M. N. Hasan and P. C. Jurs*

Department of Chemistry, 152 Davey Laboratory, The Pennsylvania State University, University Park, Pennsylvania 16802

Gas chromatographic and liquid chromatographic retention indices of polyhalogenated biphenyl compounds are successfully modeled by using descriptors derived directly from the molecular structures. A five-variable regression equation with $R^2 = 0.989$ and relative standard deviation of 2.2% was generated for the GC retention indices of 53 PHBs. A five-variable regression equation with $R^2 = 0.968$ and relative standard deviation of 8.5% was generated for the LC retention indices of 53 PHBs. The descriptors found to be important are analyzed.

INTRODUCTION

Halogenated biphenyls are a group of chemical compounds formed by substituting hydrogen in biphenyl with one of the halogens. In theory, there are 209 possible congeners for each series of halogenated biphenyl. However, the compounds which have received the most attention from environmental chemists and toxicologists are the chlorinated biphenyls (PCBs). Their chemical inertness and other desirable physical properties have made the PCBs a versatile chemical product with many industrial applications (*1*). However, due to indiscriminate use and improper disposal, PCBs have become one of the most widely spread environmental contaminants. Because of their persistence, they are still considered a major threat to the environment, despite the fact that their production has long been banned.

On the other hand, the other halogenated biphenyls such as polybrominated biphenyls (PBBs) are not as persistent as PCBs. Thus, their toxicology and environmental impact have not been as extensively studied as with PCBs. However, an accidental poisoning of dairy cattle and other farm animals in Michigan (*2*, *3*), led to more studies on the environmental effects and analytical methods for determination of PBBs (*4*, *5*).

One of the most commonly used methods of analysis for polyhalogenated biphenyls in environmental samples is high-resolution gas chromatography coupled with an electron-capture detector or mass spectrometer. Liquid chromatography is not as popular as GC for analysis of polyhalogenated biphenyls, probably due to the lack of sufficiently sensitive detectors. Nevertheless, it is still considered an important analytical method in the overall determination of halogenated biphenyls, especially for sample cleanup or fractionation prior to GC analysis. A discussion on analytical methods for analysis of PCBs has been given by Erickson (*6*).

Recently, Mullin et al. (*7*) reported the synthesis of all 209 PCBs and subsequent analysis using capillary GC. All but 11 pairs were completely separated. They noted some interesting trends in the elution order of PCB congeners which are very much influenced by their substitution pattern. Other reports also made the same generalization in the elution order of PCBs (*8–10*). For example, compounds containing ortho substituents generally have shorter retention times than those lacking ortho substituents. Retention increases as the degree of coplanarity increases. Coincidently, these so-called coplanar isomers have been shown to have higher toxicity (*11*, *12*) than the nonplanar isomers. Other researchers also find a similar trend in the elution order of other halogenated biphenyls (*4*, *5*).

Because of the high correlation between substitution pattern and retention characteristics of PCBs, a number of researchers have devised schemes for predicting the retention of PCBs from molecular structures (*13–15*). Some of these methods, however, were based on retention data measured on packed column GC. In our previous work on the prediction of retention characteristics of PCBs in capillary GC (*16*) we developed a very good equation for predicting retention using simple structural descriptors. It is desirable that a similar predictive equation be developed for all halogenated biphenyls.

Recently, Höfler et al. (*17*) described the separation of selected polyhalogenated biphenyls by both gas and liquid chromatography. In general the retention of GC and LC increases in the order F < Cl < Br < I. In each series (except for fluorinated biphenyls) there is also a good correlation between retention indices and molecular surface area. They also noted that this correlation is more significant in gas chromatography than in liquid chromatography.

The objective of the present work was to develop regression models to predict the retention of halogenated biphenyls using descriptors derived from the molecular structures. This is an extension of the previous work on PCBs (*16*). This study also includes the development of a regression model for liquid chromatography using the same methodology.

EXPERIMENTAL SECTION

Data Set. The data set consisted of 56 polyhalogenated biphenyls including 13 fluorinated, 22 chlorinated, 18 brominated, and 3 iodinated biphenyls (Table I). The gas and liquid chromatographic retention data for these compounds were taken from Höfler et al. (*17*). The GC retention data were measured on a 25 m × 0.25 mm DB-210-CB capillary column with film thickness of 0.2 μm. Retention characteristics of these compounds were expressed as Kovats retention indices. The retention index for one of the compounds, 3,3′,4,4′,5,5′-hexabromobiphenyl, was not available. Therefore, the GC retention data set consisted of 55 data points.

For the liquid chromatographic data, retention for all 56 compounds in the data set were obtained on an ODS (C_{18}) column using 100% methanol as the mobile phase. A retention index scale as described by Höfler et al. (*17*) was used. As with the Kovats retention index, the retention index of a compound is found by interpolation between flanking *n*-alkane standards.

Entry and Storage of Molecular Structures. The molecular structures were entered into the computer system by drawing them on the screen of a graphics display terminal. They were stored as connection tables for further processing.

Molecular Modeling. Since descriptors dependent on geometry were expected to be useful in modeling the retention properties of the compounds, it was necessary to obtain reasonable three-dimensional representations of the molecules. In previous studies involving PCBs (*16*), the molecules were modeled by using a force field molecular mechanics model builder with the torsional angles between the two phenyl rings being fixed using experimental values taken from the literature. It was expected that

0003-2700/90/0362-2318$02.50/0 © 1990 American Chemical Society

Table I. Polyhalogenated Biphenyls in the Data Set

no.	compound	no.	compound
1	2-fluorobiphenyl	27	2,3,4,5-tetrachlorobiphenyl
2	3-fluorobiphenyl	28	2,3,4,6-tetrachlorobiphenyl
3	4-fluorobiphenyl	29	2,3,5,6-tetrachlorobiphenyl
4	2,3-difluorobiphenyl	30	2,2′,4,4′-tetrachlorobiphenyl
5	2,4-difluorobiphenyl	31	3,3′,4,4′-tetrachlorobiphenyl
6	2,5-difluorobiphenyl	32	2,3,3′,4,5-pentachlorobiphenyl
7	2,6-difluorobiphenyl	33	2,2′,4,4′,5,5′-hexachlorobiphenyl
8	3,4-difluorobiphenyl	34	2,2′,4,4′,6,6′-hexachlorobiphenyl
9	3,5-difluorobiphenyl	35	decachlorobiphenyl
10	4,4′-difluorobiphenyl	36	2-bromobiphenyl
11	2,2′,4-trifluorobiphenyl	37	3-bromobiphenyl
		38	4-bromobiphenyl
12	2,3,5,6-tetrafluorobiphenyl	39	2,3-dibromobiphenyl
		40	2,4-dibromobiphenyl
13	decafluorobiphenyl	41	2,5-dibromobiphenyl
14	2-chlorobiphenyl	42	2,6-dibromobiphenyl
15	3-chlorobiphenyl	43	3,4-dibromobiphenyl
16	4-chlorobiphenyl	44	3,5-dibromobiphenyl
17	2,3-dichlorobiphenyl	45	4,4′-dibromobiphenyl
18	2,4-dichlorobiphenyl	46	2,4,5-tribromobiphenyl
19	2,5-dichlorobiphenyl	47	2,4,6-tribromobiphenyl
20	2,6-dichlorobiphenyl	48	3,4,5-tribromobiphenyl
21	3,4-dichlorobiphenyl	49	2,3,4,5-tetrabromobiphenyl
22	4,4′-dichlorobiphenyl	50	2,3,4,5-tetrabromobiphenyl
23	2,3,4-trichlorobiphenyl	51	3,3′,4,4′-tetrabromobiphenyl
		52	3,3′,5,5′-tetrabromobiphenyl
24	2,4,5-trichlorobiphenyl	53	3,3′,4,4′,5,5′-hexabromobiphenyl
		54	2-iodobiphenyl
25	2,4,6-trichlorobiphenyl	55	3-iodobiphenyl
		56	4-iodobiphenyl
26	3,4,5-trichlorobiphenyl		

Table II. Structural Parameters for Biphenyl

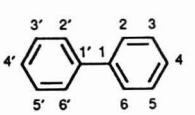

biphenyl

	expt[a]	this method	MNDO
$r(C_1–C_{1'})$	1.507	1.500	1.485
$r(C–C)_{ring}$	1.398	1.397	1.409
$r(C–H)$	1.102	1.090	1.090
$\angle C_6C_1C_2$	119.4	120.9	120.8
$\angle C_1C_2C_3$	119.4	119.0	120.4
torsional angle	44.4	44.0	76.1

[a] By electron diffraction (ref 18). All distances, r, are in Å and angles in degrees.

Table III. Structural Parameters for 2,2′-Dichlorobiphenyl

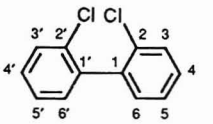

2,2′-dichlorobiphenyl

	expt[a]	this method	MNDO
$r(C_1–C_{1'})$	1.495	1.500	1.487
$r(C–C)_{ring}$	1.398	1.407	1.409
$r(C–Cl)$	1.732	1.753	1.754
$r(C–H)$	1.095	1.090	1.090
$\angle C_6C_1C_2$	–[b]	120.3	117.6
$\angle C_1C_2C_3$	–[b]	118.7	121.5
torsional angle	73.5	74	88

[a] By electron diffraction (ref 19). All distances, r, are in Å and angles in degrees. [b] Not quoted.

Table IV. Torsional Angles for Polyhalogenated Biphenyls

	torsional angle, deg
fluorinated biphenyls	
nonortho	44
one ortho substituent	56
two ortho substituents	65
chlorinated biphenyls	
nonortho	44
one ortho substituent	61
two ortho substituents	74
brominated biphenyl	
nonortho	44
one ortho substituent	63
two ortho substituents	n.e.[a]
iodinated biphenyl	
nonortho	44
one ortho substituent	64
two ortho substituents	n.e.[a]

[a] Not evaluated because there is no compound of this type in the data set.

the torsional angle for the fluorinated, brominated, and iodinated biphenyls would vary slightly from the PCBs due to differences in size. Unfortunately, structural data for most of these compounds were not readily available. Thus, the torsional angle had to be estimated with the molecular mechanics modeling approach.

Various methods have been used in the past to estimate the torsional angles of polyhalogenated biphenyls, including electron diffraction (*18*, *19*), X-ray diffraction (*20*), and photoelectron spectroscopy (*21*). In addition, theoretical methods using ab initio calculations (*22*) and molecular mechanics (MM2) (*23*, *24*) have also been used to estimate the structural parameters of polyhalogenated biphenyls. The approach taken in this study was to fix the angle in such a way that the distance between the two substituents at the opposing ortho positions just exceeds the sum of van der Waals radii of the two atoms.

Although this may appear to be a simplistic approach for estimating the torsional angle, preliminary experiments using a number of test compounds indicated that the structural parameters such as bond length, atomic distances, and torsional angles obtained by using this method agreed well with experimental and theoretical data. As examples, structural parameters for biphenyl (Table II) and 2,2′-dichlorobiphenyl (Table III) obtained by using this method are compared with structural data from the literature. Also shown are the results of molecular orbital calculations using MNDO (performed by using MOPAC molecular orbital package, version 5.0). As can be seen from the two tables, the atomic distances and the bond angles obtained by using this method did not differ very much from the experimental data. On the other hand, the torsional angles suggested by the MNDO calculation were consistently larger than the experimental values. Therefore, the simple method was employed to estimate the torsional angles of all compounds in the data set.

The results from this investigation suggested that, as far as the torsional angle is concerned, the halogenated biphenyls can be classified into three groups, depending on the number of substituents on the ortho position. The first group consisted of compounds that are not substituted at the ortho position, the compounds of the second group have one ortho substituent, and the compounds of the third group have two substituents. Also, as expected, the torsional angle increases from F to I as the van der Waals radii increase. A summary of torsional angles obtained from this investigation is shown in Table IV, and these are the angles used throughout this study.

Descriptor Generation. The molecular structure descriptors used to represent the molecules were generated by using the ADAPT software system (*25*). The descriptors can be classified into four major groups: topological, geometrical, electronic, and physicochemical descriptors. Topological descriptors include fragment descriptors, molecular connectivity indices, substructure counts, and substructure environment descriptors. Geometric descriptors include principal moments of inertia, van der Waals volume and surface area, and shape parameters. Electronic descriptors include partial charges, dipole moments, etc. Calculated

physical property descriptors include calculated log P, molecular polarizability, etc.

Recently, Kier (*26*) has developed a set of topological indices based on a graph theoretical approach to encoding the shape of molecules. These kappa indices are defined as

$$^{n}\kappa = (C \cdot {}^{n}P_{max} \cdot {}^{n}P_{min}) / ({}^{n}P_{i})^{2}$$

where $^{n}\kappa$ is the kappa index of order n, C is a constant ($C = 2$ for $n = 1$ and $n = 2$, and $C = 4$ for $n = 3$), $^{n}P_{max}$ and $^{n}P_{min}$ are the maximum and minimum number of paths of length n in a molecule with the same number of atoms as the target molecule, and $^{n}P_{i}$ is the actual number of paths of length n in the target molecule. As an example, consider the simple molecule 2-methylpentane. For this molecule, $^{2}P_{min} = 4$ (obtained from the straight-chain graph), $^{2}P_{max} = 10$ (obtained from the star graph), $^{2}P_{i} = 5$ (obtained from the structure itself), and $C = 2$, so $^{2}\kappa = 3.2$. Also, $^{3}P_{min} = 3$ (obtained from the straight-chain graph), $^{3}P_{max} = 4$ (obtained from the graph of 2,3-dimethylbutane), $^{3}P_{i} = 3$ (obtained from the structure itself), and $C = 4$, so $^{3}\kappa = 5.333$. For one of the members of the present data set, 2,3,3′,4,5-pentachlorobiphenyl, $^{2}\kappa = 5.325$ and $^{3}\kappa = 2.713$. While these kappa indices are simply related to molecular structure, they are best calculated with software due to the tedious nature of the computation, especially for larger structures.

Shadow area descriptors (*27*) are cross-sectional areas of the three-dimensional molecular models of the structures projected onto three mutually perpendicular planes. The descriptor values are highly dependent on the orientation of the molecular structures prior to the calculation, so a systematic technique for structure orientation is an essential part of the development of these descriptors. Standardized shadow areas are computed by dividing the cross-sectional areas obtained above by the areas of the largest rectangle that can enclose the molecule in the relevant orientation.

A new set of electronic descriptors, capable of encoding the amount of partial charge on the atoms in a given molecule, was developed and applied to these structures. These charges are calculated by a variation of the method of Abraham and Smith (*28*). Essentially, it calculates the σ charges from atomic electronegativity and polarizability and the π charges from Hückel molecular orbital calculations. The σ and π charges were then added to give the total atomic charge for all atoms in the molecule. The method is iterative, and recalculates the partial charges repeatedly until convergence is obtained. Partial charges for the most positive and most negative atoms were also calculated as descriptors.

From a knowledge of the partial charge of each atom in the molecule and its molecular surface area, the charge-weighted surface area of the molecule can be calculated as a descriptor. In addition, descriptors encoding the total surface area of positively or negatively charged portions of the molecule can also be calculated. These types of descriptors are quite useful to model charge-dependent intermolecular interactions in some chemical environments (*29*).

After being generated, the descriptors were subjected to an objective feature selection procedure in which descriptors with insufficient variation or with high pairwise correlations with other descriptors were discarded. These procedures are objective in that the dependent variable values are never used in the analyses. The multicollinearity among the descriptors was reduced by selecting a pool of descriptors which gave maximum orthogonality. The descriptors were then used as dependent variables in multiple linear regression analysis.

Regression Analysis. Two types of variable selection methods were used to develop regression equations for predicting the retention indices. They were stepwise regression (*30*) and leaps and bounds regression (*31*). The stepwise routine was also run several times, where in each run two or more variables already in the equation were deleted, in order to expose potentially good models which might have been left out because of intercorrelations among the variables. The equations obtained were tested for their validity and robustness by using various standard statistical tests and plotting methods.

RESULTS AND DISCUSSION

Modeling of GC Retention Indices. A number of good models for modeling GC retention indices of polyhalogenated biphenyls can be developed by using the descriptors available. One of the best equations found is the following:

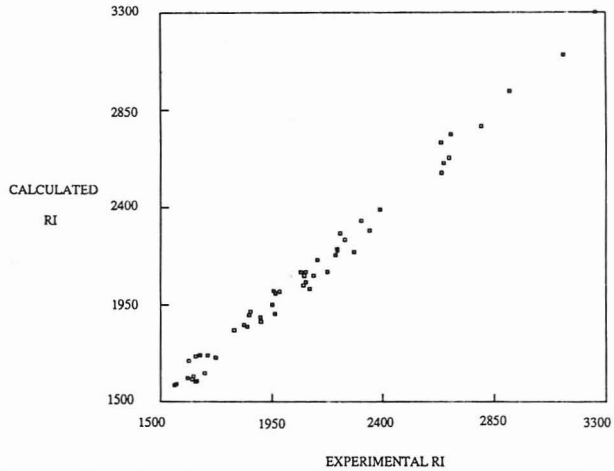

Figure 1. Calculated versus experimental gas chromatographic retention indices for 53 polyhalogenated biphenyl compounds using eq 1.

$$\begin{aligned} RI = {} & 125.4 \pm 17.3\ {}^{3}\chi_{p}^{v}\ \text{(path-3 connectivity index)} \\ & 3856 \pm 513\ \text{(std shadow area on } xy \text{ plane)} \\ & 3411 \pm 504\ \text{(std shadow area on } yz \text{ plane)} \\ & -302.7 \pm 36.0\ {}^{2}\kappa\ \text{(path-2 kappa index)} \\ & 28.0 \pm 3.3\ \text{(shadow area on } xz \text{ plane, Å}^2\text{)} \\ & -2297 \end{aligned} \quad (1)$$

$$n = 53 \qquad R^2 = 0.989 \qquad F(5,47) = 866 \qquad s = 45$$

The high value of R^2 and the F statistics indicates that this equation represents a very good model for calculating retention indices. Nearly 99% of the variance in the retention indices is accounted for by this equation. The standard error is about 45/2100 = 2.2% of the mean value of the retention index (RI) which is approaching the experimental errors of capillary GC measurements. The plot of calculated versus observed retention indices shown in Figure 1 indicates no deviation from linearity. Examination of the residuals indicates that they are normally distributed and the residual plot indicates that the error variance is constant.

The individual variables in the equation encode different aspects of the molecular structures. The variables in the equation encode different aspects of the molecular structures. The valence-corrected path-3 connectivity index, $^{3}\chi_{p}^{v}$, is a topological descriptor that encodes the size and degree of branching of the molecules. It contains corrections for the difference in the type of halogen in the molecules. The three shadow area descriptors were the two-dimensional projection of the molecules on xy, yz planes. Each area can also be normalized by dividing with the area of the rectangle defined by the maximum dimension of the projection. For this study, the molecules were oriented in such a way so that the bond connecting the two phenyl rings is parallel with the x axis and the ring with the most substituents is imbedded on the xy plane. The inclusion of these descriptors in the equation clearly indicates the importance of dispersion interactions related to molecular size in the retention mechanism. The path-2 kappa index is a topological index encoding the general shape of the molecule. It can be viewed as a ratio of the long dimension of the molecule to its shorter radial dimension (*26*).

This equation is considerably more complicated than the one previously developed for PCBs alone (*16*) in that it includes a number of more complex descriptors. This is a result of the more structurally diverse nature of the present data set, which contains all four halogens as substituents.

The correlation matrix of the variables in the equation shows the variables to be relatively uncorrelated. Examination

Table V. Experimental and Calculated Retention Indices

	GC/RI		LC/RI	
compound[a]	expt[b]	calcd[c]	expt[b]	calcd[d]
1	1627	1611	367	358
2	1654	1711	382	377
3	1651	1709	370	420
4	1672	1626	355	365
5	1604	1602	304	306
6	1636	1586	295	288
7	1622	1597	223	191
8	1609	1683	347	382
9	1636	1703	382	314
10	1684	1709	227	298
11	1558	1575	228	264
12	1639	1587	212	150
13	1550	1570	278	295
14	1717	1699	442	424
15	1845	1844	578	497
16	1853	1896	521	489
17	1957	1903	540	630
18	1897	1887	605	585
19	1900	1866	559	583
20	1832	1851	415	467
21	2082	2049	706	678
22	2113	2079	583	629
23	2170	2097	732	789
24	2098	2018	817	753
25	1952	2007	700	658
26	2278	2189	891	865
27	2339	2202[e]	978	922
28	2209	2203	832	796
29	2203	2174	794	774
30	2241	2246	682	786
31	2632	2557	871	923
32	2670	2736	982	1007
33	2662	2627	977	1003
34	2784	2520[e]	916	332
35	3254	3295	1523	1508
36	1792	1827	480	484
37	1947	1944	633	571
38	1959	1997	606	557
39	2129	2151	624	699
40	2076	2079	728	694
41	2073	2035	669	706
42	1975	2005	494	615
43	2307	2335	761	787
44	2211	2195	882	766
45	2341	2288	703	759
46	2383	2387	923	887
47	2221	2276	832	792
48	2640	4602	1000	964
49	2792	2773	1053	1035
50	2630	2697	939	966
51	3124	3099	996	1097
52	2907	2933	1031	1025
53	–[f]	3722	1365	1323
54	1858	1913	483	–[g]
55	2062	2094	663	–[g]
56	2082	2096	640	–[g]

[a] The compounds are numbered as in Table I. [b] From ref 17. [c] Using eq 1. [d] Using eq 2. [e] Suspected outliers. [f] Not available. [g] Charge-weighted surface area descriptors were not available for these compounds.

of the variance inflation factors for the five variables, showed that no serious multicollinearity exists among the variables.

The retention indices calculated by using eq 1 are listed in Table V. In general, the calculated values agree well with the observed RI, indicating high validity of the equation. Note that two observations, compounds **27** and **34** were not included in developing the equations because they were suspected outliers. Both observations had residuals of greater than 3 standard deviations and one of them (compound **34**) also has a high leverage on the regression line. No explanation is available as to why these two compounds have very high residuals. However, if included in developing the equations, these observations will pull the regression line away from the rest of the observations and undoubtedly will produce an inappropriate model for the system being studied. Furthermore, with the two observations left out, the standard error decreased by 20%.

Table VI. Statistics for GC Retention Index Equations Produced by Omitting One Halogen Group

group omitted	n	R^2	s
fluorine	40	0.988	43.6
chlorine	33	0.992	41.0
bromine	36	0.986	49.4
iodine	50	0.990	45.4

In order to validate the equation, a number of internal validation procedures were performed. First, a jackknife analysis was performed in which one observation was left out one at time and a regression equation was developed with the remaining observations. When the predicted values were compared with the observed values, a root mean square error of 51 was obtained. This in not very large compared to the standard error of the full model, indicating the regression line is quite stable over the sample space.

In the second validation experiment, the data set was divided into two sets, each containing half the number of observations. The division was performed by using the Duplex algorithm of Snee (*32*) to ensure that the two halves have similar statistical properties. A regression equation was fitted by using 27 compounds in one of the training sets, and it was used to predict the retention indices of compounds in the second set. Although it was developed by using only half the number of observations, this equation still showed a high degree of statistical significance comparable to the equation developed by using all the observations. This equation was then used to predict the retention indices of the remaining 26 compounds. For all 26 compounds, the observed retention indices were within the prediction interval of the predicted values. This clearly implies that the equation is stable over the sample space and can be used to predict the retention indices of compounds not included in developing the equation.

The majority of the descriptors which appeared in the GC retention index equations were geometric descriptors. Only the path-3 connectivity index is corrected for the type of halogen substituents, and it was the first variable selected in the equation. In order to show the effects of any particular halogen group on the overall quality of the equation, several subsets were created by omitting one halogen group from the data set. Regression equations were then fitted by using each of these subsets and the statistics were compared with those of the original equation (Table VI). Judging from the values of R^2 and standard error of the resulting equations, none of the equations was significantly inferior to the original equation. This was also the case when individual coefficients were compared. Thus, it can be concluded that the overall equation was not affected by the type of halogen substitution.

Modeling of LC Retention Indices. Several equations were evaluated for the calculation of liquid chromatographic retention indices. One of the best equations is the following:

$$\begin{aligned} RI = {} & -66511 \pm 3646\ (\text{fraction of positively charged SA}) \\ & -2469 \pm 455\ (\text{fraction of negatively charged SA}) \\ & -72.9 \pm 18.8\ (\text{number of ortho substituents}) \\ & 3351 \pm 954\ (\text{relative positive charge}) \\ & -15.8 \pm 7.0\ (^3\kappa)^3\ (\text{path-3 kappa index})^3 \\ & 840.2 \end{aligned} \qquad (2)$$

$$n = 53 \quad R^2 = 0.968 \quad F(6,48) = 285 \quad s = 55$$

The R^2 shows that almost 97% of the variance is accounted for by this equation and the standard error is about 55/650 = 8.5% of the mean value of the RI. The correlation matrix of the descriptors in this equation showed no high pairwise correlations. None of the variance inflation factors for these descriptors were large. The statistics for this equation, however, were not as good as the ones for the GC retention indices. This is understandable since it is generally more difficult to model the LC retention because more factors and interactions are involved.

The first variable in the equation is the surface area of positively charged atoms in the molecule divided by the total surface area. The values of this descriptor are affected by the number and type of substituents on the phenyl rings. The negative sign of the coefficient indicates that retention indices increase as the fraction of positively charged area in the molecule decreases. This is probably caused by an increase in the number of halogens in the molecule, since the halogens have negative partial charges. However, as observed by Höfler et al. (*17*), not every increment in the degree of substitution is accompanied by an increase in retention. The second variable, fraction of negatively charged surface area, probably served as a correction factor for this effect. The third variable is the number of halogens at the ortho position. The presence of substituents at this position causes a decrease in the retention indices. The relative positive charge descriptor is the charge of the most positive atom in the molecule divided by the total charge of the molecule. The final variable, $^3\kappa$, the path-3 kappa index, is a topological descriptor encoding the general shape of the molecules.

The charge-weighted surface area descriptors consistently appeared in several potential equations evaluated. This was expected since molecular surface area has been shown to be an important descriptor in modeling solubilities of hydrophobic compounds. However, the retention indices of fluorinated biphenyls do not correlate well with total surface area of the molecule. This is probably caused by interactions at specific sites with the solvent sites with the solvent methanol. The increase in total area of the molecule does not compensate for the increase in partial negative charges. The charge-weighted surface area descriptors were probably more effective to encode the presence of such interactions.

The descriptors contained in this equation are relatively complex. This is due to the complex nature of the interactions involved in retention in liquid chromatography. The charged partial surface area descriptors, which are contributing in a major way to the success of this equation, have been shown in a number of structure–property relationship studies to encode important structural information (*29*).

The calculated retention indices are compared with experimental values in Table V. The retention indices for iodinated biphenyls were not calculated because parameters for the calculation of partial charges for iodine were not available. Therefore, only 53 data points were used to develop the equation. The plot of calculated versus observed retention indices is shown in Figure 2. As can be seen from the plot, two observations (compounds **35** and **53**) have RI values isolated from the other data points. Although their residuals are small, these two compounds could be influential in the sense that they might have an effect of pulling the regression line away from the majority of the observations.

To determine whether the two compounds were influential, both were temporarily excluded from the data set and a new equation was fitted by using the remaining observations. In the equation that resulted, the coefficients did not significantly differ from those in eq 2. Therefore there is no reason to leave out the two observations. Furthermore, the inclusion of these two compounds in the data set will make the equation more

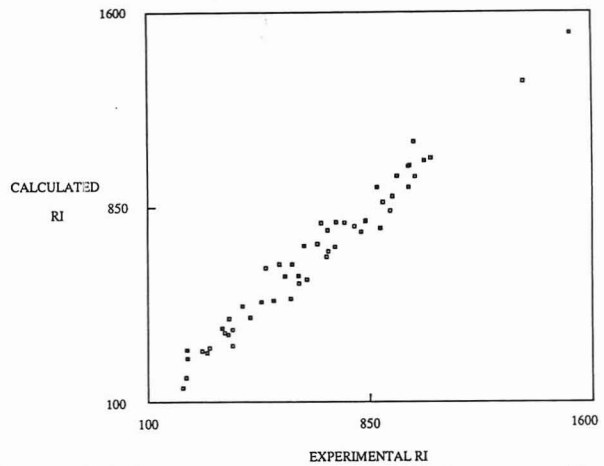

Figure 2. Calculated versus experimental liquid chromatographic retention indices for 53 polyhalogenated biphenyl compounds using eq 2.

Table VII. Statistics for LC Retention Index Equations Produced by Omitting One Halogen Group

group omitted	n	R^2	s
fluorine	40	0.945	59
chlorine	31	0.972	57
bromine	35	0.974	51

useful for prediction purposes as they represent the only compounds containing six bromine and ten chlorine substituents.

The residual plot for eq 2 showed a normal distribution and showed no evidence of nonconstancy of the error term. The last variable (path-3 kappa index) was raised to the third power in order to get a linear equation. When the original variable or its square was used, the residual plot suggested some curvature in the regression line. By use of the cubic transformation of the variable, the curvature disappeared, indicating that the transformation was appropriate.

The effects on the equation due to the identity of the halogens on a particular compound are encoded by the descriptors, but not in a straightforward way. In order to test the effects of any particular halogen group on the overall quality of the equation, several subsets were created by omitting one halogen group from the data set. Regression equations were then fitted using each of these subsets and the statistics were compared with those of the original equation (Table VII). The values of R^2 and standard errors for these equations show that the overall equation was not unduly affected by the type of halogen substitution.

Internal validation using the jackknife method resulted in a root mean square error of 63, which is not large compared to the standard error of the full model. When the data set was divided into two training sets by the Duplex method and a new regression equation was developed by using one of the training sets, a statistically strong equation was generated. This equation was then used to predict the retention indices of compounds not included in generating the equation. The results show that only one compound (**44**) has a predicted RI that deviates significantly from the observed values, while the remaining compounds have their experimental RI within the prediction interval of the predicted RI. Thus it can be concluded that the equation developed by using the five variables was internally consistent and has a high probability of being able to predict the retention indices of compounds not included in developing the equation.

CONCLUSIONS

This study indicated that the methodology used previously to model GC retention characteristics of PCBs can also be

applied to model the retention indices of other halogenated biphenyls. In addition, the LC retention indices of these compounds can also be modeled, although the model found was not as good as the one for GC retention indices. A set of more sophisticated descriptors might be able to support better models. A descriptor to encode the tendency to form hydrogen bonds is one example. With the availability of more retention data, these models can be improved by using more observations to develop the regression equations. Retention indices measured on other columns, i.e. those that have different polarities, should also be tested. Finally, the possibility of predicting elution order should also be considered since it would be of practical value of chromatographers.

LITERATURE CITED

(1) Hutzinger, O.; Safe, S.; Zitko, V. *The Chemistry of PCBs*; CRC Press: Boca Raton, FL, 1980.
(2) Carter, L. J. *Science* **1976**, *192*, 240–243.
(3) Robertson, L. W.; Chynoweth, D. P. *Environment* **1975**, *17* (6), 25–27.
(4) de Kok, J. J.; de Kok, A.; Brinkman, J. A. Th.; Kok, R. M. *J. Chromatogr.* **1977**, *142*, 367–383.
(5) Robertson, L. W.; Safe, S. H.; Parkinson, A.; Pellizari, E.; Pochini, C.; Mullin, M. D. *J. Agric. Food Chem.* **1984**, *32*, 1107–1111.
(6) Erickson, M. D. *Analytical Chemistry of PCBs*; Butterworth: Stoneham, MA, 1986.
(7) Mullin, M. D.; Pochini, C. M.; McCrindle, S.; Romkes, M.; Safe, S. H.; Safe, L. M. *Environ. Sci. Technol.* **1984**, *18*, 468–476.
(8) Bush, B.; Murphy, M. J.; Connor, S.; Snow, J.; Barnard, E. *J. Chromatogr. Sci.* **1985**, *23*, 509–515.
(9) Onuska, F. I.; Terry, K. A. *HRC & CC, J. High Resolut. Chromatogr. Chromatogr. Commun.* **1986**, *9*, 671–675.
(10) Fischer, R.; Ballschmiter, K. *Fresenius' Z. Anal. Chem.* **1988**, *332*, 441–446.
(11) McFarland, V. A.; Clarke, J. U. *Environ. Health Perspect.* **1989**, *81*, 225–239.
(12) Parkinson, A.; Safe, S. In *Polychlorinated Biphenyls (PCBs): Mammalian and Environmental Toxicology*; Safe, S., Ed.; Springer-Verlag: Berlin, 1987; pp 49–75.
(13) Sissons, D.; Welti, D. *J. Chromatogr.* **1971**, *60*, 15–32.
(14) Robbat, A.; Xyrafas, G.; Marshall, D. *Anal. Chem.* **1988**, *60*, 982–985.
(15) Devillers, J. *Fresinius' Z. Anal. Chem.* **1988**, *332*, 61–62.
(16) Hasan, M. N.; Jurs, P. C. *Anal. Chem.* **1988**, *60*, 978–982.
(17) Höfler, F.; Melzer, H.; Möckel, J.; Robertson, L. W.; Anklam, E. *J. Agric. Food Chem.* **1988**, *36*, 961–965.
(18) Almenningen, A.; Bastiansen, O.; Fernholt, L.; Cyvin, B. N.; Cyvin, S. J.; Samdal, S. *J. Mol. Struct.* **1985**, *128*, 59–76.
(19) Rømming, C.; Seip, H. M.; Aanesen Øymo, I.-M. *Acta Chem. Scand., Ser. A* **1974**, *28*, 507–514.
(20) Field, L. D.; Skelton, B. W.; Sternhell, S.; White, A. H. *Aust. J. Chem.* **1985**, *38*, 391–399.
(21) Dynes, J. J.; Baudais, F. L.; Boyd, R. K. *Can. J. Chem.* **1985**, *63*, 1292–1299.
(22) McKinney, J. D.; Gottschalk, K. E.; Pedersen, L. *J. Mol. Struct.* **1983**, *104*, 445–450.
(23) Tsuzuki, S.; Tanabe, K.; Nagawa, Y.; Nakanishi, H.; Osawa, E. *J. Mol. Struct.* **1988**, *178*, 277–285.
(24) Jaime, C.; Font, J. *J. Mol. Struct.* **1989**, *195*, 103–110.
(25) Stuper, A. J.; Brugger, W. E.; Jurs, P. C. *Computer Assisted Studies of Chemical Structure and Biological Function*; Wiley-Interscience: New York, 1979.
(26) Kier, L. B. *Quant. Struct.-Act. Relat.* **1985**, *4*, 109–116.
(27) Rohrbaugh, R. H.; Jurs, P. C. *Anal. Chim. Acta* **1987**, *199*, 99–109.
(28) Abraham, R. J.; Smith, P. E. *J. Comput. Chem.* **1987**, *9*, 288–297.
(29) Stanton, D. R.; Jurs, P. C. Unpublished results.
(30) Draper, N.; Smith, H. *Applied Regression Analysis*, 2nd ed.; Wiley-Interscience: New York, 1981; pp 307–312.
(31) Furnival, G. M.; Wilson, R. W., Jr. *Technometrics* **1974**, *16*, 499–511.
(32) Snee, R. D. *Technometrics* **1977**, *19*, 415–428.

RECEIVED for review April 16, 1990. Accepted July 30, 1990. This work was partially supported by the National Science Foundation Grant CHE-8815785. The Sun workstation was purchased with partial financial support of the National Science Foundation. The financial support of the University Teknologi Malaysia and the Malaysian Government is acknowledged.

Development and Use of Charged Partial Surface Area Structural Descriptors in Computer-Assisted Quantitative Structure–Property Relationship Studies

David T. Stanton and Peter C. Jurs*

Chemistry Department, Davey Laboratory, Penn State University, University Park, Pennsylvania 16802

Intermolecular interactions that are polar in nature contribute to observed physicochemical properties such as chromatographic retention and normal boiling point. However, these types of interactions are difficult to encode with structural parameters currently available for use in SPR studies. A new series of molecular structural parameters have been developed that combine molecular surface area and partial atomic charge information to form charged partial surface area (CPSA) descriptors. These descriptors have been shown to be useful in a variety of structure–property studies. The characteristics and properties of these parameters are discussed, and their use in several structure–property studies is described.

INTRODUCTION

There are many applications of computer-assisted quantitative structure–property relationships (QSPR) that are of value in analytical chemistry. Such relationships act as tools to augment experimental analytical techniques, allowing the chemist to extract additional information. These computer-assisted techniques can be used as an aid to understanding chemical processes such as chromatographic retention. They are also of value in the identification of materials when authentic standards are not available or quantities of available materials are limited. In addition, computer-assisted QSPRs can save time by allowing the analyst to quickly estimate a property for a given molecule which might be too time-consuming to measure experimentally. However, because of limitations inherent to methods used to study the relationship between molecular structure and physical property, QSPR studies often focus on sets of compounds that are relatively similar. Also, limitations associated with the parameters used in QSPR in the past have restricted the accuracy of predictions and the variety of properties that can be studied. Thus, it is of interest to expand the utility of QSPR to a larger variety of compounds, to increase accuracy, and to extend the use of

0003-2700/90/0362-2323$02.50/0 © 1990 American Chemical Society

QSPR to new properties of analytical interest.

In the computer-assisted study of the relationship between the structure of molecules and their physicochemical properties, several different approaches are used to characterize the structure of the molecule in terms that can be manipulated by a computer. The structural information used by the computer is in the form of numerical values termed structural *descriptors*. The information contained in these descriptors reflects the nature of the particular type of molecular representation used. For example, a graph theoretical representation describes the molecule as a set of vertices (atoms) and edges (bonds). Several descriptors found to be useful in QSPR studies which are based on graph theoretical representations of molecules have been reported in the literature (*1–3*). A more sophisticated representation views a molecule as a collection of nuclei bound together by overlapping electron orbitals. Such a representation can be used to derive electronic information such as partial atomic charges and dipole moments (*4, 5*). Another structural representation characterizes a molecule as a set of hard spheres connected by bonds possessing specific stretching, bending, and torsional energies. The shape of the molecule is determined by the strain placed on the bonds as the spheres are allowed to interact. Information that is related to the geometry (size and shape) of the molecule can be obtained from such a representation (*6–8*). The conclusions that can be drawn from these examples are that several useful, but significantly different, representations can be used to describe a molecule and that no single one is best. Rather, the true representation must lie in some combination of them, and some combinations of additional representations that have not yet been conceived. One of the limitations one encounters in QSPR studies is the lack of information concerning the particular structural features responsible for the observed differences in physical properties within a set of molecules. This information deficiency is related directly to the type of molecular representation employed. Thus, one goal of QSPR studies is to expand the set of representations in order to derive new descriptors which allow the chemist to better understand the link between structure and property.

In a previous QSPR study, regression equations were developed for the prediction of gas chromatographic retention indices for a series of 107 pyrazines on both a nonpolar OV-101 stationary phase and a polar Carbowax-20M stationary phase (*9*). Among other conclusions of that study, it was determined to be more difficult to predict the chromatographic retention for such compounds on the polar stationary phase. This had also been previously noted by Kaliszan (*10*). The difficulty is presumed to stem from the lack of information contained in the available structure-based descriptors concerning those features responsible for polar intermolecular interactions. Thus, new descriptors were sought that would improve the correlation of the structures of analytes to their retention characteristics on polar stationary phases.

The search for new parameters was based on a particular concept of how molecules might interact, particularly when the interactions are polar. Specific and nonspecific polar interactions greatly affect many physical properties, and the strength of these interactions was considered to be a function of the amount of contact between molecules. Also, the charge distribution within the molecules would act as the driving force for these interactions and should be considered in any new parameter studied. In the past, some success has been achieved by using information concerning the solvent-accessible surface area of molecules to describe intermolecular interactions that are important for different properties. For example, Camilleri et al. (*11*) reported the use of solvent-accessible surface area to correlate molecular structure with

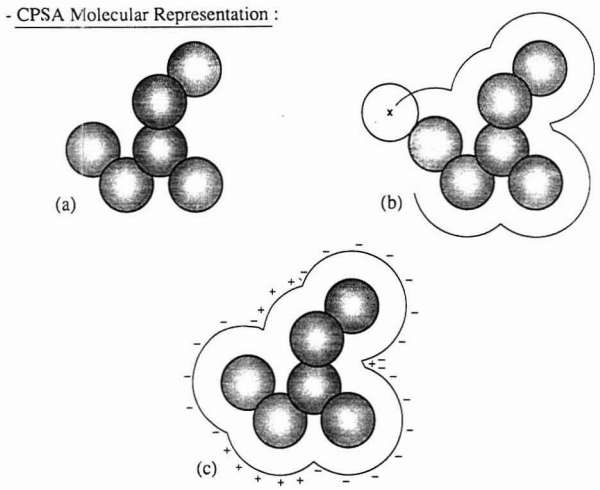

Figure 1. Diagram of the molecular representation used to derive the charged partial surface area (CPSA) descriptors.

partition coefficients for a wide variety of benzene derivatives. Modifications of surface area calculations have also been reported. Amidon and co-workers (*12*) studied the correlation of surface area, in terms of hydrocarbon portions (HYSA) and functional group portions (FGSA), with the aqueous solubility of a series of monofunctional aliphatics. Dunn et al. (*13, 14*) reported similar experiments involving the division of solvent-accessible surfaces into isotropic (nonpolar) portions and hydrated (polar or solvated) portions for the prediction of partition coefficients. Iwase et al. (*15*) employed corrections for hydrophilic interactions and hydration of polar moieties in the correlation of solvent-accessible surface area and hydrophobicity. More recently, Grigoras (*16*) has reported work involving molecular surfaces expressed in the form of electrostatic molecular surface interaction terms. These structural surface descriptors include information concerning molecular surface area, partial atomic charges, and charge scaling factors. He showed these descriptors to be useful in the prediction of such properties as critical temperature and critical volume. We decided to investigate this type of structural descriptor in more detail in an attempt to find new ways of encoding the structural features responsible for polar intermolecular interactions, which are needed for a variety of QSPR studies.

We report here a new set of molecular structure descriptors termed charged partial surface area (CPSA) descriptors that encode features responsible for polar interactions between molecules. The molecular representation used here views a molecule as having a surface defined by the overlap of hard spheres, defined by the van der Waals radii of the atoms (Figure 1a), which is traced by a sphere representing a solvent molecule (water by default). The surface traced out by the center of the solvent sphere has been termed the solvent-accessible surface (*6*) and is shown diagrammatically in Figure 1b. The molecule is further defined as having a specific electron distribution, thus yielding a representation of a charged contact surface (Figure 1c) where polar intermolecular interactions can take place.

The CPSA descriptors derived from such a representation have been shown to be useful in correlations of structural features with physical properties such as chromatographic retention, boiling point, and surface tension. The utility and characteristics of the CPSA descriptors are discussed below.

EXPERIMENTAL SECTION

All computations in this study were performed on a Sun 4/110 workstation running the ADAPT software system under the UNIX operating system. The general procedure for the development of regression equations from structural descriptors using ADAPT has been outlined previously (*17, 18*). The solvent accessible surface area calculations were performed using the SAVOL

Table I. Experimentally Derived Data Used in the Structure–Property Study of Surface Tension

compound name	surface tension, dyn cm^{-1}	compound name	surface tension, dyn cm^{-1}
decane	23.74	nitrobenzene	42.70
cyclohexane	25.16	methoxybenzene	35.00
benzene	28.81	*N*,*N*-dimethylanaline	36.04
toluene	28.52	dimethyl phthalate	41.84
1-chlorotetradecane	30.36	1-chloronaphthylene	41.04
1-bromo-tetradecane	31.17	nitromethane	37.36
		dichloromethane	27.89
acetonitrile	29.29	dibromomethane	39.74
cyanoethane	27.24	1,2-dihydroxyethane	48.49
1-cyanobutane	27.39	1,2-dimethoxyethane	24.61
1-cyanohendecane	29.82	1,4-dioxane	33.26
methanol	22.49	pyridine	37.24
ethanol	22.32	tetrahydrofuran	27.31
2-butanol	23.37	cyclohexanone	35.05
1-hexanol	26.20	dimethyl adipate	35.86
chlorobenzene	32.96		
bromobenzene	35.80		

algorithm of Pearlman (*6*), which was modified to store the surface area data for the individual atoms of a molecule in a computer file. The partial atomic charges were obtained by using a modified version of the algorithm of Abraham and Smith (*4*). This is an empirical method of calculating partial charges, which includes both σ and π contributions and which is parameterized to reproduce experimental dipole moments. The algorithm has been implemented in FORTRAN in our laboratory as part of the ADAPT system. In addition, the method has been improved and the parameter set has been expanded to include a greater variety of atom and bond types. Calculations of the surface areas and atomic partial charges included hydrogens.

The Data Sets. The data used in this study were obtained from several sources. The gas chromatographic retention data for the series of 107 pyrazines on Carbowax-20M were taken from work previously reported by the authors (*9*). Normal boiling points (boiling point recorded at 760 mmHg) and structures for a set of 209 furans and tetrahydrofurans were obtained as ASCII files from The Beilstein Institute (supplementary material). The structures, in the form of connection tables were converted to ADAPT format with a FORTRAN program and were stored on disk. Reasonable low-energy conformations for the molecules were obtained by using molecular mechanics calculations (*17*, *19*). Data for the study of surface tension were taken from Körösi and Kovâts (*20*). The structures were entered into the ADAPT files by sketching them on a graphics terminal. These structures were also placed in reasonable low energy conformations using molecular mechanics calculations. Surface tension data recorded at 20 °C (Table I) were used in the modeling process.

Descriptor Analysis. Once the structures had been stored, and desired sets of structural descriptors had been calculated, the process of descriptor analysis or objective feature selection was begun. This is an objective analysis of the calculated descriptors which is necessary to reduce the number of available descriptors in order to avoid obtaining good correlations purely by chance. The analysis involves the detection and removal of those structural descriptors which exhibit high pairwise correlations with other descriptors, or which contain little discriminatory information. Pairs of descriptors that are highly correlated ($r \geq 0.950$) contain nearly identical information, and one of the pair should be discarded. Descriptors that contain a high percentage (≥90%) of identical values or a small number (≤10%) of nonzero values are of little use and are discarded. The results of this type of analysis are a reduced pool of information-rich descriptors that can then be screened in regression analysis.

Regression Analysis. Multiple linear regression techniques are used for descriptor selection rather than other methods such as factor analysis or principle components regression, because of their ease of implementation and the interpretability of the resulting equations. In most cases, least-squares multiple linear regression analysis was carried out by using a process of stepwise addition with progressive deletion (*21*). Regression analysis of this form proceeds by a stepwise addition of terms, based on F statistic values, which is followed by a deletion process. In the deletion process, each variable (descriptor) is held out in turn, and the stepwise addition process is repeated on the remaining pool of variables. Then each combination of two, and then three, variables are held out, and the regression is repeated. This combination of steps has the effect of uncovering potentially superior equations that may have been otherwise obscured by the existence of a descriptor that was highly correlated to the dependent variable. The final models were chosen on the basis of the values for the coefficient of multiple determination (R) and standard deviation of the regression (s). The exception to this process was the study involving the correlation of molecular structure descriptors and surface tension. For this study, the process of best subsets regression (*22*) was used as implemented in the Minitab statistical package (*23*). In this process, all possible combinations of 1–15 variables are regressed together, and the best equations are reported. Selection of the final equation in this case was based on the C_p criterion (*22*).

Each model chosen from regression analysis is examined for statistical significance (overall F test) and for the significance of the individual descriptors (partial F test). Also, the models are examined for collinearities between two or more of the descriptors. Since it is common for descriptors within models of this type to be correlated to some extent, it is important that any collinearities that do exist be noted and that they are not causing any serious problems (e.g., increased uncertainty in the regression coefficients). Statistical orthogonality of the descriptors is not a requirement.

RESULTS AND DISCUSSION

A set of 25 individual descriptors was assembled that combines information on the atomic contributions to the solvent-accessible surface area of the molecule with partial atomic charge information. This particular set was originally chosen to allow the examination of a variety of combination schemes. However, it was found in subsequent studies that the descriptors contain different information from each other such that several CPSA descriptors are often combined within a single regression equation. It was also noted that different combinations of these descriptors become important depending on the physical property and data set being considered. The equations used to calculate these descriptors are given in Table II. The values are grouped by charge type and by the method used to combine the surface area and charge information. Thus, there are three partial positive surface area descriptors (PPSAs) and an equal number of the partial negative surface area descriptors (PNSAs). Also, there is a set of three difference in partial surface area descriptors (DPSAs), six fractional charged surface area (FPSA and FNSA) descriptors (three positive and three negative), and a similar set of six total surface weighted partial surface area (WPSA and WNSA) descriptors. In addition to the charged surface area parameters, it was of interest to examine the relative influence of the most highly charged (positive and negative) atom on the overall charge of the molecule. These descriptors are the relative positive and relative negative charges (RPCG and RNCG, respectively). This information was then combined with the accessible surface area of the most highly charged atoms to obtain the relative positive and relative negative charged surface area descriptors (RPCS and RNCS, respectively).

To illustrate the calculation of the CPSA descriptors, the necessary data for methyl acetate, as an example compound, is given in Table III. The surface area and charge data for each atom in the molecule are given along with the total solvent accessible surface area and greatest positive and negative partial atomic charges. Table IV gives the values of the individual CPSA descriptors derived from these data.

Chromatographic Retention. The first application of the CPSA descriptors in an QSPR study involved the correlation of molecular structure and chromatographic retention on Carbowax-20M for the 107 pyrazines. The set of 25 CPSA

Table II. Formulas Used in the Calculation of the CPSA Molecular Structure Descriptors

descriptor	descriptor label	formula[a,b]
partial positive surface area	PPSA-1	$\sum(+SA_i)$
partial negative surface area	PNSA-1	$\sum(-SA_i)$
total charge weighted PPSA	PPSA-2	$(\sum(+SA_i))Q^+_T$
total charge weighted PNSA	PNSA-2	$(\sum(-SA_i))Q^-_T$
atomic charge weighted PPSA	PPSA-3	$\sum(+SA_i)(Q^+_i)$
atomic charge weighted PNSA	PNSA-3	$\sum(-SA_i)(Q^-_i)$
difference in charged partial surface areas	DPSA-1	[(PPSA-1) − (PNSA-1)]
	DPSA-2	[(PPSA-2) − (PNSA-2)]
	DPSA-3	[(PPSA-3) − (PNSA-3)]
fractional charged partial surface areas	FPSA-1 FNSA-1	(charged partial surface area)/(total molecular surface area)
	FPSA-2 FNSA-2	
	FPSA-3 FNSA-3	
surface weighted charged partial surface areas	WPSA-1 WNSA-1	(CPSA)(total mol surf. area)/1000
	WPSA-2 WNSA-2	
	WPSA-3 WNSA-3	
relative positive charge	RPCG	(charge of most positive atom)/(sum total positive charge)
relative negative charge	RNCG	(charge of most negative atom)/(sum total negative charge)
relative positive charged surface area	RPCS	$(SA_{MPOS})(RPCG)$
relative negative charged surface area	RNCS	$(SA_{MNEG})(RNCG)$

[a] $(+SA_i)$ and $(-SA_i)$ are the surface area contributions of the ith positive or negative atom in the molecule. [b] Q^+_i and Q^-_i are the partial atomic charges for the ith positive and negative atoms, while Q^+_T and Q^-_T are the sum total positive and negative charges for the molecule.

Table III. Data Used for the Example Calculations of the CPSA Descriptors for Methyl Acetate

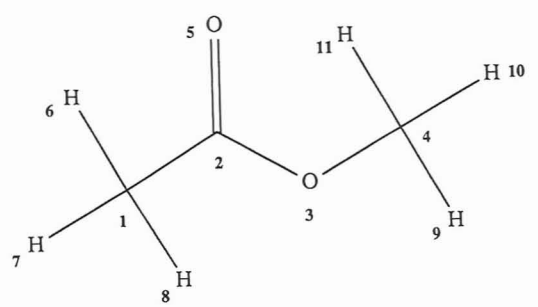

total solvent-accessible surface area = 246.7 Å²
partial atomic charge on most positive atom = 0.3194
partial atomic charge on most negative atom = −0.3818

atom no.	solvent accessible surface area, Å²	partial charge
1	10.1	−0.042
2	7.3	0.319
3	16.4	−0.212
4	11.4	0.002
5	39.6	−0.382
6	27.0	0.049
7	27.5	0.049
8	27.6	0.049
9	30.7	0.056
10	24.6	0.056
11	24.5	0.056

Table IV. Values of the CPSA Descriptors Calculated for Methyl Acetate

descriptor label	descriptor value	descriptor label	descriptor value
PPSA-1	180.7	FNSA-2	−0.171
PPSA-2	115.0	FNSA-3	−0.077
PPSA-3	10.8	WPSA-1	44.6
PNSA-1	66.1	WPSA-2	28.4
PNSA-2	−42.1	WPSA-3	2.67
PNSA-3	−19.0	WNSA-1	16.3
DPSA-1	114.6	WNSA-2	−10.4
DPSA-2	157.1	WNSA-3	−4.70
DPSA-3	29.9	RPCG	0.502
FPSA-1	0.732	RNCG	0.600
FPSA-2	0.466	RPCS	3.64
FPSA-3	0.044	RNCS	23.8
FNSA-1	0.268		

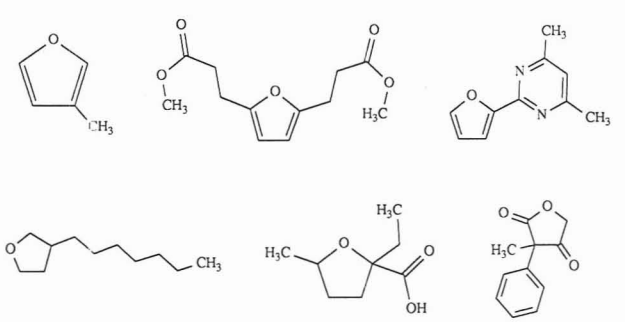

Figure 2. Examples of the compounds included in the furan and tetrahydrofuran boiling point QSPR study training set.

descriptors were combined with the variables contained in the previously reported Carbowax-20M model. After elimination of high pairwise correlations, the remaining descriptors were regressed against the retention indices for the pyrazines on Carbowax-20M. For the purpose of comparison to the previous work, the best six-variable predictive equation obtained as given in Table Va. Examination of the new model shows that three of the six descriptors are from the CPSA set. The new model yields a slightly better fit to the experimental data (R^2 = 0.988) and a 9.5% reduction in the standard deviation of the regression (s = 32.9). However, the best overall model obtained contained nine variables, six of which are of the CPSA set. The nine-variable model is shown in Table Vb. A significant improvement in the fit of the equation is obtained (R^2 = 0.994) along with a decrease of 26.5% in the standard deviation of regression (s = 26.7) as compared with the previous model. This brings the quality of the Carbowax-20M model more in line with that of the OV-101 model previously reported. Although some improvement in the fit of equations involving CPSA descriptors was expected, the number and combination of the new CPSA descriptors in the resulting models were unforeseen.

Boiling Point. As a result of the success obtained with the CPSA descriptors in modeling retention, it was of interest to study the application of the new descriptors in the modeling of other properties. In a QSPR study involving correlations of molecular structure with normal boiling point for a diverse

Table V

(a) A Six-Variable Regression Equation Obtained for the Correlation of the Molecular Structure and Gas Chromatographic Retention Indices of 107 Pyrazines on Carbowax-20M Employing CPSA Descriptors

R = 0.994 (R^2 = 0.988), s = 32.9 (2.0% of mean), n = 107
F value for analysis of variance = 1515.9, F(0.90;6,100) = 1.77

independent variable	regression coeff	std dev of regr coeff	partial F value
PNSA-1	4.68	0.44	113.74
PNSA-2	4.61	0.46	99.55
DPSA-3	19.55	1.34	213.10
no. of single bonds	−103.57	4.10	639.68
molecular polarizability	94.36	3.51	722.47
1st moment of inertia (included hydrogens)	0.031	0.0078	16.04
intercept	−272.65		

(b) A Nine-Variable Regression Equation Obtained for the Correlation of Molecular Structure and Gas Chromatographic Retention Indices of 107 Pyrazines on Carbowax-20M Employing CPSA Descriptors

R = 0.997 (R^2 = 0.994), s = 26.7 (1.6% of mean), n = 107
F value for analysis of variance = 1538.0, F(0.90;6,100) = 1.77

independent variable	regression coeff	std dev of regr coeff	partial F value
PNSA-2	3.11	0.54	32.76
DPSA-2	−0.72	0.11	40.05
DPSA-3	27.91	2.22	158.17
FNSA-2	−826.66	232.65	12.63
FPSA-3	−8776.53	1488.63	34.76
RNCS	−11.33	2.47	20.99
no. of single bonds	−116.51	5.32	479.63
molecular polarizability	94.26	3.49	729.56
1st moment of inertia (included hydrogens)	0.095	0.0079	144.78
intercept	265.98		

set of 209 furan and tetrahydrofuran related compounds, some difficulty was encountered in obtaining a good fit to experimental values. This was due in part to the great diversity of the types of substituents in the data set. To illustrate this diversity, some of the compounds from the training set are shown in Figure 2. Since the goal of the study was to model the data set as a whole, it was not possible to subset the compounds to reduce the problems related to diversity of functional groups involved. Given that properties such as the normal boiling point are functions of the strength of various intermolecular interactions in the liquid phase, it was thought that the CPSA descriptors would yield better results, based on the results obtained in the retention study of the pyrazines.

A final model based on a set of 209 furans and tetrahydrofurans was developed and was found to give good results for this diverse data set. This model, shown in Table VI, contains 11 variables. A plot of the correlation of the fitted and observed boiling points for the 209 furans and tetrahydrofurans is given in Figure 3. Results of this quality had not been obtained in the study prior to the inclusion of the CPSA descriptors to the pool available to the regression program. Five of the 11 descriptors in the model are of the CPSA variety. Again, we found it interesting that so many of the variables in the model were of the CPSA variety. We also noted that none of the five CPSA descriptors in the boiling point model were the same as those used in the pyrazine retention index model described above. This is presumably a function of the data set and property being studied. It is apparent from the examination of the gas chromatographic retention and boiling point QSPR equations that there is a significant difference in the kind of structural information contained in the individual CPSA descriptors.

Table VI. Regression Model for the Correlation of Molecular Structure and Normal Boiling Point of a Series of 209 Furans and Tetrahydrofurans Using CPSA Descriptors

R = 0.984 (R^2 = 0.968), s = 11.2 (5.7% of mean), n = 209
F value for analysis of variance = 554.5, F(0.90;11,198) = 1.55

independent variable	regression coeff	std dev of regr coeff	partial F value
PPSA-1	0.61	0.05	133.92
PPSA-3	10.78	1.04	108.40
FNSA-3	−1296.78	55.76	540.82
WPSA-3	−26.87	2.89	86.47
RPCG	145.05	13.00	124.41
path-1 simple molecular connectivity	61.61	4.46	191.05
no. of single bonds	−25.36	1.12	514.18
LUMO energy (from Hückel method)	11.52	2.97	15.07
valence corrected path-3 molecular connectivity	22.94	3.63	39.85
square root of KAPPA-3 (*24*)	47.15	7.31	41.57
av distance sum connectivity (*25*)	21.14	3.99	28.01
intercept	−280.94		

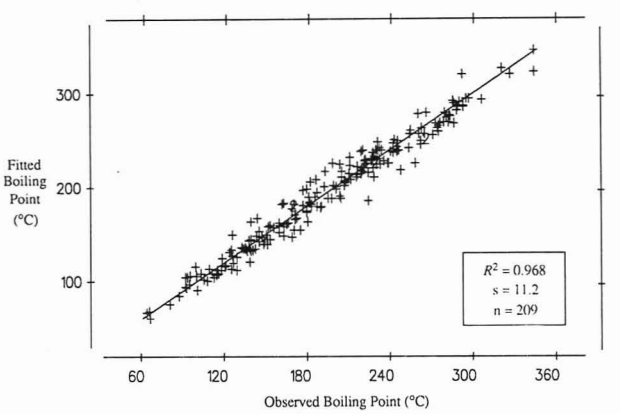

Figure 3. Correlation of the fitted and observed normal boiling points for the 209 furans and tetrahydrofurans in the boiling point QSPR study.

Surface Tension. It is a common practice in QSPR studies to use a large set of compounds to derive regression equations. This is done in order to include as much information as possible concerning the molecules under study in the resulting model. However, such large data sets are not always available, and the chemist must rely on the strength of the descriptors to encode as much information as is contained in a less than ideal data set. Since the CPSA descriptors have shown utility in studies involving quite diverse sets of compounds, it was of interest to apply them to a smaller than usual data set in order to determine the limits of our QSPR technique using the new descriptors. It was also of interest to extend the use of computer-assisted QSPR to a physical property that had not previously been studied in this fashion and is also a function of the strength of various intermolecular interactions. Examination of the literature indicated that surface tension was such a property.

By use of the methods described above, a study involving a small and very diverse series of 31 organic compounds with known surface tension values (Table I) was initiated. A regression equation that employed six descriptors was found to yield good results. This model is detailed in Table VII, and the correlation between fitted and observed surface tension

Table VII. Regression Model Obtained for the Study of the Correlation of Molecular Structure and Surface Tension Using CPSA Descriptors

R = 0.953 (R^2 = 0.908), s = 2.32 (6.9% of mean), n = 31
F value for analysis of variance = 39.14, F(0.90;6,25) = 2.02

independent variable	regression coeff	std dev of regr coeff	partial F value
FNSA-2	−29.16	3.64	64.18
FPSA-3	387.62	39.81	94.79
RPCS	−1.29	0.19	45.66
RNCS	0.28	0.06	23.39
7th order, valence corrected chain molecular connectivity[a]	106.71	22.82	21.86
topological symmetry measure[b]	−9.51	2.95	10.41
intercept	12.87	2.02	

[a] See ref 26. [b] See text.

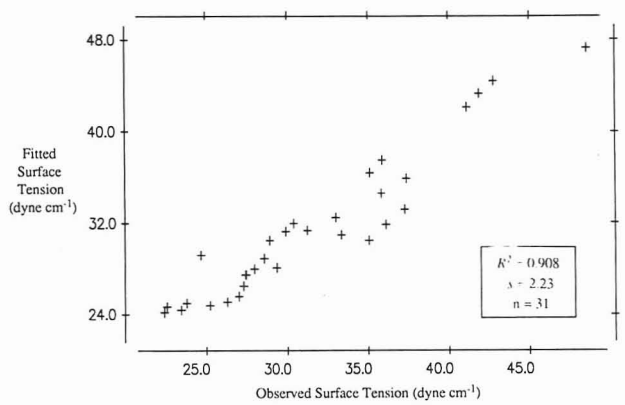

Figure 4. Correlation of the fitted and observed values for the surface tension QSPR study.

is shown graphically in Figure 4. The standard deviation of the regression (s) for this case represents 6.9% based on the mean surface tension for this data set. As was noted in other QSPRs, the majority of the information concerning the structures of the compounds in question is obtained from the CPSA type descriptors. The other descriptors within the model are topological in nature. The 7th order valence-corrected chain molecular connectivity describes the structure around the rings (*26*), while the topological symmetry describes the structural symmetry of a molecule and is calculated as the number of unique atoms in a molecule divided by the total number of atoms. A unique atom is defined as an atom having a unique chemical environment over a given bond distance. A bond distance of 1 was used in this case.

Within the model, information concerning features important for polar interactions is supplied solely by the CPSA parameters. Also, examination of the results of the regression analysis indicates that the CPSA descriptors account for the greatest amount of the variance in the training set (largest partial F values). It was also noted that only one of the four CPSA descriptors in the surface tension model had appeared in either the boiling point or retention index prediction models discussed above. While the quality of these results is not as good as that obtained for the previous QSPR examples discussed, they indicate the potential of the CPSA descriptors in the study of surface tension, and a more detailed study involving a larger data set is now in progress.

Other Characteristics of the CPSA Descriptors. Since the new CPSA descriptors were of obvious importance in the QSPR studies described, it was necessary to determine the properties of the descriptors themselves. Points of interest included degree of information overlap (intercorrelation),

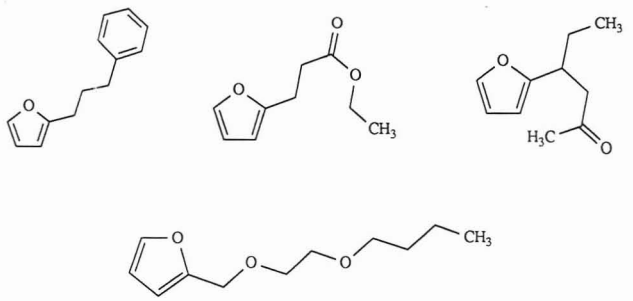

Figure 5. Structures of the furan analogues used to study the conformation dependence of the CPSA descriptors.

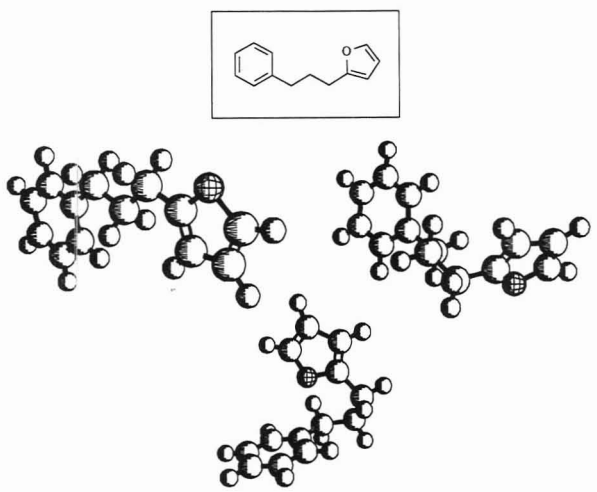

Figure 6. Conformations of 2-(propylphenyl)furan used in the study of the conformation dependence of the CPSA descriptors.

Table VIII. Average Percent Change Observed in the CPSA Descriptors as a Function of Changes in the Geometry of Four Furan Molecules

descriptor label	av % change	descriptor label	av % change
PPSA-1	2.2	FNSA-2	4.9
PPSA-2	2.2	FNSA-3	8.0
PPSA-3	2.3	WPSA-1	4.3
PNSA-1	7.3	WPSA-2	4.3
PNSA-2	7.3	WPSA-3	4.3
PNSA-3	9.0	WNSA-1	9.6
DPSA-1	5.9	WNSA-2	9.6
DPSA-2	5.9	WNSA-3	11.0
DPSA-3	4.1	RPCG	0.0
FPSA-1	2.0	RNCG	0.0
FPSA-2	2.0	RPCS	20.3
FPSA-3	2.2	RNCS	21.0
FNSA-1	4.9		

sensitivity to changes in conformation of molecules under study, and importance of inclusion of the solvent in the calculation of the surface area.

The test of sensitivity to changes in conformation was accomplished by using a set of four furan analogues (Figure 5). Each compound was placed in three different energy minimized conformations. Examples of the conformations used for the first of the test compounds are given in Figure 6. The series of 25 CPSA descriptors were then calculated for each conformation and the descriptor values were then compared. The results of the comparison are given in Table VIII. The descriptors exhibiting the largest overall variation with changing conformation are the RPCS and RPNS descriptors. Since these parameters encode information related to a single atom, changes in conformation of a molecule would have a relatively large effect on these descriptors. Also, since the remaining CPSA descriptors are based on the surface area of

several atoms, changes in surface area are averaged out, thus reducing the conformational dependence of these descriptors. Another consideration is the topological nature of the method used for calculating the partial atomic charges. Geometry is not a factor in the computation of the atomic partial charges used and thus they have a stabilizing effect on the resulting CPSA descriptors. The overall average change in the set of CPSA descriptors is 6.1%. Given that the differences in conformations were large, this value seems to be reasonable.

Another aspect of the CPSA descriptors to be considered is their connection to a solvent-accessible surface. It was of interest to determine what effect the removal of the solvent in the surface area calculation would have on the usefulness or information content of the CPSA descriptors. Normally, the calculation of the surface area is done by using a sphere with a radius of 1.5 Å to approximate the contact surface formed when a water molecule interacts with the query molecule. For the test of the effects of solvent removal, the radius of the solvent was set to zero. This results in the use of the van der Waals surface of the molecule. The study of the effect of removal of the solvent was done with the set of 107 pyrazines previously described. Calculation of the descriptors and subsequent objective feature selection and regression analysis was done as previously outlined. The first test involved the direct replacement the solvent-included CPSA descriptors in the model shown in Table Va with the corresponding solventless descriptors, followed by the recalculation of the regression coefficients. Examination of the model obtained in this fashion shows that the substitute descriptors yield a poorer fit to the experimental data (R^2 = 0.984) and a larger standard deviation of regression (s = 39.3 or 2.4% of the mean retention index) as compared with the model containing the solvent-included descriptors. Also, the standard deviation of the regression coefficients increased as well. Other tests involved building models in the usual fashion with the substitute descriptors. These equations yielded generally poorer fits to the experimental data and also exhibited a decrease in the number of CPSA type descriptors in the models. It was also noted that the descriptors based on the van der Waals surface were more highly correlated between themselves than are the normal CPSA descriptors. These results suggest that the quantity of structural information in the substitute descriptors has decreased, and that the solvent-accessible surface is an important factor in describing the molecular features which are involved in intermolecular interactions. Thus, it can be concluded that the solvent-accessible surface represents a useful approximation of the contact surface involved in such interactions between molecules.

A final comparison of the solvent-included and solventless CPSA descriptors for the 107 pyrazines involved the examination of the correlation between the two sets of descriptors. The average correlation for the two sets is 0.887, with a high of 1.00 (RPCG and RNCG) and a low of 0.406 (RPCS). The high correlations for RPCG and RNCG are expected since these descriptors contain no surface area information, and such values will be identical regardless of the surface area data used. The results of this comparison suggest that different structural information is encoded in the solvent-included CPSA descriptors. This information taken together with the significant role the CPSA descriptors have played in the three SPR studies described above indicates the importance of using the solvent-accessible surface area.

CONCLUSIONS

The CPSA descriptors represent a new set of parameters for use in QSPR studies. They appear to provide important information concerning features of molecules that are responsible for strong intermolecular interactions, which are in turn important for helping to correlate structural features to physical properties such as chromatographic retention, boiling point, and surface tension. These descriptors allow for the use of smaller sets of compounds, thus extending the use of QSPR techniques to problems were the availability of experimentally derived values is limited. Through the application of the CPSA descriptors to problems of analytical importance, it may be possible to gain additional insight into the nature of solvent–solute interactions in chromatography and allow for the extension of QSPR techniques to broader sets of compounds and a larger number of analytically important properties.

ACKNOWLEDGMENT

We are grateful to Steve Dixon for his work involving the program used to calculate the partial atomic charges used in this study.

Supplementary Material Available: Identification numbers, data, and structures for the 209 furans and tetrahydrofurans (27 pages). Photocopies of the supplementary material from this paper or microfiche (105 × 148 mm, 24× reduction, negatives) may be obtained from Microforms & Back Issues Office, American Chemical Society, 1155 16th Street, NW, Washington, DC 20036. Orders must state whether for photocopy or microfiche and give complete title of article, names of authors, journal issue date, and page numbers. Prepayment, check or money order for $46.00 for photocopy ($48.00 foreign) or $10.00 for microfiche ($11.00 foreign), is required and prices are subject to change.

LITERATURE CITED

(1) Wiener, H. *J. Am. Chem. Soc.* **1947**, *69*, 2636.
(2) Randić, M. *J. Am. Chem. Soc.* **1975**, *97*, 6609.
(3) Randić, M. *J. Chem. Inf. Comp. Sci.* **1984**, *24*, 164–175.
(4) Abraham, R. J.; Smith, P. E. *J. Comput. Chem.* **1988**, *9*, 288–297.
(5) Ośmiałowski, K.; Halkiewisz, J.; Radecki, A.; Kaliszan, R. *J. Chromatogr.* **1985**, *346*, 53–60.
(6) Pearlman, R. S. In. *Physical Chemical Properties of Drugs*; Yalkowsky, S. H., Sinkula, A. A., Valvani, S. C., Eds.; Marcel Dekker: New York, 1980.
(7) Goldstein, H. *Classical Mechanics*; Addison-Wesley: Reading, MA, 1950; pp 144–156.
(8) Jinno, K.; Kawasaki, K. *Chromatographia* **1983**, *17*, 445.
(9) Stanton, D. T.; Jurs, P. C. *Anal. Chem.* **1989**, *61*, 1328–1332.
(10) Kaliszan, R. *Quantitative Structure-Chromatographic Retention Relationships*; Wiley-Interscience: New York, 1987.
(11) Camilleri, P.; Watts, A.; Boraston, J. A. *J. Chem. Soc., Perkin Trans. 2*, **1988**, 1699–1707.
(12) Amidon, G. L.; Yalkowsky, S. H,; Anik, S. T.; Valvani, S. C. *J. Phys. Chem.* **1975**, *21*, 2239–2246.
(13) Dunn, W. J., III; Koehler, M. G.; Grigoras, S. *J. Med. Chem.* **1987**, *30*, 1121–1126.
(14) Koehler, M. G.; Grigoras, S.; Dunn, W. J., III *Quant. Struct.-Act. Relat.* **1988**, *7*, 150–159.
(15) Iwase, K.; Komatsu, K.; Hirono, S.; Nakagawa, S.; Moriguchi, I. *Chem. Pharm. Bull.* **1985**, *33*, 2114–2121.
(16) Grigoras, S. *J. Comput. Chem.* **1990**, *11*, 493–510.
(17) Stuper, A. J.; Brugger, W. E.; Jurs, P. C. *Computer-Assisted Studies of Chemical Structure and Biological Function*; Wiley-Interscience: New York, 1979.
(18) Jurs, P. C.; Chou, J. T.; Yuan, M. In *Computer-Assisted Drug Design*; Olson, E. C., Christoffersen, R. E., Eds.; American Chemical Society: Washington, DC, 1979, pp 103–129.
(19) Allinger, N. L.; Yuh, Y. H. *Molecular Mechanics, Operating Instructions for MM2 and MMP2 Programs, 1977 Force Field*; Quantum Chemistry Program Exchange, 1980; Program 395.
(20) Körösi, G.; Kováts, E. *J. Chem. Eng. Data* **1981**, *26*, 323–332.
(21) Small, G. W.; Jurs, P. C. *Anal. Chem.* **1983**, *55*, 1121–1127.
(22) Neter, J.; Wasserman, W.; Kutner, M. H. *Applied Linear Statistical Models*, 2nd. ed.; Irwin: Homewood, IL, 1985.
(23) *Minitab Reference Manual*, release 7.2; Minitab: State College, PA, 1989.
(24) Kier, L. B. *Quant. Struct.-Act. Relat.* **1985**, *4*, 109.
(25) Balaban, A. T. *Chem. Phys. Lett.* **1982**, *89*, 399–404.
(26) Kier, L. B.; Hall, L. H. *Molecular Connectivity in Structure-Activity Analysis*; Research Studies Press: Letchworth, Herts, England, 1986.

RECEIVED for review May 11, 1990. Accepted August 3, 1990. The funding for this work was provided by the Beilstein Institute. Partial funding was also provided by the National Science Foundation for the purchase of the Sun 4/110 computer system.

Whole-Column Computer Simulation in Nonlinear Liquid Chromatography. The Traveling Characteristics of the Concentration Waves of a Binary Mixture

Zidu Ma and Georges Guiochon*

Department of Chemistry, University of Tennessee, Knoxville, Tennessee 37996-1600, and Division of Analytical Chemistry, Oak Ridge National Laboratory, Oak Ridge, Tennessee 37831-6120

Computer calculations show the progressive changes in the individual elution band profiles of the components of a binary mixture during their migration and progressive separation along a chromatographic column. These changes are conveniently illustrated by the waveform surface, obtained by plotting the concentration of each component versus the column distance and time. The surface can be represented either in false 3-D views or by a contour map. Illustrated by the representations of the waveforms surface are the main features of the band interaction, the progressive erosion of the rectangular injection band plateau, the formation and collapse of a front plateau for the first component band, the slower formation of a plateau at the rear of the second component band, and its decay after the bands have separated.

INTRODUCTION

A satisfactory understanding of the mechanism of band separation in chromatography requires a representation of the individual band profiles along the column and of the progressive change of these profiles during the migration of the bands of the mixture components. The concept of this representation is not new. Thin-layer chromatography is based on the examination of the chromatographic bed after a certain time (*1*), while in column chromatography the composition of the eluent is monitored at a certain location of the chromatographic bed (its end). The difference between the methodologies of thin-layer and column chromatography have resulted from the nearly opposite viewpoints of the chromatographic bed adopted. Optimizing the experimental conditions for maximum performance leads in the former case to the use of a thin, flat bed, easily accessible for observation, and in the latter case to the use of a cylindrical column, simple to connect to a swept-through detector cell. Alternative designs, such as overpressure thin-layer chromatography (*2*) and whole-column detection (*3*, *4*), although they permit in principle the addition of the advantages of both methods, have not achieved a high degree of popularity. Few global descriptions of the behavior of chromatographic bands are available.

The purpose of the present work, however, is not to discuss the practical relative advantages of a periodic observation of the concentration profiles along the chromatographic bed versus the monitoring of the mobile-phase composition at some selected location or a combination of both methods but rather to supply a dynamic description of the progressive changes in the individual band profiles which accompany the separation of these bands during their migration along the chromatographic column. Most classical discussions of chromatography have been limited so far to linear chromatography, and elution band profiles (i.e., at column outlet) have rarely been considered in combination with band profiles along the chromatographic bed. Since the combination of the sources responsible for band spreading in linear chromatography can be made by a shift-invariant convolution (*5*) and since the behavior of each band is independent of the behavior or even the presence of any of the other component bands, the problem is entirely explained by progressive drift at constant velocity of a Gaussian profile with a variance increasing linearly with time. We note in passing that a major consequence of this simple model is that the elution profile is *not* a Gaussian curve but is skewed. Failure to understand this effect may explain in part, together with some pervasive experimental problems associated with the difficulty to achieve a true Dirac pulse injection, the success of the exponentially convoluted Gaussian curve as an empirical representation of the elution band profiles.

In nonlinear chromatography, a velocity is associated with each concentration (*6*). This velocity varies with the concentration of the compound considered, with the result that a concentration shock or rather, in real columns, a shock layer takes place on one side of the profile (*6*, *7*). Because the velocity associated with a concentration of one component is a function of the concentrations of all the mixture components, the behaviors of the band profiles of the components of a mixture are no longer independent. Furthermore, the interaction between the different contributions to band broadening is a shift-variant convolution (*5*). The band profiles have to be treated together, and the result depends on the amount of sample injected, the injection profile, and the relative feed composition (*5–12*). A number of different cases must be considered successively to provide a reasonably complete picture of a much more complex situation than in the linear case. It is especially important to understand that, even when the bands are separated at their elution, they have traveled together during most of their journey along the column and, when one of the concentrations at least is large, have interfered with each other. The band profile of the first component never recovers from this interaction but continues to carry a scar (*9*, *10*).

Most of the previous work dealing with the calculation of individual band profiles is devoted to elution profiles, as they could be recorded by an on-line detector. The calculation methods used, however, can be easily applied to the determination of individual band profiles along the column at any time during the elution of the sample. In fact, one of the calculation methods used calculates all these intermediate profiles at successive times separated by a brief increment, Δt, while another procedure calculates the elution profiles from each successive column increment, Δz (*13–15*). These intermediate profiles can be stored and displayed, which provides for the entire behavior of the sample component bands in the time, length space.

We present in this paper series of solutions permitting a complete description of the migration and separation of the

*To whom correspondence should be addressed, at the University of Tennessee.

0003-2700/90/0362-2330$02.50/0 © 1990 American Chemical Society

bands of a binary mixture. This permits a simple explanation of the mechanisms of band interaction, the rise and decay of the displacement and tag-along effects, the decay of the injection pulse plateau, and the simultaneous formation of a concentration plateau for the first component (related to the displacement effect) and of a concentration plateau for the second component at the end of the mixed band (related to the tag-along effect).

THEORY

The equilibrium and semiequilibrium models of chromatography have been reviewed recently (*16*). Whenever the kinetics of mass transfers between and across the phases of the chromatographic system are fast and the column efficiency exceeds a few hundred plates, the numerical solutions of the system of mass balance equations of chromatography calculated with the semiequilibrium model are identical with those derived from kinetic models under equivalent experimental conditions (*17*). Accordingly, the present work uses the semiideal model (*8*, *14*).

I. Equations of the Problem. In this model, the mass balance equation of the compound i (i = 1 or 2) is written

$$\frac{\partial C_i}{\partial t} + F\frac{\partial Q_i}{\partial t} + u_0\frac{\partial C_i}{\partial z} = D_a\frac{\partial^2 C_i}{\partial z^2} \quad (1)$$

where Q_i and C_i are the concentrations of the component i in the stationary and the mobile phase, respectively, z and t are the column length and the time, respectively, F is the phase ratio, equal to the ratio $(1 - \epsilon)/\epsilon$, where ϵ is the internal porosity of the packing material used, u_0 is the mobile-phase velocity, and D_a is the apparent dispersion coefficient for the compound and the conditions considered.

In order to simulate the behavior of the band of a compound under defined experimental conditions, the concentrations of the two components in the stationary and the mobile phase must be related by equations accounting for their competitive interactions with the stationary phase. The simplest and most convenient interaction model is the competitive Langmuir isotherm, written as

$$Q_i = \frac{a_i C_i}{1 + \sum_{j=1}^{2} b_j C_j} \quad (2)$$

where a_i and b_j are numerical coefficients depending on the nature of the compounds studied and on the chromatographic system.

The apparent dispersion coefficient, D_a, is related to the column height equivalent to a theoretical plate (HETP), H, for the compounds considered by the equation

$$D_a = HL/2t_0 \quad (3)$$

where L is the column length and t_0 is the hold-up time.

Equation 3 assumes that the column HETP, H, is a known parameter, constant during an experiment. Thus, the model does not account directly for the dependence of the plate height on the mobile-phase linear velocity or the retention factor of the components used, which is not a serious limitation. The mobile-phase velocity does not vary during a chromatographic experiment (*14*), unless it is programmed to do so, which is rather unusual. Furthermore, completing the system of eqs 1–3 with the Knox plate height equation gives a model that takes properly into account the influence of the velocity on the mass-transfer kinetics in HPLC columns. The model accounts correctly for the band broadening of a pure component even at high loadings, where the band is wide and covers a significant range of retention factors (*15*). In the case of a binary mixture, the model assumes that the two components have the same value of H, which is reasonable, as the dependence of H on the retention is weak for compounds that are closely related and have similar retention times.

In this model, we assume that the column is homogeneous and that its properties are independent of z. In liquid chromatography, we know that we can neglect the influence of the mobile-phase compressibility and assume that the mobile-phase linear velocity, its viscosity, and the molecular diffusion coefficients of the solutes are constant along the column (*6*, *12–15*). The inlet pressure used in preparative liquid chromatography rarely exceeds 100 atm, which makes the relative variation of these parameters along the column smaller than a few percent (*14*). Similarly, the coefficients of the Langmuir isotherms are constant. Finally, we assume that the kinetics of mass transfers in preparative columns is controlled by the diffusion in the mobile phase, either between or inside packing particles. This is true in all modes of HPLC. It is not often true in affinity chromatography nor in some special cases where other modes are used and the kinetics of adsorption/desorption or of association/dissociation are slow. In these cases a kinetic model becomes necessary and the results presented here are not valid (*12*, *17*).

Finally, the solution of the system of eq 1–3 must be found for the following set of boundary and initial conditions:

$$C_i(t, z = 0) = \phi_i(t)$$
$$C_i(t = 0, z) = 0$$
$$i = 1, 2 \quad (4)$$

The conditions given in eq 4 state that the column is empty at the beginning of the experiment and that a mixture having the profile $C_1 = \phi_1(t)$, $C_2 = \phi_2(t)$ is injected at the column inlet, in the mobile phase entering the column. In this work, $\phi_i(t)$ is chosen to simulate the injection of a rectangular band of the binary mixture. Two bandwidths have been used, 40 s and 2 min. These values are typical of those used in preparative chromatography.

II. Numerical Solutions of the Equation System. The system of eqs 1–4 written for the two components of a binary mixture can be solved by using either the finite difference (*13–15*) or the finite element (*18*) approach. The former is easier to understand as it propagates the band along a time–space grid (*14*). Two methods are available that differ by the relative emphasis given to the time and space directions. We explain here how the calculation is performed in the case of a finite difference scheme that is analogous in principle to the Craig machine (*19*). The advantage of the Craig–Czok (CC) algorithm is that it has a physical sense (*15*). Other finite difference schemes that have no physical equivalent are as correct as the CC algorithm discussed elsewhere (*15*).

The column is divided into thin slices of thickness Δz, and the concentration in each of these $L/\Delta z$ cells is determined at each time interval Δt. The mass balance relation between two successive cells at two consecutive time intervals permits the writing of an equation that describes iteratively the behavior of the entire sample zone during its migration and separation into two bands. Let us consider the jth cell at the nth time interval. If for the moment we neglect the axial dispersion (i.e., assume an ideal column), the mass balance for that cell, between the times $n\Delta t$ and $(n + 1)\Delta t$ is written

$$\frac{C_j^{n+1} - C_j^n}{\Delta t} + F\frac{Q_j^{n+1} - Q_j^n}{\Delta t} + u_0\frac{C_j^n - C_{j-1}^n}{\Delta z} = 0 \quad (5)$$

which can be rearranged into

$$(C_j^{n+1} + FQ_j^{n+1}) - (C_j^n + FQ_j^n) = \frac{u_0\Delta t}{\Delta z}(C_{j-1}^n - C_j^n) \quad (6)$$

Equation 6 states the physical evidence that the change in the total amount of the component considered, which is contained in the jth cell, is equal to the net amount of material flowing into the cell: we have assumed that there is no axial dispersion. The amount of compound which enters the jth cell during the time Δt is $Su_0\Delta t C_{j-1}^n$, while the amount which leaves that cell is $Su_0\Delta t C_j^n$, where S is the cross section area of the column. Thus, the change in concentration is

$$\frac{Su_0\Delta t(C_{j-1}^n - C_j^n)}{\Delta z S} \tag{7}$$

Following this propagation step, an equilibration step must be carried out. Since the mobile-phase concentration has been changed (eq 7), the two phases in the cell are no longer in equilibrium (*15*).

If we now take the axial dispersion (i.e., the finite character of the column efficiency) into account, the finite difference (CC type) equation equivalent to eq 1 for one component is written

$$\frac{C_j^{n+1} - C_j^n}{\Delta t} + F\frac{Q_j^{n+1} - Q_j^n}{\Delta t} + u_0\frac{C_j^n - C_{j-1}^n}{\Delta z} = D\frac{C_{j+1}^n - 2C_j^n + C_{j-1}^n}{\Delta z^2} \tag{8}$$

The change in the total amount of the compound considered, which is contained in the jth cell, is now the sum of the convection flux (the amount flowing into or out of the cell) and the dispersion term (the amounts lost to the previous and following cells and the amounts gained from them by dispersion).

The calculations performed by using either eq 6 or 8 give a staircase concentration profile. There is one concentration value for each cell at each time increment. There is no physical basis for that profile, the division of the column into a series of cells is arbitrary, and the concentration profiles observed experimentally are continuous. The problem, however, is that our calculation gives an uncertain position of the concentration obtained in the cell. Because the calculations have to be carried out a large number of times (of the order of N^2, where N is the column plate number under linear conditions), this uncertainty propagates during the calculations, the errors made accumulate, and the profile resulting from the numerical integration is not exact. It can be shown (*12*, *20–22*) that the error introduced by the calculation is a numerical dispersion, exactly equivalent to an axial dispersion.

There are several ways to accommodate the axial dispersion of numerical origin. First, we can try to make it negligible by selecting proper values of the integration increments. This would require the use of very small increments, resulting in excessively long computer time. Secondly, we can adjust it in such a way that it is equivalent to the axial dispersion due to the axial diffusion and to the mass-transfer resistances due to the finite rate of the kinetics of these transfers between and across phases. This is the basis of our earlier work (*13–15*). For example, when eq 6 is used, the increments are chosen so that (*15*)

$$H = \Delta z - \frac{u}{1 + k'}\Delta t \tag{9}$$

where H is the column height equivalent to a theoretical plate and k' is the retention factor, both under linear conditions (e.g., $\Delta z = 2H$ and $\Delta t = H(1 + k')/u$). The main difficulty is that the selection of Δt is a function of k'. In the nonlinear case, the calculation procedure contains a third-order error term that cannot be controlled. This term causes a deviation between the true and the calculated profiles, which is usually negligible (*12*, *20–22*). Some significant error takes place in the case of a binary mixture, however, when the concentration of the second component is smaller than that of the first one (*15*, *23*). This error affects almost exclusively the front of the second component.

A third approach consists of selecting values of the increments which are large enough to introduce a significant amount of numerical dispersion, thus keeping the computation time reasonable, but are small and do not permit full account of the actual band dispersion resulting from the finite column efficiency. Then, a diffusion step is added for the exact amount still unaccounted for. This step uses a dispersion coefficient that varies with the retention factor, k', and is calculated for each cell (*23*). This is the method used in the present work.

In the case of a binary mixture, two equations such as eqs 6 and 8 are written. Because of their competition for interaction with the stationary phase (e.g., for adsorption), the new concentrations of the two components must be recalculated together, which introduces some minor complication because the system of mass balance equations between the two phases in a cell, using the competitive Langmuir isotherms (eq 3), cannot be solved in closed form (*15*, *24*). The competitive nature of the equilibrium of the two components between the phases of the chromatographic system is the physical origin of the coupling between the differential mass balance of these two components.

In the following, results obtained with a FORTRAN program implementing the CC algorithm and using eq 8 are presented and discussed. The numerical values for the Langmuir isotherm coefficients and for the column-phase ratio are experimental values obtained in a study reported elsewhere (*25*), using 2-phenylethanol and 3-phenylpropanol with a (50:50) methanol/water mobile phase on C_{18} silica as the stationary phase. The efficiency is 1250 plates, a reasonable value for a typical preparative column packed with 20-μm particles and operated at a high reduced velocity.

RESULTS AND DISCUSSION

By plotting the concentration of each component as a function of the column distance and time, we obtain a waveform surface that describes completely the behavior of the sample zone during its journey along the column and its separation into the two component bands. The basic rule to understand the profiles in the following figures is that the farther down the column a concentration is, the earlier it leaves the column. Large distances at a given time correspond to short retention times. On each of the following figures, the surface is represented by the network of cross sections formed by two series of parallel planes.

Cross sections of the $C_i(z, t)$ surfaces by planes parallel to the C, z coordinate plane (i.e., t = constant) give individual band profiles along the column at the corresponding times. These profiles are similar to those recorded in thin-layer chromatography. Consideration of these cross sections shows how the band profile evolves during its migration. Conversely, cross sections of the $C_i(z, t)$ surface by planes parallel to the C, t coordinate plane (i.e., z = constant) give elution profiles at the end of a column of corresponding length. These profiles are the chromatograms that would be obtained in elution chromatography with a column of length z. The study of these elution profiles shows also how the band profile evolves and could permit the selection of the proper column length for maximum production rate. On each 3-D figure, the two sets of cross sections are shown. They are calculated together by the program and obtained by proper management of the result file. Thus, the waveform surface contains all the elution profiles, at any possible column length, and the profiles along the column, at any instant. Finally, as all 3-D surfaces, the

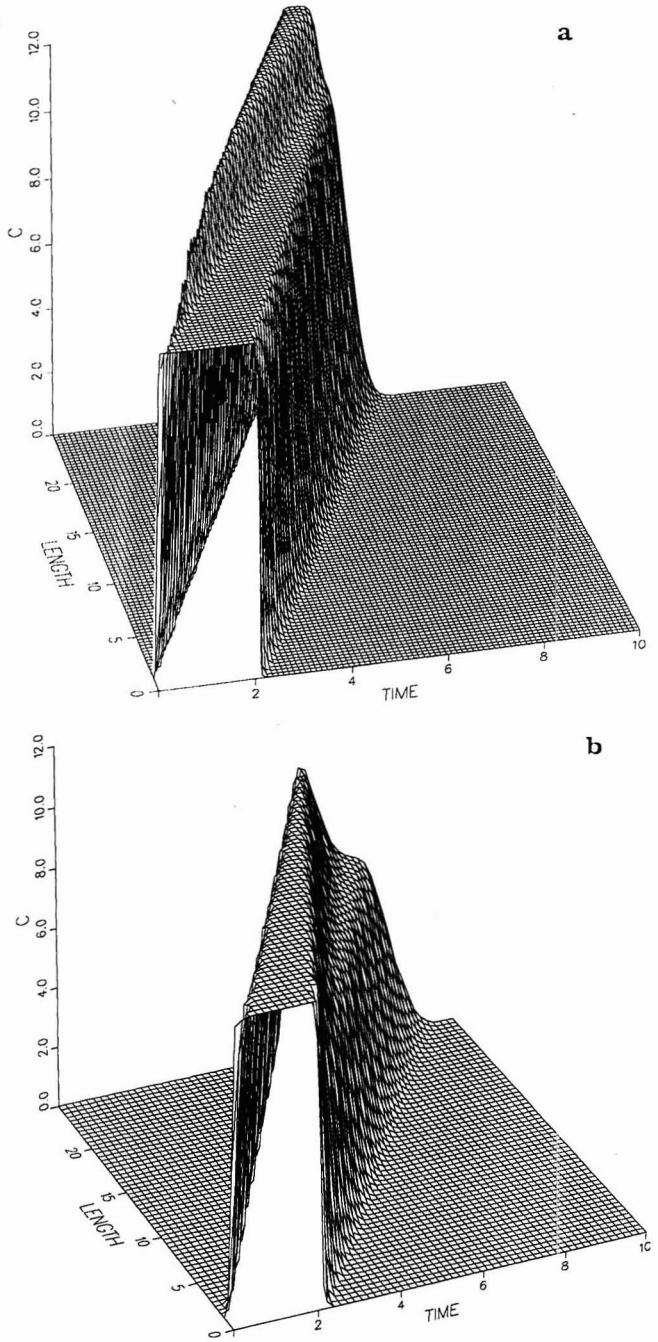

Figure 1. Individual waveform solution surfaces for a wide rectangular injection pulse (view from the injection side): (a) solution surface for the less retained component; (b) solution surface for the more retained component. Conditions: flow velocity, 0.13 cm/s; column dimensions, 250 × 4.6 mm; phase ratio, 0.31 (ϵ = 0.76); column efficiency, 1200 theoretical plates. Competitive Langmuir isotherms are a_1 = 1.92 ($k_{0,1}'$ = 0.6), b_1 = 0.0256, a_2 = 3.55 ($k_{0,2}'$ = 1.10), and b_2 = 0.0211. The injection concentration of both solutes is the same, $C_1^0 = C_2^0$ = 10.0 mg/mL, and the injection time is 2.0 min.

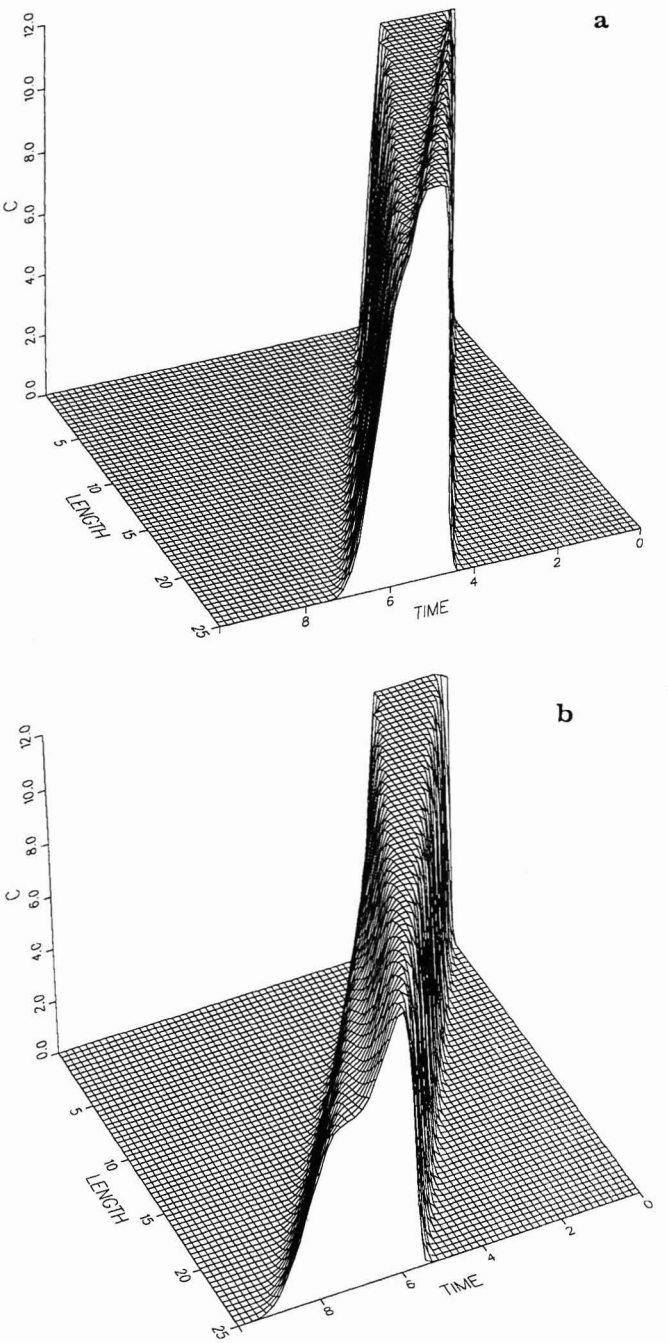

Figure 2. Individual waveform solution surfaces for a wide rectangular injection pulse (view from the elution side): (a) solution surface for the less retained component; (b) solution surface for the more retained component. System parameters are the same as for Figure 1.

concentration distribution surfaces can be mapped by considering cross sections by planes parallel to the z, t plane (i.e., C_i = constant). Some such contour maps will be presented later.

Figure 1 shows the waveform surfaces of the two components, 1 (less retained) and 2 (more retained), respectively, in the case of a wide rectangular injection. The profile $\phi_i(t)$ (eq 4) for each component is a rectangle of height C_i^0 ($C_1^0 = C_2^0$). The injection width has been chosen so that the concentration plateau of the injection remains stable until the elution of the band, at the end of a 25 cm long column. Only a small fraction (ca. 90) of the large number of profiles (1250) calculated during the total integration is shown. Some lines on these figures and in the next ones appeared jagged, especially at the beginning of the experiment. This is an artifact due to the plotter program, whose influence could not be reduced further. Figure 2 shows the same surfaces as Figure 1, respectivley, but from the opposite angle, featuring the band profiles near the end of the experiment and the elution profiles, since the surface is cut by the plane L = 25 cm.

The waveform profiles of the two components are profoundly different. For the first component (Figures 1a and 2a), an intense displacement effect prevails as soon as the analysis begins (*9*, *10*). A concentration plateau forms, which is higher than the injection pulse plateau at $C_1 = C_1^0$. The existence of this plateau has been recognized earlier (*6*) and explained theoretically (*6*, *9*, *10*, *12*, *26–30*). Its existence is central to the frontal analysis method developed by Frenz et al. (*31*) and to the simple wave method (*6*, *26–30*) developed

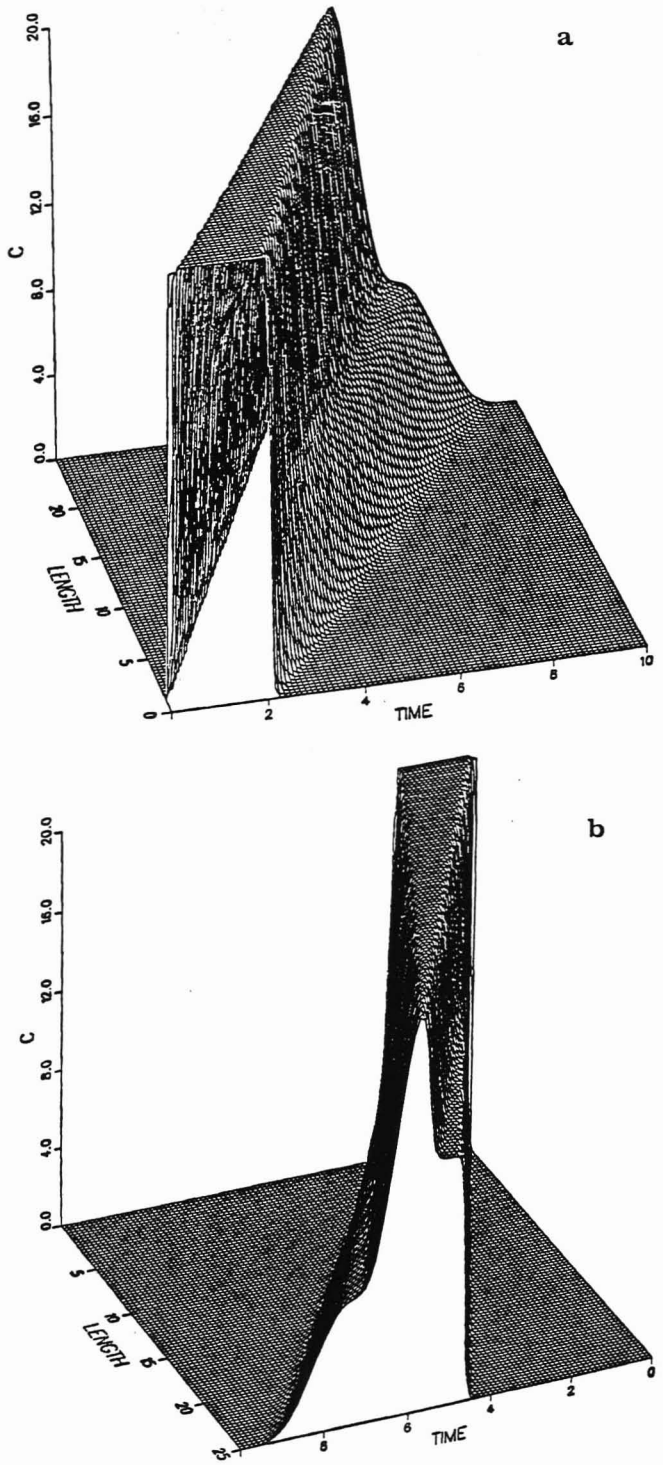

Figure 3. Total concentration waveform solution surface for a wide rectangular injection pulse: (a) view from the injection side; (b) view from the elution side. System parameters are the same as for Figure 1.

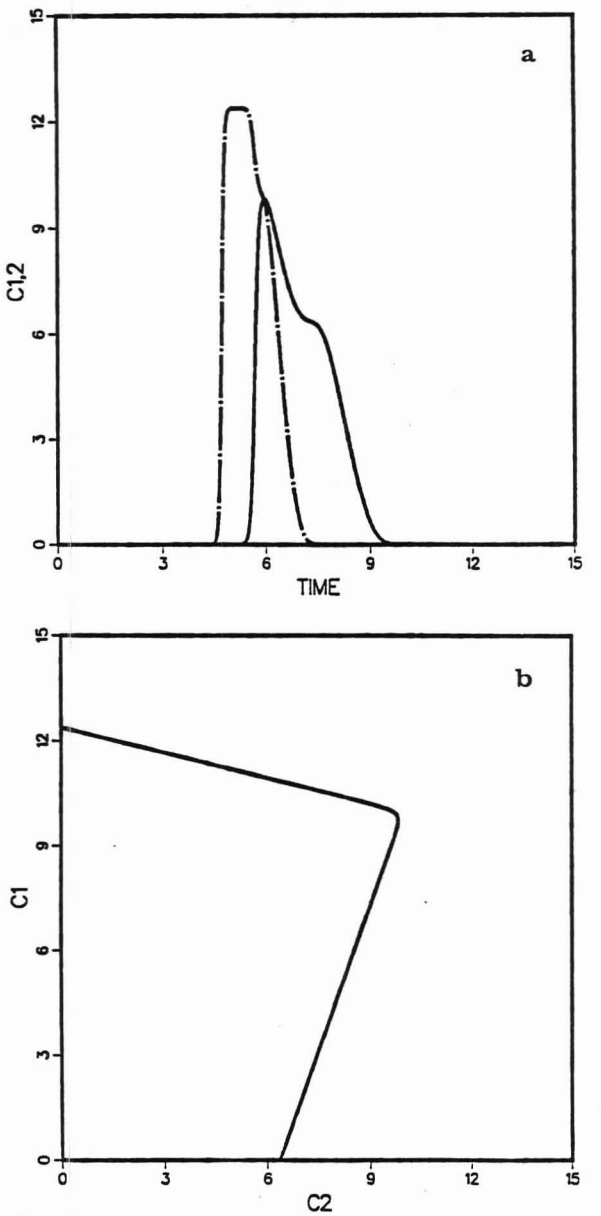

Figure 4. Hodograph transform of the elution profile of the two components of the binary mixture as shown in Figures 1–3: (a) elution profiles of the two components; (b) hodograph transform of these profiles.

by Ma et al. (*25*) for the determination of competitive isotherms. This plateau forms rapidly (Figure 1a), and it widens as long as the injection pulse plateau persists (Figure 2a). It starts to decay as soon as the concentration plateau disappears, which can be seen near the end of the waveform profile in Figure 2a.

On the contrary, in the waveform profile of the second component (Figures 1b and 2b), we see the progressive buildup of an intermediate plateau at a concentration lower than the concentration C_2^0. The velocity associated with a given concentration of the second component decreases with decreasing value of the local concentration of the first component (*9*, *11*). This is because the amount of a component adsorbed at equilibrium, at constant concentration in the mobile phase, decreases with increasing concentration of the other components. The limit of the velocity associated with a given concentration of the second component when the local concentration of the first component tends toward zero is, however, larger than the velocity associated with the same concentration of the pure second component (*11*). This explains the formation of the intermediate plateau of the second component (*9–11*).

The total concentration profile for the zone obtained with a wide injection pulse of a binary mixture is shown in Figure 3a (origin view) and b (end view). Three plateaus are observed in this figure, the injection pulse plateau, which disappears progressively, and the two plateaus of the pure component bands, in the front and rear of the zone. Within the time and column distance ranges shown, these two plateaus grow wider. The concentrations of the two components in the time–distance space between these two pure component plateaus are simply related (*6*, *25–30*). The corresponding region is called the *simple wave region*. The simple wave solution is simply related to the parameters of the competitive isotherm equation model (*25*).

These results are illustrated by the hodograph transform of the elution profile, which is similar to the transform of a zone profile along the column (see Figure 4). The hodograph transform of the elution profiles of a binary mixture is a plot of the concentration of the first component versus the concentration of the second one at the same time. For a mathematical justification of the transform and a description of its properties, see refs 12 and 25. The zone profile obtained for the injection of a large rectangular pulse of a binary mixture contains three successive bands, a band of pure first component, a mixed band, and a band of the pure second component (Figure 4a). As long as the plateau of the injection profile is not completely eroded, the plot of the concentration of one component versus the concentration of the other one gives two lines that are nearly straight (Figure 4b). These lines intersect at the point (C_1^0, C_2^0). They intersect the coordinate axes at the points corresponding to the two plateaus, on the front of the first component profile and the rear of the second component profile (Figure 4b). The formation of this latter plateau explains the origin of the tag-along effect (*8*, *10*, *11*).

When the column is long or the injection pulse is narrow, the two component bands separate (Figure 5). The simple wave region disappears first, in the same time as ends the injection pulse plateau. A deep valley forms between the two pure component bands which eventually are completely resolved. The two plateaus, now one at the top of each pure component band, start to erode as soon as the injection pulse plateau has disappeared. Their end marks the beginning of the decay of each component band height. Although with an ideal column of infinite efficiency, the front and end plateaus form always, whatever the composition of the feed pulse and its width, with a real column, the plateaus may never appear, especially when the feed composition corresponds to a mixture rich in one of the two components. In such a case, the top of the first component band becomes flat or the rear of the second component profile acquires an inflection point.

These phenomena can be illustrated as well, sometimes more clearly, by using contour maps instead of false 3-D pictures. Isoconcentration lines in a time–distance plot show the trajectory of concentrations. When the slope of these lines increases, the corresponding concentration moves faster. When the slope decreases, the corresponding concentration slows down. In Figure 6a and b are represented the isoconcentration lines of the zone obtained with a wide concentration pulse (Figures 1–3). The two wide white areas seen in the center of the band in this figure correspond to concentration plateaus, while the dark boundaries correspond to steep concentration gradients. Lines originating from the origin indicate the behavior of the front discontinuity of the injection pulse. Those originating from the rear of the injection pulse show the behavior of this second concentration discontinuity. We see that the front remains very steep (the front shock is stable (*6*, *7*)) but that a second plateau appears on the front of the first band (the concentration wedge originating from the top of the plot) while the injection pulse plateau has nearly disappeared for L = 25 cm (the wedge originating from the bottom of the plot). The spreading of the lines originating from the rear of the injection pulse shows an unstable rear shock collapsing into a diffuse rear profile (*9*, *14*).

The contour map for the second component shows also the progressive erosion of the injection pulse plateau (Figure 6b, wedge originating from the bottom of the figure) and the formation of the plateau on the rear of the profile. The widths of the fronts of the two profiles (Figure 6a and b) are nearly constant. This is in agreement with the constant thickness of the front shock layer (*7*). Comparison between parts a and b of Figure 6 shows the extent of the simple wave region (*25*): the profile considered for the experiment (in practice, the

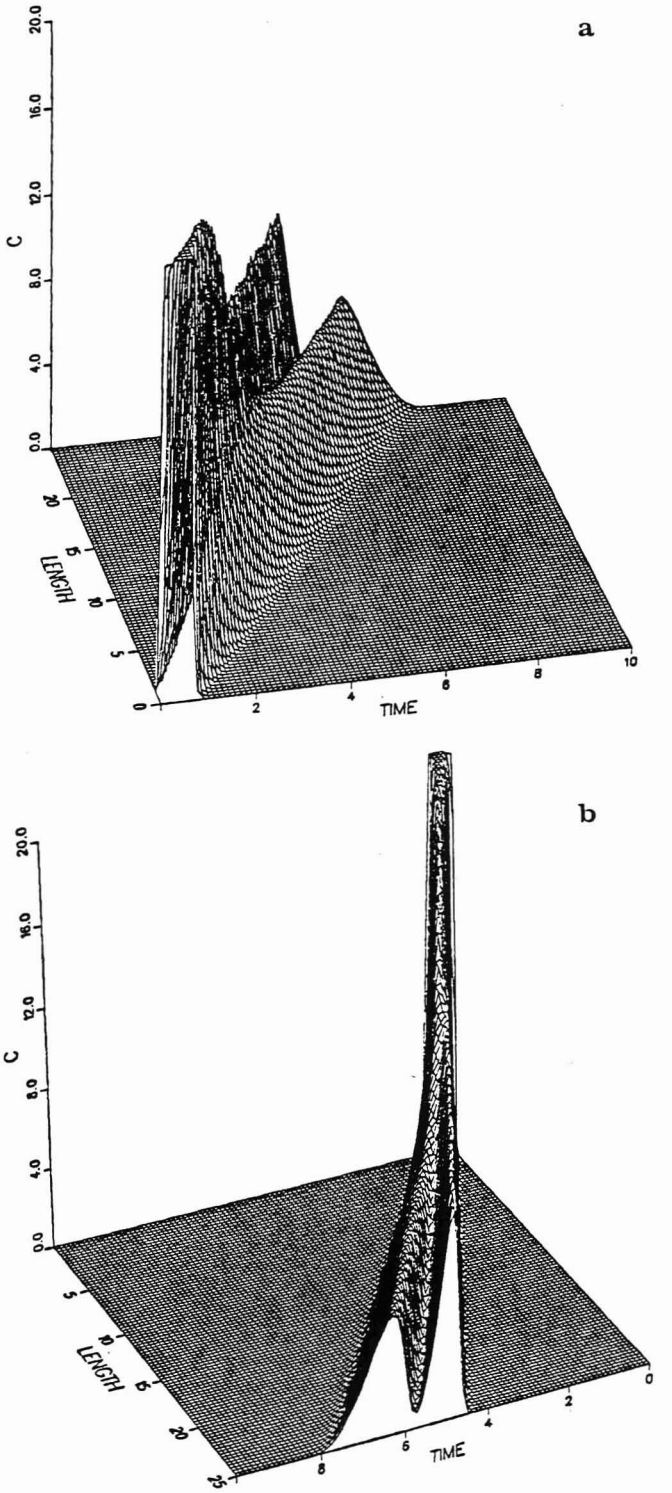

Figure 5. Total concentration waveform solution surface for a narrow rectangular injection pulse: (a) view from the injection side; (b) view from the elution side. System parameters are the same as for Figure 1, except the injection time: 0.6 min.

profile in the column at t = constant, or the elution profile, at z = constant) should intersect the z, t plane along a line that has least one point contained in the injection pulse plateau region.

In the case of a narrow pulse injection, there is no displacement or tag-along plateau (see Figure 7a and b). The thickness of the front shock layer is too large, larger than would be the width of these plateaus. With an efficient enough column, a displacement and a tag-along plateau would be observed. The existence of the displacement effect is demonstrated, however, by the increasing concentration ridge culminating around z = 9 cm and t = 2 min, with a concen-

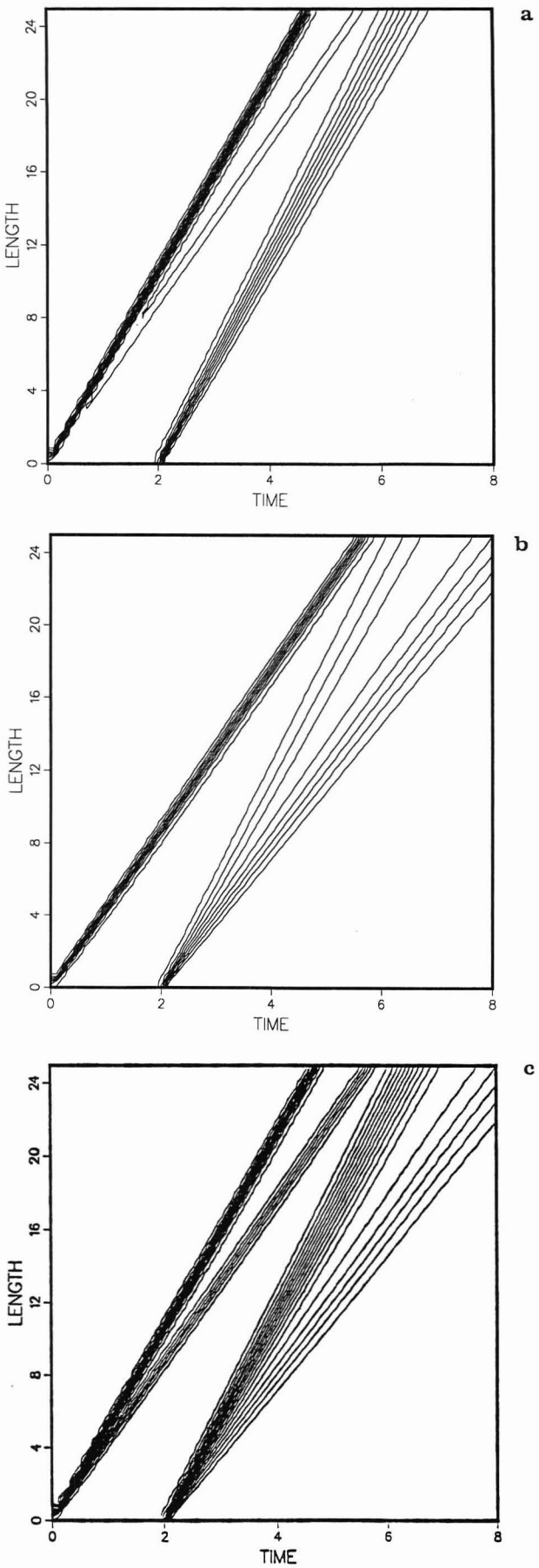

Figure 6. Contour map of the waveform solution surfaces for a wide rectangular injection pulse (isoconcentration curves for the surface shown in Figures 1 and 3): (a) contour map for the less retained component; (b) contour map for the more retained component; (c) isoconcentration curves for the surface shown in Figure 3.

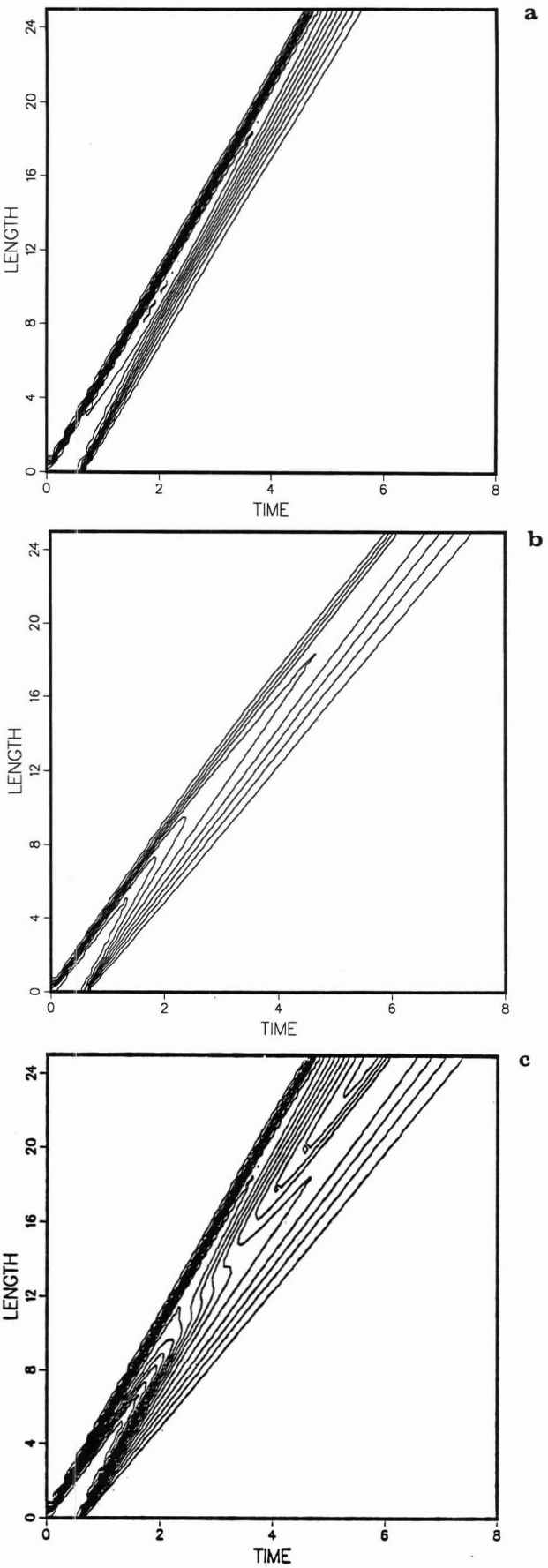

Figure 7. Contour map of the individual and total concentration waveform solution surface for a narrow rectangular injection pulse (isoconcentration curves for the waveform solution surfaces shown in Figures 4 and 5): (a) contour map for the less retained component; (b) contour map for the more retained component; (c) contour map of the total concentration waveform solution surface for a narrow rectangular injection pulse.

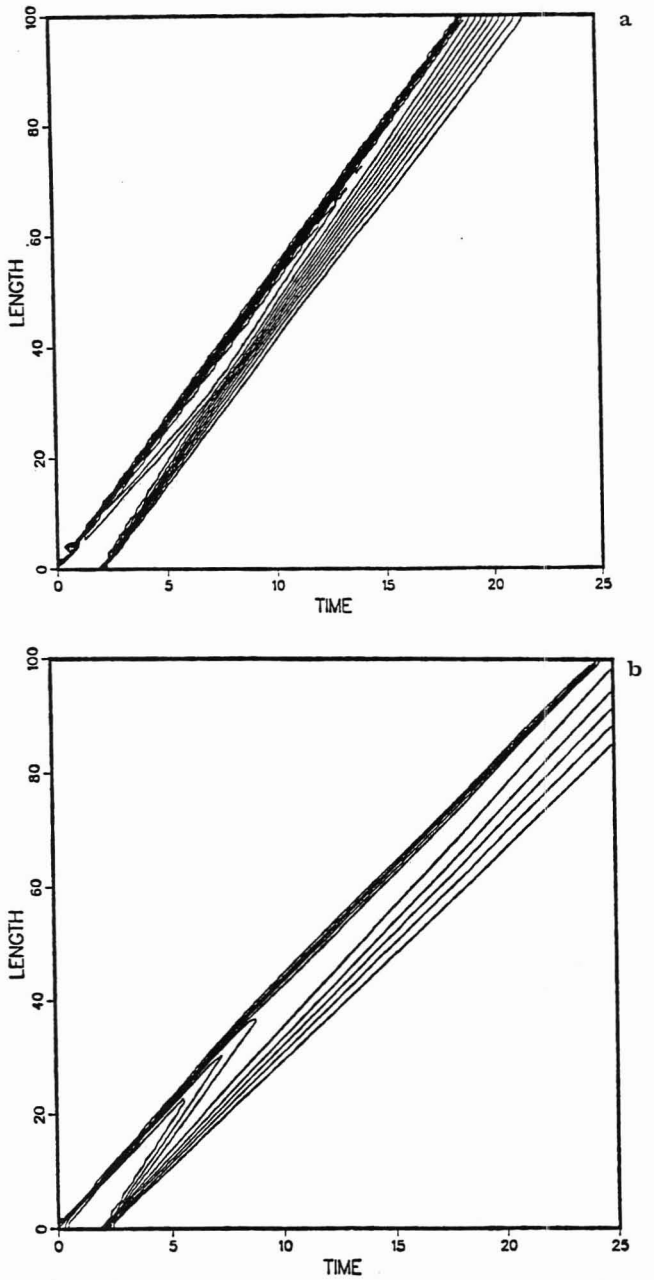

Figure 8. Contour map of the individual waveform solution surfaces for a wide rectangular injection pulse: (a) contour map for the less retained component; (b) contour map for the more retained component. Parameters are the same as for Figures 1–4 and 6, except column length: 100 cm.

tration higher than C_1^0 (Figure 7a). In Figure 7b, we see that the trajectories of the front concentration (shock layer) change slope when the separation reaches completion and the migration of a given concentration slows down. This effect is due to the interaction with the first component band, but this is all that is left of the tag-along effect.

The superimposition of the contour maps in Figures 6a and b and 7a and b, respectively are shown in Figures 6c and 7c. In the former figure, we see again the extent of the simple wave region and the formation of the two plateaus which flank it. In the latter figure (Figure 7c), the simple wave region has dramatically shrunk and can barely be identified, at the beginning of the column (first 5 cm). The wedge of the valley that forms between the two bands when they separate is clearly visible at the top of the figure. The tag-along effect is shown by the rapid widening of the second band profile during the first part of its trajectory, until about 11–13 cm, followed by a much slower broadening of the separated band.

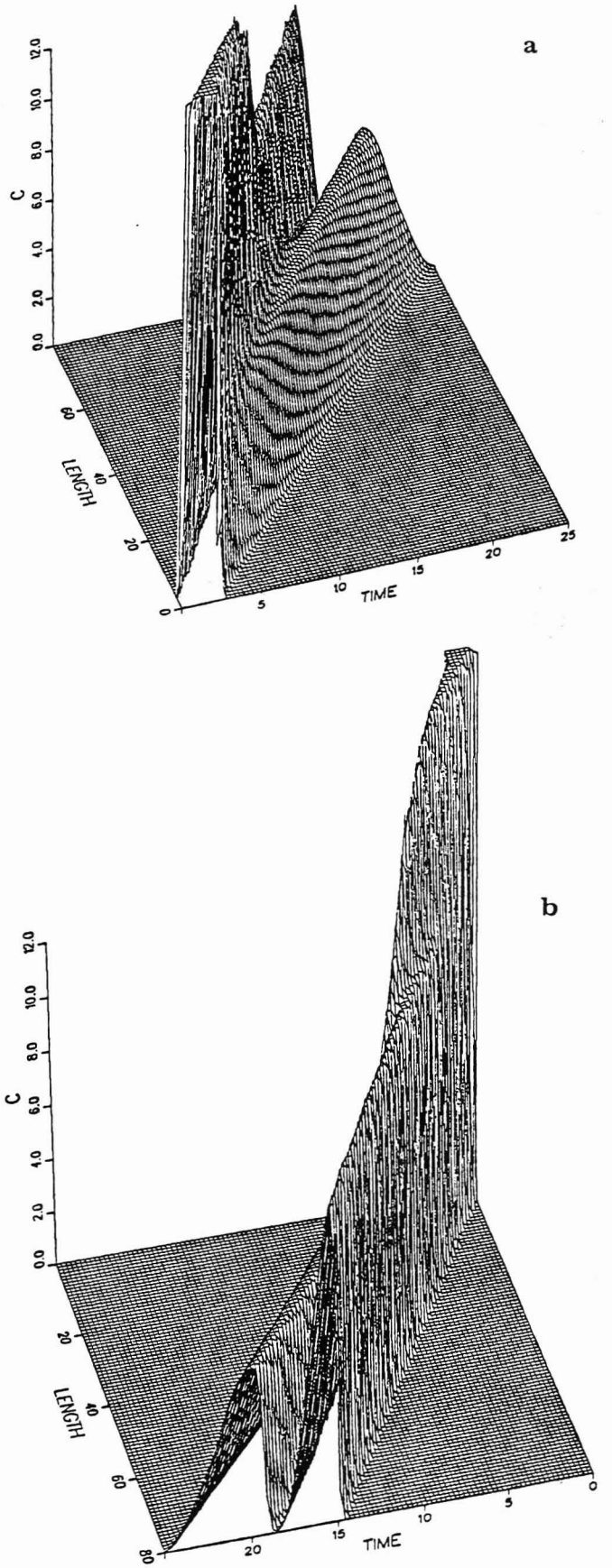

Figure 9. Total concentration waveform solution surface for a wide rectangular injection pulse, on a very long column: (a) view from the injection side; (b) view from the elution side. System parameters are the same as for Figure 1.

On the contrary, the displacement effect results in a slower broadening of the first component band at first (until z = ca. 15 cm), followed by a faster, more normal rate of band

spreading when the second band has been left behind.

Finally, in Figure 8, we show the contour maps of the individual band profiles of the two components, under the same conditions as used to calculate the maps shown in the Figures 6 and the 3-D waveform surfaces in Figures 1–3. The column used now is 4 times longer, so the result includes all features encountered in Figures 1–7, corresponding to the wide and the narrow injection pulses. The separation between the two bands reaches completion for a distance approximately equal to 60 cm, but the displacement plateau as well as the simple wave region do form at low elution distance. The displacement plateau is seen for distances up to ca. 27 cm, while the tag-along plateau remains stable beyond z = 100 cm. The tag-along plateau is the maximum of the second band profile beyond about 40 cm. We have shown previously that this plateau is eroded only slowly. The thickness of the shock layer of the first component remains nearly constant over the entire plot, which is explained by the rather narrow range of variation of the maximum concentration of this band. The thickness of the shock layer of the second band increases when the injection pulse plateau is eroded and remains constant, which is expected since the maximum concentration of this band remains also constant. Figure 9 shows the 3-D waveform surface for a 0.80 m long column and a wide injection pulse. The progressive formation and erosion of the three concentration plateaus is clearly seen.

CONCLUSION

Consideration of plots such as the ones in Figure 8 can be used to determine the optimum column length permitting the separation of the components of a binary mixture with some constraints of fraction purity. Drawing such plots requires only the calculation of one solution of the partial differential equation system of chromatography, corresponding to a column length longer than that needed to achieve total separation of the two bands. Intermediate results of this calculation have to be stored and reprocessed by the graphic program at minimum CPU time cost.

Most importantly, however, the waveform chromatograms provide a vivid description of the progressive changes in the individual band profiles that accompany their migration and separation. All the information contained in a waveform chromatography surface is also contained in a single cross section of the surface. This results immediately from the fact that these profiles are solutions of eq 1. The values of the parameters can be related simply to the properties of the profiles if the column is homogeneous. Comparison between experimental results and the profiles obtained by numerical calculations need be made only on the elution profiles corresponding to one value of the column length. The only feature that does not show on the elution profile of a 25-cm column is the displacement crest in the case of a narrow rectangular injection. It appears clearly, however, with a wide rectangular injection (*25*). If the column is not homogeneous, it is still true that all the chromatographic information is contained in one elution chromatogram but the inverse problem becomes impossible to solve with our present tools.

Finally, it must be emphasized that the calculations leading to the results presented here are based on the validity of eq 2 as a model for the competitive behavior of the mixture components. We know now that, although this model provides a good qualitative description of this behavior, it is not exact whenever the column saturation capacities for the different components are different (*32*).

LITERATURE CITED

(1) Geiss, F. *Fundamentals of Thin-Layer Chromatography*; Alfred Huethig Verlag: Heidelberg, Germany, 1987.
(2) Tyihak, E.; Mindcsowics, E.; Kalasz, H.; Nagy, J. *J. Chromatogr.* **1981**, *211*, 45.
(3) Gelderloos, D. G.; Rowlen, K. L.; Birks, J. W.; Avery, J. P.; Enke, C. G. *Anal. Chem.* **1986**, *58*, 900.
(4) Rowlen, K. L.; Kenneth, A. D.; Avery, J. P.; Birks, J. W.; Enke, C. G. *Anal. Chem.* **1989**, *61*, 2624.
(5) Dose, E. V.; Guiochon, G. *Anal. Chem.* **1990**, *62*, 1723.
(6) Aris, R.; Amundson, N. R. *Mathematical Methods in Chemical Engineering*; Prentice-Hall: Englewood Cliffs, NJ, 1973.
(7) Lin, B. C.; Golshan-Shirazi, S.; Ma, Z.; Guiochon, G. *Anal. Chem.* **1988**, *60*, 2647.
(8) Guiochon, G.; Ghodbane, S. *J. Phys. Chem.* **1988**, *92*, 3682.
(9) Golshan-Shirazi, S.; Guiochon, G. *J. Phys. Chem.* **1989**, *93*, 4143.
(10) Golshan-Shirazi, S.; Guiochon, G. *J. Chromatogr.* **1989**, *484*, 125.
(11) Golshan-Shirazi, S.; Guiochon, G. *Anal. Chem.* **1990**, *62*, 217.
(12) Lin, B. C.; Golshan-Shirazi, S.; Ma, Z.; Guiochon, G. *J. Chromatogr.* **1990**, *500*, 125.
(13) Rouchon, P.; Schoenauer, M.; Valentin, P.; Guiochon, G. *Sep. Sci. Technol.* **1987**, *22*, 1793.
(14) Guiochon, G.; Golshan-Shirazi, S.; Jaulmes, A. *Anal. Chem.* **1988**, *60*, 1856.
(15) Czok, M.; Guiochon, G. *Anal. Chem.* **1990**, *62*, 189.
(16) Golshan-Shirazi, S.; Guiochon, G. *J. Chromatogr.* **1990**, *506*, 475.
(17) Lin, B. C.; Golshan-Shirazi, S.; Guiochon, G. *J. Phys. Chem.* **1989**, *93*, 3363.
(18) Ma, Z.; Guiochon, G. Unpublished material.
(19) Craig, L. C. *J. Biol. Chem.* **1944**, *155*, 519.
(20) Lin, B. C.; Guiochon, G. *Sep. Sci. Technol.* **1988**, *24*, 31.
(21) Lin, B. C.; Ma, Z.; Guiochon, G. *J. Chromatogr.* **1989**, *484*, 83.
(22) Richtmeyer, R. D.; Morton, K. W. *Difference Methods for Initial Value Problems*, 2nd ed.; Interscience: New York, 1967.
(23) Czok, M.; Guiochon, G. *Comput. Chem. Eng.*, in press.
(24) Czok, M.; Guiochon, G. *J. Chromatogr.*, in press.
(25) Ma, Z.; Katti, A.; Lin, B. C.; Guiochon, G. *J. Phys. Chem.* **1990**, *94*, 6911.
(26) Seinfeld, J. H.; Lapidus, L. *Mathematical Methods in Chemical Engineering*; Prentice-Hall: Englewood Cliffs, NJ, 1974; Vol. 3.
(27) Lax, P. D. *Commun. Pure Appl. Math.* **1957**, *10*, 537.
(28) Whitham, G. B. *Linear and Nonlinear Waves*; Wiley: New York, 1974.
(29) Jeffrey, A. *Quasilinear Hyperbolic Systems and Waves*; Pitman Publishing: London, 1976.
(30) Schapiro, A. H. *The Dynamics and Thermodynamics of Compressible Fluid Flow*; Ronald Press: New York, 1953.
(31) Jacobson, J. M.; Frenz, J. H.; Horvath, Cs. *Ind. Eng. Chem. Res.* **1987**, *26*, 43.
(32) Golshan-Shirazi, S.; Guiochon, G. *J. Chromatogr.*, in press.

RECEIVED for review April 23, 1990. Accepted July 31, 1990. This work has been supported in part by Grant CHE-8901382 of the National Science Foundation and by the cooperative agreement between the University of Tennessee and the Oak Ridge National Laboratory. We acknowledge support of our computational effort by the University of Tennessee Computing Center.

Surface Studies of the Silver Sulfide Ion Selective Electrode Membrane

Roland De Marco, Robert W. Cattrall,* John Liesegang, and Graeme L. Nyberg

School of Physical Sciences, La Trobe University, Melbourne, Victoria 3083, Australia

Ian C. Hamilton

BHP Central Research Laboratories, Newcastle, New South Wales 2287, Australia

X-ray photoelectron spectroscopy (XPS) and scanning electron microscopy (SEM) have been used to examine the surface layers of the silver sulfide ion selective electrode membrane. It has been found that the outermost surface layer of the membrane is hydrated, and that aquated ions do not penetrate the membrane beyond this "skin" layer. The mercuric ion undergoes ion-exchange reactions with the Ag_2S surface. A study of mercuric ion interference shows that reductive Hg^{2+} ion exchange occurs in the presence of light, whereas a metathetic displacement reaction occurs in the dark. Ferric and cupric ion interference studies show that these ions exhibit relatively weaker effects. Exposure of Ag_2S to solutions of Cl^-, Br^-, and I^- in the presence of light has been found to cause crystals of the corresponding silver halide to grow on (and out of) the membrane surface. It is postulated that the reaction mechanism of the membrane involves photooxidation of Ag_2S to produce some metal deficient sulfide(s) (e.g. Ag_2S_2 and/or elemental S).

INTRODUCTION

The silver sulfide ion selective electrode membrane is normally fabricated as a dense polycrystalline disk by pressing the finely divided powder. There are two crystalline modifications of silver sulfide, acanthite (β-form), which is monoclinic and stable below 176 °C, and argentite (α form), which is cubic and stable at higher temperatures. Both forms show electrical conductivity which is accountable in terms of predominantly electronic conduction in α-Ag_2S and ionic conduction in β-Ag_2S (*1*, *2*). The latter occurs via a Frenkel crystal defect mechanism in which silver ions are the major charge carriers. It is for this reason that it is the β modification which is used in the ion-selective electrode membrane.

It is generally accepted that, when the Ag_2S electrode is immersed in solutions containing the silver ion, there is an exchange of ions between the solution and cation vacancies at the membrane surface, and an interfacial potential is thus generated by a space-charge mechanism. Little more is known, however, about the response mechanism or the reactions which are occurring at the membrane surface, particularly in the presence of interfering ions.

Ion interference with crystal-membrane ion-selective electrodes is generally assumed to be due to metathesis between the interfering ion and the membrane surface (*3*). This model is adequate when the membrane is an electrical insulator (e.g. LaF_3 (*4*, *5*) and AgCl (*6*, *7*)). It is unsatisfactory, however, for the many electrode membranes which are electrical semiconductors (e.g. PbS/Ag_2S, CuS/Ag_2S, Ag_2S, etc.), since it neglects any possibility of electron transfer between the membrane surface and adsorbates.

Our recent work with the LaF_3 electrode membrane (*4*, *5*) has demonstrated the power of surface analysis techniques such as X-ray photoelectron spectroscopy (XPS) and scanning electron microscopy (SEM) in studying ion-selective electrode membrane surfaces, and in this paper we apply these techniques to a study of the surface chemistry associated with the Ag_2S electrode membrane.

Wilson and Pool (*8*) have carried out XPS studies on a silver sulfide/tris(thiourea)copper(I) monohydrogen phosphate ion selective electrode and found that the Ag_2S component was partially oxidized to Ag_2SO_4. There is evidence from their work and from the work of Gulens and Ikeda (*9*), Buck (*10*), and Morf (*11*) that the much higher silver and sulfide ion detection limits observed for the Ag_2S electrode than are predicted from the Ag_2S solubility product may be due to the higher solubility of silver sulfate.

Gulens and Ikeda (*9*) carried out SEM studies of Ag_2S membranes which exhibited slow and non-Nernstian response after continuous use monitoring H_2S in water. The surfaces of the membranes were found to be highly pitted and porous. Also, platelike deposits were observed on the pitted surface, and energy dispersive analysis of X-rays (EDAX) spectra revealed that these plates were rich in silver and low in sulfur. It is likely the deposits are metallic silver, particularly in view of the fact that the buffer contained ascorbic acid which can act as a reductant. In fact, Gulens and Shoesmith (*12*) used X-ray diffraction to confirm this by detecting metallic silver in the surface region of the Ag_2S membrane after treatment in alkaline ascorbic acid solutions.

The limited amount of XPS and SEM work already carried out on the Ag_2S membrane suggested to us that redox reactions play a dominant role in the response mechanism of the Ag_2S electrode, particularly in the presence of interfering ions, and so a detailed surface analysis study was of considerable interest.

EXPERIMENTAL SECTION

Silver sulfide electrode membranes were obtained from several different sources (edt Research, London; Pye Unicam Ltd., Cambridge; and Dr. W. Ingold AG, Switzerland). The membranes consisted of polycrystalline β-Ag_2S pressed in disk form. Several additional membranes were prepared by pressing β-Ag_2S powder (Aldrich, >99.9% (w/w)) in a Specac punch and die at 10 tons to give disks 13 mm in diameter and approximately 1.5 mm thick.

Analytical grade reagents were used in all cases. $Hg(NO_3)_2$ and $Fe(NO_3)_3$ solutions were prepared by dissolving the salts in 0.1 M H_2SO_4. The use of acid solutions ensured minimal hydrolysis of the Hg^{2+}(aq) and Fe^{3+}(aq) species.

Potentiometric response curves were measured using the following electrochemical cell:

Ag|AgCl|KCl(satd.)||1.3 M NH_4NO_3||sample|Ag_2S|0.1 M $AgNO_3$, AgCl(satd.)|AgCl|Ag

An Orion double-junction sleeve-type reference electrode was used and potential measurements were made with an Orion Ionalyzer (Model 901). Pure silver nitrate solutions were used for the response curve measurements. Silver ion activities were calculated

0003-2700/90/0362-2339$02.50/0 © 1990 American Chemical Society

Table I. XPS Binding Energies (eV) of Different Levels of Hg, Fe, Cu, S, and O for Ag_2S Membranes[g]

levels	clean[a]	$[Hg^{2+}]h\nu$[b]	$[Hg^{2+}]$[c]	$[Fe^{3+}]h\nu$[d]	$[Fe^{3+}]$[e]	$[Cu^{2+}]h\nu$[f]
$Ag(3d_{5/2})$	367.8	nd	nd	367.9	368.0	367.8
$Ag(3d_{3/2})$	373.6	nd	nd	373.7	373.8	373.8
$Hg(4f_{7/2})$		100.7	101.9			
$Hg(4f_{5/2})$		104.2	105.1			
$Hg(4d_{5/2})$		358.7	359.6			
$Hg(4d_{3/2})$		378.0	378.9			
S(2p)	161.8	162.1	162.0	161,164	161.4	161.8
O(1s)	533.5	533.4	533.5	533.6	533.4	533.5
Fe(2p)				nd	nd	
$Cu(2p_{3/2})$						nd

[a] Clean membrane (H_2O for 7 days). [b] 0.10 M $Hg(NO_3)_2$ for 7 days (light). [c] 0.10 M $Hg(NO_3)_2$ for 7 days (darkness). [d] 0.20 M $Fe(NO_3)_3$ for 7 days (light). [e] 0.20 M $Fe(NO_3)_3$ for 7 days (darkness). [f] 0.30 M $Cu(NO_3)_2$ for 7 days (light). [g] Key: nd, not detected; blank, not examined.

by using the Debye–Hückel equation.

XPS analysis of β-Ag_2S membranes was performed by using the techniques described in previous work (*4*, *5*). Two XPS spectrometers were used. The main one (XPS-1) was a high-vacuum (HV) instrument with Al Kα X-ray source and the spectrometer chamber is maintained at a pressure of $\sim 10^{-5}$ Pa. The second instrument (XPS-2), built by Vacuum Science Workshop, Ltd., was an ultrahigh-vacuum (UHV) angle resolved multitechnique electron spectrometer with a Mg Kα X-ray tube. The pressure in the spectrometer is $\sim 10^{-8}$ Pa. The HV spectrometer has resolution or full width at half maxima (fwhm) of ~ 2 eV, while the UHV instrument possesses a resolution of ~ 1 eV. The UHV spectrometer was used in cases where higher resolution of XPS peaks was required.

Binding energies for XPS-1 were determined by using the $Cu(2p_{3/2})$ peak at 932.67 eV (referenced to the Fermi level) as the calibrant (*13*). The binding energy scale for XPS-2 was calibrated by using the Ni(3d) Fermi edge, the Cu(3p), Cu(LMM), $Cu(2p_{3/2})$, and C(1s) (adventitious hydrocarbon) peaks (*14*, *15*).

Chemical depth profiles were measured with XPS-1 by sputtering the sample in argon at 10^{-2} Pa using an ion gun (Varian, Model 981-1045). The sample was bombarded by 600-eV ions at a current density of ~ 5 μA cm^{-2}. The depth scale was calibrated by calculating the sputter rate, using the equation given by Hofmann (*16*) and used by us previously (*4*, *5*). The sputter rate was calculated to be 0.7 nm min^{-1}.

Atomic concentration ratios were calculated from photoelectron line intensities (*17*) using empirical atomic sensitivity factors reported by Wagner et al. (*18*).

SEM studies were carried out using a Siemens Autoscan microscope. This instrument incorporates an EDAX International, Inc., accessory. The microscope chamber was maintained at a pressure of 10^{-3} Pa. This instrument permitted attainment of images at a maximum magnification of 10 000.

An experiment was conducted in deoxygenated NaCl solution to examine the effect of the absence of dissolved oxygen on the photooxidation of Ag_2S. The solution was first purged with high-purity nitrogen (100 cm^3/min). The membrane was then placed in the solution, following which the membrane/solution system was continually purged with nitrogen (100 cm^3/min) for 21 days.

RESULTS AND DISCUSSION

Surface Composition of the Membrane. XPS was used to determine the surface composition of an Ag_2S membrane which was soaked in distilled water for 7 days. Silver ion exchange was also examined by carrying out XPS analysis of a membrane which had been soaked in 0.1 M $AgNO_3$ for 7 days (and blotted dry with tissue without rinsing with distilled water).

The binding energies of the O(1s), S(2p), and Ag(3d) levels of the water-treated membrane are given in Table I. The position of the O(1s) level (533.5 eV) is consistent with oxygen in H_2O (*19*, *20*), and the absence of an O(1s) peak at 529 eV eliminates the presence of Ag_2O and AgO (*21*, *22*). The position of the S(2p) peak (161.8 eV) is consistent with sulfur

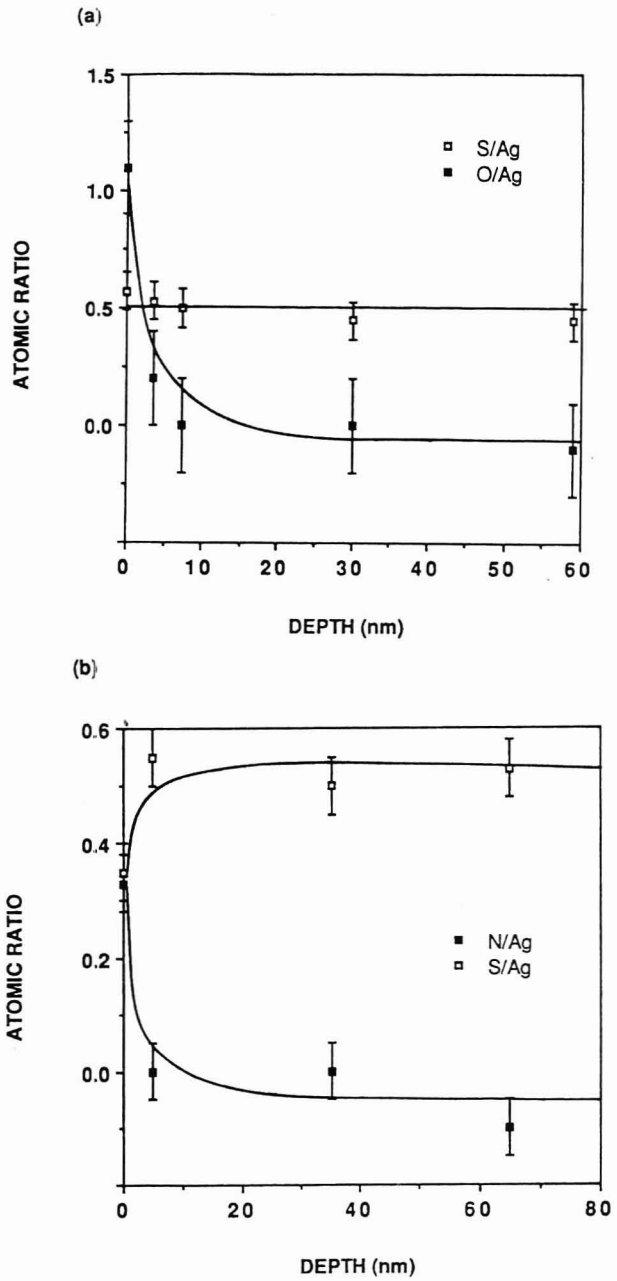

Figure 1. Chemical depth profiles for Ag_2S membranes soaked in (a) H_2O for 7 days and (b) 0.1 M $AgNO_3$ for 7 days. Instrumental error limits are indicated.

in S^{2-} (*23*, *24*). The spin–orbit splitting of the S(2p) level is ~ 1 eV, and since the fwhm values for the spectra shown are ~ 2.5 eV, the $2p_{3/2}$ and $2p_{1/2}$ components strongly overlap to give the observed single S(2p) peak. The Ag(3d) level has two peaks corresponding to the $3d_{5/2}$ and $3d_{3/2}$ spin–orbit split components. The Ag(3d) level is insensitive to changes in silver oxidation state and chemical environment (*24*), and thus cannot be used to distinguish the particular silver salts which may be present. However, the modified Auger parameter ($\alpha + h\nu = E_K[Ag(M_4N_{45}N_{45})] + E_b[Ag(3d_{5/2})]$) is equal to 723.9 $\pm$ 0.3 eV, which is consistent with Ag^+ (or Ag^{2+}), but not Ag^0 (*23*). Ag_2SO_4 can be eliminated, though, since the sulfate S(2p) peak at 168.8 eV (*24*) was not detected. The surface composition may thus be described as hydrated silver sulfide.

This is confirmed by the chemical depth profile shown in Figure 1a. It can be seen that an O/Ag ratio of ~ 1 which is obtained at the surface quickly diminishes to ~ 0, whereas the S/Ag ratio remains constant at ~ 0.5. This indicates that the surface composition may best be represented as $Ag_2S \cdot 2H_2O$.

Figure 1b shows the chemical depth profile obtained for a membrane soaked in 0.1M $AgNO_3$ for 7 days. It may be seen that the silver nitrate solution interacts only with this hydrated layer. It would seem most likely that the water in the surface region of the membrane enhances the mobility of aquated ions, and thus accelerates the rate of attainment of equilibrium of the ion-exchange process. It is evidence that the Ag_2S membrane does not possess a gel layer in the same way as does LaF_3 (*5*).

Interferences. Mercuric Ions. The mercuric ion exhibits a strong interference effect with the silver sulfide ion selective electrode, and this phenomenon was studied by XPS. Ag_2S membranes were soaked for 7 days in 0.1 M $Hg(NO_3)_2$ in both the presence and absence of light, and the surfaces then examined by XPS. The membrane surface was rinsed with distilled water and blotted dry prior to introduction to the analysis chamber.

The Hg(4f) level (Table I) for a membrane soaked in Hg^{2+} in ambient light reveals two peaks, at 100.7 and 104.2 eV, corresponding, respectively, to the $4f_{7/2}$ and $4f_{5/2}$ spin–orbit split components. The Hg($4f_{7/2}$) peak is at 1 eV higher binding energy than the 99.7 eV of the metal (*24*), which is what might be expected for mercury as Hg_2^{2+}. The surface stoichiometry of the membrane (obtained from XPS peak intensities) was consistent with Hg_2S. The lack of any Ag(3d) peaks revealed that silver was completely absent at the surface. The S(2p) level (162.1 eV) is consistent with sulfur in S^{2-} (*23*, *24*). The XPS data suggest that soaking the electrode for a long period of time in a Hg^{2+} solution tends to produce mercurous sulfide, Hg_2S, on the surface of the membrane.

The results clearly indicate an electron transfer between the Ag_2S surface and the adsorbing Hg^{2+} ions. Ag_2S is a semiconductor, possessing a band gap of 1.03 eV (*25*). Radiation of wavelengths less than 1210 nm (e.g. ambient light) may thus induce photoconductivity in Ag_2S. It is proposed that this photoconductivity accelerates the rate of the electron transfer process. To examine this more fully, an Ag_2S membrane was exposed to Hg^{2+} in the absence of light. As may be seen in Table I, the binding energies of the Hg(4f) and Hg(4d) levels are about 1 eV higher than those obtained in ambient light, which is what might be expected for Hg^{2+}. The surface stoichiometry of the membrane deduced from the measured Hg/S atomic ratio was also consistent with HgS.

It is therefore evident that a straightforward metathetic displacement reaction takes place between Ag_2S and Hg^{2+} in the absence of light, viz.

$$Ag_2S(s) + Hg^{2+}(aq) = HgS(s) + 2Ag^+(aq)$$

The reductive ion exchange of Hg^{2+} in daylight, by contrast, may be explained by the following reactions:

$$Ag_2S \overset{h\nu}{=} 2Ag^+ + S + 2e^- \quad (1)$$

$$2Ag_2S \overset{h\nu}{=} Ag_2S_2 + 2Ag^+ + 2e^- \quad (2)$$

$$2HgS + 2e^- = Hg_2S + S^{2-} \quad (3)$$

Reactions 1 and 2 represent photooxidation of the sulfide in Ag_2S to produce elemental sulfur and/or S_2^{2-}. The S and/or S_2^{2-} species are probably present underneath the Hg_2S overlayer at the Ag_2S interface, and so were not detected by XPS. The exchange mechanisms described above require Ag^+ ions to be transferred to the aqueous solution, and indeed relatively high concentrations of this ion (>0.3 mM in 50 mL solution) were detected by atomic absorption spectrometry.

Tossell and Vaughan (*26*) have used molecular orbital theory to determine the binding energies (relative to the S(3p) nonbonding level) of metal d and ligand p orbitals in the room-temperature-stable forms of HgS (cinnabar) and Ag_2S (acanthite). The calculations show that the binding energy of the Hg(5d)–S(3p) bonding orbital (3.6 eV) in HgS (an adsorbate level) is greater than that of the Ag(4d)–S(3p) bonding orbital (1.9 eV) in Ag_2S. Thus electron transfer from the Ag_2S valence band to the low lying HgS band to produce Hg_2^{2+} is energetically feasible.

Table II. Postulated Mechanism for Hg(II) Exchange at Silver Sites in the Ag_2S Ion Selective Electrode Membrane[a]

reactions	comments
(1) $2Hg^{2+}(aq) = 2Hg^{2+}(ad)$	adsorption
(2) $2Hg^{2+}(ad) \overset{h\nu}{=} Hg_2^{2+}(ad) + 2h^*$	electron transfer
(3) $Hg_2^{2+}(ad) + V'_M = (Hg_2)^+_M$	
(4) $2Ag_M = 2V'_M + 2Ag^+(ad)$	
(5) $2Ag^+(ad) = 2Ag^+(aq)$	desorption of Ag^+
(6) $S_S + h^* = S^+_S$	S^- intermediate
(7) $S^+_S + h^* = S^{2+}_S$	elemental sulfur
alternatively after reaction 6	
(8) $S^+_S + S^+_S = (S_2)_S$	S_2^{2-} species
(9) $Ag^+_i + Hg_2^{2+}(ad) = (Hg_2^{2+})_i + Ag^+(ad)$	
Overall Reactions	
(i) $2Hg^{2+}(aq) + 2Ag_M + S_S = (Hg_2)^+_M + V'_M + S^{2+}_S + 2Ag^+(aq)$	
(ii) $2Hg^{2+}(aq) + 2Ag_M + 2S_S = (Hg_2)^+_M + V'_M + (S_2)_S + 2Ag^+(aq)$	

[a] The notation scheme of Kroger and Vink (*31*) is utilized, as frequently modified in the catalysis literature (*32*). (1) Subscripts "M" and "S" refer to the metal and sulfide ion sublattices. (2) Superscripts "*n*+" and "*n*−" refer to the charge of the occupied lattice sites. (3) V'_M is a vacant lattice site in the metal sublattice with unit negative charge. (4) An interstitial ion is identified by the subscript "i". (5) "h*" represents a hole in the valence band of the membrane, with unit positive charge.

The detailed mechanism shown in Table II is proposed to explain the reductive ion exchange of Hg^{2+} on the surface of Ag_2S. Initially, Hg^{2+} ions are present at the outer Helmholtz plane (OHP) of the membrane, and the concentration of Hg^{2+} in this plane is assumed to be equal to that of the bulk solution. Adsorption (step 1) may be envisaged as Hg^{2+} ions moving from the OHP to the inner Helmholtz plane (IHP) (*27*). Electron transfer between the Ag_2S surface and $Hg^{2+}(ad)$ occurs (step 2) to produce two holes (h*) in the valence band of Ag_2S. $Hg_2^{2+}(ad)$ may enter a metal ion vacancy, V'_M (step 3); however the charge of the vacancy site (−1) is increased by two (since Hg_2^{2+} carries a charge of +2) i.e. from $V'_M(-1)$ to $(Hg_2)^+_M$. Electroneutrality of the membrane surface is maintained by silver ions in lattice sites being displaced to the IHP to produce metal ion vacancies, and the adsorbed silver ions are then desorbed from the membrane surface (steps 4 and 5). The holes in the Ag_2S valence band must of course be consumed. Reactions 6 and 7 show that elemental sulfur may be formed by the stepwise absorption of two holes by S^{2-}. Another possibility is the formation of the stable S_2^{2-} species (*28*), which may be produced by the combination of two S^- ions (step 8). $Hg_2^{2+}(ad)$ may also exchange with silver ions in interstitial sites (step 9). The overall reactions are shown at the bottom of the Table II.

Chemical depth profiles for Ag_2S membranes after exposure to Hg^{2+} in both the presence and absence of light (Figure 2) reveal a Hg_2S overlayer (ambient light), which is ≤80 nm in thickness, and a HgS overlayer (darkness), which is ≤10 nm in thickness. The thickness of the Hg_2S overlayer was unexpected in view of the fact that the hydrated surface layer in the Ag_2S membrane is less than 5 nm thick (Figure 1) and it is assumed that exchange reactions are facilitated within this hydrated layer.

The physical nature of the Hg_2S and HgS overlayers was examined by SEM, and the micrographs are shown in Figure

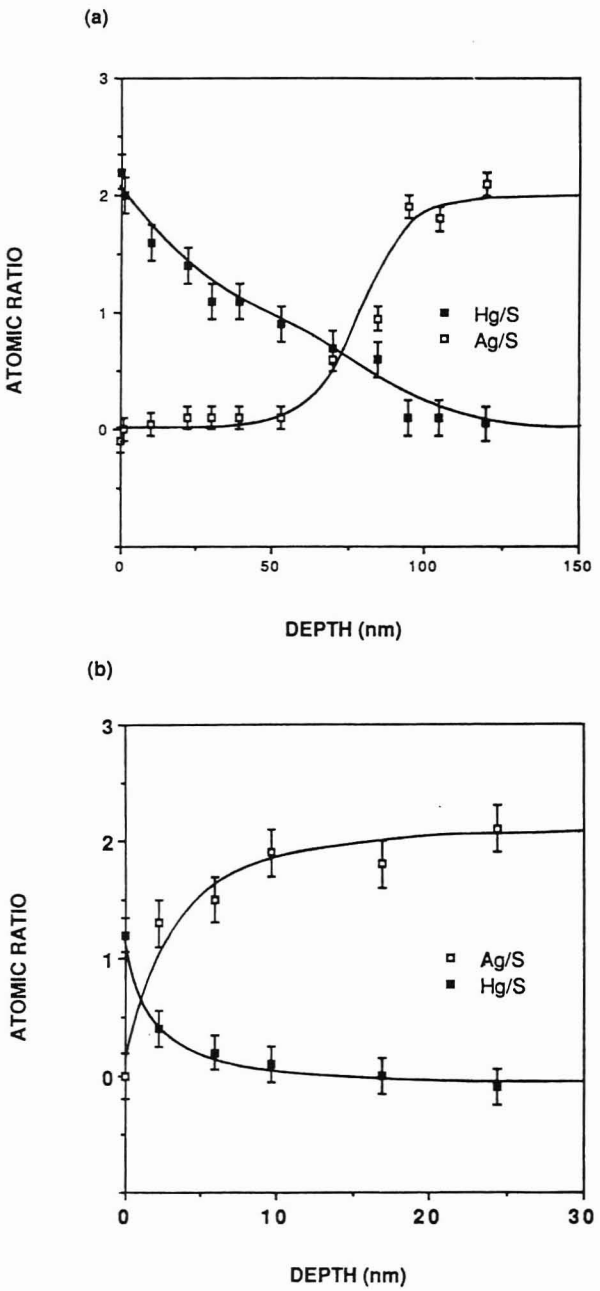

Figure 2. Chemical depth profiles for Ag_2S membranes soaked in the following solutions for 7 days; (a) 0.1 M $Hg(NO_3)_2$ (ambient light) and (b) 0.1 M $Hg(NO_3)_2$ (darkness). Instrumental error limits are indicated.

3. It may be seen in part a that large platelike crystals (~7 μm in length) are present on the surface of the membrane treated with Hg^{2+} in the presence of light, whereas for the membrane treated in darkness (part b), clusters of smaller platelike crystals (~3 μm in length) are revealed. The EDAX spectra of both the large and small plates confirmed that they each contained mercury and sulfur.

It would seem most likely that the electron transfer process which occurs in ambient light severely corrodes the membrane surface and causes crystals of Hg_2S to grow on (and out of) the membrane surface, thus explaining the observation of a thick Hg_2S overlayer.

The potentiometric response curve for an Ag_2S electrode in $AgNO_3$ solutions in the concentration range 10^{-6}–10^{-1} M before and after exposure to 0.1 M Hg^{2+} for 7 days in ambient light revealed Nernstian response in both cases; i.e. a 58-mV change in potential per decade change in silver ion activity. The intercept of the emf versus pAg plot, however, changed from 555 mV before to 570 mV after exposure to Hg^{2+}. This suggests a modification of the membrane surface after exposure to solutions containing Hg^{2+}.

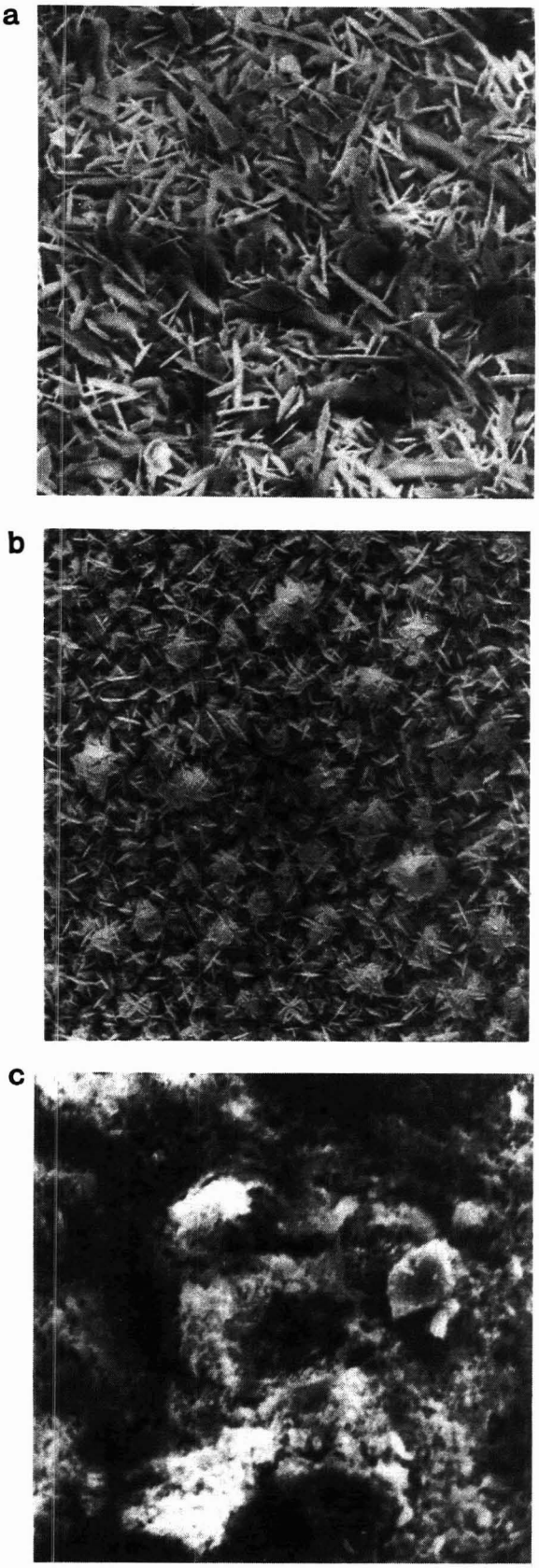

Figure 3. SEM micrographs (magnification of 2000×) of Ag_2S membranes soaked in solutions (a–b) of Figure 2 and (c) the Fe^{3+}-treated membrane (ambient light).

The exact conditions used to produce the response curve for the Hg^{2+}-treated electrode were reproduced, and XPS analysis of the Ag_2S membrane was carried out at stages corresponding to the measured points on the response curve. Atomic ratios for Hg/S and Ag/S were calculated from the

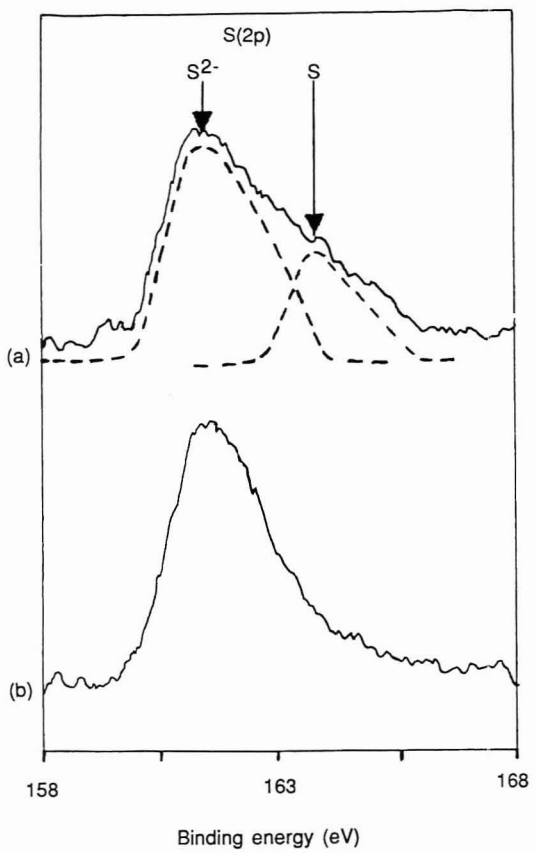

Figure 4. Photoelectron spectra of the S(2p) level for a Ag_2S membrane exposed to 0.2 M $Fe(NO_3)_3$ in the presence of light (spectrum a). Spectrum b was obtained after heating the Fe^{3+}-treated membrane to 170 °C (under vacuum). The spectra were obtained for an emission angle of the detected photoelectrons of 80°.

XPS peak intensities and plotted against pAg. It was found that the surface stoichiometry was approximately Hg_2S in the pAg range 5–6, while the surface is partially replenished to the nonstoichiometric compound $HgAg_{0.5}S$ in the pAg range 1–4. Continuous soaking of the Hg^{2+}-treated membrane in 0.1 M $AgNO_3$ for a total of 3 months produced no further restoration to the initial composition. Thus the Hg^{2+} ion-exchange reaction is only partially reversible and produces a shift in the $E°$, but nevertheless, the stable electrode surface which results responds in a Nernstian fashion to Ag^+.

Ferric Ions. Ferric ion does not exhibit a strong interference effect on the response characteristics of the Ag_2S electrode. The standard reduction potential for the Fe^{3+}/Fe^{2+} redox couple (0.77 V (*29*)) is, however, of approximately the same magnitude as the Hg^{2+}/Hg_2^{2+} couple (0.905 V (*29*)). Thus it was postulated that Fe^{3+} may exhibit reductive ion exchange in a similar fashion to that observed with Hg^{2+}.

Figure 4 shows UHV S(2p) spectra obtained for a membrane soaked in 0.2 M $Fe(NO_3)_3$ (pH ~ 1) for 7 days in the presence of light. The spectra were obtained at an emission angle of 80° from the surface normal, which accentuates the surface sensitivity. Spectrum a shows two distinct peaks. The main peak at ~161 eV is consistent with the presence of S^{2-} (*24*), while the small shoulder on the high binding energy side (~164 eV) is consistent with elemental sulfur (*24*). The stoichiometry of this surface (obtained from the XPS peak intensities) was $Ag_{1.4}S$, indicating that the outermost surface (just a few monolayers) of the membrane was rich in sulfur. In near-normal emission (which probes down to the electron escape depth, of ~5 nm) the sulfur intensity was markedly attenuated. This indicates that the sulfur-enriched overlayer, as sampled at grazing emission, was ~1 nm thick. Spectrum b was obtained after heating the same membrane to 170 °C overnight (under vacuum) and revealed that the intensity of the elemental sulfur peak was significantly reduced. The surface stoichiometry of the heated membrane was restored to Ag_2S. Mass spectrometry of the gases thermally desorbed from the Fe^{3+}-treated membrane surface revealed the presence of S(g), S_2(g), and S_3(g), which may have arisen directly from elemental sulfur on the membrane surface or from the thermal decomposition of low oxidation state sulfides (e.g. Ag_2S_2). Ferrous sulfide was not detected (by either XPS or SEM) in the surface region of the Fe^{3+}-treated membrane (ambient light). This absence is in agreement with the equilibrium calculations. The solubility products for Ag_2S ($\log K_s = -48.80$ (*29*)) and FeS ($\log K_s = -18.43$ (*29*)) suggest that the equilibrium constant for simple ion exchange of Ag^+ and Fe^{2+} is 4.3×10^{-31} M. Thus the formation of FeS on the Ag_2S surface is not thermodynamically possible.

A SEM micrograph of the ambient-light Fe^{3+}-treated membrane is given in Figure 3c and reveals the presence of amorphous deposits on the surface, in contrast to the membrane treated in darkness (not shown) which revealed a smooth surface. The EDAX spectrum of the latter gave a Ag Lα/S Kα intensity ratio of ~3, which is identical with that of the clean membrane, whereas the amorphous regions of the light-exposed surface provided a Ag Lα/S Kα intensity ratio of approximately unity. Thus the amorphous deposits are rich in sulfur and low in silver. This is consistent with the presence of species such as Ag_2S_2 and/or elemental S.

The XPS results suggest a mechanism involving photooxidation of Ag_2S by Fe^{3+} as was observed for Hg^{2+} exchange, and this may be described by reactions 1 and 2 above in combination with the redox half reaction for Fe^{3+}/Fe^{2+}, viz.

$$Ag_2S(s) + 2Fe^{3+}(aq) \overset{h\nu}{=} 2Ag^+(aq) + 2Fe^{2+}(aq) + S(s)$$

and/or

$$2Ag_2S(s) + 2Fe^{3+}(aq) \overset{h\nu}{=} Ag_2S_2(s) + 2Ag^+(aq) + 2Fe^{2+}(aq)$$

The detailed Fe^{3+} reaction mechanism is similar to that proposed for Hg^{2+} reductive ion exchange in Table II, except that Fe^{3+} is the oxidant in this case and the reduced species (Fe^{2+}) does not form an insoluble salt on the surface of the membrane. Also, as was the case with the mercury system, relatively high concentrations of the Ag^+ ion were detected in the aqueous solutions giving support to the proposed exchange mechanism.

Cupric Ions. Copper(II) is another cation that does not interfere with the response of the Ag_2S electrode. Young (*30*) has calculated band structures for CuS and Ag_2S. Young's calculations show that the relative binding energy of the Ag(4d)–S(3p) bonding orbital (11.5 eV) in Ag_2S is greater than that of the Cu(3d)–S(3p) bonding orbital (9.2 eV) in CuS (adsorbate level). Therefore, it may be predicted that electron transfer will not occur from Ag_2S to Cu^{2+}.

SEM analysis of a membrane soaked in 0.3 M Cu^{2+} (ambient light) showed that the surface was not attacked (SEM showed a smooth surface, and EDAX spectra were identical with that of the untreated membrane). XPS analysis revealed that the surface of the Cu^{2+}-treated membrane consisted almost entirely of Ag_2S (S/Ag ~ 0.5, Cu/S ~ 0, and the binding energy of the S(2p) peak (161.8 eV) was consistent with sulfur in S^{2-} (*24*)). Thus the experimental results agree with the predictions from the band structure calculations.

Halide Ions. Halide ions do not interfere significantly with the response of the Ag_2S membrane electrode in either silver or sulfide ion measurement modes, other than by contributing to the electrode becoming sluggish after prolonged use in

Table III. XPS Binding Energies (eV) for Ag_2S Membranes Exposed to Cl^-, Br^-, and I^-[i]

levels	clean[a]	$[Cl^-]h\nu$[b]	$[Cl^-]$[c]	$[Cl^-]h\nu$[d]	$[Br^-]h\nu$[e]	$[Br^-]$[f]	$[I^-]h\nu$[g]	$[I^-]$[h]
$Ag(3d_{5/2})$	367.8	367.8	367.8	367.8	368.0	368.0	368.0	368.0
$Ag(3d_{3/2})$	373.6	373.7	373.6	373.6	373.8	373.8	373.7	373.7
S(2p)	161.6	nd	161.8	161.8	161,164	161.7	161,164	161.7
Cl(2p)		198.1	nd	nd				
Br(3d)					61.0	nd		
$I(3d_{5/2})$							619.3	nd
$I(3d_{3/2})$							630.9	nd

[a] Clean membrane (H_2O for 14 days). [b] 0.4 M NaCl for 21 days (light). [c] 0.4 M NaCl for 21 days (darkness). [d] Deoxygenated NaCl (light). [e] 0.4 M NaBr for 21 days (light). [f] 0.4 M NaBr for 21 days (darkness). [g] 0.4 M NaI for 21 days (light). [h] 0.4 M NaI for 21 days (darkness). [i] Key: nd, not detected; blank, not examined.

halide media. Consequently, it was expected that the XPS study of the surface of the Ag_2S membrane after exposure to halide solutions would not show the presence of significant amounts of silver halides. This is in keeping with the solubility products for the various salts (Ag_2S, pK_s = 48.80; AgCl, pK_s = 9.81; AgBr, pK_s = 12.12; AgI, pK_s = 15.83 (*29*)) and the equilibrium constants for simple ion exchange of the sulfide ion by halide (Cl^-, $pK_{S,Cl}$ = 29.2; Br^-, $pK_{S,Br}$ = 24.6; I^-, $pK_{S,I}$ = 17.1). These values confirm that silver halides ought not to form on the surface of Ag_2S in halide solutions.

Silver sulfide membranes were exposed to solutions consisting of 0.4 M of the sodium salt of the appropriate halide ion in ambient light for 21 days, and XPS analysis revealed that significant quantities of the respective silver halide had formed on the surface. In addition, halide-treated Ag_2S electrodes displayed near-Nernstian response toward the appropriate halide ion. This halide sensitivity could be removed simply by polishing the membrane surface with alumina.

Chemical depth profiles for halide-treated membranes are shown in Figure 5. It may be seen that, for the Cl^--treated membrane, AgCl is present to a depth of about 130 nm. The I^--treated membrane (Br^- gave a similar result) suggests a mixture of species is present to a depth of about 50 nm. The surface composition (halide/Ag ~ 0.5 and S/Ag ~ 0.8) cannot be due to a mixture of Ag_2S and AgI, since any AgI-to-Ag_2S ratio does not agree with the observed atomic ratios. A mixture containing 25% Ag_2S_2, 25% S, and 50% AgI would give the observed surface composition.

The binding energies of the XPS peaks are given in Table III. The binding energy of the Cl(2p) level (198.1 eV) for the Cl^-treated membrane (ambient light) is consistent with chlorine as the Cl^- ion (*24*). Similarly, the positions of the Br(3d) and $I(3d_{5/2})$ peaks for the Br^-- and I^--treated membranes (ambient light) are consistent with bromine and iodine in Br^- and I^-, respectively (*24*). The S(2p) peak for membranes treated with Br^- and I^- in ambient light was ~2 eV higher than that of the untreated membrane. This is consistent with the presence of an oxidized form of sulfide such as S_2^{2-} and/or elemental sulfur since a chemical shift of ~2 eV to higher binding energy is expected for such species (*24*).

Further XPS analysis of the Br^-- and I^--treated membranes was carried out in the UHV spectrometer which was expected to better define the spectra. The UHV S(2p) spectrum indeed showed two peaks and looked similar to that of the Fe^{3+}-treated membrane shown in Figure 4. As was suggested previously, the peak at ~164 eV is due to elemental sulfur and the peak at ~161 eV is due to S^{2-}. Heating the membrane to 170 °C (under vacuum) for 1 h removed the high binding energy shoulder on the S(2p) spectrum. Mass spectrometry of the gases thermally desorbed from the Br^-- and I^--treated membrane surfaces indicated the presence of S(g), S_2(g), and S_3(g). Again, this may arise from the presence of sulfur on the membrane surface or from the thermal decomposition of low oxidation state sulfides (e.g. Ag_2S_2).

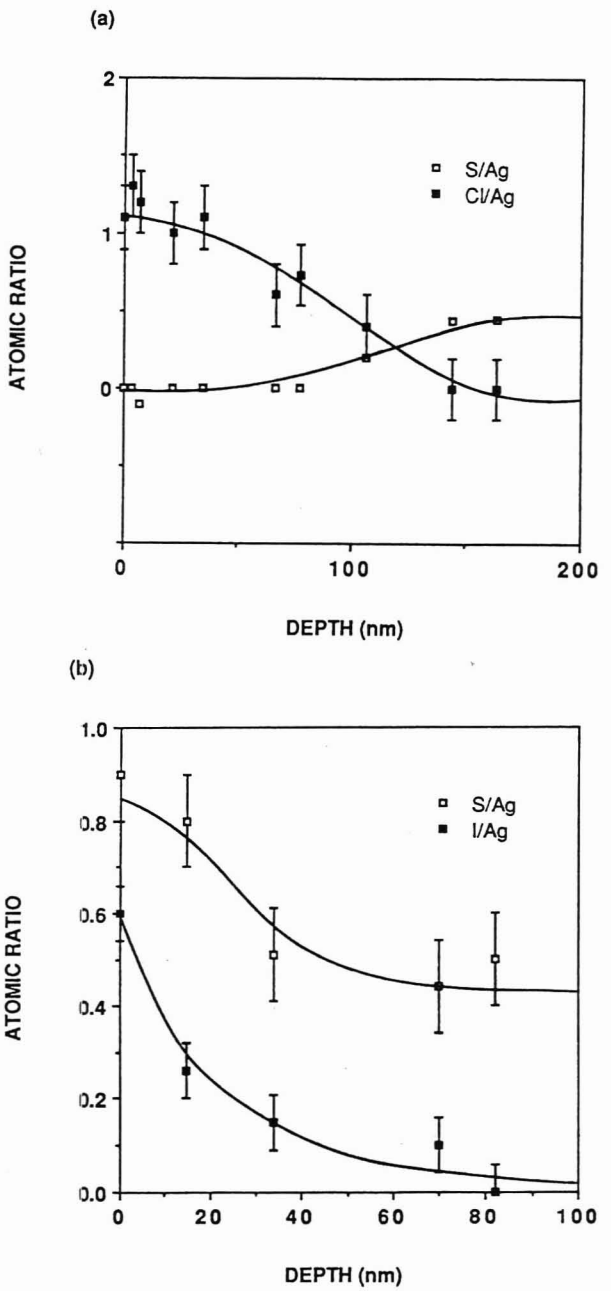

Figure 5. Chemical depth profiles of Ag_2S membranes soaked in the following solutions for 21 days in natural light: (a) 0.4 M NaCl and (b) 0.4 M NaI. Instrumental error limits are indicated.

Treatment of the Ag_2S membrane with Cl^-, Br^-, and I^- in the absence of light produced no effect. XPS analysis of these surfaces showed that they consisted almost entirely of Ag_2S (S/Ag ~ 0.5, halide/Ag ~ 0, and a S(2p) binding energy of ~161.7 eV, which is consistent with sulfur as S^{2-} (*24*)). Thus it appears that photooxidation of the surface of the Ag_2S

Table IV. Postulated Mechanism for the Formation of AgCl on the Surface of the Ag_2S Ion Selective Electrode Membrane

reactions	comments
(1) $H_2O(l) = H_2O(ad)$	adsorption
(2) $2Cl^-(aq) = 2Cl^-(ad)$	
(3) $^1/_2O_2(g) = {}^1/_2O_2(ad)$	
(4) $^1/_2O_2(ad) + H_2O(ad) \overset{h\nu}{=} 2OH^-(ad) + 2h^*$	electron transfer
(5) $2OH^-(ad) = 2OH^-(aq)$	desorption of OH^-
(6) $S_S + h^* = S^+_S$	S^- intermediate
(7) $S^+_S + h^* = S^{2+}_S$	elemental sulfur
alternatively after reaction 6	
(8) $S^+_S + S^+_S = (S_2)_S$	S_2^{2-} species
(9) $2Ag_M = 2V'_M + 2Ag^+(ad)$	
(10) $2Ag^+(ad) + 2Cl^-(ad) = 2AgCl$	insoluble AgCl salt
Overall Reactions	
(i) $2Ag_M + {}^1/_2O_2(g) + H_2O(1) + 2Cl^-(aq) + S_S = 2AgCl(s) + S^{2+}_S + 2OH^-(aq) + 2V'_M$	
(ii) $2Ag_M + {}^1/_2O_2(g) + H_2O(1) + 2Cl^-(aq) + 2S_S = 2AgCl(s) + (S_2)_S + 2OH^-(aq) + 2V'_M$	

membrane occurs in the presence of halides in ambient light, as was the case with Hg^{2+} and Fe^{3+}. This may be represented as follows:

$$2Ag_2S(s) + 2Cl^-(aq) \overset{h\nu}{=} Ag_2S_2(s) + 2AgCl(s) + 2e^-$$

and/or

$$Ag_2S(s) + 2Cl^-(aq) \overset{h\nu}{=} S(s) + 2AgCl(s) + 2e^-$$

At first glance it is not obvious what is acting as the oxidant; however dissolved oxygen seems likely

$$½O_2(g) + H_2O(l) + 2e^- = 2OH^-(aq)$$

To test this possibility, an Ag_2S membrane was exposed to deoxygenated NaCl solution in ambient light for 21 days. XPS analysis revealed that the surface consisted almost entirely of Ag_2S (S/Ag ~ 0.5, halide/Ag ~ 0, and the S(2p) peak at 161.8 eV is consistent with S^{2-} (*24*)). This therefore supports the above proposal.

Table IV gives the mechanism which is proposed for the formation of AgCl on the surface of Ag_2S. Steps 1–3 represent H_2O, Cl^-, and O_2 moving from the OHP to the IHP (adsorption). Reaction 4 shows the electron transfer between adsorbed H_2O and O_2 and the Ag_2S surface to produce OH^- and two holes (h*) in the valence band of Ag_2S. The OH^- formed in step 4 is subsequently desorbed from the membrane surface (step 5). The holes produced are consumed in steps 6–8 to produce S_2^{2-} and/or elemental S. Electroneutrality of the membrane surface is maintained by two silver ions moving from lattice sites to the IHP, producing metal ion vacancies (step 9). Finally, adsorbed Ag^+ and Cl^- combine to form the insoluble AgCl salt on the membrane surface.

SEM micrographs of the silver halide overlayers are shown in Figure 6. It may be seen that cubic crystals grow on (and out of) the surface of the ambient-light Cl^--treated membrane (Figure 6a). EDAX spectra showed that these cubic crystals contain the elements silver and chlorine. The crystal form of the AgCl deposit is similar to that of the mineral ceragyrite (*29*), ie., β-AgCl. The membrane exposed to deoxygenated NaCl solution, however, revealed a smooth surface, and EDAX spectra showed that it consisted of Ag_2S (the Ag Lα/S Kα intensity ratio was identical with that of the untreated membrane). The membrane exposed to Br^- (ambient light) showed an amorphous deposit (Figure 6b). The EDAX spectrum of this deposit showed that it contained small amounts of bromine and silver and that it was rich in sulfur (oxidation state undeterminable). The ambient-light I^--treated membrane revealed large hexagonal crystals (Figure 6c). EDAX spectra of several of these crystals showed that they contained the elements silver and iodine. The crystal form of the AgI deposit is similar to that of the mineral iodyrite (*29*), i.e. β-AgI. The I^--treated membrane also showed regions containing an

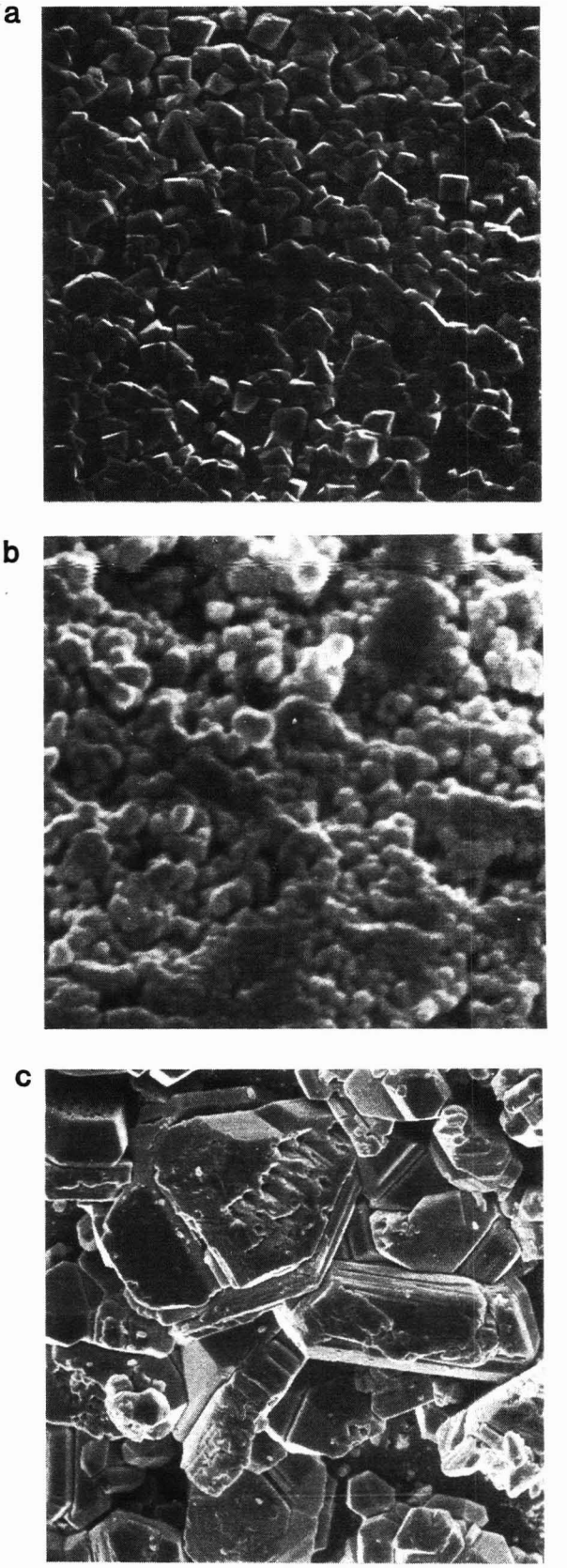

Figure 6. SEM micrographs (magnification of 2000×) of Ag_2S membranes exposed to halides for 21 days in the presence of light: (a) 0.4 M NaCl; (b) 0.4 M NaBr; (c) 0.4 M NaI.

amorphous deposit (and which looked similar to the Br^--treated membrane). EDAX spectra revealed that the amorphous deposits were rich in sulfur species and low in silver.

CONCLUSIONS

This work demonstrates the importance of surface techniques like XPS and SEM for studying the chemical and physical nature of overlayers on the surfaces of ion selective electrode membranes. The results from this study further elucidate the response mechanism of the Ag_2S membrane electrode. A simple ion-exchange mechanism is not applicable to the Ag_2S membrane alone. Consideration of electron transfer reactions that take place between adsorbates and the Ag_2S surface is also required. The photooxidation of Ag_2S in the presence of some ions in ambient light severely corrodes the membrane surface, and in some cases crystals of insoluble salts grow on (and out of) the surface of the membrane. Band structure calculations may be used to predict the effect of interfering ions on the Ag_2S membrane. The photooxidation of the surface of the Ag_2S membrane suggests that the electrode is best used in the absence of light. This may be achieved, for example, by using the electrode in a dark enclosed cell such as that used in flow methods like flow injection analysis. Nevertheless, the results of this study demonstrate that the surface of the Ag_2S membrane requires regular polishing to maintain its performance.

ACKNOWLEDGMENT

The authors wish to thank the companies (edt Research, London; Pye Unicam, Ltd., Cambridge, and Dr. W. Ingold AG, Switzerland) who kindly donated the ion selective electrode membranes used in this study. We are grateful to Mr. T. Gengenbach of the Chemistry Department, La Trobe University, for running the UHV XPS spectra and to Mr. F. Daniels of the Botany Department, La Trobe University, for assistance with the SEM studies.

LITERATURE CITED

(1) Klaiber, F. *Ann. Phys.* **1929**, *3*, 229.
(2) Hebb, M. H. *J. Chem. Phys.* **1952**, *20* (1), 185.
(3) Buck, R. P. *Anal. Chem.* **1968**, *40*, 1432.
(4) De Marco, R.; Cattrall, R. W.; Liesegang, J.; Nyberg, G. L.; Hamilton, I. C. *SIA, Surf. Interface Anal.* **1989**, *14*, 457.
(5) De Marco, R.; Hauser, P. C.; Cattrall, R. W.; Liesegang, J.; Nyberg, G. L.; Hamilton, I. C. *SIA, Surf. Interface Anal.* 1989, 14, 463.
(6) Sandifer, J. R. *Anal. Chem.* **1981**, *53*, 312.
(7) Rhodes, R. K.; Buck, R. P. *Anal. Chim. Acta* **1980**, *55*, 113.
(8) Wilson, A. C.; Pool, K. H. *Anal. Chim. Acta* 1979, 109, 149.
(9) Gulens, J.; Ikeda, B. *Anal. Chem.* **1978**, *50*, 782.
(10) Buck, R. P. *Anal. Chem.* **1976**, *48*, 26R.
(11) Morf, W. E. *The Principles of Ion-Selective Electrodes and of Membrane Transport, Studies in Analytical Chemistry*; Pungor, E., et al., Eds.; Akademial Klado: Budapest, 1981; Vol. 2.
(12) Gulens, J.; Shoesmith, D. W. *J. Electrochem. Soc.* **1981**, *128*, 811.
(13) Anthony, M. T. *Practical Surface Analysis by Auger and X-Ray Photoelectron Spectroscopy*; Briggs, D., Seah, M. P., Eds.; Wiley: Chichester, 1983; pp 429–435.
(14) Anthony, M. T.; Seah, M. P. *SIA, Surf. Interface Anal.* **1984**, *6*, 107.
(15) Anthony, M. T.; Seah, M. P. *SIA, Surf. Interface Anal.* **1984**, *6*, 95.
(16) Hofmann, S. ref 13, pp 141–179.
(17) Ebel, M. F.; Ebel, H.; Hirokawa, K. *Spectrochim. Acta* **1982**, *37B*, 461.
(18) Wagner, C. D.; Davis, L. E.; Zeller, M. V.; Taylor, J. A.; Raymond, R. M.; Gale, L. H. *SIA, Surf. Interface Anal.* **1980**, *2*, 173.
(19) *Handbook of Spectroscopy*; Robinson, J. W., Ed.; CRC Press: Cleveland, OH, 1974; Vol. I, pp 517–754.
(20) Wagner, C. D.; Zatko, D. A.; Raymond, R. H. *Anal. Chem.* **1980**, *52*, 1445.
(21) Schon, G. *Acta Chem. Scand.* **1973**, *27*, 2623.
(22) Hammond, J. S.; Garrenstroom, S. W.; Winograd, N. *Anal. Chem.* **1975**, *47*, 2193.
(23) Zingg, D. S.; Hercules, D. M. *J. Phys. Chem.* **1978**, *82*, 1992.
(24) Wagner, C. D., Riggs, W. M., Davis, L. E., Moulder, J. F., Muilenburg, G. E., Eds. *Handbook of X-ray Photoelectron Spectroscopy*; Perkin-Elmer, Physical Electronics Division: Eden Prairie, MN, 1979.
(25) Strehlow, W. H.; Cook, E. L. *J. Phys. Chem. Ref. Data* 1973, 2, 163.
(26) Tossell, J. A.; Vaughan, D. J. *Inorg. Chem.* **1981**, *20*, 3333.
(27) Bockris J. O'M.; Reddy, A. K. N. *Modern Electrochemistry*; Plenum Press: New York, 1970; Vol. 2, Chapter 7.
(28) Greenwood N. N.; Earnshaw A. *Chemistry of the Elements*, 1st ed.; Pergamon Press: Oxford, 1984; Chapter 8.
(29) *Handbood of Chemistry and Physics*, 62nd ed.; Weast, R. C., Ed. The Chemical Rubber Co.: Boca Ratan, FL, 1981.
(30) Young, V. *Anal. Chem.* **1980**, *57*, 1650.
(31) Kroger, F. A.; Vink, H. J. *Solid State Physics*; Seitz, F., Turnbull, D., Eds.; Academic Press: New York, 1956; Chapter 5.
(32) Happel, J.; Hnatow, M.; Bajars, L. *Base Metal Oxide Catalysts*; Marcel Dekker: New York, 1977.

RECEIVED for review February 26, 1990. Accepted July 10, 1990. We express our appreciation to the Australian Research Council for financial support. R.D.M. thanks La Trobe University for a postgraduate scholarship.

Stearate-Modified Carbon Paste Electrodes for Detecting Dopamine in Vivo: Decrease in Selectivity Caused by Lipids and Other Surface-Active Agents

Paul D. Lyne[1] and Robert D. O'Neill*

Chemistry Department, University College, Belfield, Dublin 4, Ireland

Electrochemical characteristics of dopamine, ascorbic acid, and ferrocyanide measured with carbon–Nujol paste electrodes (CPEs) and stearate-modified carbon paste electrodes (SMEs) before and after treatment with either surfactant (Triton-X), lipid (phosphatidylethanolamine), or brain tissue indicate that the lipophilic nature of the brain destroys the selectivity of SMEs for dopamine by removing the hydrophobic elements from the electrode surface. Measurements of the degree and time-course of changes in surface capacitance of SMEs following contact with surface-active agents support this conclusion. The results suggest that SMEs cannot be used to detect dopamine unambiguously in vivo and emphasize the need to characterize electrochemical sensors in an environment similar to that of intended applications.

INTRODUCTION

A variety of voltammetric techniques have been developed to monitor changes in the concentration of endogenous electroactive compounds in the intact central nervous system (*1*, *2*). In particular, attention has been focused on the detection of dopamine, a neuromodulatory catecholamine, in the extracellular fluid (ECF) of mammalian brain. The two main problems associated with measuring levels of this monoamine in vivo have been (i) the very low baseline concentration of dopamine (0.02–0.05 μmol/L) in the ECF (3–6) and (ii) the presence of large excesses of other substrates, such as ascorbic acid at 200–500 μmol/L (*7*) and 3,4-dihydroxyphenylacetic acid (DOPAC) at about 10 μmol/L (*5*), which oxidize at potentials similar to that of dopamine on many electrode materials. As a result of these adverse conditions, extracellular dopamine has been reliably detected with electrochemical techniques only in situations of strong physiological perturbation, such as electrical stimulation (*8*, *9*) or high potassium ion concentration (*10*, *11*), or with severe pharmacological manipulation of dopaminergic systems, i.e., total inhibition of transmitter metabolism (*12*).

In contrast, the detection of dopamine in vivo using stearate-modified carbon–Nujol paste electrodes (SMEs) has been claimed extensively for a wide variety of mild challenges to dopamine neurons (*13–28*). The basis of the modification is that the presence on SMEs of unprotonated carboxylic moieties at physiological pH retards the electrooxidation of anionic species, such as ascorbate and DOPAC, to such an extent that the cationic dopamine species can be detected in their presence. Apart from the complication of the electrocatalysis of dopamine oxidation by ascorbate already investigated (*29*), the major inconsistency posed by this technique (*2*, *30*) is the large size of the putative dopamine signal recorded in vivo which corresponds to a concentration greater than 1 μmol/L (*13*), some 2 orders of magnitude greater than that estimated by using other electrochemical (*3*, *4*) and microdialysis (*5*, *6*) techniques. Since a recent report has shown that the response of unmodified carbon paste electrodes (CPEs) is significantly altered by contact with brain tissue (*31*), we felt it necessary to reexamine the properties of SMEs in vitro following tissue contact. A preliminary report of this work showed a loss in selectivity of the SMEs for dopamine over ascorbate following implantation in the brain (*32*). In order to elucidate the processes leading to this loss of selectivity, the electrochemical behavior of ascorbic acid, dopamine, and ferrocyanide at CPEs and SMEs following treatment with a variety of surface-active agents, and at carbon powder electrodes, is described here. The results obtained emphasize the need to consider electrode–environment interactions when developing new sensors for use in biological systems.

EXPERIMENTAL SECTION

Electrodes. Stearate-modified carbon paste electrodes (SMEs) were manufactured from Teflon-coated silver wire as previously reported (*13*). Briefly, stearate-modified paste was prepared by thoroughly mixing 1.5 g of carbon powder (UCP-1-M, Ultra Carbon Corp.) with 100 mg of stearic acid (octadecanoic acid, Sigma Chemical Co.) dissolved in 1 mL of Nujol (Aldrich Chemical Co.). The stearic acid did not dissolve easily in the oil, and the mixture was warmed to approximately 55 °C for some time to achieve a solution that was very viscous. Unmodified carbon paste electrodes (CPEs) were prepared in an identical manner, omitting stearic acid. The carbon powder electrodes (CPWEs) were made by packing unpasted UCP-1-M into the Teflon-insulated cavity. The diameter of the active surface of each electrode type was 250 μm; the external diameter was 350 μm.

CPEs and SMEs were subjected to different treatments. SMEs were exposed for 24 h to either surfactant solution (0.1% Triton-X 100), SME_{surf}, or a lipid suspension (phosphatidylethanolamine, PEA, 100 mg/mL), SME_{lipid}. CPE_{tissue} and SME_{tissue} represent CPEs and SMEs inserted into brain tissue for a 24-h period. The tissue in this study was removed from the skull of rat before use, and either used immediately or stored frozen before being defrosted; the effect of fresh and stored tissue was similar. The relevance of the state of the tissue to the modification of electrodes is discussed later. Because of the relative importance of the tissue modification of SMEs to our final conclusions, eight such electrodes were treated in this way.

Apparatus. Cyclic staircase voltammograms were recorded at 25 ± 1 °C in solutions containing either ascorbate, dopamine, or ferrocyanide, using a microcomputer-based three-electrode system similar to that reported previously (*33*), at 50 mV/s with a saturated calomel electrode as reference and silver wire in an isolated compartment as auxiliary electrode. For the scan rate and electrode dimension used, this corresponds adequately to cyclic voltammetry (*34*, *35*).

Analysis. The peak separation was calculated as the difference between the anodic and cathodic peak potentials, $\Delta E_p = E_{p,a} - E_{p,c}$, and used as an index for the rate of electron transfer for the ferrocyanide couple at the various electrodes (*36*). The problem of adsorption of substrate on carbon powder-type surfaces (*37*) precludes a more direct comparison of heterogeneous rate constants for electron transfer. Due to the irreversibility of the oxidation of ascorbate and dopamine under the present experimental conditions, we have used the potential of maximum slope (*38*), $E_{s,max}$, to characterize the waves for these compounds. $E_{s,max}$ was used both as an index of the position of the waves on the voltage axis and as a measure of changes in rates of electron transfer for the two substrates at the electrodes. The foot potential, E_f (the potential at which the current first reached 1 nA

[1] Present address: Department of Inorganic Chemistry, South Parks Rd., Oxford, U.K.

0003-2700/90/0362-2347$02.50/0 © 1990 American Chemical Society

Table I. Potential of Maximum Slope, $E_{s,max}$, Recorded at 50 mV/s for Dopamine (DA) and Ascorbid Acid (AA) at pH 7.4, and Peak Separation, ΔE_p, for Ferrocyanide (pH 4) at Different Types of Carbon Paste Electrode[a]

	wave position $E_{s,max}$/mV		wave separation $\Delta E_{s,max}$/mV	peak separation ΔE_p/mV
electrode[b]	AA	DA	AA − DA	ferrocyanide
CPE	565 ± 55	140 ± 10	425 ± 56	202 ± 31
SME	880 ± 55	272 ± 15	608 ± 57	[c]
CPE_{tissue}	188 ± 27	75 ± 5	113 ± 28	108 ± 2
SME_{tissue}	275 ± 10	78 ± 9	197 ± 14	82 ± 14
SME_{lipid}	202 ± 44	94 ± 10	108 ± 45	114 ± 11
SME_{surf}	195 ± 32	75 ± 5	120 ± 33	103 ± 22
CPWE	142 ± 9	75 ± 5	67 ± 11	77 ± 7

[a] Means ± SEM, $n = 3$. The $\Delta E_{s,max}$ values for all treated SMEs and CPEs were significantly less than for the unmodified CPE ($P < 0.02$, Student's two-tailed t test). [b] Electrode types: CPE, unmodified carbon-Nujol paste electrode; CPE_{tissue}, carbon paste electrode after contact with brain tissue; SME_{tissue}, stearate-modified electrode after contact with brain tissue; SME_{lipid}, stearate-modified electrode after contact with lipid; SME_{surf}, stearate-modified electrode after contact with surfactant; CPWE, carbon powder electrode. [c] Absent.

above the baseline), was used as a further comparison of the position of the waves due to dopamine and ascorbate oxidation. The background current, recorded in the absence of substrate, was subtracted from each voltammogram before analysis. The size of the background current recorded in phosphate buffered saline (PBS) was also used as a measure of the double layer capacitance for each electrode type (*39*); the charge passed was also determined in some cases by calculating the area between oxidation and reduction background currents.

Chemicals. L-Ascorbic acid (BDH), dopamine hydrochloride, and PEA (Sigma Chemical Co.) and potassium ferrocyanide (Hopkins and Williams) were used as supplied. Separate solutions of dopamine and ascorbate were made in PBS, pH 7.4: NaCl (0.15 mol/L), NaH_2PO_4 (0.04 mol/L), and NaOH (0.04 mol/L). Solutions of ferrocyanide were made in potassium chloride (1.00 mol/L) and hydrochloric acid (0.10 mol/L), diluted to pH 4. All solutions were purged with nitrogen before use.

RESULTS AND DISCUSSION

Oxidation of Ascorbic Acid and Dopamine. As expected from previous studies (*13*, *29*), incorporating the carboxylate anion of stearic acid into carbon paste electrodes increased the separation of the oxidation waves for ascorbate (AA) and dopamine (DA), quantified as $E_{s,max}$(AA)–$E_{s,max}$(DA), from 425 ± 56 mV for CPEs to 608 ± 57 mV for SMEs at pH 7.4. Surprisingly, however, the modification increased $E_{s,max}$ for both the cationic dopamine and anionic ascorbate species (Table I). This decrease in charge transfer rate for the two substrates may be due to the approximately 12% greater hydrocarbon content of the SMEs due to the presence of the octadecanoic acid, since increasing the amount of hydrocarbon in CPEs progressively reduces the rate of electron transfer to paste electrodes of this carbon/oil ratio (*37*). The overall increase in the separation of the two waves is interpreted as the extra unfavorable electrostatic interaction between the ascorbate and stearate anions (*13*).

After a 24-h period in brain tissue, the ability of SMEs to separate dopamine and ascorbate oxidation waves was reduced from 608 ± 57 to 197 ± 14 mV, a value significantly less than that for unmodified CPEs (Table I). The same treatment of unmodified CPEs reduced the separation from 425 ± 56 to 113 ± 28 mV. Thus, the effective resolution of ascorbic acid and dopamine is comparable at CPEs and SMEs after contact

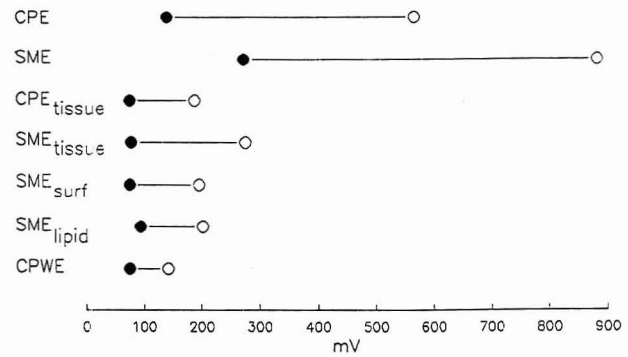

Figure 1. Ability of different types of carbon electrodes to separate ascorbic acid (open circles) and dopamine (filled circles) oxidation waves recorded in PBS (pH 7.4) at 50 mV/s. Mean values of $E_{s,max}$ and abbrevations from Table I.

with brain tissue and is insufficient to detect dopamine in the presence of large excesses of ascorbate. This conclusion is supported by the finding that the foot potential, E_f, measured using $SMEs_{tissue}$, was 27 ± 27 mV ($n = 3$) for ascorbate at a concentration of 500 μmol/L and 40 ± 5 mV ($n = 3$) for 100 μmol/L dopamine. These data indicate that for a concentration ratio of ascorbate/dopamine as low as 5:1, the current due to ascorbate is greater than that for dopamine at 40 mV vs SCE in the absence of electrocatalytic effects (discussed below). There is a general consensus that the concentration ratio of the two compounds in rat striatum (the brain area where the majority of in vivo electrochemical recordings are made) is of the order of 10000:1 (*2*); under these conditions, the separation of dopamine and ascorbate in vivo using SMEs is clearly untenable.

To investigate the possibility that lipids, which constitute about 40% dry weight of mammalian brain membranes (*40*), might be responsible for the loss of selectivity of the electrodes for dopamine, SMEs were treated with a suspension of PEA, a lipid abundant in brain tissue. The data in Table I show that these $SMEs_{lipid}$ have also lost the ability to separate ascorbate and dopamine oxidations effectively, a characteristic property of the untreated SME, and have very similar properties to the SME_{tissue}. The finding that a general-purpose surfactant, Triton-X 100, with a very different molecular structure to lipids also destroyed the selectivity of SMEs (Table I) suggests that a common surfactant mechanism may be responsible for the effects observed. We propose that when SMEs come into contact with surfactants, lipids, or brain tissue, the hydrophobic stearic acid is removed, together with pasting oil (*31*), from the exterior of the electrode to give a more powderlike surface. This interpretation of the data is supported by the measured electrochemical behavior of dopamine and ascorbate at carbon powder electrodes (Table I). The ability of the different electrodes to separate ascorbate and dopamine oxidations is illustrated in Figure 1.

Oxidation of Ferrocyanide. The ferrocyanide couple was used as a probe of the electrode surface because of the relative simplicity of its one-electron transfer reaction compared with the complex oxidations of ascorbic acid and dopamine (*41*). In addition, the charge of −4 on the substrate makes it particularly sensitive to the presence of anions at the electrode/solution interface. The oxidation of ferrocyanide at CPEs is irreversible at pH 7.4 due to ionized carboxylate moieties endogenous to the carbon material (*42*). At pH 4, however, enough of these anions are protonated to allow increaseed electron transfer at the surface; the ferrocyanide system shifts to quasi–reversible behavior, showing both anodic and cathodic peaks with a separation greater than the characteristic value for a one-electron Nernstian system. The ferrocyanide wave recorded at 50 mV/s is a pH 4 solution using a CPE exhibited quasi-reversible characteristics (Figure

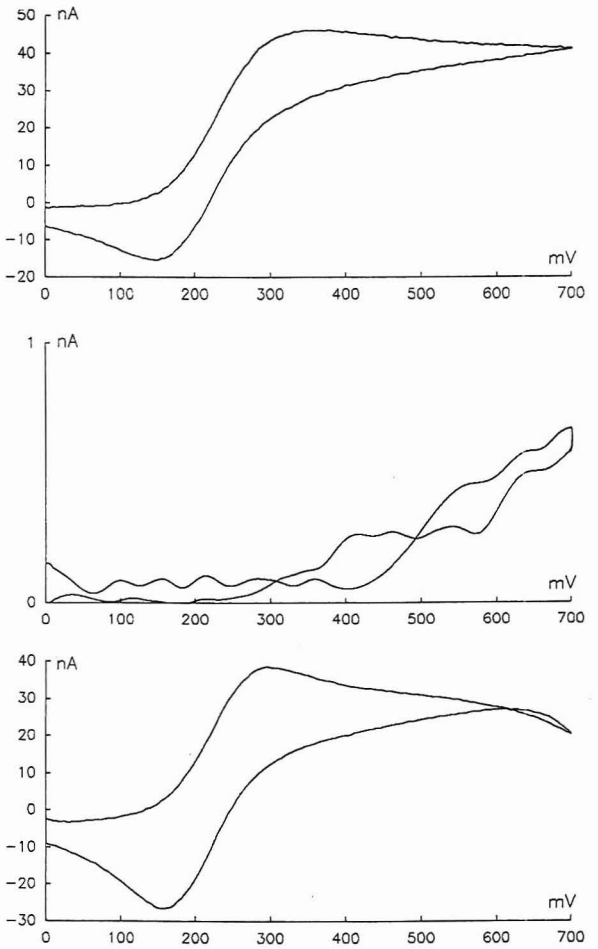

Figure 2. Examples of cyclic voltammograms for ferrocyanide recorded at 50 mV/s and pH 4 using carbon paste electrodes: top, unmodified electrode (CPE); middle, stearate-modified CPE (SME); bottom, SME after treatment with lipid (SME_{lipid}). See Table I for electrochemical data for all electrode types.

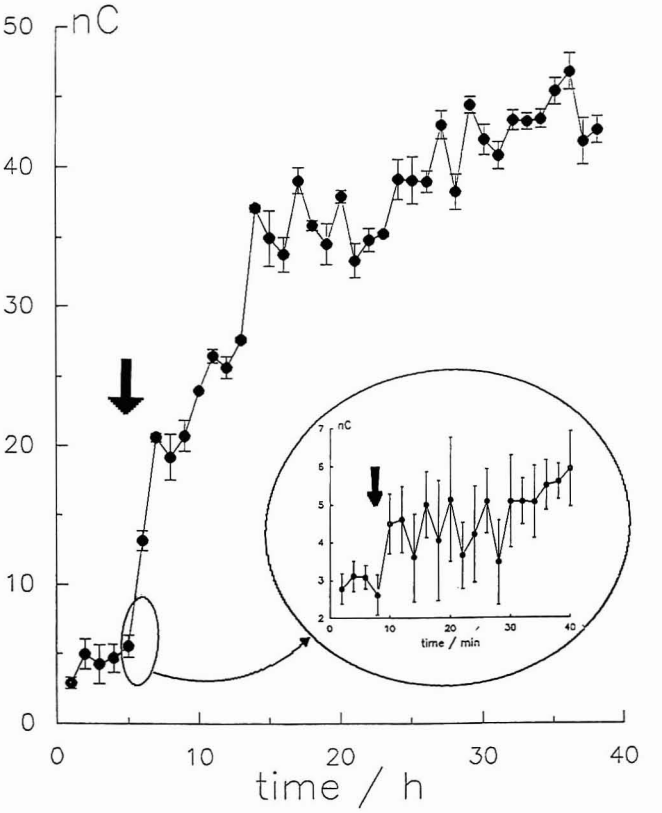

Figure 3. Time course for changes in the integral of charging current (nanocoulombs, nC) recorded with a SME at 100 mV/s between −100 and +700 mV over a 40-h period in the absence of any electroactive substrate. The arrow indicates the addition of 2 mL of 0.1% Triton-X solution to 18 mL of PBS. Mean ± SEM of three measurements. See Table II for capacitance data for all electrode types. Inset: Changes in charge passed recorded at higher time resolution over a 40-min period during which the surfactant was added.

2). The incorporation of stearic acid into the paste increased the overpotential for oxidation to the extent that hardly any faradaic current was observed up to 700 mV vs SCE. Clearly, the fraction of the surface stearic acid ($pK_a \sim 4.9$) unprotonated at this pH is sufficient to block electron transfer from the ferrocyanide anions to SMEs (Figure 2). After lipid treatment of the SME, however, the behavior of the ferrocyanide couple at this pH is similar to that at the unmodified CPE, again suggesting that the treatment abolishes the anion-repelling action of stearic acid at the electrode surface (Figure 2). A comparison of the ferrocyanide characteristics at surfactant, lipid, and tissue-treated SMEs with those at carbon powder electrodes supports this conclusion (Table I). The finding that the ΔE_p value for the treated SMEs was significantly less than that for CPEs indicates that removal of pasting oil is an additional feature of the action of surfactants on these Nujol–paste electrodes.

Capacitance Measurements and Electron Microscopy. It is possible that simple wetting of the oil surface could account for the increased activity of paste electrodes following contact with surface-active agents. To distinguish between fast wetting of the oil–water interface and the physical removal of lipophiles from the electrode surface, which one might expect to occur much more slowly, the time course for changes in the total background charge for SMEs was measured after the addition of 2 mL of 0.1% Triton-X solution to 18 mL of PBS (Figure 3). The finding that the half-life of the overall process was of the order of 5 h suggests that insulating material is displaced from the surface by the surfactant. However, at higher time resolution (inset Figure 3) the initial statistically significant jump in the charging current, observed by 2 min, may be due to a wetting effect.

Table II. Capacitance Values for Different Electrode Types[a]

electrode	capacitance/nF	electrode	capacitance/nF
CPE	9 ± 2(4)	SME_{tissue}	138 ± 19 (8)
SME	7 ± 1 (6)	SME_{lipid}	159 ± 16 (3)
CPWE	1250 ± 600 (6)	SME_{surf}	223 ± 23 (5)

[a] Means ± SEM, number of electrodes in parentheses. See Table I for abbreviations.

A comparison of capacitance values for the different electrode types (Table II) indicates that each treatment increased this parameter approximately 20-fold over the value for the paste electrodes. This finding is consistent with the proposal that all treatments expose additional conducting surface. The still greater capacitance value for powder electrodes suggest that the surfactant-treated pastes are not as porous as powder itself; i.e., the hydrocarbons are removed from only the outer surface of the paste electrodes. Similar conclusions have been reached previously to account for the effect of brain tissue on the electrochemical characteristics of carbon/silicone paste electrodes (*31*) and of surfactants on the surface resistance of three commercially available carbon pastes in addition to pastes made from mineral oil, high-vacuum grease, and hexadecane (*43*).

Further support for these conclusions comes from electron micrographs (Figure 4) which show that the carbon platelets in paste electrodes orient themselves parallel to the disk surface, forming a relatively compressed material. The to-

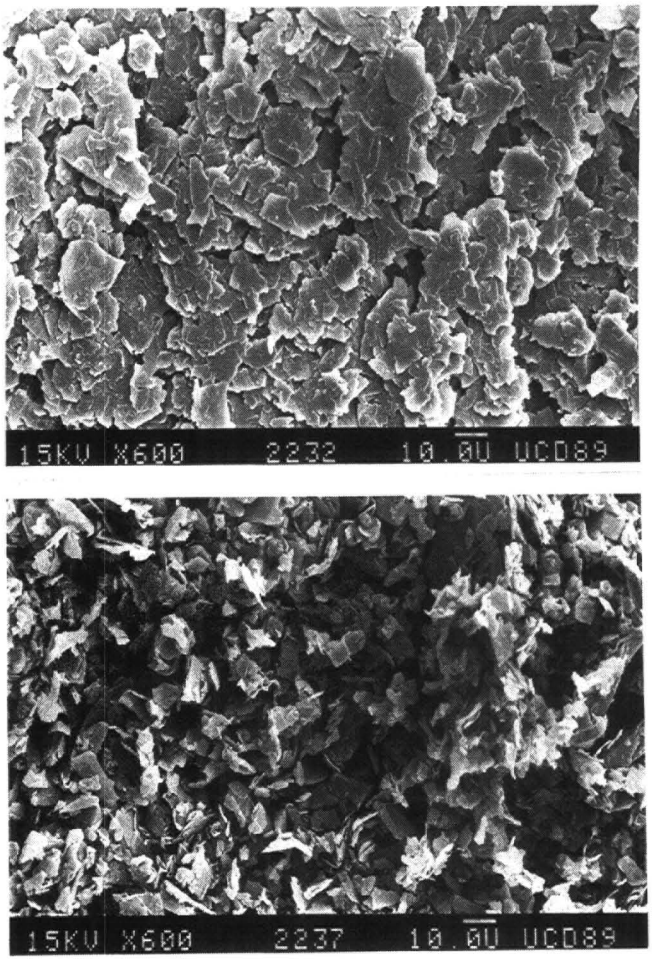

Figure 4. Scanning electron micrographs of the surface of a carbon paste electrode (top) and carbon powder electrode (bottom), magnification ×600. The appearance of surfactant-treated paste electrodes was similar to that of the untreated paste electrode.

pography of powder electrodes appeared quite different with the carbon particles showing no preferential alignment and the surface being less compact. The finding that the appearance of surfactant-treated electrodes was similar to that of the untreated paste electrodes correlates qualitatively with the difference in the capacitance values (Table II) for CPEs (compact and oil coated), treated paste electrodes (compact with reduced hydrocarbon coverage), and carbon powder electrodes (porous and oil free).

General Discussion. There are two possible explanations of the large currents reported for SMEs in vivo (*13*) where dopamine is present with a large excess of ascorbic acid (*2*): either the stearic acid is still functioning to eliminate direct ascorbic acid oxidation, but electrocatalytic reduction of electrooxidized dopamine by ascorbate increases the dopamine current (*29*), or the surface stearate is rendered ineffective by the brain tissue and ascorbic acid contributes directly to the faradaic current. Since the extracellular concentration of brain ascorbate shows diurnal variations (*44*) and can be altered by physiological (*45*) and pharmacological (*46–51*) manipulations, either of these scenarios would imply that an unambiguous dopamine signal cannot be obtained by using SMEs in vivo. The results reported here indicate that the latter explanation of the large current values is more justifiable and specifically that lipids present in brain tissue remove the lipophilic elements (stearate and pasting oil) from the electrode surface.

The finding that a simple surfactant and an isolated lipid destroy the selectivity of SMEs suggests that its destruction by brain tissue does not depend on brain structure or function. This conclusion regarding the unimportance of the state of the tissue was also drawn from earlier studies on the effect of brain tissue on CPEs made with silicone oil (*52*), where an increased rate of ascorbate oxidation was observed with electrodes following either use in living brain or immersion in brain homogenate. It is likely that the introduction of the electrode into intact tissue disrupts the lipid bilayer membrane structure of cells it comes into contact with, freeing lipid molecules. The results obtained by using brain homogenates (*52*) and lipid suspensions also suggest that the altered response induced by contact with intact tissue is not due to a mechanical disruption of the electrode surface by the brain on removal of the electrode.

Many more aspects of the electrochemical behavior of treated and untreated SMEs could have been investigated, for example, the electrocatalytic interaction of dopamine and ascorbic acid, which has already been shown to be significant at untreated SMEs (*29*). Also, the limit of detection for substrates is an important characteristic of any analytical technique. However, if the aim is to develop a sensor for dopamine in vivo, discrimination against ascorbate is a prerequisite property. Since SMEs do not possess this characteristic following implantation in the brain, we feel that further studies of SMEs would be unproductive.

The results highlight the need for caution when developing neurochemical sensors for use in vivo. The lipophilic environment of brain tissue interacts strongly with carbon paste electrodes, removing hydrophobic species that are not firmly bound to the surface. It is possible that covalently bonded modifications may prove useful in this area. We suggest, however, that it is unlikely that any manipulation of electrode characteristics which shifts ascorbate oxidation to higher potentials will be successful in detecting dopamine unambiguously, since electrocatalysis becomes a significant problem at that stage. Since the redox potential of ascorbic acid is more than 200 mV less than that of dopamine (*41*), devising modified electrodes to encourage ascorbate oxidation at lower potentials, as has been achieved for carbon fiber electrodes (*53*), might be a better strategy. Depending on its size, such an electrode sampling a restricted compartment in vivo (*7*, *54*, *55*) might deplete the pool of ascorbate before the dopamine signal appeared, making electrocatalytic contributions negligible.

ACKNOWLEDGMENT

We thank Mr. Barry Cregg for electron microscopy.

Registry No. DA, 51-61-6; AA, 50-81-7; ferrocyanide, 13408-63-4; Triton X, 9002-93-1.

LITERATURE CITED

(1) *Voltammetry in the Neurosciences: Principles, Methods and Applications*; Justice, J. B., Jr., Ed.; Humana Press: Clifton, NJ, 1987.
(2) Marsden, C. A.; Joseph, M. H.; Kruk, Z. L.; Maidment, N. T.; O'Neill, R. D.; Schenk, J. O.; Stamford, J. A. *Neuroscience* **1988**, *25*, 389–400.
(3) Gonon, F. G.; Navarre, F.; Buda, M. J. *Anal. Chem.* **1984**, *56*, 573–575.
(4) Kelly, R. S.; Wightman, R. M. *Brain Res.* **1987**, *423*, 79–87.
(5) Zetterstrom, T.; Sharp, T.; Marsden, C. A.; Ungerstedt, U. *J. Neurochem.* **1983**, *41*, 1769–1773.
(6) Church, W. H.; Justice, J. B., Jr. *Anal. Chem.* **1987**, *59*, 712–716.
(7) Amatore, C.; Kelly, R. S.; Kristensen, E. W.; Kuhr, W. G.; Wightman, R. M. *J. Electroanal. Chem. Interfacial Electrochem.* **1986**, *213*, 31–42.
(8) Stamford, J. A.; Kruk, Z. L.; Millar, J. *Br. J. Pharmacol.* **1988**, *94*, 924–932.
(9) May, L. J.; Kuhr, W. G.; Wightman, R. M. *J. Neurochem.* **1988**, *51*, 1060–1069.
(10) Rice, M. E.; Oke, A. F.; Bradbury, C. W.; Adams, R. N. *Brain Res.* **1985**, *340*, 151–155.
(11) Gratton, A.; Hoffer, B. J.; Gerhardt, G. A. *Neuroscience* **1989**, *29*, 57–64.
(12) Marcenac, F.; Gonon, F. *Anal. Chem.* **1985**, *57*, 1778–1779.
(13) Blaha, C. D.; Lane, R. F. *Brain Res. Bull.* **1983**, *10*, 861–864.
(14) Blaha, C. D.; Lane, R. F. *Eur. J. Pharmacol.* **1984**, *98*, 113–117.
(15) Howard-Butcher, S.; Blaha, C. D.; Lane, R. F. *J. Pharmacol. Exp. Ther.* **1985**, *233*, 58–61.
(16) Lane, R. F.; Blaha, C. D.; Phillips, A. G. *Brain Res.* **1986**, *397*, 200–204.

(17) Blaha, C. D.; Lane, R. F. *Neurosci. Lett.* **1987**, *78*, 199–204.
(18) Lane, R. F.; Blaha, C. D. *Brain Res. Bull.* **1987**, *18*, 135–138.
(19) Lane, R. F.; Blaha, C. D. *Brain Res.* **1987**, *408*, 317–320.
(20) Lane, R. F.; Blaha, C. D.; Hari, S. P. *Brain Res. Bull.* **1987**, *19*, 19–27.
(21) Broderick, P. A. *Life Sci.* **1985**, *36*, 2269–2275.
(22) Broderick, P. A. *Neurosci. Lett.* **1988**, *95*, 275–280.
(23) Yamamoto, B. K.; Lane, R. F.; Freed, C. R. *Life Sci.* **1982**, *30*, 2155–2162.
(24) Broderick, P. A. *Neuropeptides* **1987**, *10*, 369–386.
(25) Signs, S. A.; Yamomoto, B. K.; Schechter, M. D. *Neuropharmacology* **1987**, *26*, 1653–1656.
(26) Yamamoto, B. K.; Spanos, L. J. *Eur. J. Pharmacol.* **1988**, *148*, 195–203.
(27) Glynn, G. E.; Yamamoto, B. K. *Brain Res.* **1989**, *481*, 235–241.
(28) Phillips, A. G.; Pfaus, J. G.; Blahm, C. D.; Fibiger, H. C. *J. Neurosci. Methods* **1989**, *29*, 275.
(29) Gelbert, M. B.; Curran, D. J. *Anal. Chem.* **1986**, *58*, 1028–1032.
(30) Crespi, F.; Martin, K. F.; Marsden, C. A. *Neuroscience* **1988**, *27*, 885–896.
(31) Ormonde, D. E.; O'Neill, R. D. *J. Electroanal. Chem. Interfacial Electrochem.* **1989**, *261*, 463–469.
(32) Lyne, P. D.; O'Neill, R. D. *Anal. Chem.* **1989**, *61*, 2323–2324.
(33) O'Neill, R. D.; Fillenz, M.; Albery, W. J.; Goddard, N. J. *Neuroscience* **1983**, *9*, 87–93.
(34) Saralathan, M.; Osteryoung R.; Osteryoung, J. *J. Electroanal. Chem. Interfacial Electrochem.* **1986**, *214*, 141–156.
(35) Penczek, M.; Stojek, Z. *J. Electroanal. Chem. Interfacial Electrochem.* **1987**, *227*, 271–274.
(36) Nicholson, R. S. *Anal. Chem.* **1965**, *37*, 1351–1355.
(37) Rice, M. E.; Galus, Z.; Adams, R. N. *J. Electroanal. Chem. Interfacial Electrochem.* **1983**, *143*, 89–102.
(38) Oldham, K. B. *J. Electroanal. Chem. Interfacial Electrochem.* **1985**, *184*, 257–267.
(39) Bard, A. J.; Faulkner, L. R. *Electrochemical Methods*; John Wiley & Sons: New York, 1980; p 13.
(40) Reinis, S.; Goldman, J. M. *The Chemistry of Behavior*, Plenum Press: New York, 1982; p 7.
(41) Deakin, M. R.; Kovach, P. M.; Stutts, K. J.; Wightman, R. M. *Anal. Chem.* **1986**, *58*, 1474–1480.
(42) Deakin, M. R.; Stutts, K. J.; Wightman, R. M. *J. Electroanal. Chem. Interfacial Electrochem.* **1985**, *182* 113–122.
(43) Albahadily, F. N.; Mottola, H. A. *Anal. Chem.* **1987**, *59*, 958–962.
(44) O'Neill, R. D.; Fillenz, M. *Neurosci. Lett.* **1985**, *60*, 331–336.
(45) Boutelle, M. G.; Svensson, L.; Fillenz, M. *Neuroscience* **1989**, *30*, 11–17.
(46) Clemens, J. A.; Phebus, L. A. *Life Sci.* **1984**, *35*, 671–677.
(47) Brose, N.; O'Neill, R. D.; Boutelle, M. G.; Fillenz, M. *Neuropharmacology* **1989**, *28*, 509–514.
(48) Louilot, A.; Gonon, F.; Buda, M.; Simon, H.; Le Moal, M.; Pujol, J. F. *Brain Res.* **1985**, *336*, 253–263.
(49) Wilson, R. L.; Kamata, K.; Bigelow, J. C.; Rebec, G. V.; Wightman, R. M. *Brain Res.* **1986**, *370*, 393–396.
(50) Gonzalez-Mora, J. L.; Sanchez-Bruno, J. A.; Mas, M. *Neurosci. Lett.* **1988**, *86*, 61-66
(51) Mueller, K.; Haskett, C. *Pharmacol. Biochem. Behav.* **1987**, *27*, 231–234.
(52) O'Neill, R. D.; Grunewald, R. A.; Fillenz, M.; Albery, W. J. *Neuroscience* **1982**, *7*, 1945–1954.
(53) Gonon, F.; Fombarlet, C. M.; Buda, M.; Pujol, J. F. *Anal. Chem.* **1981**, *53*, 1386–1389.
(54) Albery, W. J.; Goddard, N. J.; Beck, T. W.; Fillenz, M.; O'Neill, R. D. *J. Electroanal. Chem. Interfacial Electrochem.* **1984**, *161*, 221–233.
(55) Cheng, H. Y. *J. Electroanal. Chem. Interfacial Electrochem.* **1982**, *135*, 145-151.

RECEIVED for review January 2, 1990. Accepted July 11, 1990. We thank EOLAS for a grant to P.D.L. under the Basic Research Awards scheme.

Polynomial Filters for Data Sets with Outlying or Missing Observations: Application to Charge-Coupled-Device-Detected Raman Spectra Contaminated by Cosmic Rays

G. R. Phillips and J. M. Harris*

Department of Chemistry, University of Utah, Salt Lake City, Utah 84112

Occasionally data sets contain points with excess error so that no information about the underlying signal is available from these observations. Such points should be considered lost and be given no influence on the results. Polynomial filters suitable for smoothing data sets containing outlying or missing observations are presented. Outliers are first identified by their deviation from the trends of the surrounding data, relative to a robust estimate of the standard deviation. In the vicinity of an outlying point thus identified, the missing-point filter employs a polynomial fit to the points surrounding, but not including, the outlying or missing point. In the absence of outliers, the procedure reverts to ordinary Savitzky–Golay polynomial filtering. The equations for generating these filters and predicting their statistical properties are derived. Their performance is evaluated on charge-coupled-device-detected Raman spectra contaminated with cosmic ray events and is compared with nonlinear smoothing algorithms. The linear, missing-point polynomial filters are found to be efficient, both in speed and in ability to bridge gaps in data with minimal distortion.

Least-squares polynomial digital filters, introduced by Savitzky and Golay (*1*), are frequently used to remove high-frequency noise and enhance the signal-to-noise ratio of spectroscopic or time-dependent data (*2*). Errors in the original smoothing coefficients published by Savitzky and Golay were corrected by Steiner (*3*), while Madden (*4*) published equations for calculating the convoluting coefficients. Polynomial filters are moving weighted averages computed by convoluting a set of regression-generated filter coefficients with a moving data window (*5*). These filters can be applied to any data set of equally spaced observations with locally constant variance (i.e. within the filter width). For data with normally distributed errors, least-squares polynomial filters are maximum likelihood estimators. The efficiency of least-squares estimators is severely degraded by the presence of deviant observations, as shown by the distortion of spectra containing outliers when smoothed by Savitzky–Golay filters.

Outliers are a common problem in analytical techniques such as Raman spectroscopy that utilize ultrasensitive detection methods. The high sensitivity and low noise of charge-coupled device (CCD) detectors make them ideal for the weak signal levels produced in these experiments (*6–9*). The characteristics of CCD detectors have been recently reviewed (*10–11*). A significant problem with CCD detectors is their sensitivity to cosmic rays (*6–12*). Cosmic ray events produce enormous charge spikes (10^3–10^4 photoelectrons), which cause large distortions in the spectrum when ordinary linear smoothing procedures are used. Outliers in Raman spectroscopy may also arise from particles or bubbles in the

* To whom correspondence should be addressed.

0003-2700/90/0362-2351$02.50/0 © 1990 American Chemical Society

focused laser beam. Whatever the cause, outliers should be removed before background subtraction, peak fitting, or other data processing.

In this work, a linear smoothing algorithm suitable for outlier-contaminated data is presented. The method is also effective in bridging gaps in data sets where observations are missing or lost. In the vicinity of an outlying or missing point, filters similar in design to those of Savitzky and Golay (*1*) employ a polynomial fit to the points surrounding, but not including, the outlying or missing point. In the absence of outliers, the procedure reduces to a Savitzky–Golay polynomial filter. After equations for generating these filters and predicting their precision are derived, their performance is tested on CCD-detected Raman spectra contaminated with cosmic ray events; the results are compared with those produced by two nonlinear smoothing algorithms proposed by Hillig and Morris (*13*) and Bussian and Härdle (*14*). The linear, missing-point polynomial filters are found to be efficient, both in speed and ease of implementation and in their ability to bridge gaps in data with minimal distortion.

EXPERIMENTAL SECTION

The linear polynomial filters (and the comparison nonlinear smoothing algorithms) were written in Microsoft FORTRAN and executed on a PC-AT compatible computer with an 80827 math coprocessor using subroutines from the GRAFMATIC library (Microcompatibles, Inc., Silver Spring, MD). Analytical equations for filter coefficients were derived on a VAX 8300 computer by using the algebraic programming language REDUCE (Rand Corp., Santa Monica, CA.).

Raman spectra of 0.4 mM ferriprotoporphyrin chloride (hemin) in aqueous solution buffered at pH 7 were produced by using 514.5-nm incident laser radiation and a CCD (Thomson, Model CSF THF7882CDA) detector housed in a cryogenic dewar (Photometrics, Model CH210) cooled to -115 °C. The two-dimensional (384 columns by 576 rows) CCD was positioned such that the spectrum was dispersed along the horizontal (576 channel) detector axis and photoelectrons were binned (summed) along the vertical axis to minimize readout noise. The complete Raman instrument has been described elsewhere (*15*).

RESULTS AND DISCUSSION

Missing-Point Polynomial Filters. Occasionally data sets contain a few erroneous points, contaminating an otherwise usable spectrum or other data record. If the error in these points is so large that no information about the underlying signal is available from the observation, then the points should be considered missing or lost and should have no influence on the results. In these cases, a desirable smoothing procedure should automatically detect and replace these outliers with a statistically valid estimate of the point derived from adjacent data. The missing-point filtering method described in this section accomplishes this goal. Presently, the only restrictions with the method are that the data be evenly spaced, that any spike or outlier occupy no more than two adjacent data channels, and that such outlying events be separated by at least one filter width. The latter two restrictions can easily be relaxed with further development, as discussed below.

Outliers in the data are identified by first smoothing with a quadratic Savitzky–Golay filter. Standardized residuals

$$r_i/s = (y_i - \hat{y}_i)/s \tag{1}$$

are formed, where y_i and $\hat{y}_i$ denote the original and filtered points, respectively. The standard deviation, s, is estimated from the inner quartile range (*16*) by

$$s = (\mu_{75} - \mu_{25})/1.3490 \tag{2}$$

where μ_{25} and μ_{75} are the 25th and 75th percentiles (or first and third quartiles) of the distribution of residuals. This estimate of the standard deviation requires sorting the residuals but is insensitive to a small number of outliers, in contrast to the more familiar root mean square estimate of the standard deviation (*16*). Observations whose standardized residuals are greater than some constant, $r_i/s > c$, are considered to be outliers (note: we are only testing for positive outliers in the present study since cosmic ray events and particles in the sample generate excess charge in the detected spectrum). For this work, a value, $c = 3.5$, was chosen to reject points outside the 99.98% one-sided confidence interval of a normal error distribution. Normalization of the residuals by an estimate of the standard deviation means that c does not require adjustment as the noise in the spectrum changes, eliminating the need for the subjective selection of error parameters.

For an isolated outlier or spike, y_s, identified by the above procedure with a filter width equal to $2m + 1$, all the filtered points within the interval y_{s-m} to y_{s+m} have been contaminated by the outlier during the Savitzky–Golay smooth and must be recalculated. Each of the contaminated intensities $\hat{y}_{s+k}$, $k = -m, ..., m$, is replaced by a quadratic polynomial least-squares fit to the m points on each side of y_{s+k}, excluding y_s. These least-squares estimates are computed by using the filter or convoluting coefficients $C_{2,k,i}$

$$\hat{y}_{s+k} = \sum_{i=-m}^{m} C_{2,k,i} y_{s+k-i} \tag{3}$$

for $k = -m, ..., m$. The convoluting coefficient for the outlier, $C_{2,k,i=k}$, should be zero in all $2m + 1$ sets of coefficients.

The convoluting coefficients are computed by using a matrix formulation (*3*, *17–19*) of least-squares polynomial filters. This approach to the polynomial regression problem (*20*, *21*) simplifies the design of new filters for initial point estimation, for example (*17*), and allows the statistical properties of polynomial filters to be predicted from first principles (*18*, *19*). For quadratic filtering, the best fit quadratic function is defined by the $n + 1 = 3$ parameters, $\beta_{n,j}$, which best fit $2m + 1$ simultaneous equations, one equation for each point within the $2m + 1$ data segment, of the form

$$y_i = \sum_{j=0}^{n} \beta_{n,j} i^j + \epsilon_i \tag{4}$$

where ϵ_i is the difference between the observation signal and the polynomial fit. Since there are more observations than parameters, this is an overdetermined problem that can be solved by least squares. The set of $2m + 1$ equations represented by eq 4 can be expressed in matrix notation, where letters capped by an arrow denote column vectors and boldface letters denote matrices.

$$\vec{y} = \mathbf{X}\vec{\beta} + \vec{\epsilon} \tag{5}$$

In this equation, $\vec{y}$ contains the $2m + 1$ observations of the dependent variable, the vector $\vec{\beta}$ contains the $n + 1 = 3$ unknown parameters, and $\vec{\epsilon}$ is a vector of $2m + 1$ errors (in the absence of any deviation between the underlying signal and the polynomial model, this vector will contain the residuals, r_i). The design matrix $\mathbf{X}$ has dimensions $2m + 1$ by $n + 1$ and contains the i^j factors from eq 4. The least-squares estimate of $\vec{\beta}$, denoted $\vec{b}$, is obtained by minimizing the sum of squares of error and is given by (*20*, *21*)

$$\vec{b} = (\mathbf{X}^t\mathbf{X})^{-1}\mathbf{X}^t\vec{y} \tag{6}$$

From eq 4, one sees that the value of the polynomial at $i = 0$ (midpoint of the $2m + 1$ data segment) is just the zeroth-order parameter, $\beta_{n,0}$. Combining eq 2 and 6 with this observation indicates that the convoluting coefficients, $C_{2,k,i}$, for quadratic midpoint smoothing are found in the first row of the matrix $\mathbf{T} = (\mathbf{X}^t\mathbf{X})^{-1}\mathbf{X}^t$.

The problem of having an outlier in the data vector, $\vec{y}$, is solved by eliminating its influence on the estimate of $\vec{b}$ in eq

Table I. Quadratic Missing-Point Filter $C_{2,k,i,1}$

k \ i	-4	-3	-2	-1	0	+1	+2	+3	+4
-4	0	-588/14112	1764/14112	3276/14112	3948/14112	3780/14112	2772/14112	924/14112	-1764/14112
-3	-1764/29988	0	5544/29988	7308/29988	7812/29988	7056/29988	5040/29988	1764/29988	-2772/29988
-2	-1872/33228	3354/33228	0	9126/33228	9672/33228	8658/33228	6084/33228	1950/33228	-3744/33228
-1	-2844/31932	3084/31932	7272/31932	0	10428/31932	9396/31932	6624/31932	2112/31932	-4140/31932
0	-3780/30960	2520/30960	7020/30960	9720/30960	0	9720/30960	7020/30960	2520/30960	-3780/30960
+1	-4140/31932	2112/31932	6624/31932	9396/31932	10428/31932	0	7272/31932	3084/31932	-2844/31932
+2	-3744/33228	1950/33228	6084/33228	8658/33228	9672/33228	9126/33228	0	3354/33228	-1872/33228
+3	-2772/29988	1764/29988	5040/29988	7056/29988	7812/29988	7308/29988	5544/29988	0	-1764/29988
+4	-1764/14112	924/14112	2772/14112	3780/14112	3948/14112	3276/14112	1764/14112	-588/14112	0

6. This is easily accomplished by replacing the corresponding row in the design matrix, **X**, by zeros. For example, for a quadratic fit of a 9-point segment where the point at $k = -2$ (or two increments before the midpoint) has been identified as an outlier, the design matrix, $\mathbf{X}_{n,k}$ would be given by

$$\mathbf{X}_{2,-2} = \begin{array}{c|ccc} k \backslash j & 0 & 1 & 2 \\ \hline -4 & 1 & -4 & 16 \\ -3 & 1 & -3 & 9 \\ -2 & 0 & 0 & 0 \\ -1 & 1 & -1 & 1 \\ 0 & 1 & 0 & 0 \\ 1 & 1 & 1 & 1 \\ 2 & 1 & 2 & 4 \\ 3 & 1 & 3 & 9 \\ 4 & 1 & 4 & 16 \end{array} \quad (7)$$

In order to estimate all of the points within the interval $k = -m, \ldots, m$ or $-4, \ldots, 4$ of the outlier, $2m + 1$ or nine of these design matrices must be constructed and the convoluting coefficients determined by solving for the first row of the matrix $\mathbf{T} = (\mathbf{X}^t\mathbf{X})^{-1}\mathbf{X}^t$.

Convoluting coefficients, thus derived, for quadratic filtering of points within an interval of ±4 from a single outlier are listed in Table I. A similar approach is used when a spike event contaminates two adjacent points in the data. Here, two rows of the design matrix are replaced by zeros (except at the ends of the filter, $k = -m$ and $m + 1$, where only one element of the spike event overlaps the filter, and hence only one row of zeros is needed). The convoluting coefficients appropriate for two adjacent outlying points are listed in Table II for 9-point quadratic filtering. To build other missing-point quadratic filters of arbitrary width, analytical expressions for the coefficients of these filters were derived from eq 6 for a design matrix having an arbitrary number of rows, $2m + 1$. These expressions are listed in Table III; included in the table are filter coefficients for a spike consisting of a single channel or two adjacent channels. The design of missing-point filters is not limited to quadratic fitting functions or to two adjacent outliers. Higher-order polynomial filtering can be implemented by expanding the number of columns in the design matrix; similarly, other patterns of missing or outlying points can be accommodated by choosing different rows of the design matrix to replace with zeros.

Smoothing Performance. The matrix derivation for least-squares polynomial filters can also be used to predict the statistical consequences of applying these filters to noisy data (*18*, *19*). The elements of the matrix $\mathbf{V} = \sigma o^2(\mathbf{X}^t\mathbf{X})^{-1}$ predict the variance and covariance of the parameters, $\vec{b}$, estimated by eq 5 (*20*, *21*), where σ_o^2 is the variance of the noise in the raw data. The first diagonal element of **V** contains the expected variance of $b_{n,0}$, the estimated or smoothed value at the origin or midpoint, $i = 0$. This method was applied to the design matrices for missing-point quadratic filters like the example shown in eq 7. Dividing the predicted variance of the smoothed midpoint by the variance of the raw data, σ_o^2, and taking the square root gives the relative change in standard deviation due to the filtering process, as plotted in Figure 1 for 9-point quadratic filters for one or two missing points. The results show that the greatest uncertainty is in estimating the missing point itself, $k = 0$. For a single missing point, the standard deviation of this estimate is <20% more than for 9-point quadratic filtering with no missing points (see the error prediction for the region beyond $k = \pm 4$). For two missing points, the error in predicting their values is 40% larger than the surrounding filtered signal; nevertheless, the two missing points are estimated with greater precision than the original data, since (σ/σ_o) at the peak is less than unity.

Table II. Quadratic Missing-Point Filter $C_{2,k,i,2}$ for Two Outliers

k \ i	-4	-3	-2	-1	0	+1	+2	+3	+4
-4	0	-588/14112	1764/14112	3276/14112	3948/14112	3780/14112	2772/14112	924/14112	-1764/14112
-3	0	0	2646/37044	7938/37044	10584/37044	10584/37044	7938/37044	2646/37044	-5292/37044
-2	1323/202041	0	0	60453/202041	61857/202041	54108/202041	37206/202041	11151/202041	-24057/202041
-1	-8397/215649	35271/215649	0	0	85329/215649	75033/215649	51246/215649	13968/215649	-36801/215649
0	-25596/193536	27756/193536	65448/193536	0	0	84564/193536	59616/193536	19008/193536	-37260/193536
+1	-37260/193536	19008/193536	59616/193536	84564/193536	0	0	65448/193536	27756/193536	-25596/193536
+2	-36801/215649	13968/215649	51246/215649	75033/215649	85329/215649	0	0	35271/215649	-8397/215649
+3	-24057/202041	11151/202041	37206/202041	54108/202041	61857/202041	60453/202041	0	0	1323/202041
+4	-5292/37044	2646/37044	7938/37044	10584/37044	10584/37044	7938/37044	2646/37044	0	0
+5	-1764/14112	924/14112	2772/14112	3780/14112	3948/14112	3276/14112	1764/14112	-588/14112	0

Table III. Equations for a Quadratic Missing-Point Filter

Single Outlying or Missing Point

$$C_{2,k,i,1} = \begin{cases} 0 & i = k \\ \dfrac{(a_1 - 3a_2k^2 - 15k^4) + 3k(a_2 - 5k^2)i + 5(6k^2 - a_3)i^2}{\text{NORM}} & i \neq k \end{cases}$$

$a_1 = m(m + 1)(2m + 1)(3m^2 + 3m - 1)$
$a_2 = 3m^2 + 3m - 1$
$a_3 = m(m + 1)(2m + 1)$
NORM $= (2m + 1)((m - 1)m^2(m + 1)(8m + 11) + 9k^2(2m^2 + 2m + 1 - 5k^2))/3$

Two Adjacent Outlying or Missing Points

$$C_{2,k,i,2} = \begin{cases} C_{2,-m,i,1} & k = -m \\ 0 & -m < k \leq m,\ i = k,\ k - 1 \\ \dfrac{n_1 + n_2i + n_3i^2}{\text{NORM}} & -m < k \leq m,\ i \neq k,\ k - 1 \\ C_{2,m,i,1} & k = m + 1 \end{cases}$$

$n_1 = (m - 1)m(m + 1)(2m + 1)(6m^4 + 21m^3 + 31m^2 + 22m + 12) + 18km(m + 1)(2m + 1)(m^2 + m + 3) - 3k^2(12m^5 + 30m^4 + 80m^3 + 90m^2 + 28m - 15) - 15k^3(k - 2)(2m - 1)(2m^2 + 4m + 3)$

$n_2 = -9(m - 1)m(m + 1)(m + 2)(2m + 1) + 3k(12m^5 + 30m^4 - 10m^3 - 45m^2 - 17m - 15) - 15k^2(2k - 3)(2m^3 + 3m^2 + m + 3)$

$n_3 = -5(m - 1)m(m + 1)(2m + 1)(2m^2 + 5m + 6) + 15k(k - 1)(8m^3 + 12m^2 + 4m + 3)$

NORM $= [2(m - 1)^2m^2(m + 1)(4m^2 + 13m + 12) - 36k(m - 1)m(m + 1)(m + 3) + 9k^2(4m^4 + 12m^3 - 14m^2 - 32m - 15) - 45k^3(k - 2)(2m^2 + 4m + 3)](2m - 1)(2m + 1)/3$

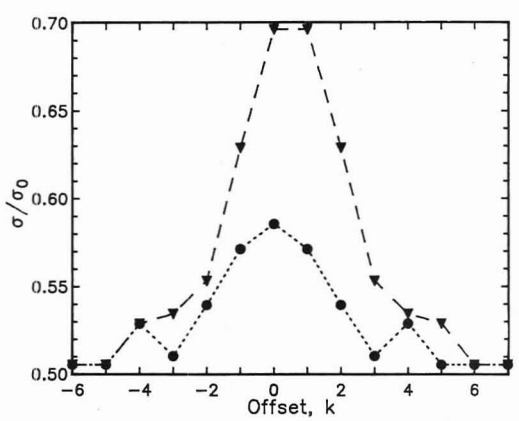

Figure 1. Standard deviation of smoothed data relative to raw data. k points away from missing observation(s). The missing-point (quadratic, 9-point) filter is applied to the data having one outlier (circles) and two adjacent outliers (triangles).

The theoretical predictions of the statistical performance of missing-point filters are encouraging. To test their application on laboratory data, a Raman spectrum of 0.4 mM ferriprotoporphyrin chloride (hemin) in aqueous buffer at pH 7 is collected over a 20-s observation time with a CDD detector; the results are shown in Figure 2. The spikes in the spectrum are typical of cosmic ray events. They carry significant charge (10^3–10^4 photoelectrons) and occupy only one or two pixels, and their probability of appearance and location in the spectrum are random. Outliers occupying two adjacent pixels are less common for cosmic ray events in CCD detectors but can occasionally arise from "blooming", in which on pixel in

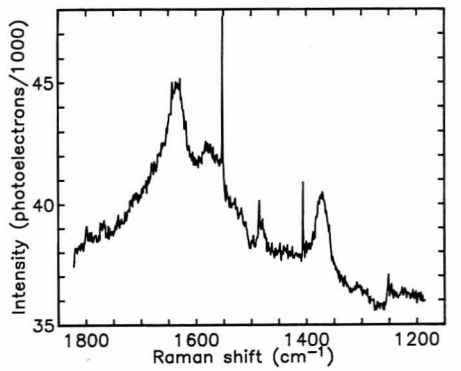

Figure 2. CCD-detected Raman spectrum of 0.4 mM ferriprotoporphyrin (hemin) chloride in aqueous buffer, pH 7.

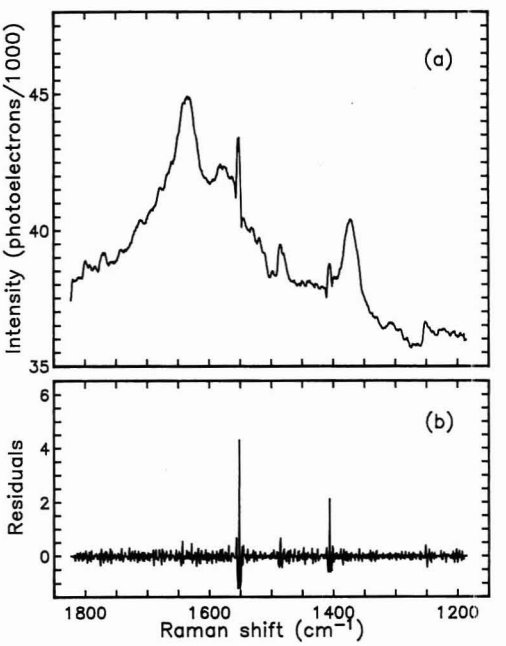

Figure 3. Nine-point quadratic Savitzky–Golay filter (*1*) applied to Figure 2: (a) smoothed spectrum; (b) residual differences between the original and smoothed spectra.

the CCD is saturated and charge leaks to an adjacent pixel. Spikes occupying more than one channel are more common for other sources of outliers in laser spectroscopy, such as particles in solution drifting through the observation volume.

A 9-point smooth of the data using an ordinary, Savitzky–Golay quadratic filter is shown in Figure 3a. In the regions where there are no outliers, the variation in signal intensity over any 9-point data segment is <5%; this indicates that the variance of the photon shot noise is locally constant, which validates the statistical assumptions underlying the least-squares derivation of these filters. In regions of the raw data where there are cosmic ray events, the enormous charge density in one or two channels has an overwhelming influence within the interval of the filter width around the spikes, which distorts the smoothed spectrum. Figure 3b shows the residual differences between the original and smoothed spectra. The peak magnitude of the spike has been reduced by filtering; however, points on each side of the spike have been elevated to much higher intensities (negative residuals), beyond which distortion is to lower intensity, since the convoluting coefficients (*1*) change sign at the edge of the filter.

The filtered spectra and residuals from the missing-point (9-point, quadratic) filter described above are shown in parts a and b of Figure 4, respectively. From a value of $c = 3.5$ in the outlier detection step, six pixels out of 568 filtered points in the spectrum were flagged as outliers; four of these outliers were isolated pixels, and one spike comprised two adjacent

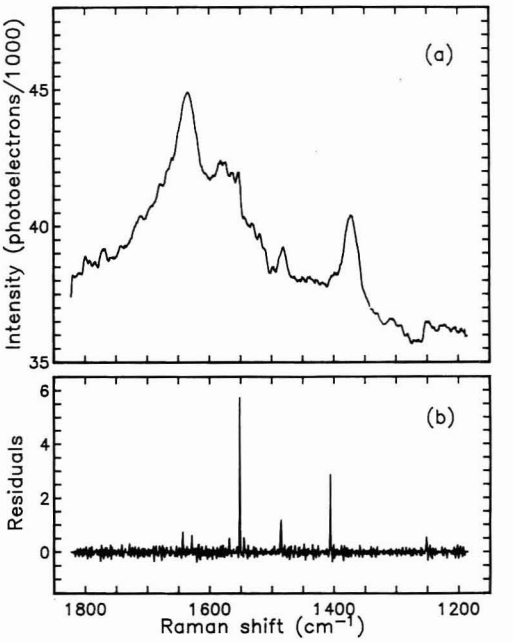

Figure 4. Missing-point (quadratic, 9-point) filter applied to Figure 2: (a) smoothed spectrum; (b) residual differences between the original and smoothed spectra.

pixels. For normally distributed errors with no outliers, 0.02% of the residuals will be larger than the cutoff value of 3.5 times the standard deviation (*21*); thus, there is a small (11%) chance that one pixel out of 568 will be flagged as an outlier even when no cosmic ray events are in the spectrum. The penalty for treating such a point as an outlier is not excessive, however, since the single missing-point filter increases the standard deviation of filtering by less than 20% (see Figure 1). Points beyond the immediate vicinity (±4 points) of outliers are smoothed by using an ordinary 9-point Savitzky–Golay quadratic filter (which is accomplished during the outlier detection step). The missing-point filtering step does not affect these results, so that smoothed spectrum and residuals in these regions of the data are identical with the results in Figure 3. In the region of a spike or outlier, however, the missing-point filter elminates the outlier with no distortion of adjacent data (compare residuals in Figures 3b and 4b).

Confidence intervals can easily be constructed around the smoothed spectra by using the variance–covariance matrix, $\mathbf{V} = \sigma_0^2(\mathbf{X}^t\mathbf{X})^{-1}$. Symmetric confidence limits for the smoothed curve are $\pm[t(\alpha/2,\nu)\sqrt{\mathbf{V}(1,1)}]$, where α is the probabilty of a type I error and ν equals the number of degrees of freedom in the estimate of σ_0. For the Raman spectra in Figure 3a, the standard deviation of the raw data is $\sigma_0 = 126$ photoelectrons, estimated from the innerquartile range (*16*) over the entire 568-point spectrum, and the square root of the 1,1 elements of $\mathbf{X}^t\mathbf{X}^{-1}$ are shown in Figure 1. For a 95% confidence level where $\alpha = 0.05$, $\nu = (568)(0.368) = 209$ (*16*), and $t(0.025,209) = 1.97$, the confidence interval is ±145 around a single missing point and ±173 about two adjacent missing points, compared with ±126 in the absence of outliers. This variation is very small compared to the magnitude of the signal (35 000–45 000 photoelectrons); a visual examination of a plot of the upper and lower confidence bands does not reveal the location of the missing points after smoothing.

Nonlinear smoothing algorithms have previously been used to address the problem of outliers in spectra. Hillig and Morris (*13*) have approximated each point in the spectrum by using a cubic spline in a local region around, but not including, that point. If the derivation between the observed and predicted observation is greater in magnitude than a predetermined limit, the observed point is replaced by a point closer to the spline approximation. The cutoff limit and the relative change

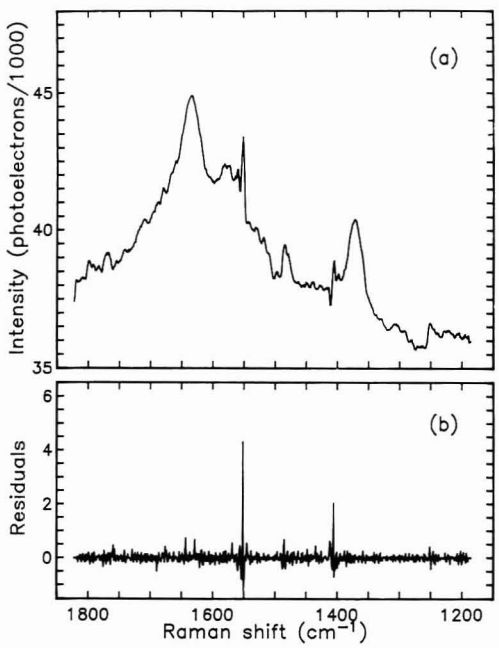

Figure 5. Hillig and Morris 9-point robust filter (*13*) applied to Figure 2: (a) smoothed spectrum; (b) residual differences between the original and smoothed spectra.

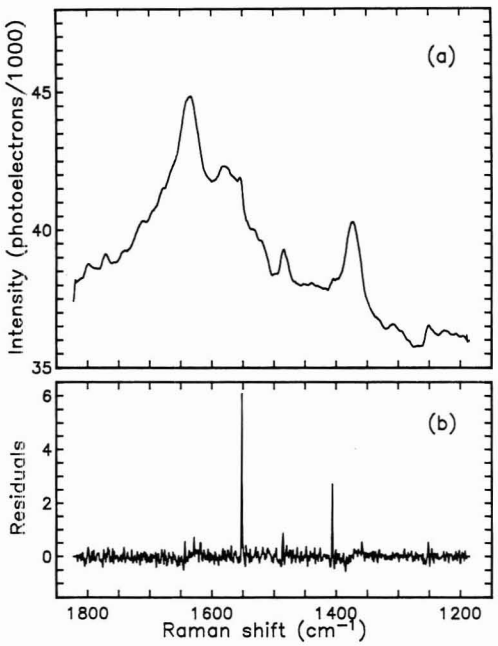

Figure 6. Bussian and Härdle robust smooth using a 9-point kernel filter (*14*) applied to Figure 2: (a) smoothed spectrum; (b) residual differences between the original and smoothed spectra.

are user-supplied parameters. After a complete pass along the spectrum, the procedure is repeated until all points are brought within the specified error limit. A final smooth is made with a Savitzky–Golay filter.

Bussian and Härdle (*14*) have proposed a robust version of a kernel smoother for this problem. The robust estimates of the intensity $\hat{y}_n$ is obtained by solving the following equation

$$\sum_{j=-m}^{m} [c_j \psi(y_{n+j} - \hat{y}_n)] = 0 \qquad (8)$$

where c_j is a weighing coefficient and ψ is a robust influence function. The robust function used was Huber's function, and the window was a quadratic kernel smoother. An iterative Newton–Raphson algorithm solves the implicit eq 8. Tuning is accomplished by adjusting the width of the window and the cutoff point of the ψ function according to the S/N ratio of the spectrum. Bussian and Härdle tested this method (*14*) on a data set from the literature (*13*); Peck and Morris subsequently used the technique to smooth data from a thermal lens experiment (*22*).

These methods share two drawbacks. First, both are nonlinear procedures, requiring that filter coefficients be calculated for each data window. Second, smoothing parameters must be supplied subjectively by the experimenter and must be changed to optimize the filters as noise levels change. The performance of these nonlinear smoothing procedures was evaluated on the CCD Raman data of Figure 2, to compare against the missing-point quadratic filter. Figure 5a is the spectrum smoothed by the procedure of Hillig and Morris; both the spectrum and the residuals in Figure 5b show distortion in points adjacent to the spikes. A robust smooth of the spectrum using the algorithm of Bussian and Härdle is plotted in Figure 6. This smooth eliminates the spikes with little influence on surrounding points; however there is a suggestion of bandwidth reduction relative to Figure 3. The window function, rather than the smoothing procedure appears to account for this behavior. For comparison, when Bussian and Härdle's method is applied with coefficients from a quadratic Savitzky–Golay filter, the bandwidth remains high. The execution time for this smoothing combination remains significantly longer, however, than for the missing-point filter.

Execution times for all four smoothing techniques are listed in Table IV. The cubic splines were computed by using the efficient subroutine, QINTERP from the GRAFMATIC library; the

Table IV. Execution Times for 9-Point Smooth

method	t, s	method	t, s
Savitzky–Golay (*1*)	0.4	Hillig–Morris (*13*)	18.3
missing-point	0.9	Bussian–Härdle (*14*)	4.3

subroutine published by Bussian and Härdle was used to determine the zero of a function. Execution times for the nonlinear smoothing methods are sensitive to the values of the user-supplied parameters. Efforts were made to choose optimal parameter values, small deviations from which did not greatly affect excution time. Clearly, both nonlinear smoothers require longer calculations, and neither is superior in performance to the simple missing-point quadratic filter.

The linear missing-point filter presented here allows a small number of outliers to be present in a spectrum without affecting the quality of the smoothed result. The procedure is designed to detect and reject outlying points when they occur. The filters are easily designed and implemented, and they retain the powerful statistical properties of least-squares polynomial filters. The application to CCD-detected Raman spectra has emphasized their usefulness in smoothing data-containing outliers. They should be equally valuable in bridging small gaps in data records where observations are lost or missing.

ACKNOWLEDGMENT

We thank K. L. Rowlen for acquiring the Raman data.

LITERATURE CITED

(1) Savitzky, A.; Golay, M. J. E. *Anal. Chem.* **1964**, *36*, 1627.
(2) Enke, C. G.; Nieman, T. A. *Anal. Chem.* **1976**, *48*, 705A.
(3) Steiner, J.; Termonia, Y.; Deltour, J. *Anal. Chem.* **1972**, *44*, 1906.
(4) Madden, H. M. *Anal. Chem.* **1978**, *50*, 1383.
(5) Edwards, T. R. *Anal. Chem.* **1982**, *54*, 1519.
(6) Murray, C. A.; Dierker, S. B. *J. Opt. Soc. Am. A* **1986**, *3*, 2151.
(7) Dierker, S. B.; Murray, C. A.; Legrange, J. D.; Schlotter, N. E. *Chem. Phys. Lett.* **1987**, *137*, 453.
(8) Harris, T. D.; Lamont, M. G.; Seibles, L. *Mat. Res. Soc. Symp. Proc.* **1987**, *104*, 479.
(9) Harris, T. D.; Lamont Schnoes, M.; Seibles, L. *Anal. Chem.* **1989**, *61*, 994.
(10) Bilhorn, R. B.; Epperson, P. M.; Sweedler, J. V.; Denton, M. B. *Appl. Spectrosc.* **1987**, *41*, 1114, 1125.
(11) Sweedler, J. V.; Bilhorn, R. B.; Epperson, P. M.; Sims, G. R.; Denton, M. B. *Anal. Chem.* **1989**, *60*, 282A.
(12) Eccles, M. J.; Sin, M. E.; Tritton, K. P. *Low Light Level Detectors in Astronomy*; Cambridge University Press: Cambridge, U.K., 1983; Chapter 8.
(13) Hillig, K. J. D.; Morris, M. D. *Appl. Spectrosc.* **1982**, *36*, 700.

(14) Bussian, B. M.; Gasser, T. J. R. Statist. Soc., Ser. B 1980, 46, 42.
(15) Simpson, S. F.; Harris, J. M. J. Phys. Chem., 1990, 94, 4649.
(16) Fenstat, G. U.; Kjaernes, M.; Walloe, L. J. J. Statist. Comput. Simul. 1980, 10, 113.
(17) Leach, R. A.; Carter, C. A.; Harris, J. M. Anal. Chem. 1984, 56, 2304.
(18) Bialkowski, S. E. Anal. Chem. 1989, 61, 1308.
(19) Phillips, G. R.; Harris, J. M. Unpublished work.
(20) Deming, S. N.; Morgan, S. L. Clin. Chem. 1979, 25, 840.
(21) Draper, N. R.; Smith, H. Applied Regression Analysis, 2nd ed.; John Wiley & Sons: New York, 1981; Chapter 2.
(22) Peck, K.; Morris, M. D. Anal. Chem. 1986, 58, 2876.

RECEIVED for review March 21, 1990. Accepted July 27, 1990. This research was supported in part by the National Science Foundation under Grants CHE85-06667 and CHE90-10319.

Chemiresistor Gas Sensors Based on Photoconductivity Changes in Phthalocyanine Thin Films: Enhancement of Response toward Ammonia by Photoelectrochemical Deposition with Metal Modifiers

Rossella Brina, Greg E. Collins, Paul A. Lee, and Neal R. Armstrong*

Department of Chemistry, The University of Arizona, Tucson, Arizona 85721

Determination of NH_3 in flowing N_2 or air is demonstrated by monitoring changes in the photoconductivity of chloroindium phthalocyanine (InPc-Cl) and chlorogallium phthalocyanine (GaPc-Cl) thin films vacuum deposited on platinum silicide interdigitated array microcircuits. Photoconductivity changes were measured, as opposed to the more commonly measured dark conductivity changes, yielding reasonable sensitivity to the adsorption of submonolayer amounts of gas analytes such as NH_3. Photoelectrochemical modification of Pc-coated microcircuits was carried out in order to obtain submonolayer coverages of a variety of different metals (Ag, Au, Cu, Pt, and Hg) on the Pc film. This modification apparently provides new chemisorption sites for NH_3, thus improving the performance of these microcircuit assemblies as NH_3 sensors in N_2 and in air. The Hg-modified microcircuits demonstrated a superior performance compared to the microcircuits modified with other metals, by showing a linear photocurrent response as a function of NH_3 concentration in N_2 at room temperature over the range from ca. 1.5 to 5.4 ppm, and a logarithmic relationship above that level (up to ca. 84 ppm). Photoconductivity measurements in NH_3–air mixtures were carried out on microcircuit assemblies "as-prepared" and after photoelectrochemical modification. The presence of the metal modifier on the InPc-Cl film markedly improves the assembly performance in air, providing a detection limit for NH_3 in air of ca. 1.0 part per thousand (ppt). The effect on the photoconductivity of O_2 and other impurities present in GaPc-Cl and InPc-Cl is discussed, and a mechanism is proposed to explain the variations observed in the photocurrent response to NH_3 in these assemblies before and after modification.

INTRODUCTION

The electrical properties of many organic thin films are significantly affected by the incorporation or chemisorption of electron-accepting or electron-donating molecules (*1–8*). Among molecular materials manifesting sensitivity to added impurities, phthalocyanine (Pc) thin films are particularly interesting because of their chemical and thermal stability, ease of preparation and compatibility with vacuum deposition, and their light absorbing properties in the visible and near-infrared region (*9*). Photoelectrochemical studies performed on thin films of trivalent and tetravalent metal Pc's (*10–13*) have demonstrated that these materials can have reasonable energy conversion efficiencies (*14, 15*) and that the contrast between dark conductivity (σ_{dk}) and photoconductivity (σ_{ph}) is higher in these films (as much as 1000:1) (*10–18*) than in the more commonly studied divalent metal Pc's (2:1 at most). The effect of added or adventitious impurities on these electrical properties has been noted, and particularly, the open-circuit photovoltages appeared to be affected by impurities collected at an interface with the organic material (*8, 11, 19*). This sensitivity to adsorbed impurities is an important factor in the use of these materials as gas-phase chemical sensors (chemiresistors, surface acoustic wave microgravimetric devices, etc.) (*20–26*).

In chemiresistor applications of Pc thin films, the role of O_2 as an impurity already present in the film, or as a component of the gaseous mixture to be analyzed, is extremely important (*12, 19, 23, 27–31*). As a weak electron acceptor, O_2 at low concentrations appears to increase the dark conductivity by providing low concentrations of $Pc^{+\bullet}$ and $O_2^{-\bullet}$. Additionally, it may also bind (coordinate) to transition-metal impurities within the thin film (e.g. FePc, a ubiquitous impurity in all Pc thin films) which have a particular affinity for O_2. The resulting O_2 impurity complex may have a greater electron affinity and, therefore, may act as an energetically deep trap for photogenerated electrons. At much higher concentrations of O_2 (atmospheric conditions), the creation of $O_2^{-\bullet}$ and host $Pc^{+\bullet}$ states as sites of fixed charge appears to increase photoconductivity by facilitating exciton dissociation (*32*).

In the case of NH_3 (a weak donor), there is interest in understanding how O_2 affects the chemisorption of NH_3 and in determining the detection limit for NH_3 in N_2 and in air using the response of a Pc chemiresistor. Previous experiments performed in this laboratory (*33, 34*) have shown that NH_3 and O_2 may be in competition for at least one chemi-

* To whom correspondence should be addressed.

0003-2700/90/0362-2357$02.50/0 © 1990 American Chemical Society

sorption site at the surface of InPc-Cl and GaPc-Cl thin films but that only one of the NH_3 chemisorption sites affects σ_{ph}.

Most of the literature available on chemiresistor gas sensors focuses on the changes in σ_{dk} caused by the adsorption of the analyte gas on the film, and generally on sensors with much larger active areas than those discussed here (*24–28*, *35*, *36*). The responses appear to depend on several parameters, such as the relative electron affinity of the gas (donor or acceptor), the particular Pc chosen, the purification and preparation techniques used for the Pc, the nature and purity of the substrate, and the interferences produced by other molecules. We have explored an alternative detection mode which consists of measuring photoconductivity instead of dark conductivity changes with analyte adsorption. Photocurrent generation is primarily a near-surface phenomenon in these materials, and an amplification of the response to analyte adsorption may be expected when compared to the dark current case. This can be attributed to the higher concentration of charge carriers (photogenerated in the near surface region) whose effective concentration and collection probabilities are affected by chemisorbed species. Since the sensitivity of chemiresistor gas sensors scales with the active electrode area, higher sensitivities to molecules such as NH_3 are seen with microcircuit assemblies larger than those reported in these studies. The use of photoconductive modes of detection may provide a means of enhancing sensitivity on smaller devices.

The presence of small amounts of impurities (*6*, *24–28*, *32*, *37*) in these Pc thin films is critical in determining their photoresponse in the presence of chemisorbed species. Highly purified phthalocyanines still contain impurities such as Fe, Cu, and Ni at the parts-per-million level, which are capable of affecting the photoconductivity. The introduction of additional "impurity sites" by photoelectrochemical deposition of submonolayer coverages of a metal (Ag, Au, Cu, Pt, Hg), onto the Pc surface, is effective in promoting the chemiresistor sensitivity to NH_3, through the apparent creation of new chemisorption sites. The amplified response to NH_3 appears to be the result of detrapping photogenerated electrons in the near-surface region through the metal adatom sites, because of the σ-donor character of NH_3. The weakness of the interaction of NH_3 with Pc surfaces, in the presence of O_2, has previously required operating chemiresistor NH_3 sensors at elevated temperatures (*22*, *30*, *36*). In the studies discussed here, even in the presence of O_2, NH_3 appears to be preferentially adsorbed on the metal adatom centers, thus improving the response of these assemblies in air at room temperature.

EXPERIMENTAL SECTION

Chloroindium and chlorogallium phthalocyanines were synthesized from $InCl_3$ or $GaCl_3$ and *o*-phthalonitrile, according to the procedure described in refs 38 and 39. The Pc products of the reaction were Soxhlet extracted for 48 h using absolute ethanol. The solid was dried in air and then washed with 1% ammonium hydroxide, 1.5% hydrochloric acid, and triply distilled water. The final products were purified by entrainer sublimation in a flowing stream of ultrahigh-purity argon.

Analysis of the InPc-Cl sample by means of X-ray fluorescence was performed in order to establish the nature of the impurity sites that may act as electron traps. The InPc-Cl contained impurities of copper (ca. 100 ppm), iron (ca. 10–50 ppm), and chromium and nickel (below 10 ppm).

The microcircuits (MC) used as substrates for the InPc-Cl thin films for these and previous experiments were provided by Burr-Brown (Tucson, AZ) or by Motorola (Phoenix, AZ). The MC provided by Burr-Brown consisted of two interdigitated electrode arrays, each with ca. 400 platinum silicide ($PtSi_x$) fingers 100 nm high, 4 or 6 μm wide, and with a finger center-to-finger center separation of either 4 or 6 μm. The other form of MC used had 59 Au fingers (100 nm high), spaced at 3 μm. The active length of the $PtSi_x$ interdigitated array was 3 mm, giving a geometric active area of 0.09 cm^2. The effective active area of the $PtSi_x$ array was calculated as the product of the perimeter length around each of the array fingers and the height of each finger, giving $A_{eff} = 3.9 \times 10^{-4}$ cm^2 for the 6 μm wide MC and $A_{eff} = 5.9 \times 10^{-4}$ cm^2 for the 4 μm wide MC, which are small areas relative to most previously reported systems (*19–21*, *36*, *37*). All results reported in this article were obtained by using the 6 μm wide microcircuits from Burr-Brown at a finger-to-finger bias potential of 2.0 V with a Pc film thickness of 40 nm; these parameters give a geometrical factor of 0.77 $(V \cdot cm)^{-1}$ for converting the photocurrent into conductivity. The interdigitated Au mcirocircuits were used in previously reported studies (*33*) and produced equivalent responses to those shown here. The Au microcircuits continue to be the principal circuit used in our ultrahigh-vacuum mechanistic studies (*34*, *40*). Microcircuits were cleaned in a radio frequency plasma chamber (Harrick Scientific, ca. 10^{-3} Torr in air) to remove traces of hydrocarbons present on the as-received microcircuit (*33*). Immediately after plasma cleaning, the MC was introduced inside the high-vacuum Pc deposition chamber (base pressure ca. 10^{-8} Torr), where deposition of the Pc onto the MC occurred. A schematic diagram of the vacuum chamber used has been described elsewhere (*8*). The deposition chamber uses a system of effusion sources and shutter assemblies to direct a beam of the molecular material at the substrate located ca. 10 cm above the aperture at the top of the effusion sources. Inside the chamber, the MC was held at a temperature of 95 °C during pump down and during deposition of the Pc thin film, to prevent condensation of impurities on the MC. A quartz crystal microbalance (QCM) was also simultaneously coated with Pc, thus enabling the Pc surface coverage to be estimated. By use of the same deposition chamber, several additional microbalances were coated on both surfaces with Pc films whose thicknesses were comparable to those of the MC, in order to later perform microgravimetric measurements simultaneously with the chemiresistor gas-sensing experiments, once inside the sensing cell (described below). Deposition rates from two to four equivalent Pc monolayers per minute were used for coating both the QCM and MC. The MC was transferred directly from the deposition chamber to the atmospheric-pressure-sensing cell.

The gas-sensing cell was configured from a UHV 2.75-in. conflat flange and nipple assembly. It incorporated entrance and exit ports for the gases and a wide-angle quartz window for illumination of the MC. The cell was fabricated from stainless steel, with the exception of the TO-99 socket (Bakelite) where the MC was mounted. (Later versions of this cell have dispensed with the TO-99 socket in order to facilitate higher temperature experiments.) The temperature inside the cell was monitored with a thermocouple in close proximity to the MC and to the housing for the QCM. The inner volume of the cell was ca. 100 cm^3.

Photocurrent yield spectra were obtained by illuminating the MC with a 600-W tungsten–halogen lamp (Sylvania) monochromatized with a Jobin-Yvon H-20 or with a H-10IR holographic grating monochromator. The photon output of the monochromator was normalized with a calibrated thermopile to correct the photocurrent spectra for lamp fluctuations. A 10-mW He–Ne laser (Hughes) was used as the light source in most of the gas-sensing experiments. The laser was kept defocused, so that the entire MC was illuminated. The dark and photocurrents were measured with a Keithley 485 picoammeter placed in series with the potentiostat and the gas-sensing cell. A Model 362 scanning potentiostat (EG&G Princeton Applied Research) was used to control the potential drop between the interdigitated electrode arrays. Unless otherwise stated, a difference in potential of 2.0 V was maintained between the electrode arrays. In later experiments, the He–Ne laser was replaced by the tungsten light source in order to maximize the polychromatic photon flux to the sensor surface, and to evaluate the response to a more practical light source. In these experiments, the full output of the lamp was directed through an IR filter and modulated at 10 Hz with a chopper. Because the photocurrents generated were now much larger, the modulated MC response was monitored directly with the current-to-voltage convertor of the potentiostat. The output was then demodulated with a lock-in-amplifier (EG&G 5209).

The composition of the gas flowing through the sensing cell was controlled by adjusting the flow rates of the analyte gas (NH_3) in the presence of a predetermined flow rate of the carrier gas

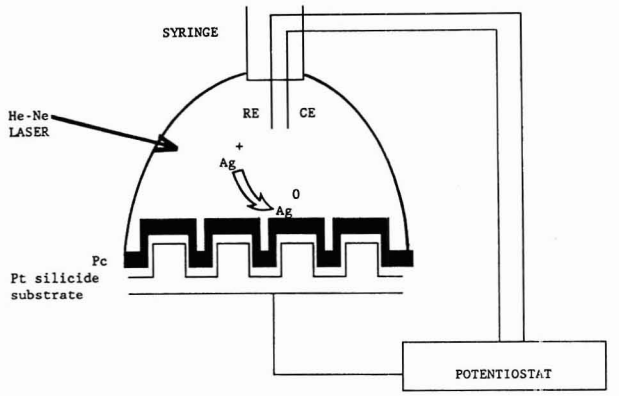

Figure 1. Schematic of the experimental arrangement used for the photoelectrochemical modification of the Pc-coated microcircuit: RE, reference electrode; CE, counter electrode.

(nitrogen or air). The gases used were Matheson 99.99% purity N_2, 99.99% purity anhydrous NH_3, 1023 and 59 ppm NH_3 in N_2, and dry air. The nitrogen was passed over copper turnings and molecular sieves before introduction into the gas-sensing cell. The air and NH_3 were passed over molecular sieves. The analyte and the carrier gas were mixed thoroughly in a coil before the mixture entered the sensing cell to avoid any inhomogeneity effects.

Each MC was heated overnight in a nitrogen atmosphere at 90 °C when first positioned inside the sensing cell and after the completion of each set of gas-sensing experiments. This treatment was adopted since it restored the initial properties of the microcircuit/Pc assembly (e.g. a large photo-to-dark current ratio with an extremely low dark current level). The photoresponse in N_2, air or NH_3 was recorded with a Omniscribe D5000 strip chart recorder (Houston Instrument). After each addition of the analyte gas, the photoresponse was monitored for 10 min.

The photoelectrochemical modification of Pc-coated microciruits has been previously described (*13*, *33*); these experiments were carried out with aqueous solutions of nitrate or chloride salts of various metals (Ag, Au, Pt, Cu, Hg) at concentrations between 10^{-4} and 10^{-6} M. All the solutions were prepared with triply distilled water, and they were degassed with nitrogen before the electrochemical experiment. Supporting electrolyte was purposely omitted in the preparation of these solutions, in order to prevent the deposition of these salts on the Pc surface. Figure 1 shows schematically the experimental configuration used in all of the photoelectrochemical modifications. A small drop (1 μL) of the electrolyte solution was positioned on the microcircuit surface by means of a silver-plated syringe. The syringe acted as the reference electrode (RE), while a platinum wire mounted on the same syringe served as the counter electrode (CE). The syringe and the MC were located inside a chamber that also served as a Faraday cage to reduce electrical noise. The chamber was filled with nitrogen saturated with triply distilled water, to avoid rapid evaporation of the solution drop. A window on the upper part of the cell was used to illuminate the MC/solution drop system with a 5-mW He–Ne laser, which was kept defocused as described earlier. Both sets of grids in the interdigitated arrays were used as the working electrode, which was held at a potential where the reduction of the metal ion in the solution occurred photoelectrochemically, but where reduction in the dark was not significant (the photoelectrochemical properties of these Pc thin films makes this possible) (*13*, *33*). The electrolysis was continued until the metal ion had been exhaustively reduced (coverages corresponding to 0.5 to 1.0 equivalent monolayer were deposited). The MC was then washed extensively with triply distilled water to eliminate any excess electrolyte and heated overnight in N_2 at 90 °C to facilitate evaporation of the solvent and return of the electrical properties to values near those recorded before the photoelectrochemical modification. The experimental arrangement described in Figure 1 was also used for the photoelectrochemical modification carried out on the QCM coated with Pc, using the same metals and under the same conditions employed for the modification of the corresponding MC assembly. In this manner, each set of MC assemblies had a corresponding QCM coated with Pc and then modified electrochemically.

RESULTS AND DISCUSSION

Photoconduction Mechanism. Previous studies involving the exposure of GaPc-Cl/MC assemblies to NH_3 in N_2 at the part-per-thousand level showed that the chemisorption of NH_3 proceeded through at least two different chemisorption sites, with only one site affecting σ_{ph} (*33*). Lower concentrations of NH_3 in N_2 were difficult to detect, and an even poorer sensitivity was observed for NH_3 in air. The competition with O_2 for producing changes in photoconductivity was also noted, although the reasons for this behavior were not clear. Recently, the investigation of the interaction of GaPc-Cl thin films with O_2, NH_3, NO_2, TCNQ, etc., starting with films grown under ultrahigh-vacuum (UHV) environments, has elucidated some of the mechanisms that determine the influence of these dopant molecules on the electrical properties of these thin films (*40*). Starting with Pc thin films prepared under UHV conditions, O_2 interacts with the Pc in two distinct steps. At O_2 pressures of ca. 10^{-5} Torr, and exposure levels below 10^3 langmuirs, σ_{ph} is reduced by ca. 30%, apparently because of the formation of O_2·Pc complexes, acting as electron traps, arising from FePc and CuPc impurities present in these films at 10–100 ppm levels (*31*). At O_2 pressures above 10^{-5} Torr, and exposure times as long as several hours, σ_{ph} is restored to its initial UHV level and then steadily increases to several times its initial value. The origin of this effect appears to be the photoassisted formation of $O_2^{-\bullet}$ and $Pc^{+\bullet}$ through

$$Pc + h\nu \rightleftarrows Pc^* \quad (1)$$

$$Pc^* + O_2 \rightleftarrows Pc^{+\bullet} + O_2^{-\bullet} \quad (2)$$

This type of photoassisted charge transfer has been previously observed for O_2 complexes and for complexes with other weak electron acceptors (*9*). The formation of $O_2^{-\bullet}$ and $Pc^{+\bullet}$ increases the dark and photoconductivity in the near surface region in a reversible fashion; i.e., the σ_{dk} and σ_{ph} values can be restored to near their original levels by pumping back to UHV.

The interaction of NH_3 with the UHV-prepared MC assembly initially shows a decrease in σ_{ph} and σ_{dk} (at partial pressures below 10^{-5} Torr). This initial decrease is likely due to the compensation of some of the charged species indicated in the reactions above and may be the origin of conductivity decreases seen for NH_3 adsorption on thin film Pc's in the past. These conductivity decreases have been used as the analytical response for chemiresistor NH_3 sensors (*20*, *27*). Higher subsequent exposures of NH_3 cause a steady increase in σ_{ph} (see also next section, Figure 3A and Table I). At least part of the increase in current may be related to the formation of the complex NH_3·MPc (M = Fe, Cu) through the reaction

$$(MPc)^{-\bullet} + NH_3 \rightleftarrows (NH_3{\cdot}MPc) + e^- \quad (3)$$

which displaces electrons bound in trap sites arising from the transition-metal Pc's. These reactions only occur at pressures of NH_3 that may be analytically uninteresting and do not cause detectable changes in σ_{ph} in the presence of O_2 concentrations like those seen in air.

For inorganic and organic photoconductors the photocurrent yield (i_{ph}) has been reported to vary with the light intensity (I_0) according to (*41*)

$$i_{ph} = KI_0^{\alpha} \quad (4)$$

where K is a constant determined by the quantum efficiencies for the absorption of the photon and α is determined by the efficiencies of radiative and nonradiative energy transfer back to the ground state and by the inefficiencies in collection of mobile electrons and holes. Values of α from ca. 0.2 to 1.0 (or larger) have been reported for various Pc thin films (*42*, *43*). For the InPc-Cl and GaPc-Cl thin films studied here, the value of the exponent (α) varied between 0.61 and 0.74

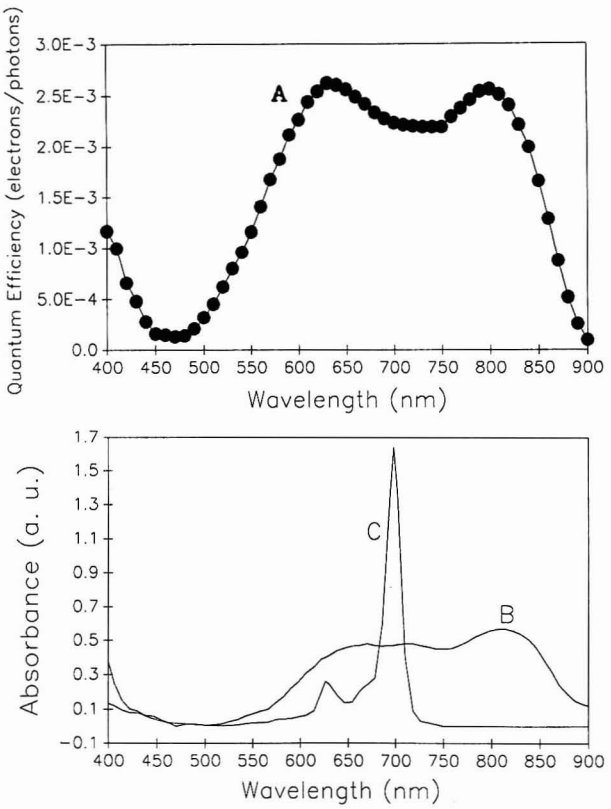

Figure 2. (a) Photocurrent yield spectrum of a InPc-Cl coated MC (40 nm) in atmospheric pressure N_2 at room temperature: bias potential, 4.0 V. (b) Absorbance spectrum of a 50-nm InPc-Cl film vacuum deposited on Au-MPOTE. (c) Absorbance spectrum of a 2×10^{-5} M InPc-Cl solution in chloronaphthalene.

at room temperature in N_2 in the spectral range from 500 to 900 nm, when measured at successive 25-nm intervals. These values of α were then used to correct the photoaction spectra by multiplying the photocurrent by a normalized photon flux (as determined from a calibrated thermopile) which includes the wavelength-dependent intensity exponent, α, as per eq 4.

We have recently shown (*40*) that by considering the molecular aspects of photoconduction in these Pc thin films, a more exact expression for photocurrent generation in these assemblies can be written

$$i_{ph} = kI_0(1 - e^{-\beta x})\phi_{ct}\phi_{diss}\phi_{coll} \quad (5)$$

where I_0 is the photon flux, β is the solid-state absorptivity, which is ca. 2×10^4 cm^{-1} at 632.8 nm for these Pc films, x is the depth to which photon absorption occurs and is the film thickness in this case, ϕ_{ct} represents the probability of creating a charge transfer state in the Pc matrix that can lead to generation of mobile charges, ϕ_{diss} is the probability of dissociating the charge transfer state into mobile charges and is strongly affected by the applied electric field as well as local fields created in the vicinity (less than 2–3 nm) of sites of fixed charge (e.g. $O_2^{-\bullet}$), and ϕ_{coll} represents the probability of collecting mobile charges, is electric field dependent, and is also strongly dependent on trap concentrations and trapping probability (controlled by donors such as NH_3 bound at, or adjacent to, the trap site) (*34*). It is the variation of ϕ_{coll} that is most strongly affected by the chemisorption of an analyte such as NH_3, especially in the presence of a metal surface modifier. The fact that one chemisorption event can result in the detrapping of multiple photogenerated electrons may lead to considerable "amplification" of the response to the analytically important event.

Microcircuit Assembly Characterization in Atmospheric Pressure Nitrogen. All the measurements presented in this section were performed by using 40 nm thick InPc-Cl films (results for the GaPc-Cl films have been described elsewhere) (*33*), in atmospheric pressure N_2. Figure 2A shows a typical photocurrent yield spectrum (electrons produced per *incident* photon), which is in qualitative agreement with the absorbance spectrum of a thin film of similar thickness (50 nm) vacuum deposited on a semitransparent substrate, as shown in Figure 2B. The Q-band absorbance region is broadened and red shifted in the condensed phase spectra compared to the solution phase spectrum in Figure 2C, which was recorded for a 2×10^{-5} M InPc-Cl solution in chloronaphthalene. The dark current response at room temperature was in the range of 0.1–0.3 pA at 2.0 V, with a ratio between σ_{ph} and σ_{dk} of ca. 10^3 (dependent on the photon flux). The variation of dark or photocurrent with the temperature gives an activation energy for σ_{ph} of 0.23 eV and 1.3 eV for σ_{dk} (*41*). No changes in shape of the photocurrent yield spectra were noted with the introduction of O_2 or NH_3 at any concentration.

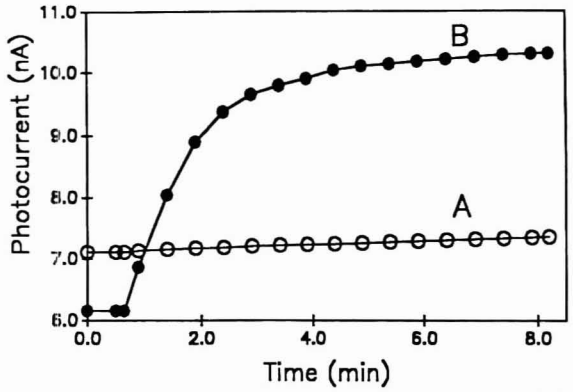

Figure 3. Photocurrent response as a function of time for a InPc-Cl coated MC (40 nm) at room temperature: (a) response to 48 ppm NH_3 in N_2 before electrochemical modification; (b) response to 31 ppm NH_3 in N_2 after electrochemical modification with a submonolayer coverage of Ag. Bias potential was 2.0 V.

Measurements of Sensitivity to NH_3 in N_2 and in Air for Unmodified Microcircuits. In flowing N_2, the initial introduction of NH_3 from UHV conditions always caused a decline in the photoconductivity, presumably because of the interaction of NH_3 with $Pc^{+\bullet}$ sites generated (a) through the reaction of Pc with residual O_2 (eq 2) and/or (b) through the decomposition of the Pc during vacuum deposition. Previous ESR measurements of various sublimed Pc powders have shown persistent signals due to stable radicals (ca. 10^{17} spins per cm^3 are typical). These radicals can be increased in concentration by O_2 treatment and decreased by treatment with reductants like H_2 (*9*, *31*, *42*). The initial response of a Pc/MC assembly to NH_3 in flowing N_2, i.e., the extent of the photocurrent decrease prior to the steady increases seen later (Figure 3A), was variable from circuit to circuit. This suggests that slight differences in film preparation, exposure to atmosphere, and pretreatment in N_2 can produce sizable differences in levels of traps and dopant sites. For these unmodified circuits, pretreatment in N_2 for several hours appears to be essential for establishing the predictable operation of these devices. Figure 3A shows the typical photoresponse obtained for these MC assemblies "as prepared", with 48 ppm NH_3 in N_2 following the initial decline in σ_{ph}. Analogous features were observed in the dark current response. Table I lists the percent changes in photocurrent for several MC assemblies after exposure to NH_3/N_2 mixtures before modification. Although the responses to NH_3 were slightly different for each MC assembly, depending upon the conditions of preparation and history of the film, very small changes in photocurrent were generally observed for the MC "as prepared" following the introduction of NH_3 at this level. Similar results were obtained for the dark current. No sig-

Table I. Percent Changes in the Room Temperature Photocurrent after Exposure of the MC Assemblies to NH_3/N_2 and NH_3/Air Mixtures[a]

$[NH_3]$, ppm	carrier gas	% change i_{ph}[b]	metal modifier
48	N_2	0.9	none
31	N_2	84	Ag
6	N_2	2	none
8.9	N_2	18	Au
9.3	N_2	4	none
6	N_2	13	Cu
8.9	N_2	1	none
8.2	N_2	10	Pt
10.2	N_2	0	none
6	N_2	43	Hg
56000	air	2	none
6000	air	26	Hg

[a] For MC "as prepared" and after photoelectrochemical modification with the specified metal. [b] Each horizontal section in the table refers to the same MC assembly.

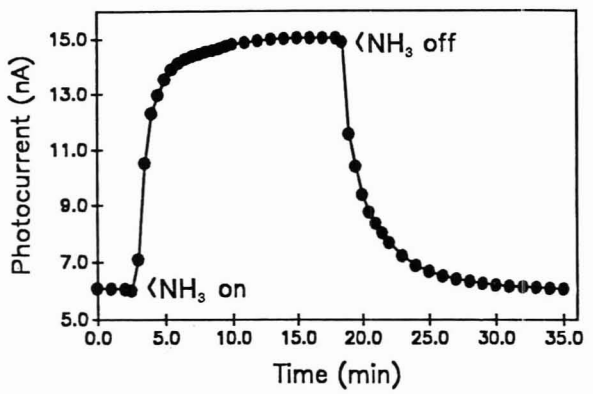

Figure 4. Photocurrent response to 6.5 ppt NH_3 in N_2 for a InPc-Cl coated MC (40 nm), at room temperature: bias potential, 2.0 V.

nificant QCM frequency shifts (less than 1 Hz in 10 MHz) were noted at these NH_3 concentrations, suggesting that the amount of NH_3 chemisorbed on these films corresponds to a fraction of a monolayer (*33*). When the NH_3 concentration reached ca. 4 ppt in N_2, the dark and photocurrents began increasing rapidly (increases of ca. a factor of 20 for the σ_{dk} and a factor of 3 for σ_{ph} in 3 min). This effect appeared to be reversible for both dark and photocurrents once the ammonia flow had been stopped.

Figure 4 shows the typical photocurrent response obtained from the microcircuits described above after introduction of 6.5 ppt of NH_3 in N_2. The response appears to be reversible (over a period of 35–40 min), reproducible, and linear in NH_3 concentration. In the range of NH_3 concentrations tested (4.0–25 ppt), a correlation coefficient of 0.99 and a slope of 1.0×10^{-11} A/ppt were obtained from the plot of the change in photocurrent versus NH_3 concentration. A noise level corresponding to 4 pA was recorded for these MC assemblies. We estimated the detection limit as the concentration of NH_3 needed to produce a change in the photocurrent twice the noise level, yielding a detection limit of ca. 800 ppm for NH_3 in N_2 for these unmodified microcircuit assemblies.

The MC assemblies tested had dark currents of 1–5 pA and photo-to-dark current ratios of 10^3 (using a 10 mW He–Ne laser) before the introduction of NH_3. Following repeated exposure to NH_3 (up to 80 ppt), the ratio of photo-to-dark current showed a decrease to ca. 10^2 in some cases. Overnight heating in N_2 tended to restore the original properties of the MC, although complete regeneration of the initial values never occurred. Repeated exposures to NH_3, followed by overnight heating in N_2 showed a gradual and irreversible deterioration of the response (increase in dark current, decrease in photo-to-dark-current ratio to ca. 10) after several weeks of continuous testing.

The dark current changes were monitored for the microcircuit assemblies described above when the carrier gas in the gas-sensing cell was switched from atmospheric pressure N_2 to dry air. A decrease of more than 60% in dark current was generally observed in the first hour of exposure to air, followed by a gradual increase over the next 12 h. The equilibrium value for the dark current in air was generally close to the equilibrium value in N_2 before exposure to air. After equilibration of the MC assemblies in air in the dark, the light from a 10 mW He–Ne laser was directed onto the MC assembly, and the photocurrent response in air was monitored for several hours. As a result of illumination, the σ_{dk} and σ_{ph} increased rapidly, reaching equilibrium after ca. 24 h. Increases in dark current up to a factor of 100 and increases up to a factor of 10 in photocurrent were observed.

When NH_3 (4 ppm) was first introduced inside the gas-sensing cell, a notable decrease in dark and photocurrent was observed during the first 3 min, then both currents reached constant values again. Further increases in NH_3 concentration caused a similar change in both dark and photocurrent, but on a much smaller scale. This behavior was observed until a concentration of ca. 45 ppt of NH_3 in air was reached, when both the dark and photocurrent start increasing linearly with the NH_3 concentration. On the basis of the definition given previously, and with a noise level of 4 pA, a detection limit of 16 ppt was obtained for NH_3 in air for these MC assemblies. The decrease in dark and photocurrent observed following the introduction of NH_3 (up to ca. 45 ppt) is attributed to the displacement of O_2 adsorbed on the Pc film.

Response to NH_3 in N_2 and in Air after Photoelectrochemical Modification. The interaction of NH_3 with the Pc thin film at room temperature is sufficiently weak that photoelectrochemical modification of the Pc surface was undertaken in order to (a) provide chemisorption sites that were more selective for electron donors such as NH_3 and (b) change the surface chemistry of the Pc film to make it less responsive to weak electron acceptors such as O_2.

The photoelectrochemical modification process itself affects both dark and photocurrent, causing a decrease in σ_{ph} by 20–50% in pure N_2 for all the MC assemblies tested. This decrease in photocurrent could be caused by the destruction, occurring during the electrolytic process, of some of the Pc sites which acted as centers for exciton dissociation (*32*). Some nonreproducible changes in dark current baselines were also observed after the photoelectrochemical modification in the majority of the MC assemblies studied. The changes in dark current are generally more significant compared to changes in photocurrent. These effects were also observed when the blank solution (triply distilled water) was electrolyzed on the MC assembly surface.

Sensitivity to NH_3 in N_2. Figure 3B shows the typical photoresponse obtained at room temperature upon the initial exposure to NH_3 (31 ppm) following electrochemical modification of the MC assembly with the metal salt solution. The change in photocurrent response is compared to the one obtained for the same MC in 48 ppm NH_3 before electrochemical modification, and it is comparable to previous results obtained by using GaPc-Cl thin films (*33*, *34*). The MC assembly in Figure 3b was modified by using a 10^{-5} M $AgNO_3$ solution, but analogous responses were observed for the MC modifications using Au, Pt, Cu, and Hg solutions at 10^{-6} M concentrations. Surface coverages of the various electrodeposited transition metals were calculated to be near one equivalent monolayer. Table I lists the percent changes in photocurrent upon exposure to the NH_3/N_2 mixtures after photoelectro-

chemical modification of the MC assemblies. The percent changes in photocurrent are now significantly higher than before the electrochemical modification of the MC assemblies with Ag and Hg. In some cases large changes in dark current were also observed, although these values have limited quantitative interest, since the dark currents for these small area microcircuits were still low and close to the limit of detection of our instrumentation even after the electrochemical modification. The Pc thin film on the QCM was simultaneously modified with each respective metal, but once again, no significant frequency shifts were observed when exposed to the low concentrations of NH_3 employed. Metal modification of the MC appears to provide significant amplification of response from the chemisorption of submonolayer amounts of NH_3.

For all the electrochemically modified MC assemblies, the initial introduction of NH_3, even at the 1 ppm level, caused the largest increase in photocurrent, independent of the nature of the metal deposited. With the exception of Hg, further increases in the NH_3 concentration led to only small photocurrent changes (analogous to the one observed before electrochemical modification), suggesting that saturation of the new adsorption sites had occurred. When log i_{ph} vs log [NH_3] plots were constructed, the response was linear, but not with as large a slope as for the Hg-modified assemblies described below.

When the MC assembly was electrochemically modified with a 10^{-4} M $HgCl_2$ solution, a steplike response of the kind shown in Figures 3B and 4 was observed for the photocurrent after *each* addition of NH_3 in N_2, up to a concentration of 85 ppm, revealing that saturation of the NH_3 chemisorption sites did not occur in this case (no pretreatment was necessary to achieve this response). At NH_3 concentrations higher than ca. 85 ppm, the near saturation response, typical of the MC before modification, was observed once again. Even at 85 ppm NH_3, the modified or unmodified Pc-coated QCM's in the same sensing cell showed that the total amount of NH_3 adsorbed was less than an equivalent monolayer, even without correction for the roughness of the Pc film (less than 1 Hz frequency shift in a 10 MHz crystal), further confirming the sensitivity of this approach.

At the parts-per-million level, the adsorption of NH_3 on most of these metal-modified MC assemblies is followed by a slow desorption step to completely restore the original photo and dark conductivities. At room temperature, several hours was needed to restore the original value of σ_{ph} (before NH_3 had been introduced), once the flow of NH_3 had been stopped. Generally, the MC assembly had to be heated overnight in N_2 in order to restore the initial properties, including the steplike response to NH_3 shown in Figure 3B.

The Hg-modified MC, however, appeared to behave in a markedly different fashion. Once saturation of the Hg sites had occurred, 1–2 h of degassing in N_2 at room temperature was successful in restoring the original σ_{dk} and σ_{ph} of the MC assembly. For NH_3 concentrations below the saturation level, the Hg-modified microcircuit assemblies *showed reproducible and reversible photoresponses* (see also next section, Figure 7A).

Figure 5 shows the room temperature photocurrent response of the Hg-modified MC as a function of the NH_3 concentration (1.5 to 84 ppm). The relationship between the photocurrent and the NH_3 concentration is linear at the lowest concentrations tested (1.5–5.5 ppm NH_3 in N_2, Figure 5A), with a correlation coefficient of 0.99 and a slope of 1.9×10^{-11} A/ppm. A noise level corresponding to 3 pA was recorded for these MC assemblies. If the detection limit is defined as the concentration of NH_3 needed to produce a change in photocurrent twice the noise level, a detection limit of 300 ppb is expected

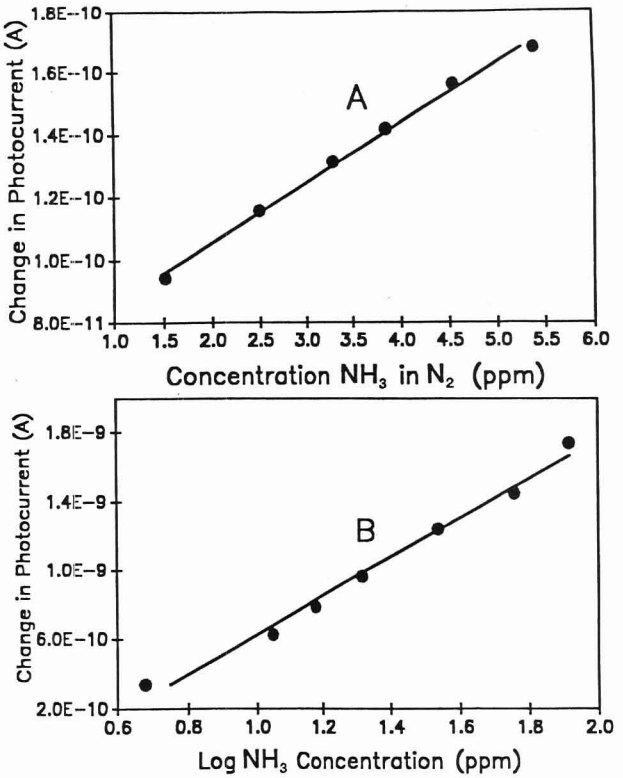

Figure 5. (a) Photocurrent response as function of the NH_3 concentration in N_2 for a InPc-Cl coated MC (40 nm) electrochemically modified with Hg at room temperature. (b) Photocurrent response as function of the log of the NH_3 concentration in N_2 for the same MC in part a. Conditions were as follows: concentration range, 4.8–84 ppm; bias potential, 2.0 V.

for NH_3 in N_2 for the Hg-modified MC assemblies. At higher NH_3 concentrations (4.8–84 ppm, Figure 5B) the photocurrent versus NH_3 concentration plot is logarithmic in nature. A linear relationship between photocurrent response and NH_3 concentration is observed again at NH_3 concentrations higher than ca. 4 ppt.

A higher operational temperature was attempted in order to improve the sensitivity and reversibility of these metal modified assemblies. The results obtained at 50 °C in the range of NH_3 concentrations between 700 ppb and 48 ppm on MC assemblies modified with Hg or Ag revealed that increased photoresponses (up to 40% higher) can be obtained at higher temperatures. Unfortunately, in both cases saturation of the metal sites seems to occur at lower NH_3 concentrations, generally after the second addition of NH_3. It seems plausible that the higher temperatures result in a removal of surface-adsorbed impurities on the metal modifier, in particular O_2, which gives rise to stronger binding sites for the NH_3.

Sensitivity to NH_3 in Air. For the Hg-modified MC, when the carrier gas was changed from N_2 to dry air ($H_2O < 3$ ppm), the behavior observed previously for the unmodified MC assembly was obtained once again. The initial introduction of NH_3 (ppm level) resulted in a dramatic decrease in both dark and photocurrent; with further increases in the NH_3 concentration, both currents were affected less notably. After the addition of ca. 5.5 ppt NH_3 in this pretreatment phase, further increases in the NH_3 concentration produced the steplike increase in photocurrent response observed previously (Figures 3B and 4), with both the dark and photocurrent increasing linearly with NH_3 concentration. A plot of the photoresponse versus the concentration of the NH_3 in air (8.4 to 28 ppt) is linear (Figure 6), with a correlation coefficient of 0.99 and a slope of 7.8×10^{-12} A/ppt. According to the definition of detection limit given previously, with a noise level

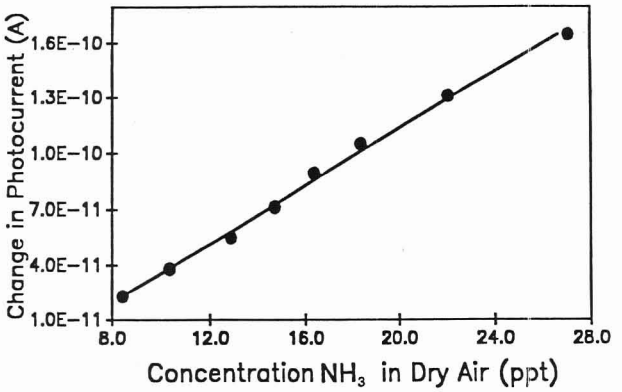

Figure 6. Photocurrent response as a function of the NH_3 concentration in air for a InPc-Cl coated MC electrochemically modified with Hg, at room temperature: bias potential, 2.0 V.

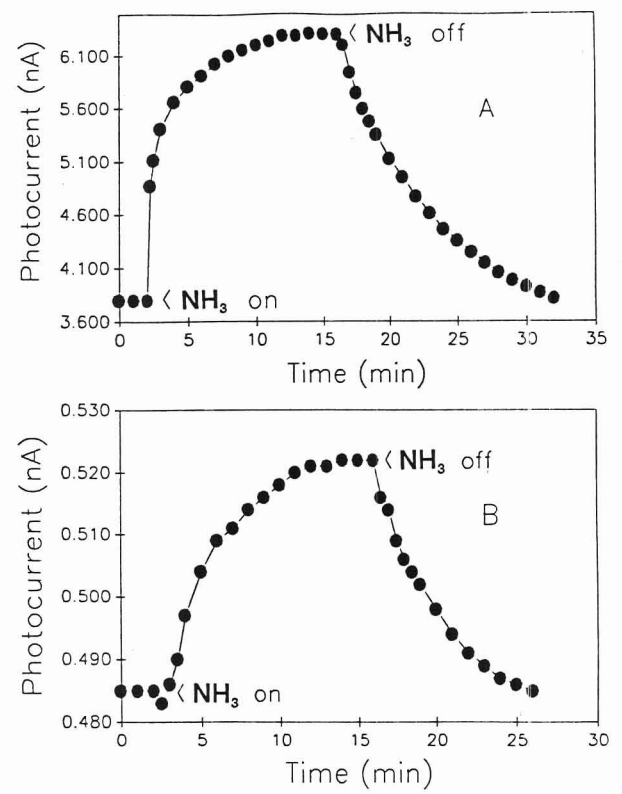

Figure 7. (a) Photocurrent response to 3.1 ppt NH_3 in N_2 for a InPc-Cl coated MC electrochemically modified with Hg at room temperature. (b) Photocurrent response to 6.0 ppt NH_3 in air for the MC in part a. Bias potential was 2.0 V.

of 4 pA, a detection limit of 1.0 ppt was obtained for NH_3 in air with the Hg-modified MC assemblies. It should be noted at this point that the detection limit for NH_3 in air (1.0 ppt) is now considerably lower than the value obtained for the unmodified MC assemblies (16 ppt, see previous section). This effect is attributed to the presence of the metal modifier on the surface of the PC film. Similar results were obtained for the MC assemblies modified with other metals (Au, Pt, Cu, Ag), with the detection limits varying slightly for each circuit (between 1.6 and 3.2 ppt NH_3 in air, depending on the MC).

The changes in photocurrent as a function of time for a given NH_3 concentration in N_2, and in air, for the Hg-modified MC are compared in Figure 7. Figure 7A shows the photocurrent response after the introduction of 3.1 ppt of NH_3 in N_2, while Figure 7B is relative to 6.0 ppt of NH_3 in air. In both cases equilibrium was reached in approximately the same time, although the slope of the initial part of the plot was steeper when the carrier gas was N_2. The opposite is true when the NH_3 was turned off, and the photocurrent returned faster

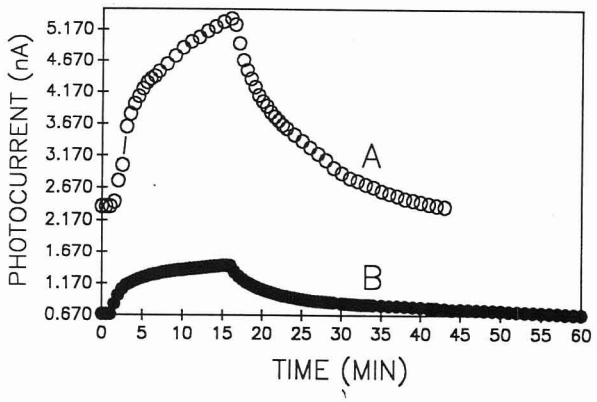

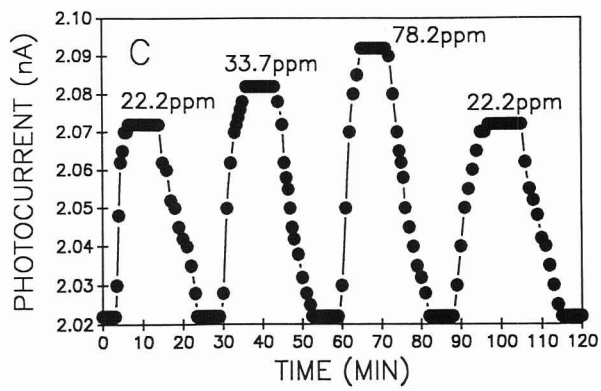

Figure 8. Photocurrent responses of the Hg-modified MC to NH_3 in N_2 using (a) white light illumination from the tungsten–halogen light source and (b) illumination from the He–Ne laser source, for NH_3 levels of 4.4 and 3.6 ppt, respectively. Part a represents the photocurrent output as measured from the calibrated lock-in-amplifier output, while part b represents the photocurrent measured directly from the picoammeter. Part c represents the photocurrent response of the same MC after introduction and removal of a sequence of NH_3 concentrations, demonstrating response times, reversibility of response, and reproducibility.

to its initial value in air. This behavior can be explained assuming that at least some of the NH_3 adsorbed on the film (the portion of NH_3 which affects the photocurrent response) may be displaced by O_2, once the flow of NH_3 is stopped.

In the attempt to increase the sensitivity and reversibility of the Hg-modified MC assemblies in air, higher temperatures of operation were studied. Despite the higher value of photocurrent generally obtained, no notable gain in sensitivity or reversibility was observed at 50 °C. After a few days of measurements at this higher temperature, deactivation of the metal modifier seems to be occurring, since the detection limits for NH_3 began to increase. Temperatures higher than 50 °C were not attempted because of this deactivation process. The MC assemblies electrochemically modified with Au behaved differently, showing faster on and off response times and no significant deactivation of the metal centers even after exposure to NH_3 in air at 50 °C.

Response of the Hg-Modified MC to White Light Illumination. Any application of photoconductivity-based chemiresistors will likely involve polychromatic light sources, with higher power densities than the He–Ne laser used in most of these studies. Figure 8 shows the type of responses obtained from the Hg-modified MC described above, when illuminated with either the full output of the tungsten–halogen light source or the 10 mW He–Ne laser. The tungsten–halogen light source output was chopped by using a 10 Hz modulation, with the output of the current-to-voltage converter being demodulated with a lock-in amplifier. A substantial increase in the total photocurrent response was seen when the polychromatic light source was used at nearly the same NH_3 concentration.

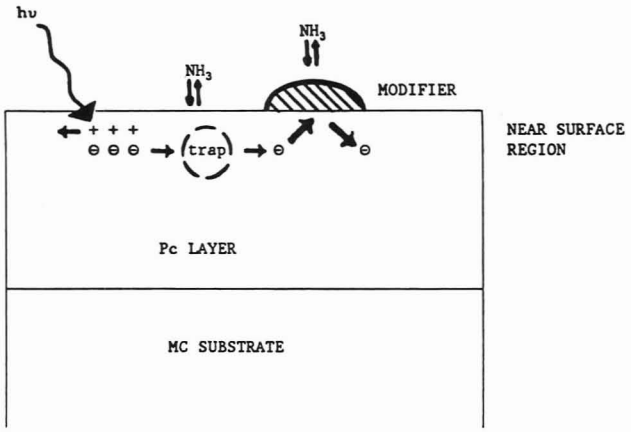

Figure 9. Schematic of the chemisorption process for NH_3 on the InPc-Cl and GaPc-Cl surface region for the photoelectrochemically modified MC assemblies. The dark area at the surface of the modifier represents the metal possibly present in an oxidized state.

Corresponding increases in sensitivity were observed for NH_3 when the white light source was used (a factor of ca. 5 times the sensitivities noted above using the He–Ne laser). This enhancement can be expected to improve with even brighter light sources. The photocurrent yield was found to be essentially linear over the range of light intensities available with the tungsten–halogen source, although it may saturate at higher light intensities (*33*). It was also noted that when using the white light source, the length of time necessary to achieve nearly steady-state photocurrents after introduction of NH_3 and after removal of NH_3 from the gas stream, improved by ca. 25% when compared to the response obtained by using the He–Ne light source.

The issues of reversibility and reproducibility of response were also addressed by using the white light source, as shown in Figure 8C. Several different concentrations of NH_3 were introduced and allowed to reach a steady-state response, whereupon the NH_3 was removed from the gas stream and followed by higher or lower levels of NH_3. Provided that the concentration of NH_3 was kept below the saturation levels described above, reasonably fast response times to steady state were achieved, and the steady-state responses to identical NH_3 levels were reproducible to within 10%.

CONCLUSIONS

Photoconductivity-based microcircuit/phthalocyanine gas sensors show promise for the detection of certain molecules, provided that the mechanism(s) for gas/Pc interactions can be further modified to improve the analytical response in the presence of O_2. Most previous gas sensing studies, based upon organic thin film chemiresistors, have acknowledged the complexity of the mechanisms for charge generation, electron and hole trapping, charge collection, and the multiple surface interaction modes experienced by gas phase analytes (*1*, *7*, *9*, *21*, *26–28*, *33–37*). The studies discussed here, and those presented previously (*33*, *34*), suggest the interaction models shown in Figure 9 for O_2 and NH_3, as discussed above. Our findings can be summarized as follows:

(a) Submonolayer amounts of O_2 appear to bind to impurity sites in the Pc film, forming electron traps, which are probably only affected by high concentration levels of NH_3 (greater than 10 ppt) (*33*, *34*).

(b) The majority of O_2 bound in the Pc film acts (through eqs 1 and 2) to increase the photoconductivity (and the dark conductivity) of the film, and its displacement by NH_3 is the cause of the decline in σ_{ph} during sensor pretreatment stages. This effect is a serious limitation regarding the use of these sensors in air, in that the effect of O_2 on σ_{dk} and σ_{ph} can only be overcome (in an analytically significant way) at high NH_3 concentrations and after pretreatment.

(c) The photoelectrodeposition of metal modifiers, occurring at sites of highest Pc photoactivity (which may also be sites of high O_2 concentration and high defect densities), provides a new electron trap site, whose affinity for electrons is strongly affected by binding of a donor molecule such as NH_3. Because each trap site affects the collection of several charges (depending upon their concentration, average lifetime, and the photon flux), significant "amplification" of each analyte chemisorption event is possible. The optimization of response may be achieved through the appropriate modification of the photoconductive thin film with respect to the type and distribution of modifier sites, thereby selectively introducing trap sites of choice into the pure Pc thin film to enhance the sensitivity and analytical response. For the measurements in air, the pretreatment stage, consisting of exposing the modified MC assemblies to constant and continuous flows of NH_3 at a few parts per million in air before the analytical measurement, appeared to improve the stability and reproducibility of these assemblies, allowing for detection of NH_3 in air as low as 1 ppt.

The nature of the surface composition of the metal modifier is as yet unclear, but it must be important in determining the analytical utility of the technology. Metal modifiers have been widely used to enhance the response of certain chemiresistor and FET sensors (*26*), although never, to our knowledge, with Pc-based chemiresistors. Recent studies of lead phthalocynine (PbPc) based chemiresistors for NO_2 have demonstrated that the surface of the PbPc thin film is converted to a lead oxide form as a result of sensor pretreatment steps (*26*, *44*). The action of such modifiers on both NO_2 and NH_3 chemiresistors, as well as sensors for other weak acceptor and donor molecules, is under investigation.

One should also note the inherent differences in dark and photoconductivity detection modes in chemiresistors. Obviously, maximizing the surface-to-volume ratios of sensor thin films for a given device size will further enhance sensitivity for either mode of detection. This idea was taken to its extreme by Hirschfeld through the use of highly porous gold films as a substrate for an organic thin film (*45*). The resultant chemiresistors had high signal strength and would undoubtedly benefit further by the photoconductivity detection modes discussed here. In a related fashion, our attempts to increase the photocurrent yield of these assemblies with the use of polychromatic light sources with high power densities may ultimately ensure the maximum interaction of traps and adsorbed analytes in the near surface region of the Pc film with photogenerated charges. Other chemiresistor studies have tended to use much larger electrode arrays than ours (and hence thicker organic layers) which is less desirable for photoconductive detection modes. Pc films with thicknesses less than the step height of the individual microcircuit legs optimize the photocurrent yield (*8*). Such thin films ensure that many of the photogenerated charges are close enough to the surface to interact with the added modifiers. Ultrathin films of Pc's, etc., produced by Langmuir–Blodgett or other self-assembly methods, may be attractive alternatives to the vacuum-deposited thin films described here, provided that the resistance of the thin film is not excessive (*21*, *36*). In addition, one can speculate that the alteration of the photoconductivity would be an attractive addition to detection modes of recently described FET-based gas sensors (*6*). Changes in dark conductivities of a Pc thin film, used to indirectly modulate a source-drain current, could be further amplified by the analyte adsorption/photoconductivity changes described here.

LITERATURE CITED

(1) Meier, H. *Organic Semiconductors*; Verlag Chemie: Berlin, 1974; pp 143 and 473.
(2) Marks, T. J. *Science* **1985**, *227*, 881.

(3) Dirk, C. W.; Inabe, T.; Schoch, K. F.; Marks, T. J. *J. Am. Chem. Soc.* **1983**, *105*, 1539.
(4) Inabe, T.; Gaudiello, J. G.; Maguel, M. K.; Lyding, J. W.; Burton, R. L.; McCarthy, W. J.; Kammewurf, C. R.; Marks, T. J. *J. Am. Chem. Soc.* **1986**, *108*, 7595.
(5) Nohr, R. S.; Kuznesof, P. M.; Wynne, K. J.; Kenney, M. E.; Siebernmann, P. G. *J. Am. Chem. Soc.* **1981**, *103*, 4371.
(6) Kolesar, E. S.; Wiseman, J. M. *Anal. Chem.* **1989**, *61*, 2355.
(7) Nieuwenhuizen, M. S.; Barendsz, A. W. *Sens. Actuators* **1987**, *11*, 45.
(8) Armstrong, N. R.; Lee, P.; Pankow, J.; Danzinger, J.; Nebesny, K. W. In *Photoelectrochemistry and Electrosynthesis on Semiconducting Materials*; Ginley, D., Armstrong, N., Nozik, A., Honda, K., Fujishima, A., Sakata, T., Eds.; Electrochemical Society Publications: Pennington, NJ, 1987.
(9) Simon, J.; André, J.-J. *Molecular Semiconductors*; Springer-Verlag: New York, 1985; pp 73–148.
(10) Rieke, P. C.; Armstrong, N. R. *J. Am. Chem. Soc.* **1984**, *106*, 47.
(11) Klofta, T.; Rieke, P. C.; Linkous, C. A.; Buttner, W. J.; Nanthakumar, A.; Mewborn, T. D; Armstrong, N. R. *J. Electrochem. Soc.* **1985**, *132*, 2134.
(12) Klofta, T. J.; Danziger, J.; Lee, P.; Pankow, J.; Nebesny, K. W.; Armstrong, N. R. *J. Phys. Chem.* **1987**, *91*, 5646.
(13) Sims, T. D.; Pemberton, J. E.; Lee, P.; Armstrong, N. R. *Chem. Mater.* **1989**, *1*, 26.
(14) Rieke, P. C.; Linkous, C. L.; Armstrong, N. R. *J. Phys. Chem.* **1984**, *88*, 1351.
(15) Hor, A. M.; Loutfy, R. O.; Hsiao, C. K. *Appl. Phys. Lett.* **1983**, *42*, 165.
(16) Lee, P.; Pankow, J.; Danziger, J.; Nebesny, K. W.; Armstrong, N. R. In *Deposition and Growth, Frontiers for Microelectronics*; Rubeloff, G. W., Ed.; American Institute of Physics: New York, 1988.
(17) Belanger, D; Dodelet, J.-P.; Dao, L. D.; Lombos, B. A. *J. Phys. Chem.* **1984**, *88*, 4288.
(18) Guay, D.; Cote, R.; Marques, R.; Dodelet, J.-P.; Lawrence, M. F.; Gravel, D.; Langford, C. H In *Photoelectrochemistry and Electrosynthesis on Semiconducting Materials*; Ginley, D., Armstrong, N., Nozik, A., Honda, K., Fujishima, A., Sakata, T., Eds. Electrochemical Society Publications: Pennington, NJ, 1987.
(19) Martin, M.; André, J.-J.; Simon, J. *J. Appl. Phys.* **1983**, *54* (5), 2792.
(20) Barger, W. R.; Wohltjen, H.; Snow, A. W.; Jarvis, N. L. In *Fundamentals and Applications of Chemical Sensors*; Schuetzle, D., Hammerle, R., Eds.; American Chemical Society: Washington, DC, 1986.
(21) Snow, A. W.; Barger, W. R.; Klusty, M.; Wohltjen, H.; Jarvis, N. L. *Langmuir* **1986**, *2*, 513.
(22) Ricco, A. J.; Martin, S. J.; Zippeman, T. E. *Sens Actuators* **1985**, *8*, 319.
(23) Swalen, J. D.; Allara, D. L.; Andrade, J. D.; Chandross, E. A.; Garoff, S.; Israelachvili, J.; McCarthy, T. J.; Murrar, R.; Pease, R. F.; Rabolt, J. F.; Wynne, K. J.; Yu, H. *Langmuir* **1987**, *3*, 932.
(24) Loutfy, R. O.; Hor, A. M.; Di Paola-Baranyi, G.; Hsiao, C. K. J. *Imaging Sci* **1985**, *29* (3), 116.
(25) Wagner, H. J.; Loutfy, R. O.; Hsiao, C. K. *J. Mater. Sci.* **1982**, *17*, 2781.
(26) Mockert, H.; Schmeisser, D.; Gopel, W. *Sens. Actuators* **1989**, *19*, 159.
(27) Collins, R. A.; Mohammed, K. A. *J. Phys. D: Appl. Phys.* **1988**, *21*, 154.
(28) Dahlberg, S. C.; Musser, M. E. *J. Chem. Phys.* **1980**, *72* (12), 6706.
(29) Collins, R. A.; Mohammed, K. A. *Thin Solid Films* **1986**, *145*, 133.
(30) Wilson, A.; Collins, R. A. *Phys. Status Solids A* **1986**, *98*, 633.
(31) (a) Klofta, T. J.; Sims, T. D.; Pankow, J. W.; Danziger, J.; Nebesny, K. W.; Armstrong, N. R. *J. Phys. Chem.* **1987**, *91*, 5651. (b) Klofta, T. K. Ph.D. Dissertation, University of Arizona, 1986.
(32) Popovic, Z. D. *J. Chem. Phys.* **1982**, *77*, 498.
(33) Waite, S.; Pankow, J.; Collins, G.; Lee, P.; Armstrong, N. R. *Langmuir* **1989**, *5*, 797.
(34) Arbour, C.; Armstrong, N. R.; Brina, R.; Collins, G.; Danziger, J.; Dodelet, J.-P.; Lee, P.; Nebesny, K. W.; Pankow, J.; Waite, S. *Mol. Cryst. Liq. Cryst.* **1990**, *183*, 307.
(35) Honeybourne, C. L.; Ewen, R. J. *J. Phys. Chem. Solids* **1983**, *44*, 215 and 833.
(36) Wohltjen, H.; Barger, W. R.; Snow, A. W.; Jarvis, N. L. *IEEE Trans. Electron Devices* **1985**, *32*, 1170.
(37) Wilson, A.; Collins, R. A. *Sens. Actuators* **1987**, *12*, 389.
(38) Linsky, J. P.; Paul, T. R.; Nohr, R. S.; Kenney, M. E. *Inorg. Chem.* **1980**, *19*, 3131.
(39) Varmuza, K.; Maresch, G.; Meller, A. *Monatsh. Chem.* **1974**, *105*, 327.
(40) Pankow, J.; Arbour, C.; Armstrong, N. R. Unpublished work.
(41) Meier, H. *Organic Semiconductors*; Verlag Chemie: Berlin, 1974; pp 317–328.
(42) Laurs, H.; Heiland, G. *Thin Solid Films* **1987**, *149*, 129.
(43) van Ewyk, R. L.; Chadwick, A. V.; Wright, J. D. *J. Chem. Soc., Faraday Trans. 1* **1981**, *77*, 73.
(44) Rager, A.; Gompf, B.; Dürselen, L.; Mockert, H.; Schmeisser, D.; Göpel, W. *J. Mol. Electron.* **1989**, *5*, 227.
(45) Hirschfeld, T. B. U.S.P.N. 4,674,320, 1987.

RECEIVED for review April 11, 1990. Accepted July 27, 1990. Support for this work by the National Science Foundation, Motorola (University Partnerships in Research), Burr-Brown, and the Materials Characterization Program—University of Arizona is gratefully acknowledged.

Environmental Factors Affecting Micellar Stabilized Room-Temperature Phosphorescence Lifetimes

Haidong Kim[1] and Stanley R. Crouch*

Department of Chemistry, Michigan State University, East Lansing, Michigan 48824

Matthew J. Zabik* and Salah A. Selim

Pesticide Research Center, Michigan State University, East Lansing, Michigan 48824

Triplet lifetimes of organic compounds at low temperature are well established compared to the room-temperature phosphorescence (RTP) lifetimes. The RTP lifetimes may vary from system to system depending on the experimental conditions employed. The environmental factors affecting micellar-stabilized RTP lifetimes are investigated. It was found that solution deoxygenation method, temperature, and heavy atoms are the major contributor to the variations of observed RTP lifetimes. A kinetic decay model of triplet molecules is proposed to describe the effects of triplet quenchers and external heavy atoms on phosphorescence lifetimes in micellar solution.

* To whom correspondence should be addressed.
[1] Present address: 204 Pesticide Research Center, Michigan State University, East Lansing, MI 48824.

INTRODUCTION

Micelle stabilized room-temperature phosphorescence (MS-RTP) spectrometry is a convenient and useful analytical technique compared to classical low-temperature phosphorescence spectrometry (*1*, *2*). Aqueous surfactant solutions exhibit the phenomenon of self-organization. Above a certain concentration, the critical micelle concentration (cmc), surfactant molecules associate spontanously to build up structural entities of colloidal dimensions called micelles. The protective screening effect of micelles from external quenchers by compartmentalization of solubilized lumiphore molecules greatly reduces collisional quenching of triplet molecules. Thus, by using external heavy atoms which increase the phosphorescence yield, phosphorescence of many polynuclear aromatic hydrocarbon (PAH) compounds can be observed in micellar solutions at room temperature (*3*, *4*).

0003-2700/90/0362-2365$02.50/0 © 1990 American Chemical Society

The decay lifetimes of the excited triplet state are important in studies of kinetic processes associated with the triplet state of compounds (*5*). The lifetime of the excited triplet state is a characteristic property of a molecule and its molecular environment. Phosphorescence lifetimes frequently provide a diagnostic tool since compounds having very similar spectral characteristics may have greatly different triplet lifetimes (*6*). Although triplet lifetimes of organic compounds have been well established in rigid media at low temperature (77 K), RTP lifetimes in fluid media are far more variable and difficult to use for chemical analysis. In the frozen state, at liquid nitrogen temperature, collisional quenching of the triplet state by molecular oxygen and other impurities is significantly minimized, and the temperature of the sample remains constant. These conditions give reliable and consistent phosphorescence lifetimes that can be used as qualitative descriptors of the luminescent species.

However, RTP lifetimes of compounds are extremely sensitive to such environmental conditions as temperature, the presence of heavy atoms, the oxygen content, and the presence of other triplet quenchers. Solid-surface RTP utilizes interactions of lumiphors with solid matrices such as filter paper or ionic salts (*7–9*). The interactions between lumiphors and solid matrices such as hydrogen bonding provide more rigid molecular environment for lumiphors than micellar solution as evidenced by much longer RTP lifetimes (*10*, *11*). This is attributed to the fact that triplet molecules in micellar solutions are in dynamic equilibrium with various sources of triplet quenchers. Therefore, RTP lifetimes in fluids may vary from system to system. This variability can prevent RTP lifetimes from being used for analytical purposes.

In this work, various environmental factors affecting MS-RTP lifetimes are investigated. Factors such as temperature of the sample solution, the presence of heavy atoms, the purity of the sample, the oxygen content of the sample, and the presence of other triplet quenchers are considered as the sources of the observed RTP lifetime fluctuations. A kinetic decay model is proposed to use alternative parameters in place of RTP lifetimes, which are less dependent on environmental conditions of the sample solution.

THEORY

Studies of micelle dynamics were performed to understand the quenching and decay kinetics of luminescence in micellar solutions. Almgren et al. (*12*) studied the kinetics of solubilization and the solubilities of neutral arenes in ionic micellar systems using phosphorescence, fluorescence, and steady-state absorption techniques. Infelta et al. (*13*) proposed a kinetic model describing the kinetics of quenching reactions in micelles. Triplet lifetime measurements with solutions containing micellized cetyltrimethylammonium bromide (CTAB), anthracene, and Cu^{2+} ions show that the rate constant for the exit of anthracence from CTAB micelles into the aqueous bulk phase is as low as $2 \times 10^2\ s^{-1}$. Cline Love et al. (*14*) studied the influence of analyte–heavy atom micelle dynamics on RTP lifetimes and spectra. They proposed limiting rates determining MS-RTP lifetimes of analyte for long-lived, intermediate, and short-lived cases. Although all the previous kinetic decay models adequately treat quenchers, they all neglect external heavy atoms simply because heavy atoms are not triplet quenchers. The triplet decay model proposed below focuses on the influence of external heavy atoms on MS-RTP lifetimes.

The main difference between this model and previous kinetic models is the incorporation of heavy atom terms. The proposed triplet decay model is shown schematically in Figure 1. To successfully apply this proposed model, the following assumptions are made:

(i) The detectable RTP comes mainly from triplet molecules located inside the micelles. This assumption is valid because RTP cannot be observed in the absence of micelles.

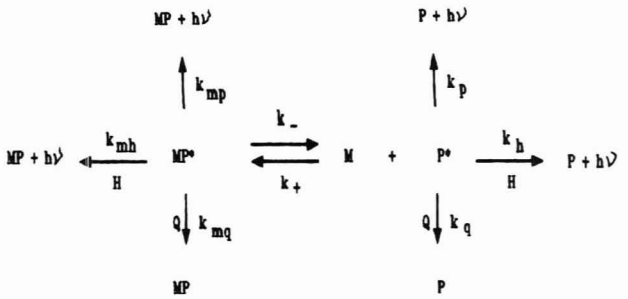

Figure 1. Kinetic model of micellar-stabilized RTP: M, micelle; P, triplet probe; Q, quencher; H, heavy atom. MP* represents excited triplet probe located inside micelle.

(ii) Quenching of the triplet state occurs mainly at the micellar surface and in the aqueous phase. It has been observed that RTP lifetimes of lumiphors in micellar solution decrease with increasing quencher concentration until a plateau level is reached (*15*). If quenching occurs mainly inside or outside the micelle, the triplet lifetime must decrease continuously as the quencher concentration increases. With a fixed micelle concentration, the micellar surface area is also fixed to a limiting value for triplet quenching. This supports the assumption of micellar surface quenching.

(iii) The probe molecules must be far more soluble in the micellar phase than in the aqueous phase. This condition is necessary for the application of steady-state approximation.

(iv) The concentration of the phosphorescent probe is so low that self-quenching of the excited state is unimportant.

The partitioning of a phosphorescent probe P* between an aqueous phase and micelle M is given by

$$\mathrm{MP^*} \underset{k_+}{\overset{k_-}{\rightleftharpoons}} \mathrm{M} + \mathrm{P^*} \tag{1}$$

where MP* and P* denote the triplet probe located inside and outside the micelle, respectively. The triplet emission mainly comes from the phosphorescent probe located inside the micelle

$$\mathrm{MP^*} \xrightarrow{k_{mp}} \mathrm{MP} + h\nu \tag{2}$$

Triplet quenching by quencher Q, and reaction of heavy atom H with excited triplet probes occur at the micellar surface and in the aqueous phase

$$\mathrm{MP^*} + \mathrm{H} \xrightarrow{K_{mh}} \mathrm{MP} + \mathrm{H} \tag{3}$$

$$\mathrm{P^*} + \mathrm{H} \xrightarrow{k_h} \mathrm{P} + \mathrm{H} \tag{4}$$

$$\mathrm{MP^*} + \mathrm{Q} \xrightarrow{k_{mq}} \mathrm{MP} + \mathrm{Q} \tag{5}$$

$$\mathrm{P^*} + \mathrm{Q} \xrightarrow{k_q} \mathrm{P} + \mathrm{Q} \tag{6}$$

As a result, the rates of disappearance of MP* and P* are given by

$$-\mathrm{d[MP^*]}/\mathrm{d}t = k_-[\mathrm{MP^*}] - k_+[\mathrm{M}][\mathrm{P^*}] + k_{mp}[\mathrm{MP^*}] + k_{mh}[\mathrm{MP^*}][\mathrm{H}] + k_{mq}[\mathrm{MP^*}][\mathrm{Q}] \tag{7}$$

$$-\mathrm{d[P^*]}/\mathrm{d}t = k_+[\mathrm{M}][\mathrm{P^*}] + k_h[\mathrm{P^*}][\mathrm{H}] + k_q[\mathrm{P^*}][\mathrm{Q}] - k_-[\mathrm{MP^*}] \tag{8}$$

If the phosphorescent probe P* is far more soluble in the micellar solution than in aqueous phase, such that [MP*] ≫ [P*], the steady-state approximation can be applied

$$-\mathrm{d[P^*]}/\mathrm{d}t = 0 \tag{9}$$

From eqs 7, 8, and 9 we obtain

$$-\mathrm{d[MP^*]}/\mathrm{d}t = [\mathrm{MP^*}][k_- + k_{mp} + k_{mh}[\mathrm{H}] + k_{mq}[\mathrm{Q}] - \{k_+k_-[\mathrm{M}]/(k_+[\mathrm{M}] + k_h[\mathrm{H}] + k_q[\mathrm{Q}])\}] \tag{10}$$

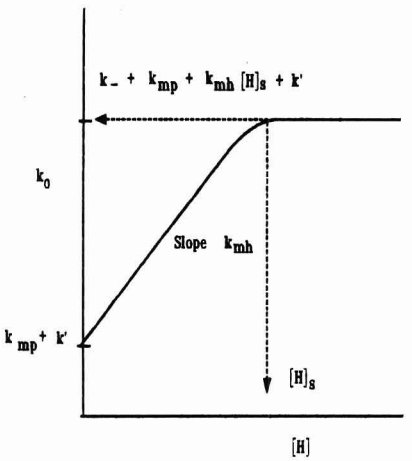

Figure 2. Decay rate constants of triplet probe with different heavy atom concentrations in ideal conditions. k_o is reciprocal of the observed MS-RTP lifetime and $[H]_s$ is the saturated heavy atom concentration at which k_o reaches steady state.

Therefore, the observed disappearance rate constant of MP*, k_o, which is the reciprocal of lifetime τ is given by

$$k_o = 1/\tau = k_- + k_{mp} + k_{mh}[H] + k_{mq}[Q] - \{k_+k_-[M]/(k_+[M] + k_h[H] + k_q[Q])\} \quad (11)$$

This equation shows that at a fixed concentration of micelle, the observed lifetime decreases as the heavy atom and quencher concentrations increase. In a given system, if the concentration of quencher remains constant, then eq 11 becomes

$$k_o = 1/\tau = k_- + k_{mp} + k_{mh}[H] + k' - \{k_+k_-[M]/(k_+[M] + k_h[H] + k'')\} \quad (12)$$

where $k' = k_{mq}[Q]$ and $k'' = k_q[Q]$, respectively. If [H] is zero and $k_+[M] \gg k''$, the $k_o = k_{mp} + k'$. Also, if heavy atoms react with the triplet probe mainly at the micellar surface, the observed RTP lifetime will decrease continuously until [H] reaches a saturated value $[H]_s$ as shown in Figure 2.

EXPERIMENTAL SECTION

Reagents. Sodium sulfite (J. T. Baker) was recrystallized from warm water (0.5 mL/g). Thallium(I) nitrate (99.99%, Aldrich), sodium bromide (99.9%, J. T. Baker), sodium dodecyl sulfate, SDS (99%, Sigma), and methanol (GR grade, EM Science) were used as received. The analytes used in this research, naphthalene (Eastman), pyrene (J. T. Baker), 2-bromonaphthalene (97%, Aldrich), and biphenyl (J. T. Baker), were all recrystallized twice from absolute ethanol. Distilled–deionized water was used for RTP sample preparation throughout the experiment.

Apparatus. RTP spectra and RTP lifetimes were measured by a Perkin-Elmer LS-5B spectrometer. Data were acquired with an IBM-XT compatible personal computer interfaced to the LS-5B. Software written with Turbo Pascal (Borland International) and Macro Assembler (MicroSoft) was used to control the instrument, acquire luminescence data, and perform data analysis. RTP lifetimes were calculated by linear least-squares method. The ranges of delay times and gate times for RTP measurements were 0.03–0.05 ms and 1–3 ms, respectively.

Sample Preparation and General Procedure. Stock solutions of naphthalene, pyrene, biphenyl, and 2-bromonaphthalene were made by dissolving appropriate amounts of analytes in 10 mL of methanol and diluting to 100 mL with water. For the external heavy atom source, a 0.25 M thallium nitrate stock solution was used. A 0.05 M sodium dodecyl sulfate stock solution was prepared for the micellar solution, and a 0.4 M sodium sulfite stock solution was used for deoxygenation of the sample solution.

An aliquot of analyte stock solution was pipetted into a 10-mL volumetric flask and solvent was evaporated to a minimum volume using nitrogen gas. Sample solutions were made by adding appropriate amounts of stock solutions of thallium nitrate, SDS, and sodium sulfite into the 10-mL volumetric flask containing analyte. These solutions were diluted to a 10 mL final volume with distilled–deionized water. After thorough mixing, the solution was transferred to a cuvette covered with a Teflon stopper. The cuvette holder was maintained at constant temperature. The progress of chemical oxygen scavenging was monitored by measuring the RTP intensity development at the emission maximum with the appropriate excitation wavelength on the spectrometer. Uncorrected RTP spectra were obtained after the RTP intensity reached steady state and remained constant for at least 5 min.

RESULTS AND DISCUSSION

Experimental Conditions for MS-RTP. Deoxygenation of the micellar solution was the most experimentally troublesome of the early MS-RTP studies. The use of an inert gas such as nitrogen to remove dissolved oxygen generate foams. Furthermore, degassing time and quality of inert gas generally affect the observed MS-RTP lifetimes. Chemical deoxygenation method by sulfite ions was used for this work because of its simplicity and reliability (*16*).

To find the optimum concentration of sodium sulfite, various amounts of sodium sulfite were added to a solution of a fixed amount of naphthalene (2×10^{-5} M), SDS, and heavy atom (Tl^+). The concentration of SDS and Tl^+ were 3.5×10^{-2} and 1.5×10^{-2} M, respectively. RTP intensities were measured 15 min after mixing. The optimum concentration range of sodium sulfite was found to be 0.8×10^{-2} to 1.5×10^{-2} M. Below this range, the RTP intensity decreased due to incomplete and slow deoxygenation. Above the optimum range, the RTP of naphthalene showed a reduced intensity due to a high concentration of sodium ions, which at such levels can displace thallium ions from the micellar surface.

The reported value of the critical micelle concentration (cmc) of SDS is 8.2×10^{-3} M (*17*). Effective screening of the triplet sample molecules by the micelle is expected at surfactant concentrations above the cmc. To find the optimum SDS concentration, various amounts of SDS were added to a solution containing fixed amounts of Tl^+, sodium sulfite, and naphthalene. The maximum RTP intensity was observed when the SDS concentration was in the 1.5×10^{-2} to 5.0×10^{-2} M range. The RTP intensity began to decrease at SDS concentrations above 5.0×10^{-2} M. MS-RTP lifetimes of PAHs are found to increase upon increasing the surfactant concentration up to 0.05 M. At higher surfactant concentrations, the lifetime decreased possibly because of increase in impurities.

There are several possible reasons for the reduced RTP intensity at high SDS concentrations. First, the number of heavy atoms per micelle should decrease with increasing SDS concentration. As a result, the effective concentration of heavy atom will decrease; this results in reduced spin–orbital interactions between the singlet molecules and heavy atoms. Second, the size, shape, and dynamic motion of the micelle will change at high SDS concentration and this could affect the stability of triplet molecules. Third, it has been reported that the removal of dissolved oxygen by sodium sulfite becomes more difficult as the surfactant concentration increases (*16*). Also, there are more possibilities of RTP quenching by impurities in the SDS at higher SDS concentration.

MS-RTP Lifetimes of Polyaromatic Hydrocarbon Molecules. The MS-RTP lifetimes of PAHs were measured at room temperature. The MS-RTP lifetimes of selected PAHs under optimum conditions are shown in Table I. These MS-RTP lifetimes are considerably longer than other reported

Table I. MS-RTP Lifetimes of Selected Arenes

compound	wavelength, nm excitation	emission	lifetime,[a] ms
naphthalene	290	511	1.05 ± 0.07
2-bromonaphthalene	293	527	0.82 ± 0.08
biphenyl	280	475	1.12 ± 0.07
pyrene	337	595	7.81 ± 0.05

[a] All sample concentrations were 5×10^{-5} M, [SDS] = 0.05 M, $[Na_2SO_3]$ = 0.02 M, and $[TlNO_3]$ = 0.025 M. Above lifetimes were calculated with the linear least-squares method and correlation coefficients were above 0.998 in all cases.

Table II. Effect of Temperature on RTP of Pyrene

temp, °C	RTP intensity	RTP lifetime,[a] ms
15	656	6.02 ± 0.03
20	590	5.36 ± 0.04
25	532	5.02 ± 0.04
30	502	4.93 ± 0.06
35	468	4.89 ± 0.06

[a] Sample solutions were deoxygenated with 0.02 M sodium sulfite; concentrations of SDS and Tl^+ were 0.05 and 0.035 M, respectively: excitation wavelength 337 nm, emission wavelength 595 nm.

lifetime values. Cline Love et al. (*18*) reported MS-RTP lifetimes of selected PAHs. Their reported values for several compounds rarely exceed 1.2 ms. On the other hand, Kalyanasundaram et al. (*19*) observed much longer MS-RTP lifetimes of several PAHs in various surfactant solutions. Their reported MS-RTP lifetime values lie in the 1.2–20 ms range, which are, in some cases, much longer than our values (*20*). The differences in MS-RTP lifetimes among different systems indicate that RTP lifetimes are extremely sensitive to environmental conditions. The concentrations of dissolved oxygen and heavy atom, the temperature, and the presence of impurities in the sample solution can directly affect the observed RTP lifetime.

The effect of temperature on MS-RTP intensities and lifetimes was investigated. The RTP intensity of pyrene decreased by 29%, and the RTP lifetime also decreased by 19% from 6.02 to 4.89 ms as the temperature increased from 15 to 35 °C as shown in Table II. Although temperature variations will be under 10 °C in most cases, the changes in RTP intensity and RTP lifetimes of compounds are still significant. Therefore, temperature control of the sample solution seems to be necessary for accurate and consistent RTP data.

Heavy Atom Effect on MS-RTP Lifetimes. The use of external heavy atoms to increase phosphorescence yield has become a common practice in RTP. The interactions between the heavy atoms and the sample molecules frequently result in an increase in the phosphorescence quantum yield and a corresponding decrease in the fluorescence yield. Also, the observed phosphorescence lifetimes with heavy atoms are usually shorter than those without heavy atoms. As a result, RTP lifetimes of many PAHs may vary significantly depending on the concentration of heavy atoms used.

The effect of the external heavy atom on the RTP lifetime was investigated by using thallium ions as the heavy atom source. The RTP intensity and lifetime of pyrene were measured with various amounts of thallium ion concentrations. The RTP intensity increased up to 0.06 M thallium ion concentration as shown in Figure 3. At concentrations higher than 0.06 M thallium, precipitation occurred in the solution. On the other hand, the RTP lifetimes of pyrene decreased continuously up to 0.05 M thallium concentration. The same trend was observed with naphthalene even though the RTP

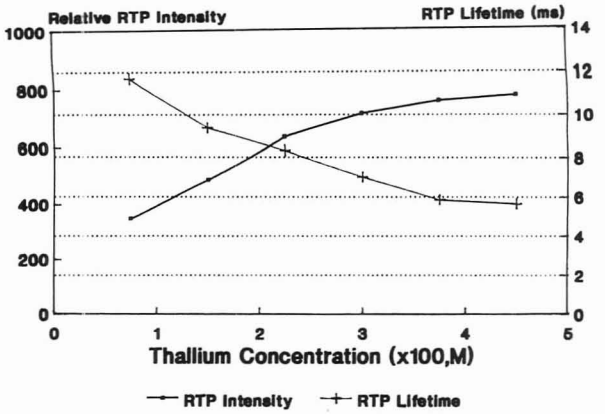

Figure 3. Heavy atom (Tl^+) effect on MS-RTP intensity and MS-RTP lifetime of pyrene: [pyrene] = 5×10^{-5} M, [SDS] = 0.05 M, $[SO_3^{2-}]$ = 0.02 M; excitation 337 nm, emission 595 nm.

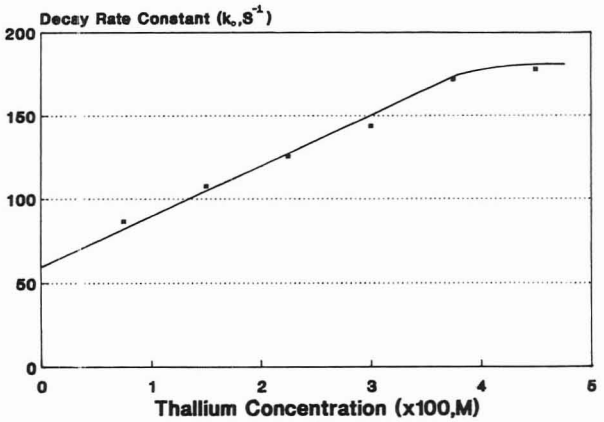

Figure 4. Plot of observed decay rate constant of pyrene versus heavy atom (Tl^+) concentration in SDS micellar solution: [pyrene] = 5×10^{-5} M, [SDS] = 0.05 M, $[SO_3^{2-}]$ = 0.02 M; excitation 337 nm, emission 595 nm.

lifetimes were rather unstable at lower heavy atom concentrations. The use of silver ion instead of thallium as external heavy atom did not work in this system due to the very low solubility of Ag_2SO_3, which was formed by the reaction of dissolved silver ions and sulfite ions.

It was found that the decrease in RTP lifetime is a function of heavy atom concentration. The plot of reciprocal lifetime, k_o, versus thallium ion concentration was linear (Figure 4) as is expected from eq 12. In eq 12, the reciprocal of lifetime is a function of the concentrations of micelle and heavy atom. If the concentration of micelle is fixed in a given system, then rate constant k_0 mainly depends on $k_{mh}[H]$ and $k_h[H]$ terms. It is expected that reaction rate constant k_{mh} of excited triplet molecule with heavy atom at micellar surface should be much larger than k_h because micelles and heavy atoms have opposite polarity in most cases. Therefore, eq 12 can be simplified as a linear function of $k_{mh}[H]$. Also, as the concentrations of heavy atom increases, micelle surface will become saturated to give $k_{mh}[H]_s$, which will yield a plateau value. From the slope and intercept of the plot, k_{mh} and $k_{mp} + k'$ were found to be 2560 and 65, respectively. Sulfite ions are known to form light-absorbing complexes with thallium ions in micellar solutions (*21*), particularly at wavelengths below 275 nm. It is not clear whether Tl^+–sulfite complexes quench the triplet state of molecules as well as attenuate the exciting radiation. It is also possible that triplet molecules may have multiple collisions with heavy atoms during their relatively long lifetimes. However, it may not be reasonable to call heavy atoms triplet quenchers since increased phosphorescence yield is observed with heavy atoms. It may be more reasonable to say that heavy atoms affect triplet states by other mechanisms (*22–24*).

It is well-known that heavy atoms reduce phosphorescence lifetimes through spin–orbital interactions (*25*). The spin and orbital motions of the electrons are not independent, even in atoms with very small nuclear charge. The orbital motion of the electron induces a magnetic field that interacts with its spin magnetic momentum. This spin–orbital interaction leads to a change in the direction of the spin–angular momentum of an electron, thereby changing a singlet state into triplet state, and vice versa.

The external heavy atom effect may take place in two ways: one, by a complex formation with the heavy atom, and another, by a long range interaction through a statistical distribution of the heavy atoms around the phosphorescing molecule (*26*). It has been shown that the rate constants of both $S_1 \rightarrow T_1$ and $T_1 \rightarrow S_0$ processes are increased (*27*). This is evident from the reduced RTP lifetimes of the probe molecules at high heavy atom concentrations. Furthermore, it has also been demonstrated that the $T_1 \rightarrow S_0$ radiationless transition is only slightly enhanced and the observed reduction in the triplet lifetimes is mainly due to an increase in the radiative transition probability (*28*).

While various mechanisms to explain the enhanced spin–orbital interaction and the reduced triplet lifetime have been proposed, they are still not well understood (*29*). The various schemes that have been previously proposed share a common factor in that the singlet state is ultimately responsible for introducing reduced phosphorescence lifetimes. That is, the triplet state of the emitting molecule is mixed with the singlet state of another molecule. The source of the singlet state can be the same molecule (*30*), the perturber (*31*), or a charge transfer state of the molecule–perturber complex (*32*).

CONCLUSIONS

The RTP lifetimes of PAHs in micellar solution are a function of various environmental factors. Major contributors to the magnitude of the observed RTP lifetimes are the nature and concentration of the external heavy atoms used. Also, the method of deoxygenation and solution temperature affect observed RTP lifetimes significantly. This results in different RTP lifetimes under different experimental conditions, which is undesirable from an analytical point of view. Therefore, it is necessary to carefully analyze observed RTP lifetimes according to the system employed to correctly interpret RTP lifetime data. The proposed triplet decay model clearly indicates that external heavy atoms along with triplet quenchers affect observed RTP lifetimes significantly.

It is recommended that the use of other constants such as k_{mp} or k_{mh} instead of RTP lifetimes will give a more valid criterion in identifying different compounds in MS-RTP. Although k_{mp} cannot be calculated directly, k_{mh} can be obtained from the slope of the plot of k_o versus [H]. The observed MS-RTP lifetimes may vary drastically depending on the experimental conditions employed, but the triplet decay rate constant (k_{mp}) and reaction rate constant (k_{mh}) with heavy atoms in the micelle should give more consistent values.

LITERATURE CITED

(1) Turro, N. J.; Liu, K. C.; Chow, M. F.; Lee, P. *Photochem. Photobiol.* **1978**, *27*, 523.
(2) Thomas, J. K. *Acc. Chem. Res.* **1977**, *10*, 133.
(3) Cline Love, L. J.; Skrilec, M.; Habarta, J. G. *Anal. Chem.* **1980**, *52*, 754.
(4) Cline Love, L. J.; Habarta, J. G.; Dorsey, J. G. *Anal. Chem.* **1984**, *56*, 1132A.
(5) Winefordner, J. D. *Acc. Chem. Res.* **1969**, *2*, 361.
(6) Bacon, J. R.; Demas, J. N. *Anal. Chem.* **1983**, *55*, 653.
(7) Schulman, E. M.; Walling, C. *Science* **1972**, *178*, 53.
(8) Hurtubise, R. J. *Solid Surface Luminescence Analysis: Theory, Instrumentation, Applications*; Marcel Dekker: New York, 1981.
(9) Ward, J. L.; Walden, G. L.; Winefordner, J. D. *Talanta* **1981**, *28*, 201.
(10) Scharf, G.; Smith, B. W.; Winefordner, J. D. *Anal. Chem.* **1985**, *57*, 1230.
(11) Nithipatikom, K.; Pollard, B. D. *Appl. Spectrosc.* **1985**, *39*, 109.
(12) Almgren, M.; Grieser, F.; Thomas, J. K. *J. Am. Chem. Soc.* **1979**, *101*, 279.
(13) Infelta, P. P.; Gratzel, M.; Thomas, J. K. *J. Phys. Chem.* **1974**, *78* (2), 190.
(14) Cline Love, L. J.; Habarta, J. G.; Skrilec, M. *Anal. Chem.* **1981**, *53*, 437.
(15) Bolt, J. D.; Turro, N. J. *J. Phys. Chem.* **1981**, *85*, 4029.
(16) Diaz Garcia, M. E.; Sanz-Medel, A. *Anal. Chem.* **1986**, *58*, 1436.
(17) Cline Love, L. J.; Habarta, J. G.; Dorsey, J. G. *Anal. Chem.* **1984**, *56*, 1132A.
(18) Skrilec, M.; Cline Love, L. J. *Anal. Chem.* **1980**, *52*, 1559.
(19) Kalyanasundaram, K.; Grieser, F.; Thomas, J. K. *Chem. Phys. Lett.* **1977**, *51*, 501.
(20) Kraus, Paul. Ph.D. Thesis, Department of Chemistry, Michigan State University, 1987.
(21) Nugara, N. E.; King, A. D., Jr. *Anal. Chem.* **1989**, *61*, 1431.
(22) Lin, K. C.; Lin, S. H. *Mol. Phys.* **1971**, *21*, 1105.
(23) Giachina, G. G.; Kearns, D. R. *J. Chem. Phys.* **1970**, *52* (6), 2964.
(24) Tsubomura, H.; Mulliken, R. S. *J. Am. Chem. Soc.* **1960**, *82*, 5966.
(25) McGyynn, S. P.; Sunseri, R.; Christodouleas, N. *J. Chem. Phys.* **1962**, *37*, 1818.
(26) Ebara, N.; Yajima, Y.; Watanabe, H. *Bull. Chem. Soc. Jpn.* **1979**, *52*, 2866.
(27) Humphry-Baker, K. R.; El-Sayed, M. A. *Chem. Phys. Lett.* **1978**, *58*, 207.
(28) Eisenthal, K. R.; El-Sayed, M. A. *J. Chem. Phys.* **1965**, *42*, 794.
(29) Chaudhurl, N. K.; El-Sayed, M. A. *J. Chem. Phys.* **1965**, *42*, 1947.
(30) Isubomura, H.; Mulliken, R. S. *J. Am. Chem. Soc.* **1966**, *82*, 5966.
(31) Hoijtink, G. J. *Mol. Phys.* **1960**, *3*, 67.
(32) Murrel, J. N. *Mol. Phys.* **1960**, *3*, 319.

RECEIVED for review May 30, 1990. Accepted July 31, 1990.

Anal. Chem. 1990, 62, 2370-2376

Figures of Merit for Furnace Atomization Plasma Emission Spectrometry

R. E. Sturgeon,* S. N. Willie, V. Luong, and S. S. Berman

Division of Chemistry, National Research Council of Canada, Ottawa, Ontario, Canada K1A 0R9

Analytical figures of merit for nine elements (viz. Ag, Cd, Pb, Ni, Be, Fe, Bi, Cu, and P) are presented that serve to broadly characterize the furnace atomization plasma emission spectrometry technique. Detection power lies in the low picogram region; precision of replicate signals obtained with injection of samples by hand ranges from 2.2 to 12.1% relative standard deviation and the linear range of calibration spans 2–4 orders of magnitude. Relative sensitivities of alternative atom and ion lines are given for each element. Sufficient energy is available to efficiently detect analyte ion lines having excitation energies of up to 13 eV. Static and dynamic background spectra are presented which reveal broad-band contributions from molecular species such as CO, N_2, NO, and OH as well as atom lines from the He support gas.

Although widely recognized as an atomizer for atomic absorption, the graphite furnace (GF) has also been successfully utilized as an emission source for thermal excitation of atomic vapor (*1*, *2*). Unfortunately, the relatively low temperatures attained preclude detection of elements having emission lines with excitation potentials much greater than 4.5 eV (*2*). This problem can be partially circumvented by relying on the high sample vaporization efficiency of the GF as a means of introducing analyte vapor into hotter excitation sources, such as the inductively coupled plasma (*3*). With these processes decoupled, such tandem devices provide a promising means of achieving relatively efficient yet independent optimization of both sample introduction/atomization and analyte excitation.

A somewhat more advantageous arrangement is a combined source, wherein a single device permits retention of independent control over these two processes. Falk et al. (*4*) have earlier addressed the advantages of the low pressure FANES (furnace atomic nonthermal excitation spectrometry) system, which combines the attractive thermal vaporization attributes of the GF with nonequilibrium excitation in a hollow cathode discharge for high multielement detection power. Subsequently, Ballou et al. (*5*) described a low pressure hollow anode plasma source, also based on a GF (anode) but containing a coaxially centered graphite rod (cathode) extending the length of the tube. Although work with this hollow anode based FANES system appears equally promising (*5*), both sources suffer from the need to operate at low pressures (<200 Torr) such that analyte residence times are reduced and sample introduction is more complex.

Establishment of an atmospheric pressure radio frequency (rf) He plasma inside a GF containing a coaxially placed graphite rod antenna has recently been described (*6–8*) and its analytical utility demonstrated for real samples (*9*). This FAPES (furnace atomization plasma emission spectrometry) system offers the full advantage of such a coupled source in that the GF is operated at atmospheric pressure (permitting straightforward sample introduction) and independent analyte excitation occurs in the rf plasma. To date, little information is available characterizing analyte emission with FAPES. This study was undertaken to broadly assess the analytical performance of this novel source in that figures of merit (limits of detection, sensitivity, precision and linear range) for several elements as well as associated background spectra are presented and compared with those available with the FANES technique.

* To whom correspondence should be addressed.

Table I. Instrumentation and Operating Conditions

plasma power	50–75 W, 13.56-MHz Model RFX-600 solid-state rf generator (Advanced Energy Ind., Ft. Collins, CO)
impedance match	Heathkit Model SA 2060A antenna tuner
graphite furnace	modified Perkin-Elmer HGA-2200; pyrolytic graphite coated electrographite tubes; Ar external gas at 1 L/min; He internal purge gas at 200 mL/min
optics	0.5-m Varian monochromator (Springvale, Australia) equipped with Hamamatsu R446 PMT operated at −600 V; nominal spectral bandpass of 0.082 nm FAPES source focused with $f/2$ lens, imaging the space between the wall and center electrode, incandescent tube wall emission masked
wavelength calibration	hollow cathode lamps operated at dc via a Kepco Model HB2AM power supply (Flushing, NY)
data aquisition	12-bit digitization, 8000 points per scan processed in Turbo Pascal (version 4.0, Borland International) using in-house software and an IBM AT PC

EXPERIMENTAL SECTION

Apparatus. A brief summary of instrumentation and operating parameters is presented in Table I. The FAPES workhead, based on a Perkin-Elmer Model HGA-2200 GF, has been described in detail earlier (*8*, *9*). A 13.56-MHz rf He plasma is supported inside the graphite tube. An internal He gas flow rate of 200 mL/min was used for all measurements. An external Ar sheath gas was maintained at a flow rate of 1 L/min. All signals were digitised with 12-bit resolution and acquired at rate of 8000 points per transient (irrespective of the sampling period).

Reagents. Stock solutions (1000 mg/L) were prepared by dissolution of the high-purity metals (Cd, Pb, Cu, Fe, Bi, Ni, Be, Ag) or their salts ($(NH_4)_2HPO_4$). Working standards were obtained by dilution of the stocks with high-purity deionized distilled water (DDW) acidified to 1% (v/v) with quartz sub-boil distilled HNO_3 (Ag, P, Pb, Cd, Cu, Bi, Ni,) or HCl (Fe and Be).

Procedure. All wavelengths were tuned to the appropriate resonance lines by using hollow cathode lamps. For P I, a Co hollow cathode lamp was used to locate the lines of interest at 253.6, 255.3, and 213.6 nm. An Fe lamp was used to peak in the P II 525.3-nm line.

Compromise analytical conditions were selected for study in that a forward plasma power of 50 W (3–4 W reflected power at 300 K) and a nominal spectral bandwidth (SBW) of 0.082 nm were used. The effect of forward plasma power on analyte response

0003-2700/90/0362-2370$02.50/0 Published 1990 by the American Chemical Society

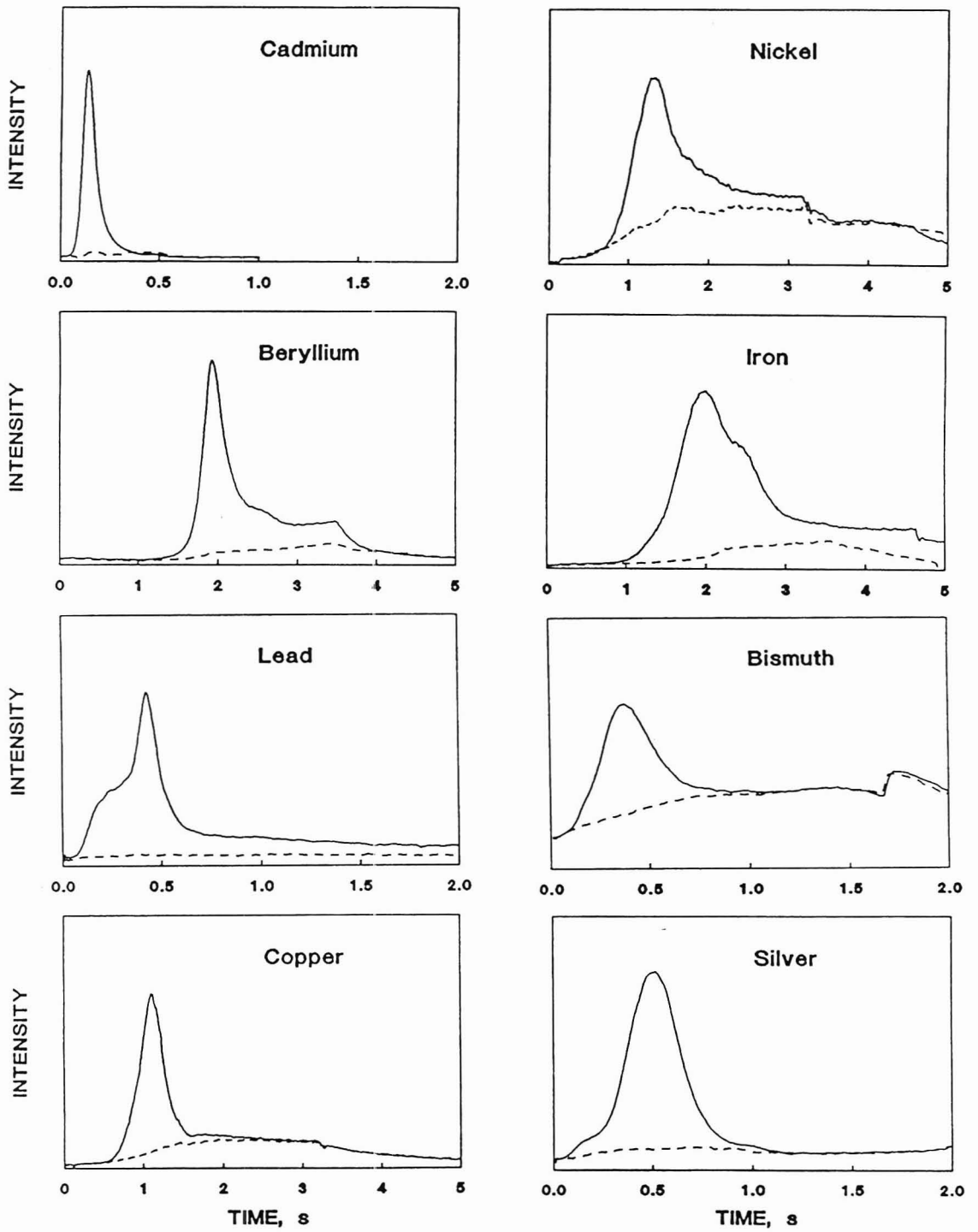

Figure 1. Time-resolved analyte emission transients: (—) analyte response, (---) background; Cd, 250 pg, 228.8 nm; Ni, 5 ng, 232.0 nm; Be, 500 pg, 234.8 nm; Fe, 5 ng, 248.3 nm; Pb, 2.5 ng, 283.3 nm; Bi, 500 pg, 306.7 nm; Cu, 500 pg, 324.8 nm; Ag, 50 pg, 328.1 nm.

was also examined. Atomization conditions were not exhaustively studied and thus should not be considered as optimum. These are presented in Table II. No matrix modifiers were used with the result that char temperatures are relatively low.

Analytical figures of merit (sensitivity, detection limit, precision, linear range) were obtained for each element and at least one alternative line as well as an ion line were studied in order to determine relative sensitivities. Samples (5-μL volume) were dispensed into the furnace by hand through a Hamilton syringe fitted with a short length of Teflon tubing and dried at a temperature of 110 °C for 30 s. Following a 15-s char stage, the rf power was applied and the plasma spontaneously ignited. After a further 5-s stabilization period the high-temperature atomization stage was activated, the emission transient recorded, the furnace subjected to a high temperature cleanout cycle, and the plasma extinguished. For P, the furnace was briefly cooled to room temperature after the char stage. The plasma was allowed to self-ignite only during the high-temperature atomization ramp. Attempts to ignite the plasma during the char stage resulted in significant loss of this element from the analysis volume prior to atomization.

Blank signals were recorded for each analyte line wherein 5-μL volumes of 1% HNO_3 or HCl in DDW was pipetted into the furnace and atomized.

A wavelength scan from 200 to 700 nm was recorded in order to characterize the background emission from a "clean" plasma operating at 50-W forward power and at a furnace temperature of 500 K. Shorter wavelength scans, covering an interval of ±1.0 nm centered about the line of study were also obtained.

RESULTS AND DISCUSSION

Typical examples of the emission signal transients from the elements studied are presented in Figures 1 and 2. Also given are the associated blank signals characterizing the response

Table II. Furnace Program[a]

element	temperature, °C	
	char	atomization
Ag	500	2700
Be	500	2700
Bi	250	2700
Cd	180	1100 (mp)
Cu	700	2300 (mp)
Fe	600	2500
Ni	800	2700 (mp)
P	300	1600 (mp)
Pb	250	1100 (mp)

[a] Temperatures refer to setting on the power supply and were not measured: dry 110 °C, 5-μL sample in 1% HNO_3, except Be and Fe (1% HCl); plasma power, 50 W; He flow, 200 mL/min; nominal SBW, 0.082 nm.

from DDW. These signals are similar to those observed with graphite furnace atomic absorption spectroscopy (GFAAS) in terms of their general shape and half-width although residence times are somewhat shorter because of more rapid diffusive loss of the analyte in a flowing He atmosphere as compared to the usual stagnant Ar gas used for absorption measurements.

Estimated appearance temperatures for all elements except P are in reasonable agreement with those published in the GFAAS literature. For P, an estimated appearance temperature of 950 K is 400–500 K lower than expected (*10*). This suggests that P atoms arise from plasma-induced dissociation of volatile molecular P containing species and also accounts for the loss in sensitivity (due to plasma induced heating) for this element if the plasma is permitted to burn prior to sample atomization.

The early appearance of signals from Cd, Pb, Bi, and P suggests that use of chemical modifiers or atomization from a platform would serve to favorably delay their release into the plasma, with corresponding benefits commensurate with those observed in GFAAS, i.e., improved sensitivity and reliability of measurement. In the case of P, this would also allow increased time for the plasma background to stabilize before the signal evolved (cf. Figure 2).

Introduction of Fe and Be in 1% HCl resulted in an increased sensitivity (2-fold) over that obtained in a 1% HNO_3, as well as improved precision.

In the absence of the plasma, atomization of these elements produced no measurable emission response, indicating that thermal excitation by the hot wall plays no role in the production of the signal. Sputtering of the analyte by the He plasma is expected to be very inefficient because of the low mass of He.

Figure 3 illustrates the effect of forward plasma power on net analyte response. As power increases there is a corresponding increase in analyte emission intensity, in both peak height and area. The interesting feature is the temporal displacement of the position of peak intensity for Cd and Cu as the incident power changes. Similar early shifts were observed for Cu, Ni, and Be whereas no shifts were evident with Fe, Pb, P, and Bi. This effect must be related in some manner to the increased plasma volume and density which occurs with increased rf power, more efficient excitation via electron collision, possible changes in the actual observation zone, and reduced self-absorption in the larger, hotter plasma. Beyond this simple mention, however, a comprehensive explanation as to why the peak intensities for some elements shift earlier in time whereas others move later or not at all remains elusive.

Plasma Background. There are numerous potential sources of background in this emission source: continuous radiation from free–free and free–bound electrons, stray light,

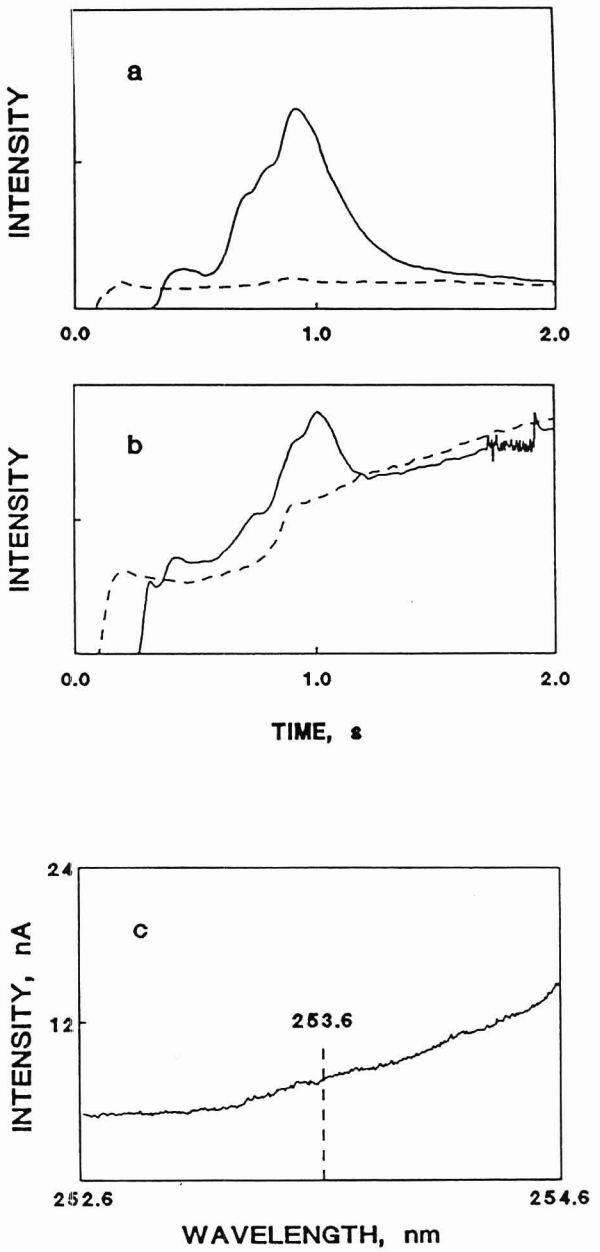

Figure 2. Signal transients and background spectra for phosphorus: (a) 2.5 ng, P I 253.6 nm; (b) 5 μg, P II 525.3 nm; (c) background wavelength scan: 50 W plasma, 0.082 nm SBW, furnace at 700 K.

quasi-continua from line wings, molecular bands from the discharge gas impurities or from reaction products between such impurities and sample constituents, spectral lines emitted by free atoms or ions of the discharge gas and its impurities, spectral lines emitted by free atoms or ions of the concomitants of the sample, and blackbody radiation from the atomizer tube wall. The majority of these sources is active in contributing to the background observed in the FAPES source. A wavelength scan covering the spectral interval 200–700 nm is presented in Figure 4. This scan was obtained at a furnace temperature of 700 K and a forward plasma power of 50 W. A highly structured background is evident in the region 200–500 nm, containing intense molecular bands arising from CO, NO, OH, and N_2 as well as intense lines from He I. Bands arising from the fourth positive system of CO have not been labeled on Figure 4a in an effort to keep the congestion of information to a minimum. However, the following band heads are evident: (3,10), (4,11), (5,12), (3,11), (6,14), (7,15), (4,13), (8,16), and (7,16) at 204.6, 206.8, 209.0, 212.8, 219.7, 222.2, 223.8, 224.7, 231.2 nm, respectively. The highly structured feature centered at 283 nm reflects both OH as well

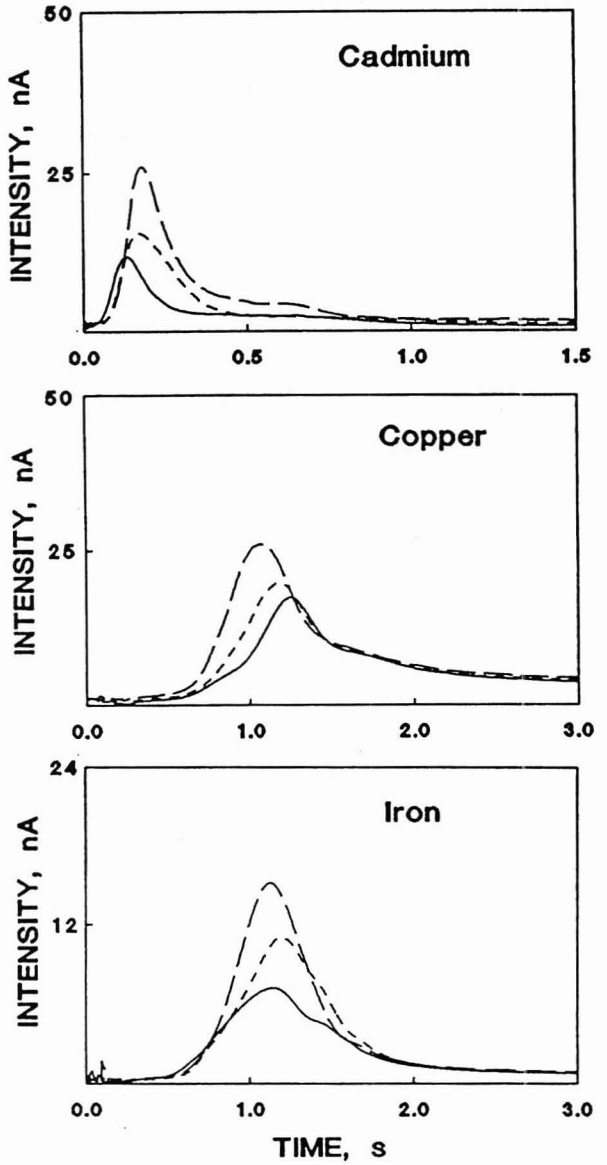

Figure 3. Effect of forward plasma power on signal intensities: (—) 50 W, (---) 60 W, (– –) 75 W; Cd, 250 pg; Cu, 500 pg; Fe, 5 ng.

as the presence of other additional (unidentified) species. Beyond 500 nm, the plasma background is relatively structureless and, with the exception of some discharge gas lines, the few features evident in Figure 4e have not been identified. The molecular bands arise predominantly from impurities in the He gas and from ingress of ambient atmosphere into the furnace through the sample introduction port (*11*, *12*).

Dynamic background signals arising from the "atomization" of acidified DDW blanks are illustrated in Figures 1 and 2. Two cases can be discerned: a relatively flat background that is associated with the more volatile elements and a background that increases with time, eventually achieving a plateau. This latter feature is characteristic of the less volatile elements that atomize at elevated temperature (Ni, Be, Fe, Cu) when blackbody continuum from the hot furnace wall reaches the detector. Such a continuum photon flux is orders of magnitude greater than that arising from the plasma continuum itself (*4*). An efficient optical mask will significantly reduce this problem.

Figures 2 and 5 illustrate the structure of the static background in the neighborhood of the analytical lines selected (±1.0 nm). These wavelength scans were obtained with the furnace set at the appropriate char temperature used for each element (cf. Table II). It is obvious that there is highly structured background in the vicinity of many of the analysis

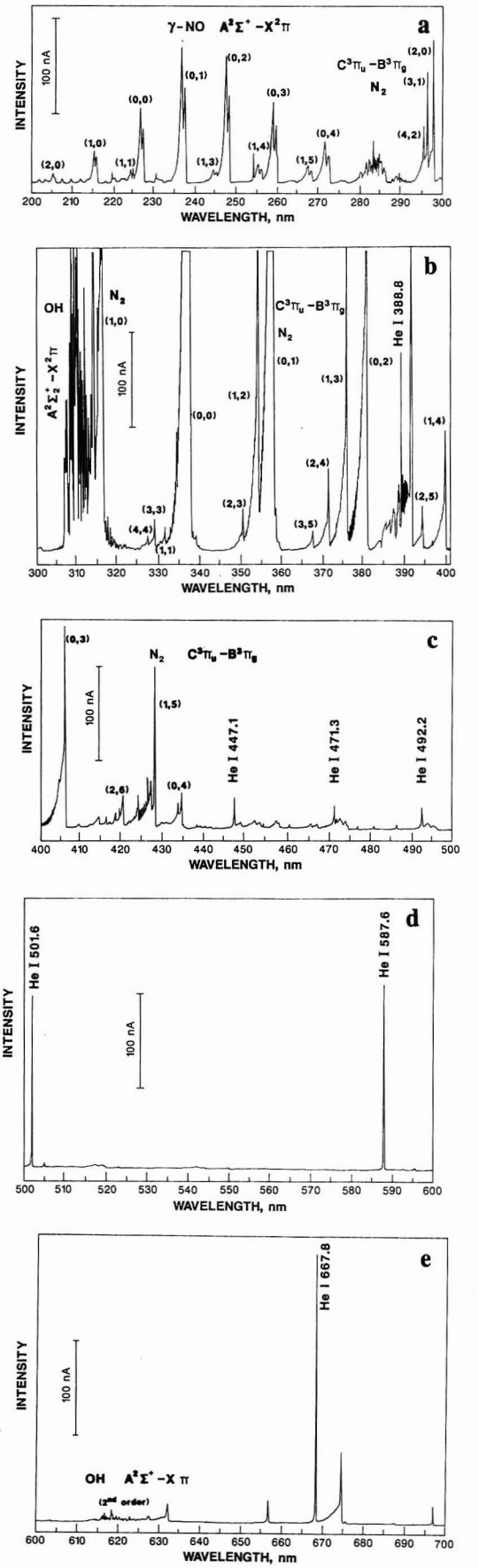

Figure 4. Plasma background in the 200–700 nm region: 50 W plasma; 0.082 SBW; furnace at 700 K.

lines: NO bands near lines for Cd, Fe, and Be; CO bands near Ni and OH bands near Bi and Pb. Although the intensities of these structures are quantitatively presented in these figures, they refer to conditions prevailing at the char temper-

Table III. Absolute Detection Limits, pg

element	λ, nm	FAPES[a] peak	FAPES[a] area	FANES peak
Ag	328.1	1.2	4.8	
	320.1			4.0
Be	234.8	5.0	16	
Bi	306.7	25	55	45
Cd	228.8	2.0	6.8	2
Cu	324.8	4.9	14	1.5
Fe	248.3	50	51	6.8
	302.1			0.7
Ni	232.0	164	405	
	341.5			2.3
P	253.6	94	152	
	214.9			210
Pb	283.3	21	46	12

[a] LOD based on $3\sigma_b$ criterion where σ_b is the estimate of the SD of repetative measurements of the blank.

ature. It can be experimentally seen that the intensities of the NO bands decrease dramatically as the temperature of the furnace increases while there is a corresponding increase in the intensities of the CO bands. This simply reflects the increasingly reducing atmosphere within the furnace as the temperature rises (*11*, *12*). Cleanup of the He gas and enclosure of the furnace in a more efficient housing to eliminate ingress of ambient atmosphere, such as that described by Ballou et al. (*5*), should significantly reduce molecular background and permit access to elements having sensitive emission lines in the 305–320 nm (Al, Mo, V) and 350–360 nm (Cr, U) regions.

It is evident that use of a high-resolution spectrometer and efficient transfer optics coupled with rapid dynamic background correction should eliminate many potential spectroscopic problems that may be encountered with the present system.

Figures of Merit. Table III compares absolute limit of detection (LOD) for the FANES system with those obtained in this study by FAPES. The former data are compiled from the work of Littlejohn (*13*). The LOD for the FAPES system is based on the $3\sigma_b$ criterion where σ_b is the estimate of the standard deviation of repetitive measurements of the background or blank signal. No information is given in ref 13 as to the manner in which the FANES LOD is calculated. In general, detection power lies in the picogram range and compares favorably with those data reported for the FANES system. Room for significant improvement in these data is expected with use of more efficient transfer optics, dynamic background correction, a high-resolution spectrometer, chemical modifiers, and an isothermal furnace such as that described by Frech et al. (*14*).

Of the several lines for each element that were investigated, those reported in Table III resulted in the best detection limits. Peak height quantitation was found to result in LOD's superior to those obtained with signal integration, particularly for the more volatile elements possessing small signal half-widths. It is noteworthy that nonmetals such as P can be detected with the FANES and FAPES systems. In the present case, the LOD reported for P is superior to the best values obtained from either GFAAS, i.e., 3000 pg (*15*), or FANES, i.e., 150 pg (*16*).

Table IV summarizes the sensitivities of the elements in terms of absolute response per nanogram for both peak height (nanoamperes) and area (nanoamperes seconds); Table V gives the precision of replicate measurements and approximate linear range of calibration curves. Precision is largely determined by the repeatability of injection of samples into the furnace by hand. Evidently, a precision as good as 2% relative

Table IV. Sensitivity[a]

element	peak height, nA/ng	peak area, nA·s/ng
Ag	370	120
Be	89	37
Bi	46	15
Cd	51	7.4
Cu	45	16
Fe	4.4	4.3
Ni	3.1	2.1
P	71	36
Pb	4.7	1.1

[a] Data obtained under conditions given in Tables I and II.

Table V. Precision and Linear Range[a]

	precision, %		log (linear range)	
	peak	area	peak	area
Ag	9.4	6.0	3.9	3.3
Be	2.2	2.2	3.3	2.8
Bi	6.5	7.7	3.3	3.0
Cd	7.5	3.5	4.4	4.5
Cu	2.3	2.5	2.9	2.1
Fe	5.8	3.7	4.4	4.3
Ni	2.5	4.0	2.0	1.6
P	12.1	12.5	1.7	1.7
Pb	7.7	3.5	2.4	2.7

[a] Precision expressed as % RSD for $n > 8$ at concentrations 10–100-fold estimated LOD.

Table VI. Plasma Gas Lines

line, nm	excitation energy, eV	rel sens
He I 667.8	23.07	1.0
He I 587.6	23.06	0.70
He I 501.6	23.08	0.64
He I 492.2	23.72	0.07
He I 471.3	23.58	0.06
He I 447.1	23.72	0.11
He I 388.9	23.00	0.57

standard deviation can be achieved for this operation since this was attained for Be and Ni. Relatively poor precision is seen with volatile elements, possibly reflecting variable preatomization losses of molecular species (particularly P) and any instability in the plasma which occurs during this early period of rapid heating of the furnace and expulsion of the internal gas. It is expected that these data could be improved with the use of chemical modifiers and/or atomization from a platform which would serve to shift the signals to higher temperatures.

The linear ranges of calibration curves are shorter than expected for an emission source and typically span only 3 orders of magnitude, not significantly greater than those for GFAAS. It is possible that self-absorption may limit the linear range in this system because of the extremely large temperature gradient that exists between the center and ends of the furnace (*17*). This shortcoming could be eliminated with the use of an isothermal integrated contact cuvette type of furnace (*14*). Alternatively, a higher powered plasma of expanded volume may extend the linear range, but this aspect was not investigated.

Analyte Excitation. Analyte excitation and ionization likely occur via electron impact. As noted earlier, no analyte emission was detected during sample atomization if the plasma was not on, thermal excitation being negligible. A number of intense He atom and ion lines were observed in a 50-W plasma. Their relative sensitivities are summarized in Table VI along with their corresponding excitation energies. Strong

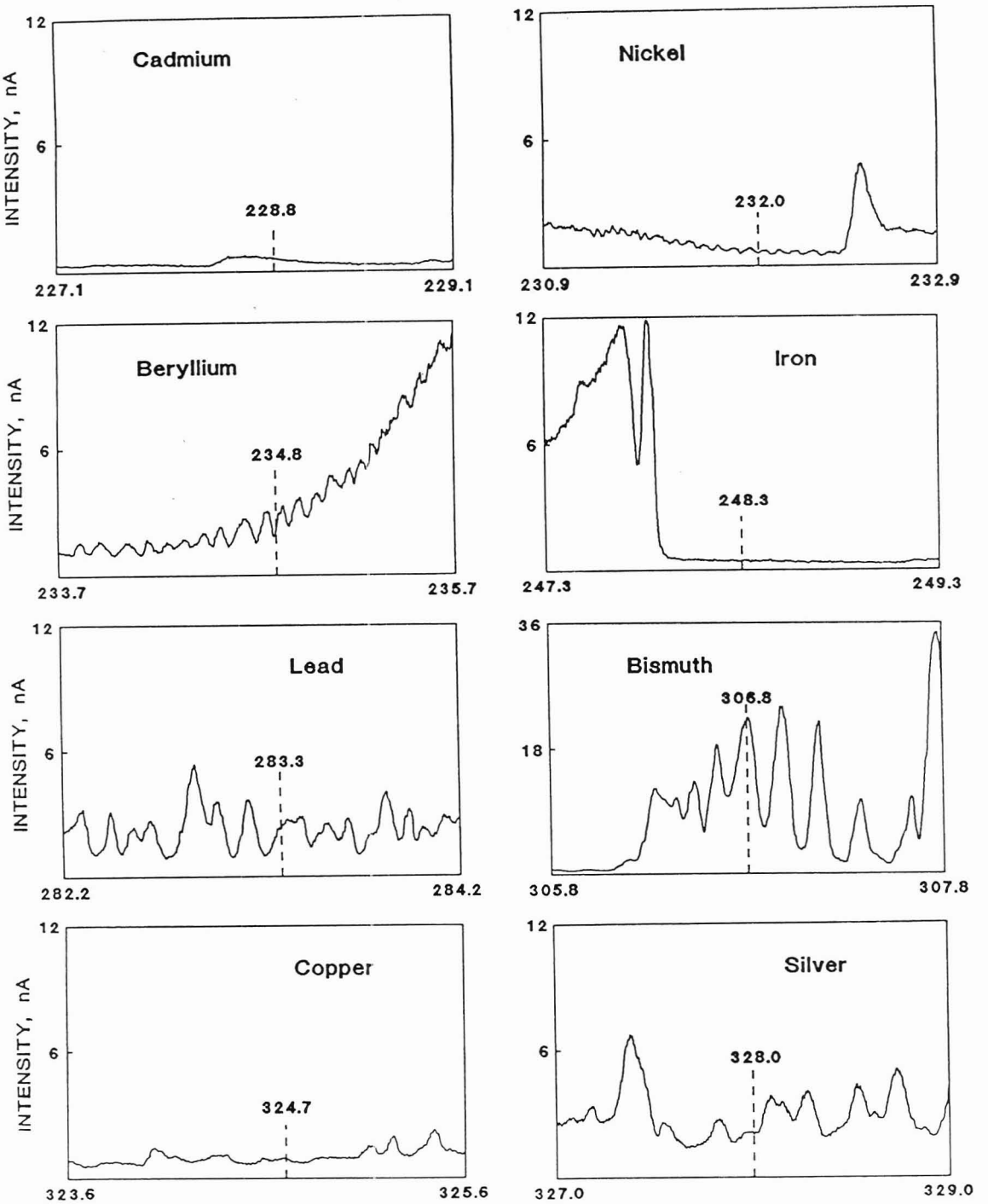

Figure 5. Wavelength scans covering ±1 nm about the analyte emission lines: 50 W plasma; 0.082 nm SBW; furnace temperature as given for each element in Table I (char temperature).

excitation of He should be indicative of strong analyte excitation. As the forward power to the plasma was increased from 50 to 75 W, the intensities of the He I 587.6- and 447.1-nm lines increased 3-fold. No study of the effect of internal He gas flow rate on the intensity of plasma gas lines was made. Although not possible to undertake with the present setup, it is expected that plasma gas line intensities will be markedly affected by the ambient pressure (*18*) and future investigations will be aimed at elucidating this.

Table VII presents a summary of the relative sensitivities of several alternative emission lines of each analyte. Also given are the relative sensitivities of these lines observed in an Ar inductively coupled plasma (ICP) (*19*). It is evident that sufficient energy is available in the He plasma to ionize and excite populations of a number of analytes, including nonmetals. In most cases, the alternative atom line is comparable in relative intensity to that observed in the ICP. However, large discrepancies are evident with ion line intensities, leading to the obvious conclusion that the degree of ionization of analytes is significantly lower in the FAPES source. The excitation temperature of the FAPES source has been measured (Boltzmann plot with both He I and Fe I thermometric species) to be 3200 ± 200 K (*20*).

The data in Table VII also point to the utility of utilizing the major compilations of wavelength tables that are available, such as Boumans' (*19*), to select appropriate analyte lines for measurement and take advantage of the wealth of information presented in this literature concerning potential spectroscopic interferences.

CONCLUSIONS

This study has demonstrated the analytical characteristics of the FAPES technique. Detection power is comparable to or better than that available with FANES and operation is

Table VII. Analyte Response[a]

line, nm	excitation energy, eV	relative sensitivity FAPES	relative sensitivity ICP[b]
Be I 234.8	5.28	1.0	0.48
Be I 249.5	7.68	0.03	0.05
Be II 313.0	13.28	0.95	1.0
Ag I 328.1	3.78	1.0	1.0
Ag I 338.3	3.66	0.30	0.49
Ag II 243.8	17.5	0.002	0.025
Ni I 232.0	5.54	1.0	0.64
Ni I 234.5	5.28	0.30	0.29
Ni II 221.6	14.56	0.05	1.0
Bi I 306.8	4.04	1.0	1.0
Bi I 223.1	5.55	0.05	0.93
Bi II 190.3	>7.29	6×10^{-5}	0.06
Cd I 228.1	5.41	1.0	0.88
Cd I 361.1	7.37	0.02	0.04
Cd II 214.4	14.77	2×10^{-4}	1.0
Cu I 324.8	3.82	1.0	1.0
Cu I 327.4	3.78	0.40	0.51
Cu II 224.7	13.23	2×10^{-3}	0.39
Pb I 283.3	4.40	1.0	0.51
Pb I 217.0	5.67	0.10	0.38
Pb II 220.4	14.67	5×10^{-3}	1.0
Fe I 248.3	4.99	1.0	
Fe I 372.0	3.32	0.41	
Fe I 302.1	4.11	0.27	
Fe II 238.2	13.07	0.04	
P I 253.6	7.21	1.0	
P I 255.3	7.18	1×10^{-3}	0.28
P I 213.6	7.18	0.05	1.0
P II 525.3	13.38	1×10^{-5}	

[a] Atomization and measurement conditions as given in Tables I and II. [b] From ref 19.

unencumbered by the need to establish a low-pressure discharge. Since furnace programming is similar, the cycle time per analysis is comparable to conventional GFAAS. Graphite tube lifetime is identical to GFAAS methodology and that of the center electrode is in excess of 200 cycles. Although the background spectrum exhibits many molecular bands, most of these can be eliminated or severely attenuated by working with a more enclosed furnace. The rapid signal transients that are developed require a fast response (<1 ms) detection system for accurate recording.

FAPES offers great latitude for use in both metal and nonmetal analyses and there are substantial data to suggest that the technique has considerable potential for future development. A number of improvements can be relatively easily implemented with this system that should have a significant impact on improving performance. These include analyte atomization from a platform and use of chemical modifiers, use of an isothermal integrated contact cuvette furnace, more efficient transfer optics, and imaging coupled to a high resolution spectrometer and dynamic background correaction (e.g., wavelength modulation). An improvement of 10–100-fold in LOD can be expected.

Future work must also consider the areas of plasma characterization and the influence of matrix concomitants (interferences) on analyte response. Work is presently in progress to address these issues.

LITERATURE CITED

(1) Littlejohn, D.; Ottaway, J. M. *Analyst* **1979**, *104*, 208.
(2) Bezur, L.; Marshall, J.; Ottaway, J. M.; Fakhrul-Aldeen, R. *Analyst* **1983**, *108*, 553.
(3) Crabi, G.; Cavalli, P.; Achilli, M.; Rossi, G.; Omenetto, N. *At. Spectrosc.* **1982**, *3*, 81.
(4) Falk, H.; Hoffmann, E.; Ludke, Ch. *Prog. Anal. Spectrosc.* **1988**, *11*, 417.
(5) Ballou, N. E.; Styris, D. L.; Harnly, J. M. *J. Anal. At. Spectrom.* **1988**, *3*, 1141.
(6) Liang, D. C.; Blades, M. W. *Spectrochim. Acta* **1989**, *44B*, 1059.
(7) Smith, D. L.; Liang, D. C.; Steel, D.; Blades, M. W. *Spectrochim. Acta* **1990**, *45B*, 493.
(8) Sturgeon, R. E.; Willie, S. N.; Luong, V. T.; Berman, S. S.; Dunn, J. G. *J. Anal. At. Spectrom.* **1989**, *4*, 669.
(9) Sturgeon, R. E.; Willie, S. N.; Luong, V. T.; Berman, S. S. *J. Anal. At. Spectrom.*, in press.
(10) Ohta, K.; Sugiyama, T.; Mizuno, T. *Analyst* **1990**, *115*, 279.
(11) Sturgeon, R. E.; Falk, H. *Spectrochim. Acta* **1988**, *43B*, 421.
(12) Sturgeon, R. E.; Siu, K. W. M.; Gardner, G. J.; Berman, S. S. *Anal. Chem.* **1986**, *58*, 42.
(13) Littlejohn, D. *Anal. Proc.* **1989**, *26*, 92.
(14) Frech, W.; Baxter, D. C.; Hutsch, B. *Anal. Chem.* **1986**, *58*, 1973.
(15) Slavin, W.; Carnrick, G. R.; Manning, D. C.; Pruszkowska, E. *At. Spectrosc.* **1983**, *4*, 69.
(16) Dittrich, K.; Fuchs, H. *J. Anal. At. Spectrom.* **1989**, *4*, 705.
(17) Welz, B.; Sperling, M.; Schlemmer, G.; Wenzel, N.; Marowsky, G. *Spectrochim. Acta* **1988**, *43B*, 1187.
(18) Evans, J. C.; Olsen, K. B.; Sklarew, D. S. *Anal. Chim. Acta* **1987**, *194*, 247.
(19) Boumans, P. W. J. M. *Line Coincidence Tables for Inductively Coupled Plasma Atomic Emission Spectrometry*; Pergamon Press: New York, 1976.
(20) Sturgeon, R. E.; Willie, S. N.; Luong, V.; Berman, S. S. Unpublished work, 1990.

RECEIVED for review May 2, 1990. Accepted July 26, 1990.

Oxygen Optrode for Use in a Fiber-Optic Glucose Biosensor

Maria C. Moreno-Bondi[1] and Otto S. Wolfbeis*

Analytical Division, Institute of Organic Chemistry, Karl-Franzens University, 8010 Graz, Austria

Marc J. P. Leiner and Bernhard P. H. Schaffar

AVL-List GmbH, Biomedical Division, Kleist-Strasse 48, 8020 Graz, Austria

An optical fiber oxygen sensor, based on the dynamic quenching of the luminescence of tris(1,10-phenanthroline)-ruthenium(II) cation by molecular oxygen, is presented. The complex is adsorbed onto silica gel, incorporated in a silicone matrix possessing a high oxygen permeability, and placed at the tip of the optical fiber. Oxygen has been monitored continuously in the 0–750 Torr range, with the detection limit being as low as 0.7 Torr. The device has been applied to the development of a fast responding and highly sensitive fiber-optic glucose biosensor based on this highly sensitive oxygen transducer. The sensor relates oxygen consumption (as a result of enzymatic oxidation) to glucose concentration. The enzyme is immobilized on the surface of the oxygen optrode; carbon black is used as an optical isolation in order to prevent ambient light and sample fluorescence to interfere. Measurements have been performed in a flow-through cell in air-equilibrated glucose standard solutions of pH 7.0. The effects of enzyme immobilization procedures (including enzyme immobilization on carbon black) as to response times (around 6 min), analytical ranges (0.06–1 mM glucose), reproducibility in sensor construction, and long-term stability have been studied as well.

INTRODUCTION

Given the widespread demand for glucose sensing devices, the development of glucose biosensors displaying the required sensitivity, long-term stability, and fast response has been a main target in sensor research during the last few years. Glucose sensing devices can be divided into three main classes, namely the electrochemical, optical, and enthalpy sensors (*1*, *2*). In most cases, the sensing scheme includes the use of glucose oxidase (GOx), an enzyme catalyzing the oxidation of glucose according to

$$\text{D-glucose} + O_2 \xrightarrow{\text{GOx}} \text{D-gluconolactone} + H_2O_2$$

$$\text{D-gluconolactone} + H_2O \rightarrow \text{D-gluconic acid}$$

Therefore, by measuring the decrease in oxygen partial pressure (pO_2) when glucose is oxidized by the enzyme gives an indirect indication of glucose concentration. In the amperometric enzyme electrode (*3*), an oxygen electrode is covered with a layer of immobilized GOx. Numerous modifications of this sensing scheme are known (*1*). Uwira et al. (*4*) briefly report on the development of an optical glucose sensor. In this device, changes in pO_2 are measured via quenching of the fluorescence of an oxygen-sensitive dye. However, this system is not compatibile with conventional fiber-optic components.

Other optical approaches have been made by Goldfinch and Lowe (*5*) who used bromocresol green immobilized on cellophane in order to measure the decrease in pH produced during the GOx-catalyzed oxidation of glucose by following the changes in light absorption of a pH-sensitive dye. Trettnak et al. (*6*) describe a fiber-optic fluorosensor for glucose that uses a pH sensor as the transducer. However, the response of biosensors based on pH transducers strongly depends on the buffer capacity of the medium. In the recent approach of Weigel et al. (*7*), a GOx film was spread onto a germanium crystal. Fourier transform infrared attenuated total reflection (FTIR-ATR) spectroscopy was applied to measure the 1153-cm^{-1} absorption band of gluconic acid, the intensity of which can be related to glucose concentration.

Schultz et al. (*8*) have described an immunoaffinity glucose sensor based on the reversible competitive binding of glucose and fluorescein-labeled dextran for the sugar binding sites of concanavalin-A. This device is very slow in response. The intrinsic fluorescence of GOx is another parameter that has been utilized in a glucose sensing device described by Trettnak et al. (*9*), following the observation that the intrinsic fluorescence of the enzyme slightly changes upon interaction with glucose. While glucose biosensors based on pO_2 and, in particular, hydrogen peroxide transduction (*10*, *11*) are to be preferred over those based on pH transduction for a number of reasons, the current sensitivity limits of oxygen sensors (in terms of signal resolution) determine the glucose detection limits.

Existing optical glucose biosensors, for instance, cannot be applied for determination of "normal" glucose levels in urine simply because the existing oxygen optrodes are not sensitive enough. More recently, the new indicator tris(2,2′-bipyridine)ruthenium(II) dichloride, [$Ru(bpy)_3^{2+}$], has been applied to monitor oxygen via a fiber-optic device (*12–14*). Its quenching constant still is too poor for use in biosensors for urine glucose levels. We report here the development of a new pO_2 sensor based on the quenching of the luminescence of a closely related metal complex, tris(1,10-phenanthroline)ruthenium(II) [$Ru(phen)_3^{2+}$] immobilized in a silicone matrix. The use of this sensing material substantially improves the characteristics of the optical sensors described to date. The material also has been applied to highly sensitive glucose determination by coupling it to the above GOx reaction.

EXPERIMENTAL SECTION

Instrumentation. Optical measurements were performed with two different arrangements. System I consists of an Oriel 3090 fiber-optic photometer (Chelsea Instruments, London) equipped with a 150-W xenon lamp pulsed at 9 Hz. After passing a 450-nm interference filter (band-pass 10 nm), light was guided through the input bundle of a bifurcated optical fiber to a flow-through cell and luminescence was collected and guided back to the photometer through the output bundle. A 570-nm cut-off filter (Schott, Mainz, FRG) was used to remove the scattered light. The 1.5-m light guide is made of poly(methyl methacrylate) (PMMA) (Faseroptik Henning, Allersburg, FRG), with an internal diameter of 3.5 mm per single bundle (30 fibers per bundle) and 4.5 mm at the common end.

The home-made flow-through cell was machined from stainless steel and possesses a volume of ca. 20 μL. The biosensor forms one wall of the flow-through cell and is separated from the optical fiber end by a 4 mm PMMA spacer (for a more detailed description of the cell see Trettnak et al. (*10*)). The buffer and

[1] Present address: Departamento de Quimica Analitica, Facultad de Ciencias Quimicas, Universidad Complutense, 28040 Madrid, Spain.

0003-2700/90/0362-2377$02.50/0 © 1990 American Chemical Society

glucose solutions are pumped through the cell at a typical total flow rate of 1.0 mL min^{-1}. An autosampler (Ventilomat R08, Fa. Ziegler, Graz, Austria) was utilized to calibrate the glucose sensor using standard solutions.

System II was used for calibration of the oxygen sensor performances, in order to compare the latter results with those obtained with the Oriel device. This home-made system has been described in some detail (*13*). Basically, it consists of a 6-W, 4.6-V tungsten halogen lamp focused onto a 460-nm interference filter and launched into a bifurcated fiber-optic waveguide bundle (Volpi AG, CH-8952 Schlieren, Switzerland), the common end of which (10 mm o.d.) is thermostated and contains the sensing layer. Luminescence and scattered light return through the second half of the fiber bundle, pass a 550-nm cut-off filter, and are detected with a photodiode (BPW 21, Siemens, D-8000 Munich, FRG). The collected data are then transferred to, and stored in, an IBM-XT personal computer, which also governs the automated measurement procedure including gas supply and sample flow.

Chemicals. Oxygen, air, and nitrogen of +99.99% purity where obtained from cylinders. Oxygen and nitrogen are mixed by using a RMD 280 mass flow controller (Air Liquide, Vienna) to yield mixtures of defined oxygen percentage. The gas mixtures are bubbled through an aqueous buffered solution before entering the flow cell for measurements with moist gases. The precision of the mixing device is specified to be within ±1% of the actual value. All experiments were performed at barometric pressure of about 736 Torr and room temperature of 25 ± 2 °C.

Tris(1,10-phenanthroline)ruthenium(II) dichloride was purchased from Aldrich (Steinheim, FRG). Glucose oxidase (EC 1.1.3.4, Type VII-S, from *Aspergillus niger*), with a specific activity of 200 units mg^{-1} of solid was obtained from Sigma (Munich, FRG). Glucose oxidase (from *Penicillium amagasakiense*) with a specific activity of 320 units mg^{-1} of solid was from Nagase Biochemicals (Tokyo, Japan). Glutaraldehyde (a 25% solution in water) from Sigma has been used to cross-link the GOx. Immunodyne immunoaffinity membranes, made of Nylon 6-6 having a porosity of 200 nm, an approximate thickness of 150 μm, and chemically activated carboxyl groups on the surface, were obtained from Pall Co. (Glen Glove, NY).

Glucose solutions have been prepared by diluting a 20 mM stock in 0.1 M phosphate buffer of pH 7.0 (when affinity membranes were used) or 0.02 M phosphate buffer of pH 7.0 containing 0.9% (w/v) NaCl and 0.1% sodium azide (referred to as phosphate buffered saline, PBS) when combined pO_2-glucose measurements were performed. All other chemicals were of analytical reagent grade.

Sensing Membranes. Oxygen sensors have been prepared according to a published procedure (*14*) but using $Ru(phen)_3^{2+}$ as the oxygen-sensitive dye. Glucose oxidase was immobilized by two different methods. In the first one, a 2-cm disk of the immunoaffinity membrane was immersed into a solution of 2 mg of the enzyme in 1 mL of pH 7 phosphate buffer for 24 h. The membrane was then washed with phosphate buffer and stored in the refrigerator at 4 °C in the same buffer containing sodium azide as a bactericide. The membrane was placed on top of the oxygen sensor membrane and kept in position with an O-ring.

The second procedure is a modification of the one described by Schaffar et al. (*11*). In this case, the oxygen sensing layer was covered with a thin layer of carbon black (ca. 1 μm) before curing and allowed to polymerize for 1 week at room temperature. The resulting black oxygen optrodes were washed with 70% ethanol as a desinfectant. Squares (2 × 5 cm) of these foils were first soaked with PBS and then treated with a mixture of 6 mg of the corresponding enzyme in 240 μL of PBS and 30 μL of a 2.5% glutardialdehyde solution. The solution is allowed to evaporate while the cross-linking reaction occurs on the carbon black surface at room temperature. When the enzyme film is completely dry, 2-cm disks were punched out and stored in the refrigerator at 4 °C in PBS, with 0.1% sodium azide being added when not in use. Figure 1 shows a cross section of this type of glucose sensing membrane.

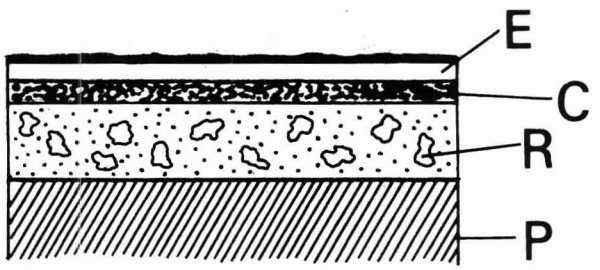

Figure 1. Cross-section through the sensing layer of the fiber-optic glucose sensor consisting of a polyester film as a support (P), a silicone matrix with suspended dyed kieselgel particles (R), a carbon black optical isolation (C), and a GOx/glutardialdehyde gel (E).

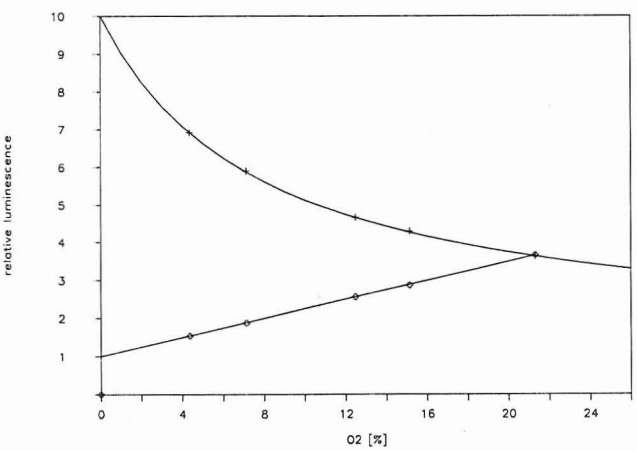

Figure 2. Effect of oxygen on the relative luminescence intensity of the oxygen sensor (+), and corresponding Stern–Volmer plot (◇), corrected for false light according to eq 1, at a total gas pressure of 736 Torr.

RESULTS AND DISCUSSION

Choice of the Indicator. The $[Ru(bpy)_3^{2+}]$ complex displays a fairly strong absorption in the visible region of the spectrum (λ_{max} 452 nm, ϵ 13 600 M^{-1} cm^{-1}, in water), a large Stokes' shift (fluorescence λ_{max} = 603 nm, corrected), and a sufficiently long excited-state lifetime (0.6 μs in oxygen-free aqueous solution) at room temperature (*15*, *16*). However, it has an emission quantum yield of 0.042 only (*15*). Similarly, the [Ru(diphenyl-1,10-phenanthroline)$_3^{2+}$] complex was found (*16*) to exhibit poor luminescence and moderate quenchability as well. While this was found to be of sufficient sensitivity for determination of oxygen over the usual range encountered in blood gas analysis, its quenching constant is too small to detect traces of glucose when used in a urine glucose biosensor with an oxygen transducer.

We therefore looked for a dye with improved Stern-Volmer quenching constants and found ruthenium tris(1,10-phenanthroline) dichloride $[Ru(phen)_3^{2+}]$ to have improved indicator properties particularly when adsorbed on a hydrophilic support. The excitation and emission wavelengths of this complex in water are 447 nm (ϵ 18 100 M^{-1} cm^{-1}) and 604 nm (corrected), respectively, and the luminescence quantum yield has been determined to be 0.058 (*17*). The luminescence lifetime in oxygen-free aqueous solutions is 1.0 μs at room temperature. Therefore, the indicator is subject to more efficient quenching than the bipyridine complex. It has been immobilized in a silicone matrix as described in the experimental part to give a sensor material useful for oxygen sensing.

Analytical Features of the O_2 Sensor. Silicone is considered to be an ideal material for the preparation of most oxygen sensors. It can be easily spread in thin layers and has the best permeability for gases when compared to other polymers (*18*, *19*). Figure 2 is a plot of the relative signal change of the $Ru(phen)_3^{2+}$-based oxygen sensor as a function of the oxygen concentration, together with a Stern–Volmer type representation. This curve has been obtained by using eq 1, which takes into account the contributions of the so-

$$(I'_o - I_f)/(I' - I_f) = 1 + K_{sv}[O_2] \quad (1)$$

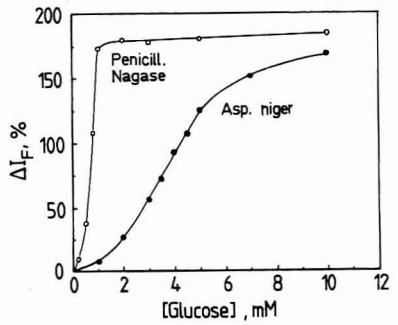

Figure 3. Calibration graph (obtained for sensors based on the use of the immunoaffinity membrane: (○) GOx with a specific activity of 320 units mg^{-1}; (●) GOx of 200 units mg^{-1}.

called *false light* (*10*). This term (I_f) includes all components responsible for a constant background of light not associated with quenchable indicator fluorescence and which cannot be removed by electronic or manual subtraction. As expected, the K_{sv} shown by the $Ru(phen)_3^{2+}$ complex is larger by a factor of 2.2 than the values described (*13*) for the same type of sensor using the $Ru(bpy)_3^{2+}$. Data reproducibility is mostly limited by the instrument performance. This is mainly due to the difficulty of getting a calibration point for a perfectly oxygen-free sample. The standard deviation for the determination of 7.3% oxygen in nitrogen is ±0.7% and ±0.5% for 21.9% oxygen at barometric pressure. The detection limit as defined by the analyte concentration giving a fluorescence of 3 times the standard deviation of the background is calculated to be 0.7 Torr when dry gases are used. The response time for a complete signal change to occur is about 40 s.

Preparation of the Glucose Sensor. In order to make the oxygen sensor a glucose biosensor, it has to be covered with a membrane containing immobilized GOx. The oxygen sensor then acts as a transducer for the rate at which oxygen is consumed during enzymatic oxidation. Hence, the response is the result of a dynamic balance in diffusion of glucose and oxygen into the sensor, and consumption of oxygen in the reaction, resulting in a steady-state decreased oxygen level and, consequently, an increase in fluorescence.

Two different immobilization procedures have been studied with respect to their effect on the sensor performance. When immunoaffinity membranes were used to immobilize GOx, the response time turned out to become very long. This may be attributed to the characteristics of the sensing layer, formed by a nylon membrane with the immobilized GOx deposited onto the oxygen sensor described before. This configuration is the limiting factor for the development of sensors prepared in this fashion because the glucose and oxygen transport across the membranes is very slow due to the thickness of the layers (particularly the 150-μm nylon membrane), yielding a 32-min response time in the most unfavorable case.

Figure 3 shows a calibration curve of two glucose sensors prepared from two different glucose oxidases. Not surprisingly, the enzyme with higher activity gives a more pronounced signal change, but at the same time the saturation point of the sensor is reached earlier because oxygen is consumed in the membrane at a faster rate during the enzymatic reaction or the enzyme is saturated earlier. The analytical range for the 320 units mg^{-1} enzyme is from 0.1 to 1.0 mM glucose. The standard deviation for 10 replicate measurements was ±3.5%. The useful range is between pH 5.5 and 7.5. However, it should be pointed out that if the membranes are treated with pH 9.0 phosphate buffer, its activity decreases dramatically and irreversibly. The analytical range for the 200 units mg^{-1} GOx lies between 0.3 and 5 mM glucose and the standard deviation for the measurements with this membrane was calculated to be ±4.8%.

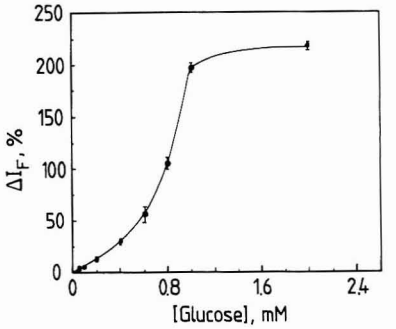

Figure 4. Calibration graph (expressed as the % increase in fluorescence over the value of air-saturated buffer) for the glucose biosensor with an oxygen sensor as a transducer and GOx immobilized directly on carbon black which also acts as an optical isolation to prevent ambient light and sample fluorescence to interfere. Standard deviations are given for 12 replicate measurements.

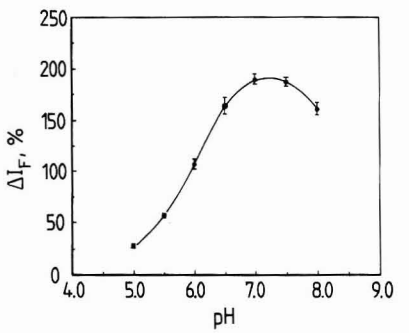

Figure 5. pH dependence of the response of the biosensor to 1 mM glucose solutions at different pH values (standard deviations for five replicate measurements).

When compared with sensors of this type known in the literature (*10*, *20*), the use of $Ru(phen)_3^{2+}$ as the oxygen-sensitive indicator obviously leads to a tremendous enhancement in relative signal change even at low glucose concentrations. Nevertheless, since long response times turned out to be a limitation of this sensor, we decided to apply a different immobilization procedure to produce thinner sensor layers and achieve faster oxygen diffusion. Both enzymes were cross-linked with glutardialdehyde onto the oxygen-sensitive layer covered with carbon black, as described in the Experimental Section. The biosensor layer made from *Penicillium amagasakiense* yielded an active membrane, while the other one showed no sensitivity to glucose changes, pointing to the possibility that the active centers of the enzyme were somehow affected during the immobilization procedure.

The calibration curve of this new sensor type which incorporates the oxygen-sensitive complex and the enzyme in the same membrane is depicted in Figure 4. The maximum signal change measured with this device is a 2.2-fold increase of the optrode luminescence intensity in air-equilibrated buffer upon exposure to 2 mM (or more) glucose solutions. In terms of both relative signal change and detection limits, this is a 50% increase over the values obtained with optical biosensors of this kind so far (*11*). The signal-to-noise ratio is 200:1, and the response times are about 2 min for a 90% signal change (t_{90}) and around 6 min for t_{100}. The time required to reach the base line again is approximately 7 min. The dynamic range of the sensor is 0.06–1.0 mM glucose, similar to that obtained with the sensor using the immunoaffinity membrane. However, the former provides response times substantially shorter and the signal change is larger as can be observed from Figures 3 and 4. The sensor performance is insensitive to flow rates between 0.9 and 1.7 mL min^{-1}.

Figure 5 shows the response of the sensor to 1 mM glucose solutions of different pH. The maximum signal is obtained in the pH 7.0–7.5 range, which is in agreement with previous

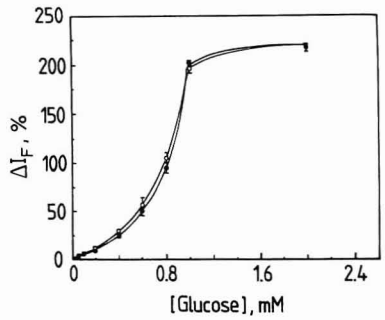

Figure 6. Reproducibility check for two different glucose biosensors.

Table I. Effect of Sensor Lifetime to the Response of the Glucose Biosensor toward 1.0 and 0.8 mM Glucose Solutions

	increase in fluorescence intensity,[a] arbitrary units	
time, weeks	1 mM glucose	0.8 mM glucose
1	203 (±9)	110 (±6)
2	194 (±7)	111 (±4)
4	187 (±3)	85 (±0.7)

[a] Standard deviations of five measurements given in parentheses.

findings on immobilized enzyme (*21*) whose optimum activity is at pH 5.6 in free form. No signal changes were observed when 100 mM saccharose, fructose, lactose, or galactose were tested. The reproducibility in the fabrication of the biosensor is demonstrated by the calibration curves for two different membranes in Figure 6. It is evident that both sensors exhibit a very similar behavior. However, it is essential to precisely follow the standardized procedure for enzyme gel preparation in order to obtain reproducible results. When stored at room temperature in PBS containing sodium azide, the sensors lost 16–18% of their activity within 4 weeks when used daily. They were found still to be operative 12 months after preparation and storage a 4 °C.

The activity of the enzyme does not decrease in a constant rate; in fact, during the period monitored only a slight decrease of the sensor response was observed as appears from the data in Table I. During this time the biosensor was flashed at 9 Hz for ca. 150 h but no photobleaching was observed.

CONCLUSIONS

The advantages displayed by this biosensor over other optical biosensors described in the literature include (a) an excitation and emission wavelength within the visible range, (b) a large Stokes' shift which facilitates the separation of fluorescence from straylight, and (c) an improved quenching efficiency. The dynamic range of this biosensor makes it adequate for glucose determinations in urine, where normal glucose levels are at around 0.8 mM (*22*). Any increase in this value is indicative of a pathological situation and appears to be detectable with this biosensor. Experiments are underway to couple this optical fiber system to flow injection analysis of urine glucose.

ACKNOWLEDGMENT

The authors gratefully acknowledge the help of W. Trettnak in the preparation of the immobilized membranes and Dr. G. Orellana for suggesting the use of $Ru(phen)_3^{2+}$ as an oxygen indicator and reading the manuscript.

LITERATURE CITED

(1) Turner, A. P. F.; Karube, I.; Wilson G. S. *Biosensors*; Oxford University Press: Oxford, 1987.
(2) *Molecular Luminescence Spectroscoy: Methods and Applications*; Schulman, S. G., Ed.; Wiley: New York, 1988; Vol 2, Chapter 3.
(3) Clark, L. G.; Lyons, C. *Ann. N.Y. Acad. Sci.* **1962**, *102*, 29.
(4) Uwira, N.; Opitz, N.; Lübbers, D. W. *Adv. Exp. Med. Biol.* **1984**, *169*, 915.
(5) Goldfinch, M. J.; Lowe, C. R. *Anal. Biochem.* **1984**, *138*, 430.
(6) Trettnak, W.; Leiner, M. J. P.; Wolfbeis, O. S. *Biosensors* **1989**, *5*, 245.
(7) Weigel, Ch.; Kellner, R. *Proc. SPIE—Int. Soc. Opt. Eng.* **1989**, *1145*, 134.
(8) Schultz, J. S.; Mansouri, S.; Goldstein, L. J. *Diabetes Care* **1982**, *5*, 245.
(9) Trettnak, W.; Wolfbeis, O. S. *Anal. Chim. Acta* **1989**, *221*, 195.
(10) Trettnak, W.; Leiner, M. J. P.; Wolfbeis, O. S. *Analyst* **1988**, *113*, 1519.
(11) Schaffar, B. P. H.; Wolfbeis, O. S. *Biosensors Bioelectronics* **1990**, *5*, 137.
(12) Wolfbeis, O. S.; Weis, L. J.; Leiner, M. J. P.; Ziegler, W. E. *Anal. Chem.* **1988**, *60*, 2028.
(13) Wolfbeis, O. S.; Leiner, M. J. P.; Posch, H. E. *Mikrochim. Acta* **1986**, *III*, 359.
(14) Lippitsch, M. E.; Pusterhofer, J.; Leiner, M. J. P.; Wolfbeis, O. S. *Anal. Chim. Acta* **1988**, *205*, 1.
(15) Juris, A.; Balzani, V.; Barigeletti, F.; Campagna, S.; Belser, P.; von Zelewski, A. *Coord. Chem. Rev.* **1988**, *84*, 85.
(16) Hoffman, M. Z.; Bolletta, F.; Moggi, L.; Hug, G. L. *J. Phys. Chem. Ref. Data* **1989**, *18*, 219.
(17) Bacon, J. R.; Demas, J. N. *Anal. Chem.* **1987**, *59*, 2780.
(18) Cox, M. E.; Dunn, B. *J. Polym. Sci.* **1986**, *24*, 621 and 2395.
(19) Bandrup, J.; Immergut, E. H. *The Polymer Handbook*; Wiley: New York, 1975; p III-232 ff.
(20) Dremel, B. A. A.; Schaffar, B. P. H.; Schmid, R. D. *Anal. Chim. Acta* **1989**, *225*, 293.
(21) Hartmeier, W. *Immobilisierte Biokatalysatoren*; Springer Verlag: Berlin, 1986.
(22) Peter, G. *Lehrbuch der Klinischen Chemie*, edition medizin; Verlag Chemie: Weinheim-Deerfield Beach-Basel, 1982; p 172f.

RECEIVED for review May 15, 1990. Accepted July 16, 1990. M. C. Moreno-Bondi thanks the Community Council of Madrid for a grant.

Nonenzymatic Method for the Determination of Hydrogen Peroxide in Atmospheric Samples

Jai H. Lee* and Ignatius N. Tang

Environmental Chemistry Division, Brookhaven National Laboratory, Upton, New York 11973

Judith B. Weinstein-Lloyd

Chemistry/Physics Program, State University of New York/Old Westbury, Old Westbury, New York 11568

A nonenzymatic method is developed and compared with the well-known enzymatic (*p*-hydroxyphenyl)acetic acid (pOHPAA) method for the determination of hydrogen peroxide in aqueous atmospheric samples. The new method is based on the Fe(II)-catalyzed oxidation of benzoic acid by H_2O_2 to form hydroxylated products (OHBA), which are analyzed by fluorescence detection. The limit of detection and linear response range of the new method are comparable to those of the pOHPAA technique. In addition, the new Fenton-OHBA method has the advantage of using inexpensive, stable, easily available chemical reagents that do not require refrigeration. The new method is insensitive to moderate transition-metal concentrations often found in atmospheric samples.

INTRODUCTION

As a principal oxidant of atmospheric S(IV), hydrogen peroxide is believed to play an important role in acid deposition (*1–4*), and its availability may control the aqueous-phase conversion of SO_2 to sulfate in the Eastern United States (*5*). In recent years, numerous field measurements have mapped the temporal, seasonal, and geographical concentrations of atmospheric hydrogen peroxide in gas and aqueous phases. H_2O_2 concentrations averaging several micromolar, but occasionally exceeding 100 μM in precipitation (*6–8*) and cloudwater (*5, 8, 9*), 200 ppb in ice (*10*), and several ppbv in air (*11, 12*), have been reported.

Techniques for the determination of atmospheric hydrogen peroxide have been the subject of substantial research efforts. Early measurements employing the absorbance of the violet complex formed in a solution of Ti(IV), H_2O_2, and 8-quinolinol (*13, 14*) suffered from low sensitivity and substantial interference from organic hydroperoxides and ozone. A similar technique, involving absorbance measurements of the oxo–dioxo complex formed when V(V) reacts with dioxopyridine-2,6-dicarboxylate and H_2O_2, exhibited comparable sensitivity (*15*). Kok et al. made use of the chemiluminescent oxidation of luminol (1,4-phthalazinedione) by H_2O_2 in the presence of copper as a catalyst (*16*). In addition to requiring purification of the luminol, this technique exhibited negative interference from transition metals (*17*). A modification of the technique, using hemin as a catalyst, led to improved sensitivity but still suffered from interferences (*18*). Klockow and Jacob developed a fluorescence method based on the oxidation of bis(trichlorophenyl) oxalate by H_2O_2 in the presence of perylene (*19*). The authors note that an Fe(III) impurity interferes at 10^{-5} M. The horseradish peroxidase (HRP) catalyzed destruction of scopoletin fluorescence upon reaction with H_2O_2 was used as the basis of an analytical technique by Zika et al. (*20, 21*). Because it makes use of fluorescence quenching, the scopoletin method is not as convenient or sensitive as direct fluorescence methods.

Among the more widely used methods is a fluorescence technique originated by Guilbault (*22*) and further developed by Lazrus et al. (*23*). This method is based upon the reaction between peroxide and (*p*-hydroxyphenyl)acetic acid (pOHPAA), catalyzed by HRP, to generate a fluorescent dimer. Although the technique is highly sensitive and relatively free from interferences, it suffers the disadvantages common to many enzyme assays, notably reagent instability and high cost.

Several investigators have compared H_2O_2 analysis methods by simultaneous determination of samples by two or more techniques. In one comparison, Lazrus (*23*) found that luminol consistently gave a higher reading for H_2O_2 concentration than pOHPAA. The luminol technique did, however, produce reasonable agreement with the Ti(IV)–H_2O_2–quinolinol method (*24*). Analysis by pOHPAA agreed well with the peroxyoxalate chemiluminescence technique (*25*). Measurement of gaseous H_2O_2 by scrubbing air on a common manifold revealed the pOHPAA technique to be 1 order of magnitude more sensitive than the luminol technique and less subject to gas-phase interferences (*26*).

We have developed an analytical scheme based upon the well-known Fenton reaction, in which ferrous ion reacts with hydrogen peroxide to yield the hydroxyl radical (*27*). The hydroxyl radical is scavenged by benzoic acid (BA) to form isomeric hydroxybenzoic acids (OHBA), which fluoresce strongly (*28*). In this work, the validity of the nonenzymatic method is established by simultaneous analysis of H_2O_2-spiked atmospheric precipitation samples by the Fenton-OHBA and pOHPAA methods.

EXPERIMENTAL SECTION

Chemicals. Ferrous sulfate, sulfuric acid, and hydrochloric acid (Mallinckrodt AR), *o*- (Aldrich ACS reagent), *m*- (Aldrich 99%), and *p*-hydroxybenzoic acid (Aldrich 99+% gold label), and benzoic acid (Baker 99.8%) were used without further purification. All reagents were prepared by using high-purity water from a Millipore ultrapurification system.

pOHPAA reagent contained 4.5 mM pOHPAA, 0.20 mM EDTA, and 1.8 units/mL horseradish peroxidase. The solution pH was adjusted to 8.5 with Tris buffer and HCl. (*p*-Hydroxyphenyl)acetic acid (Eastman 98% minimum), hydrochloric acid (Mallinckrodt AR), EDTA (Sigma 99.5%), Tris buffer (Sigma reagent), and horseradish peroxidase (Sigma Type VI, P8375) were used without further purification.

Apparatus and Procedures. Fenton-OHBA analysis was carried out by using a single-channel modification of the apparatus developed by Lazrus (*23*), represented schematically in Figure 1. Three inlet ports are used, one each for the H_2O_2 sample, ferrous sulfate/benzoic acid solution, and NaOH. The air-stripping coil was retained for future application of the technique to the measurement of gaseous H_2O_2, and aqueous H_2O_2 samples were introduced through the stripping solution port. Room air entering the stripping coil at a rate of 1.05 L min^{-1} was freed of gaseous H_2O_2 by a Hopcalite column. After separation of air from the liquid phase in a vertical tube, the H_2O_2 stream joined the liquid stream containing ferrous sulfate and benzoic acid. Hydroxyl radicals produced from the H_2O_2–Fe(II) reaction were scavenged by benzoic acid in a reaction coil. The solution containing hydroxylated products was made alkaline with 0.18 M NaOH to enhance fluorescence intensity (*28*). Air bubbles were

0003-2700/90/0362-2381$02.50/0 © 1990 American Chemical Society

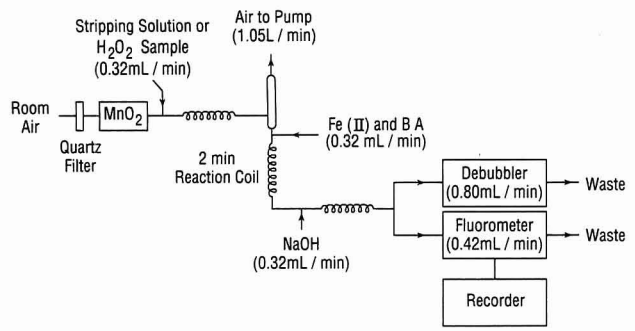

Figure 1. Schematic diagram of the Fenton-OHBA analytical system.

introduced into the flow stream to enhance mixing and were removed by a debubbler before analysis. Fluorescence measurements were made with a Kratos 950 filter fluorometer equipped with a 0.1-cm flow-through cell, mercury lamp, Schott UG11 wide-band excitation filter (λ_{ex} = 313 nm), and an L399 cutoff emission filter (λ_{em} > 399 nm).

Ferrous sulfate/benzoic acid solution contained 1.5 mM ferrous sulfate and 3.0 mM benzoic acid dissolved in 0.016 M sulfuric acid. Reagents generally contained a low concentration of fluorescent impurities; the signal reported in this work is the difference between the fluorescence intensity with and without H_2O_2.

The system used for hydrogen peroxide analysis by the pOHPAA technique has been described elsewhere (*8*). Briefly, each peroxide sample was mixed with an equal volume of pOHPAA reagent and introduced through an injection valve into a flow of deionized water. The formation of a fluorescent dimer from the HRP-catalyzed reaction between pOHPAA and H_2O_2 is complete before injection, and the dimer is stable for several hours. The flow stream passed through a 1.0-cm flow-through cell, and fluorescence was monitored by a Perkin-Elmer Model 201 spectrofluorometer. The excitation and emission monochromators were set at 321 and 401 nm, respectively.

Calibration curves for both methods were obtained daily, by using hydrogen peroxide standards prepared from 3% H_2O_2, which had been titrated against standardized potassium permanganate.

Precipitation samples for peroxide analysis were collected at ground level in polyethylene containers and refrigerated in rigorously cleaned Pyrex vessels. These samples were spiked with microliter quantities of H_2O_2 stock solution for the comparison study.

RESULTS AND DISCUSSION

Reaction Scheme. The Fenton-OHBA analytical technique is summarized by the following scheme:

$$Fe(II) + H_2O_2 \rightarrow Fe(III) + OH^- + OH \quad (1)$$

$$OH + C_6H_5COOH \rightarrow o\text{-}OHC_6H_5COOH, \; m\text{-}OHC_6H_5COOH, \text{ and } p\text{-}OHC_6H_5COOH \quad (2)$$

$$OH + Fe(II) \rightarrow Fe(III) + OH^- \quad (3)$$

The rate constant for eq 1, known as the Fenton reaction, is 57.8 M^{-1} s^{-1} (*29*) in solutions containing ferrous sulfate in sulfuric acid. Under our experimental conditions, complexation of Fe(II) with benzoate may alter the rate of reaction 1. Reaction 2 is nearly diffusion-controlled, at 4.3 × 10^9 M^{-1} s^{-1} (*30*). To minimize scavenging of OH radicals by reaction 3, which is characterized by a second-order rate constant of 4.3 × 10^8 M^{-1} s^{-1} (*31*), we maintained the BA and Fe(II) concentration in at least a 2:1 ratio.

Reaction Conditions. The optimum conditions for production of OHBA were determined by varying the pH for reaction 1, Fe(II) concentration, reaction time, and pH of the fluorescent products.

Solutions of benzoic acid and ferrous sulfate are stable to air oxidation for several days as long as the pH is kept below 2.5. At a higher pH, one observes a large, nonreproducible background fluorescence signal. This effect can be attributed to ferrous ion catalyzed air oxidation of benzoic acid, as no

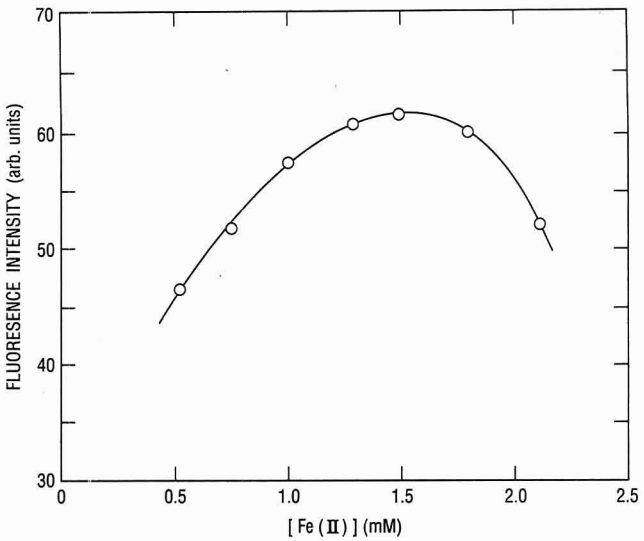

Figure 2. Dependence of the fluorescence signal on Fe(II) concentration. Experimental conditions: pH = 1.8, $[H_2O_2]$ = 4.1 × 10^{-6} M, 2-min reaction time, 3.0 > [BA]/[Fe(II)] > 2.0.

significant fluorescence is observed in neutral air-saturated benzoic acid solutions in the absence of Fe(II) or in such solutions containing Fe(II) if they are deoxygenated.

The fluorescence signal is virtually insensitive to changes in pH when reaction 1 is carried out below pH 2.5. In these experiments, OHBA isomers were produced in the reaction coil at pH 1.8. Before detection, the solution pH was rapidly raised to 11.6 to optimize the fluorescence intensity of OHBA (see below). However, at this pH, the ferrous ion is rapidly oxidized to the ferric ion. Fe(III) is unstable in the resulting solution and slowly precipitates on standing, presumably as the hydroxide and/or oxide. The presence of colloidal iron decreases the signal, an interference that worsens as the Fe(III) concentration increases. However, it is desirable to keep the Fe(II) concentration as high as possible to accelerate the rate of reaction 1. This reasoning prompted us to seek an Fe(II) concentration that would maximize the rate of formation of OHBA while minimizing the quenching of the fluorescence signal by Fe(III). The dependence of the fluorescence signal on Fe(II) concentration, shown in Figure 2 for a single peroxide concentration and a 2-min reaction time, indicates that the optimum ferrous ion concentration lies between 1 and 2 mM.

The dependence of fluorescence signal on reaction time for reaction 1 is shown in Figure 3 for several concentrations of Fe(II). As expected from kinetic considerations, the signal reaches a plateau at earlier times for higher Fe(II) concentrations. The figure also illustrates the fluorescence quenching described earlier, which diminishes the ultimate plateau signal for solutions with higher iron concentrations. It is evident from Figure 3 that the highest signal is produced by using the lowest possible concentration of Fe(II). However, this increased sensitivity occurs at the expense of an unacceptably long analysis time. In these experiments, we utilized a 1.5 mM Fe(II) solution, which produced the highest fluorescence signal under the constraint of a 2-min reaction time.

The pH dependence of the fluorescence intensities of isomeric hydroxybenzoic acids has been studied (*28*). The fluorescence signal increases dramatically at the pK of the OHBA isomers and reaches a plateau at pH 5 and 11.6 for the ortho and meta isomers, respectively. In calibration studies using our apparatus, the fluorescence of the meta isomer was approximately twice that of the ortho at pH 11.6 (Figure 4). However, upon increasing the pH of the OHBA product flow stream from 5 to 11.6 in actual analyses, we observed an increase in fluorescence intensity by a factor of 2.2. This suggests that *o*- and *m*-OHBA are produced in a

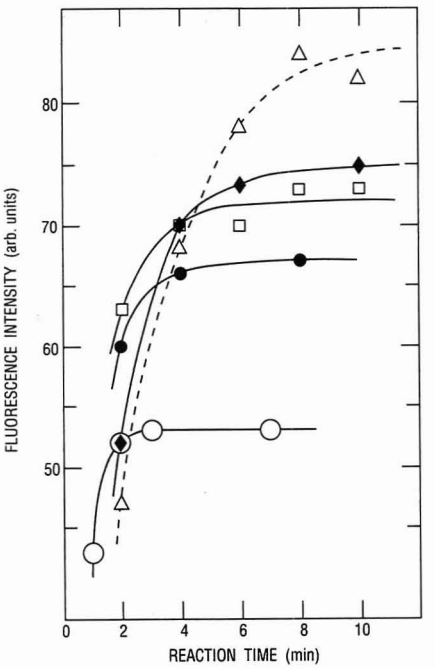

Figure 3. Dependence of fluorescence signal on reaction time: (△) 0.55 mM; (◆) 0.75 mM; (□) 1.49 mM; (●) 1.80 mM; (○) 2.09 mM. Experimental conditions: pH = 1.8, $[H_2O_2] = 4.1 \times 10^{-6}$ M, 3.0 > [BA]/[Fe(II)] > 2.0, [Fe(II)]. Data for 1.49 mM has reached 90% of the plateau value at 2 min.

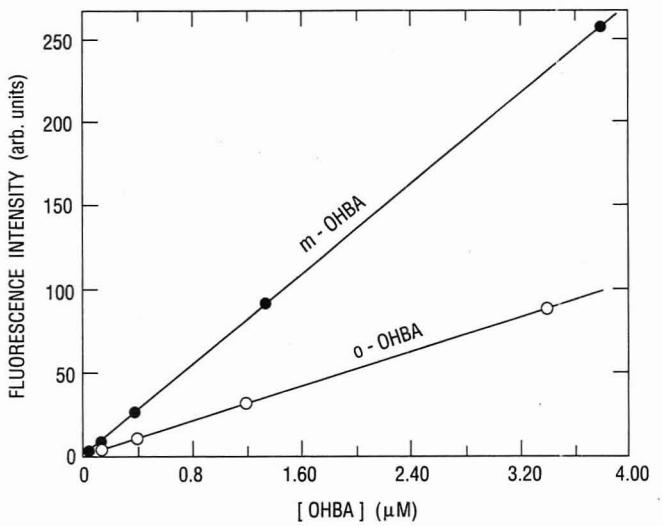

Figure 4. Dependence of fluorescence signal on concentrations of *o*- and *m*-OHBA at pH 11.6.

2:1 ratio. The para isomer does not fluoresce under the conditions employed.

Calibration and Sensitivity. The calibration curve for Fenton-OHBA analysis under our experimental conditions is linear for H_2O_2 concentrations between 10^{-8} and 10^{-5} M. The detection limit of this technique is 2×10^{-8} M, based on a signal to noise ratio of 1. However, as shown in Figure 5, the fluorescence intensity begins to deviate from a linear response to H_2O_2 concentrations above 5×10^{-5} M. Regression analysis of the linear portion of the calibration curve gives a standard deviation of 1% for the slope and a correlation coefficient of 0.999.

It has been reported that various EDTA complexes of Fe(II) produce OH via reaction 1 but at significantly faster rates (*32*). Such a rate increase would enhance the sensitivity of the Fenton-OHBA technique by decreasing the concentration of Fe(II) required for analysis and thereby decreasing the extent of fluorescence quenching by Fe(III). Our experiments utilizing Fe(II) complexes in reaction 1 resulted in a large, unstable background reading, apparently due to Fe-complex-catalyzed air oxidation of benzoic acid, and were therefore discontinued.

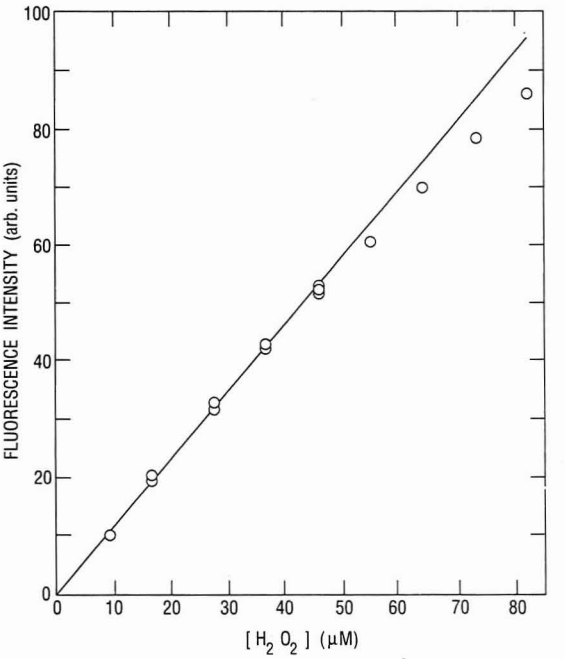

Figure 5. Calibration curve for Fenton-OHBA analysis. Experimental conditions: pH = 1.8, 2.0-min reaction time, [BA]/[Fe(II)] = 2.0.

Interferences. Chemical analysis of precipitation samples from the Northeastern United States has shown the presence of the following species: H_2O_2, HCHO, H^+, NO_3^-, SO_4^{2-}, NH_4^+, Na^+, Cl^- (*6*). In our experiments, the presence of 0.4 mM NH_4NO_3, 0.4 mM NaCl, and 0.08 mM HCHO did not affect H_2O_2 concentrations measured by the Fenton-OHBA technique. To address the possibility of a spurious signal due to reaction of S(IV) with Fe(III), we observed the fluorescence signal of a sample containing 10 μM S(IV) (*33*). The absence of a signal under these conditions demonstrates that S(IV) does not interfere.

Field investigations have shown that organic hydroperoxides can comprise a significant fraction of the total peroxides in atmospheric samples (*8*, *34–37*). Unlike the Fe(II)–H_2O_2 reaction (1), the Fe(II)–ROOH reaction does not give rise to an OH radical, and is therefore not expected to produce OHBA (*38*, *39*). Because of the presence of millimolar levels of the ferrous ion, this technique is also insensitive to the micromolar levels of transition metals often found in atmospheric samples.

Comparison of Fenton and pOHPAA Techniques. Precipitation samples collected on Long Island, NY, were spiked with H_2O_2 and analyzed simultaneously by the Fenton-OHBA and the pOHPAA methods. Linear regression analysis of H_2O_2 concentration determined by the Fenton-OHBA method versus that determined by the pOHPAA method gives a slope of 0.96 and a correlation coefficient of 0.997 (Figure 6). The comparison showing good agreement over a wide range of H_2O_2 concentration clearly indicates the utility of the Fenton-OHBA method for analysis of atmospheric samples.

CONCLUSION

We have developed and demonstrated the use of the Fenton reaction as an analytical tool for the measurement of H_2O_2 and have shown it to be sensitive, linear, and to give results consistent with that of the frequently used pOHPAA method. Moreover, the present technique has the advantage of using inexpensive, easily available nonenzymatic reagents that do not require refrigeration and of being insensitive to the moderate concentration of inorganic ions and transition metals

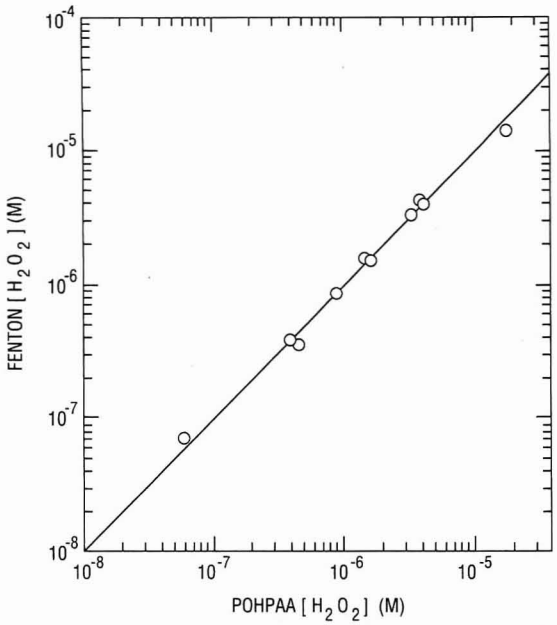

Figure 6. Comparison of Fenton-OHBA and pOHPAA technique. Measurements are made on precipitation samples containing added H_2O_2; the solid line represents a slope of 1.

often found in atmospheric samples. Because of its high sensitivity and lack of interferences, the Fenton-OHBA method can easily be adopted for gaseous H_2O_2 measurement at ambient concentration levels.

ACKNOWLEDGMENT

Helpful discussions with B. H. J. Bielski, D. Cabelli, J. Fajer, S. E. Schwartz, and L. Newman during this study are appreciated. We are indebted to Y.-N. Lee and S. Springston for providing instruments for this work and to D. Leahy for technical assistance.

Registry No. $FeSO_4$, 7720-78-7; benzoic acid, 65-85-0; water, 7732-18-5; H_2O_2, 7722-84-1.

LITERATURE CITED

(1) Penkett, S. A.; Jones, B. M. P.; Brice, K. A.; Eggleton, A. E. *Atmos. Environ.* **1979**, *13*, 123–127.
(2) Calvert, J. G.; Lazrus, A.; Kok, G.; Heikes, B.; Walega, J.; Cantrell, C. A. *Nature* **1985**, *317*, 27–38.
(3) Schwartz, S. E. In *SO_2, NO and NO_2 Oxidation Mechanisms: Atmospheric Considerations*; Calvert, J. G., Ed.; Acid Precipitation Series, Vol. III; Butterworth: London, 1984; Chapter 4, pp 173–208.
(4) Martin, L. R.; Damschen, D. E. *Atmos. Environ.* **1981**, *15*, 1615–1621.
(5) Daum, P. H.; Kelly, T. J.; Schwartz, S. E.; Newman, L. *Atmos. Environ.* **1984**, *18*, 2671–2684.
(6) Lee, Y.-N.; Shen, J.; Klotz, P. J. *Air Soil Pollut.* **1986**, *30*, 143–152.
(7) Kok, G. L. *Atmos. Environ.* **1980**, *14*, 653–656.
(8) Kelly, T. J.; Daum, P. H.; Schwartz, S. E. *J. Geophys. Res.*, [*Atmos.*] **1985**, *90*, 7861–7871.
(9) Daum, P. H.; Kelly, T. J.; Strapp, J. W.; Leaitch, W. R.; Joe, P.; Schemenauer, R. S.; Isaac, G. A.; Anlauf, K. G.; Weibe, H. A. *J. Geophys. Res.* **1987**, *92*, 915–931.
(10) Neftel, A.; Jacob, P.; Klockow, D. *Tellus* **1986**, *38B*, 262–270.
(11) Heikes, B.; Kok, G. L.; Walega, J. G.; Lazrus, A. L. *J. Geophys. Res.* **1987**, *92*, 915–932.
(12) Daum, P. H.; Kleinman, L. I.; Hills, A. J.; Lazrus, A. L.; Leslie, A. C. D.; Busness, K.; Boatman, J. *J. Geophys. Res.* **1990**, *95*, 9857–9872.
(13) Cohen, I. R.; Purcell, T. C. *Anal. Chem.* **1967**, *39*, 131–132.
(14) Bufalini, J. J.; Gay, B. W.; Brubaker, K. L. *Environ. Sci. Technol.* **1972**, *6*, 816–821.
(15) Hartkamp, H.; Bachhausen, P. *Atmos. Environ.* **1987**, *21*, 2207–2213.
(16) Kok, G. L.; Holler, T. P.; Lopez, M. B.; Nachtrieb, H. A.; Yuan, M. *Environ. Sci. Technol.* **1978**, *12*, 1072–1076.
(17) Ibusuki, T. *Atmos. Environ.* **1983**, *17*, 393–396.
(18) Yoshizumi, K.; Aoki, K.; Nouchi, I.; Okita, T.; Kobayashi, T.; Kamakura, S.; Tajima, M. *Atmos. Environ.* **1984**, *18*, 345–401.
(19) Klockow, D.; Jacob, P. In *The Chemistry of Multiphase Systems*; Jaeschke, W., Mohnen, V., Eds.; Springer-Verlag: Berlin, 1985.
(20) Perschke, H.; Broda, E. *Nature* **1961**, *190*, 257–258.
(21) Zika, R.; Saltzman, E.; Chameides, W.; Davis, D. *J. Geophys. Res.* **1982**, *87*, 5015–5017.
(22) Guilbault, G.; Brignac, P. J.; Juneau, J. M. *Anal. Chem.* **1968**, *40*, 1256–1263.
(23) Lazrus, A.; Kok, G.; Gitlin, S.; Lind, J. A.; McLaren, S. *Anal. Chem.* **1985**, *57*, 917–922.
(24) Kok, G. L.; Darnell, K. R.; Winer, A. M.; Pitts, J. N., Jr.; Gay, W. B. *Environ. Sci. Technol.* **1978**, *12*, 1077–1080.
(25) Beltz, N.; Jaeschke, W.; Kok, G. L.; Gitlin, S. N.; Lazrus, A. L.; McLaren, S.; Shakespeare, D.; Mohnen, V. A. *J. Atmos. Chem.* **1987**, *5*, 311–322.
(26) Kleindienst, T. E.; Shepson, P. B.; Hodges, D. N.; Nero, C. M.; Arnts, R. R.; Dasgupta, P. K.; Hwang, H.; Kok, G. L.; Lind, J. A.; Lazrus, A. L.; Mackay, G. I.; Mayne, L. K.; Schiff, H. I. *Environ. Sci. Technol.* **1988**, *22*, 53–61.
(27) Fenton, H. J. H. *J. Chem. Soc.*, **1894**, *65*, 899–910.
(28) Thommes, G. A.; Leininger, E. *Anal. Chem.* **1958**, *30*, 1361–1363.
(29) Po, H.; Sutin, N. *Inorg. Chem.* **1968**, *7*, 621–624.
(30) Wander, R.; Neta, P.; Dorfman, L. M. *J. Phys. Chem.* **1968**, *72*, 2946–2949.
(31) Christensen, H.; Sehested, K. *Radiat. Phys. Chem.* **1981**, *18*, 723–731.
(32) Borggaard, O. K.; Farver, O.; Andersen, V. S. *Acta Chem. Scand.* **1971**, *25*, 3541–3543.
(33) MAP3S/RAINE Research Community. *Atmos. Environ.* **1982**, *16*, 1603–1631.
(34) Lazrus, A. L.; Kok, G. L.; Lind, J. N.; Gitlin, S. N.; Heikes, B. G.; Schetter, R. E. *Anal. Chem.* **1986**, *58*, 594–597.
(35) Hellpointner, E.; Gab, S. *Nature* **1989**, *337*, 631–634.
(36) Kok, G. L.; Walega, J. G.; Heikes, B. G.; Lind, J. A.; Lazrus, A. L. *Aerosol Sci. Technol.* **1990**, *12*, 49–55.
(37) Kok, G. L.; Hewitt, C. N. *Eos* **1989**, *170*, 1019.
(38) Kolthoff, I. M., Medalia, A. I. *Anal. Chem.* **1951**, *23*, 595–60.
(39) Winston, G. W.; Harvey, W.; Berl, L.; Cederbaum, A. I. *Biochem. J.* **1983**, *216*, 415–421.

RECEIVED for review April 27, 1990. Accepted July 30, 1990. This material is based upon work supported in part by National Science Foundation Grants ATM-8808480 and ATM-8911296 to J.W.-L. and performed under the auspices of the United States Department of Energy under Contract No. DE-AC02-76CH00016.

Spatially Resolved Laser Transfer of Organic Surface Films for Infrared Analysis

M. S. de Vries, H. E. Hunziker,* and H. R. Wendt

Almaden Research Center, IBM Research Division, San Jose, California 95120

D. D. Saperstein

IBM General Products Division, San Jose, California 95193

The technique of laser transfer sampling is described and applied to obtain IR spectra of organic surface films. Spatially resolved transfer across a vacuum gap is demonstrated at 1064 and 248 nm, occurring by different, highly directional mechanisms. Laser interference in the gap and surface topography of the sample are shown to modulate the transferred film patterns.

INTRODUCTION

Chemical analysis of thin surface films is a task frequently encountered in areas such as the microelectronics industry and environmental monitoring. Intentionally deposited coatings as well as contamination layers need to be characterized. For molecular identification of organic layers the selection of techniques is rather limited. IR spectroscopy is often preferred because it is specific, quantitative, and nondestructive. It can, however, rarely be applied in situ: Difficulties arise when the substrate is highly IR absorbing or has metallic reflection (only absorptions with transition moment perpendicular to the surface are seen, requiring grazing incidence which limits spatial resolution) or if for some other reason an object cannot be directly examined with an IR spectrometer. In all these cases a sampling technique is desirable that separates the organic film from the substrate before analysis. This paper presents such a technique, which we call laser transfer sampling.

We have used laser transfer sampling with some success for analyzing contaminants and lubricants on parts of data storage devices. The principle of the method is shown in Figure 1: A transfer target substrate is mounted close to the surface to be analyzed, separated from it by a vacuum gap. Transfer without a gap at ambient pressure may be feasible, but we have not investigated this possibility. This substrate is transparent for both IR and the laser wavelength used for transfer. A single laser pulse applied through it vaporizes all or part of the surface film and drives it across the gap onto the target. The latter is then dismounted and subjected to transmission IR analysis.

This sampling techniques has the advantage of preserving some or all of the spatial information about the surface deposit, as indicated by the transferred pattern in Figure 1. Thus one can examine the transferred pattern with an IR microscope and recover the spatial distribution present on the original sample. The main purpose of this paper is to characterize the transfer of patterns and its limitations in detail. The results provide a basis for applications and shed some light on the transfer mechanism.

Laser transfer of organic films for other purposes and without spatial imaging has been described in the literature. UV laser ablation of polymer films (*1*) and partial vaporization of frozen DNA solutions with 581-nm laser pulses (*2*) were found to be highly directional processes. Transfer of dust (*3*) and ice (*2*) particles driven by laser vaporization of water has also been observed. A theoretical analysis of the strongly forward-peaked expansion plumes encountered in laser sputtering has been given by Kelly (*4*). The technique described here is suitable for obtaining spatially resolved transfer samples from large or stationary objects by appropriate modification of the basic device shown in Figure 1. It suffices that a vacuum seal can be made against the surface to be examined. Transfer sampling may also be useful with analytical techniques other than IR, where special substrates are required to give optimal results. Examples include secondary ion mass spectrometry (SIMS) (*5*) (Ag substrate), surface photoionization mass spectrometry (*6*) (Au substrate), scanning electron microscopy (SEM), and scanning tunneling microscopy.

EXPERIMENTAL SECTION

Coronene was chosen as the test substance for pattern transfer experiments. It has negligible vapor pressure at room temperature ($p < 10^{-12}$ Torr), yet was conveniently vapor-deposited under vacuum (10^{-5} Torr) from a crucible heated to about 225 °C. A mask with a lithography test pattern was pressed against the stainless steel and KBr sample substrates during evaporation, producing a patterned film as shown in Figure 3a. The micrographs of Figures 3 and 4 were obtained by using the fluorescence of coronene under UV illumination. Film thicknesses were measured during evaporation with a quartz crystal balance.

The apparatus used for transfer is shown in Figure 1. Standard 25 mm diameter NaCl windows were used as transfer targets. Some visible coloration due to color centers appeared when using 248-nm laser pulses for transfer, but did not interfere with IR analysis of coronene deposits. A 0.25-mm vacuum gap between the sample and target was maintained by a spacer. Forepump vacuum of about 50 mTorr was sufficient to make the mean free path of vaporized molecules larger than the gap width. The vacuum also served to press and seal the transfer target plate against an O-ring, which made it easy to remove. A complete transfer experiment took no longer than 1 to 2 min including pump-down.

Two different lasers were used to effect the transfers: a Nd:YAG system (1064 nm) with 10-ns pulse duration and maximum fluence of 400 mJ/cm^2, and a KrF exciplex laser (248 nm) with 25-ns pulse duration and 250 mJ/cm^2 maximum fluence. Because the beam profile of the Nd:YAG laser is very inhomogeneous at the laser exit, the transfer experiments were set up 10 m away in the far field where the profile is more even. The exciplex laser was operated with the unstable resonator cavity, which produces a beam profile (approximately 0.5 × 2.0 cm) much more uniform than that of the Nd:YAG laser.

Figure 2 compares the Fourier transform infrared (FTIR) spectra of an original coronene film with one that was transferred with a 1064-nm pulse. Obviously no decomposition occurs due to the transfer process. The same observation was made at the 248-nm transfer wavelength. Two strong IR absorption bands

* To whom correspondence should be addressed.

0003-2700/90/0362-2385$02.50/0 © 1990 American Chemical Society

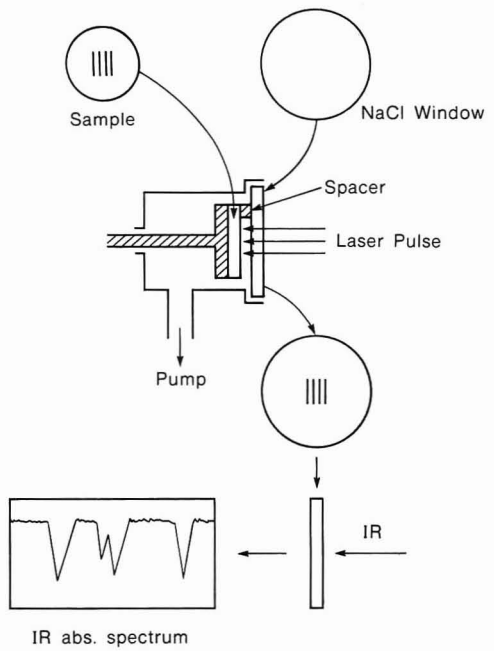

Figure 1. Schematic representation of the laser transfer technique, as applied for obtaining transmission IR spectra of patterned organic films.

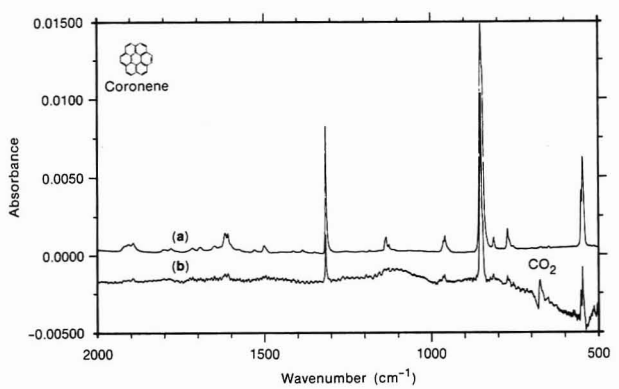

Figure 2. IR spectra of coronene (a) in KBr and (b) 54 nm thick film transferred with one 1064-nm laser pulse from stainless steel substrate to NaCl target; resolution, 2 cm^{-1}.

of coronene at 845 and 1314 cm^{-1} can readily be oberved at 1-nm film thickness, in the 50 × 50 μm^2 minimum area which can be resolved with the FTIR microscope attachment (Bruker IR/85 or IR/44 with a high gain MCT detector).

RESULTS

(a) 1064-nm Laser, Stainless Steel Substrate. Figure 3a shows the pattern of coronene stripes before transfer. The film was 23 nm thick, the smallest bars measured 160 × 800 μm and were spaced 120 μm apart, about half the vacuum gap distance (250 μm). The substrate was polished stainless steel. Exposure to a single pulse of 1064-nm radiation (200 mJ/cm^2) resulted in near-quantitative transfer of the coronene pattern to the NaCl target which is shown in Figure 3b. The transferred pattern is inverted as a result of the geometry of the experiment. Comparison with a film of known thickness evaporated directly on NaCl showed that the transferred pattern contained at least 95% of the original material. Its structure was grainy under higher magnification. The transferred deposit of Figure 3b also shows random, spotlike inhomogeneities which were attributed to imperfections of the transfer target.

Most strikingly the features of the original pattern are reproduced almost exactly in the transferred deposit. Fill-in between the smallest stripes is negligible and amounts to less

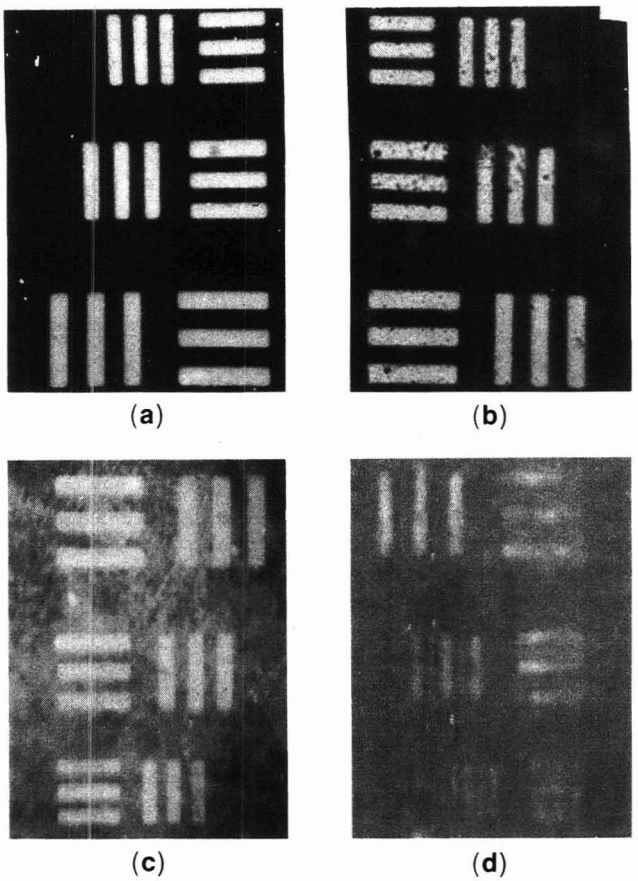

Figure 3. Fluorescence micrographs of patterned coronene films: (a) original pattern on polished stainless steel substrate, (b) same sample after transfer to NaCl target with one 1064-nm pulse, (c) residue on KBr substrate after exposure to one 248-nm pulse, (d) transferred portion of same sample on NaCl target.

than 1 nm of coronene according to IR measurements. Broadening of the stripes is no more than the standard error of the measurement which is about 6 μm.

Figure 4b presents the result of transfer from a rough sample surface shown in Figure 4a, using 400 mJ/cm^2 fluence. The surface topography is modulated by turning marks. This modulation shows up in the film thickness of the transferred deposit. The transfer process is obviously not just the reverse of the original vapor deposition of coronene.

A quite different modulation effect is exhibited in parts c and d of Figure 4. The latter is an enlargement of the target picture Figure 3b (longest bars, rotated 180°), the former shows its corresponding residue on the steel sample surface after transfer. Both images exhibit a pattern of parallel stripes unrelated to sample topography. This pattern is due to laser intensity variation caused by interference in the vacuum gap. The stripe separation distance of 28 μm can be accounted for with an angle of about 0.5° between sample and target surfaces. Interference patterns generated in this way contain useful information and permit structuring of surface films without using a mask.

(b) 248-nm Laser, KBr Substrate. Figure 3c shows the KBr sample and Figure 3d the NaCl transfer target, both after applying a single, 248-nm laser pulse with about 50 mJ/cm^2 fluence. The coronene film thickness was 50 nm. Clearly transfer at this fluence was incomplete. At higher fluences, up to 160 mJ/cm^2, the coronene pattern was completely removed from the sample surface but no transfer image was formed on the target. The transferred stripes in Figure 3d are 20–30% narrower than the original ones, Figure 3c. Surprisingly a thin extra stripe appears in the gap between the bars of the pattern, becoming more pronounced (albeit

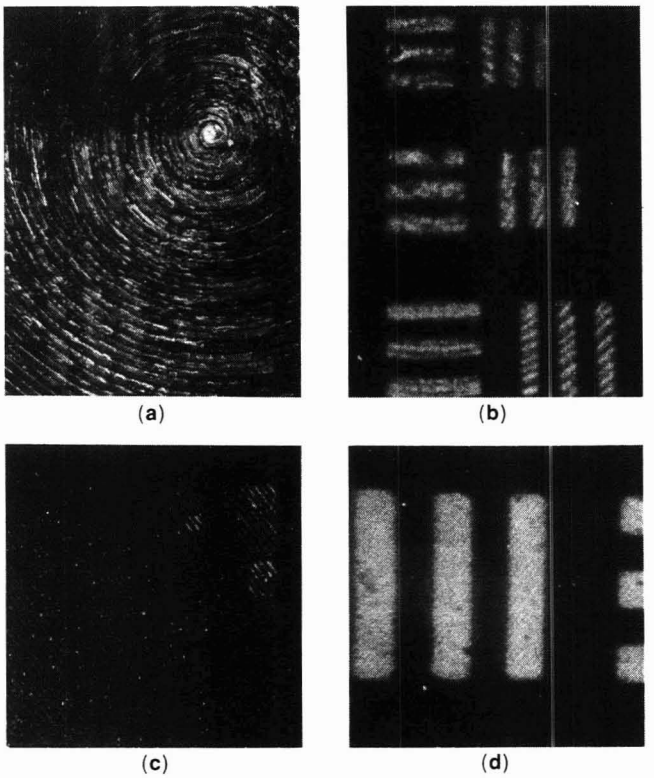

Figure 4. Micrographs in visible light (a) and in fluorescence (b to d) of patterned coronene films: (a) 25 nm thick film pattern before transfer, on stainless steel surface corrugated by turning marks; (b) same pattern after transfer to NaCl target with one 1064-nm pulse; (d) enlargement of the longest bars in Figure 3b, rotated 180°, exhibiting interference fringes; (c) corresponding residue on polished stainless steel sample.

poorly visible in the micrograph) as the bars get narrower.

DISCUSSION

The 1064- and 248-nm experiments are complementary in the sense that the substrate but not the coronene film absorbed the laser radiation in the former, while in the latter the opposite was the case. It is obvious from Figure 3 that in both cases the deposit leaves the surface in a highly directional way with an angular distribution sharply peaked at the surface normal, $\theta = 0$. If the transfer followed a $\cos^2 \theta$ distribution, as is often observed in laser desorption of small surface coverages, the pattern should be obliterated and no image formed. Instead the angular spreading is no more than about 1.4° at 1064 nm. Apart from this directionality the results point to different mechanisms at 1064 and 248 nm.

The grainy deposit formed in 1064-nm transfers indicates that a large fraction of the film is driven across the vacuum gap in the form of solid or liquid particles. Most likely this is due to a blasting mechanism. Rapid heating of the interface between sample and film generates a rapidly expanding vapor layer which breaks up the bulk of the film and drives the fragments vertically from the surface. The process in the latter phase resembles one being used to lift contaminant particles off surfaces (*3*). Its high directionality, even at film edges, as evident from Figure 3b, is astonishing.

At 248 nm heat is deposited mainly in the top portion of the organic film, generating a dense vapor layer at the vacuum interface. Under these conditions a highly directional, adiabatic expansion of the vapor occurs (*4*). We speculate that the extra stripes appearing in the transferred pattern, Figure 3d, are due to shock fronts, which are formed when the supersonic expansion plumes coming from adjacent bars of the pattern collide. At high laser fluences, excessive heating of the expanding vapor by light absorption may be responsible for complete disappearance of a transferred pattern.

CONCLUSIONS

Our results demonstrate that pulsed laser heating is a useful method for transferring an organic surface film to a substrate on which it can be analyzed by transmission IR spectroscopy. When a moderate vacuum gap width between sample and transfer target is used, the method preserves spatial information with a precision exceeding the resolution of an IR microscope. This is especially true, and the method works best, when the substrate rather than the film itself is heated by the laser, as was the case in our 1064-nm experiments. Under these conditions particulate matter is transferred by a highly directional blasting mechanism. If the laser light is mainly absorbed by the film, directional transfer again occurs by a strongly forward-peaked expansion of the vapor. Both directional mechanisms depend on formation of a dense vapor layer and will therefore fail eventually when the surface coverage gets very small. Sample surface topography translates into modulation of the transferred film thickness by effects including optical interference.

LITERATURE CITED

(1) Lazare, S.; Granier, V. *Laser Chem.* **1989**, *10* (1), 25.
(2) Nelson, R. W.; Rainbow, M. J.; Lohr, D. E.; Williams, P. *Science* **1989**, *246*, 1585.
(3) Imen, K.; Lee, S. J.; Allen, S. D. *Conference on Lasers and Electro-Optics*; 1990 Technical Digest Series; Optical Society of America: Washington, DC, 1990; Vol. 7, p 228.
(4) Kelly, R. *Proc. SPIE—Int. Soc. Opt. Eng.* **1989**, *1056*, 258.
(5) Bletsos, I. V.; Hercules, D. M.; van Leyen, D.; Benninghoven, A. *Macromolecules* **1987**, *20*, 407.
(6) Yang, M.; Millard, J. R.; Reilly, J. P. *Opt. Commun.* **1985**, *55*, 41.

RECEIVED for review June 18, 1990. Accepted August 6, 1990.

Endothermic Ion–Molecule Reactions. 4. Site-Directed Fragmentation in N-Acetylated Oligosaccharides at Low Beam Energies

Ron Orlando* and Catherine Fenselau

Structural Biochemistry Center, Department of Chemistry and Biochemistry, University of Maryland Baltimore County, Baltimore, Maryland 21228

Robert J. Cotter*

Middle Atlantic Mass Spectrometry Facility, Department of Pharmacology and Molecular Sciences, Johns Hopkins University School of Medicine, Baltimore, Maryland 21205

Reactive endothermic collisions between N-acetylated oligosaccharides and ammonia have been carried out at very low beam energies. At energies slightly above those for which the proton collision complex is observed, the major fragment ions include those resulting from cleavages localized at the amide bond. At somewhat higher energies, localized fragmentation gives way to cleavages of the glycosidic bond. Such studies indicate that fine tuning of the beam energy can be employed for *site-directed* fragmentation in endothermic collision complexes.

INTRODUCTION

In a series of reports we have advocated the use of endothermic reactions between protonated molecular ions of peptides and ammonia as alternatives to low-energy and high-energy *collision-induced decomposition* (CID) for the purpose of obtaining structural (sequence) information (*1–4*). Ammonia was chosen as the target gas since the reaction

$$NH_4^+ + CH_3CONH_2 \rightarrow NH_3 + CH_3CONH_3^+ \quad (1)$$

is slightly exothermic [−0.16 eV (*5*), −0.10 eV (*6*)] and could be used to estimate the endothermicity of proton transfer from a peptide to ammonia, in peptides where the proton was associated with the amide bond.

We were then able to demonstrate that (near-threshold) proton-transfer reactions occur via a proton-bound *collision complex* and that additional beam energy results in opening new dissociation channels that lead to the desired, structurally informative fragment ions (*1*). In our initial studies, we followed the relative intensities of product ions from the reaction of protonated *leucine-enkephalin* and ammonia as a function of primary-ion beam energy. The proton-transfer reaction (i.e. formation of NH_4^+) occurred with a threshold of 6 eV (or 0.18 eV in the *center-of-mass* frame, consistent with thermodynamic data). In addition, the formation of the collision complex itself (MNH_4^+) could be observed and had a similar threshold. At 10 eV (in the laboratory frame), the proton-transfer reaction gave way to the formation of fragment ions of leucine-enkephalin at m/z 279, 397, and 425. At this energy, the observed intensity of the collision complex also decreased, reflecting an increase in the number of dissociation channels for a complex with higher internal energy. These product ions are clearly associated with a collision intermediate, since their intensities decrease rapidly at 15 eV, and thereafter exhibit behavior identical with that observed for collisions with helium at corresponding relative energies (*4*).

* To whom correspondence should be addressed.

In that initial study we noted that collisions between protonated molecular ions of the oligosaccharide *stachyose* and ammonia did not produce a reaction threshold and that (in this case) the increasing intensity for proton transfer as the beam energy approached zero was consistent with an exothermic reaction (*1*).

We subsequently confirmed the assumption that proton transfer occurred for protons attached to the amide bond by examining the behavior of several other peptides that contained very basic residues, had no free amino or carboxy termini, or had a mixture of amide and ester linkages (*2*). A hexapeptide, *Leu-Trp-Met-Arg-Phe-Ala*, and *luteinizing hormone releasing hormone* (LHRH), both containing arginine residues, failed to produce fragment ions from a collision complex prior to the onset of *direct* processes (i.e. low-energy CIDs). In these cases it is supposed that the positive charge is carried on the arginine and that proton transfer is, therefore, highly endothermic. *Valinomycin* is a *depsipeptide* having alternate amide and ester linkages. In this case, mixed exothermic and endothermic (threshold = 0.16 eV) behavior reflected protonation at either amide or ester bond sites. Finally, the cyclic *cyclosporin* revealed behavior similar to that of leucine-enkephalin: the formation of a collision complex at 9 eV (0.14 eV in the center-of-mass frame) and fragmentation at slightly higher energies. In this very hydrophobic, cyclic peptide, the amide bonds offered the only sites for protonation.

We have been interested in developing similar schemes for carbohydrates. Because reactions of protonated molecular ions of neutral carbohydrates (i.e. stachyose) with ammonia are exothermic, our first studies have involved N-acetylated glucosamines, which contain amide bonds. Our results (described below) confirm the formation of a collision complex at energies that are consistent with proton transfer from the amide bond. In addition, increases in the beam energy sequentially open channels for fragmentation localized at the N-acetyl moiety and at the glycosidic bond. The results suggest that fine-tuning of the beam energy can be used for directed, *site-specific* fragmentation.

EXPERIMENTAL SECTION

The studies reported here were carried out on a JEOL (Tokyo, Japan) Model HX110/HX110 tandem mass spectrometer with four-sector (*EBEB*) geometry. Protonated molecular ions were produced by fast atom bombardment, accelerated to 10 keV and mass-selected by MS1. These were then passed through a collision chamber containing ammonia gas and focused to the detector at the end of MS2. The collision gas pressure was adjusted for 80% attenuation of the molecular beam, with the collision cell maintained at 10kV − V_{lab}, where $E_{lab} = eV_{lab}$ corresponds to the *beam energy*. *Product ion* mass spectra were obtained for beam energies ranging from 1 to 60 eV, by scanning the magnetic field (B) in

0003-2700/90/0362-2388$02.50/0 © 1990 American Chemical Society

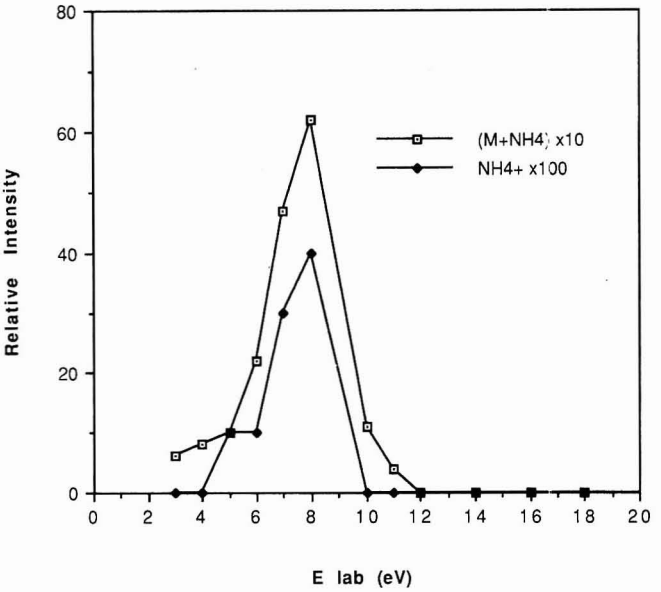

Figure 1. Relative intensities for the MNH_4^+ ion (collision complex) and NH_4^+ ion (proton transfer) for the reaction between *N,N′,N″*-triacetylchitobiose and ammonia in the threshold region.

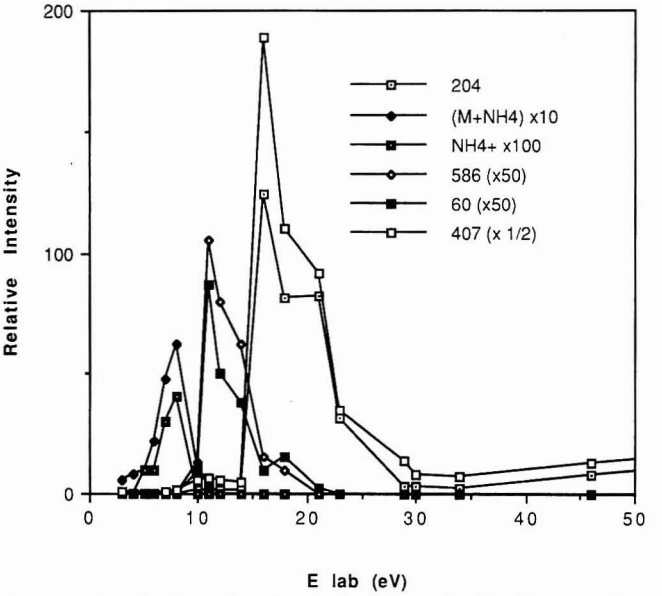

Figure 2. Relative intensities for product ions vs ion kinetic energy for the reaction of *N,N′,N″*-triacetylchitotriose with ammonia.

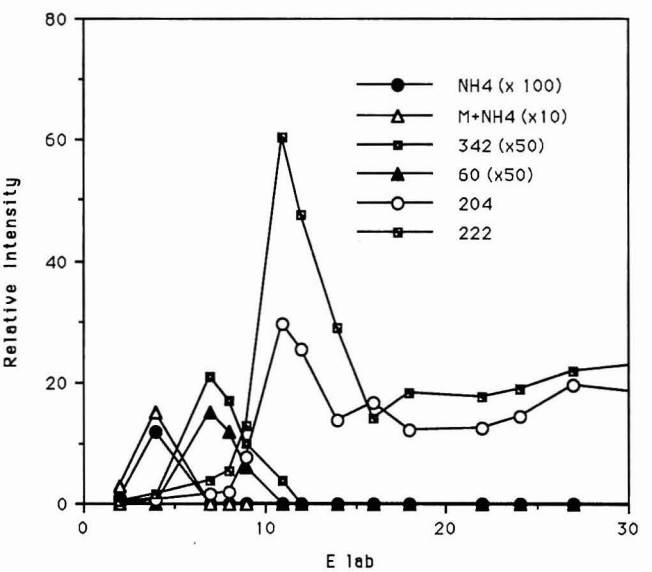

Figure 3. Relative intensities for product ions vs ion kinetic energy for the reaction of GalGlcNAc with ammonia.

MS2. *N,N′,N″*-Triacetylchitobiose and GalGlcNAc were used in this study and were obtained from Sigma (St. Louis, MO) and Biocarb, Inc. (Lunde, Sweden), respectively.

RESULTS AND DISCUSSION

***N,N′,N″*-Triacetylchitotriose.** As in the case of the peptides studied earlier, we assumed that protonation of N-acetylated amino sugars is associated (predominantly) with one or another of the amide bonds and that proton transfer to ammonia would be an endothermic process, in contrast to the exothermic behavior of stachyose. Thus, one possible structure for the protonated molecular ion of *N,N′,N″*-triacetylchitobiose is shown in I. While the proton and charge

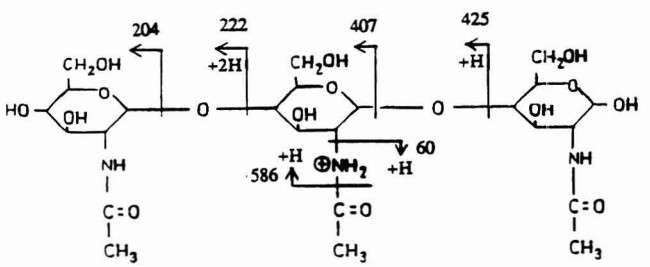

I

are shown as localized on the nitrogen atom of the amide bond, we note that numerous studies of amides in solution (*7*, *8*) suggest that the proton may be attached to the oxygen (II and III).

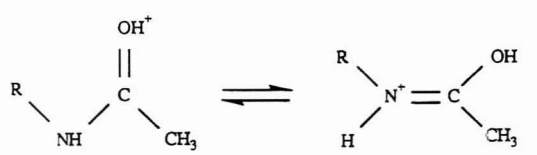

II III

Figure 1 shows the threshold region for the formation of the collision complex (MNH_4^+) and the ammonium ion in the reaction of *N,N′,N″*-triacetylchitobiose with ammonia. The reaction is exclusively endothermic, and the thresholds at approximately 5 eV (0.14 eV in the center-of-mass) are again consistent with proton transfer to ammonia from a protonated amide.

The major fragment ions observed in the product ion mass spectra of *N,N′,N″*-triacetylchitobiose are also shown in structure I. These include cleavage of the amide bond with charge retention on the nitrogen (m/z 586) and cleavage of the C2–N bond to form $+NH_3COCH_3$ at m/z 60 (both of which could presumeably occur at any of the three N-acetyl side chains), cleavage of the O–C4 bonds (m/z 222 and 425), and the formation of oxonium ions at m/z 204 and 407. Figure 2 is a plot of the product ions for the reaction of *N,N′,N″*-triacetylchitobiose with ammonia over a wider range of beam energy. Beginning at 10 eV, the intensities of the ammonium ion and the collision complex decrease considerably as channels for fragmentation of the N-acetyl moiety (leading to the ions at m/z 60 and 586) are opened up. As the beam energy is further increased (around 15 eV), these fragmentation channels give way to those in which the C1″–O and C1′–O bonds are cleaved, leading to the formation of the oxonium ions at m/z 204 and 407, respectively. Intensities for the ions formed by cleavage of O–C4′ and O–C4 bonds (m/z 222 and 425, respectively (not shown)) follow the same behavior. At still higher energies (around 30 eV), fragmentation associated with the proton-bound collision complex decreases, and formation of the oxonium ions from direct processes (collision-

induced dissociations) occurs, with the intensity of these ions rising slowly with beam energy.

GalGlcNAc. The maxima in product ion intensities observed at low beam energies for peptides (*1*, *2*) and *N,N′,N″*-triacetylchitotriose (Figure 2) do not occur when inert target gases (e.g helium) are used and are associated with the formation of a collision complex. The two distinct maxima observed for the reaction of *N,N′,N″*-triacetylchitotriose with ammonia suggest that cleavage of the glycosidic bonds occurs when the internal energy of the collision complex is somewhat higher than that needed for cleavages localized at the charge site. Because it is difficult to establish which fragment ions are associated with each of the three possible amide protonation sites, similar studies were carried out on GalGlcNAc, a disaccharide containing a single N-acetylated site. The structure of the protonated molecular ion is shown as structure IV, along with the major fragment ions observed in the product ion mass spectra.

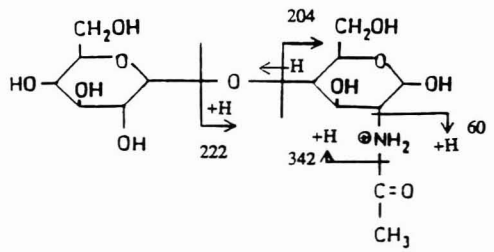

IV

The intensities of the product ions for the reaction of GalGlcNAc with ammonia as a function of beam energy are shown in Figure 3. The NH_4^+ (proton transfer) and MNH_4^+ (collision complex) ions have thresholds of approximately 3 eV (0.13 eV in the center-of-mass). At 7 eV, the major ions (m/z 60 and 342) correspond to cleavages localized at the charge site. At 11 eV, cleavages of the glycosidic bond (m/z 204 and 222) predominate, with retention of the charge on the sugar containing the protonated amide site.

CONCLUSIONS

In an earlier paper (*4*) we noted that the b and y fragment ions of leucine-enkephalin are produced most abundantly at endothermicities of 0.3 eV (center-of-mass) and that the product ion spectra (in particular: the ratio of m/z 278/279 intensities) resembles those produced by high-energy (rather than low-energy) collision-induced dissociation with helium. These ions result from the cleavage of the peptide (amide) bond. Similarly, cleavages localized at the amide bond in N-acetylated sugars also occur when the endothermicity is approximately 0.3 eV (11 and 7 eV for *N,N′,N″*-triacetylchitotriose and GalGlcNAc, respectively, on the laboratory scale). In contrast, cleavages of the glycosidic bond occur at endothermicities of 0.43 and 0.47 eV (for *N,N′,N″*-triacetylchiotriose and GalGlcNAc, respectively). While such cleavages may result from rearrangement reactions, we have also considered the possibility that they are *remote-site* fragmentations conistent with the idea that remote-site fragmentation is observed primarily in higher energy collisions (*9*) and that endothermic reactions result in product ion spectra which mimic those from high-energy collisions. That possibility has been borne out by subsequent studies (*10*) on the endothermic reactions of protonated *N,N′*-dimethylmyristamide with methylamine, in which increases in the collision energy just above threshold resulted in a shift from cleavages localized at the amide bond to (exclusively) cleavages along the hydrocarbon chain.

Endothermic reactions of peptides with ammonia were designed initially as a strategy for reducing the relative (and laboratory) energies required for efficient fragmentation of large molecules (*1*, *2*). We have subsequently been able to show that product ion mass spectra involving reactive collisions could produce spectra resembling those of high-energy CIDs at low energies (*4*, *10*), that adjustment of the beam energy over a small range can be used to direct fragmentation (this study), and that such fragmentation may be directed toward remote-site cleavages (*10*).

Thus, it should be possible to obtain spectra resembling those of high-energy CIDs on less expensive triple-quadrupole and hybrid instruments. The observation of remote-site fragmentation is an advantage for molecules that contain cationic (or anionic) sites, for which there is often little structural information on remote sites of the molecule. In addition, the ability to select energies that will alternately produce localized and remote-site fragmentation will provide two distinct structural views of the molecule.

LITERATURE CITED

(1) Orlando, R.; Murphy, C.; Fenselau, C.; Hansen, G.; Cotter, R. J. *Anal. Chem.* **1990**, *62*, 125–129.
(2) Orlando, R.; Fenselau, C.; Cotter, R. J. *Org. Mass Spectrom.* **1989**, *24*, 1033–1042.
(3) Orlando, R.; Cotter, R. J.; Fenselau, C. *J. Am. Chem. Soc.* **1990**, *112*, 5742–5749.
(4) Orlando, R.; Fenselau, C.; Cotter, R. J. *Rapid Commun. Mass Spectrom.* **1990**, *4*, 259–262.
(5) Yamdagni, R.; Kebarle, P. *J. Am. Chem. Soc.* **1973**, *95*, 355–358.
(6) Lias, S. G.; Bartmess, J. E.; Liebman, J. F.; Holmes, J. L.; Levin, R. D.; Mallard, W. G. *J. Phys. Chem. Ref. Data* **1988**, *17* (Suppl. 1).
(7) Martin, R. B. *J. Chem. Soc., Chem. Commun.* **1972**, 793–794.
(8) Molday, R. S.; Kallen, R. G. *J. Am. chem. Soc.* **1972**, *94*, 6739–6745.
(9) Adams, J.; Gross, M. L. *J. Am. Chem. Soc.* **1986**, *108*, 6915–6921.
(10) Orlando, R.; Fenselau, C.; Cotter, R. J. *Org. Mass Spectrom.*, in press.

RECEIVED for review May 24, 1990. Accepted July 20, 1990. This work was supported by a grant (BBS 87-14238) from the National Science Foundation. Mass spectral measurements were carried out at the Structural Biochemistry Center, an NSF supported Biological Instrumentation Center at the University of Maryland Baltimore County.

Recognition of Trypsin Autolysis Products by High-Performance Liquid Chromatography and Mass Spectrometry

Martha M. Vestling,*[1] Constance M. Murphy, and Catherine Fenselau

Department of Chemistry and Biochemistry, University of Maryland Baltimore County, Baltimore, Maryland 21228

Potential artifactual contributions are assessed in high-pressure liquid chromatograms and fast atom bombardment mass spectra from autolysis of different preparations of the widely used protease trypsin. Both commercially supplied and laboratory-purified samples were examined. Bovine pancreatic trypsin (1 mg/mL) was found to be completely destroyed in 2 h at pH 8.5, degraded to a complex mixture of small peptides which were characterized by their molecular weights. Some identifications were supported by sequencing by tandem mass spectrometry or by mass spectrometric analysis of the mixture resulting from a single Edman degradation. Autolysis of porcine pancreatic trypsin produced a completely different set of peptides. Five sites of hydrolysis at asparagine residues in bovine trypsin were also identified.

INTRODUCTION

The serine protease trypsin, also called β-trypsin, is widely used to catalyze the hydrolysis of proteins to produce mixtures of peptides suitable for Edman sequencing and mapping by high-pressure liquid chromatography (HPLC) and mass spectrometry. Pancreatic bovine trypsin is a single chain of 223 amino acids with six disulfide bonds. Its structure has been firmly established by X-ray crystallography (*1*), and its primary structure is shown in Figure 1. Trypsin functions optimally at pH 8–9 and shows high specificity for catalyzing the hydrolysis of amide bonds whose carbonyls are part of lysine or arginine (*2*). Since trypsin's own structure contains 14 lysines and 2 arginines, it is a substrate for its own action, and this autolysis has long been recognized as a potential source of artifacts in structure studies (*3*). This paper reports a determination of the autolysis products that are preferentially detected by fast atom bombardment mass spectrometry when the product mixture is analyzed directly and when it is fractionated by HPLC. The autolysis products from trypsin from two different suppliers and from freshly purified material were characterized both by HPLC and mass spectrometry.

EXPERIMENTAL SECTION

Bovine pancreatic, TPCK treated trypsin, phenyl isothiocyanate, and thioglycerol were obtained from Sigma Chemical Co., St. Louis, MO. Two different lots of trypsin were used. The trypsin, labeled sequence grade, bovine (lots 11594921-02 (Nov 89) and 12058920-03 (Nov 90)), obtained from Boehringer Mannheim Biochemicals, Indianapolis, IN, was actually porcine trypsin. See Results and Discussion below. Sigma trypsin was used in the studies reported, unless otherwise specified. Trifluoroacetic acid (TFA) was obtained from Aldrich Chemical Co., Milwaukee, WI.

High-Performance Liquid Chromatography. HPLC was performed on a Shimadzu dual pump system (Model LC-6A pumps) with a variable wavelength UV detector (Model SPD-6A) equipped with a Brownlee Aquapore RP300 (C8) (4.6 × 250 mm) column: mobile phase A, 0.1% TFA/water; mobile phase B, 0.1% TFA/acetonitrile. Fractions collected every 3 min in iced polypropylene tubes were frozen and lyophilized.

Mass Spectrometry. Conventional magnetic scans were made on the first two sectors (EB) of a JOEL HX110/HX110 mass spectrometer (Tokyo, Japan) using either a JOEL FAB gun or a JOEL cesium ion gun and the JOEL DA5000 data system. The FAB (fast atom bombardment) gun was operated at 6 kV and the Cs ion gun at 23 kV. Resolution was 3000. Tandem measurements were obtained by utilizing all four sectors (EBEB) on the JOEL HX110/HX110 instrument. Linked B/E scans were made on MS-2, following mass selection of precursor ions by MS-1. In these experiments, helium was used as the collision gas between the two mass spectrometers, at pressure sufficient to attenuate the precursor ion beam by 80%. The accelerating voltage was 10 kV, and the collision cell was floated at 4 kV. Resolution in both MS-1 and MS-2 was 1000. For both scanning modes, the peptides dissolved in 0.1% trifluoroacetic acid were measured from thioglycerol. The computer program, RESIDUES, written by David Heller (Middle Atlantic Mass Spectrometry Center, Johns Hopkins University, Baltimore, MD) was used to assist interpretation of tandem mass spectra while MacProMass (Terry D. Lee and Sunil Vemuri, Beckman Research Institute, City of Hope, Duarte, CA) and PROCOMP (P. C. Andrews, Department of Biochemistry, University of Michigan, Ann Arbor, MI) supported interpretation of the conventional magnetic scans.

Trypsin Autolysis. Trypsin (1 mg) was placed in a 1-dram vial and 1 mL of a solution that was 0.1 M NH_4HCO_3 and 0.1 mM $CaCl_2$ (pH 8.5) was added. The mixture was allowed to stand at room temperature for 2 h before it was frozen and lyophilized. The reaction was monitored by HPLC: gradient, 10–25% B over 10 min then 25% B for 5 min then 25–40% B for 5 min then 40% B for 5 min then 40–60% B for 5 min; flow rate, 1.0 mL/min.

Trypsin Purification. TPCK treated trypsin from Sigma Chemical Co. (3–5 mg) was dissolved in 0.1 mM $CaCl_2$ (600–1000 μL) and immediately iced. Trypsin was separated from residual chymotrypsin and autolysis products by reverse-phase HPLC (*4*): gradient, 10–35% B over 5 min, 35–45% B over 10 min, 45–70% B over 5 min, 70% B for 5 min making a 25-min run; flow rate, 1.0 mL/min; 215 nm; 200 μL sample injected.

Edman Degradation. Trypsin autolysis and Edman degradation were carried out sequentially in one 1-dram vial with a Teflon-lined cap. A modified version of the Edman method of Bradley et al. (*5*) was used.

RESULTS AND DISCUSSION

Purified and unpurified trypsin dissolved in buffer suitable for incubation with substrate proteins, i.e. pH 8–9, undergo rapid autolysis. In 0.1 M NH_4HCO_3 (pH 8.5) (1 mg/mL) trypsin is completely autolyzed after 2 h at room temperature, based on HPLC analysis. The same HPLC pattern was obtained after 30 min with a higher trypsin concentration (4 mg/mL). Trypsin dissolved in 0.1 mM $CaCl_2$ (pH 6) or in 0.1% trifluoroacetic acid (pH 2) and kept on ice for several hours showed no change in its HPLC pattern.

Comparison of the HPLC traces of autolysis products from purified and unpurified bovine pancreatic trypsin (Figure 2a,b) shows more similarities than differences. The higher molecular weight peptides elute at the longer retention times and are not fully separated by the gradient shown. The sample from unpurified trypsin has a few more components. This is consistent with the mass spectrometric data, and attributable to the presence and action of chymotrypsin and previous autolysis (*4*).

*To whom correspondence should be addressed.
[1] On sabbatical leave from the Department of Chemistry, State University of New York College at Brockport, Brockport, NY 14420

0003-2700/90/0362-2391$02.50/0 © 1990 American Chemical Society

Table I. Observed Autolysis Products from Bovine Pancreatic Trypsin

total hydrolysate purified trypsin[a] m/z	HPLC fractions unpurified trypsin[a] m/z	assignment residues	assignment cuts[b]	calculated monoisotopic MH^+	additional information[c]
	3210.5	[140–149]-[150–170]	K/K, K/K	3209.51	
	3140.8				
2612.9	2611.8	[201–223]	K/–	2613.35	
	2552.5	[100–125][d]	R/K	2552.25	
	2304.8	[70–89][e]	K/K	2305.16	
2273.5	2272.5	[70–89][d]	K/K	2273.16	E
2193.0	2192.9	[150–170][d]	K/K	2193.01	
	2163.0	[50–69][d]	R/K	2163.06	
1901.1	1900.9				
1775.0	1775.1	[1–14]-[137–139]	–/Y,K/K	1774.86	
	1578.7				
	1433.8	[187–200][d]	K/K	1433.72	
	1375.9	[78–89]	N/K	1375.73	E
1174.8	1174.9	[80–89]	N/K	1174.65	S, ES
		[160–170]	N/K	1174.54	S, E
1153.8	1153.8	[126–136][d]	K/K	1153.57	S, ES
1117.7	1117.6	[70–79]	K/N	1117.53	
	1111.8	[209–217][d]	K/K	1111.56	
1037.7	1037.6	[150–159]	K/N	1037.49	ES
1018.8	1020.7	[140–149][d]	K/K	1019.52	
	916.4	[70–77]	K/N	916.45	
906.7	906.6	[201–208][d]	K/K	906.50	
	867.7	[15–22]	Y/Y	867.42	S
805.6	805.5	[92–99][d]	K/R	805.42	S, E
	802.7	[70–76]	K/Y	802.41	
659.8	659.5	[44–49][d]	K/R	659.38	S, E
633.7	633.4	[218–223][d]	K/–	633.32	S, E
	562.3	[92–97]	K/N	562.28	S
560.7	560.4	[15–19]	Y/N	560.30	S

[a] Monoisotopic masses were measured (*6*). [b] Residues that contributed the carbonyls from each hydrolyzed bond. [c] S, sequenced by tandem mass spectrometry; E, N-terminus residue confirmed by Edman degradation; ES, peptide product from one Edman degradation sequenced by tandem mass spectrometry. [d] Predicted. [e] Methionine sulfone.

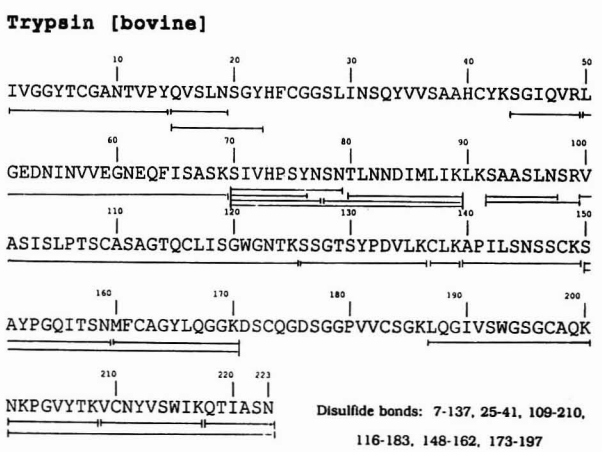

Figure 1. Primary structure of bovine pancreatic trypsin from ref 1. See Table I for the protonated monoisotopic weights of the underlined peptides.

Table I summarizes the mass spectra of the autolysis products of bovine trypsin. Determinations are reported for an unfractionated mixture from autolysis of purified trypsin and of seven fractions collected at 3-min intervals during the chromatographic separation of the autolysis mixture from unpurified bovine trypsin. Only ions with a signal to noise ratio greater than 3 are reported and only ions that appeared in determinations using both lots of Sigma trypsin. Additional ions were detected in the composite of the HPLC fractions, compared to the unfractionated sample, due both to the chymotryptic contamination and to the preferential desorption of peptides in mixtures that has been previously demonstrated (*7*). All the peaks detected in the mixture were also found in the fractions.

Formation of 16 peptides is predicted, based on the specificity for lysine and arginine, and assuming that all the disulfide bonds are reduced. Lysine at position 200 is regarded as not hydrolyzable because of the proline at position 201. Although these assumptions are qualified to some extent by the peptides identified in Table I, nonetheless, 12 of the predicted peptides are observed (starred). In five cases these assignments are confirmed by sequencing by tandem mass spectrometry (*8*) and/or by a single cycle of Edman degradation. The predicted autolysis fragments that are not observed include the heaviest, >4000 u and the three lightest, <400 u. Two disulfide bonded products were identified, [140–149]-[150–170] and [1–14]-[137–139], and five peptides were assigned as having been released from disulfide bonds, perhaps by reduction in the thioglycerol matrix used for fast atom bombardment mass spectrometry. Control of pH and/or a nonreducing matrix might preserve disulfide bonds and shift some of the potential autolysis background to a higher mass range, albeit with potentially altered solubility and sensitivity. Some peaks were assigned to peptides formed by incomplete hydrolysis, such as m/z 2612 to peptide [201–223]. Note also that m/z 2163 supports glutamic acid not glutamine at positions 52 and 62 in agreement with the X-ray data of Bode and Schwager (*1b*).

A number of ions were observed that could not be explained by cleaving only disulfide linkages and bonds containing lysine and arginine carbonyl groups. To assign structures to these ions, the primary structure of trypsin was searched for peptides of appropriate masses. In most cases this generated several candidates. In seven cases the final assignment is based on sequencing by tandem mass spectrometry and/or analysis of the products after one Edman degradation cycle (Table I). Edman degradation indicated that the m/z 1175

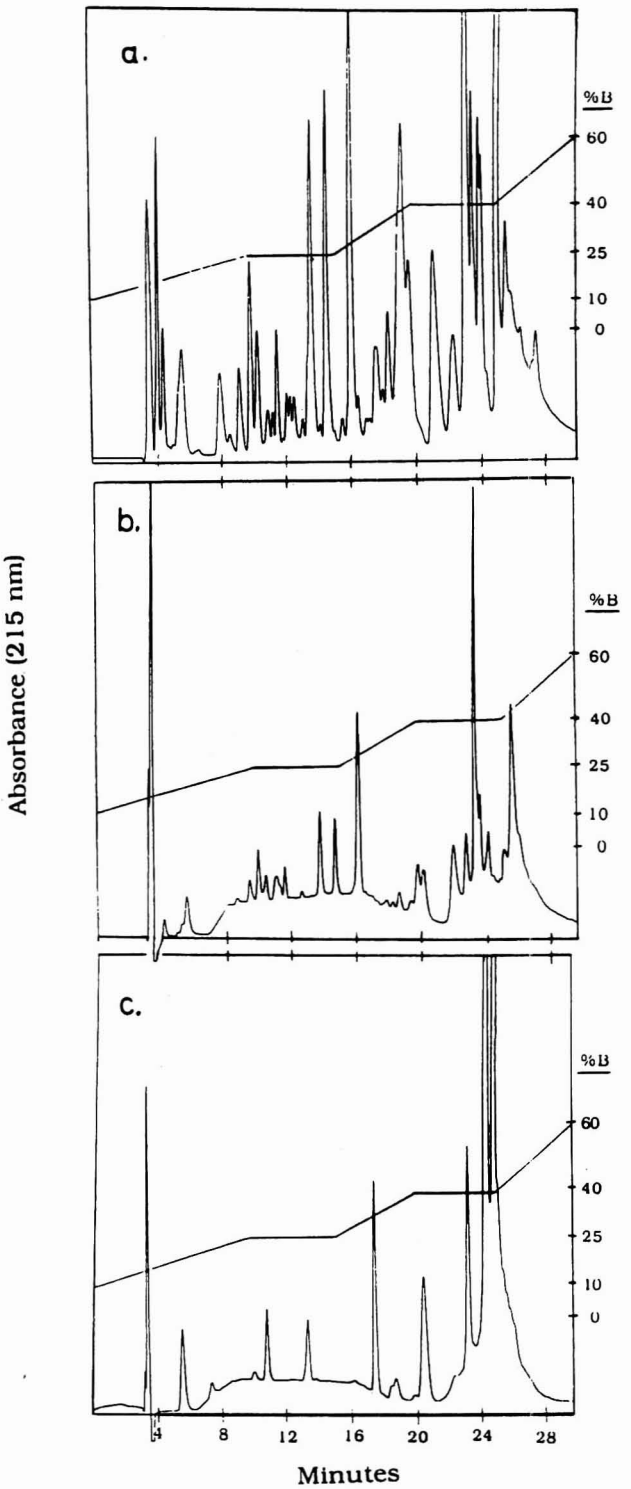

Figure 2. Reverse-phase HPLC of trypsin autolysis products: (a) trypsin from Sigma, (b) HPLC purified trypsin, and (c) sequence grade trypsin from Boehringer-Mannheim. See text for details.

peak corresponds to two isobaric peptides. To obtain assignments for the rest of the ions, priority was given to sequences that would be formed with at least one cut at lysine (K) or arginine (R) and, secondarily to peptides formed with the proteolytic selectivity expected from chymotrypsin (*9*) or ψ-trypsin (*10*), an early trypsin autolysis product with proteolytic activity like chymotrypsin. Four peptides in Table I {[70–76], [70–77], [70–79], and [1–14]-[137–139]} should be viewed as suggestions since additional experimental confirmation was not obtained.

It is of interest that formation of six of the peptides whose structures are confirmed by additional experiments (Table I) requires cleavage at five amide bonds whose carbonyl group

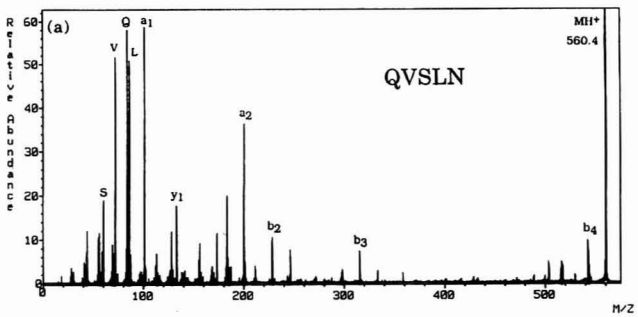

Figure 3. Mass spectrum obtained by collisional activation in a tandem mass spectrometer of QVSLN [15–19]. Assignment of sequence ions follows Biemann (*8*).

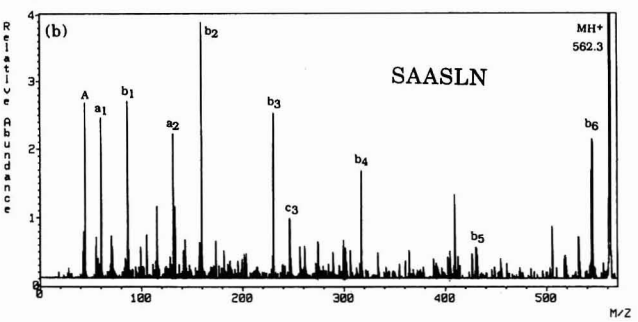

Figure 4. Mass spectrum obtained by collisional activation in a tandem mass spectrometer of SAASLN [92–97].

Table II. Observed Autolysis Products from Porcine Pancreatic Trypsin

total hydrolysate[a] m/z	assignment residues	assignment cuts[b]	calculated monoisotopic MH^+	additional information[c]
2283.3	[70–89][d]	K/K	2283.18	S
2211.1	[50–69][d]	R/K	2211.10	S
1768.9	[108–125][d]	R/K	1768.80	
1737.0	1736.84	K/–	1736.84	S
1469.9	[126–139][d]	K/K	1469.73	S
1143.0	[203–212]	K/Y	1143.55	
1106.7	[77–86]	F/M	1106.48	
1045.8	[90–99][d]	K/R	1045.56	
1006.7	[140–149][d]	K/K	1006.49	S
842.8	[100–107][d]	R/R	842.51	S
515.8	[46–49][d]	R/R	515.33	S

[a] Monoisotopic masses were measured (*6*). [b] Residues that contributed the carbonyls from each hydrolyzed bond. [c] S, sequenced by tandem mass spectrometry. [d] Predicted, assuming complete hydrolysis at lysine and arginine and reduction of all disulfide bonds.

is donated by asparagine. Spectra of two of these, [15–19] and [92–97] obtained by tandem mass spectrometry are presented in Figures 3 and 4. Fragment ions are identified following the nomenclature of Biemann (*8*) and support the assignment indicated. This detailed examination identifies 5 of the 16 asparagine residues as hydrolyzable under autolysis conditions. Nonenzymatic degradation of proteins at asparagine has been previously observed (*11*).

Autolysis of sequence grade trypsin from two different lots provided by Boehringer Mannheim produced a different HPLC pattern (Figure 2c) and mass spectra with no coincident peaks when compared to that from Sigma bovine trypsin. However, the peptide molecular weights observed in Table II are consistent with the structure of porcine trypsin (*12*) shown in Figure 5. Cleavage occurred primarily, but not exclusively at lysine and arginine. Although 80% or 179 of the amino acids are identical in bovine and porcine trypsins, the remaining 20% or 44 amino acid differences are sufficient

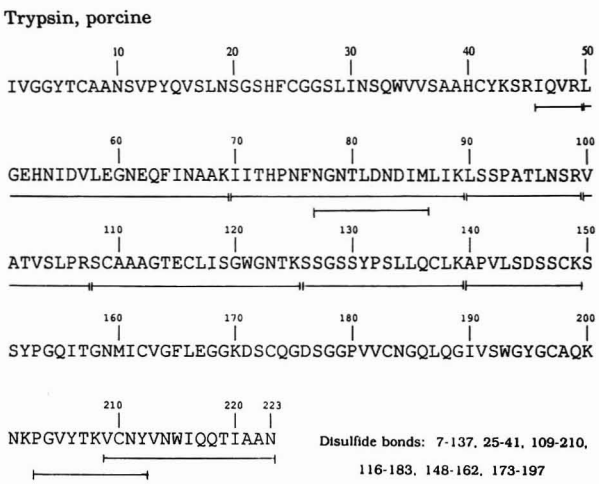

Figure 5. Primary structure of porcine pancreatic trypsin from ref 11. See Table II for the protonated monoisotopic weights of the underlined peptides.

to completely change the HPLC and mass spectrometric maps. In Table II (peaks observed from both lots), the number of peaks observed is smaller than that in column 1 of Table I; however, this may only reflect the slower proteolysis rate of porcine trypsin.

The autolysis studies reported here were carried out in the absence of substrate in order to produce the most inclusive set of potential artifactual peptides. The level and also the selection of autolytic peptides encountered will vary with the length of exposure of trypsin at pH 8, in stock solutions as well as in the proteolytic reaction itself. The level and selection of artifactual peaks that might be observed in mass spectra of total or partially fractionated trypsin digests may also vary with the protein substrate, since the peptides produced from different substrates may affect selective desorption in the FAB source differently and may inhibit autolysis at different rates. The value of the present experimental determination of autolysis products is confirmed by significant deviations from prediction based on trypsin's known specificity. Hydrolysis of bovine trypsin at asparagine under standard trypsin digestion conditions was documented.

LITERATURE CITED

(1) (a) Huber, R.; Kukla, D.; Bode, W.; Schwager, P.; Bartels, K.; Deisenhofer, J.; Steigeman, W. *J. Mol. Biol.* **1974**, *89*, 73–101. (b) Bode, W.; Schwager, P. *J. Mol. Biol.* **1975**, *98*, 693–717.
(2) (a) Walsh, K. A. *Methods Enzymol.* **1970**, *19*, 41–63. (b) Keil-Dlouha, V.; Zylber, N.; Tong, N.-T.; Keil, B. *FEBS Lett.* **1971**, *16*, 287–290. (c) Poncz L.; Dearborn, D. G. *J. Biol. Chem.* **1983**, *258*, 1844–1850.
(3) For example, Andrews, P. C.; Dixon, J. E. *Methods Enzymol.* **1989**, *168*, 97.
(4) Titani, K.; Sasagawa, T.; Resing, K.; Walsh K. A. In *High-Performance Liquid Chromatography of Proteins and Peptides*; Academic Press: New York, 1982; pp 23–27.
(5) Bradley, C. V.; Williams, D. H.; Hanley, M. R. *Biochem. Biophys. Res. Commun.* **1982**, *104*, 1223–1230.
(6) Yergy, J.; Heller, D.; Hansen, G.; Cotter, R. J.; Fenselau, C. *Anal. Chem.* **1983**, *55*, 353–357.
(7) (a) Hemling, M. E.; Carr, S. A.; Capiau, C.; Petre, J. *Biochemistry* **1988**, *27*, 699–705. (b) Gibson, B. W.; Biemann, K. *Proc. Natl. Acad. Sci. U.S.A.* **1984**, *81*, 1956–1960. (c) Naylor, S. A.; Findeis, A. F.; Gibson, B. W.; Williams, D. H. *J. Am. Chem. Soc.* **1986**, *108*, 6359–6363.
(8) Biemann, K. *Biomed. Environ. Mass Spectrom.* **1988**, *16*, 99–111.
(9) (a) Baumann, W. K.; Bizzozero, S. A.; Dutler, H. *FEBS Lett.* **1970**, *8*, 257–260. (b) Berezin, I. V.; Martinek, K. *FEBS Lett.* **1970**, *8*, 261–262.
(10) Keil-Dlouha, V.; Zylber, N.; Imhoff, J.-M.; Tong, N.-T.; Keil, B. *FEBS Lett.* **1971**, *16*, 291–295.
(11) Geiger, T.; Clarke, S. *J. Biol. Chem.* **1987**, *262*, 785–794.
(12) Hermodson, M. A.; Ericsson, L. H.; Neurath, H.; Walsh, K. A. *Biochemistry* **1973**, *12*, 3146–3153.

RECEIVED for review October 30, 1989. Revised manuscript received June 29, 1990. Accepted July 30, 1990. The work was supported in part by a grant from the National Science Foundation, BB5-8714238, and was presented at the 37th ASMS Conference on Mass Spectrometry and Allied Topics.

Fast Atom Bombardment Mass Spectrometric Quantitative Analysis of Methionine-Enkephalin in Human Pituitary Tissues

Jozef J. Kusmierz,[1] R. Sumrada,[2] and Dominic M. Desiderio*[1,3,4]

Charles B. Stout Neuroscience Mass Spectrometry Laboratory and Departments of Immunology-Virology, Neurology, and Biochemistry, University of Tennessee—Memphis, 800 Madison Avenue, Memphis, Tennessee 38163

Picomole amounts of endogenous methionine-enkephalin (ME = YGGFM) were quantified in 11 individual human pituitaries by fast atom bombardment mass spectrometry methods. Quantification was based either upon the comparison of the molecular ion (MH^+) current of endogenous ME versus the current of a deuterated ME internal standard (d_5-ME) or, similarly, upon the unimolecular decomposition $MH^+ \rightarrow YGGF-^+$ in the first field-free region to produce the unique tetrapeptide fragment ion. The latter method used the multiple reaction monitoring (MRM) mode. Native ME was purified with an octadecylsilyl (ODS) disposable cartridge and with multidimensional reversed-phase high-performance liquid chromatography. The amounts of ME determined were 18.26 ± 19.98 ng of ME/mg of protein with the MH^+ method and 15.28 ± 16.59 ng of ME/mg of protein with the MRM method. A fraction (ca. 4%) of the total amount of ME from one pituitary was used to acquire these quantitative data, and ca. half of the remaining amount of a separate sample (no d_5-ME added) was used to obtain a linked scan at constant B/E (B, magnetic field; E, electric field) of the ME MH^+ at 574 u to produce the amino acid sequence determining fragment ions at *m/z* 297, 354, 411, 397, 278, and 425 u corresponding to Y_2'', Y_3'', Y_4'', A_4, B_3, and B_4, respectively. That product ion spectrum was similar to a scan of 100 ng of synthetic ME. We calculated that the amount of pentapeptide for the MRM experiments corresponded to a total of 30 ng (52 pmol) of ME on the probe tip during quantification. On the other hand, we estimated that 3 times more, or 90 ng (156 pmol), ME was on the probe tip during acquisition of the product ion spectrum.

INTRODUCTION

Neuropeptides play a role in a wide range of biological processes (*1–6*), the accurate analysis of those endogenous peptides is crucial to understanding their action (*7, 8*), and a variety of different chromatographic separation and detection methods is currently in use for their analysis (*9–11*). Radioreceptorassay (RRA) is used in some cases (*12, 13*), but in most laboratories, radioimmunoassay (RIA) (*3, 5, 14*) is used because of its high level of detection sensitivity (femtomole) and also because of its putative high level of molecular specificity. We disagree (*7, 15*) with any claims of molecular specificity made for RIA, RRA, or high-performance liquid chromatography (HPLC) (*16*) analytical methods, and thus we developed MS methods to quantify neuropeptides extracted from human tissues and fluids (*17–19*).

This paper describes the measurement of the neuropeptide methionine-enkephalin (ME = YGGFM) in 11 individual human pituitaries. First, it was necessary to optimize the extraction efficiency of endogenous ME from human pituitary and from canine pituitary and cortex tissues, then a multidimensional chromatographic system was used to obtain the ME fraction. Qualitative analysis of endogenous ME in another pituitary (to which no d_5-ME was added) was performed by using amino acid sequence determining fragment ions from the precursor ion MH^+, and FAB-MS quantitative analysis in the MRM mode of ME was optimized by using the deuterated internal standard, d_5-^{4}Phe-ME. ME was studied here because of its prevalence in many different biological tissues, and because it was present in a significant amount in our human postmortem pituitary extracts (*13*).

EXPERIMENTAL SECTION

1. Tissue Acquisition. Postmortem human pituitaries were obtained as soon as feasible after death, frozen immediately, and kept at −70 °C until processed as described (*13*). During autopsy, tissue samples containing anterior and posterior pituitary lobes were obtained. Canine cortex and pituitary tissue samples were obtained in the Department of Comparative Medicine under NIH guidelines.

2. Tissue Homogenization. To minimize enzymolysis, frozen tissue was weighed, and placed immediately into cold (4 °C) acetic acid (1 N, 1/20 (w/v)) and homogenized for 30 s in a Polytron (setting = 6). After 2 h, the homogenate was centrifuged (31000*g*; 30 min). One microgram of d_5-^{4}Phe-ME was added before tissue homogenization, except for the spectra shown in Figures 1 and 2. Proteins were measured with a Sigma diagnostic kit (No. 690).

3. Synthetic ME was purchased from Sigma Chemical Company (St. Louis, MO), and ^{3}H-ME (26 Ci/mmol specific activity), from Amersham (Arlington Heights, IL). That specific activity of ^{3}H-ME corresponded to 52 000 ((counts/min)/ng)/1.7 pmol (instrument counting efficiency = 52%). Both peptides were HPLC-purified before use.

4. Octadecysilyl (ODS) disposable cartridges (Sep-Pak, Waters, Milford, MA) were prepared for use (*11*) by pretreatment with a methanol–water–trifluoroacetic acid (TFA, 0.1%) wash, and then air-dried. Supernatant was applied to the cartridge, and CH_3CN was used as the eluting solvent (50/50 CH_3CN–0.1% TFA (v/v), other percentages used are described below). A new ODS cartridge was used for each experiment. Collected effluent was lyophilized to dryness and reconstituted into 150 μL of mobile phase (10/90 acetonitrile–TEAF (v/v)); this total volume was injected onto the HPLC column.

5. Reversed-phase high-performance liquid chromatography (RP-HPLC) analyses used either a Waters HPLC system or a microprocessor-driven Varian 5000, with either an ODS μBondapak (0.4 × 30 cm) (10-μm bead diameter; pore size, 30 Å) (Waters) or a synthetic polymer (polystyrene, poly(vinylbenzene); Polymer Laboratories, Amherst, MA) analytical column (PLRP-S, 5-μm bead, 100-Å pore size, 0.46 × 15 cm) (*20*). The volatile buffer was triethylamine–formate (*21*) (40 mM; pH 3.1), and CH_3CN (HPLC grade; Burdick and Jackson, Muskegon, MI) was the organic modifier.

a. Gradient Elution from an ODS Analytical Column. The gradient was described previously (*20*). UV adsorption at 200 nm was monitored, and the mobile phase flow rate was 1.5 mL min^{-1}. Fractions eluting from the ODS column were collected manually to optimize the chromatographic resolution and to decrease the amount of background material collected. ME

[1] Charles B. Stout Neuroscience Mass Spectrometry Laboratory.
[2] Department of Immunology-Virology.
[3] Department of Neurology.
[4] Department of Biochemistry.

0003-2700/90/0362-2395$02.50/0 © 1990 American Chemical Society

fractions collected after gradient elution were lyophilized and reconstituted into 150 μL of mobile phase (16/84 CH_3CN–TEAF (v:v)), and this entire volume was injected onto the polymer column.

b. Isocratic Elution from a Polymer Analytical Column. Isocratic elution was performed with CH_3CN–TEAF (16/84 (v/v)). The mobile phase flow rate was 1.2 mL min^{-1}. The ME fraction was collected manually, lyophilized, and reconstituted into 50 μL of 0.1% TFA. That volume permitted several separate fast atom bombardment mass spectrometry (FAB-MS) measurements and sufficed to optimize several different FAB-MS experimental parameters (i.e. resolution, sweep time, and multiplier gain).

6. Mass Spectrometry. A Finnigan MAT 731 mass spectrometer (Bremen, West Germany) with an Apple II microcomputer data acquisition system (22) was used. Fast atom bombardment used 7-keV xenon atoms from an Ion Tech (Teddington, U.K.) ion gun.

In general, the following experimental procedure was used to quantify ME. Sample (2 μL) was deposited onto the FAB probe tip, which contained a glycerol matrix (0.2 μL), water was evaporated in the MS probe vacuum lock, and the probe was inserted into the MS ion source. Ten oscillographic recordings were obtained (five d_5-ME and five d_0-ME scans) for each sample. Triplicate measurements were obtained for each sample. The same experimental protocol was used for the MH^+ and MRM measurements.

For the MH^+ quantitative measurement, the magnetic field (B) was set to center the MH^+ of d_0-ME (574 u) on the oscilloscope screen. In the peak-matching mode, the MH^+ of d_5-ME (579 u) was centered. The microcomputer system acquired the ion current due to each separate MH^+ during alternating scans between d_0-ME and d_5-ME as the peak-matching electronics swept alternately those MH^+ ion profiles across the collector slit (22).

Similarly, in the MRM quantitation mode, the ion current due to the transition $MH^+ \rightarrow YGGF-^+$ was monitored in alternate sweeps of the d_0-ME and the d_5-ME transitions.

For construction of calibration curves corresponding to the MH^+ and MRM data, solutions of synthetic ME (d_0, d_5) were prepared and analyzed. Individual standard solutions contained 2000, 1000, 500, 250, 125, and 62.5 ng of d_0-ME, respectively. Each dilution also contained 1000 ng of d_5-ME. These amounts of d_0-ME and d_5-ME were chosen to bracket the amount of endogenous ME contained in one human pituitary. The ratio of the area under the FAB desorption curves for the MH^+ and MRM ion currents was plotted versus amount (nanograms) of d_0-ME.

For a scan over a limited mass range for the MH^+ ion (see parts C and D of Figure 1), a 2% sweep of the accelerating voltage was used.

A separate pituitary fragment, to which no d_5-ME was added, was purified by multidimensional RP-HPLC as described above. The ME fraction was analyzed to determine the amino acid sequence data. For the linked scan at constant B/E (B, magnetic field; E, electric field), which produces a product ion spectrum from the selected precursor ion MH^+, the MS linear scan rate was 96 s $decade^{-1}$, and the oscillographic recorder paper speed was 2.5 cm min^{-1}. Product-ion spectra were obtained for glycerol (0.2 μL), 100 ng of synthetic ME, and a portion (50%) of one human pituitary tissue extract to which no d_5-ME had been added (see Figure 2).

The mass values on the product ion spectra were measured manually from the oscillographic trace, using the equation $M_{product} = (M_{precursor}M_{measured})^{1/2}$. We observed consistently an error of ±0.5 u in our product ion spectra.

7. Deuterated Internal Standard. YGG-[d_5-F]-M was synthesized by using the automated Merrifield solid phase method.

Deuterated Phe was purchased from Merck (St. Louis, MO). Di-*tert*-butyl dicarbonate $(t\text{-Boc})_2O$ was purchased from Fluka Chemical Corp. (Ronkonkoma, NY). Boc-d_5-Phe was synthesized as described (23), the yield was 89%, and the FAB-MS mass spectrum was similar to spectra reported elsewhere (24). The Boc-d_5-Phe sample contained 98.7% deuterium.

YGG-[d_5-F]-M was synthesized on an Applied Biosystems (Foster City, CA) Model 430A peptide synthesizer using standard solid phase *t*-Boc chemistry. Methionine residue and all reagents except for Boc-d_5-Phe were purchased from Applied Biosystems. All reaction times and volumes were standard for the current level of computer software (version 1.34). The pentapeptide resin was treated with HF (Immunodynamics, San Diego, CA) to deblock the peptide and to remove the pentapeptide from the resin. The yield of crude, deprotected, and deblocked peptide was 344 mg.

The crude d_5-ME was purified by RP-HPLC and analyzed by FAB-MS to determine the MH^+ ion of ME at 579 u, and appropriate amino acid sequence determining fragment ions were obtained in a product-ion spectrum (25).

8. Pellet Tissue Solubilization. In some of the recovery studies described below, the tissue pellet formed by centrifugation of the tissue homogenate was incubated (20 h, 50 °C) with Fisher Scintigest tissue solubilizer (Fisher Scientific, Fairlawn, NJ).

Table I. FAB-MS Measurement of ME in Canine Cortex, Using MH^+ and MRM ($MH^+ \rightarrow YGGF-^+$) Data[a]

weight, g	added ME, ng	ME, ng		n
		MH^+	MRM	
0.25 ± 0.07	0	60 ± 26	11 ± 7	3
0.30 ± 0.05	400	465 ± 23	450 ± 14	4
0.30 ± 0.16	800	830 ± 15	805 ± 38	4

[a] One microgram of d_5-ME was added to each cortex sample. Three determinations were made for each sample. *n* is the number of individual cortex samples.

RESULTS AND DISCUSSION

1. Optimizing Extraction Efficiency of Endogenous ME from Tissue Homogenates. A minimum amount of canine tissue was used for methods development. Three separate canine pituitary tissue homogenates were incubated (4 °C) with ^{3}H-ME (42 000 counts/min) for 18 h and three others for 2 h. The amount of recovered ^{3}H-ME in the supernatant and pellet was, for 18 h, 98.5 ± 0.9% and 0.8 ± 0.1% (n = 3), respectively, and for 2 h, 98.0 ± 0.1% and 0.9 ± 0.12%, respectively. The average weight of these six pituitaries was 48 mg. One microgram of d_5-ME was also added to each sample to simulate those experimental conditions used below to analyze human pituitaries. The amount of recovery of ^{3}H-ME in these two equilibration methods did not differ significantly.

The next step was to study the recovery of the ^{3}H-ME that was added to a canine cortex tissue homogenate and that was eluted from an ODS cartridge with CH_3CN. The amount of ^{3}H-ME recovered in the effluent was ca. 7%; in the water-wash, 0.4%; and in the 50% CH_3CN, 76%. The use of 100% CH_3CN eluted only an additional 0.1%. These data are to be contrasted with the elution, in the absence of any tissue, of pure ^{3}H-ME from an ODS cartridge, where 50% CH_3CN eluted 95% of the ^{3}H-ME. Thus, the presence of the biological matrix reduced the recovery of ^{3}H-ME by ca. 19% (95 − 76%).

^{3}H-ME recovered from ODS cartridge chromatography from five human pituitaries was: effluent, 13%; wash, 0.7%; and 50% CH_3CN, 70.8%.

2. Method Evaluation. During our method development, the standard addition method was used with cortex tissue (which contains a very small amount of ME and which served as a control). Eleven samples (ca. 0.3 g each) of that cortex were used as follows. One microgram of d_5-ME was added to each cortex sample. To one group of three samples (n = 3), no d_0-ME was added; to a second group of samples (n = 4), 400 ng of d_0-ME was added; and to a third group of samples (n = 4), 800 ng of d_0-ME was added. These 11 samples were processed by the ODS cartridge/HPLC procedure.

Table I contains FAB-MS measurements of ME using the ion current corresponding to either MH^+ or to the unimolecular decomposition $MH^+ \rightarrow YGGF-^+$. Thus, for 0 ng of ME added, 60 ng was measured; for 400 ng added, 465 ng; and for 800 ng, 830 ng was measured. these data (60, 65, 30 ng) corresponded to 68 ± 19 ng of endogenous ME in canine

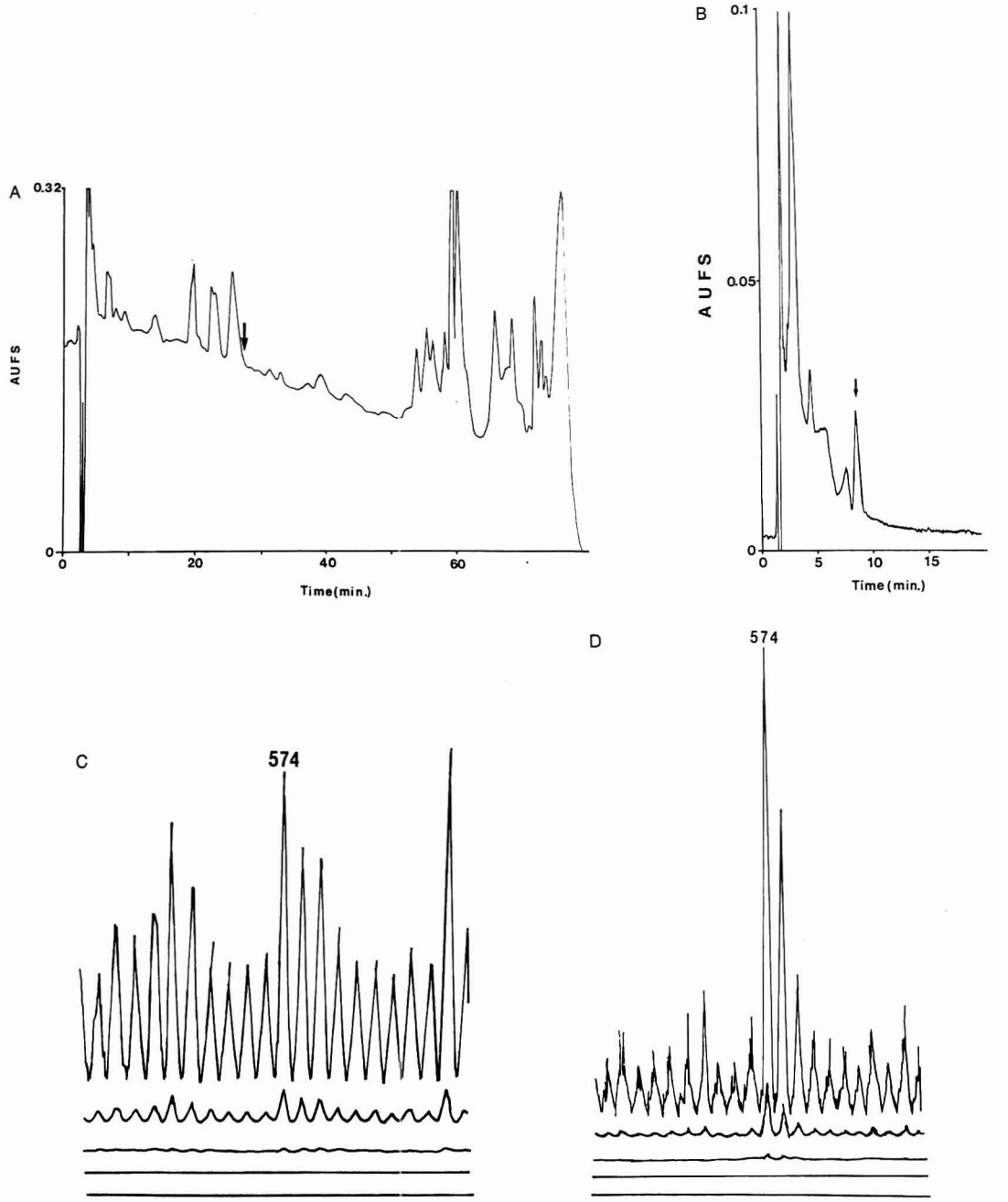

Figure 1. RP-HPLC chromatography of one human pituitary (no IS added), arrow denotes ME retention time: (A) ODS, gradient; (B) polymer, isocratic (16% CH_3CN) elution of the fraction indicated in part A; (C) FAB-MS analysis of ME MH^+ at 574, corresponding to the fraction (arrow) collected from the gradient profile in part A; (D) FAB-MS analysis of ME MH^+ at 574, corresponding to the fraction (arrow) collected from the isocratic profile in part B.

cortex. The MRM data indicated that, for 0 ng of added synthetic ME, 11 ng was measured; 400 ng added yielded 450 ng; and for 800 ng added, 805 ng. The average of these MRM data was 22 ± 25 ng of measured endogenous ME. The lower MRM average correlated with the inherently greater specificity of the MRM versus the MH^+ data. Furthermore, the data in Table I for 400 and 800 ng added ME indicated the low coefficient of variation (2–5%) within one assay for the analytical measurement of ME in the control tissue.

These standard addition data indicated the analytical utility of combining ODS chromatography (cartridge, two RP-HPLC steps) with FAB-MS measurement of ME in a biological extract using the MH^+ and MRM quantification methods, and we proceeded to measure endogenous ME in 11 individual human pituitaries.

3. Optimization of Chromatographic Resolution. Over the years, we have found that it is effective to use several different chromatography steps to analyze endogenous neuropeptides in brain and other biological tissues (*20*, *26*, *27*). First, an ODS cartridge was used to desalt and to produce a peptide-rich fraction for subsequent analytical HPLC purification. An ODS analytical column was used either in the isocratic or in the gradient mode to purify a particular peptide, which was collected into one tube, and was purified further by an isocratic elution from a polymer column (*26*).

To demonstrate the chromatographic resolution obtained for endogenous ME from one human pituitary to which no d_5-ME was added, Figure 1A contains the gradient elution chromatogram from an ODS analytical column and Figure 1B the isocratic elution chromatogram (of the ME fraction collected from the gradient) from a synthetic polymer analytical column.

The MH^+ ion current at 574 u due to ME collected from the gradient elution of Figure 1A had a signal-to-noise ratio of 2.8 (see Figure 1C), and from the isocratic elution of Figure 1B, 8.3 (see Figure 1D). Thus, the second stage of RP-HPLC

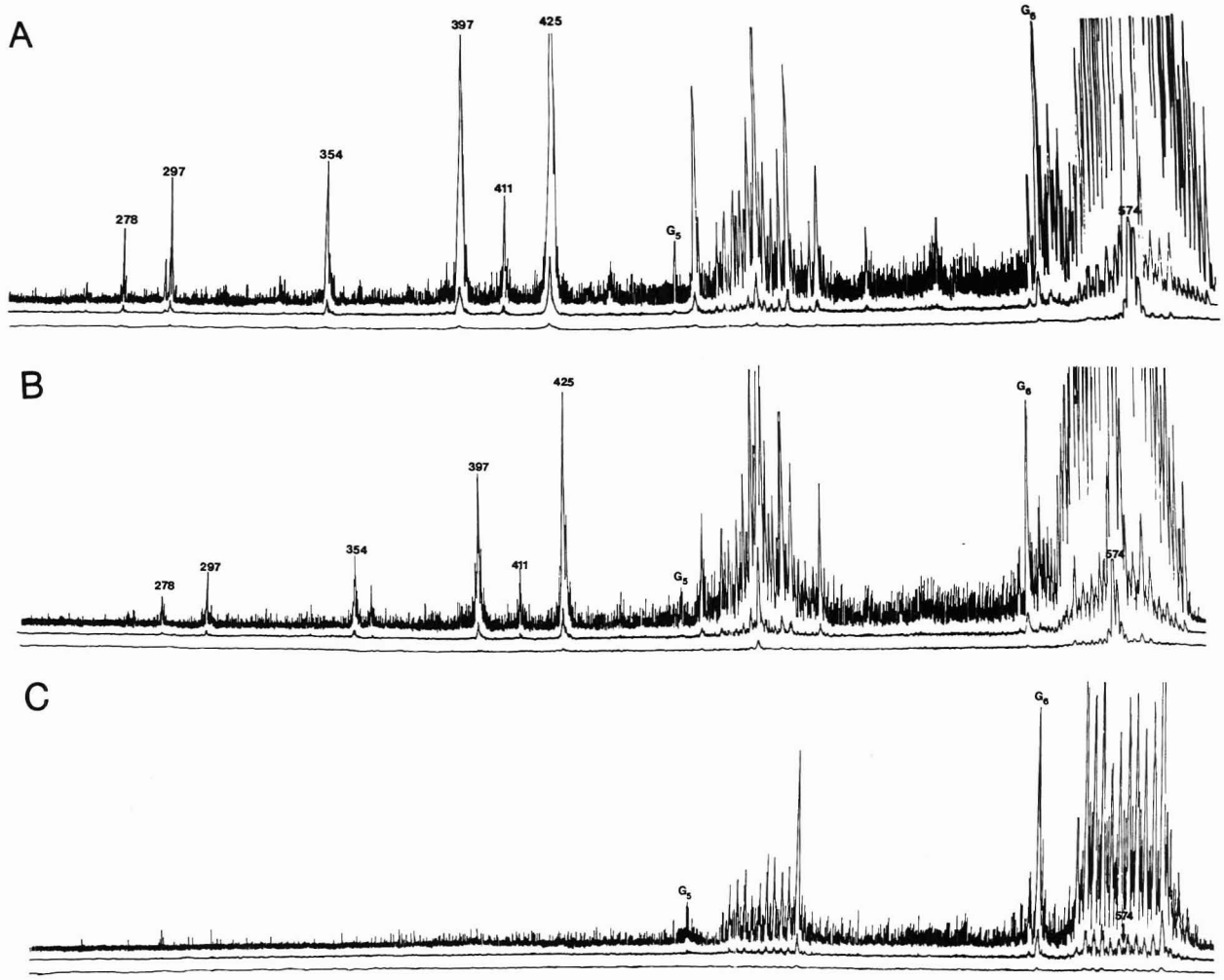

Figure 2. B/E linked-field product-ion scans of synthetic ME (A) (100 ng); one pituitary tissue extract (no IS) (B); and glycerol (C).

purification improved the FAB-MS measurement of the ME MH^+ ion by ca. 300%. Furthermore, these MS data were significant because only ca. 4% of the total available sample was used for FAB-MS quantification.

4. Qualitative Analysis of ME in One Human Pituitary. It was important to demonstrate that these multidimensional chromatographic separation steps yielded an HPLC fraction that contains the pentapeptide ME and thus that the human pituitary tissues contained ME. Therefore, we obtained amino acid sequence determining fragment ions from a FAB-MS product-ion spectrum to demonstrate that this peptide was Y-G-G-F-M. Data from the analysis of approximately half of an extract from one pituitary tissue (to which no d_5-ME was added) are shown in Figure 2B. Figure 2A contains the similar product-ion spectrum of the precursor ion MH^+ ion is seen at 574 u, obtained from 100 ng of synthetic ME. Scheme I contains the observed fragmentation and ion nomenclature (*28*) for ME.

In both product-ion spectra, the MH^+ ion is seen at 574 u, and amino acid sequence determining fragment ions at 425 (B_4), 411 (Y_4''), 397 (A_4), 354 (Y_3''), 297 (Y_2''), and 278 u (B_3) (*25*). The equivalency of these two product-ion spectra verifies, for the first time, the ME amino acid sequence Y-G-G-F-M in the extract from one human pituitary. Other workers showed a FAB B-scan mass spectrum of ME; however, those researchers required the analysis of a pool of ten pituitaries (*3*). Figure 2C contains the product ion spectrum obtained from the FAB matrix glycerol.

It is important to note the glycerol product-ion spectrum in Figure 2C because we used a forward-geometry (E, B) two-sector MS instrument, and a range of masses (ca. 560–580 u) could be selected along with the ME MH^+ precursor ion

Scheme I. ME, Observed Fragmentation Pattern and Ion Nomenclature

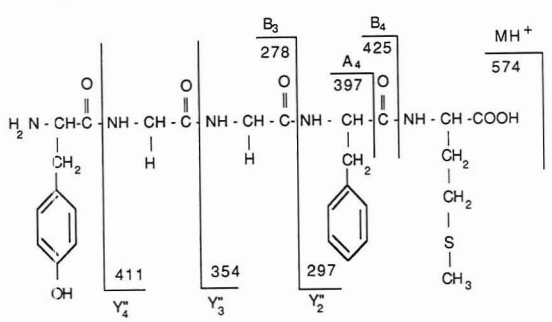

at 574 u. However, the equivalency of the two product-ion spectra in parts A and B of Figure 2 and the easy subtraction of the two glycerol ions (G_5 and G_6) from parts A and B of Figure 2 demonstrate unambiguously that ME is present in Figure 2B and in that pituitary tissue.

5. Quantitative Analysis of ME in Human Pituitary. Once it was determined that ME (=YGGFM) was present in these pituitary tissue extracts, the amount of ME was quantified in each pituitary, using the stable-isotope-incorporated internal standard d_5-ME.

We obtained the RP-HPLC elution profiles of endogenous ME in one human pituitary to which 1 μg of d_5-ME was added, and the corresponding FAB-MS data for the MH^+ ions of d_0-ME and d_5-ME at 574 u and 579 u, respectively (data not shown).

The calibration data for the MH^+ ion of solutions of synthetic ME yielded the following equation for the best-fit regression line: ratio (d_0/d_5-ME) = 0.00101 (ME, ng) + 0.019.

Table II. FAB-MS Analysis of ME in 11 Separate Human Pituitaries Based on MH^+ and MRM ($MH^+ \rightarrow YGGF-^+$) Data[a]

		MH^+		MRM	
sample no.	weight, mg	μg/g[b]	ng/mg[c]	μg/g[b]	ng/mg[c]
I	160	3.22	13.61	2.74	11.56
J	303	1.01	5.43	0.86	4.60
K	127	3.09	13.11	2.98	12.64
L	573	0.38	4.84	0.20	2.50
M	185	2.91	31.21	2.22	23.86
N	175	2.85	76.51	2.34	62.70
O	432	1.79	12.29	1.26	8.66
P	440	4.75	22.27	5.20	24.37
Q	275	1.93	10.01	1.55	8.12
R	610	0.99	6.22	0.68	4.27
S	760	0.62	5.23	0.57	4.81
	376 ± 225	2.14 ± 1.28	18.26 ± 19.98	1.87 ± 1.37	15.28 ± 16.59

[a] One microgram of d_5-ME was added to each pituitary sample. Three determinations were made for each pituitary sample. [b] μg of ME/g tissue. [c] ng of ME/mg of protein.

One microgram of d_5-ME was added with decreasing amounts of ME. The corresponding MRM calibration data for the unimolecular decomposition $MH^+ \rightarrow YGGF-^+$ obtained from the same solutions of synthetic ME correlated to the best-fit regression line: ratio (d_0/d_5-ME) = 0.0016 (ME, ng) − 0.072.

Data were obtained for the FAB-MS quantitative analysis of ME in two separate canine pituitary extracts, based on the MH^+ ion and on the unimolecular decomposition $MH^+ \rightarrow YGGF-^+$. For the two pituitaries, 8.52 and 31.1 ng of ME/mg of protein were measured for MH^+, whereas for MRM, 6.49 and 24.5 ng of ME/mg of protein were measured. These picomole amounts of endogenous ME were quantified easily by either MS method. The decrease in the amount of ME between the MH^+ ion and the MRM data was rationalized by the improved molecular specificity (*28*) and, thus, decreased noise level, of the MRM method.

Table II contains the MS measurements of ME from 11 individual human pituitary extracts, based on the MH^+ and MRM methods. Except for sample P, all of the MRM data were lower than the MH^+ ion data. The average weight of the human pituitaries was 376 ± 225 mg. The MH^+ data averaged to 2.14 ± 1.28, and the MRM data to 1.37 ± 1.37 μg of ME/g of tissue, respectively. Thus, the MH^+ data correlated to 18.26 ± 19.98 ng of ME/mg of protein and the MRM data to 15.28 ± 16.59 ng of ME/mg of protein. The coefficients of variation (both 109%) of the two measurement methods did not reflect the reproducibility of the analytical measurement, but rather reflected the biological variation observed usually in human tissues. The coefficient of variation for the measurement was much smaller (2–5%, see Table I data).

The two sets of data (MH^+; MRM) correlated well. For example, for the 11 individual human pituitary measurements collected in Table II, a linear regression line (r^2 = 0.98) best-fitted to the MH^+ vs the MRM data showed that the relationship between the amounts calculated by the two methods is MRM = [0.824 × MH^+] + 0.240. The slope of this line (0.824) indicated that the MRM transition data were more specific (slope less than one) and had less chemical noise than the MH^+ data.

On average, we calculated that 52 pmol of ME was on the FAB probe tip during MH^+ and MRM quantification, and we estimated that only 3 times more, or ca. 156 pmol of ME, was on the tip during the acquisition of the product-ion spectrum shown in Figure 2B.

A most important criterion in this analytical scheme was the post-HPLC detector sensitivity (*7*, *15*, *30*). The limit of detection for pure synthetic ME is approximately 250 pg (see also ref 31).

To increase significantly the molecular specificity of the FAB-MS quantification method, we used the MRM mode. For quantification, the FAB-MS MRM mode ensured that the observed amino acid sequence determining fragment ions derived from the MH^+ precursor. Whereas the detection sensitivity was nearly the same for the MH^+ and MRM methods (see Table II), the molecular specificity increased significantly for the MRM mode because we monitored a specific unimolecular decomposition $MH^+ \rightarrow YGGF-^+$ that produced a unique tetrapeptide fragment ion; we also used d_5-ME as the internal standard. The level of detection sensitivity in both quantification methods was sufficient to analyze picomole amounts of endogenous ME in one human pituitary.

The amounts of endogenous ME measured in this study (ca. 2 μg of ME/g of tissue) compared favorably to the data obtained in another study (*3*) that used FAB-MS to identify the ME MH^+ ion from a pool of ten pituitaries. In that latter study, 1.3 μg of immunoreactive-ME (ir-ME)/g of tissue was found for whole pituitary, 1.8 μg of ir-ME/g of tissue for the anterior lobe, and 0.1 μg of ir-ME/g of tissue for the posterior lobe. These data were compatible with the fact that the anterior lobe of the pituitary contains opioid precursors (*1*).

It is significant that a stable isotope-incorporated internal standard of ME was used in this study, and it is important that this internal standard is chemically more stable than our previously used ^{18}O internal standard (*32*). The location of the stable isotope in the peptide is important, and in our present internal standard, the ^{4}Phe position is included in both the abundant fragment ion ($YGGF-^+$) at 425 u, which was monitored in this study, and the C-terminal containing tripeptide ($-GFL^+$ at 336 u) ion (*31*).

CONCLUSIONS

We describe a process that was FAB-MS for qualitative and quantitative analysis of ME in a single human pituitary, where that analytical procedure has several desirable analytical characteristics, including a very high level of molecular specificity, a high level of detection sensitivity (femtomole), accuracy, precision, and speed. The specificity and speed of MS should be contrasted with the more commonly used radioimmunoassay method (*33*, *34*). For example, within eight working hours, we could process completely one human pituitary, including homogenization, ODS cartridge purification, multidimensional RP-HPLC, and mass spectrometry with a full standard curve. Concurrent in our laboratory, we also perform opioid RRA (*13*) and RIA (*11*) measurements. Neither of the latter methods can be performed at the same speed as with MS. But most importantly, RRA and RIA cannot provide the same level of molecular specificity as

FAB-MS MRM methods (*7*, *15*, *34*, *35*).

ACKNOWLEDGMENT

The authors acknowledge gratefully the support of Drs. Francisco, Haruff, and Berryman (Department of Pathology) for pituitary tissue, Genevieve Fridland for editing and artwork assistance, Deanna Reid and Dianne Cubbins for typing assistance, and Dianne Cubbins for data analysis.

Registry No. ME, 58569-55-4.

LITERATURE CITED

(1) Krieger, D. T., Brownstein, M. J., Martin, J. B. Eds. *Brain Peptides*; Wiley: New York, 1983; 1032 pp.
(2) Roth, K. A.; Makk, G.; Beck, O.; Faull, K.; Tatemoto, K.; Evans, C. J.; Barchas, J. D. *Regul. Pept.* **1985**, *12*, 185–199.
(3) Roth, K. A.; Lorenz, R. G.; McKeel, D. W.; Leykam, J.; Barchas, J. D.; Tyler, A. N. *J. Clin. Endocrinol. Metabol.* **1988**, *66*, 804–810.
(4) Eipper, B. A.; Mains, R. E. *J. Biol. Chem.* **1982**, *257*, 4907–4915.
(5) Higa, T.; Wood, G.; Desiderio, D. M. *Int. J. Pept. Protein Res.* **1989**, *33*, 446–451.
(6) Orth, D. M.; Guillemin, R.; Ling, N.; Nicholson, W. E. *J. Clin. Endocrinol. Metab.* **1978**, *46*, 849–852.
(7) Desiderio, D. M. *Analysis of neuropeptides by liquid chromatography and mass spectrometry*; Elsevier: Amsterdam, 1984; 235 pp.
(8) Voyksner, R. D.; Pack, T. W. *Biomed. Environ. Mass Spectrom.* **1989**, *18*, 897–903.
(9) Bennett, H. P. J. *J. Chromatogr.* **1986**, *359*, 383–390.
(10) Wiedemann, K.; Teschemacher, H. *Pharm. Res.* **1986**, *3*, 142–149.
(11) Higa, T.; Desiderio, D. M. *Int. J. Pept. Protein Res.* **1989**, *33*, 250–255.
(12) Simon, E. J. *Future Directions in Opioid Peptides: Molecular Pharmacology, Biosynthesis, and Analysis*; Rapaka, R. S., Hawks, R. L., Eds.; NIDA: Rockville, MD, 1986; pp. 155–174.
(13) Desiderio, D. M.; Fridland, G. H.; Francisco, J. T.; Sacks, H.; Robertson, J. T.; Cezayirli, R. C.; Killmar, J.; Lahren, C. *Clin. Chem.* **1988**, *34*, 1104–1107.
(14) Boarder, M. R.; Weber, E.; Evans, C. J.; Erdelyi, E.; Barchas, J. *J. Neurochem.* **1983**, *40*, 1517–1522.
(15) Desiderio, D. M. Mass spectrometry of biologically important neuropeptides In *Mass Spectrometry of Peptides*; Desiderio, D. M., Ed.; CRC Press: Boca Raton, FL., 1990.
(16) Mifune, M.; Krehbiel, D. K.; Stobaugh, J. F.; Riley, C. M. *J. Chromatogr.* **1989**, *496*, 55–70.
(17) Tanzer, F. S.; Tolun, E.; Fridland, G. H.; Dass, C.; Killmar, J.; Tinsley, P. W.; Desiderio, D. M. *Int. J. Pept. Protein Res.* **1988**, *32*, 117–122.
(18) Dass, C.; Fridland, G. H.; Tinsley, P. W.; Killmar, J. T.; Desiderio, D. M. *Int. J. Pept. Protein Res.* **1989**, *34*, 81–87.
(19) Liu, D.; Desiderio, D. M.; Wood, G.; Dass, C. *J. Chromatogr.* **1989**, *500*, 395–412.
(20) Fridland, G. H.; Desiderio, D. M. *J. Chromatogr.* **1986**, *379*, 251–268.
(21) Desiderio, D. M.; Cunningham, M. D. *J. Liq. Chromatogr.* **1981**, *4*, 721–733.
(22) Desiderio, D. M.; Laughter, J. S.; Katakuse, I.; Kai, M.; Trimble, J. *Comput. Enhanced Spectrosc.*, **1984**, *2*, 21.
(23) Itoh, M.; Hagiwara, D.; Kamiya, T. *Tetrahedron Lett.* **1975**, *49*, 4393.
(24) Garner, G. V.; Gordon, D. B.; Tetler, L. W. *Org. Mass Spectrom.* **1983**, *18*, 486–488.
(25) Dass, C.; Desiderio, D. M. *Int. J. Mass Spectrom. Ion Processes* **1989**, *92*, 267–287.
(26) Tinsley, P. W.; Fridland, G. H.; Killmar, J. T.; Desiderio, D. M. *Peptides* **1989**, *9*, 1373–1379.
(27) Liu, D.; Desiderio, D. M. *J. Chromatogr.* **1987**, *422*, 61–71.
(28) Roepstorff, P.; Fohlmann, J. *Biomed. Mass Spectrom.* **1984**, *11*, 601.
(29) Feistner, G. J.; Hojrup, P.; Evans, C. J.; Barofsky, D. F.; Faull, K. F.; Roepstorff, P. *Proc. Natl. Acad. Sci. U.S.A.* **1989**, *86*, 6013–6017.
(30) Kim, C.; Cheng, R. *J. Chromatogr.* **1989**, *494*, 67–76.
(31) Tolun, E.; Dass, C.; Desiderio, D. M. *Rapid Commun. Mass Spectrom.* **1987**, *1*, 77–79.
(32) Desiderio, D. M.; Kai, M. *Biomed. Mass Spectrom.* **1983**, *10*, 471–479.
(33) Tomer, K. B. *Mass Spectrom. Rev.* **1989**, *8*, 445–482.
(34) Desiderio, D. M.; Fridland, G. H. In *Mass Spectrometry in Biomedical Research*; Gaskell, S., Ed.; Wiley: New York, 1986; pp 443–448.
(35) Lovelace, J. L.; Kusmierz, J. J.; Desiderio, D. M. *J. Chromatogr. Biomed. Appl.*, in press.

RECEIVED for review July 12, 1990. Accepted August 2, 1990. This research was supported by NIH (GM 26666).

Laser Ionization Gas Chromatography/Mass Spectrometry of Tetraethyltin

Steven M. Colby, Michael Stewart, and James P. Reilly*

Department of Chemistry, Indiana University, Bloomington, Indiana 47405

A new method for detecting tetraethyltin that combines the high efficiency of laser ionization, the selectivity of capillary column gas chromatography, and the large throughput of a time-of-flight mass spectrometer is demonstrated. Detection limits of 2.5 pg of tetraethyltin/mL or 1.5 fg of tetraethyltin absolute have been obtained. These values correspond to 1.3 pg of tin/mL or 750 ag of tin absolute. This method should be generalizable to other elements.

INTRODUCTION

The use of organotin compounds has increased dramatically in the last 30 years (*1–3*). They find applications in catalysts, biocides, antifouling paints, and as stabilizers for poly(vinyl chloride). Their roles in biocides and paints have had significant environmental impact, particularly in estuaries near harbors (*1*, *2*, *4–10*). Approximately 10% of the organotin compounds used as biocides and in antifouling paints enter the aquatic environment (*11*). Recent legislation, limiting the use of organotins in paint, is not expected to reduce their environmental impact in the near term because of the large number of vessels to which they have already been applied. Paint chips scraped from these vessels are expected to be a continuing source of contamination (*2*). Once organotins have entered the environment they can have long term chronic effects on marine life (*2*, *10*). The toxicity of organotin compounds is roughly dependent on the number of alkyl groups, with the greatest number, 3 and 4, being the most toxic (*2*, *9*, *11*). The magnitude of the toxicity with regard to individual species and the probability that a compound will be incorporated in the food chain are determined by the identity of the alkyl groups (*9*, *12*). Among the most visible effects is shell deformation of the oyster *Crassostrea virginica* and development of male sexual organs in the female dogwhelk *Nucella lapillus* (*1*, *2*). Growth retardation of some bivalves occurs with organotin concentrations as low as 100 pg/mL (*5*).

In the environment, organotins are partitioned into several different media (sediment, biota, and water layers) (*8*, *13*). Each of these must be analyzed to properly model the bioaccumulation processes and fully understand the lifetime of the environmental impact (*9*). The analysis of organotin compounds at the concentrations found within these media requires techniques that can measure concentrations as low as 1 pg/mL in water and less than 1 ng/g in sediments (*9*, *14*). New, very sensitive methods that can accomplish this need to be developed.

0003-2700/90/0362-2400$02.50/0 © 1990 American Chemical Society

A number of techniques have been applied for detecting tin in sediment and solution (*3, 12, 14–26*). All involve a series of extraction and/or derivatization steps before the tin compounds are analyzed. In general, derivatizations involve alkylation or hydride generation and extraction is performed by using nonpolar solvents. The requirements of the extraction and detection methods determine the choice of final organotin derivative. In these experiments we have chosen tetraethyltin as our analyte because it is compatible with gas chromatography. Extraction techniques can be over 90% efficient (*8, 14, 23, 25*). Regardless of the preparation steps the sensitivity of the sample analysis depends critically on the final detection scheme. Ion spray MS/MS (*3, 19*), gas chromatography with flame photometric detection (*14, 16, 17, 21, 23, 26, 27*), and liquid chromatography with either inductively coupled plasma mass spectrometry (*20*), or laser enhanced ionization (*15*), have all been employed.

Laser ionization gas chromatography/time-of-flight mass spectrometry is an analytical method well suited to the detection of organotin compounds. It has previously been shown that resonant multiphoton ionization can be a highly efficient and selective process. Atoms (*28, 29*) can be ionized somewhat more efficiently than molecules (*30*) because atomic cross sections are comparatively large and atoms cannot undergo rapid nonradiative excited-state relaxation (*31*). With sufficient intensity the laser light can function as both the atomizer and ionization source as has been demonstrated a number of times. For example, ArF laser light yields copious quantities of C^+ ions when irradiating benzene (*32, 33*). This is possible because the high-energy photons efficiently fragment the molecule into single atoms and the ($3s\ ^1P \leftarrow 2p^2\ ^1D$) transition of the carbon atom is in resonance with the 193-nm light. Similar results have been obtained for organotin compounds by using laser-enhanced ionization (*15, 29, 34*). In this case, however, a flame is used as the atomizer and the laser light is only used for exciting the atoms. It is well-known that organometallic compounds irradiated by high intensity laser pulses fragment to form metal atoms and free radicals (*35–39*). Therefore any analytical method for detecting these species by laser ionization should be based on observing atomic ions. Detecting atomic rather than molecular ions has two distinct advantages. First, organometallic compounds containing different metallic elements are readily distinguished. Second, sensitivity is improved because the atomic signal is fixed within a limited mass range. In contrast, molecular ions can fragment leading to the distribution of signal over a number of masses. This increases the possibility of detecting background ions and therefore decreases sensitivity. The combination of these factors, along with the high throughput of TOFMS, results in a detection method for organotins that is more sensitive than those previously reported.

EXPERIMENTAL SECTION

Reagents. Tetraethyltin was purchased from Aldrich Chemical Co. Samples were prepared by dilution in Spectranalyzed methylene chloride from Fisher Scientific. Final concentrations were 10 ng/mL and 100 pg/mL of tetraethyltin. Gas chromatography/flame ionization delection (GC/FID) analysis of the sample determined the chromatographic retention time of tetraethyltin and established that the sample contained only one solute detectable with the FID. Blanks using the same solvent, glassware, and syringe were tested to verify that there was no contamination. No attempts were made to account for loss of tetraethyltin due to irreversible adsorption onto glassware or the syringe. All sample injections contained 0.6 μL of the above solutions.

Instrumentation. Chromatography was performed on a Varian 3700 gas chromatograph with on-column injection and a 30 m long, 250 μm i.d. fused silica capillary column (Supelco SPB-1). Nitrogen carrier gas was used at a flow rate of ≈0.6 mL/min. The chromatographic temperature program was started at 40 °C. This was followed by an increase, at a rate of 10 °C/min, to 200 °C. For gas chromatography/mass spectrometry (GC/MS) experiments, a 250 °C interface connected the gas chromatograph and time of flight mass spectrometer. The end of the capillary column was positioned between the first two accelerating grids of a linear time-of-flight mass spectrometer that has been described earlier (*30*). The mass spectrometer was evacuated through a liquid nitrogen trap by a Varian VHS-6 diffusion pump. The base pressure, with the carrier gas flowing, was 5.0×10^{-5} Torr. In the mass spectrometer, ions were accelerated to an energy of 2000 eV. They passed through four 90% transmitting grids (Buckbee Meers) before being detected by a pair of tandem microchannel plates (Galileo). The detector signal was amplified (LeCroy VV101ATB) and then digitized by a high-speed waveform recorder (Biomation 6500). The data were transferred to a microcomputer where software was used to record mass spectra and integrate the ion signal over the isotopic mass envelope of tin. The chromatogram was generated by recording the integrated signal once per second.

Table I. Relevant Tin Atom Transitions

transition	wavelength, nm
($8d\ ^3D_2^o \leftarrow 5p^2\ ^3P_2$)	193.412
($8d\ ^3F_3^o \leftarrow 5p^2\ ^1D_2$)	192.912
($8d\ ^1P_1^o \leftarrow 5p^2\ ^1D_2$)	193.110

The light source used for these experiments was a Lumonics TE-861 excimer laser operating at the ArF wavelength of 193 nm with a pulse duration of about 8 ns. The spectral range of this laser is approximately 193.1 to 193.6 nm (*41*). The profile of the laser light overlaps a number of tin atom transitions (*42, 43*). The closest one to this wavelength range, originating from the ground state, is ($6d\ ^3D_1^0 \leftarrow 5p^2\ ^3P_0$) at 194.269 nm. Three others that originate from low lying metastable states are in resonance with the ArF laser. They are listed in Table I. Note that transitions from the $5p^2\ ^1D_2$ state reach autoionizing levels. Atoms in this state can actually be one-photon ionized. Because of the large amount of energy involved in the atomization process, it is likely the $5p^2\ ^3P_2$ and $5p^2\ ^1D_2$ excited states will be highly populated.

The laser beam was apertured and then focused into the source of the mass spectrometer using either a 1000 or 500 mm focal length lens. The rectangular focal spots produced by these lenses were 4.5×0.6 mm and 2.5×0.4 mm (full width at half maximum), respectively. They were measured by passing a sharp edged blade through the focal plane and monitoring the transmitted light intensity. Their size affects both the mass resolution and the number of sample molecules ionized. The lens was positioned so that the narrow edge of the focal spot intercepted the chromatographic effluent approximately 1.5 mm from the tip of the chromatographic column. The laser energy, as measured with a Gentec ED-500 joulemeter at the exit of the mass spectrometer, was between 1.0 and 6.2 mJ. The pulse repetition rate was 20 Hz.

RESULTS

Figure 1 shows a chromatogram resulting from the injection of 6 pg of tetraethyltin in a 0.6 μL sample. The integrated area of the peak is 26985 relative units; the mean and standard deviation of the background integrated over the same amount of time are 6.2 and 3.8 in the same units, respectively. These data were recorded with a 500-mm lens and an average laser pulse energy of 1.0 mJ. From these results we project a detection limit at 3σ of 3.9 fg of tetraethyltin. Because this was a long and potentially unreliably extrapolation, additional data were recorded for much lower sample concentrations.

Chromatograms obtained by injecting 60 fg of tetraethyltin in 0.6 μL of solvent are shown in Figure 2. Figure 2A displays the data obtained by using a 500-mm lens and an average pulse energy of 4.1 mJ. Figure 2B displays that obtained by using a 1000-mm lens and an average pulse energy of 6.2 mJ. A comparison of the results is shown in Table II. Detection limits of 6.8 and 1.5 fg of tetraethyltin can be projected from parts A and B of Figure 2. This is in reasonable agreement

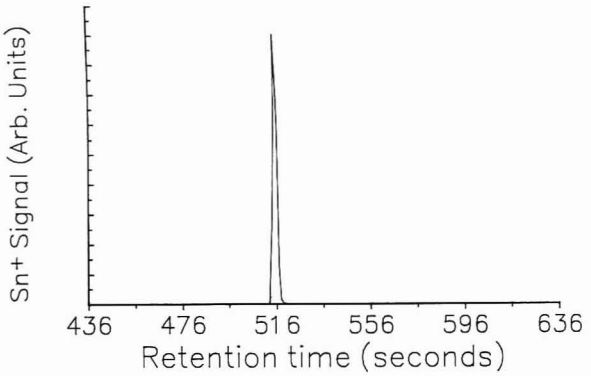

Figure 1. Chromatogram resulting from the injection of 6 pg of tetraethyltin.

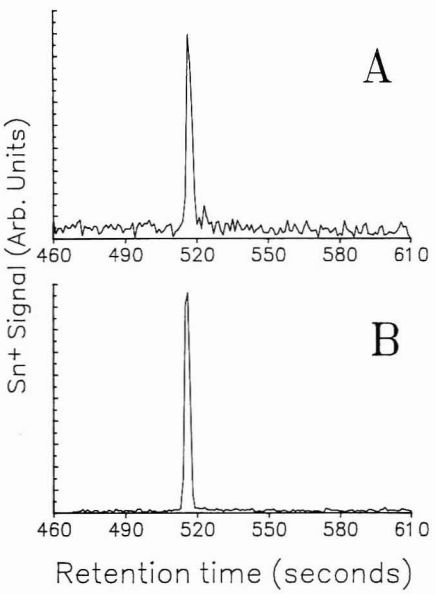

Figure 2. Chromatograms resulting from the injection of 60 fg of tetraethyltin: (A) 500 mm focal length lens; (B) 1000 mm focal length lens.

Table II. Quantitative Comparison of Data from Figures 1 and 2

sample size[a]	lens f.l., mm	rel peak area	background mean	background std	S/N^b	limit of detection,[c] fg
6.0 pg	500	26985	6.2	3.8	1500	3.9
60 fg	500	599	30	12	8.8	6.8
60 fg	1000	2341	28	9.5	41	1.5

[a] Mass of tetraethyltin in a 0.6-μL sample. [b] Peak area divided by the sum of the mean background plus 3 times the standard deviation of the background. [c] The sample size divided by the signal to noise ratio.

with the value extrapolated from the 6-pg sample.

A typical mass spectrum obtained during elution of a tetraethyltin peak is shown in Figure 3. The expected isotopic envelope for tin atoms is seen between masses 112 and 122. No signal corresponding to organotin ions was detected. For the recording of chromatograms the signal was integrated within the mass range 115.3–120.9 amu. The limited mass resolution is due to the relatively large focal spot of the laser beam and the presence of the chromatography column in the center of the ionization region. The instrument used in this experiment can achieve much higher resolution under optimal conditions (*44*).

Note that we have been discussing our detection limits in terms of the mass of tetraethyltin. If we refer to the mass of tin itself, then our best detection limit is 750 ag.

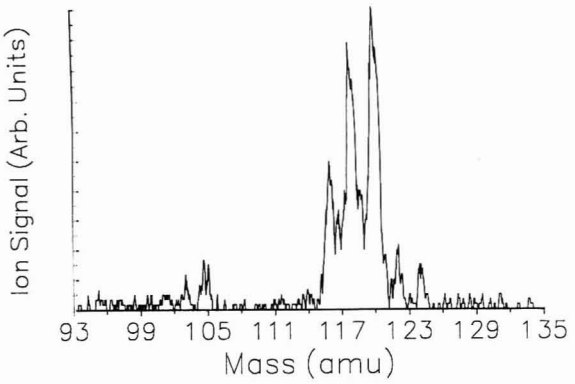

Figure 3. ArF laser ionization mass spectrum obtained during the elution of a tetraethyltin peak.

Table III. Detection Limit Comparison

method	detection sensitivity[a] concn, ng/mL	absolute, pg
LC/laser enhanced ionization (*15*)	3[b]	60
GC/flame photometric detection (*16*)	16[c]	80[c]
GC/flame photometric detection (*17*)		30[d]
GC/flame photometric detection (*14*)		3[e]
GC/flame photometric detection (*27*)		0.04[f]
GC/flame photometric detection (*26*)		<1.0[g]
LC/graphite furnace AAS (*12*)		5000
direct current plasma (*18*)	20	
ionspray tandem mass spectrometry (*3*, *19*)		5
GC/flame ionization-quenching (*40*)		0.5[h]
ion pair chromatography/ICP-MS (*20*)		400[i]
ICP-AAS (*18*)	80	
quartz furnace AAS (*22*)		30[j]
current work:		
GC/laser ionization/time-of-flight MS	0.0013	0.00075

[a] As Sn except where noted. [b] In 20 μL as tributyltin. [c] As hydride derivatives in 5 μL. [d] In 1 μL. [e] As tri-*n*-butylethyltin. [f] As tetrapropyltin. [g] Using on-column derivatization. [h] For tetraethyltin. [i] As trimethyltin chloride. [j] Based on 100-mL samples.

DISCUSSION

The results presented here demonstrate the use of an experimental method for molecular analysis whose sensitivity for organotins is a significant improvement over that of other methods. A comparison of these approaches is shown in Table III.

The detection limits achieved in this experiment are dependent upon the number of sample ions and the number of background ions that are detected. Variation of experimental parameters can affect either or both of these. For example, increasing the intensity of the laser light increases both the analyte and background signals by the same proportion. However, changing the position of the laser beam relative to the capillary column mainly affects the sample signal. In all of the above measurements the background due to ionization of pump oil is the primary factor limiting the sensitivity. Molecules in the pump oil have masses that are generally over 200 amu. However, the ArF laser produces a large number of fragment ions. A significant improvement in sensitivity would result from the use of a cleaner vacuum system.

Once the source of the background has been significantly reduced, factors that maximize the number of ions generated and detected will increase the sensitivity of this method. These include increasing the laser repetition rate, the light intensity, and the transmission of the grids. In these experiments only a fraction of the ArF laser output has been

used because higher intensities increased both the signal and background.

The fundamental limit on the sensitivity of this method is determined by the fraction of molecules eluting from the capillary column that interact with the laser radiation. Because of the low duty cycle of the pulsed laser and its finite focal volume, most of the eluting molecules are not irradiated and therefore cannot be ionized. The laser emits a light pulse 8 ns in duration, 20 times a second, resulting in a duty cycle of 1.6×10^{-7}. However, the residence time of an analyte molecule within the focal spot is much longer than 8 ns and this can be used to determine an effective duty cycle. This is done by assuming that the effluent from the capillary column sprays into the vacuum chamber with a cosine squared angular distribution and an average speed corresponding to the temperature of the interface between the GC and the mass spectrometer. This angular distribution was found to roughly describe the flow of molecules out of our capillary column as detected in a fluorescence excitation experiment (*45*). We also assume a two-dimensional system in which all of the effluent is within a plane containing the capillary column and the ion flight tube. This plane is intersected by a rectangular laser beam whose dimensions depend on the focal length of the lens used. The time that a molecule spends within the focal volume is equal to the length of the intersection of its flight path with the beam spot divided by its speed. Those trajectories that miss the laser beam are considered to have a time of zero. The average time molecules spend within the beam spot can be found by integrating over all possible flight paths and then dividing by their number. These are assumed to be collision free and are allowed to originate at any point within the 250-μm diameter of the column orifice. The resulting average time is multiplied by the repetition rate of the laser to find the fraction of molecules that are exposed to the laser light. This fraction is 8.3×10^{-7} for the 500 mm focal length lens and a 5.0×10^{-6} for the 1000 mm focal length lens. The experimental results do not show such a large difference between the sensitivity achieved with the two lenses because in this experiment the use of a larger beam spot also reduces the flux of photons per unit area. With the use of sufficient laser intensity, all of the molecules exposed to the light can be ionized regardless of which lens is used. Under these conditions the theoretical minimum mass of tin required for the production of at least one Sn^+ ion is 4.5 ag. Because of the detection efficiency of the microchannel plates, the probability of detecting an ion once it is produced is approximately 50%. The theoretical minimum detection limit is, therefore, 9 ag of tin or 18 ag of tetraethyltin.

These experiments have focused on a single compound. It is expected that any organotin compound or tin derivative that is compatible with gas chromatography could be detected in a similar manner. ArF laser light can excite and ionize atoms of various elements. Through the use of additional excimer laser wavelengths and Raman shifting (*37*, *46*, *47*) this technique of molecular photofragmentation followed by atomic ionization can be applied to almost all elements except the halogens and rare gases. Its selectivity would be particularly enhanced if a tunable excimer laser were employed.

CONCLUSIONS

A new experimental method for detecting low concentrations of organotin compounds has been developed. A detection limit of 2.5 pg/mL or 1.5 fg of tetraethyltin absolute has been achieved. These values correspond to 1.3 pg/mL or 750 ag of tin absolute. A principal factor limiting the sensitivity of the current system is the background signal due to the ionization of pump oil. However, a more fundamental limit to the sensitivity of this technique is established by the duty cycle of the laser and the geometry of the ionization region. Despite this, a detection limit of approximately 9 ag of tin is theoretically attainable.

LITERATURE CITED

(1) Salazar, M. H.; Champ, M. A. *Oceans '88*; Baltimore, MD, 1988; pp 1497–1506.
(2) Greaves, J. *Proceedings of the 37th ASMS Conference on Mass Spectrometry and Allied Topics, Miami Beach, FL, May 1989*; American Society for Mass Spectrometry: East Lansing, MI, 1989; pp 803–805.
(3) Siu, K. W. M.; Gardner, G. J.; Berman, S. S. *Rapid Commun. Mass Spectrom.* **1988**, *2* (10), 201–204.
(4) Salazar, M. H.; Salazar, S. M. *Oceans '88*; Baltimore, MD, 1988; pp 1188–1196.
(5) Henderson, R. S. *Oceans '88*; Baltimore, MD, 1988; p 1645.
(6) Adema, C. M.; Thomas, W. M., Jr.; Mangum, S. R. *Oceans '88*; Baltimore, MD, 1988; pp 1656–1667.
(7) Blair, W. R.; Olson, G. J.; Trout, T. K.; Jewett, K. L.; Brinckman, F. E. *Oceans '88*; Baltimore, MD, 1988; pp 1668–1672.
(8) Maguire, B. J. *Environ. Sci. Technol.* **1984**, *18*, 291–294.
(9) Donard, O. F.; Weber, J. H. *Environ. Sci. Technol.* **1985**, *19*, 1104–1110.
(10) Wade, T. L.; Garcia-Romero, B.; Brooks, J. M. *Oceans '88*; Baltimore, MD, 1988; pp 1198–1201.
(11) Craig, P. J. In *Comprehensive Organometallic Chemistry*; Wilkinson, G., Ed.; Pergamon Press: Oxford, U.K., 1983; Vol. 2, pp 979–1020.
(12) Jewett, K. L.; Brinckman, F. E. J. *J. Chromatogr. Sci.* **1981**, *19*, 583–593.
(13) Randall, L.; Weber, J. H. *Sci. Total Environ.* **1986**, *57*, 191–203.
(14) Müller, M. D. *Anal. Chem.* **1987**, *59*, 617–623.
(15) Epler, K. S.; O'Haver, T. C.; Turk, G. C.; MacCrehan, W. A. *Anal. Chem.* **1988**, *60*, 2062–2066.
(16) Olson, G. J.; Brinckman, F. E.; Matthias, C. L.; Bellama, J. M. *Natl. Bur Stand.*, [*Tech. Rep.*] *NBSIR (U.S.)* **1985**; *NBSIR-3295*, 50 pp.
(17) Siu, K. W. M.; Maxwell, P. S.; Berman, S. S. *J. Chromatogr.* **1989**, *475*, 373–379.
(18) Leis, F.; Broekaert, J. A. C.; Waechter, H. *Fresenius' Z. Anal. Chem.* **1989**, *333*, 2–5.
(19) Siu, K. W. M.; Gardner, G. J.; Berman, S. S. *Anal. Chem.* **1989**, *61*, 2320–2322.
(20) Suyani, H.; Creed, J.; Davidson, T.; Caruso, J. *J. Chromatogr. Sci.* **1989**, *27*, 139–143.
(21) Aue, W. A. and Flinn, C. G. *J. Chromatogr.* **1977**, *142*, 145–154.
(22) Donard, O. F. X.; Rapsomanikis, S.; Weber, J. H. *Anal. Chem.* **1986**, *58*, 772–777.
(23) Maguire, R. J.; Huneault, H. *J. Chromatogr.* **1981**, *209*, 458–462.
(24) Whang, C.; and Yang, L. *Analyst* **1988**, *113*, 1393–1395.
(25) Randall, L.; Han, J. S.; Weber, J. H. *Environ. Technol. Lett.* **1986**, *7*, 571–576.
(26) Aue, W. A.; Flinn, B. J.; Flinn, C. G.; Paramasigamani, V.; Russell, K. A. *Can. J. Chem.* **1989**, *67*, 402–410.
(27) Aue, W. A.; Flinn, C. G. *Anal. Chem.* **1980**, *52*, 1537–1538.
(28) Axner, O.; Lejon, M.; Magnusson, I.; Rubinsztein-Dunlop, H.; Sjöström, S. *Appl. Opt.* **1987**, *26* (17), 3521–3525.
(29) Young, J. P.; Shaw, R. W.; Smith, D. H. *Anal. Chem.* **1989**, *61*, 1271A–1279A.
(30) Rhodes, G.; Opsal, R. B.; Meek, J. T.; Reilly, J. P. *Anal. Chem.* **1983**, *55*, 280–286.
(31) Wilkerson, C. W., Jr.; Colby, S. M.; Reilly, J. P. *Anal. Chem.* **1989**, *61*, 2669–2673.
(32) Sekreta, E.; Owens, K. G.; Reilly, J. P. *Chem. Phys. Lett.* **1986**, *132*, (4, 5), 450–455.
(33) Sausa, R. C.; Alfano, A. J.; Miziolek, A. W. *Appl. Opt.* **1987**, *26*, (17), 3588–3593.
(34) Cool, T. A.; Goldsmith, J. E. M. *Appl. Opt.* **1987**, *26* (17), 3542–3551.
(35) Larciprete, R.; Fontana, S.; Borsella, E. *Chemtronics* **1989**, *4* (3), 184–188.
(36) Duncan, M. A.; Dietz, T. G.; Smalley, R. E. *Chem. Phys.* **1979**, *44*, 415–419.
(37) Lichtin, D. A.; Bernstein, R. B.; Vaida, V. *J. Am. Chem. Soc.* **1982**, *104*, 1830–1834.
(38) Leutwyler, S.; Even, U.; Jortner, J. *Chem. Phys.* **1981**, *58*, 409–421.
(39) Harrison, W. W.; Rider, D. M.; Zare R. N. *Int. J. Mass Spectrom. Ion Processes* **1985**, *65*, 59–68.
(40) Hansen, D. R.; Lillie, C. H.; Hill, H. H., Jr. *J. Chromatogr. Sci.* **1985**, *23*, 208–213.
(41) Loree, T. R.; Butterfield, K. B.; Barker, D. L. *Appl. Phys. Lett.* **1978**, *32* (3), 171–173.
(42) Moore, C. E. *Atomic Energy Levels*; *As Derived From the Analyses of Optical Spectra*; U.S. Government Printing Office: Washington, DC, 1971; pp 74–79.
(43) Reader, J.; Corliss, C. H.; Wiese, W. L.; and Martin, G. A. In *Wavelengths and Transition Probabilities for Atoms and Atomic Ions*; U.S. Government Printing Office: Washington, DC, 1980; p 221.
(44) Opsal, R. B.; Owens, K. G.; Reilly, J. P. *Anal. Chem.* **1985**, *57*, 1884–1889.
(45) Colby, Steven M.; Reilly, J. P. Unpublished results.
(46) Döbele, H. F.; Hörl, M.; Röwekamp, M. *Appl. Phys. B* **1987**, *42*, 67–72.
(47) Wilkerson, C. W., Jr.; Sekreta, E.; Reilly, J. P. Unpublished results.

RECEIVED for review June 12, 1990. Accepted August 8, 1990. This work has been supported by the National Science Foundation.

CORRESPONDENCE

Enzyme Immunoassay of Insulin by Semiconductor Laser Fluorometry

Sir: A laser has a large photon flux and is useful as a light source in fluorescence spectrometry. There are many reports to show analytical advantages of laser fluorometry. For example, a biological molecule such as insulin has been determined at ultratrace levels by laser-induced fluorescence immunoassay (*1*) and enzyme immunoassay (*2*, *3*). However, laser fluorometry has seldom been used in practical trace analysis. This is due to expensiveness, complexity, poor reliability, etc. of the laser. However, a recently developed semiconductor laser has no such limitations and can possibly be used in practical applications (*4*).

In biological assay, the semiconductor laser has been used in fluorometric determination of protein labeled with fluorescent dyes in the near-infrared (*5*) and deep-red regions (*6*). An enzyme reaction has been monitored by the fluorescence quenching effect: the fluorescence intensity of indocyanine green (ICG) decreases with an increase in the concentration of the OH radical produced from H_2O_2 by a catalytic reaction. Thus an enzyme reaction producing H_2O_2 can be monitored (*7*).

In this study we report enzyme immunoassay of insulin based on sandwich assay. The enzyme activity is determined by measuring the fluorescence quenching effect of ICG by an OH radical produced by peroxidase from H_2O_2. The analytical advantage of semiconductor laser fluorometry in immunological assay is further discussed.

EXPERIMENTAL SECTION

Apparatus. The apparatus used is already reported in detail elsewhere (*7*) and is briefly described here. The GaAlAs semiconductor laser oscillating at 780 nm (Sharp, LT 024MD, 20 mW) was used as an exciting source in fluorometry. The output power was regulated by an integrated circuit (Sharp, IR3CO2N) for feedback control. Fluorescence was collected by a glass lens, transmitted through an interference filter (Ditric, 15-20785, transmission maximum 830 nm, transmittance 45%) and measured by a monochromator (Jasco, CT-10) equipped with a red-sensitive photomultiplier (Hamamatsu, R928).

Procedure. The pH dependence of ICG fluorescence was investigated by diluting 20 μL of 2.8×10^{-5} M ICG to 5 mL with various buffer solutions, which were prepared by following the protocol given in ref 8: pH 1–5, 1 M CH_3COONa + HCl; pH 6–8, 0.2 M KH_2PO_4 + NaOH; pH 9 and 10, 0.2 M H_3BO_3 + KCl + NaOH; pH 12.5, NaOH. The fluorescence intensity was measured by using an 1-cm quartz cuvette.

For determination of enzyme activity, a specified amount of peroxidase, ICG (1×10^{-6} M, 100 μL), and H_2O_2 (2×10^{-3} M, 200 μL) were mixed and the solution was diluted to 5 mL with a buffer (pH 7). The buffer contained albumin (500 mg), a preservative of sodium salicylate (100 mg), KH_2PO_4 (1.4 g), $NaHCO_3$ (0.58 g), and NaCl (0.9 g) in water (100 mL). The fluorescence intensity was measured at 15 min after initiation of the enzyme reaction.

The experimental procedure for enzyme immunoassay was mostly followed by the protocol attached to the commercial kit for enzyme immunoassay of insulin based on colorimetry (Insulin B test, Wako Pure Chemical). Insulin (0–160 μunits/mL, 0.5 mL), peroxidase-labeled antibody (kit reagent, 0.5 mL), and an immunobead were reacted for 1 h at 37 °C. The solution was rinsed three times with a copious amount of 0.9% NaCl solution to remove an excess amount of enzyme-labeled antibody. The immunobead was transferred to a new test tube and was reacted with a solution consisting of ICG (4×10^{-8} M) and H_2O_2 (1×10^{-3} M) for 15 min at 37 °C. The immunobead was taken out of the test tube, and the solution was mixed with 2 mL of buffer solution (pH 7). The fluorescence intensity of ICG was measured at 810 nm by the semiconductor laser fluorometer.

Reagents. A fluorescent dye of ICG was purchased from Daiichi Seiyaku. Insulin, peroxidase, and other chemical reagents for immunoassay (e.g. enzyme-labeled antibody, immunobead, etc.) were obtained from Wako Pure Chemical.

RESULTS AND DISCUSSION

Effect of pH. The optimum pH for measurement of ICG fluorescence was investigated from pH 1 to pH 12.5. The fluorescence intensity rapidly increased from pH 2 and reached an almost constant value at pH 5. The signal intensity slightly increased above pH 5, but the fluorescence intensity was less stable above pH 8. Then, the fluorescence measurement was carried out between pH 5 and pH 7 throughout this experiment.

Determination of Peroxidase. In the previous study, ICG was found to be quenched by an OH radical produced from H_2O_2 in the presence of a catalyst, an Fe(II) ion (*7*). A metabolite of xanthine producing H_2O_2 was indirectly measured by using this reaction scheme. In this study, we more directly measured peroxidase by producing an OH radical from H_2O_2: i.e. peroxidase acts as a catalyst. The fluorescence quenching effect was evaluated by calculating $(I_0 - I)/I$, where I_0 and I are initial and final fluorescence intensities (*7*). A straight analytical curve (correction coefficient 0.990) was observed from 0 to 400 μunits/mL, and the signal changed from 0 to 8.3. The detection limit was $\sim$20 μunits.

Determination of Insulin. According to the procedure described in the experimental section, insulin was determined at trace levels. The constructed analytical curve is shown in Figure 1. The insulin concentration is measured from 0 to 160 μunits/mL, the detection limit being $\sim$10 μunits/mL. The detection sensitivity was limited by a base line drift of the fluorescence intensity for ICG. The analytical range and the detection sensitivity are similar to those for the conventional method using standard absorption spectrometry. No optimization in the analytical procedure was carried out in this study, and further investigation may be necessary for substantial improvement of the sensitivity, e.g. a search of a stabilizing reagent giving stable ICG fluorescence, an optimization of the ICG concentration, etc.

Analytical Advantage. In clinical assay, radioimmunoassay is most frequently used due to its high sensitivity. Since radioactive substances are quite few in the environment, the background signal is almost completely negligible. Recently, enzyme immunoassay has become more popular, which might be due to safety in the use of a nonradioactive substance and a signal enhancement by an enzyme catalytic reaction. Needless to say, the background signal should be reduced as much as possible in enzyme immunoassay for the best use of its high sensitivity, though impurity fluorescence can be substantially reduced through a washout process. To our best knowledge, only a polymethine dye is fluorescent in the near-infrared region (*9*), so that near-infrared semiconductor laser fluorometry is potentially useful due to its high sensitivity and low background signal, as in the case of radioimmunoassay.

0003-2700/90/0362-2404$02.50/0 © 1990 American Chemical Society

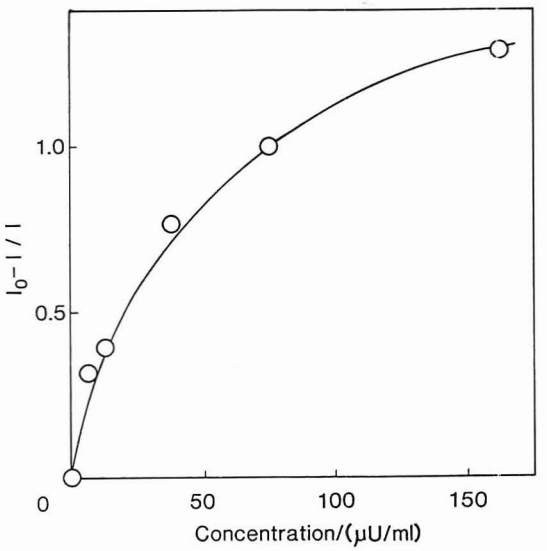

Figure 1. Analytical curve for insulin. I_0 and I are fluorescence intensities at 0 and 15 min after initiation of the enzyme reaction, respectively.

In heterogeneous enzyme immunoassay, an additional incubation time is required for the enzyme reaction. However, more rapid competitive binding assay is used in radioimmunoassay: the sample is readily measured after the immunological reaction and the succeeding phase separation of bound and free (B/F) antigens. Competitive binding fluorescence immunoassay based on semiconductor laser spectrometry may provide us with a more practical means for fluorometric determination of protein: low background fluorescence in the near-infrared region is essential in ultratrace analysis, and furthermore, the B/F separation in immunoassay will be achieved by polarization or time-resolved fluorometry. For this purpose, a new fluorometric reagent is necessary for labeling protein in the near-infrared region.

Registry No. Insulin, 9004-10-8.

LITERATURE CITED

(1) Lidofsky, S. D.; Imasaka, T.; Zare, R. N. *Anal. Chem.* **1979**, *51*, 1602.
(2) Lidofsky, S. D.; Hinsberg, W. D., III.; Zare, R. N. *Proc. Natl. Acad. Sci. U.S.A.* **1981**, *78*, 1901.
(3) Hinsberg, W. D., III.; Milby, K. H.; Zare, R. N. *Anal. Chem.* **1981**, *53*, 1509.
(4) Imasaka, T.; Ishibashi, N. *Anal. Chem.* **1990**, *62*, 363A.
(5) Sauda, K.; Imasaka, T.; Ishibashi, N. *Anal. Chem.* **1986**, *58*, 2649.
(6) Imasaka, T.; Tsukamoto, A.; Ishibashi, N. *Anal. Chem.* **1989**, *61*, 2285.
(7) Imasaka, T.; Okazaki, T.; Ishibashi, N. *Anal. Chim. Acta* **1988**, *208*, 325.
(8) *Handbook of Chemical Substances* (*Kagaku Binran*), *Fundamental II*; The Chemical Society of Japan, Ed.; Maruzen: Tokyo, 1975; p. 1490.
(9) Imasaka, T.; Yoshitake, A.; Ishibashi, N. *Anal. Chem.* **1984**, *56*, 1077.

* To whom correspondence should be addressed.

Totaro Imasaka
Hiroyuki Nakagawa
Takashi Okazaki
Nobuhiko Ishibashi*

Faculty of Engineering
Kyushu University
Hakozaki, Fukuoka 812, Japan

RECEIVED for review May 7, 1990. Accepted July 19, 1990. This research is supported by Grants-in-Aid for Scientific Research from the Ministry of Education of Japan and Naito Foundation.

TECHNICAL NOTES

Reversed Injector Loading Technique for Simultaneous Determinations by Flow Injection Analysis

José Luis Pérez Pavón,* Carmelo García Pinto, Bernardo Moreno Cordero, and Jesús Hernández Méndez

Department of Analytical Chemistry, Bromatology and Food Sciences, University of Salamanca, Salamanca, Spain

Usually flow injection methods are based on the measurement of a single signal depending on the analyte concentration. However, this methodology also permits multidetection and multidetermination, the difference between these two terms having been established by Luque de Castro et al. (*1*). The same authors have reviewed the proposed configurations allowing multidetection and multidetermination by flow injection analysis (FIA) (*2*).

The more usual ways to carry out multidetermination are sequential injection and sample splitting (*3*, *4*). The use of a two-valve injector (*5*, *6*) or an eight-port valve (*7*) allow simultaneous determinations in FIA. In this paper a six-port valve is used for the first time to carry out multidetermination by a single injection.

PRINCIPLE

The term "reversed injector loading technique" is used to indicate that in the inject mode the flow through the sample loop is opposite to the flow in the loading mode (Figure 1). If a chemical reactor (i.e. a reducing column) is included in the loop, when the valve in turned to the inject mode, two zones of sample are inserted into the carrier stream, one of them having undergone a differentiating chemical process, thus originating two signals in the detector.

EXPERIMENTAL SECTION

Reagents. Stock solutions of uranium and thorium (2.0×10^{-3} M) prepared by dissolving appropriate amounts of uranyl nitrate hexahydrate (Merck) and thorium nitrate pentahydrate (Merck) in water. Stock solutions (10^{-2} M) of Fe(III) and Fe(II) were prepared by dissolving appropriate amounts of their chlorides in 0.1 M HCl. Stock solutions of nitrate and nitrite (10^{-2} M) were also prepared from sodium nitrate (Panreac) and sodium nitrite (Panreac) in aqueous 1% NH_4Cl (Panreac).

Carrier solutions: 3.6 M HCl for the spectrophotometric determination of Th and U; 0.1 M HCl in 0.3 M NaCl for the spectrophotometric simultaneous determination of Fe(II) and Fe(III); aqueous 1% NH_4Cl for the amperometric determination of nitrate and nitrite.

Reagent solutions: 2.0×10^{-4} M Arsenazo III in 3.6 M HCl (in the presence of 1% Triton X-100) for the spectrophotometric

0003-2700/90/0362-2405$02.50/0 © 1990 American Chemical Society

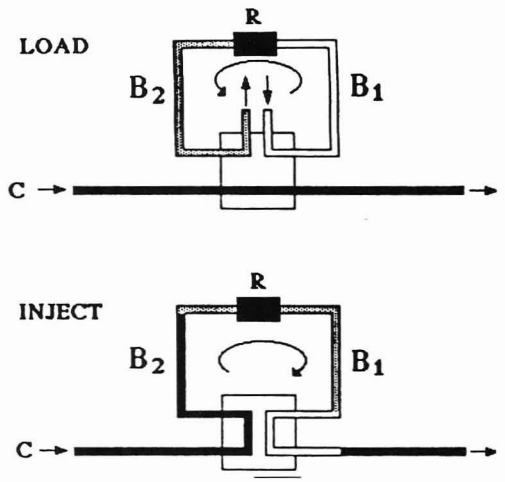

Figure 1. Injection system: C, carrier; R, reducing minicolumn; B_1, nonreduced sample loop; B_2, reduced sample loop.

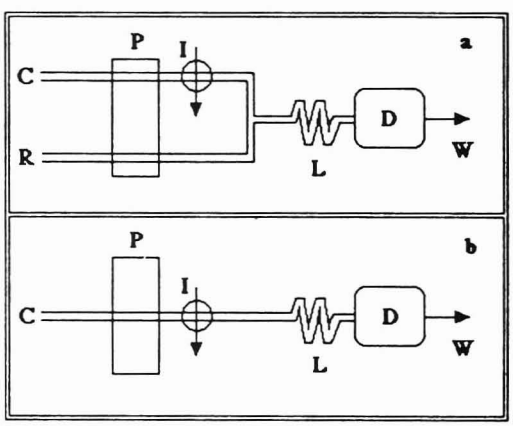

Figure 2. Manifolds: a, spectrophotometric determinations; b, amperometric determination; C, carrier; R, reagent; P, peristaltic pump; I, injection system; L, reaction coil; D, detector; W, waste.

determination of Th and U; 0.25% 1,10-phenantroline monohydrate (Panreac) in 0.2 M citrate buffer (pH = 5.2).

Apparatus. The flow system (Figure 2) comprised a peristaltic pump (Gilson Minipuls 2 HP-4) and a Rheodyne 5020 six-port injection valve. All connections were 0.5 mm i.d. Teflon tubing. For the spectrophotometric determinations (Figure 2a) a Perkin-Elmer Coleman 55 with a 1-cm flow-through cell (18 μL, Hellma 178 12-QS) was used. For the amperometric determination (Figure 2b) a Metrohm E-656 electrochemical detector furnished with glassy carbon, silver/silver chloride, and gold as working, reference, and counter electrodes, respectively, a Metrohm E-611 potentiostat, and a E-586 Labograph recorder were used. The reducing minicolumn was a 5 cm length of 2 mm i.d. glass tubing; it was packed with 0.1–0.3 mm lead powder for Th/U and Fe(II)/Fe(III) systems or with ≈0.5 mm copperized cadmium (NO_3^-/NO_2^-). Small glass wool beds at each end prevent the escape of the material.

Procedures. *Spectrophotometric Determinations.* The carrier solution and the reagent solution are pumped into their respective lines at equal flow rates of 1.7 mL min^{-1} (total flow rate Q_t = 3.4 mL min^{-1}). The sample is injected into the carrier stream from the sample loop (B_1, 3-m knotted tube; B_2, 2-m coiled tube) which includes the reducing minicolumn. The length of the reaction coil L is 1 m. Absorbance is monitored at 665 nm for Th/U and 512 nm for Fe(II)/Fe(III).

Amperometric Determination. The carrier solution is pumped at a flow rate of 1.7 mL min^{-1}. The sample is injected from the sample loop and the signal provided by the nitrite was measured at +1.000 V. The coil between the injection valve and the electrochemical cell was a 1-m coiled Teflon tube.

RESULTS AND DISCUSSION

This new injection mode has been tested in three systems: (A) the simultaneous spectrophotometric determination of Th and U with Arsenazo III, (B) the simultaneous spectrophotometric determination of Fe(II) and Fe(III) with 1,10-phenantroline, and (C) the amperometric simultaneous determination of nitrate and nitrite

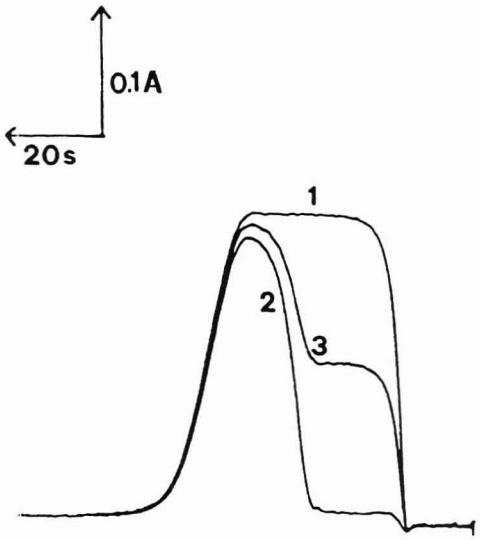

Figure 3. Fiagrams for the simultaneous determination of Th and U: 1, 4.0 × 10^{-6} M Th; 2, 4.0 × 10^{-6} M U; 3, 2.0 × 10^{-6} M Th + 2.0 × 10^{-6} M U.

A. Simultaneous Spectrophotometric Determination of Th and U with Arsenazo III. The injection mode described above is adapted for the simultaneous determination of thorium and uranium. Most of chemical and FIA variables were kept the same as in the previous work (*6*, *8*, *9*) and the values are given in the Experimental Section. A typical recorder output (fiagram) for solutions of thorium and uranium and for a mixture of both ions is shown in Figure 3. When an uranium solution is injected into the system, the plateau signal (section B_1, nonreduced sample) is much lower than the peak signal due to the low molar absortivity of the U(VI)–Arsenazo III complex; the peak signal (section B_2, reduced sample) corresponds to the U(IV)–Arsenazo III complex and is similar to the signal obtained when a thorium solution is injected into the system. We optimize the length of the two sections in order to get enough separation between the plateau signal and the peak signal. The influence on the dispersion of increasing the B1 loop length is less significant for knotted tubes; thus a 3-m knotted loop was chosen for the determination because it provides adequate fiagrams to measure both plateau and peak signals.

The signals were found to be proportional to the cation content for concentrations up to 10^{-5} M, the data fitting the following equations:

uranium plateau

$$h = ((1.91 \pm 0.05) \times 10^3)[\mathrm{U}] + (0.0016 \pm 0.0004)$$

$$r = 0.9971$$

uranium peak

$$h = ((4.12 \pm 0.03) \times 10^4)[\mathrm{U}] + (0.005 \pm 0.003)$$

$$r = 0.9997$$

thorium plateau

$$h = ((5.57 \pm 0.03) \times 10^4)[\mathrm{Th}] - (0.0002 \pm 0.0017)$$

$$r = 0.9999$$

The calculated detection limits (2 × noise) were 9.59 × 10^{-8} M for uranium and 7.18 × 10^{-8} M for thorium. The relative standard deviations (10 identical samples, 2.0 × 10^{-6} M) for U and Th were 0.91% and 0.51%, respectively.

After the accuracy of the method was tested with synthetic mixtures and with a standard ore (pitchblende S-12) it is being currently used in our laboratory for the simultaneous determination of thorium and uranium in ores provided by ENUSA (National Uranium Enterprise).

B. Simultaneous Spectrophotometric Determination of Fe(II) and Fe(III) with 1,10-Phenantroline. Several procedures have been proposed for the determination of Fe(II) and Fe(III) by flow injection techniques (*10–12*) based on the spectrophotometric measurement of the iron(II)–1,10-phenantroline complex. We used a procedure including the injector proposed in this paper and using lead as reductor with 0.1 M HCl + 0.3 M NaCl as carrier as well as reduction medium. NaCl was added to the carrier solution and to the samples in order to avoid the formation of lead chloride in the column. The signals were found to be proportional to the cation concentration, the data fitting the following equations:

Fe(II) plateau

$$h = ((4.32 \pm 0.01) \times 10^3)[\text{Fe(II)}] + (0.001 \pm 0.001)$$

$$r = 0.9999$$

Fe(III) peak

$$h = ((4.36 \pm 0.01) \times 10^3)[\text{Fe(III)}] + (0.004 \pm 0.001)$$

$$r = 0.9999$$

The calculated detection limit (2 × noise) for both Fe(II) and Fe(III) was 9.2×10^{-7} M and the relative standard deviations (10 identical samples, 2.0×10^{-5} M) for Fe(II) and Fe(III) were 0.73% and 0.91%, respectively.

C. Simultaneous Amperometric Determination of Nitrate and Nitrite. The reversed injection mode was also adapted to the simultaneous amperometric determination of nitrate and nitrite with a glassy carbon electrode. The electrode was electrochemically pretreated at +1.750 V for 5 min as recommended by Fogg et al. (*13*). The reduction minicolumn was filled with copperized cadmium. The carrier solution and reaction medium were a 1% (w/v) NH_4Cl as recommended by Trojanowicz et al. (*14*). Typical recordings for blank, nitrate, nitrite, and a mixture are shown in Figure 4.

The signal provided by the blank solution (when using carrier as a sample) could be attributed to some impurities in the carrier and in the minicolumn that can be oxidized at +1.000 V. In fact a change in the baseline is observed when the valve is turned to the inject mode, which implies the carrier passing through the reducing minicolumn before reaching the detector. In addition, owing to the strong influence that changes in the medium may exert on the electrode response, a decrease in the nitrite signal is observed for the subsample that passes through the minicolumn. However, no special difficulties arise from this fact and the measurement is made in each sample zone from the corresponding baseline.

The signals were found to be proportional to the ion concentration up to 8.0×10^{-5} M, the data fitting the following equations:

nitrite plateau

$$h(\text{nA}) = ((4.294 \pm 0.009) \times 10^7)[NO_2^-] - (14 \pm 3)$$

$$r = 0.9999$$

nitrite peak

$$h(\text{nA}) = ((2.98 \pm 0.01) \times 10^7)[NO_2^-] + (2 \pm 3)$$

$$r = 0.9999$$

nitrate peak

$$h(\text{nA}) = ((2.759 \pm 0.003) \times 10^7)[NO_3^-] - (1 \pm 1)$$

$$r = 0.9999$$

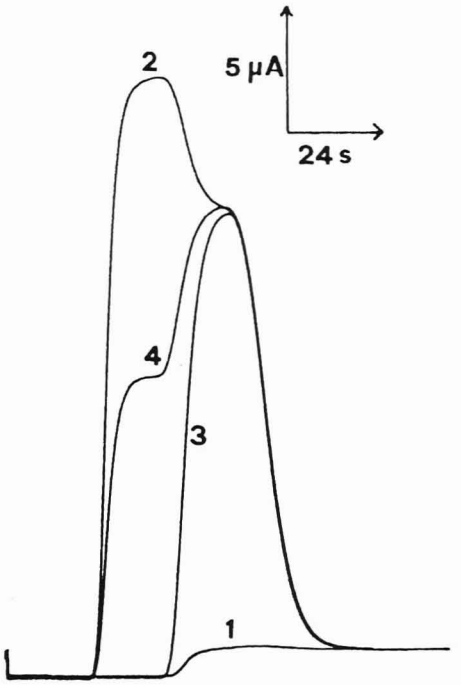

Figure 4. Fiagrams for the simultaneous amperometric determination of nitrate and nitrite: 1, blank; 2, 5.0×10^{-5} M nitrite; 3, 5.0×10^{-5} M nitrate; 4, 2.5×10^{-5} M nitrite + 2.5×10^{-5} M nitrate.

The calculated detection limits ($3 \times s/m$; s, standard deviation of the blank signal; m, slope of the calibration graph) were 2.5×10^{-7} M for nitrite peak and 2.8×10^{-7} M for nitrate peak.

The reproducibility of the signal was studied for three different concentrations: 5.0×10^{-5} M, 2.5×10^{-5} M, and 5.0×10^{-6} M. After 20 consecutive injections 9% and 3% loss of signal are observed for 2.5×10^{-5} M and for 5.0×10^{-5} M, respectively. No appreciable loss of signal is observed for 5.0×10^{-6} M (relative standard deviation 1.0%).

CONCLUSIONS

In this work a reversed injector loading technique is proposed as a new way for FIA simultaneous determinations with a six-port injection valve. Neither sequential injections nor sample splitting is required.

The simplicity and the tested applicability of this injection mode offer interesting perspectives for those simultaneous determinations and speciations which involve a differentiating chemical process.

An interesting possibility is the creation of more than two zones in the sample loop by including several differentiating chemical reactors. Work along these lines is presently under development.

Registry No. Th, 7440-29-1; U, 7440-61-1; Fe, 7439-89-6; NO_3^-, 14797-55-8; NO_2^-, 14797-65-0.

LITERATURE CITED

(1) Luque de Castro, M. D.; Valcárcel Cases, M. *Trends Anal. Chem.* **1986**, *5*, 71–74.
(2) Luque de Castro, M. D.; Valcárcel Cases, M. *Analyst* **1984**, *109*, 413–419.
(3) Valcárcel Cases, M.; Luque de Castro, M. D. *Flow Injection Analysis. Principles and Applications*. Elis Hoorwood: Chichester, 1987.
(4) FIAstar Flow Injection Analysis Bibliography. 1974–1984, 1985, 1986, 1987–1988.
(5) Dasgupta, P. K.; Hwang, H. *Anal. Chem.* **1985**, *57*, 1009–1012.
(6) Pérez Pavón, J. L.; Moreno Cordero, B.; Hernández Méndez, J.; Isidro Agudo, R. M. *Anal. Chem.* **1989**, *61*, 1789–1791.
(7) Alonso, J.; Bartroli, J.; del Valle, M.; Escalada, M.; Barber, R. *Anal. Chim. Acta* **1987**, *199*, 191–196.
(8) Pérez Pavón, J. L.; Moreno Cordero, B.; Rodríguez García, E.; Hernández Méndez, J. *Anal. Chim. Acta* **1990**, *230*, 217–220.
(9) Pérez Pavón, J. L.; Moreno Cordero, B. *Anal. Chim. Acta*, in press.

(10) Faizullah, A. T.; Townshend, A. *Anal. Chim. Acta* **1985**, *167*, 225-231.
(11) Mortatti, J.; Krug, F. J.; Pessenda, L. C. R.; Zagatto, E. A. G.; Jørgensen, S. S. *Analyst* **1982**, *107*, 659-663.
(12) Alonso, J.; Bartroli, J.; del Valle, M.; Barber, R. *Anal. Chim. Acta* **1989**, *219*, 345-350.
(13) Charnsi, A. Y.; Fogg, A. G. *Analyst* **1988**, *113*, 1723-1727.
(14) Hulanicki, A.; Matuszewski, W.; Trojanowicz, M. *Anal. Chim. Acta* **1987**, *194*, 119-127.

RECEIVED for review April 16, 1990. Accepted June 26, 1990.

Bottle-Calibration Static Head Space Method for the Determination of Methane Dissolved in Seawater

Kenneth M. Johnson,*[1] Jeffrey E. Hughes, Percy L. Donaghay, and John McN. Sieburth

Graduate School of Oceanography, University of Rhode Island, Narragansett, Rhode Island 02882

Interactions between physical structure and microbial populations play a critical role in controlling the bacterial production and consumption of gases in estuarine and oceanic environments, especially in poorly ventilated water bodies. In the permanently stratified anoxic lower basin of the Pettaquamscutt River in southern RI, fine-scale profiles (1-cm vertical resolution) of the physical structure (salinity, temperature, density, light intensity), particle structure (chlorophyll *a* fluorescence, light transmission, microbial abundance), and chemical structure (oxygen, methane, hydrogen sulfide, and carbon dioxide) showed an approximately 2 m thick oxic–anoxic transition zone (OATZ) of intense microbial activity usually situated between the 2.5- and 5.5-m depths (*1*). To determine the association between gases and the chemical, physical, and particle structure would require gas profiles of similar resolution. Current methods for the collection and analysis of gases, however, allow only a small fraction of the 200 or so required samples to be processed in a reasonable time.

The primary techniques for gas analysis are dynamic and static head space techniques (*2*). In dynamic analysis the analytes are stripped from solution with a purging gas (nitrogen, helium, etc.), trapped, and then desorbed or refocused prior to detection. Dynamic analyses for dissolved CO_2 in seawater followed by coulometric detection (*3*, *4*) showed quantitative recoveries of CO_2 with high precision but at a rate too slow for this work (7–10 min sample^{-1}). In static analysis a sealed sample container (usually a serum bottle) is incompletely filled with solution so that the dissolved gases in the liquid phase can partition into the small head space (gas phase) until the partial pressure of the gas is equal in the two phases. The equilibrium gas concentration in the head space can be increased by reducing the pressure in the head space, heating, adding electrolytes, or by keeping the ratio of head space volume (gas phase) to sample volume (liquid phase) small (*5–8*). The latter technique is simplest in terms of manipulation and calculation but requires tedious gravimetric phase volume determinations for each analysis.

In this paper we describe a simple technique for simultaneously calibrating serum bottles for both gas and liquid phases to better than ±0.1 mL. Once calibrated, the bottles may be reused without recalibration and volume changes due to temperature and salinity can be calculated. These bottles can serve for sample collection, preservation, gas concentration, incubation, and possibly as a reaction vessel in other analytical sequences. With this calibration technique and the static head space method, we have collected up to 100 samples during a profiling run, equilibrated them, and analyzed them for CH_4 by gas chromatography (GC) in a single day.

*To whom correspondence should be addressed.
[1]Present address: Department of Applied Science, Oceanographic and Atmospheric Sciences Division, Brookhaven National Laboratory, Upton, NY 11973.

EXPERIMENTAL SECTION

Gas- and liquid-phase volumes of 50-mL serum bottles (Wheaton, Millville, NJ, No. 223745) were calibrated with distilled water. The empty bottles and a gas impermeable butyl rubber septum stopper (Belco Glass, Vineland, NJ, No. 2048-11800) were weighed to four decimal places to get a total tare weight (W_1). After weighing, the bottles were immersed in a distilled water constant-temperature bath (Model RTE-8, Neslab, Portsmouth, NH) at a calibration temperature of 25 °C. When the bottles came to temperature, a Gilson 5-mL white polypropylene disposable pipet tip (Gilson Medical Electronics, Middleton, WI, No. P-5000), hereafter called the calibrator, was forced into the filled serum bottle until the tip contacted the bottle bottom, as shown in Figure 1. The calibrator sealed the bottle, which was then inverted and shaken gently from side to side until water no longer drained from the calibrator. After the calibrator was carefully removed from the upright bottle, leaving both a liquid and gas phase, the bottle was stoppered, dried, and reweighed (W_2). The liquid-phase volume in milliliters at the calibration temperature ($V_{l,ct}$) was calculated from the difference ($W_2 - W_1$) (*9*) corrected for the buoyancy of air (*10*). The bottle was reimmersed to displace the gas phase, and the bottle's stopper, pierced with a 20-gauge syringe needle, was reinserted so that the water displaced by the stopper flowed through the needle until the stopper was completely seated. After the needle was removed, the stoppered bottle was dried and reweighed (W_3). The gas-phase volume in milliliters at the calibration temperature ($V_{g,ct}$) was calculated from the corrected (*10*) weight difference in grams ($W_3 - W_2$). The total volume of the bottle at the calibration temperature ($\sum V_{ct}$) equals $V_{l,ct} + V_{g,ct}$. This procedure was repeated three times for each bottle with a different calibrator tip each time.

Field samples were collected from a stable donut-shaped floating platform (*11*) moored in the deepest basin of the Pettaquamscutt River (*12*) by siphoning through a 1 cm i.d. black polyethylene hose (*13*) to prevent alterations by pumping. The siphon tubing was attached to an electronic profiler (Sea Bird Electronics, Belvue, WA), and the siphon was maintained by discharging into a sump tank extending 1 m below the water surface in the center of the platform. Gas samples were obtained as in Figure 1. The serum stopper used to seal the bottle was pierced with a 20-gauge hypodermic needle to ensure that the gas phase remained at ambient pressure when the stopper was seated. After seating, it was secured with a 20-mm aluminum seal (Belco Glass, No. 2048-00150 or equivalent) and hand crimper (Wheaton No. 224303). A simple plastic tool shown in Figure 2 was fabricated to aid in the insertion and withdrawal of the calibrator from the serum bottles. By use of the tool, the average time for insertion, withdrawal, and crimping was about 25 s, but insertion and removal can be made without the tool in about the same time if bottles with narrow mouths that cause the calibrator to seal too tightly are discarded. To retard microbial activity, the sample bottles were placed on ice until the liquid and gas phases were equilibrated in a constant-temperature shaking bath at 100 revolutions min^{-1} for at least 12 h.

0003-2700/90/0362-2408$02.50/0 © 1990 American Chemical Society

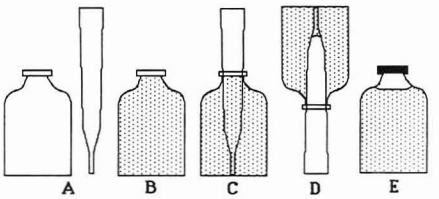

Figure 1. Steps in the calibration of both the liquid- and gas-phase volume of serum bottles using a hydrophobic disposable pipet tip: (A) serum bottle and pipet tip; (B) serum bottle filled with seawater sample; (C) pipet tip fully inserted into the bottle; (D) bottle inverted to drain excess sample and create gas phase; (E) gastight sealed sample with known liquid and gas volumes.

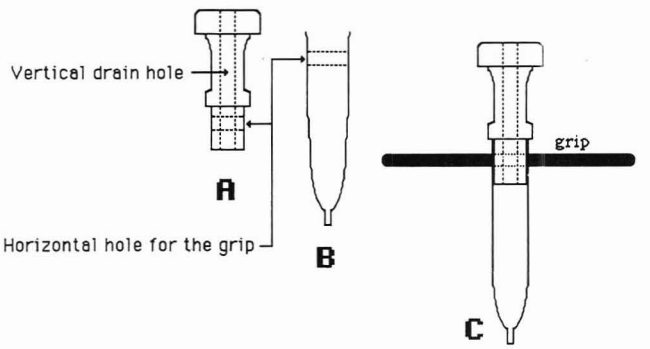

Figure 2. (A) A 7-cm long plastic tool bored through lengthwise with a 6 mm i.d. drain hole to facilitate the insertion and removal of (B) calibrator tips into and from serum bottles as shown in Figure 1. (C) Friction-fitted tool forming a water-tight seal with the calibrator tip. A stainless steel rod (grip) is inserted through horizontally aligned holes bored in both the calibrator tip and tool.

After equilibrium, the gas phase was analyzed for CH_4 by injecting 200 μL of the gas phase into a 2.5 m × 1.5 mm i.d. column of stainless steel or Teflon (PFA) packed with Porapak N of 100/120 mesh (Alltech Associates, Deerfield, IL). Before removal of the 200-μL subsamples of the gas phase for analysis, 200 μL of helium was injected into the bottle to keep the total pressure of the gas phase at 1 atm (*14*). Methane was determined on a Varian Model 1740 dual column gas chromatograph with flame ionization detection (Varian Associates, Palo Alto, CA). The detector block was at 175 °C, injector at 125 °C, and the column isothermal at approximately 55 °C. Injections were made with a Hamilton 500-μL gastight syringe (Reno, NV, No. 1750 Npt-5) equipped with a Chaney adapter. The carrier gas was helium (99.999%) at a flow rate of 20 mL min^{-1}. The output of the detector was integrated on an Infotronics Model CRS 208 digital integrator (Columbia Scientific, Austin, TX). For standards, we used gas mixtures of 100 and 1000 ppm CH_4 in helium (Alltech Associates, Deerfield, IL, Nos. G0111 and G0112, respectively). These gas mixtures were withdrawn from their containers via an Alltech septum syringe adapter (No. 8810) and injected directly into the chromatographic column. Calibration curves were made by least-squares analysis.

To calculate the in situ CH_4 concentration, we assumed that the initial CH_4 concentration in the gas phase of the sealed serum bottle was zero. We used the relationships given by Vitenberg et al. (*15*) for the equilibrium condition

$$C_l^\circ V_l = C_l V_l + C_g V_g \quad (1)$$

where C_l° is the concentration of CH_4 in the liquid phase before equilibration, C_l is the concentration of CH_4 in the liquid phase after equilibration, C_g is the concentration of CH_4 in the gas phase after equilibration, V_l is the volume of the liquid phase, V_g is the volume of the gas phase, and

$$C_l = K_d C_g \quad (2)$$

K_d is the partition or distribution coefficient. Substituting and simplifying yield

$$C_l^\circ = C_g(K_d + V_g/V_l) \quad (3)$$

The relationships given by Stumm and Morgan (*16*) relate K_d to the Henry's law constant and the Bunsen solubility coefficient (β)

$$K_H = K_d/RT \qquad \beta = K_H(22.356)$$

where K_H is the Henry's law constant in mol L^{-1} atm^{-1}, β is the Bunsen solubility of CH_4 in L L^{-1} atm^{-1}, 22.356 is the molar volume of CH_4 in L mol^{-1}, R is the gas constant in L atm mol^{-1} K^{-1}, and T is in K. Combining yields a dimensionless quantity

$$K_d = (\beta/22.356)RT \quad (4)$$

Substituting for K_d in eq 3 gives

$$C_l^\circ = C_g((\beta/22.356)\mathrm{RT} + V_g/V_l) \quad (5)$$

From $PV = nRT$, the concentration of CH_4 in the gas phase in mol L^{-1} is P/RT where P is the partial pressure of CH_4 at 1 atm of total pressure after equilibration as measured by gas chromatography. Substituting into eq 5 yields the relationship

$$C_l^\circ = (P/RT)((\beta/22.356)RT + V_g/V_l) \quad (6)$$

Equation 6 is used to solve for the liquid-phase CH_4 concentration before equilibration (mol L^{-1}). Multiplying the molar volume of CH_4 by the sample density at the equilibration temperature gives C_l° in mol kg^{-1}. For this calculation, V_g/V_l is known from the calibration procedure, the partial pressure of methane is measured directly, and the Bunsen solubility can be obtained from the tables of Wiesenburg and Guinasso (*17*) or calculated according to the Bunsen solubility equation of Weiss (*18*)

$$\ln \beta = A_1 + A_2(100/T) + A_3 \ln (T/100) + S(B_1 + B_2(T/100) + B_3(T/100)^2)$$

where A_1, A_2, A_3, B_1, B_2, and B_3 are constants and T is in K.

Alternatively, the concentration of CH_4 in the liquid phase before equilibration (C_l°) in mol L^{-1} can be found by calculating the moles of CH_4 in the liquid phase (mol_{aq}) after equilibration from

$$mol_{aq} = (PB/22.356)(V_{l,e}/1000) \quad (7)$$

where $V_{l,e}$ is the volume of the liquid phase at the equilibration temperature, and the moles of CH_4 in the gas phase (mol_g) from

$$mol_g = (P/RT)(V_{g,e}/1000) \quad (8)$$

and adding the two

$$C_l^\circ = ((mol_{aq} + mol_g)/V_{l,e})1000 \quad (9)$$

RESULTS AND DISCUSSION

To date, 157 bottles have been calibrated at least three times each. The mean liquid-phase volume ($V_{l,ct}$) was 55.11 ± 1.6 mL. The pooled standard deviation, calculated according to Youden (*19*), for three determinations of $V_{l,ct}$ was ±0.029 mL, and the relative standard deviation (rsd) was 0.053%. For the same bottles, the mean gas-phase volume ($V_{g,ct}$) was 3.95 ± 0.06 mL, the pooled standard deviation was ±0.043 mL, and the rsd was 1.0%. The mean phase ratio ($V_{g,ct}/V_{l,ct}$) was approximately 0.07. For $V_{l,ct}$, the interbottle variation was much greater than the pooled standard deviation of the calibration method (±1.6 and ±0.029 mL, respectively), but for $V_{g,ct}$ it was not significantly different from the pooled standard deviation of the calibration method (±0.06 and ±0.043 mL, respectively) so that the gas-phase volume was nearly constant for these bottles. Repeated calibrations using the same calibrator tip and stoppers (possibly improving precision) were not made because we wanted the precision of the calibration determination to reflect the interchangeability of the tips and stoppers.

The calibration method was checked with field samples. Table I shows that for samples collected at 6 °C with a salinity of 30 ppt the mean difference between the calibrated volume of the liquid phase ($V_{l,ct}$) and the liquid-phase volume at 6 °C ($V_{l,s}$) was −0.03 mL, which was equivalent to the pooled standard deviation of the calibration procedure (±0.03 mL).

Table I. Determination of the Difference between the Calibrated Serum Bottle Liquid-Phase Volume ($V_{l,ct}$) and the Liquid-Phase Volume ($V_{l,s}$) of Seawater (S = 30 ppt) Collected at 6 °C and the Difference between the Calibrated Serum Bottle Gas-Phase Volume ($V_{g,ct}$) and the Gas-Phase Volume Determined Empirically ($V_{g,g}$) When These Samples Were Equilibrated at 25 °C[a]

bottle no.	$V_{l,s}$, mL	$V_{l,ct}$, mL	diff	$V_{g,g}$, mL	$V_{g,ct}$, mL	diff
6	54.22	54.17	+0.05	3.70	3.93	−0.23
9	53.99	54.08	−0.09	3.56	3.73	−0.17
13	54.96	54.98	−0.02	3.60	3.80	−0.20
28	54.61	54.69	−0.08	3.70	3.84	−0.14
36	54.31	54.41	−0.10	3.73	3.87	−0.14
61	54.12	54.10	+0.02	3.78	3.92	−0.14
82	54.12	54.16	−0.04	3.61	3.78	−0.17
84	54.17	54.24	−0.07	3.57	3.75	−0.18
89	54.13	54.12	+0.01	3.68	3.87	−0.19
90	54.21	54.23	−0.02	3.65	3.79	−0.14
124	54.01	54.03	−0.02	3.71	3.92	−0.21
mean	54.26 ±0.28	54.29 ±0.29	−0.03[b]	3.66 ±0.07	3.83 ±0.07	−0.17

[a] The density of the sample water was 1.023604 g mL^{-1}. [b] Absolute mean difference = 0.05 mL.

However, Table I shows that after the bottles were warmed to the calibration temperature, there was a mean difference of −0.17 mL between the gas-phase volume ($V_{g,g}$) determined and the calibrated gas-phase volume ($V_{g,ct}$). This difference exceeded the pooled standard deviation of the calibration procedure (±0.04 mL) by a factor of 4. The smaller value for $V_{g,g}$ compared to $V_{g,ct}$ was due to the increased volume of the liquid phase upon warming the sample to the calibration temperature, thus reducing the observed gas-phase volume. Therefore, it was necessary to correct the gas-phase volume for the differences between the calibration, in situ, and equilibration temperatures. The gas-phase volume of a calibrated bottle at any equilibration temperature ($V_{g,e}$) for a sample of any salinity or in situ temperature equals

$$V_{g,e} = \sum V_{ct}(1 + a(t_e - t_{ct})) - V_{l,ct}(d_s/d_e) \quad (10)$$

where d_e is the density of the sample at the equilibration temperature, d_s the density at the in situ temperature, t_e the equilibration temperature, t_{ct} the calibration temperature, and a the volume coefficient of expansion of the Wheaton serum bottle glass (1.9 × 10^{-5} mL mL^{-1} °C^{-1}). The first term of eq 10 corrects for the expansion of the glass bottle due to cooling or heating, while the second term corrects the liquid-phase volume for salinity and temperature differences. For 33 samples collected at 6 (Table I), 9.6, and 17 °C with salinities of 30, 24.1, and 0, respectively, the mean differences between the gas-phase volumes at an equilibration temperature of 25 °C calculated from eq 10 ($V_{g,e}$) and the gas-phase volumes actually measured at 25 °C ($V_{g,g}$) were −0.034, −0.022, and −0.011 mL, respectively. There were 11 samples at each temperature, and the equilibration temperature equaled the calibration temperature. The mean differences never exceeded the pooled standard deviation (±0.04 mL) of the original gas-phase volume determination ($V_{g,ct}$). However, the difference between $V_{g,e}$ and $V_{g,g}$ increased with salinity. The regression line ($y = mx + b$) calculated from these data (n = 33) was $V_{g,e} = 0.94(V_{g,g}) + 0.25$ ($r = 0.93$). The coefficient of determination (r^2) was 0.87 so that eq 10 accounts for 87% of the observed variation in the measured gas-phase volumes from $V_{g,ct}$.

Table II shows the precision of the static head space CH_4 determinations with calibrated serum bottles on samples from the lower basin of the Pettaquamscutt River. These samples include discrete samples siphoned directly into the serum bottle from an apparently constant depth and batch samples siphoned to an aspirator bottle, mixed, and then dispensed in the serum bottles. These data encompassed a 100-fold variation in the concentration of CH_4 (10^{-6}–10^{-8} M). The mean rsd was not significantly different throughout this range, but the mean standard deviation was proportional to the concentration, decreasing from 0.16 μmol kg^{-1} for 10^{-6} M samples to 0.0018 μmol kg^{-1} for 10^{-8} M samples. The batch samples gave the best precision (1.4%), but none of the sample procedures including the equilibration of portions of the same sample at different temperatures adversely affected precision, and eq 6 gave the same results at the three different equilibration temperatures (2, 12, and 22 °C). The overall precision for the method was 1.6%. The mean daily precision of the CH_4 standard gases (100 and 1000 ppm in He) analyzed at

Table II. Precision of the Precalibrated Serum Bottle Static Head Space CH_4 Analysis for Pettaquamscutt River Samples

date	type	depth, m	in-situ T, °C	salinity, ppt	equilibration, T, °C	n	mean, μmol kg^{-1}	sd	rsd
10/12/87	discrete[a]	4.9	9.68	24.10	25.0	5	1.52	0.030	1.9
26/8/88	discrete	8.0	17.50	26.10	2.0[b]	4	5.44	0.400	7.5
27/8/22	discrete	8.0	17.50	26.10	2.0	2	5.42	0.040	0.8
29/9/22	discrete	2.0	19.00	16.00	3.1	3	1.34	0.026	1.9
mean[c]									2.2%
5/12/88	batch[d]	1.0	4.50	14.50	3.5	3	0.06	0.001	2.5
5/12/88	batch	2.0	8.00	20.11	3.5	3	0.29	0.004	1.5
5/12/88	batch	3.0	8.00	24.89	3.5	3	2.28	0.030	1.3
5/12/88	batch	4.0	8.00	25.56	3.5	3	2.90	0.077	2.6
5/12/88	batch	5.0	8.00	25.83	3.5	3	2.99	0.049	1.6
5/12/88	batch	6.0	9.00	26.26	3.5	3	4.07	0.046	1.1
11/8/89	batch	3.5	23.00	11.70	2.0[b]	2	3.90	0.014	0.4
12/8/89	batch	3.5	23.00	11.70	2.0	4	3.90	0.058	1.5
mean[c]									1.4%
16–18	discrete	0.75	25.39	8.29	2, 12, 22[e]	3	0.06	0.002	3.7
8/89	discrete	1.75	25.65	9.03		3	1.04	0.030	3.8
	discrete	2.75	25.49	9.95		3	2.85	0.010	0.3
	discrete	4.80	14.32	24.02		3	6.27	0.150	2.4
mean[c]									1.8%
overall mean									1.6%

[a] See text for explanation. [b] These samples were equilibrated 4 h. [c] Geometric mean. [d] See text for explanation. [e] Three serum bottles were filled at each depth, but each was equilibrated at a different temperature (either 2, 12, or 22 °C).

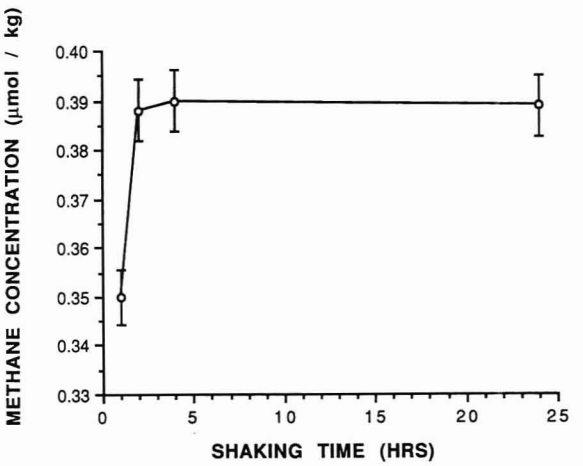

Figure 3. Time course for the equilibrium of the liquid and gas phases in calibrated serum bottles at 2 °C, as shown by the sample concentration of CH_4 calculated from the gas-phase CH_4 concentration. Water was from 3.5 m in the lower anoxic basin of the Pettaquamscutt River, August 11, 1989. The precision (error bars) of the method is ±1.6%.

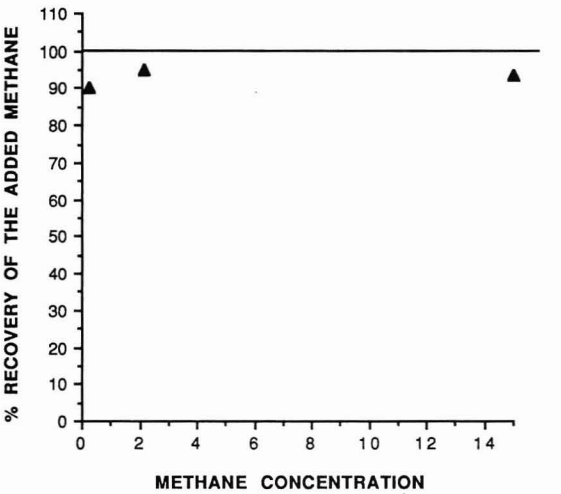

Figure 4. Recovery of CH_4 from samples analyzed by the static head space method as a percent of the apparent CH_4 concentration of these samples. The apparent concentration (µg/kg) was obtained by calculation for the gas addition samples.

the same time was 2.5 and 1.8%, respectively. Daily precision ranged from 0.3 to 5.0% for three to seven standard gas replicates per day. The identical results for both standard and sample analyses were consistent with syringe-based techniques. Better precision would require the implementation of the recommendations given by Weiss (*20*) for the gas chromatographic determination of CH_4 (thermostated gas sampling valves, etc.).

Regarding sensitivity, inspection of eq 5 illustrates the effect of reducing the ratio V_g/V_l on the concentration of CH_4 in the gas phase. A decrease in V_g/V_l increases the gas-phase concentration (C_g), assuming $C_l°$ remains constant. The mean phase ratio (V_g/V_l) of 0.07 for the serum bottles in this work gave a 10-fold enrichment of CH_4 in the gas phase compared to equilibrations of the same samples with equal liquid- and gas-phase volumes. This increased sensitivity reduced the size of the subsample (50–200 µL) needed for gas chromatographic analysis and made in possible to resample without disturbing the phase equilibrium as long as the total pressure in the bottle was kept constant. For waters undersaturated or in equilibrium with respect to atmospheric CH_4 concentrations, eqs 6 and 9 hold, but for gas chromatographic detection, larger subsamples would be needed (2000 µL).

The time needed for the equilibration of CH_4 at 2 °C was determined as shown in Figure 3. Because the calibrated bottles were to be used in subsequent incubation experiments, we equilibrated and stored our samples at 2 °C to retard microbial activity instead of risking contamination with a chemical preservative. In Figure 3, the sample CH_4 concentration calculated from the measured gas phase CH_4 concentration was unchanged after 2 h of shaking (0.388 µmol kg^{-1} compared to 0.390 and 0.389 µmol kg^{-1} at 4 and 24 h, respectively). During this experiment, three bottles were equilibrated (shaken) for 24 h and then stored at approximately 2 °C for 78 h before analysis. The mean (0.389 µmol kg^{-1}) and standard deviations (±0.008 µmol kg^{-1}) for these three samples were identical with the 24-h result. Table II shows that for samples taken on August 26, 1988, from a depth of 8.0 m, and run on August 26 and 27 equilibration was complete after 4 h even though these samples had a 10-fold higher CH_4 concentration. The 4-h samples exhibited a lower precision than the bottles analyzed at 24 h.

Figure 4 shows the recovery when a volume of a Matheson-certified mixture of 1% CH_4 in He or a volume of pure CH_4 (99.0%) was added to sealed head space bottles by using the sample syringes previously described. The highest concentration of CH_4 was prepared by adding CH_4 to head space bottles containing sulfide-free Pettaquamscutt River water from a depth of 2.0 m and a salinity of 16.0 ppt, while the other concentrations were obtained by adding CH_4 to head space bottles containing distilled water. After addition, the bottles were equilibrated at 2 °C and then analyzed after 24 h. Three bottles were prepared for each gas addition experiment, and the overall precision of these analyses was 2.9%, which is consistent with the results shown in Table II. The mean recovery for the additions was 92.7% of the calculated value, and there was no relationship between concentration and the

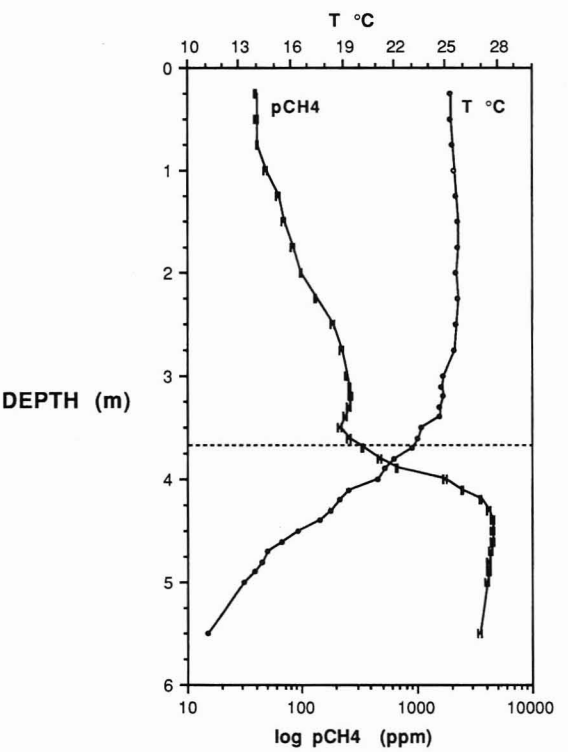

Figure 5. Vertical distribution of the log of the partial pressure of CH_4 (pCH_4 in ppm) and temperature through the oxidized and reduced layers of waters on either side of the oxic–anoxic interface (Eh = 0 = dotted line at 3.7 m) in the lower basin of the Pettaquamscutt River estuary. The profile was made on August 15, 1989, and the CH_4 samples were equilibrated at 2 °C and analyzed on August 16. The error bars are ±3.2% of the measured partial pressure, which is twice the mean precision of the analysis (1.6%).

percent recovery over the concentration range tested (0.2–15.0 μmol kg^{-1}).

A representative CH_4 profile obtained in the lower basin of the Pettaquamscutt River is presented in Figure 5. It depicts temperature and the log of the partial pressure of CH_4 (pCH_4) in ppm above and below the oxic–anoxic interface. Given the magnitude and variation (39–4200 ppm) of the in situ CH_4 concentrations in the lower basin, the precision of the method (<5% of the absolute concentration) was adequate for studies of the vertical structure of CH_4 in these waters. Figure 5 shows a very steep gradient in CH_4 concentration between 3.5 and 4.3 m. The pCH_4 rises from 211 to 3937 ppm (0.28–5.74 μmol kg^{-1}) in this interval, a ΔCH_4 of 49 ppm cm^{-1} (0.07 μmol cm^{-1}). This suggests that the precision for discrete field samples would be adversely affected by vertical motion in the sampling platform, and close-interval sampling may never be as precise as the method. Indeed, Winkler samples taken between 2.0 and 3.5 m also showed a sharp concentration gradient in O_2 (267.0–10.1 μmol kg^{-1}), with standard deviations for three replicates ranging all the way from ±1.0 to 23.1 μmol kg^{-1}.

ACKNOWLEDGMENT

We thank Geoff Laurence and Tom Halavik of the National Marine Fisheries Service Laboratory (NMFS) in Narragansett, RI, for the use of the sampling platform. Henry Rines ran the profiler and assisted with the sampling. We are grateful to Lynnea Nehring for the completion of the bottle calibrations. We acknowledge the valuable discussions with Mike Bender and Dana Kester concerning the behavior of gases, and we thank Dana for reading the manuscript and suggesting improvements.

LITERATURE CITED

(1) Sieburth, J. McN. In *Microbes in the Sea*; Sleigh, M. A., Ed.; Ellis Horwood Ltd.: Chinchester, U.K., 1987; pp 11–38.
(2) Dietz, E. A., Jr.; Singley, K. F. *Anal. Chem.* **1979**, *51*, 1809.
(3) Johnson, K. M.; King, A. E.; Sieburth, J. McN. *Mar. Chem.* **1985**, *16*, 61.
(4) Johnson, K. M.; Williams, P. J. leB.; Brandstrom, L.; Sieburth,J. McN. *Mar. Chem.* **1987**, *21*, 117.
(5) Kaiser, L. E.; Oliver, B. G. *Anal. Chem.* **1976**, *48*, 2207.
(6) Bassette, R.; Ozeris, S.; Whitnah, C. H. *Anal. Chem.* **1962**, *34*, 1540.
(7) Novak, J.; Zluticky, J.; Kubelka, V.; Mostecky, J. *J. Chromatogr.* **1973**, *76*, 45.
(8) Flett, R. J.; Hamilton, R. D.; Campbell, N. E. R. *Can. J. Microbiol.* **1976**, *22*, 43.
(9) Weast, R. C., Ed. *CRC Handbook of Chemistry and Physics*, 63rd ed.; CRC Press: Boca Raton, FL, 1982–83.
(10) Skoog, D. A.; West, D. M. *Fundamentals of Analytical Chemistry*; Saunders College: Philadelphia, PA, 1976; pp 686–689.
(11) Laurence, G. C.; Halavik, T. A.; Burns, B. R.; Smiegielski, A. S. *Trans. Am. Fish. Soc.* **1979**, *108*, 197.
(12) Gaines, A. G., Jr.; Pilson, M. E. Q. *Limnol. Oceanogr.* **1972**, *17*, 42.
(13) Lindholm, T. *Acta Bot. Fenn.* **1979**, No. 110, 91.
(14) Ioffe, B. V.; Vitenberg, A. G. *Head-Space Analysis and Related Methods in Gas Chromatography*; John Wiley and Sons: New York, 1984; pp 72–73.
(15) Vitenberg, A. G.; Ioffe, B. V.; Borisov, V. N. *Chromatographia* **1974**, *7*, 610.
(16) Stumm, W.; Morgan, J. J. *Aquatic Chemistry*; John Wiley and Sons: New York, 1981; pp 179–180.
(17) Wiesenburg, D. A.; Guinasso, N. L., Jr. *J. Chem. Eng. Data* **1979**, *24*, 356.
(18) Weiss, R. F. *Deep-Sea Res. Oceanogr. Abstr.* **1970**, *17*, 721.
(19) Youden, W. J. *Statistical Methods for Chemists*; John Wiley & Sons: New York, 1951; pp 8–23.
(20) Weiss, R. F. *J. Chromatogr. Sci.* **1981**, *19*, 611.

RECEIVED for review January 29, 1990. Accepted July 20, 1990. Principal support for this work came from the Biological Oceanography Program of the National Science Foundation through Grant OCE-8710085 and the URI Sea Grant College Program through Grant M/PD-8703.

Separation of Yttrium-90 and Strontium-90 on Papers Impregnated with Ionizable Crown Ethers

C. M. Wai* and H. S. Du

Department of Chemistry, University of Idaho, Moscow, Idaho 83843

It has been reported recently that lariat crown ethers with an attached carboxylate group and a suitable cavity size can be made highly selective for the extraction of trivalent lanthanides (*1*, *2*). The extraction is reversible with respect to pH and requires no special counteranions. In the case of extraction of La^{3+} with *sym*-dibenzo-16-crown-5-oxyacetic acid, spectroscopic data indicate that both the cavity and the carboxylate group of the macrocycle are involved in the complexation (*1*). The extraction efficiency of this ionizable crown ether for La^{3+} is much greater than that for Na^+, an alkali metal ion of similar size. The poor efficiency for Na^+ has been attributed to its high degree of ionization with the carboxylate group of the macrocycle. The crown ether carboxylic acid, therefore, behaves like a bifunctional ligand that forms chelates with cations according to their size as well as their chemical nature. This type of ionizable crown ether may have special applications for selective separation of radioactive rare-earth elements from their alkaline-earth-metal precursors as in the case of ^{90}Sr and ^{90}Y. Complexation of Y^{3+} and Sr^{2+} with these ionizable crown ethers has not been reported.

^{90}Sr is an important fission product that decays to ^{90}Y by β emission with a half-life of 28.9 years. The daughter product ^{90}Y is also a pure β emitter, which decays to stable ^{90}Zr with a half-life of 64 h. Simultaneous measurement of these two radioisotopes is difficult because of the continuous energy distribution of β radiation. A chemical separation method is usually employed prior to the determination of ^{90}Sr or ^{90}Y by β counting (*3*). Besides analytical significance, separation of ^{90}Y from its generator ^{90}Sr is also interesting in nuclear medicine because ^{90}Y has a number of potential applications in this area including making labeled antibodies for tumor therapy studies (*4*). This report describes a simple chromatographic method of separating ^{90}Y from ^{90}Sr by using papers impregnated with ionizable crown ethers *sym*-dibenzo-16-crown-5-oxyacetic acid (I) and its analogue 2-(*sym*-dibenzo-16-crown-5-oxy)stearic acid (II).

EXPERIMENTAL SECTION

Crown ether carboxylic acids I and II were synthesized in our laboratory according to the procedures described in the literature (*2*, *5*). Initial paper chromatographic separation experiments were performed by using ^{87m}Sr and ^{90m}Y produced in a 1-MW TRIGAR nuclear reactor. These isotopes have characteristic γ radiations associated with their decay (388.5 keV for ^{87m}Sr and 479.4 keV for ^{90m}Y), which can be measured simultaneously with a γ spectrometer. The radioisotope ^{90}Sr, in equilibrium with ^{90}Y, was purchased from Isotope Products Laboratories (Burbank, CA).

0003-2700/90/0362-2412$02.50/0 © 1990 American Chemical Society

Table I. R_f Values of Sr^{2+} and Y^{3+} as a Function of the pH of the Elution Solution[a]

	I		II	
pH	Sr^{2+}	Y^{3+}	Sr^{2+}	Y^{3+}
4	0.95	0.81	0.96	0.72
5	0.97	0.39	0.95	0.33
6	0.94	0.02	0.94	<0.02
7	0.96	0.02	0.96	<0.02

[a] I = paper treated with *sym*-dibenzo-16-crown-5-oxyacetic acid. II = paper treated with 2-(*sym*-dibenzo-16-crown-5-oxy)stearic acid. Concentration of crown ether carboxylic acid in chloroform = 1×10^{-2} M.

Alizarin, the spray reagent used in the identification of spots, was obtained from Pfaltz and Bauer, Inc. Other chemicals used in this study were Baker-analyzed reagents. Deionized water was prepared by passing distilled water through an ion-exchange column (Barnstead Ultrapure water purification cartridge) and a 0.2-μm filter assembly (Pall, Ultipor DFA).

The chromatographic paper strips (1 × 25 cm) were Whatman No. 1. They were immersed for 30 s in chloroform solutions containing known concentrations of crown ether carboxylic acids. After soaking, the paper strips were removed, allowed to drip, and finally dried in air at room temperature. All chromatograms were run by the descending technique in a closed jar at room temperature (24 ± 1 °C). Sample spots (10 μL in volume each) were applied to a paper strip about 2 cm from one end on a marked line and then allowed to dry in air. The dry strip with sample spots was suspended in a beaker containing the eluent solution, which was made of 5×10^{-2} M sodium acetate at different pH. Each run usually took less than 1 h for the front of the eluent to reach the other end of the strip. Spray reagent (0.1% Alizarin in ethanol) was used to identify Sr and Y spots in the initial tests. In the radioisotope experiments, the strip was cut into sections of different length for β or γ counting. An Ortec Ge(Li) detector was used to measure γ radiations from ^{87m}Sr and ^{90m}Y. The detector had a resolution of about 2.3 keV at 1336 keV γ from ^{60}Co. A conventional Geiger-Muller counter was used to measure β emitters ^{90}Sr and ^{90}Y. The procedures of γ spectrometry as well as neutron irradiations are given elsewhere (*6*).

RESULTS AND DISCUSSION

Separation of ^{90}Sr and ^{90}Y on papers treated with crown ether carboxylic acids depends on the pH of the eluent and concentration of the impregnated ligand. The effects of the pH of the eluent solution on R_f values (defined as the distance of the center of the solute spot divided by the distance of the eluent front) of Sr^{2+} and Y^{3+} are given in Table I. At pH < 4, Sr^{2+} and Y^{3+} were found near the front of the eluent, showing little retention of both cations. The R_f value of Sr^{2+} does not change appreciably with increasing pH, whereas the value of Y^{3+} decreases rapidly at pH > 4. At pH 5, the R_f value of Y^{3+} becomes much smaller than that of Sr^{2+}, and the two spots are definitely separated. At pH 6 and 7, the R_f value of Y^{3+} decreases to near zero and that of Sr^{2+} is still close to unity. Complete separation of Y^{3+} and Sr^{2+} can be achieved in the pH range 6–7 with papers impregnated with either I or II. A major difference between these two ionizable crown ethers is that in the former case the Y^{3+} spot appears to show tailing. This must be related to the solubility of I (ca. 10^{-4} M) in water. With the substitution of a large alkyl group ($C_{16}H_{33}$) to the side arm of I, the solubility of II in water is reduced by about 1 order of magnitude (*2*). As illustrated in Figure 1, the Y^{3+} peak observed on paper impregnated with II does not show significant tailing. It should also be noted that the R_f values of Y^{3+} are always smaller for the papers impreganated with II relative to I, suggesting a stronger complexation of Y^{3+} with the former relative to the latter. It has been shown that the R_f values for a given ion on papers treated with a liquid extractant and eluted with a given

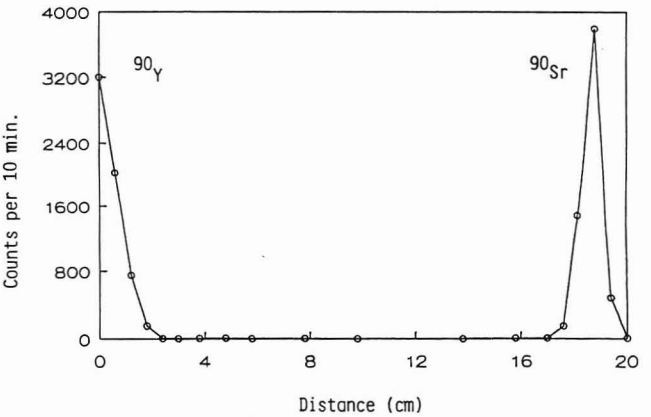

Figure 1. Separation of ^{90}Y from ^{90}Sr on papers impregnated with 2-(*sym*-dibenzo-16-crown-5-oxy)stearic acid. The elution solution was sodium acetate (5×10^{-2} M) at pH 6.5.

Table II. R_f Values of Sr^{2+} and Y^{3+} Obtained from Papers Treated with Different Ligand Concentrations

	I		II	
[ligand], M	Sr^{2+}	Y^{3+}	Sr^{2+}	Y^{3+}
1×10^{-3}	0.96	0.51	0.95	0.37
5×10^{-3}	0.94	0.06	0.97	0.02
2×10^{-2}	0.97	0.02	0.97	0.01
5×10^{-2}	0.95	<0.02	0.96	0.01

[a] I = paper treated with *sym*-dibenzo-16-crown-5-oxyacetic acid. II = paper treated with 2-(*sym*-dibenzo-16-crown-5-oxy)stearic acid. pH of eluent = 6.5.

aqueous solution are related to the extraction coefficients (D) of the same ion in the analogous liquid–liquid system by the equation (*7*)

$$\log [(1/R_f) - 1] = \log D + \text{constant} \qquad (1)$$

The R_f values of Y^{3+} and Sr^{2+} given in Tables I and II suggest at least 3 orders of magnitude difference in their relative D values at pH 6–7 according to eq 1. The D values of Sr^{2+} and Y^{3+} measured between chloroform and water at pH 6.5 with an acetate buffer and a concentration of II at 5×10^{-3} M were found to be about 0.01 and 70, respectively. The corresponding D values with I under the same solvent extraction conditions were 0.1 for Sr^{2+} and 8.0 for Y^{3+}. The ionic radius of Y^{3+} and Sr^{2+} are 1.02 and 1.26 Å, respectively, assuming a coordination number (CN) of VIII for both cations. The difference in ionic radius is probably not an important factor in determining the relative stability of the Y^{3+} and Sr^{2+} complexes. The D values of other alkaline-earth metal ions such as Ca^{2+} and Ba^{2+} were all found to be less than 0.01, although the ionic radius of Ca^{2+} (1.12 Å, CN = VIII) is close to that of Y^{3+}. Formation of a stable complex structure involving both the cavity and the carboxylate group of the ligand with the entrapping cation is probably a major factor favoring trivalent rare-earth ions over the alkaline-earth metal ions. Ionic radius makes a difference in relative D values among the lanthanides, as reported in our previous papers (*1*). Our solvent extraction results indicate that Sr^{2+} behaves like Na^+ (ionic radius 1.02 Å, CN = VI), which is virtually not extractable by the crown ether carboxylic acids ($D < 0.01$). The crown ether carboxylic acids are capable of distinguishing different groups of cations and exhibit high selectivity for trivalent rare-earth cations relative to the alkali-metal and alkaline-earth metal ions.

The concentration of the ligand impregnated in the paper also affects the separation of Sr^{2+} and Y^{3+}. Table II shows the results obtained from papers treated with chloroform containing different concentrations of the crown ether car-

boxylic acids. The pH of these experiments was fixed at 6.5. For the papers treated with a initial concentration of 1×10^{-3} M of the ligands in chloroform, the R_f value for Y^{3+} is 0.51 in I and 0.37 in II. Above a concentration of 5×10^{-3} M, the R_f values of Y^{3+} in both cases are nearly 0. Less than this concentration, there is apparently an insufficient amount of the impregnated ligand to retain Y^{3+} on the paper during elution.

To test the separation of carrier-free ^{90}Y from ^{90}Sr, we used papers treated with 1×10^{-2} M of II and an eluent solution (5×10^{-2} M sodium acetate) at pH 6.5. A typical radiochromatogram showing separation of ^{90}Y and ^{90}Sr peaks is given in Figure 1. The half-life of the ^{90}Y fraction has been measured to be 64.1 ± 0.1 h, consistent with the value reported in the literature (*8*). The growth of ^{90}Y in the ^{90}Sr fraction also followed the equation required for the secular equilibrium between a long-lived parent and a short-lived daughter.

We have demonstrated that separation of ^{90}Y and ^{90}Sr can be achieved by using papers impregnated with ionizable crown ethers I and II. This new chelation system combined with paper chromatography appears to provide a simple and efficient way of separating radioactive rare-earth isotopes from their alkaline-earth metal precursors for analytical purposes. This method can also be used to obtain carrier-free ^{90}Y from a ^{90}Sr–^{90}Y mixture because the complexation process is reversible with respect to pH. Therefore, by use of a dilute acid solution, the retained ^{90}Y can be removed from the paper into the acid solution for radioisotope applications. In theory, ^{90}Y can be repeatedly removed from its generator ^{90}Sr after reestablishment of secular equilibrium. The growth of ^{90}Y in a separated ^{90}Sr fraction was found to reach 94% of the saturation value after 11 days, consistent with the theoretical prediction for a pure ^{90}Sr source.

LITERATURE CITED

(1) Tang J.; Wai, C. M. *Anal. Chem.* **1986**, *58*, 3233.
(2) Tang J.; Wai, C. M. *Analyst* **1989**, *114*, 451.
(3) Das, N. R. *J. Radioanal. Nucl. Chem.* **1987**, *109*, 413.
(4) Vaughan, A. T. M.; Keeling, A.; Yankuba, S. C. S. *Int. J. Appl. Radiat. Isot.* **1985**, *36*, 803.
(5) Bartsch, R. A.; Heo, G. S.; Kang, S. I.; Liu, Y.; Strzelbicki, J. *J. Org. Chem.* **1982**, *47*, 457.
(6) Mok, W. M.; Wai, C. M. *Anal. Chem.* **1987**, *59*, 233.
(7) Cerrai, E.; Ghersini, G. *J. Chromatogr.* **1966**, *24*, 383.
(8) Yoshihara, K.; Kudo, H.; Sekine, I. *Periodic Table with Nuclides and Reference Data*; Springer-Verlag: Berlin, 1985; p 18.

RECEIVED for review June 8, 1990. Accepted July 30, 1990. This material is based upon work supported by the Idaho EPSCoR Program of the National Science Foundation under Grant No. RII 8902065. Neutron irradiations were performed at the Washington State University Nuclear Radiation Center under a reactor sharing program supported by DOE.

On-Valve Electrochemical Detector for High-Speed Flow Injection Analysis

Joseph Wang* and Ruiliang Li

Department of Chemistry, New Mexico State University, Las Cruces, New Mexico 88003

Flow injection analysis (FIA) has proved highly useful in practical applications in fields as varied as clinical or agricultural analysis, process analytical chemistry, and environmental control (*1–3*). The method offers distinct advantages in flexibility, reproducibility, and sample throughput over conventional methods. Because of their inherent sensitivity and selectivity toward electroactive species, amperometric detectors have been proved to be extremely useful for FIA operation. A variety of electrochemical flow cells have been employed in connection with FIA, with the thin-layer and wall-jet designs representing the most popular ones. Other devices, based on porous, micro-, or mercury-drop electrodes, have also been employed. Despite their low dead volumes, traditional amperometric detectors are too bulky to address recent trends toward miniaturization of FIA systems (*2, 4*).

This note describes a novel on-valve amperometric detector for FIA. Such a detector couples recent advances in areas of modified and microelectrodes (*5*) to achieve the desired selectivity and miniaturization. Rational tailoring of electrode surfaces permits extrapolation of well-defined solution chemistries to electrode surfaces, and hence to minimize/eliminate sample manipulation steps, commony performed in the FIA manifold channels. By coupling the selectivity advantage of modified surfaces with the miniaturization feature of ultramicroelectrodes, it is thus possible to integrate the detector into the injection valve. The small size of ultramicroelectrodes has been exploited by Jorgenson (*6, 7*) and Ewing (*8*) for on-column amperometric detection for open-tubular liquid chromatography and capillary zone electrophoresis, respectively. As applied to FIA operation, the present on-valve detector offers an exceptionally high sample throughput (3600 injections/h), associated with a unique coupling of fast response, minimized dispersion effects, small sample volumes, and miniaturization. Analytes can thus be rapidly detected while they are still in the injection valve. In addition to minimum time and reagent expense, the limited dispersion thus obtained can benefit other aspects of FIA. While the concept of on-valve detection is presented here within the framework of amperometric measurements, it could be extended to other type of miniaturized selective probes.

*To whom correspondence should be addressed.

EXPERIMENTAL SECTION

Apparatus. The carbon fiber electrochemical detector is shown in Figure 1. It is based on placing a cylinder ultramicroelectrode within the valve outlet. The microelectrode was prepared from Thornell 300 grade WYP-90 1/10 fibers (Union Carbide Corp.), with a diamter of 7 μm. The fibers were soaked and washed in acetone and dried thoroughly at room temperature. A single fiber was then inserted into a 0.3-mm-i.d. tip of a glass pipet, and sealed with epoxy resin; microcylinders of 4-mm length were used in most experiments. The pipet was back-filled with mercury, and electrical contact was established with a copper wire. Glucose oxidase modified carbon fibers were prepared by electrochemical platinization, as was described earlier (*9*). The carbon fiber microcylinder electrode was inserted to the center of a Teflon tubing (0.6 mm i.d.) that was placed and sealed within the outlet fitting of the Rheodyne 7010 injection valve. A small hole, in the other side of the tubing served as the solution outlet and provided electrolytic contact to the Ag/AgCl (3 M NaCl) reference electrode (placed downstream in the external solution compartment). The metallic sample loop of the valve served as the auxiliary electrode. Some experiments were performed with a glassy carbon thin-layer detector (Model TL-5, Bioanalytical Systems) that was placed 4 cm from the valve. The flow injection system consisted also of the carrier reservoir and interconnecting Teflon tubing (1.0 mm i.d.). Solution flow to the cell was governed by gravity. The injection valve was operated manually.

0003-2700/90/0362-2414$02.50/0 © 1990 American Chemical Society

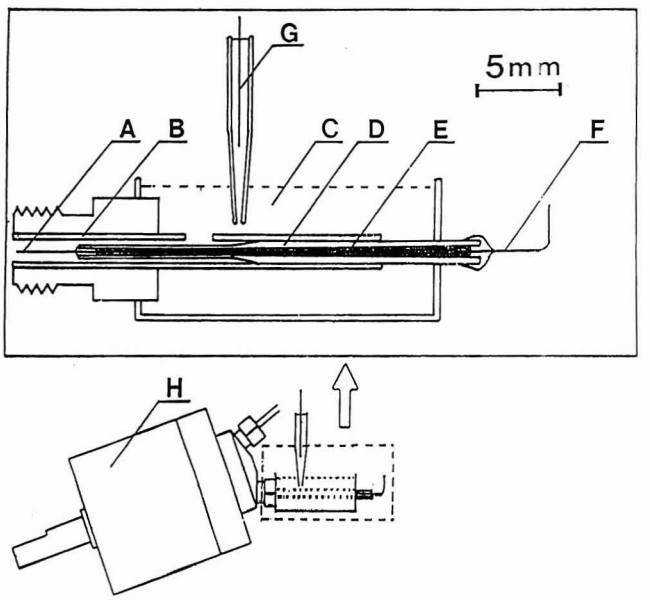

Figure 1. Schematic of the on-valve carbon fiber electrochemical detector: A, carbon fiber working electrode; B, Teflon tubing, C, electrolyte solution; D, glass pipet; E, mercury; F, metal contact; G, reference electrode; H, injection valve.

Electrochemical detection was performed in the amperometric mode with an EG&G PAR Model 264A voltammetric analyzer, the output of which was displayed on a Houston Omniscribe strip-chart recorder.

Reagents. All solutions were prepared from double-distilled water. The supporting electrolyte was a 0.05 M phosphate buffer (pH 7.4). Glucose (Sigma) and potassium ferrocyanide (Baker) were used as received.

RESULTS AND DISCUSSION

Response Characteristics. The contributions of the individual parts of FIA systems to the overall dispersion have been reviewed (*10*). Since dispersion dictates the time between injections, maximum sampling frequency is achieved by using the shortest possible residence time of the sample in the system (i.e. minimum dispersion). The ability to place the detector into the injection valve, reported in this study, offers the minimum possible dispersion, while maintaining the FIA advantage of reproducible sample introduction. The dynamic response characteristics of an on-valve detector were evaluated first by using an unmodified carbon fiber microelectrode. Figure 2 illustrates characteristic flow-injection current/time profiles for 4×10^{-3} M ferrocyanide, at an injection rate of 1800 samples/h, obtained with the on-valve microelectrode (a) and a conventional (commercial) glassy-carbon transducer (b). The on-valve detector exhibits a very rapid increase and decrease of the current during this ultrafast operation. The peak widths (at $0.6C_{max}$ and baseline) are extremely short (0.4 and 1.2 s, respectively). This indicates limited peak broadening (to a 20-μL volume), which is attributed to the injection contribution (*10*). The baseline resolution indicates rapid replenishment of the solution from the surface. In contrast, due to significant dispersion, the glassy carbon detector results in substantial peak broadening (with width at $0.6C_{max}$ of 1.3 s). The latter exhibits baseline resolution only at significantly lower injection rates of less than 300 samples/h (not shown). Under the conditions of Figure 1, the microelectrode detector yielded defined peaks for injections carried out every 1 s (not shown). To the best of our knowledge, such injection rate (3600 samples/h) is the highest ever reported for FIA systems. Further speed improvements may be attained by using smaller sample volumes.

Other parameters affecting the response of the on-valve detector were investigated. The 4×10^{-3} M ferrocyanide peak current was not affected by a change of the injection frequency over the 360 to 1800 per hour range. Similar peak widths (at $0.6C_{max}$) were observed over this range. The effect of varying the solution flow rate was examined using a 5×10^{-3} M ferrocyanide solution at 900 samples/h (other conditions, as in Figure 1). Only a slight increase of the current, from 0.39 to 0.46 μA was observed over the 0.4–1.7 mL/min range. Such a flow rate effect is attributed to the steady-state diffusional flux characterizing ultramicroelectrodes. A rapid current increase and fall-off were observed at all flow rates. A slight peak broadening was observed at lower flow rates, as expected from the longer passage of the sample over the working electrode. Different injection volumes were examined in connection with the response to 5×10^{-3} M ferrocyanide at 900 samples/h. The current increases only slightly (from 0.18 to 0.20 μA) upon increasing the volume from 10 to 50 μL. A rapid fall-off to the baseline level was observed for all volumes. Such flow-rate and sample-volume effects indicate that the on-valve detector permits high-speed assays of small samples with reduced carrier consumption.

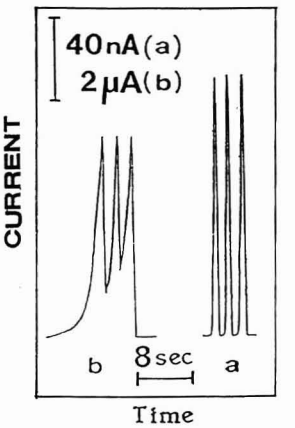

Figure 2. Flow injection current–time profiles for 4×10^{-3} M ferrocyanide at the on-valve microelectrode (a) and a glassy carbon thin layer detector (b): sample volume, 10 μL; injection frequency, 1800 per hour; operating potential, +0.7 V; flow rate, 1.0 mL/min; carrier and electrolyte, 0.05 M phosphate buffer (pH 7.4).

Analytical Performance. Quantitative work is not compromised by the ability of rapidly detecting electroactive solutes while they are still in the injection valve. Figure 3A is a typical recording of detection peaks for ferrocyanide solutions of increasing concentrations (0.5–1.5 mM (a–c)) at an injection rate of 900 samples/h. The ultrafast response is proportional to the solute concentration. These measurements are a part of a series of eight concentration incremenets over the 0.5–4 mM range. The resulting calibration plot (not shown) was linear, with a slope of 25.4 nA/mM and correlation of 0.999. A detection limit around 13 μM is estimated based on the signal-to-noise (S/N = 3) characteristics of the response. This corresponds to 27 ng in the 10-μL sample volume. The response is highly reproducible. For example, 90 repetitive injections of a 0.1 mM ferrocyanide solution (within a 6-min period) yielded a mean peak response of 1.8 nA, with a range of 1.7–1.9 nA and a relative standard deviation 2.2%.

In order for the on-valve detector to exhibit significant advantages for practical analytical work, it must possess high selectivity (hence circumventing the needs for sample manipulation steps, currently performed in the flow manifold). This may be accomplished by integrating desired reactions onto the detector surface. One promising avenue is to couple the inherent specificity of biological recognition processes with microelectrode probes. Advances in the area of biologically tailored surfaces offer the incorporation of biological entities onto miniaturized electrodes. For example, we demonstrate earlier (*9*) that glucose oxidase can be electrodeposited (to-

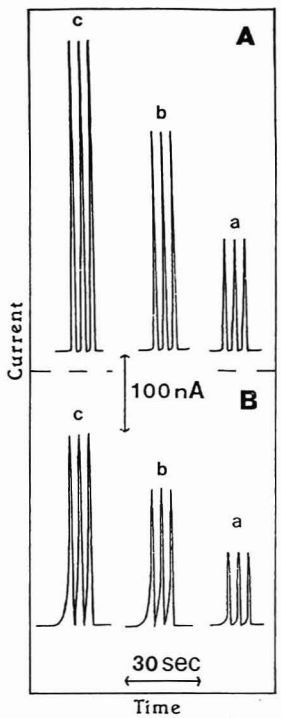

Figure 3. Flow injection peaks for solutions containing increasing ferrocyanide (A) and glucose (B) concentrations: (0.5–1.5) × 10^{-3} M (A(a–c)) and (4–12) × 10^{-3} M (B(a–c)); injection frequency, 900 per hour; other conditions, as in Figure 2.

gether with platinum) onto carbon-fiber surfaces. The use of such a glucose oxidase modified microelectrode as an on-valve FIA detector holds great promise for ultrafast clinical screening and/or rapid bioprocess monitoring of glucose. For example, Figure 3B is a typical recording of detection peaks for injections of glucose solutions of increasing concentration (4–12 mM, a–c). These are a part of a series of eight increments over the 2–16 mM range, performed at a rate of 900 per hour. Linearity prevailed up to 10 mM, with a curvature at higher levels (characteristic of enzyme-based sensing). A detection limit of 95 μM glucose can be estimated (i.e. 0.17 μg in the 10-μL sample). The limited dispersion (characterizing the on-valve detector) should minimize interferences from blood cells in enzyme-based flow injection blood analysis (*11*). Other, more cumbersome schemes to minimize dispersion, e.g. use of segmented sample injection, have been suggested recently for such applications (*11*). Modification of the on-valve carbon fiber with other enzymes (or biocomponents), as well as with appropriate chemical moieties, should lead to selective and ultrafast detection of other analytes. Additional advantages may be achieved by coverage with an appropriate protective coating.

In conclusion, we have demonstrated the significant speed advantage obtained by moving the detector from the end of the FIA system to the injection valve. Extrapolation of well-defined (e.g. enzymatic) reactions from the solution to electrode surfaces results in highly selective detectors that eliminate the need for sample manipulation (in the flow manifold). Further improvements may be achieved by "pushing" the carbon fiber, within the valve, closer to the sample loop. Other highly selective miniaturized detectors, e.g. ion-selective microelectrodes, should offer similar advantages. Placement of the detector within the valve can be attractive also for partially selective electrodes, through coverage with a permselective film (for in situ separation) or via fast potential scanning (for multipeak recordings). Even though the concept is presented in terms of amperometric detection, the on-valve detection approach could be extended to nonelectrochemical measurement strategies.

LITERATURE CITED

(1) Ruzicka, J.; Hansen, E. H. *Flow Injection Analysis*; Wiley: New York, 1981.
(2) Ruzicka, J. *Anal. Chem.* **1983**, *55*, 1040A.
(3) Christian, G.; Krull, I.; Tyson, J. *Anal. Chem.* **1990**, *62*, 455A.
(4) Ruzicka, J.; Hansen, E. H. *Anal. Chim. Acta* **1984**, *161*, 1.
(5) Johnson, D. C.; Ryan, M. D.; Wilson, G. S. *Anal. Chem.* **1988**, *60*, 147R.
(6) Knecht, L. A.; Guthrie, E. J.; Jorgenson, J. W. *Anal. Chem.* **1984**, *56*, 479.
(7) White, J. G.; St. Claire, R. L., III; Jorgenson, J. W. *Anal. Chem.* **1986**, *58*, 293.
(8) Wallingford, R. A.; Ewing, A. G. *Anal. Chem.* **1987**, *59*, 1762.
(9) Wang, J.; Li, R.; Lin, M. S. *Electroanalysis* **1989**, *1*, 151.
(10) van der Linden, W. E. *TrAC, Trends Anal. Chem.* **1982**, *1*, 188.
(11) Buch-Rasmussen, T. *Anal. Chem.* **1990**, *62*, 932.

RECEIVED for review May 29, 1990. Accepted August 6, 1990. This work was supported by the National Institutes of Health through Grant No. GM 30913-06.

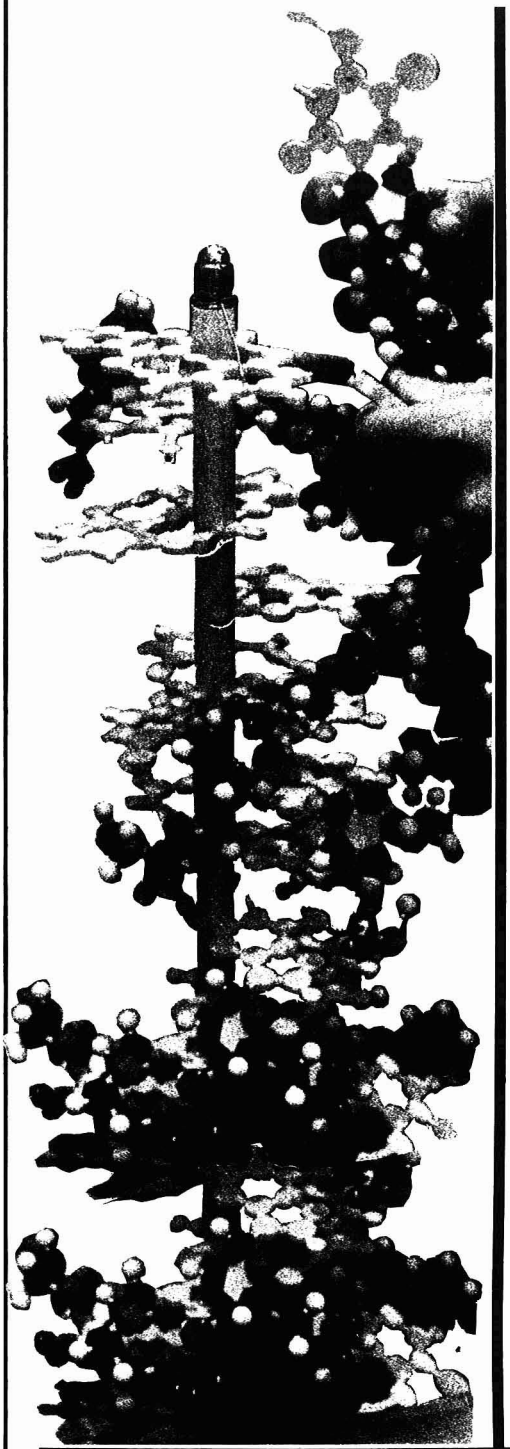

ORGANICALLY SOUND!

The Journal of Organic Chemistry...

the leading journal devoted to organic chemistry

Containing roughly 1,400 articles, notes, and communications per year—over 6,000 pages—The Journal of Organic Chemistry offers the organic chemist critical accounts of original work in a given field, and interpretive reviews of existing data that present new viewpoints.

Areas comprehensively covered are
- many facets of organic reactions
- natural products
- studies of mechanism, bioorganic chemistry, theoretical organic chemistry
- various aspects of spectroscopy related to organic chemistry

Join thousands of organic chemists who find this journal essential in keeping current.

Call Toll Free: 800-227-5558

The Journal of Organic Chemistry published biweekly. One volume per year. Volume 55 (1990)
ISSN 0022-3263

	U.S.	Canada and Mexico	Europe Air Service Included	All Other Countries Air Service Included
ACS Members				
One Year	$ 56	$ 98	$134	$162
Two Years	$100	$184	$256	$312
Nonmembers	$428	$470	$506	$534

Subscriptions at ACS member rates are for personal use only.
Journal subscriptions start January 1990.

Editor: Clayton H. Heathcock, Univ. of California, Berkeley
Assistant Editor: C.R. Hadley, Univ. of California, Berkeley
Senior Editors: P. Beak, Univ. of Illinois, Urbana; R.M. Coates, Univ. of Illinois, Urbana; C.D. Poulter, Univ. of Utah; H. Rapoport, Univ. of California, Berkeley; A. Streitwieser, Jr., Univ. of California, Berkeley; S.M. Weinreb, Penn. State Univ.
Advisory Board: P.A. Aristoff, Upjohn Co.; P.A. Bartlett, Univ. of California, Berkeley; D.E. Bergbreiter, Texas A&M Univ.; B. Carpenter, Cornell Univ.; P.N. Confalone, E.I. du Pont de Nemours & Co.; R.L. Danheiser, Massachusetts Institute of Technology; J. Faulkner, Scripps Inst. of Oceanography; R. Freidinger, Merck, Sharp & Dohme Res. Labs; B. Ganem, Cornell Univ.; R.H. Grubbs, California Institute of Technology; D. Hart, Ohio State Univ.; A. Hassner, Bar-Ilan Univ., Israel; D. Lynn, Univ. of Chicago; F.B. Mallory, Bryn Mawr College; A.I. Meyers, Colorado State Univ.; J.J. Partridge, Glaxo, Inc.; M. Platz, Ohio State Univ.; K.L. Rinehart, Univ. of Illinois; G.B. Schuster, Univ. of Illinois; I. Shinkai, Merck, Sharp & Dohme Res. Labs; W.C. Still, Columbia Univ.; C.A. Townsend, Johns Hopkins Univ.; E. Vedejs, Univ. of Wisconsin; J.J. Gajewski (ex-officio)

American Chemical Society, 1155 16th St., NW, Washington, DC 20036

This publication is available on microfilm, microfiche, and electronically through Chemical Journal Online on STN International.

Another FT-IR First From Bio-Rad:

"GC/IR With The Sensitivity of GC/MS"

Tell me about the new Tracer™ GC/IR system.

Our new Tracer GC/IR system offers the sensitivity of mass spectrometry and the specificity of infrared spectroscopy at an affordable price. For more information on the Tracer GC/IR system, fill out and return this coupon to the Bio-Rad Digilab Division, 237 Putnam Ave., Cambridge, MA 02139. Or call (617) 868-4330.

Name: _____

Title: _____

Company: _____

Street & No.: _____

City & State: _____ Zip: _____

Phone No.: _____

BIO-RAD *Digilab Division*

CIRCLE 20 ON READER SERVICE CARD